

# **Bio-inspired Design and Self-Assembly of Nucleobase- and Ion-Containing Polymers**

Keren Zhang

Dissertation submitted to the faculty of the Virginia Polytechnic Institute and State University in partial fulfillment of the requirements for the degree of

Doctor of Philosophy  
In  
Chemistry

Timothy E. Long, Chair

Robert B. Moore

S. Richard Turner

Tijana Z. Grove

May 2<sup>nd</sup>, 2016  
Blacksburg, VA

Keywords: noncovalent interaction, hydrogen bonding, ionic interaction, nucleobase, DABCO salt, self-assembly, microphase-separation, non-isocyanate polyurethane

Copyright 2016 Keren Zhang

# **Bio-inspired Design and Self-Assembly of Nucleobase- and Ion-Containing Polymers**

Keren Zhang

## **ABSTRACT**

Bio-inspired monomers functionalized with nucleobase or ionic group allowed synthesis of supramolecular polymers using free radical polymerization and controlled radical polymerization techniques. Comprehensive investigations for the structure-property-morphology relationships of these supramolecular polymers elucidated the effect of noncovalent interactions on polymer physical properties and self-assembly behaviors.

Reverse addition-fragmentation chain transfer (RAFT) polymerization afforded acrylic ABC and ABA triblock copolymers with nucleobase-functionalized external blocks and a low- $T_g$  central block. The hard-soft-hard triblock polymer architecture drove microphase-separation into a physically crosslinked hard phase in a low  $T_g$  matrix. Hydrogen bonding in the hard phase enhanced the mechanical strength and maintained processability of microphase-separated copolymers for thermoplastics and elastomers. A thermodynamically favored one-to-one stoichiometry of adenine and thymine yielded the optimal thermomechanical performance. Intermolecular hydrogen bonding of two thymine units and one adenine unit allowed the formation of base triplets and directed self-assembly of ABC triblock copolymers into remarkably well-defined lamellae with long-range ordering. Acetyl protected cytosine and guanine-containing random copolymers exhibited tunable cohesive strength and peel strength as pressure sensitive adhesives. Post-functionalization converted unprotected cytosine pendent groups in acrylic random

copolymers to ureido-cytosine units that formed quadruple self-hydrogen bonding. Ureido-cytosine containing random copolymers self-assembled into nano-fibrillar hard domains in a soft acrylic matrix, and exhibited enhanced cohesive strength, wide service temperature window, and low moisture uptake as soft adhesives.

A library of styrenic DABCO salt-containing monomers allowed the synthesis of random ionomers with two quaternized nitrogen cations on each ionic pendant group. Thermomechanical, morphological, and rheological analyses revealed that doubly-charged DABCO salts formed stronger ionic association and promoted more well-defined microphase-separation compared to singly-charged analogs with the same charge density. Bulkier counterions led to enhanced thermal stability, increased phase-mixing, and reduced water uptake for DABCO salt-containing copolymers, while alkyl substituent lengths only significantly affected water uptake of DABCO salt-containing copolymers. Step growth polymerization of plant oil-based AB monomer and diamines enabled the synthesis of unprecedented isocyanate-free poly(amide hydroxyurethane)s, the first examples of film-forming, linear isocyanate-free polyurethanes with mechanical integrity and processability. Successful electrospinning of segmented PAHUs afforded randomly orientated, semicrystalline fibers that formed stretchable, free-standing fiber mats with superior cell adhesion and biocompatibility.

## **ABSTRACT TO GENERAL PUBLIC**

Nature widely employs noncovalent interactions to construct biomacromolecules with complex three dimensional structures. For example, the double helical structure of DNA relies on complementary hydrogen bonding between nucleobase pairs and electrostatic repulsion of the phosphate backbone. These noncovalent interactions are weaker than chemical bonds but stronger than van der Waals interaction. This dissertation focus on designing polymers based on bio-inspirations from natural biomacromolecules. Firstly, scalable reactions were optimized to synthesize innovative functional monomers that contain nucleobase and ionic group. Secondly, several polymerization techniques allowed the incorporation of these functional monomers into polymers. Lastly, chemical modification of the polymers further tuned their chemical structures.

The incorporation of these functional groups largely influenced the physical property of polymers through noncovalently associating with each other and forming transient networks. The polymer network formation contributed to enhanced mechanical strength and widened service temperature window during which the modulus remained constant with increasing temperature. Furthermore, noncovalent interactions proved reversible upon external triggers such as heat, solvent, and salt, which preserved the processability and recyclability of polymers. Noncovalent interactions-containing polymers potentially solve the paradox of enhancing mechanical strength while sacrificing processability. Nucleobase- and ion-containing polymers enable potential applications as soft adhesive, thermoplastic, elastomer, biomedical materials, and membranes with excellent mechanical performance and processability. The unique self-



assembly behaviors of nucleobase-containing block copolymers formed remarkably periodic patterns with nanometer size, useful in nano-patterning and microelectronic fabrication.

Another research direction focuses on developing novel thermoplastic polyurethanes to mitigate usage of reactive and toxic isocyanates in conventional polyurethane synthesis. A novel monomer based on plant-oil and CO<sub>2</sub> afforded the synthesis of green polyurethanes with mechanical integrity and crystallinity. Electrospinning produced nanofiber mats with excellent biocompatibility and cell adhesion for tissue scaffold and wound dressing materials.

## Acknowledgements

Firstly, I would like to thank and acknowledge Dr. Tim Long, who is the best advisor one can possibly have for his/her graduate career. I sincerely appreciate his guidance and mentorship for the past five years. Every research project, every presentation practice, every manuscript revision have prepared me to be an independent researcher. His scientific curiosity, enthusiasm of innovation, and optimistic attitude have imprinted on my perspectives towards challenges and obstacles. All the achievements I have obtained during graduate school wouldn't be possible without Dr. Long's continuous support and encouragement. I would like to thank my committee members Dr. Robert Moore, Dr. Richard Turner, and Dr. Tijana Grove for their insightful comments and help during all the milestone exams and tasks. Dr. Moore's expertise on scattering and morphology furnished me with thorough understanding of structure-morphology relationships for all the polymers studied in this dissertation. Dr. Turner introduced career path in industry and taught me the importance of details in scientific writing. Dr. Grove graciously shared her experience as a female scientist and encouraged me to pursue my own interest. I am grateful for Dr. David Dillard to open me the door to the world of viscoelasticity and adhesives. I also thank Dr. Webster Santos for accepting me to VT chemistry and encouraging me to follow my passion in polymer chemistry.

I am very fortunate to be a Long group member and have the pleasure to spend my graduate school years with many talented students. I must thank Mana Tamami first for being a great mentor when I first joined the group. I am also grateful for all the help and advice from Renlong Gao, Tianyu Wu, and Shijing Cheng. Renlong and I came from the same beautiful city of Qingdao and graduated from the same polymer department of University of Science and Technology in China. Shijing left the legacy of nucleobase-containing acrylics before her

graduation, which was the initiator for my research. The torch has been passed on to Kevin Drummey. Hopefully he will continue the supramolecular polymer project and let it blossom. I am very grateful to get to know Mike Allen, Musan (Nancy) Zhang, Dan Buckwalter, David Inglefield, and Sean Hemp, who taught me many things from running RAFT polymerization to playing cornhole. I will always remember my Florida trip with Nancy, tailgating parties with Mike Allen and Matt Hunley, all the bluegrass music Dan used to play in the lab, and all the extra short T-shirt Dingles wore every day. I am glad to become friend with Ashley Nelson during our collaboration on the polyurethane project. I will always remember the girls' nights with Chainika Jangu and Alie Schultz. To all the senior students in the Long group, I owe much of my success and research to the ground work they laid out and group tradition they passed along.

Special thanks to my favorite labmate and dearest friend from the first day of graduate school, Evan Margareta. He is the cup of hot chocolate in ice-cold winter days. I am so lucky to have Evan on my side through this graduate school journey, and those warm hugs will always help me get through tough time. I am always glad to share my passion on rheology and snowboarding with Joe Dennis, who was voted the most handsome dude in the department, by me. Being a skilled chemist and expert on step growth polymers, I have no doubt Joe will be an excellent leader for our group being the only graduate student in his year. It was a pleasure to see many young brilliant researchers joined the long group: Justin Serrine, Mingtao Chen, Allison Pekkanen, Ryan Mondschein, Katie Valentine, Kevin Drummey, and Philip Scott, as well as post-doc researchers: Maruti Hedge, Nick Moon, Makito Yokoe, Sachin Bobade, Daisuke Yamamoto, Asem Abdulahad, Charles Carfagna, and Zhiyang Zhang. I appreciate all their support and wish them successful careers.

I would like to thank all the administrative personnel who helped me greatly during my graduate school years. Brent Bowden is simply the best organizer in the world. His hard work

has made a lot of things happened on time and kept the Long group together and functionable. I also thank Steve McCartney, Tammy Jo Hiner, Naya Sou, Joli Huynh, Tom Bell, Tom Wertalik, Geno Iannaccone, Laurie Good, Donnie Neel, and Narasimhamurthy Shanaiah for their keen service in our Chemistry department and all their help for instrument, scheduling, documentation, visa, and ordering.

I acknowledge funding from Henkel and Elevance Renewable Science that supported my research assistantship for most of my graduate school years. I appreciate all the collaboration and discussion with Charles Paul, Eric Silverberg, Cristina Dejesus, and Peter Palasz for sharing their knowledge of adhesives. I would like to thank Emmett O'Brien and Yong Li for the summer internship opportunity at Eastman Chemical in Kingsport, TN. I also would like to acknowledge various academic collaborators, including Motohiro Aiba, Don Aduba, Akanksha Kanitkar, Mitsu Murayama, Ya Peng Yu, Amanda Hudson, Lindsey Anderson, and Gregory Fahs.

I am thankful for all the friends I met in Blacksburg. Especially Bo Dong, who has been a very close friend for years, has helped me tremendously. He drove me and Chennan to buy our first car in 2011. His strive for perfection, attention to details, and dedication to work have always impressed me as much as his kindness to friends. I appreciate the help from Xi Guo, Yafen Zhang, Jessica Wynn, Yumin Dai, Wenyu Zhang, Mingqiang Zhang, Haoyu Liu, and Jianbo Hou on research, especially organic synthesis. I am gracious for the friendship with Jing Huang and Tinghui Li, we always have a lot to chat about. Many other good friends have contributed to unforgettable memory here in this small town: Tianle Meng, Kuier Li, Zhizheng Chen, Winston Hu, Junjie Liang, Zhihao Yu, Xinghua Zhang, Guigui Wan, Liyun Ye, Lei Pan, He Liao, Liang Han, Xiaokui Shu, Wenjun Wu, Shen Li, Tianxiang Chen, Di Hu. They shared many hobbies and good time with Chennan and me.

I am very appreciative for the professors and friends in UT Southwestern Medical Center, who helped me tremendously during my first year in the US, when I had the language barrier and a new major in molecular biology. Dr. Benjamin Tu, Dr. Wen-Hong Li, Dr. Dean Sherry, and Dr. Zoltan Kovacs have graciously trained me as a rotation student in their lab. Leilani Marty and Shah Nawaz Zaheer graciously tutored me on biology. My big sib Mian Zhou and many other senior students Yindi Jiang, Rui Zhong, and Ling Cai all helped me tremendously by providing transportation, offering advice, and organizing events on the weekends. I also thank my roommate Fang Zhang for keep me company, as well as Wenlin Li and Rui Li for being great friends.

I would like to thank all the professors, my class of 0620, and all my friends from USTC, especially our class advisor and my undergraduate research advisor, Dr. Weidong He. He cared about our entire class from his heart and supported us selflessly. He is one of the driving force for me to continue my career in polymer chemistry. I know I can't let him down. I'm so proud to be a member of our 0620 family, and to be an USTC'er. Hopefully one day, I can make them proud as well. I would like to thank my dearest friends, Lu Lu, Yelu Shi, and Hao Zhou, who shared a dorm with me for four years. I will always remember the book, the food, the good time we shared. I want to acknowledge Jinglin Liu, Mingzhe Yu, Wentao Li, and Wan Zheng for their continuous friendship and help after graduation. I appreciate the entire roller skating club crew whom I had so much fun with, especially Sheng Feng, Jixin Si, Wuming Luo, Yiran Li, and Chennan Hu, who turned out to be my boyfriend after three years knowing each other. Those days skating on the street were the most memorable time during my college. And Chennan and I are continuing our passion for roller skating to skiing and snowboarding.

Finally and most importantly, I am forever grateful to my parents and my dearest boyfriend for their unconditional love, understanding, and support. My mother, Dongmei Li is such a talented and strong woman, who taught me to independent, indestructible, and courageous. She is the rock I can hold on to in rapids and storms. She can always get me back on my feet when I was defected and thought I would never stand again. My father, Tianlin Zhang is a dedicated chemist who has led my path in chemistry. I basically grew up in my father's lab. I still vividly remembered the first reaction he showed me and the explosion when I was just learning how to write. My father is so fearless in pursuing his passion in chemistry and so hard-working to provide for his family. Both my parents have devoted all their love to me, to my little brother Kexin Li, and to thousands of students they taught over many years. My family will always be the safe haven for my heart and I will always find my way home. I am so grateful for all the love, caring, and company from my boyfriend Chennan Hu ever since we met. He is the most adventurous, yet the most reliable man I've ever met. It has been quite a journey and I know life will never ever be bored with him. He brought so many fun things to our life which turned to be my favorite hobbies like snowboarding and fishing. These six years together with Chennan have been filled with enjoyable memory and so many "first-times". He brought a bigger and more colorful world to me. I can't wait to continue our life journey together. My little brother Kexin has grew out of the cutest little boy into a big man when I'm away from home. I truly hope he will find his way into this big wild world smoothly and discover his career passion. I appreciate my grandparents for their love and belief in me. I wish both of my grandmas live long and healthy. I hope I will make my grandpas in heaven proud. I also would like

to thank my cousin Hua Li and her family for their warm welcome and support every time I travel to Shanghai.

I realize there are many more friends, seniors, and even strangers who have helped me tremendously and guided my way to this point than I can ever listed. I sincerely thank everybody that have helped or interacted with me. I am so fortunately to meet everyone and have you in my life. There is a saying in Chinese, “glancing back five hundred times in my prelife, only to passing by you on the street.” I truly wish everyone joy, happiness, and prosperity.

All Hail Chemistry!

All Hail Polymer!

## Attributions

Prof. Timothy E. Long  
Professor of Chemistry at Virginia Tech and Research Advisor

Prof. Robert B. Moore  
Professor of Chemistry at Virginia Tech and collaborator on Chapters 3, 4, 5, 6, 7, 9, and 10

Dr. Motohiro Aiba  
Past visiting student in Dr. Long's research group who contributed to Chapters 3 and 4

Gregory B. Fahs  
Graduate student in Dr. Moore's research group who contributed to Chapters 3, 4, 7, and 9

Dr. Amanda G. Hudson  
Past graduate student in Dr. Moore's research group who contributed to Chapters 3, 7, and 10

William D. Chiang  
Past undergraduate student in Dr. Long's research group who contributed to Chapters 3 and 8

Prof. Mitsuru Ueda  
Professor of Organic and Polymeric Materials at Tokyo Institute of Technology who contributed to Chapter 3

Mingtao Chen  
Graduate student in Dr. Long's research group who contributed to Chapters 6 and 10

Kevin J. Drummey  
Graduate student in Dr. Long's research group who contributed to Chapters 6, 8, and 9

Samantha J. Talley  
Graduate student in Dr. Moore's research group who contributed to Chapters 5, 6, and 10

Evan Margareta  
Graduate student in Dr. Long's research group who contributed to Chapter 10

Ashley M. Nelson  
Graduate student in Dr. Long's research group who contributed to Chapter 10

Ya Peng Yu  
Graduate student in Dr. Murayama's research group who contributed to Chapter 5

Prof. Mitsu Murayama,



Professor of Materials Science and Engineering at Virginia Tech who contributed to Chapter 5

Lindsey J. Anderson

Graduate student in Dr. Moore's research group who contributed to Chapter 6

Dr. Nicholas G. Moon

Postdoctoral researchers in Dr. Long's research group who contributed to Chapter 8

Dr. Donald C. Aduba, Jr.

Postdoctoral researchers at Department of Mechanical Engineering of Virginia Tech who contributed to Chapter 11

Justin Sirrine

Graduate student in Dr. Long's research group who contributed to Chapter 11

Dr. Akanksha Kanitkar

Postdoctoral researchers at Department of Biomedical Engineering and Mechanics of Virginia Tech who contributed to Chapter 11

Kristen S. Wek, Ye-Won Rhee, and Andrea Sweet

Past undergraduate students in Dr. Long's research group who contributed to Chapters 12

## Table of Contents

|   |    |
|---|----|
| Chapter 1. Introduction.....  | 1  |
| 1.1 Dissertation Overview.....  | 1  |
| Chapter 2. Design and Performance of Reversible Adhesives .....   | 4  |
| 2.1 Abstract .....  | 4  |
| 2.2 Introduction .....  | 5  |
| 2.2.1 Conventional Adhesives Concept and Limitation .....   | 5  |
| 2.2.2 Concept and Potential Impact: Reversible Adhesive.....  | 6  |
| 2.2.3 Methodologies in Reversibility in Adhesives Fabrication.....                                      | 10 |
| 2.3 Reversible Chemically Linked Adhesives .....  | 13 |
| 2.3.1 Thermally Reversible Diels-Alder Adhesives .....  | 14 |
| 2.3.2 Photo Reversible Cyclobutane Adhesives .....  | 16 |
| 2.3.3 Redox Reversible Adhesion.....  | 18 |
| 2.4 Biomimetic Reversible Adhesives .....   | 20 |
| 2.4.1 Mussel Inspired Fibrillar Reversible Adhesives .....  | 22 |
| 2.4.2 Wrinkled Fibrillar Reversible Adhesives.....  | 23 |
| 2.4.3 Interlocked Fibrillar Reversible Adhesives .....  | 25 |
| 2.4.4 Electro-Fibrillar Reversible Adhesives.....   | 26 |
| 2.4.5 Shape Memory Fibrillar Reversible Adhesives .....   | 27 |
| 2.5 Hydrogen Bonding Based Reversible Adhesives.....  | 28 |
| 2.5.1 Acrylic Reversible Adhesives.....   | 29 |
| 2.5.2 Solvent Reversible Adhesion.....  | 34 |
| 2.6 Other Method of Introducing Reversibility.....  | 37 |
| 2.7 Conclusion.....   | 39 |
| 2.8 References .....  | 40 |
| Chapter 3. Nucleobase-Functionalized Acrylic ABA Triblock Copolymers and<br>Supramolecular Blends ..... | 44 |
| 3.1 Abstract .....  | 44 |
| 3.2 Introduction .....  | 45 |
| 3.3 Experimental Section .....  | 49 |
| 3.4 Results and Discussion.....   | 53 |
| 3.5 Conclusions .....   | 70 |
| 3.6 Acknowledgements .....  | 71 |
| 3.7 References .....  | 71 |

|  |                              |     |
|--|------------------------------|-----|
| 3.8  | Supporting Information ..... | 74  |
| Chapter 4. Nucleobase-Functionalized ABC Triblock Copolymers: Self-assembly of Supramolecular Architectures..... |                              |     |
|  |                              | 82  |
| 4.1  | Abstract .....               | 82  |
| 4.2  | Introduction .....           | 82  |
| 4.3  | Results and discussion.....  | 85  |
| 4.4  | Conclusions .....            | 93  |
| 4.5  | References .....             | 93  |
| 4.6  | Supporting Information ..... | 94  |
| Chapter 5. Influence of Adenine and Thymine Binding Ratio on ABC Block Copolymer Self-Assembly.....              |                              |     |
|  |                              | 99  |
| 5.1  | Abstract .....               | 99  |
| 5.2  | Introduction .....           | 99  |
| 5.3  | Results and Discussion.....  | 102 |
| 5.4  | Conclusions .....            | 114 |
| 5.5  | Acknowledgements .....       | 114 |
| 5.6  | References .....             | 115 |
| 5.7  | Supporting Information ..... | 116 |
| Chapter 6. Ureido-Cytosine and Cytosine Containing Supramolecular Polymers.....                                  |                              |     |
|  |                              | 124 |
| 6.1  | Abstract .....               | 124 |
| 6.2  | Introduction .....           | 125 |
| 6.3  | Experimental Section .....   | 128 |
| 6.4  | Results and Discussion.....  | 134 |
| 6.5  | Conclusions .....            | 153 |
| 6.6  | Acknowledgements .....       | 155 |
| 6.7  | References .....             | 155 |
| 6.8  | Supporting Information ..... | 157 |
| Chapter 7. Acetyl-Protected Cytosine- and Guanine-Containing Acrylics for Supramolecular Adhesives.....          |                              |     |
|  |                              | 164 |
| 7.1  | Abstract .....               | 164 |
| 7.2  | Introduction .....           | 165 |
| 7.3  | Experimental Section .....   | 168 |
| 7.4  | Results and Discussion.....  | 174 |
| 7.5  | Conclusion.....              | 190 |
| 7.6  | Acknowledgements .....       | 191 |

|   |                              |     |
|---|------------------------------|-----|
| 7.7   | References .....             | 191 |
| 7.8   | Supporting Information ..... | 193 |
| Chapter 8. Styrenic DABCO Salt-Containing Monomers for the Synthesis of Novel Charged Polymers .....          |                              | 202 |
| 8.1   | Abstract .....               | 202 |
| 8.2   | Introduction .....           | 202 |
| 8.3   | Results and Discussion.....  | 204 |
| 8.4   | Conclusions .....            | 213 |
| 8.5   | Acknowledgements .....       | 214 |
| 8.6   | References .....             | 214 |
| 8.7   | Supporting Information ..... | 215 |
| Chapter 9. Doubly-Charged Random Ionomers with Enhanced Microphase-Separation .....                           |                              | 228 |
| 9.1   | Abstract .....               | 228 |
| 9.2   | Introduction .....           | 229 |
| 9.3   | Experimental Section .....   | 231 |
| 9.4   | Results and Discussion.....  | 235 |
| 9.5   | Conclusions .....            | 254 |
| 9.6   | Acknowledgements .....       | 255 |
| 9.7   | References .....             | 255 |
| 9.8   | Supporting Information ..... | 257 |
| Chapter 10. Non-Isocyanate Poly(amide-hydroxyurethane)s from Sustainable Resources .....                      |                              | 267 |
| 10.1  | Abstract .....               | 267 |
| 10.2  | Introduction .....           | 268 |
| 10.3  | Experimental Section .....   | 272 |
| 10.4  | Results and Discussion.....  | 278 |
| 10.5  | Conclusions .....            | 300 |
| 10.6  | Acknowledgements .....       | 301 |
| 10.7  | References .....             | 301 |
| 10.8  | Supporting Information ..... | 303 |
| Chapter 11. Electrospinning of Plant Oil-based, Non-Isocyanate Polyurethanes for Biomedical Applications..... |                              | 318 |
| 11.1  | Abstract .....               | 318 |
| 11.2  | Introduction .....           | 319 |

|   |  |     |
|---|--|-----|
| 11.3  | Experimental Section .....   | 321 |
| 11.4  | Results and discussion.....  | 329 |
| 11.5  | Conclusions .....  | 346 |
| 11.6  | Acknowledgements .....   | 347 |
| 11.7  | References .....   | 348 |
| Chapter 12. Nucleobase Functionalized Polymers for Enhanced Interlayer Adhesion<br>in 3D Printing 350 |  |     |
| 12.1  | Abstract .....   | 350 |
| 12.2  | Introduction .....   | 351 |
| 12.3  | Experimental Section .....   | 352 |
| 12.4  | Results and Discussion.....  | 355 |
| 12.5  | Conclusions .....  | 362 |
| 12.6  | References .....   | 363 |
| 12.7  | Supporting Information.....  | 363 |
| Chapter 13. Overall Conclusions .....   |  | 366 |
| Chapter 14. Suggested Future Work.....  |  | 370 |
| 14.1  | Ureido-cytosine functionalized triblock copolymers .....   | 370 |
| 14.2  | Synergy of hydrogen bonding and ionic interaction in random copolymers ...   | 371 |
| 14.3  | Bis(ureido cytosine) diacrylate crosslinkers for 3D printing .....   | 373 |
| 14.4  | Ureido-cytosine containing resins for extrusion 3D printing and self-healing<br>materials .....                    | 374 |
| 14.5  | Synthesis of poly(ureido-cytosine ester) .....   | 376 |
| 14.6  | Chirality, pi-pi stacking, complement hydrogen bonding in concert for<br>supramolecular polymer self-assembly..... | 377 |
| 14.7  | Synthesis of guanine-containing acrylamide monomer .....   | 378 |
| 14.8  | Doubly-charged monomers .....  | 378 |
| 14.9  | References .....   | 378 |

## **Chapter 1. Introduction**

### **1.1 *Dissertation Overview***

The overall theme of this dissertation revolves around synthesis and structure-property-morphology relationships of novel supramolecular polymers. Chapter 2 reviews current progress in developing reversible adhesives which represents a promising application for polymers containing noncovalent interactions. Chapters 3 to 7 mainly focus on nucleobase-containing random and block copolymers with mechanical integrity and self-assembled morphologies. Chapters 8 and 9 introduce the effect of doubly-charged pendant groups on random ionomer morphology and properties. Chapters 10 and 11 discuss synthesis and electrospinning of non-isocyanate poly(amide-hydroxyurethane) thermoplastics based on renewable resources. Chapter 12 shows preliminary results on how noncovalent interaction impacts interlayer adhesion for mask projection micro-stereolithography.

Chapter 3 details the synthesis of adenine- and thymine-functionalized ABA triblock copolymers using RAFT polymerization. The supramolecular blend of complementary nucleobase-functionalized ABA triblock copolymers self-assembled into a microphase-separated morphology with enhanced mechanical performance and maintained processability. Chapter 4 reports RAFT polymerization of acrylic ABC triblock copolymers that contain self-complementary nucleobase-functionalized external blocks and a low- $T_g$  soft central block. ABC triblock copolymers self-assembled into well-defined lamellar microphase-separated morphologies for potential applications as thermoplastic elastomers. Complementary hydrogen bonding within the hard phase facilitated self-assembly and enhanced mechanical performance. Chapter 5 further investigates influence

of the binding ratio between thymine to adenine on ABC triblock copolymers mechanical performance and morphology. Intermolecular hydrogen bonding formed thymine-adenine triplets and promoted self-assembly into well-defined lamellae with long-range order, while thymine-adenine duplets contributed to superior mechanical property. Chapter 6 expands the synthesis of nucleobase-containing copolymers to cytosine, which allows facile post-functionalization into ureido-cytosine. Ureido-cytosine formed quadruple self-hydrogen bonding that contributed to microphase-separated morphology with superior cohesive strength, wide service temperature window, and low moisture uptake for applications as adhesives and thermoplastic elastomers. Chapter 7 focuses on synthesis of cytosine and guanine-containing monomers and polyacrylates with acetyl-protection groups. Acetyl cytosine and acetyl guanine-containing acrylics with relatively low polar monomer incorporation served as promising candidates for pressure sensitive adhesives.

Chapter 8 describes a facile synthesis for styrenic DABCO salt monomers bearing two covalently linked quaternary ammonium cations, which allow the synthesis of novel charged polymers with a double ion pair on each pendant group. DABCO salt monomers expand the current library of ionic monomers and demonstrate the potential of multi-charged ionic groups in forming strong ionic interactions and driving microphase-separation. Chapter 9 shows that DABCO salts afford stronger ionic association of compared to singly-charged trialkyl ammoniums, which resulted in superior thermomechanical and tensile properties of DABCO salt-containing ionomers. The counterion choices and alkyl substituent lengths affected thermal stability, phase-separation, and water uptake for both DABCO salt-containing copolymers and their singly-charged controls.

Chapter 10 describes a unprecedented one-pot synthetic platform for nonsegmented and segmented poly(amide-hydroxyurethane) with polyether soft segments using plant-oil based monomers, which represents the first example of film-forming, linear isocyanate-free polyurethanes with crystallinity, mechanical integrity, and processability. Chapter 11 demonstrates the successful electrospinning of these isocyanate-free polyurethanes into randomly orientated, semicrystalline fibers that formed stretchable, free-standing fiber mats. These fiber mats showed good cell attachment and no negative effect on cell viability, which enabled potential applications as biomedical materials. Chapter 12 introduces testing method development and nucleobase-containing UV-curable resin synthesis. Preliminary results of the nucleobase-containing samples showed similar weak interfaces compared to the controls. Finally Chapter 13 provides the overall conclusion comparing the structure-property-morphology relationships of polymers with varied noncovalently associating groups. Chapter 14 suggests future directions to continue the research efforts on supramolecular polymer synthesis and characterization.



## Chapter 2. Design and Performance of Reversible Adhesives

(*In preparation* as a chapter in a book volume for *Advances in Polymer Science* planned to be published by Springer)

Keren Zhang and Timothy E. Long\*

*Department of Chemistry, Macromolecules and Innovation Institute  
Virginia Tech, Blacksburg, VA 24061, US*

### 2.1 ***Abstract***

The potential advantages and versatility of reversible adhesives continue to catalyze advances in this area. This review summarizes recent achievements in designing and fabricating adhesives with reversible chemical structures, surface interactions, morphology, mechanical properties, and adhesion performance. There are many key components that introduce reversibility into conventional adhesives or assist designs of novel compositions, including reversible chemical bonds, noncovalent interactions, tailored morphology, and physical transitional of polymers. Different reversible mechanisms also correspond to various debonding methods of the adhesives, such as temperature, photo-irradiation, solvent, and mechanical peeling. Reversible chemical bonds contribute to one type of reversible adhesives with controllable molecular weight and crosslinking density. For example, adhesives that contain diene and alkene functional groups go through thermal reversible Diels-Alder reaction, providing a reversible chemically crosslinked network with enhanced mechanical strength. Noncovalent interactions like hydrogen bonding,  $\pi$ - $\pi$  stacking, and ionic interaction also allow reversible surface interactions and apparent molecular weight variation. Hydrogen bonding-containing adhesives show potential with enhanced cohesive strength at application temperature while dissociation upon heating or

solvent regains their processibility. Nature also inspires a wide variety of biomimetic adhesives based on gecko, spider, and mussels. The fibrillar structure of the gecko footpad guarantees its survival for the ability to easily attach and detach to a variety of surfaces. The abundant catecholic groups in mussel foot proteins contribute to strong and reversible adhesion to rocks underwater. Numerous efforts have been devoted in matching and preceding adhesion performance of biological systems with synthetic adhesives over the past few decades. Other reversible adhesives involve engineered composite materials, shape memory materials, and geometric isomers. This review categorizes each reversible adhesive based on its main design feature that introduces reversibility. However, many high functional reversible adhesives combine multiple mechanisms of reversibility and showed promising adhesion strength compared to their predecessors. Exploiting the synergy of various reversible mechanisms is becoming the dominating concept of next generation, reversible adhesive design.

## **2.2 *Introduction***

### **2.2.1 Conventional Adhesives Concept and Limitation**

Adhesives are everywhere: nature makes adhesives like bee wax, gecko foot pad, and glue droplets on spider web; synthetic adhesives are widely used in commodity, construction, manufacturing industry, and medical treatment. The importance of adhesives lays in their ability to bind two surfaces together without tempering the surface integrity and aesthetic value, while lowering the cost and bringing additional advantages like vibration damping. Adhesive and cohesive strength are two vital parameters to measure adhesive performance.<sup>1</sup> Adhesive strength describes the capacity of bonding at the interface between the surface and adhesive, and cohesive strength represents the internal

strength of the adhesive. Conventional adhesives are often low viscosity liquids for easy application, which subsequently solidify through chemical crosslinking or physical transition such as cooling or solvent evaporation. As adhesives harden between two surfaces, sufficient adhesive and cohesive strengths provide suitable mechanical properties at the joint. However, many adhesive applications require debonding of the adhesives after uses for modification or recycling. The separation of two assembled surfaces is challenging in most cases, especially for structural adhesives such as epoxy, which often requires demanding conditions such as high temperature. Debonding surfaces with thermoplastic adhesives requires at least 200 °C during the wafer thinning process in advanced microelectronic device manufacturing process.<sup>2-4</sup> Thermoset adhesives require thermal decomposition temperature above 350 °C, which largely limits further processing and recycling.<sup>5,6</sup> Some pressure sensitive adhesives (PSA), that temporarily bond to diverse substrates, are removable later with only moderate peeling force. Removable PSAs are usually tacky solids that adhere to surfaces with applied pressure and detach with peeling force.<sup>7,8</sup> However, low cohesive strength of removable PSAs limits their industrial significance to applications that only require weak adhesion at the joints, such as skin care, surface protections, labels, and office supplies.<sup>9</sup>

### **2.2.2 Concept and Potential Impact: Reversible Adhesive**

An exciting direction in adhesive development emphasizes reversibility in mild conditions while maintaining adherence strength.<sup>10</sup> Optimal reversible adhesives undergo multiple bonding and debonding cycles to a substrate when triggered with external stimuli. The adhesive and cohesive strength of reversible adhesives must meet criteria for conventional adhesives and maintain stability under certain conditions such as varied

temperature and moisture according to specific application requirements. More importantly, either or both adhesive and cohesive strength must vary significantly in response to external bonding and debonding triggers. Commercially available removable adhesives such as the Post-It Notes® typically show relatively weak adhesive strength and poor durability. Applied peeling force as the only debonding method largely limits these products in more demanding industrial applications. Unlike their predecessors, next generation reversible adhesives will gain significant industrial potential if they can substitute conventional adhesives with comparable adhesion performance. Such novel adhesives offer opportunities for repairing and recycling multilayered or multi-component structures and laminates without collateral damages. Reuse of adhesives also provides economic and environmental advantages, especially for structural adhesives, which are mostly thermosets such as epoxy, polyurethanes, acrylics, cyanoacrylates, polyimides. Structural adhesives are mechanically strong to withhold stress similar to their adherents for long period without failure. They are widely used in automotive, construction, appliances, and furniture.<sup>11</sup> However, the chemically crosslinked networks of thermosets are so strong that degradation of the adhesives is necessary for debonding, which prohibits repair, recycle, or reuse of either the adhesives or adherents. Reversible thermosets will open a window for cost-efficient, sustainable, and recyclable structural adhesives. Most promising direction for designing reversible structural adhesives as of now is utilizing reversible chemical reactions that form chemically crosslinked network and dissociate upon external triggers, such as UV radiation, pH changes, and mechanical stress.<sup>5,6,12,13</sup>

Markets for “softer” adhesives such as hot melt and pressure sensitive adhesives also embrace development of their novel reversible competitors. Soft adhesives for medical

and hygiene products is a big and important market for reversible adhesives. Current commercial medical skin care products are facing an impasse to provide sufficient skin adhesion while alleviating pain and trauma during removal. Applications such as wound dressing and bandages widely recognize the importance of alternative debonding mechanisms.<sup>14-16</sup> In other applications such as packaging, appliances, textiles, automotive, electronics, and office supplies, reversibility of adhesives is also crucial in processing, applying, removal, and recycling. Higher molecular weight polymers generally increase the cohesive strength while compromising the processability of adhesives. So an adhesive formulation with enhanced adhesive performance often comes with higher processing temperature for hot melt PSA, or higher volatile organic compounds (VOC) for solution-based PSA. Incorporations of reversible bonding will allow fabrication of PSAs with enhanced strength and maintained processability.<sup>17,18</sup>

In addition, the future of reversible adhesives goes beyond just improving current adhesive products. There is a high potential for reversible adhesives in enabling transformative applications and innovative products such as portable devices, new sportswear, medical cares, and artificial intelligence designs. The climbing ability of geckos intrigues many researchers to fabricate reversible adhesives for “Spider-Man gloves”. Geim *et al.* showed gecko-inspired adhesive supporting a toy hanging in 2003 (Figure 2.1a),<sup>19</sup> Hawkes *et al.* demonstrated the capability of their gecko-inspired adhesives, allowing an adult climbing on a glass wall.<sup>20</sup> Who is to say after several years it won’t be possible to pull off what Tom Cruise did in Mission impossible with gecko-inspired adhesives instead of wires and pulleys.



**Figure 2.1.** A spider-man toy hanging from glass ceiling using a microfabricated gecko-inspired adhesive pad on its hand 2003. Reprinted with permission<sup>19</sup> Copyright 2003 Nature Publishing Group.

Currently, the field of reversible adhesives development is relatively new with limited industrial impact. Most studies remain preliminary and focus on verifying the possibility of incorporating triggerable reversible mechanisms with enhanced adhesive strength. Many opportunities await in improving the performance of synthetic reversible adhesives. Besides strength and reversibility, durability in multiple adhesion cycles and versatility for various surfaces still limit the applications of current synthetic reversible adhesives. On the contrary, animals such as geckos, beetles, and flies have the ability to firmly adhere to a variety of surfaces and swiftly detach. And the bioadhesives are durable throughout their lifespan. To achieve similar strength, reversibility, versatility, and durability of these biological reversible adhesive systems, most studies start with one aspect in developing synthetic substitutes. A confluence of all the superior features still

remains elusive in many present adhesive systems. Despite the challenging goals of matching Nature's creations, several recently developments show potential as scalable reversible adhesives that afford more than two features of the biological system.<sup>20-22</sup> This review mainly focuses on summarizing methodologies for design and fabrication of reversible adhesive and interfaces, and probing the effect of incorporating reversibility on adhesive performance.

### **2.2.3 Methodologies in Reversibility in Adhesives Fabrication**

Researchers have explored various methods for designing new types of reversible adhesives to obtain tunable reversibility with sufficient adhesive strength. Reversible chemical reactions provide various avenues to incorporate reversibility into adhesive systems. Many thermally reversible polymers are based on a thermally reversible 4+2 cyclo-addition reaction Otto Diels and Kurt Alder designed in 1928.<sup>23,24</sup> One of the most investigated DA reactions involves [4+2] cycloaddition reaction of furan as a diene and maleimide as a dienophile when heated below 60°C.<sup>25,26</sup> The resulting cyclohexene adduct undergoes a retro-Diels-Alder reaction, which reverses the cyclic system upon heating above 90°C (Figure 2.2a).<sup>27</sup> The thermally reversible nature of DA reactions suggests the facile reversibility of adhesives. Photo reversible cycloaddition also provides an avenue to incorporate reversibility through cyclobutane crosslinking groups. Functional groups such as coumarin, thymine, stilbene and cinnamate undergo reversible [2+2] cycloaddition upon UV irradiation of certain wavelength (Figure 2.2b).<sup>12</sup> The reversible [4+4] cycloaddition of anthracene also introduces photo reversibility to polymeric materials.<sup>28</sup> Thirdly, pH is an potential external debonding trigger for reversible adhesives. The reaction of an amine with paraformaldehyde yields a triazine, which reverses back to the starting materials in acidic

conditions (Figure 2.2c).<sup>5</sup> In addition, redox-reversible chemical reactions such as formation of the disulfide bond present another route for designing reversible adhesives (Figure 2.2d).<sup>29,30</sup> Reversible chemical reactions either increase the polymer molecular weight when placing on the backbones, or introduce branching and crosslinking when placing on the pendant groups. Either way, the reversible chemical bonds improve adhesive performance under application conditions and weaken cohesive strength when exposed to debonding triggers.

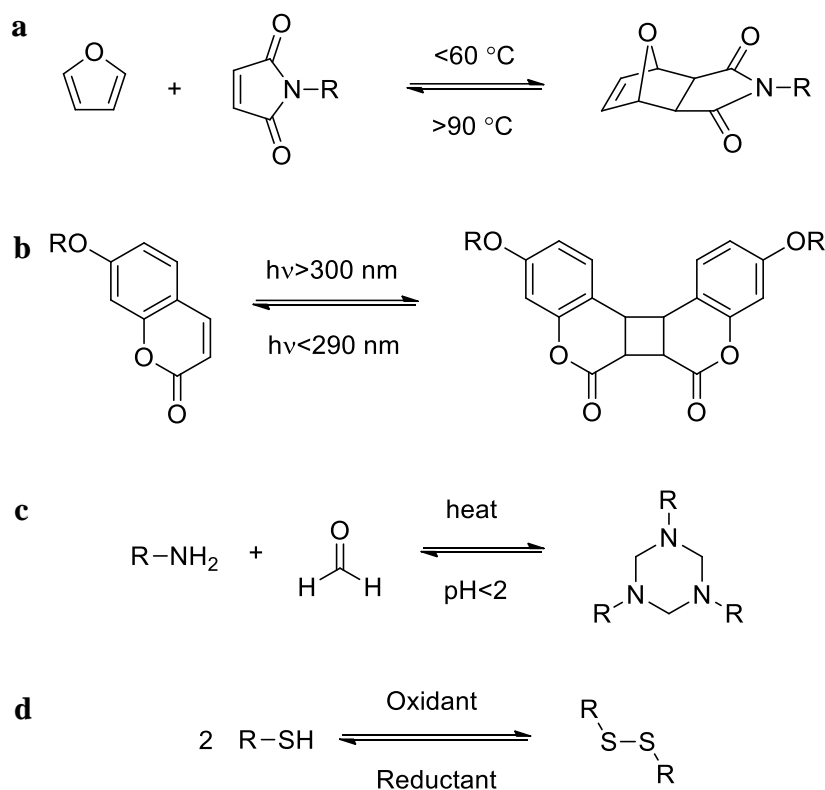


**Figure 2.2.** (a) Diels Alder and retro-DA reaction of furan and maleimide.<sup>25</sup> (b) Photo reversible dimerization reaction of coumarin groups.<sup>31</sup> (c) pH reversible triazine formation from paraformaldehyde with primary amine.<sup>5</sup> (d) Redox reversible disulfide bond formation.



Noncovalent interactions also serve as reversible mechanisms in adhesive systems. Noncovalent interactions include hydrogen bonding, electrostatics,  $\pi$ - $\pi$  stacking, van der Waals force, and coordination bonds. They are ubiquitous and significant in nature. In addition, the well-known double helix structure of DNA is a synergistic combination of hydrogen bonding, electrostatics,  $\pi$ - $\pi$  stacking, and hydrophobic-hydrophilic interactions. Inspiration from DNA structure motivates massive studies for synthetic nucleobase-containing polymers, as well as supramolecular systems bearing multiple noncovalent interactions.<sup>32-34</sup> Similar applicable strategies to design reversible adhesives highlight nucleobase functional groups and other hydrogen bonding motifs.<sup>35-40</sup> Researchers continue to recognize the supramolecular systems' potential for the reversibility and amendability through incorporating different noncovalent interactions, especially hydrogen bonding.<sup>33,41</sup>

One example is the gecko's ability to climb onto a variety of substrates, which solely depends on the weakest noncovalent interaction: van der Waals forces. Researchers devote many efforts to fabricate dry reversible adhesives that mimic the multiscale hierarchy hairy structure of gecko foot. Multiple extensive reviews summarized achievements so far in this emerging field for further reading.<sup>42-47</sup> Furthermore, mussel foots' strong and reversible attachment to wet surfaces intrigue researchers to study the mechanism and design similar wet adhesives.<sup>22,48-51</sup> The key to strong cohesion and adhesion strength is the high content of catecholic amino acid L-3,4-dihydroxyphenylalanine (DOPA) in adhesive protein mussel secrete.<sup>52-55</sup> Inspirations from beetles' wing locking device and ripple surface morphology also brings in fresh concepts of reversibility.<sup>56-60</sup> Applying electronic voltage on conductive adhesive materials and

utilizing shape memory polymers (SMP) are the most recent advances of improving fibrillar reversible adhesives.<sup>61,62</sup>

Finally, there are several reports on thermally controlled dry reversible adhesives using delicate designs of composite materials with unique shape and morphological changes.<sup>63-65</sup> A few groups reported reversible adhesion of polyelectrolytes coated surfaces using ionic interactions and reversible cell adhesion substrates based on photoreversible azobenzene isomerization.<sup>66,67</sup>

This review discusses details of various paths to prepare reversible adhesives in four main sections introduced above: chemically reversible adhesives, biomimetic reversible adhesives, hydrogen bonding supramolecular adhesives, and others types of reversible adhesives. Discussion sorts achievements of reversible adhesive according to the pivotal theory behind the fabrication of reversible adhesives. Yet a majority of polymer performances result from synergistic or antagonistic combination of multiple interactions. Many novel complex adhesives systems united two or more concepts to tune adhesion strength and enhance reversibility. This review also discusses the advantages and disadvantages among different categories of reversible adhesives, followed by promising applications reported in literature.

### **2.3 *Reversible Chemically Linked Adhesives***

Covalent bonds require tough conditions to dissociate because of the high energy nature ( $\sim 360$  kJ/mol)<sup>68</sup>. Consequently, debonding of chemically cured adhesives is difficult to accomplish. Reversible chemical reactions with mild conditions are valuable tools for such purpose.

### 2.3.1 Thermally Reversible Diels-Alder Adhesives

Previous studies have utilized DA reactions to form polymer backbones as well as chemical crosslinks. Chen *et al.* reported a self-healing polymeric material, which has comparable mechanical properties with epoxy resin, using monomers with multiple furan and maleimide functional groups to form a highly crosslinked polymer network.<sup>69</sup> Solid state Nuclear Magnetic Resonance spectroscopy (NMR) revealed 30% reversibility of DA adducts-containing materials in multiple cycles of heating and cooling using cyclohexene chemical shifts. Chen's study proved capability of DA reaction to polymerize, providing thermal reversibility to resulting polymeric materials.

Aubert first presented reversible adhesives using the same furan and maleimide DA reaction to form polymer backbone.<sup>70,71</sup> Epoxy resin, prepared with DA reaction between furfuryl glycidyl ether and bismaleimide (Figure 2.3), was cured with diamine to form adhesives that have lap-shear of 4.56 MPa on stainless coupons. Immeasurable lap-shear and  $10^3$  storage modulus drop at 90°C allowed debonding to occur in multiple heat-and-cool cycles. Loss of cohesion and adhesion strength resulted from the loss of crosslinking networks above the retro-DA reaction temperature. Nevertheless, reversibility loss occurred when adhesives were held above 90°C for longer than an hour cumulatively, which was due to side reaction between the amines and maleimides according to the author.

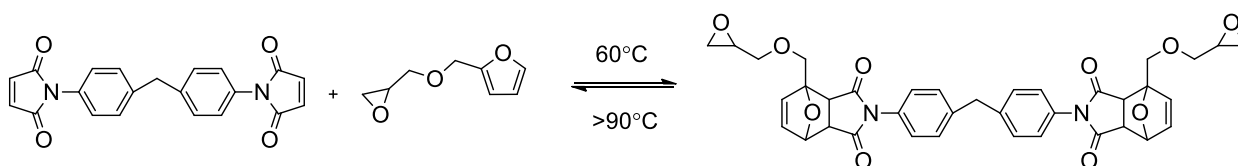


**Figure 2.3.** DA reaction of furfuryl glycidyl ether and 1,1'-(methylenedi-4,1-phenylene)-bismaleimide.<sup>71</sup>

Later, Wouters *et al.* presented crosslinked acrylic copolymers networks capable of temporally bind wafers during semiconductors manufacture.<sup>72</sup> Wouters *et al.* copolymerized a series of *n*-alkyl (meth)acrylate and furfuryl methacrylate in different feed ratios. Characterization methods including rheology assessed copolymer properties in presence of bismaleimide crosslinker (Figure 2.4). Complex viscosity measurements in multiple heat-and-cool circles demonstrated that the novel copolymer system possessed thermal reversibility without loss of properties. These networks also had sufficient thermal stability, chemical resistance and cleanability. New DA crosslinked adhesives exhibited higher viscosity at lower temperature and better processability at high temperature compared to benchmark adhesive samples. More importantly, Wouters *et al.* proved the possibility of tailoring various adhesives properties for different applications using DA crosslinked adhesives systems.

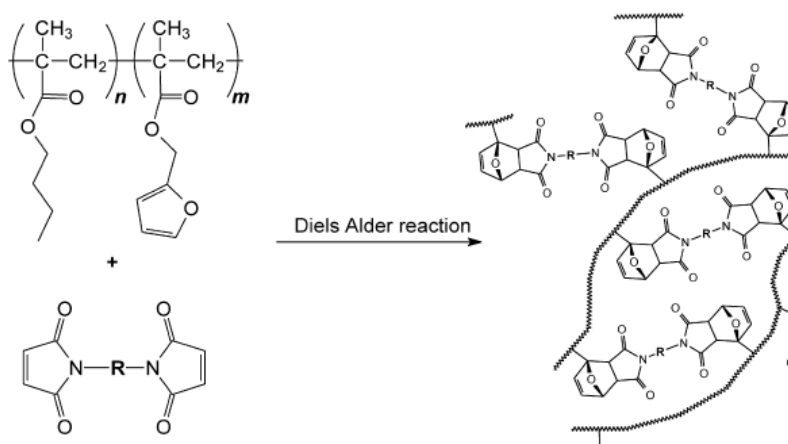


**Figure 2.4.** Crosslinking reaction of poly(furfuryl methacrylate-*co*-*n*-butyl methacrylate) with bismaleimide. Reprinted with permission<sup>72</sup> Copyright 2012 Elsevier.

### 2.3.2 Photo Reversible Cyclobutane Adhesives

Our group designed a series of reversible adhesives based on the photo reversibility of [2+2] cycloaddition in the past few years.<sup>73-75</sup> The removable pressure sensitive adhesives (PSA) with light initiated crosslinking mechanism from Webster and coworkers<sup>76,77</sup> inspired many researchers to develop reversible PSA for non-trauma wound dressing. Long *et al.* were the first to show the possibility of incorporating reversibility into PSA via photodimerization forming cyclobutane crosslinking sites.<sup>73</sup> In Figure 2.5, coumarin functional groups that attached to poly(2-ethylhexyl acrylate-co-hydroxyethyl acrylate) side chain dimerized when exposed to ultraviolet-A (UVA) (>300nm), forming a cyclohexane crosslinking site which dissociated upon irradiation of UVC (<290nm). Conversion of dimerization was monitored by UV absorption at signature wavelength. Peel strength decreased by 97% upon UVA irradiation, resulting from the low viscous flow and difficulty to form adhesive bonds, corresponding to 90% gel fraction. Whereas UVA irradiation only recovered up to 6% peel strength. Long *et al.* continued more systematic study on coumarin-containing poly(alkyl acrylate/methacrylate).<sup>74</sup> This work showed how the glass transition temperature ( $T_g$ ) largely affected the photodimerization efficiency when deviating from irradiation temperature. This occurred as mobile chains allowed more chances for coumarin side groups to collide. However, photodimerization efficiency was irrelevant to the  $\alpha$ -methyl on poly(alkyl methacrylate) on the main chain compared to corresponding polyacrylates and polymethacrylates. These photo reactions followed the Bunsen-Roscoe reciprocity law, which allowed low intensity of irradiation to be compensated with longer time. Another advantage was the stability of cyclobutane groups to ambient light. However, the author did not address the problem of poor reversibility,

which might result from the equilibrium nature of the reversible reaction under certain wavelengths. Previously, Chen and coworkers conducted a thorough investigation of the conditions that affected reversibility efficiency. They include chemical environment of the moieties, wavelength of irradiation, and addition of photosensitizer.<sup>78-82,31</sup>

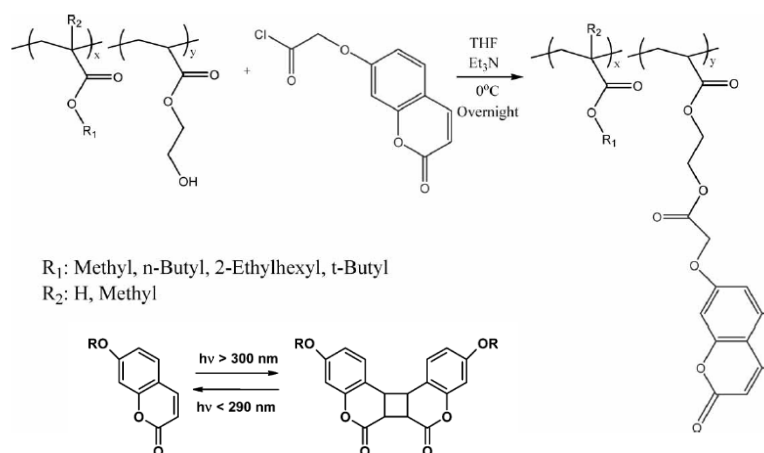


**Figure 2.5.** Copolymers modification with coumarin groups and the photoreversible dimerization reaction. Reprinted with permission<sup>73,74</sup> Copyright 2005, 2007 Taylor & Francis.

Besides photocrosslinking on the side chain, our group also demonstrated the possibility of utilizing cyclobutane photocleavage to decrease molecular weight. This mechanism diminished adhesion strength and established reversibility. Long *et al.* synthesized microphase separated poly(siloxane imides) that were made from maleic anhydride dimers, providing photoreversible cyclobutane groups on the polymer backbone (Figure 2.6).<sup>75</sup> Polymers were thermally stable up to 360 °C, until retro-DA reactions led to degradation.<sup>83</sup> Dynamic Mechanical Analysis (DMA) showed a rubbery plateau from - 50 °C to 100 °C, which was attributed to the microphase separated nature (Figure 2.7).

Having a modulus drop for less than 100MPa, this adhesives displayed promising applications for requirements of high performance in a large temperature range. Increasing intensity of maleimide signature peaks shown on  $^1\text{H}$  NMR upon UVC irradiation demonstrated reversibility of cyclobutane moieties.

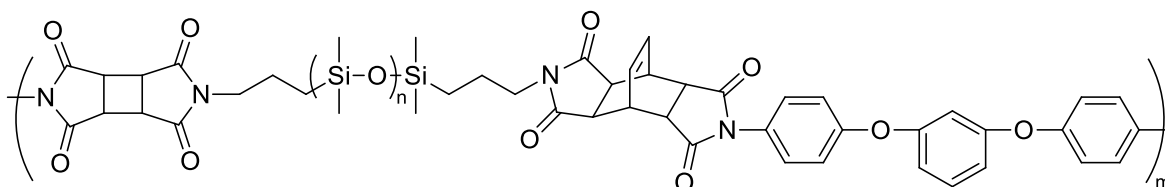


**Figure 2.6.** Poly(siloxane imides) containing cyclobutane diimide functionality. Reprinted with permission<sup>75</sup> Copyright 2010 Taylor & Francis.

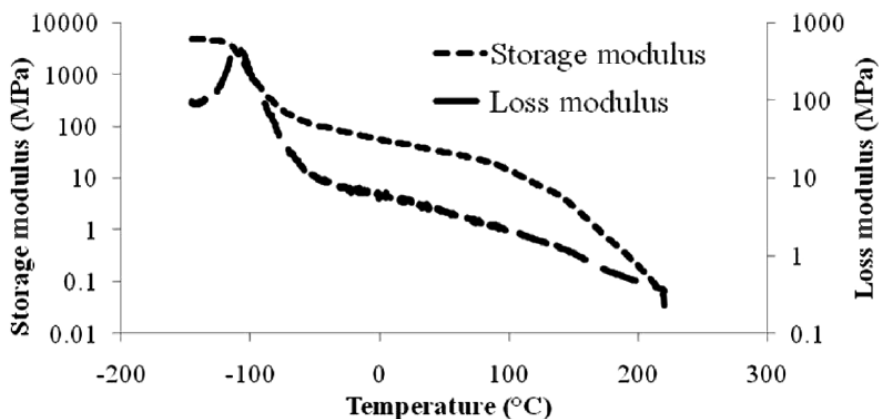


**Figure 2.7.** DMA of cyclobutane diimide-containing poly(siloxane imides) demonstrates a rubbery plateau. Reprinted with permission<sup>75</sup> Copyright 2010 Taylor & Francis.

### 2.3.3 Redox Reversible Adhesion

Disulfide bond is another reversible chemical moiety that can lead to reversibility in adhesive materials. Wu *et al.* discussed the possibility of cleaving disulfide bonds to redissolve cured polyimides, thus increasing the reprocessing ability of materials.<sup>29</sup>

Anumolu *et al.* designed a hydrogel based on crosslinking of disulfide bridges on the end of 8-arm-Polyethylene glycol (PEG), using H<sub>2</sub>O<sub>2</sub> as an oxidizing agent or thiopyridine as a good leaving group.<sup>30</sup> Adding glutathione (GSH) as a reducing agent broke down crosslinked networks, resulting in gel to sol changes (Figure 2.8). This mechanism has potential in removable dermatological treatment for wounds healing without peeling. High crosslink density of the hydrogel provided sufficient mechanical strength and low swelling degree. This hydrogel also showed sustained drug release of doxycycline for extended periods of time. Both *in vivo* and *in vitro* histology tests demonstrated the benefits of this doxycycline loaded removable hydrogel wound healing efficiency for mustard-induced skin wounds. Furthermore, this work initiated multifunctional wound dressing materials



design with drug releasing potential and removability that alleviated pain and trauma to the patients from peeling.

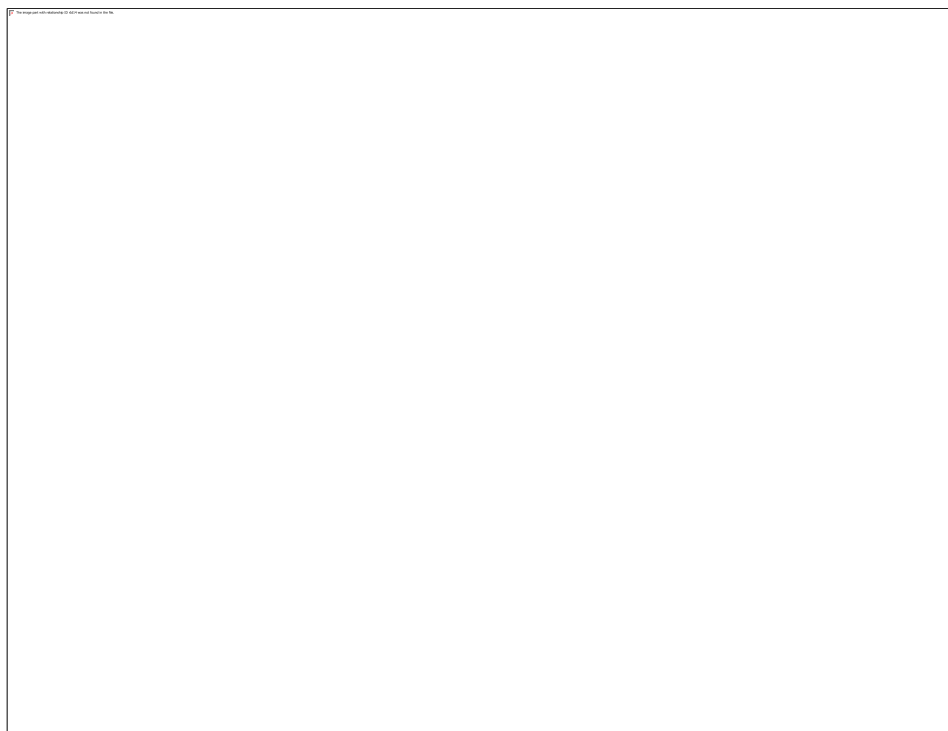


**Figure 2.8.** GSH induced gel to sol transformation resulting from the cleavage of disulfide bridges. Reprinted with permission<sup>30</sup> Copyright 2011 Elsevier.

In summary, reversible chemical reactions offer versatile tools to design reversible adhesives for various applications. Through applying thermal, photo and redox conditions, chemical structure changes can result in significant adhesive performance tunability. In spite of all inspiring results reviewed above, there are still many aspects and opportunities to improve and explore.

## 2.4 *Biomimetic Reversible Adhesives*

Autumn *et al.* first measured the adhesive force of a single hair on the gecko footpads.<sup>84</sup> Those pads require multiscale hierarchical fibrillar structure for maximum

surface contact in order to maintain sufficient adhesive force due to the weak van der Waals force nature. Animals' locomotions require easy and fast detachment from the surface while remaining good durability and adaptability on a variety of surfaces. A series of feature articles cover different aspects of this area: cell biological nature of the keratin-associated beta-proteins (KA $\beta$ Ps) enriched setae<sup>42</sup>, fibrillar adhesives parameters and fabrication methods<sup>45,85</sup>, theoretical and experimental measurement of adhesion forces<sup>86</sup>, mechanical principle of contact splitting and adhesion testing methods<sup>43,45</sup>, nano-based systems<sup>46,87</sup>, and potential applications<sup>44,47</sup> etc.

Nevertheless, limitations present in many gecko-inspired fibrillar adhesives. Gecko footpad KA $\beta$ Ps protein provides both rigidity and hydrophobicity. To achieve similar performance, the substrate materials require certain properties for fabricating fibrillar structure surface. They demand mechanical stiffness to prevent fibers collapsing or sticking. Softness is also crucial for sufficient adhesion strength. Poly(dimethylsiloxane) (PDMS) is a common polymer for fabricating the microfibrillar surface with easy prototyping and good adhesion strength. However, high aspect ratio fibers are hard to achieve without surface contamination and fibers collapse. Conversely, poly(methyl methacrylate) (PMMA) replicates nanofibrillar with high aspect ratio, yet brittleness limit the durability and adhesion performance. Moreover, most fibrillar adhesives lack durability and debonding mechanism, whereas reversible adhesive that will respond to external stimuli such as heat, light, and solvent are highly useful. Their applicability on real surface in various environments such as moisture and heat are limited. The major drawback of all gecko-inspired adhesive is the cost and complexity of manufacturing. Safety issue of manufacturing and using nanomaterials also restrict the applications. Below are the most

significant and recent achievements with potential of addressing drawbacks of traditional fibrillar adhesives.

#### 2.4.1 Mussel Inspired Fibrillar Reversible Adhesives

Another well-known bio-adhesive system is the dihydroxyphenylalanine (DOPA)-containing mussel foot which has unique strong binding to wet surface. Moisture usually decrease the adhesives performance significantly due to complex reasons,<sup>88</sup> whereas mussel foot bind to the rock underwater. Waite *et al.* first extracted mussel foot proteins and identified the key amino acid: DOPA.<sup>55</sup> However, the molecular binding mechanism remained unclear until 25 years later Messersmith *et al.* found the metal chelating ability of DOPA.<sup>52</sup> Later, the molecular interactions were found to be a combination of several interaction including metal coordination,  $\pi$ - $\pi$  interaction, covalent interchain crosslink and hydrophobic/hydrophilic interactions.<sup>52,89</sup> Since then, synthetic polymers with DOPA functional groups were proved to be promising in developing reversible adhesives and antifouling applications. Lee and coworkers have been pioneered in this area and published an extensive review on mussel-related theoretical and practical studies.<sup>22,50,52,90</sup>

Combining the strategies of gecko and mussel adhesives, Lee *et al.* presented a unique “geckel” nanoadhesive that had superior adhesive performance in air and water per pillar.<sup>90</sup> They coated poly(dopamine methacrylamide-co-methoxyethyl acrylate) (p(DMA-co-MEA)) on to PDMS nanofibrillar through dipping (Figure 2.9a). The hybrid adhesive exhibited much higher adhesion compared to nanofibrillar adhesive without catecholic coating in air and the enhancement is much more significant in water (Figure 2.9b). And durability is phenomenal in more than a thousand cycles (Figure 2.9c). Macroscopic adhesion showed 9 N/cm<sup>2</sup> in water, which is close to the gecko dry adhesive with hierarchy

structure. Applying two inspirations from nature, Geckel nanoadhesives improved the durability and applicability on wet environment. Besides, improved adhesion using coating compensated the loss of surface area from eliminating the complex hierarchy, providing a way of simplifying manufacturing process. Later, Glass *et al.* modified the fabricating procedure and prepared a DOPA-containing polymer coated microfibrillar with mushroom-shape tips. The new adhesive showed enhanced adhesion strength to nonflat surface in wet conditions over uncoated and unpatterned materials.<sup>91</sup>

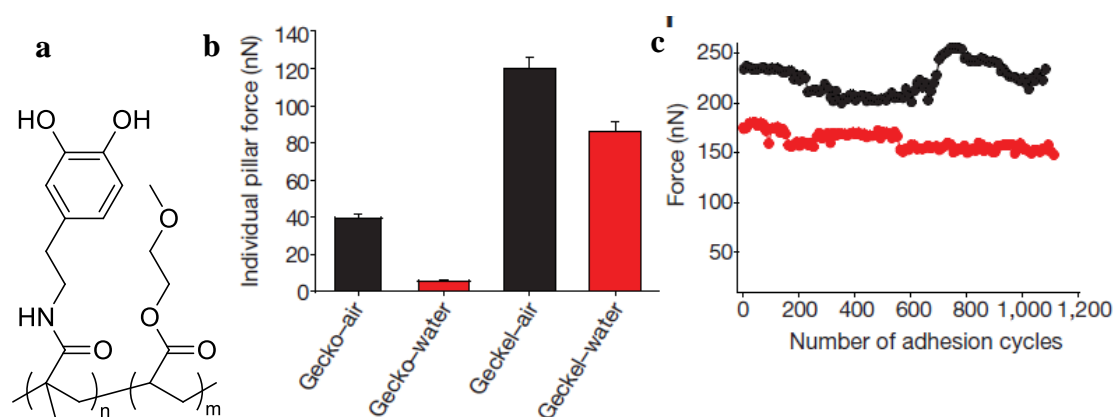


**Figure 2.9.** a) Chemical structure of DOPA-containing polymer coating. b) Adhesion force per pillar for non-coated nanoadhesive (gecko) and coated nanoadhesive (geckel) in air and water. c) Adhesion force per pillar for geckel nanoadhesive in multiple contact cycles in air and water. Reprinted with permission<sup>90</sup> Copyright 2007 Nature Publishing Group.

#### 2.4.2 Wrinkled Fibrillar Reversible Adhesives

Wrinkled (Rippled) elastomeric adhesive surface is another way of designing patterned reversible adhesives. Chan *et al.* prepared poly(n-butyl acrylate) (PnBA) surface wrinkled elastomer using swelling a laterally confined PnBA film with improved adhesion.<sup>56</sup> Theoretical study showed that adhesion enhancement only occur when

wavelength of ripples small than critical wavelength which largely varies over different surface. Lin *et al.* used simple yet robust mechanical strain methods to generate wrinkled PDMS surface with different amplitude.<sup>57</sup> Their studies were aiming at preparing surface with roughness to enhance adhesion properties while lowering the cost of micro/nano surface fabrication. Jeong and Suh et al. combined the prototyping fibrillar surface with mechanical strain induced wrinkling to design a wrinkled microfibrillar PDMS switchable adhesive.<sup>58</sup> This adhesive had relatively good peel and shear force in the range of 10 N/cm<sup>2</sup> and extraordinary durability over 100 cycles. Moreover, full contact with surface when applied with prestrain yielded good adhesion while no prestrain lead to very weak adhesion due to a point contact with the substrates (Figure 2.10). This switch-on/off adhesive is an excellent example of joining different technique to improve the drawback of the original gecko adhesive addressed before.

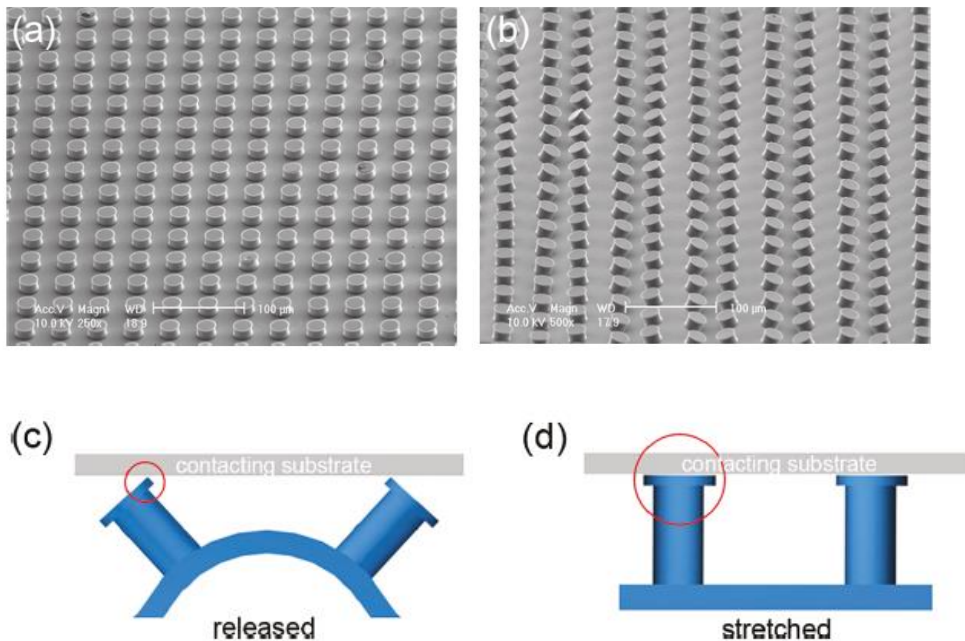


**Figure 2.10.** SEM images of the wrinkled microfibrillar adhesive a) with prestrain and (b) without prestrain. The illustration of c) point contact and d) area contact mechanism to the surface. Reprinted with permission<sup>58</sup> Copyright 2010, American Chemical Society.

### 2.4.3 Interlocked Fibrillar Reversible Adhesives

There are some other most recent advances on improving gecko adhesive with integration of other inspiration. Pang and Suh *et al.* designed reversible interlocking adhesives with high shear force up to 40 N/cm<sup>2</sup> using micro/nanofibrillar with high aspect ratio while maintain easy peeling off availability in vertical direction.<sup>59,60</sup> The inspiration comes from beetles' wing locking device showed in Figure 2.11. The shear force depended on a variety of conditions: polymeric material properties, fiber aspect ratio, fiber diameter and preload force. Shear strength decreased over cycles of attaching and detaching resulting from the breakage of fibers during pulling, yet 10 nm coating of Pt preserved the reversibility up to 300 cycles without much surface damage. As a result, a versatile system of reversible adhesive with exceptional high and tunable shear strength and facile removal which will be promising in many applications.

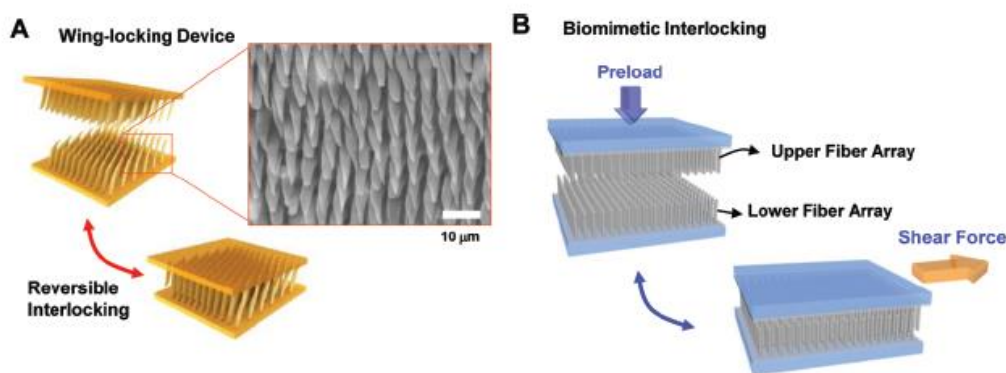


**Figure 2.11.** A) SEM image of microtrichia on the cuticular surface of a beetle and schematic illustration of the interlocking of beetle wings. B) Biomimetic interlocking

adhesive system of two dense fiber arrays. Reprinted with permission<sup>59</sup> Copyright 2012 American Chemical Society.

#### 2.4.4 Electro-Fibrillar Reversible Adhesives

Krahn and Menon reported a novel conductive gecko-based microfibrillar adhesive, which was made of cured carbon black with PDMS mixture.<sup>61</sup> Experiment set up in Figure 2.12c was used to measure shear force of conductive fibrillar adhesion to nonconducting substrated with high applied voltage. Result in Figure 2.12b showed microfibrillar structure and conductive composite material both contribute to higher shear strength with high voltage applied. Preload using electrostatics force also lead to better shear strength than comparable normal pressure preload. Even though shear force achieved is not optimal compared to other adhesive system, using electrostatics to enhance adhesion strength explore a novel perspective of improving gecko adhesives performance.

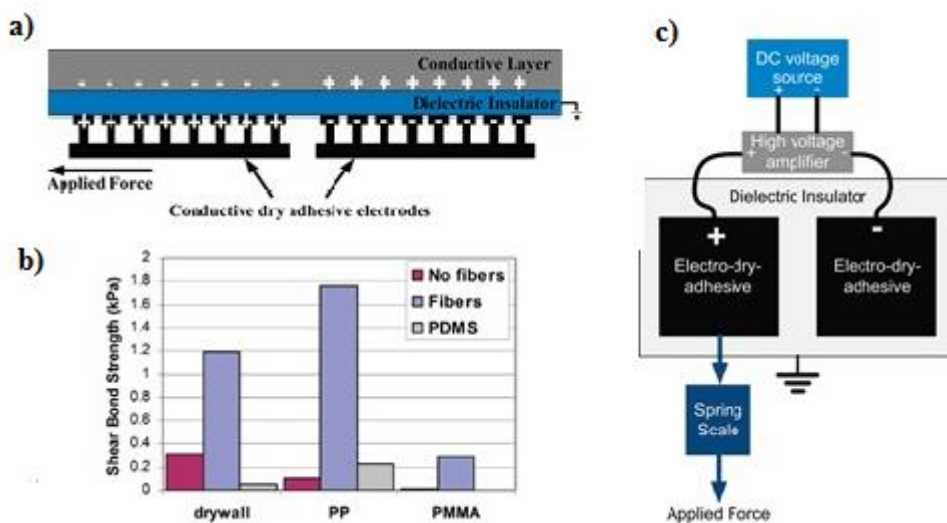


**Figure 2.12.** a) Illustration of two conductive dry adhesive electrodes generate attractive electrostatic force to substrate when applied voltage. b) Shear bond strength of fiber

conductive, flat conductive and fiber nonconductive PDMS samples to different substrates with applied voltage. c) Experiment setup to measure shear force with applied voltage. Reprinted with permission<sup>61</sup> Copyright 2012 American Chemical Society.

#### **2.4.5 Shape Memory Fibrillar Reversible Adhesives**

Kim et al. produced a novel microfibrillar reversible adhesive system by coating a continuous thin layer adhesive polymers onto shape memory polymers (SMP) microfibrillar array using a dipping and cure method.<sup>62</sup> The thin layer AP-coated SMP microfibrillar array showed 4 times weaker peeling strength at 80 °C than room temperature. Deformation of adhesive during peeling can recover thermally due to the shape memory properties. Fibrillar structure was also proved to enhanced rough surface adaptation.

From the leading edge of developing gecko inspired fibrillar adhesives, we can draw the conclusion that combining other concept of adhesion and interactions is the way out for conquering the limitations of existing fibrillar surface. Uniting external boost of molecular interaction other than the weak van der Waals force with large contact areas, elavation of adhesion strength is expected as “geckel” system<sup>22</sup> showed enhanced adhesion performance. Furthermore, adaptation and responsiveness to different conditions can be expanded due to the nature of the additional interactions. A new direction could involve incorporating reversible chemical reaction functional group on fibrillar surface to gain more adhesion strength while introduce thermal/photo responsiveness of reversibility. Other noncovalent interations like hydrogen bonding and ion interactions are also promising on giving thermal and solvent detachment mechanism. However, the fabrication may become complex due to the necessity of coating both adhesive and substrate surface. Using



polymeric materials that have both optimal mechanical property and functional moiety to provide extra enhancement to adhesion strength will be a challenging while promising route of improving fibrillar surface adhesives. The next section will be focusing on studies of some very promising hydrogen bonding adhesive system.

## 2.5 *Hydrogen Bonding Based Reversible Adhesives*

Hydrogen bonding is a directional attractive force between hydrogen bonding donor and acceptor with a medium strength stronger than van der Waals force while weaker than covalent bonds. The nature of thermal and solvent reversibility makes it a versatile tool of incorporating reversibility into smart materials like self-healing<sup>33</sup>, self-assembly<sup>93</sup> and stimuli responsive materials<sup>94</sup>. Having multiple hydrogen bonding donors and acceptors on one molecule creates complementary multiple hydrogen bondings (CMHB) with higher association constant than single hydrogen bonding unit. Nucleobase pairs are natural examples of CMHB: double hydrogen bonding between adenine and thymine (uracil); triple hydrogen bonding between cytosine and guanine (Figure 2.13a).<sup>95</sup> There are also many synthetic CMHB for preparing supramolecular polymers<sup>96-98</sup>, for example, Meijer's 2-ureido-4[1H]-pyrimidinone (UPy) quadruple unit which can self-dimerize with high association constant in Figure 2.13b.<sup>96</sup> Our group has been focusing on designing novel reversible adhesive and investigating the effect of incorporating hydrogen bonding on adhesive performance.

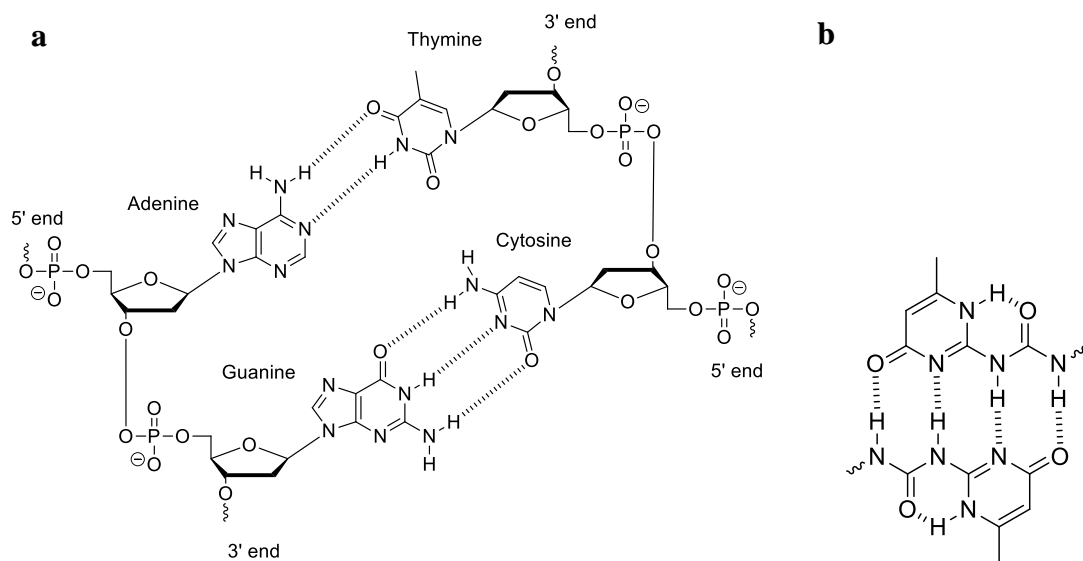
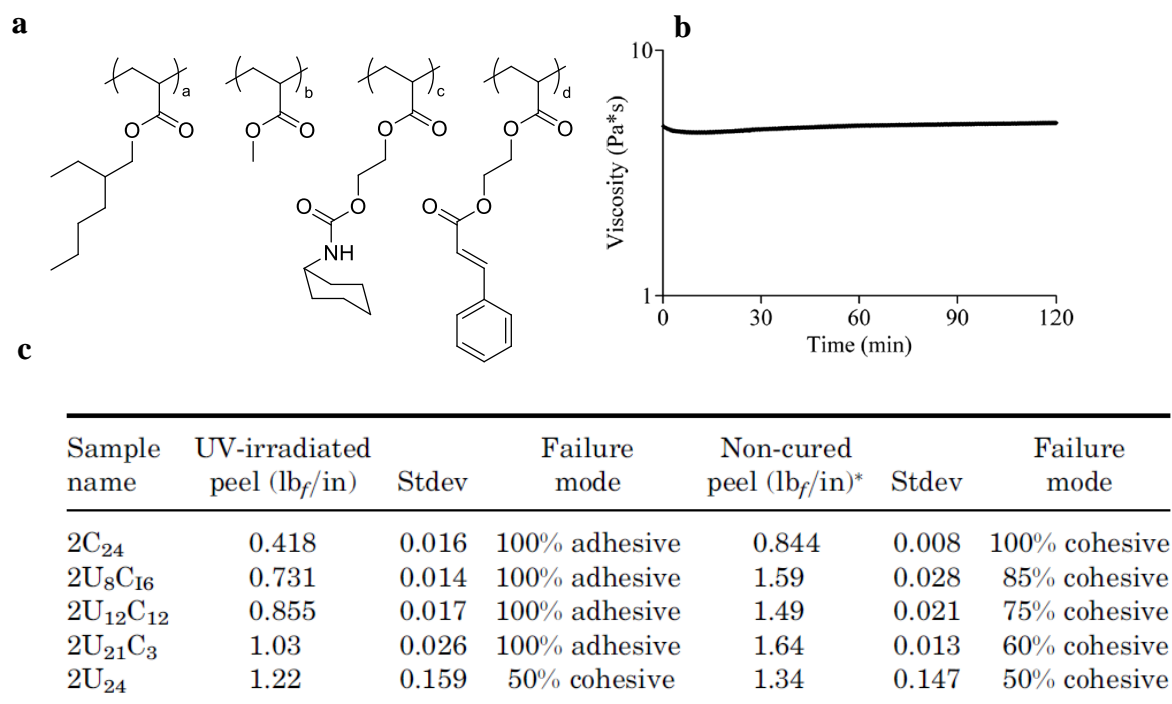


**Figure 2.13.** a) Chemical structure of double strand DNA showing nucleobase pairs of adenine/thymine and cytosine/guanine. Reprinted with permission<sup>95</sup> Copyright 2012 WILEY-VCH Verlag GmbH & Co. KGaA, Weinhei. b) Hydrogen bonding self-dimerization of UPy group.

### 2.5.1 Acrylic Reversible Adhesives

Acrylic copolymers are widely used in adhesives manufacturing because of the low  $T_g$  and sufficient tackiness without additives. Long *et al.* copolymerized nBA with UPy-methacrylate to synthesize a novel reversible adhesive.<sup>37</sup> 3.3 mol % of Upy-containing monomer in nBA resulted in triple peel strength with glass substrate compared to PBA, which can be attributed to hydrogen bonding with substrate and increased apparent molecular weight. Melt viscosity dropping at 80 °C suggested the thermal reversibility, while solution viscosity and thin-layer chromatography indicated the solvent reversibility potential of this copolymer system. With a recent study of spacer length effect on the CMHB efficiency<sup>99</sup>, we can possibly increase the peel strength by changing to a longer spacer between the Upy and the polymer backbone.

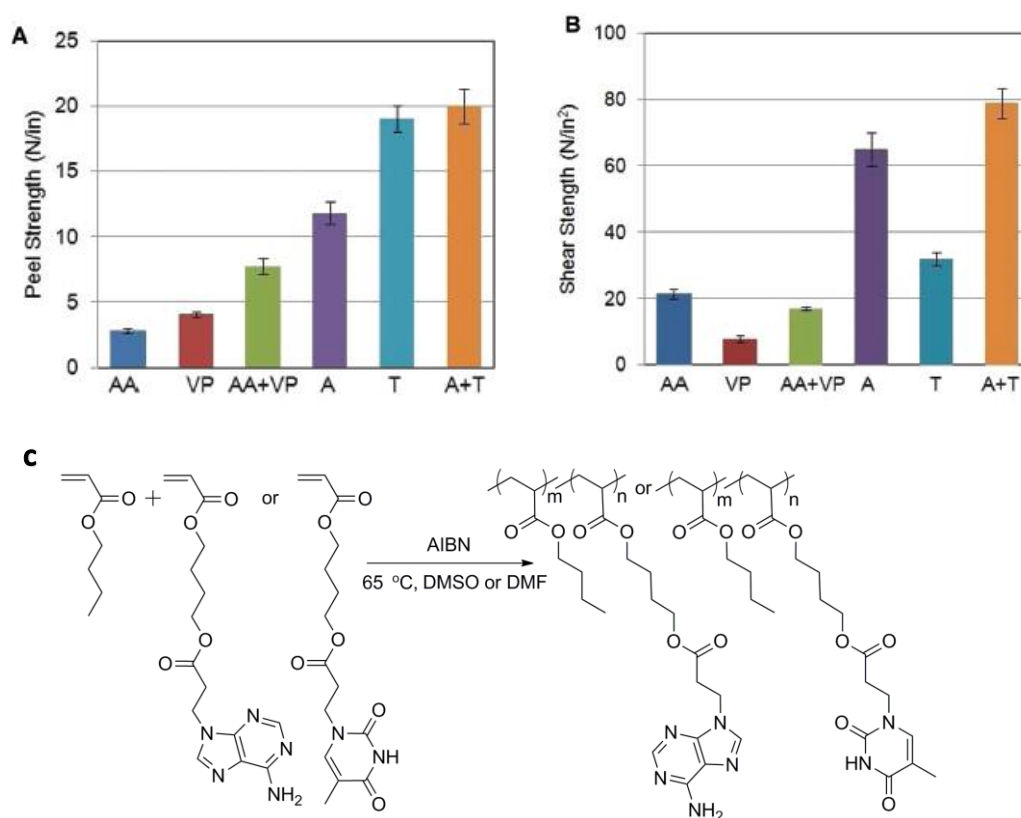
Long *et al.* later reported acrylic copolymer adhesives that took advantage of the synergistic effect of hydrogen bonding and photo reversible reaction. Urethane and cinnamate group were used as hydrogen bonding and photocrosslinking sites respectively, as shown in Figure 2.14a. High content of urethane groups assisted photo dimerization rate of cinnamate for bringing in a proximity benefit. Hydrogen bonding enhanced the adhesive strength of UV-cured sample, while photocrosslinking of cinnamate enhanced the cohesive strength and reduced adhesive strength. The content of hydrogen bonding and photocrosslinking groups can serve as two parameters to tune the adhesives performance (Figure 2.14c). Thermally dissociation of hydrogen bonding provides low viscosity for melt processing and reversibility. High melt stability from the isothermal rheology test also makes the copolymer system a strong candidate for hot melt pressure sensitive adhesives (Figure 2.14b).



**Figure 2.14.** a) Chemical structure of cinnamate and urethane containing acrylic copolymers as HMPSA. b) Isothermal melt rheology at 150 °C for 2h. c) Peeling strength and failure mode of cinnamate and urethane containing acrylic copolymers. Reprinted with permission<sup>38</sup> Copyright 2009 Taylor & Francis.

Recently, Long *et al.* presented novel nucleobase-containing acrylic supramolecular adhesives with chemical structure shown in Figure 2.15.<sup>35</sup> Adenine-containing copolymer (A) showed microphase separated with needle-like structure of the hard phase which was attributed to the more pronounced  $\pi$ - $\pi$  stacking of the aromatic adenine ring than thymine-containing copolymer (T). CMHB between pendant adenine and thymine moiety significantly enhanced the peel and shear strength between two copolymers, compared to the adhesion performance of single copolymer and single hydrogen bonding copolymers: poly(acrylic acid) (AA) and 4-vinylpyridine (VP) based copolymers. The strong CMHB acts as physical crosslinking to increase apparent

molecular weight which results in enhanced adhesive properties. More study on explaining the mechanism behind the difference performance of single nucleobase adhesive and reversibility are being pursued in our laboratory. However, one can speculate the adhesion strength of A+T would decrease when heated above the hydrogen bonding dissociation temperature based on the variable temperature (VT) Fourier Transform Infrared spectra (FT-IR), which showed the stretching vibration of hydrogen bonded carbonyl peak disappearance upon heating.



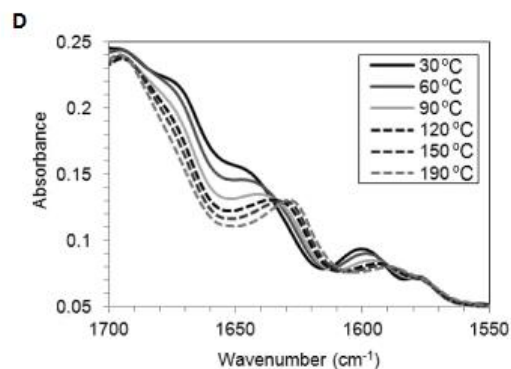


**Figure 2.15.** A) Peel and B) shear strength of nucleobase-containing copolymers and control of AA and VP containing copolymers. C) Reaction scheme of copolymerization of *n*BA and acrylic adenine/thymine. D) VT FT-IR for the complex of A and T. Reprinted with permission<sup>35</sup> Copyright 2012, American Chemical Society.

The relatively weak single hydrogen bonding can be compensated with increased quantity of hydrogen bonding groups. Wang and Xie designed a reversible adhesive using shape memory-epoxy with dense hydroxyl groups and nitrogen atoms in the material.<sup>40</sup> Extraordinary high adhesion force ( $453 \text{ N/cm}^2$ ) was achieved with preload pressure at  $90^\circ\text{C}$  (above  $T_g$ ) aided by low amount of methanol and cooling with load. Heating to  $90^\circ\text{C}$  again decrease the peeling force to  $0.2 \text{ N/cm}^2$ . The shape memory property of epoxy recovered the deforming during heating and preserved the original adhesion strength to 67% after two cycles. Incorporating more hydrogen bonding groups through grafting polyethyleneimine on epoxy surface resulted in a  $640 \text{ N/cm}^2$  pulling off strength and pH dependence with strong adhesion after treatment with acid solution. This study certainly illustrates the power and potential of hydrogen bonding containing adhesives with comparable adhesion strength to conventional liquid adhesive and superior reversibility for a variety of applications.

## 2.5.2 Solvent Reversible Adhesion

Solvent reversible adhesion is also an important aspect of hydrogen bonding containing polymers, especially for applications that require temperature like human skin. Based on the previous work of a photo-crosslinked poly(D,L-lactide)s network to be used potentially as bioadhesive<sup>36</sup>, Long *et al.* introduce reversibility to the network via changing to hydrogen bonding as a physical crosslinking method.<sup>100</sup> Biocompatible star-shaped poly(D,L-lactide)s (PDLLA) were end capped with adenine and thymine using Michael addition. Solution viscosity increased significantly when mixing polymers with two complementary nucleobases in nonpolar solvent, followed by a decrease to original range when polar solvent were added to disrupt the hydrogen bonding (Figure 2.16a). Moreover, <sup>1</sup>H NMR shift as function of temperature demonstrated the thermal reversibility of H-bonded network (Figure 2.16b). This study points out a promising direction of designing biomedical adhesives through crosslinking of star-shaped low molecular weight precursors with end hydrogen bonding groups, which will be removable upon contact of water.

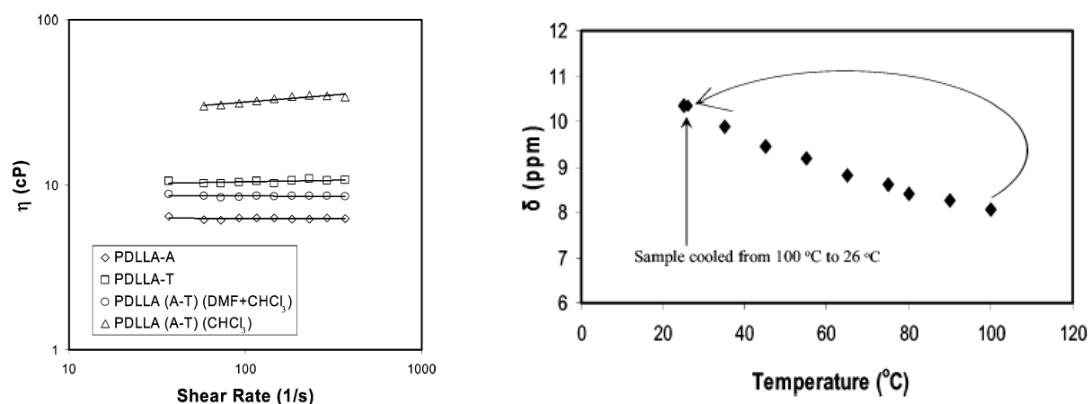


**Figure 2.16.** a) Solution viscosities of star-shaped PDLLA end functionalized with adenine/thymine and their 1:1 mixture in CHCl<sub>3</sub> and CHCl<sub>3</sub>/DMF. b) <sup>1</sup>H NMR NH

chemical shift of PDLLA-AT mixture vs temperature. Reprinted with permission<sup>100</sup>  
Copyright 2006 American Chemical Society.

Hydrogen bonding of nucleobase pair can also be used to design solvent reversible adhesion. Viswanathan and Long illustrated the solvent reversibility of the adhesion between terminal thymine-functionalized polystyrenes (PS-T)<sup>101</sup> and silicon surface that covalently modified with adenines.<sup>39</sup> Binding was specific and reversible confirmed with water contact angle measurement and X-ray photoelectron spectroscopy (XPS) in multiple solvent treatment cycles, shown in Figure 2.17. Herein, covalent coating of surface with hydrogen bonding groups was proved to be a possible method to adhere materials reversibly and selectively. Potential applications also exist in biomedical field, column chromatography and molecular recognition.



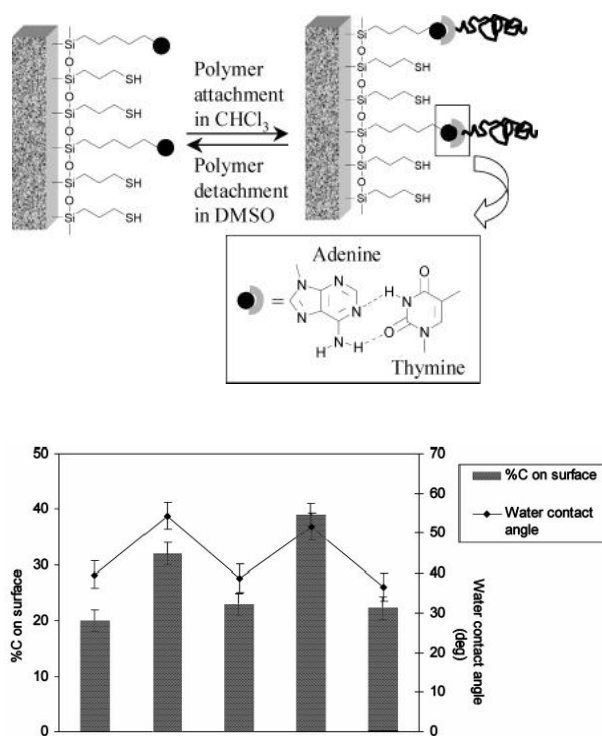


**Figure 2.17.** a) Scheme of solvent reversible adhesion of PS-T to adenine modified silicon surface. b) Water contact angle and XPS result of silicon surface upon solvent wash cycles of PS-T treatment/wash and DMSO rinse. Reprinted with permission<sup>39</sup> Copyright 2006 American Chemical Society.

Even though most of the results are preliminary studies, they all show the advantages and possibility of incorporating hydrogen bonding groups into adhesives. With relatively strong physical interactions, adhesion on the interface rises due to the additional holding force preventing break on interface. Moreover, increasing apparent molecular weight and networking forming increase the  $T_g$  and modulus of the adhesive material itself which could lead to improved cohesive strength. Hydrogen bonding also brings in thermal and solvent reversibility which ensure easy detachment upon heating and polar aprotic solvent rinsing. Resistance to moisture could be an extra advantage if adhesive is

hydrophobic like acrylates. Hydrogen bonding on the interface could be protected by water repelling acrylates if sufficient contact can be guaranteed with preload force, while speculation still needs evidence.

## 2.6 *Other Method of Introducing Reversibility*

There are some other methods of introducing reversibility in adhesives. Luo et al. presented a uniquely designed thermal reversible composite adhesive.<sup>64,65</sup> The blend of poly(3-caprolactone) (PCL) and epoxy precursor formed a “bricks-and-mortar” morphology through polymerization-induced phase separation (Figure 2.18A). When heated above the melting point of PCL for enough period of time under preload, the rigid composite adhesives wet the surface and formed a PCL thin layer at the interface due to the “differential expansive bleeding (DEB)” which is termed for the PCL volume expansion in excess of epoxy components. Cooling resulted in strong adhesive and cohesive strength as the thin layer of PCL provides good wetting and high modulus crystalline with highest pull-off strength to be about 9MPa. Melting of PLC thin layer at 80 °C resulted in easy detachment of adhesives. Xie et al. also designed a reversible composite adhesive using a special shape memory polymer layer with small curvature and a low  $T_g$  intrinsic sticky adhesive layer.<sup>63</sup> Preloading at 90 °C deformed the composite adhesive to comply with substrate surface, resulting in 60 N/cm<sup>2</sup> pull-off strength. Repeated heating to 90 °C recovered the curved structure, correspondingly minimized the contact area and decrease the pull-off force to 10% of the original. Schematic illustration is shown in Figure 2.18E.

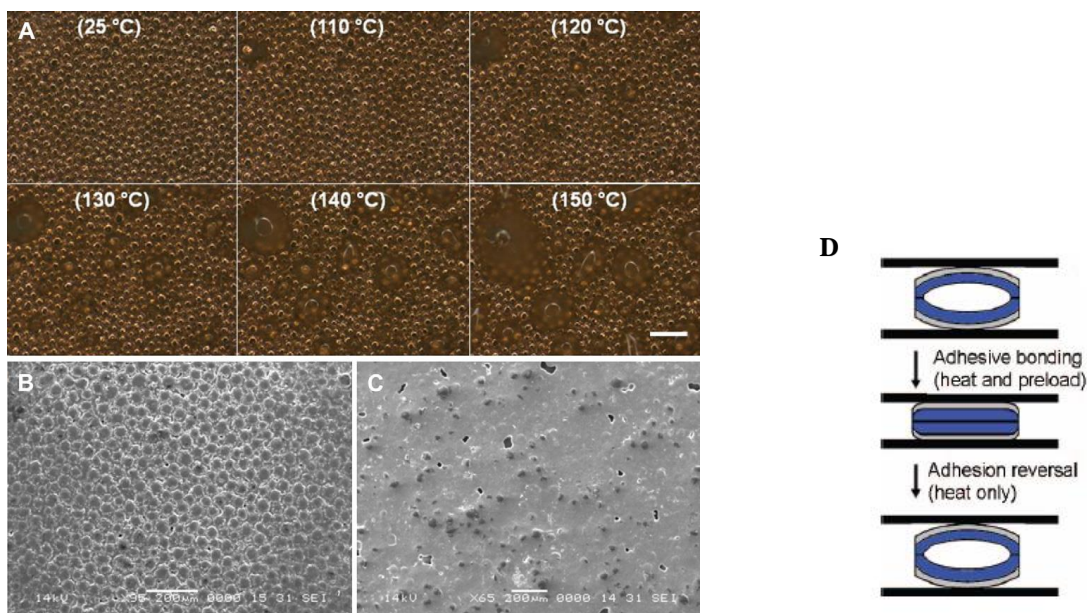


**Figure 2.18.** A) Stereo optical microscope images of DEB phenomenon at different temperatures of the Epoxy/PLC surface. B) and C) Scanning electron microscope (SEM) images of Epoxy/PLC surface before and after heating. Reprinted with permission<sup>65</sup> Copyright 2010 Elsevier. D) Scheme of reversible adhesion of SMP-based composite adhesives. Reprinted with permission<sup>63</sup> Copyright 2008, American Chemical Society.

Kobayashi studied reversible adhesion of positively and negatively charged polyelectrolytes brushes prepared with surface initiated polymerization on substrates.<sup>66</sup> Small amount of deionized water generated strong binding of two oppositely charge surface with a lap shear rate of 1.5 MPa. NaCl solution easily separated the surface through screening charges interactions. Polyelectrolytes remained on original surface in both detaching mechanism which proved the capability to go through multiple attaching and detaching cycles. La Spina et al. also reported switchable adhesion of a polyacid gel to polybase grafted substrate. The environmental pH value served as mechanism for reversible adhesion in this study.<sup>102</sup>

## 2.7 *Conclusion*

With the potential to recycle, repair, and reuse, reversible adhesives have received significant attention from chemists, engineers, and material scientists. Achievements in fabricating reversible adhesive and surface adhesion so far mainly include three routes: reversible chemical reaction, biomimetic reversible system, which is primarily based on van der Waals interaction, and hydrogen bonding-containing polymers. The reversibility of chemical reactions can result in significant adhesion strength difference with certain thermal, photo, and redox external condition changes. Researchers successfully incorporated thermal reversible Diel Alder adducts and photoresponsive cyclobutane groups to achieve reversible adhesion, which is attributed to molecular weight changing or crosslink network forming. While the development of gecko-inspired fibrillar adhesive seems to reach a bottleneck of fabricating complicated hierarchy structure, new directions of utilizing additional mechanism of adhesion open another window to enhanced adhesion strength as well as simplified manufacture. Uniting other noncovalent interactions and special shape design of adhesive materials not only overcomes the weakness from van der Waals nature of original gecko adhesives, but also introducing new detaching mechanism while maintaining weak peel strength for single fiber compared to overall adhesion strength. Incorporating hydrogen bonding enhances both interfacial adhesion strength and internal cohesive strength of the adhesive materials. Having multiple hydrogen acceptors and donors on one CMHB unit provides strong and specific interactions which further improve the apparent molecular weight and form network. Researchers further demonstrated large number of hydrogen bonding compensated relatively weak hydrogen bonding. Thermal

and solvent reversibility from hydrogen bonding provide detaching mechanism for adhesives and surface adhesion.

## 2.8 **References**

1. Onusseit, H.; Wefringhaus, R.; Dreezen, G.; Wichelhaus, J.; Schall, J.; Thiele, L.; van Halteren, A. In *Ullmann's Encyclopedia of Industrial Chemistry*; Wiley-VCH Verlag GmbH & Co. KGaA: 2000.
2. Puligadda, R.; Pillalamarri, S.; Hong, W.; Brubaker, C.; Wimplinger, M.; Pargfrieder, S. *Mater. Res. Soc. Symp. Proc.* 2007, 970, 239.
3. Niklaus, F.; Stemme, G.; Lu, J.-Q.; Gutmann, R. J. *J. Appl. Phys.* 2006, 99, 031101.
4. Zussman, M.; Milasincic, C.; Rardin, A.; Kirk, S.; Itabashi, T. *Journal of Microelectronics and Electronic Packaging* 2010, 7, 214.
5. García, J. M.; Jones, G. O.; Virwani, K.; McCloskey, B. D.; Boday, D. J.; ter Huurne, G. M.; Horn, H. W.; Coady, D. J.; Bintaleb, A. M.; Alabdulrahman, A. M. S.; Alsewailem, F.; Almegren, H. A. A.; Hedrick, J. L. *Science* 2014, 344, 732.
6. Long, T. E. *Science* 2014, 344, 706.
7. Creton, C. *MRS Bull.* 2003, 28, 434.
8. Chang, E. P. *J. Adhes.* 1991, 34, 189.
9. Satas, D. *Handbook of pressure sensitive adhesive technology*; Satas & Associates Warwick, RI, 1999.
10. Creton, C.; Papon, E. *MRS Bull.* 2003, 28, 419.
11. Committee, A. I. H. *Engineered Materials Handbook: Adhesives and Sealants*; CRC, 1990; Vol. 3.
12. Kaur, G.; Johnston, P.; Saito, K. *Polym. Chem.* 2014, 5, 2171.
13. Davis, D. A.; Hamilton, A.; Yang, J.; Cremar, L. D.; Van Gough, D.; Potisek, S. L.; Ong, M. T.; Braun, P. V.; Martinez, T. J.; White, S. R.; Moore, J. S.; Sottos, N. R. *Nature* 2009, 459, 68.
14. Zhang, C.; Orosco, M. M.; Yu, X.; Kirkbir, F. N.; Thompson, M. E.; Alfred E. Mann Institute for Biomedical Engineering At the University of Southern California, USA . 2012, p 31pp.
15. Anumolu, S. S.; Menjoge, A. R.; Deshmukh, M.; Gerecke, D.; Stein, S.; Laskin, J.; Sinko, P. J. *Biomaterials* 2011, 32, 1204.
16. Kim, S.; Wu, J.; Carlson, A.; Jin, S. H.; Kovalsky, A.; Glass, P.; Liu, Z.; Ahmed, N.; Elgan, S. L.; Chen, W.; Ferreira, P. M.; Sitti, M.; Huang, Y.; Rogers, J. A. *Proc. Natl. Acad. Sci. U. S. A.* 2010, 107, 17095.
17. Zhang, K.; Aiba, M.; Fahs, G. B.; Hudson, A. G.; Chiang, W. D.; Moore, R. B.; Ueda, M.; Long, T. E. *Polym. Chem.* 2015, 6, 2434.
18. Zhang, K.; Fahs, G. B.; Aiba, M.; Moore, R. B.; Long, T. E. *Chem. Comm.* 2014, 50, 9145.
19. Geim, A. K.; Dubonos, S. V.; Grigorieva, I. V.; Novoselov, K. S.; Zhukov, A. A.; Shapoval, S. Y. *Nat Mater* 2003, 2, 461.
20. Hawkes, E. W.; Eason, E. V.; Christensen, D. L.; Cutkosky, M. R. *Human climbing with efficiently scaled gecko-inspired dry adhesives*, 2015; Vol. 12.

21. Bartlett, M. D.; Croll, A. B.; King, D. R.; Paret, B. M.; Irschick, D. J.; Crosby, A. *J. Adv. Mater. (Weinheim, Ger.)* 2012, *24*, 1078.
22. Lee, H.; Lee, B. P.; Messersmith, P. B. *Nature (London, U. K.)* 2007, *448*, 338.
23. Diels, O.; Alder, K. *Justus Liebigs Ann. Chem.* 1928, *460*, 98.
24. Tasdelen, M. A. *Polym. Chem.* 2011, *2*, 2133.
25. Bergman, S. D.; Wudl, F. *J. Mater. Chem.* 2008, *18*, 41.
26. Toncelli, C.; De, R. D. C.; Picchioni, F.; Broekhuis, A. A. *Macromol. Chem. Phys.* 2012, *213*, 157.
27. Gandini, A.; Belgacem, M. N. *ACS Symp. Ser.* 2007, *954*, 280.
28. Froimowicz, P.; Frey, H.; Landfester, K. *Macromol. Rapid Commun.* 2011, *32*, 468.
29. Wu, Y.; Tesoro, G.; Engelberg, P. I. *Polym. Prepr. (Am. Chem. Soc., Div. Polym. Chem.)* 1991, *32*, 140.
30. Anumolu, S. N. S.; Menjoge, A. R.; Deshmukh, M.; Gerecke, D.; Stein, S.; Laskin, J.; Sinko, P. J. *Biomaterials* 2010, *32*, 1204.
31. Trenor, S. R.; Shultz, A. R.; Love, B. J.; Long, T. E. *Chem. Rev. (Washington, DC, U. S.)* 2004, *104*, 3059.
32. Sivakova, S.; Rowan, S. J. *Chem. Soc. Rev.* 2005, *34*, 9.
33. Burattini, S.; Colquhoun, H. M.; Greenland, B. W.; Hayes, W.; John Wiley & Sons Ltd.: 2012; Vol. 7, p 3221.
34. McHale, R.; O'Reilly, R. K. *Macromolecules* 2012, *45*, 7665.
35. Cheng, S.; Zhang, M.; Dixit, N.; Moore, R. B.; Long, T. E. *Macromolecules* 2012, *45*, 805.
36. Karikari, A. S.; Edwards, W. F.; Mecham, J. B.; Long, T. E. *Biomacromolecules* 2005, *6*, 2866.
37. Yamauchi, K.; Lizotte, J. R.; Long, T. E. *Macromolecules* 2003, *36*, 1083.
38. Cashion, M. P.; Park, T.; Long, T. E. *J. Adhes.* 2009, *85*, 1.
39. Viswanathan, K.; Ozhalici, H.; Elkins, C. L.; Heisey, C.; Ward, T. C.; Long, T. E. *Langmuir* 2006, *22*, 1099.
40. Wang, R.; Xie, T. *Langmuir* 2010, *26*, 2999.
41. Lehn, J. M. *Supramolecular Chemistry: Concepts and Perspectives*; VCH, 1995.
42. Alibardi, L. *Zoology (Munich, Ger.)* 2009, *112*, 403.
43. Kamperman, M.; Kroner, E.; del, C. A.; McMeeking, R. M.; Arzt, E. *Adv. Eng. Mater.* 2010, *12*, 335.
44. Kroner, E.; Kamperman, M.; Arzt, E. *Adhaes.--Kleben Dichten* 2011, *55*, 40.
45. Boesel, L. F.; Greiner, C.; Arzt, E.; del, C. A. *Adv. Mater. (Weinheim, Ger.)* 2010, *22*, 2125.
46. Jeong, H. E.; Suh, K. Y. *Nano Today* 2009, *4*, 335.
47. Kwak, M. K.; Pang, C.; Jeong, H.-E.; Kim, H.-N.; Yoon, H.; Jung, H.-S.; Suh, K.-Y. *Adv. Funct. Mater.* 2011, *21*, 3606.
48. Nicklisch, S. C. T.; Waite, J. H. *Biofouling* 2012, *28*, 865.
49. Zeng, H. *Proceedings of the Annual Meeting of the Adhesion Society* 2011, *34th*.
50. Lee, B. P.; Messersmith, P. B.; Israelachvili, J. N.; Waite, J. H. *Annu. Rev. Mater. Res.* 2011, *41*, 99.
51. Waite, J. H. *CHEMTECH* 1987, *17*, 692.
52. Lee, H.; Scherer, N. F.; Messersmith, P. B. *Proc. Natl. Acad. Sci. U. S. A.* 2006, *103*, 12999.

53. Waite, J. H. *Integr. Comp. Biol.* 2002, 42, 1172.
54. Papov, V. V.; Diamond, T. V.; Biemann, K.; Waite, J. H. *J. Biol. Chem.* 1995, 270, 20183.
55. Waite, J. H.; Tanzer, M. L. *Science (Washington, D. C., 1883-)* 1981, 212, 1038.
56. Chan, E. P.; Smith, E. J.; Hayward, R. C.; Crosby, A. J. *Adv. Mater. (Weinheim, Ger.)* 2008, 20, 711.
57. Lin, P.-C.; Vajpayee, S.; Jagota, A.; Hui, C.-Y.; Yang, S. *Soft Matter* 2008, 4, 1830.
58. Jeong, H. E.; Kwak, M. K.; Suh, K. Y. *Langmuir* 2010, 26, 2223.
59. Pang, C.; Kang, D.; Kim, T.-i.; Suh, K.-Y. *Langmuir* 2012, 28, 2181.
60. Pang, C.; Kim, T.-i.; Bae, W. G.; Kang, D.; Kim, S. M.; Suh, K.-Y. *Adv. Mater. (Weinheim, Ger.)* 2012, 24, 475.
61. Krahm, J.; Menon, C. *Langmuir* 2012, 28, 5438.
62. Kim, S.; Sitti, M.; Xie, T.; Xiao, X. *Soft Matter* 2009, 5, 3689.
63. Xie, T.; Xiao, X. *Chem. Mater.* 2008, 20, 2866.
64. Luo, X.; Ou, R.; Eberly, D. E.; Singhal, A.; Viratyaporn, W.; Mather, P. T. *ACS Appl. Mater. Interfaces* 2009, 1, 612.
65. Luo, X.; Lauber, K. E.; Mather, P. T. *Polymer* 2010, 51, 1169.
66. Kobayashi, M.; Terada, M.; Takahara, A. *Soft Matter* 2011, 7, 5717.
67. Goulet-Hanssens, A.; Lai, W. S. K.; Kennedy, T. E.; Barrett, C. J. *Biomacromolecules*, Ahead of Print.
68. Weinhold, F.; Landis, C. R. *Valency and bonding : a natural bond and orbital donor-acceptor perspective*; Cambridge University Press New York, 2005.
69. Chen, X.; Dam, M. A.; Ono, K.; Mal, A.; Shen, H.; Nut, S. R.; Sheran, K.; Wudl, F. *Science (Washington, DC, U. S.)* 2002, 295, 1698.
70. Aubert, J. H.; Sandia Corp., USA . 2003, p 10 pp.
71. Aubert, J. H. *J. Adhes.* 2003, 79, 609.
72. Wouters, M.; Burghoorn, M.; Ingenhut, B.; Timmer, K.; Rentrop, C.; Bots, T.; Oosterhuis, G.; Fischer, H. *Prog. Org. Coat.* 2011, 72, 152.
73. Trenor, S.; Long, T.; Love, B. *J. Adhes.* 2005, 81, 213.
74. Huyck, R. H.; Trenor, S. R.; Love, B. J.; Long, T. E. *J. Macromol. Sci., Part A: Pure Appl. Chem.* 2008, 45, 9.
75. June, S. M.; Suga, T.; Heath, W. H.; Long, T. E.; Lin, Q.; Puligadda, R. *J. Adhes.* 2010, 86, 1012.
76. Webster, I. *Int. J. Adhes. Adhes.* 1999, 19, 29.
77. Boyne, J. M.; Millan, E. J.; Webster, I. *Int. J. Adhes. Adhes.* 2001, 21, 49.
78. Chen, Y.; Geh, J. L. *Polymer* 1996, 37, 4481.
79. Chen, Y.; Jean, C.-S. *J. Appl. Polym. Sci.* 1997, 64, 1759.
80. Chen, Y.; Chou, C.-F. *J. Polym. Sci., Part A: Polym. Chem.* 1995, 33, 2705.
81. Chen, Y.; Chen, K.-H. *J. Polym. Sci., Part A: Polym. Chem.* 1997, 35, 613.
82. Chen, Y.; Wu, J. D. *J. Polym. Sci., Part A: Polym. Chem.* 1994, 32, 1867.
83. Itamura, S.; Yamada, M.; Tamura, S.; Matsumoto, T.; Kurosaki, T. *Macromolecules* 1993, 26, 3490.
84. Autumn, K.; Liang, Y. A.; Hsleh, S. T.; Zesch, W.; Chan, W. P.; Kenny, T. W.; Fearling, R.; Full, R. J. *Nature (London)* 2000, 405, 681.
85. del, C. A.; Arzt, E. *Macromol. Biosci.* 2007, 7, 118.
86. Arzt, E. *Mater. Sci. Eng., C* 2006, 26, 1245.

87. Greiner, C.; Wiley-Blackwell: 2010; Vol. 7, p 1.
88. Comyn, J. *Dev. Adhes.* 1981, 2, 279.
89. Yamamoto, H.; Sakai, Y.; Ohkawa, K. *Biomacromolecules* 2000, 1, 543.
90. Lee, H.; Dellatore, S. M.; Miller, W. M.; Messersmith, P. B. *Science (Washington, DC, U. S.)* 2007, 318, 426.
91. Glass, P.; Chung, H.; Washburn, N. R.; Sitti, M. *Langmuir* 2009, 25, 6607.
92. Ruffatto, D.; Parness, A.; Spenko, M. *Improving controllable adhesion on both rough and smooth surfaces with a hybrid electrostatic/gecko-like adhesive*, 2014; Vol. 11.
93. Whitesides, G. M.; Grzybowski, B. *Science* 2002, 295, 2418.
94. Brunsveld, L.; Folmer, B. J. B.; Meijer, E. W.; Sijbesma, R. P. *Chem. Rev.* 2001, 101, 4071.
95. Hemp, S. T.; Long, T. E. *Macromol. Biosci.* 2012, 12, 29.
96. Sijbesma, R. P.; Beijer, F. H.; Brunsveld, L.; Folmer, B. J. B.; Hirschberg, J. H. K. K.; Lange, R. F. M.; Lowe, J. K. L.; Meijer, E. W. *Science* 1997, 278, 1601.
97. Park, T.; Zimmerman, S. C.; Nakashima, S. *J. Am. Chem. Soc.* 2005, 127, 6520.
98. Fouquey, C.; Lehn, J. M.; Levelut, A. M. *Adv. Mater.* 1990, 2, 254.
99. De, G. T. F. A.; Kade, M. J.; Feldman, K. E.; Kramer, E. J.; Hawker, C. J.; Meijer, E. W. *J. Polym. Sci., Part A: Polym. Chem.* 2011, 49, 4253.
100. Karikari, A. S.; Mather, B. D.; Long, T. E. *Biomacromolecules* 2006, 8, 302.
101. Yamauchi, K.; Lizotte, J. R.; Long, T. E. *Macromolecules* 2002, 35, 8745.
102. La, S. R.; Tomlinson, M. R.; Ruiz-Perez, L.; Chiche, A.; Langridge, S.; Geoghegan, M. *Angew. Chem., Int. Ed.* 2007, 46, 6460.



## Chapter 3. Nucleobase-Functionalized Acrylic ABA Triblock Copolymers and Supramolecular Blends

(Published in *Polymer Chemistry* **2015**, 6, 2434)

Keren Zhang,<sup>a</sup> Motohiro Aiba,<sup>b</sup> Gregory B. Fahs,<sup>a</sup> Amanda G. Hudson,<sup>a</sup> William D. Chiang,<sup>a</sup> Robert B. Moore,<sup>a</sup> Mitsuru Ueda,<sup>b</sup> and Timothy E. Long<sup>\*a</sup>

<sup>a</sup> *Department of Chemistry, Macromolecules and Interfaces Institute  
Virginia Tech, Blacksburg, VA 24061, USA*

<sup>b</sup> *Department of Organic and Polymeric Materials, Graduate School of Science and  
Engineering, Tokyo Institute of Technology, 2-12-1, O-okayama, Meguro-ku, Tokyo 152-  
8552, Japan*

Keywords: nucleobase, RAFT polymerization, ABA triblock copolymers, noncovalent interactions, self-assembly, thermoplastic elastomer, supramolecular blend.

### 3.1 *Abstract*

Reversible addition-fragmentation chain transfer (RAFT) polymerization afforded the unprecedented synthesis of well-defined acrylic ABA triblock copolymers with nucleobase-functionalized external blocks and a central poly(*n*-butyl acrylate) (*Pn*BA) block. Size exclusion chromatography (SEC) confirmed the molecular weight and molecular weight distribution of the central block. <sup>1</sup>H NMR spectroscopy revealed the successful chain extension of the *Pn*BA macro-chain transfer agent (CTA) using adenine or thymine-functionalized acrylic monomers. The acrylic monomer with a flexible spacer to the pendant nucleobases promoted intermolecular recognition of nucleobases and long range segmental motion of polymer main chains. The external block glass transition temperatures (*T<sub>g</sub>*'s) of thymine (T) and adenine (A) functionalized blocks were 52 °C and 76 °C, respectively. Thermomechanical and morphological analysis revealed the effect of processing conditions on self-assembly and microphase-separated morphology of

nucleobase-functionalized ABA copolymers. Thymine and adenine-functionalized ABA triblocks formed a thermodynamically stable, hydrogen-bonded complex upon blending. The supramolecular blend exhibited a cylindrical microphase-separated morphology with an extended plateau window compared to the individual block copolymers. The complementary hydrogen bonding between adenine and thymine formed a thermally labile, physically crosslinked, network that exhibited enhanced mechanical performance with melt processibility. Thus, these ABA nucleobase-functionalized block copolymers demonstrate potential as thermoplastic elastomers for hot melt adhesives and coatings.

### 3.2 *Introduction*

Specific noncovalent interactions are a critical design feature for tailoring polymeric material properties.<sup>1</sup> Noncovalent interactions, including hydrogen bonding and pi-pi stacking, create supramolecular physically crosslinked networks that significantly influence polymer properties. The intermediate bond strength between van der Waals forces and covalent bonds leads to reversible bonds that respond to external stimuli such as temperature, moisture, solvent, and pH.<sup>1,2</sup> Noncovalent interactions also improve cohesive strength for adhesives,<sup>3,4</sup> enhance temperature dependence of melt viscosity,<sup>5</sup> and promote self-assembly.<sup>4-9</sup> Block copolymers containing physical crosslinking attract both academia and industry due to the potential synergy between microphase-separation and noncovalent interactions. Localized hydrogen bonding within the hard phase induces or reinforces microphase separation of block copolymers.<sup>1,10-12</sup> Long *et al.* observed a phase-separated morphology of triblock copolymers with short nucleobase external blocks of molecular weights between 1-4 kDa.<sup>12</sup> Long *et al.* also recently showed the capability of hydrogen bonding to facilitate self-assembly of ABC block copolymers.<sup>13</sup> Nowick *et al.*

and McHale *et al.* both noted enhanced molecular recognition through segregation of block copolymers in solution.<sup>14,15</sup> The commercial impact of block copolymer thermoplastic elastomers (TPEs) continues to increase, including hot melt adhesives, synthetic elastomers, automobile parts, and membranes. The past two decades have also witnessed various fundamental studies of block copolymer TPEs with structure-property relationships and emerging applications.<sup>16-21</sup> The microphase-separated morphology of block copolymers is crucial for their thermoplastic properties and elasticity. The hard phase (high  $T_g$  or semicrystalline) provides mechanical integrity, while the soft phase (low  $T_g$ ) affords flexibility. ABA triblock copolymers, such as styrene-butadiene-styrene (SBS) and styrene-isoprene-styrene (SIS), represent TPEs with wide industrial appeal due to their unique synergy of elastomeric properties and melt processibility. Noncovalent interactions have shown great potential for inducing thermal responsiveness and enhancing mechanical strength of polymers.<sup>1,5,12,22,23</sup> It is hypothesized that reversible physical crosslinking in block copolymers allows supramolecular thermoplastic elastomers with a self-assembled morphology, enhanced mechanical integrity, and tailored thermal responsiveness.

Nucleobases in deoxyribonucleic acid (DNA) exemplify biology-inspired candidates for introducing noncovalent interactions to synthetic polymers due to their thermal stability and synthetic versatility.<sup>24</sup> The unique molecular recognition between purine and pyrimidine rings is of particular interest for their potential in self-assembly, template polymerization, thermal responsiveness, and information storage.<sup>25,26</sup> Nucleobase-functionalized polymers also offer unique biological properties including selective protein adsorption, suppressed bacterial adherence, and biocompatibility.<sup>27</sup> Furthermore, nucleobase-containing polymers suggest potential as biosensors, molecular probes,

biomedicine, biomimetic information storage, and materials with enhanced mechanical properties.<sup>25,28-30</sup> However, introducing nucleobases to synthetic polymers is challenging due to their limited solubility and susceptibility to multiple substitutions during monomer synthesis.<sup>22</sup>

Most nucleobase-containing polymers in the literature are synthesized through the polymerization of nucleobase-functionalized monomers, and styrenic and methacrylic adenine/ thymine monomers are extensively described. Various controlled polymerization strategies are amendable to synthesize nucleobase-functionalized polymers, including ring-opening metathesis polymerization,<sup>31,32</sup> nitroxide mediated polymerization,<sup>12,14,33</sup> and atom transfer radical polymerization (ATRP).<sup>34-36</sup> Lutz *et al.* synthesized nucleobase-functionalized styrenic polymers and observed the association and dissociation of hydrogen bonding in solution.<sup>36,37</sup> McHale *et al.* combined segregation in solution with templating to obtain well-controlled, high molecular weight styrenic nucleobase polymers.<sup>14</sup> Our research group reported styrenic triblock copolymers with adenine and thymine external blocks and showed their potential as drug delivery vehicles and biological probes.<sup>12,33</sup> Inaki *et al.* synthesized methacrylamide adenine and uracil polymers with an ethylene spacer for template polymerization.<sup>38-40</sup> Others probed the effect of molecular recognition on copolymer composition with nonpolar and hydrogen-bonding disrupting solvent using methacrylic adenine and thymine monomers with ethylene diester spacers.<sup>30</sup> Haddleton *et al.* synthesized methacrylic and acrylic nucleoside monomers for subsequent template polymerization.<sup>29,41</sup> Other researchers synthesized and observed assembly of PEGylated methacrylic nucleobase polymer in water, and also reported nucleobase-

functionalized monomers for step-growth polymerization including norbornene derivatives.<sup>31,32,42-44</sup>

Despite the intensive research interest in nucleobase-containing polymers, most nucleobase-containing polymers mentioned above either presented sterically constrained side groups or rigid polymer backbones with  $T_g$ 's above the hydrogen bonding dissociation temperature range. Literature values for styrenic and methacrylic adenine-functionalized polymer  $T_g$ 's range from 105 °C to 204 °C; thymine-functionalized polymers show a  $T_g$  from 87 °C to 191 °C, depending on the monomer structure.<sup>12,29,30,41,45</sup> The only previously reported acrylic nucleoside homopolymers also showed  $T_g$ 's around 140-170 °C.<sup>29</sup> Steric effects and polymer chain rigidity significantly restricted molecular association and dissociation in the bulk.<sup>46</sup> This also accounts for predominate research focus in literature on supramolecular polymer self-assembly and template polymerization in solution, where solvation and mobility promote molecular recognition. Previous investigations of bulk and mechanical properties of supramolecular polymers only include telechelic polymers with physical crosslinking sites located only at the chain ends.<sup>5,47-49</sup> As a result, nucleobase-functionalized block copolymers with sufficiently low  $T_g$  backbone and less steric hindrance are of particular interest for ascertaining the influence of nucleobase pendant groups on solid-state properties.

Acrylic polymers exhibit 20-100 °C lower  $T_g$  values than their methacrylic analogs due to the absence of a pendent methyl on the backbone.<sup>50</sup> However, controlled polymerization of acrylate monomers is more challenging due to the presence of an  $\alpha$ -proton, which facilitates branching due to chain transfer to polymer.<sup>51</sup> Long *et al.* previously synthesized acrylic adenine and thymine polymers with  $T_g$  of 65 °C and 43 °C, respectively, with

flexible spacers to promote molecular recognition. Both rheological and adhesive analyses demonstrated the effect of A-T complementary hydrogen bonding on random copolymer blends due to supramolecular association in the bulk.<sup>4</sup>

This manuscript focuses on the synthesis of novel, bio-inspired, supramolecular block copolymers with well-defined compositions and nanoscale phase-separated morphologies. An optimized, two-step, RAFT polymerization afforded ABA triblock copolymers with either adenine acrylic (AdA) or thymine acrylic (ThA) external blocks and a *Pn*BA central block. The structural design of an acrylic backbone with a flexible spacer to the nucleobase pendant groups ensured sufficiently low  $T_g$ 's and flexibility for molecular recognition.<sup>4</sup> Dynamic mechanical analysis (DMA), small angle X-ray scattering (SAXS), and atomic force microscopy (AFM) revealed the effect of noncovalent interactions on block copolymer morphologies and thermomechanical properties. We further discuss the effect of processing conditions on film performance. The complementary hydrogen bonding between adenine and thymine contributed to a microphase-separated supramolecular blend with an elongated plateau region and similar melt processibility compared to the precursors. The reversible supramolecular network provided enhanced mechanical properties and thermal responsiveness.

### 3.3 *Experimental Section*

**Materials.** *n*-butyl acrylate (*n*BA, 99+%) was purchased from Aldrich and passed through a neutral alumina column before use.  $\alpha,\alpha'$ -Azobis(isobutyronitrile) (AIBN, Fluka, 99%) was recrystallized from methanol. *N,N'*-dicyclohexylcarbodiimide (DCC, 99%), 4-(dimethylamino) pyridine (DMAP,  $\geq 99\%$ ), and 1,4-butanediol diacrylate (Alfa Aesar, 99%) were used without further purification. Adenine (A, 99%), thymine (T, 99%), triethylamine

(TEA, 99%), potassium carbonate (99%), 1,6-hexanediamine (98%), 4-cyano-4-(dodecylsulfanylthiocarbonylsulfanyl)pentanoic acid (CDP, 97%), and 2,6-di-*tert*-butyl-4-methylphenol (BHT, 99%) were purchased from Aldrich and used without further purification. Hexane (HPLC grade), chloroform (CHCl<sub>3</sub>, HPLC), tetrahydrofuran (THF, HPLC grade), *N,N*-dimethylsulfoxide (DMSO, HPLC grade) and *N,N*-dimethylformamide (DMF, HPLC grade, anhydrous) were purchased from Fisher Scientific and used as received.

**Analytical Methods.** <sup>1</sup>H NMR and <sup>13</sup>C NMR spectra were collected in CDCl<sub>3</sub> or DMSO-d<sub>6</sub> on a Varian INOVA spectrometer operating at 400 MHz at 23 °C. Size exclusion chromatography (SEC) was performed using a Waters size exclusion chromatograph. The instrument was equipped with an auto sampler, three 5 μm PLgel Mixed-C columns, a Waters 2410 refractive index (RI) detector operating at 880 nm, and a Wyatt Technologies miniDAWN multi-angle laser light scattering (MALLS) detector operating at 690 nm with a flow rate of 1 mL/min at 30 °C in THF. Reported molecular weights are absolute values from the light scattering detector with dn/dc value of 0.07. Differential scanning calorimetry (DSC) was performed under a nitrogen flush of 50 mL/min at a heating rate of 10 °C/min on a TA instruments Q1000 DSC, which was calibrated using indium (mp = 156.60 °C) and zinc (mp = 419.47 °C) standards. Glass transition temperatures were measured as the midpoint of the transition in the second heating scan. DMA was conducted on a TA Instruments Q800 in tension mode at a frequency of 1 Hz, an oscillatory amplitude of 8 μm, and a static force of 0.01 N. The temperature ramp was 3 °C/min. The glass transition temperature (T<sub>g</sub>) was determined at the peak maximum of the tan δ curve. All FTIR experiments were performed using a Varian 670-IR spectrometer (DTGS detector)

with Pike Technologies variable temperature GladiATR™ attachment (Diamond crystal). The spectra were collected at 4 cm<sup>-1</sup> resolution and as an average of 32 scans. The samples were subjected to a temperature ramp of 1 °C /min, starting from 30 °C to 180 °C and FTIR spectra were collected every 10 °C beginning from 30 °C.

A Veeco MultiMode scanning probe microscope was used for tapping-mode AFM imaging. Samples were imaged at a set-point ratio of 0.60 with a magnification of 1 μm×1 μm. Veeco nanosensor silicon tips with a spring constant of 42 N/m were utilized for imaging. SAXS experiments were performed using a Rigaku S-Max 3000 3 pinhole SAXS system, equipped with a rotating anode emitting X-ray with a wavelength of 0.154 nm (Cu Kα). The sample-to-detector distance was 1600 mm, and q-range was calibrated using a silver behenate standard. Two-dimensional SAXS patterns were obtained using a fully integrated 2D multiwire, proportional counting, gas-filled detector, with an exposure time of 2 h. All SAXS data were analyzed using the SAXSGUI software package to obtain radially integrated SAXS intensity *versus* scattering vector q, where  $q = (4\pi/\lambda)\sin(\theta)$ ,  $\theta$  is one half of the scattering angle and  $\lambda$  is the wavelength of X-ray.

**Polymerization of difunctional PnBA macro-CTA.** 1,6-bis(4-cyano-4-(dodecylsulfanylthiocarbonylsulfanyl)pentanoic acid)-hexane diamide (dCDP-NH<sub>2</sub>) was synthesized according to previous literature.<sup>52</sup> DMF (13.0 g, 20 wt%), dCDP-NH<sub>2</sub> (35.6 mg, 0.4 mmol), nBA (3.2 g, 25.1 mmol), and AIBN (0.7 mg, 0.04 mmol) were charged into a single-necked Schlenk flask. The monomer: initiator: CTA ratio was 630:1:10. The flask was subjected to four freeze-pump-thaw cycles with subsequent refilling with argon. The flask was then sealed and thermostated at 65 °C for 6 h. <sup>1</sup>H NMR determined a monomer conversion of 55%. After the polymerization, residual monomer and solvent were removed by distillation.



SEC analysis in THF revealed molecular weight data  $M_n = 44.8$  kDa.  $M_w/M_n = 1.13$ . Yield was approximately 50%.

**Polymerization of adenine-functionalized ABA triblock copolymers.** AdA (613.8 mg, 1.8 mmol), AIBN (0.2 mg, 1.2  $\mu$ mol), PnBA macro-CTA (549.0 mg, 12.3  $\mu$ mol), and DMF (4.6 g, 20 wt%) were charged into a single-necked Schlenk flask and subjected to four cycles of freeze-pump-thaw and subsequent refilling with argon. The flask was then sealed and maintained at 65 °C for 6 h. The copolymer was isolated from precipitation into methanol and dried in vacuo at room temperature for 24 h. The monomer: initiator: CTA ratio was 1500:1:10.  $^1\text{H}$  NMR revealed the number-average molecular weight for each external block of poly(AdA-*b*-nBA-*b*-AdA)  $M_n = 13.8$  kDa, monomer conversion 56%, assuming an equal chain growth rate from both macro-CTA ends.

**Polymerization of thymine-functionalized ABA triblock copolymers.** ThA (613.0 mg, 1.9 mmol), AIBN (0.2 mg, 1.2  $\mu$ mol), PnBA macro-CTA (549.0 mg, 12.3  $\mu$ mol), and DMF (4.7 g, 20 wt%) were charged into a single-necked Schlenk flask and subjected to four cycles of freeze-pump-thaw and subsequent refilling with argon. The flask was then sealed and maintained at 65 °C for 6 h. The copolymer was isolated from precipitation into methanol and dried under vacuum at room temperature for 24 h. The monomer: initiator: CTA ratio was 1600:1:10.  $^1\text{H}$  NMR revealed number-average molecular weight for each external block of poly(ThA-*b*-nBA-*b*-ThA)  $M_n = 15.0$  kDa for each block, monomer conversion 56%, assuming an equal chain growth rate from both macro-CTA ends..

**Triblock copolymer films and supramolecular blend preparation.** Poly(AdA-*b*-nBA-*b*-AdA) and poly(ThA-*b*-nBA-*b*-ThA) were melt pressed at 120 °C for 1 h and annealed at 120 °C in vacuo for 24 h. poly(AdA-*b*-nBA-*b*-AdA)/poly(ThA-*b*-nBA-*b*-ThA) were also

dissolved in DMSO (2 wt% solids) at 50 °C for 18 h and casted to a Teflon<sup>®</sup> mold. A Teflon<sup>®</sup> mold was used to minimize deformation of the polymeric films during removal. The mold was placed at 80 °C for 48 h to slowly evaporate DMSO. The dried copolymer film was then annealed under vacuum at 120 °C for 24 h. To obtain the supramolecular blend, poly(AdA-*b*-nBA-*b*-AdA) (50 mg) and poly(ThA-*b*-nBA-*b*-ThA) (47 mg) (A:T=1:1) were dissolved in DMSO (5 mL) at 50 °C for 18 h and casted to a Teflon<sup>®</sup> mold, using an identical drying and annealing procedure.

### 3.4 *Results and Discussion*

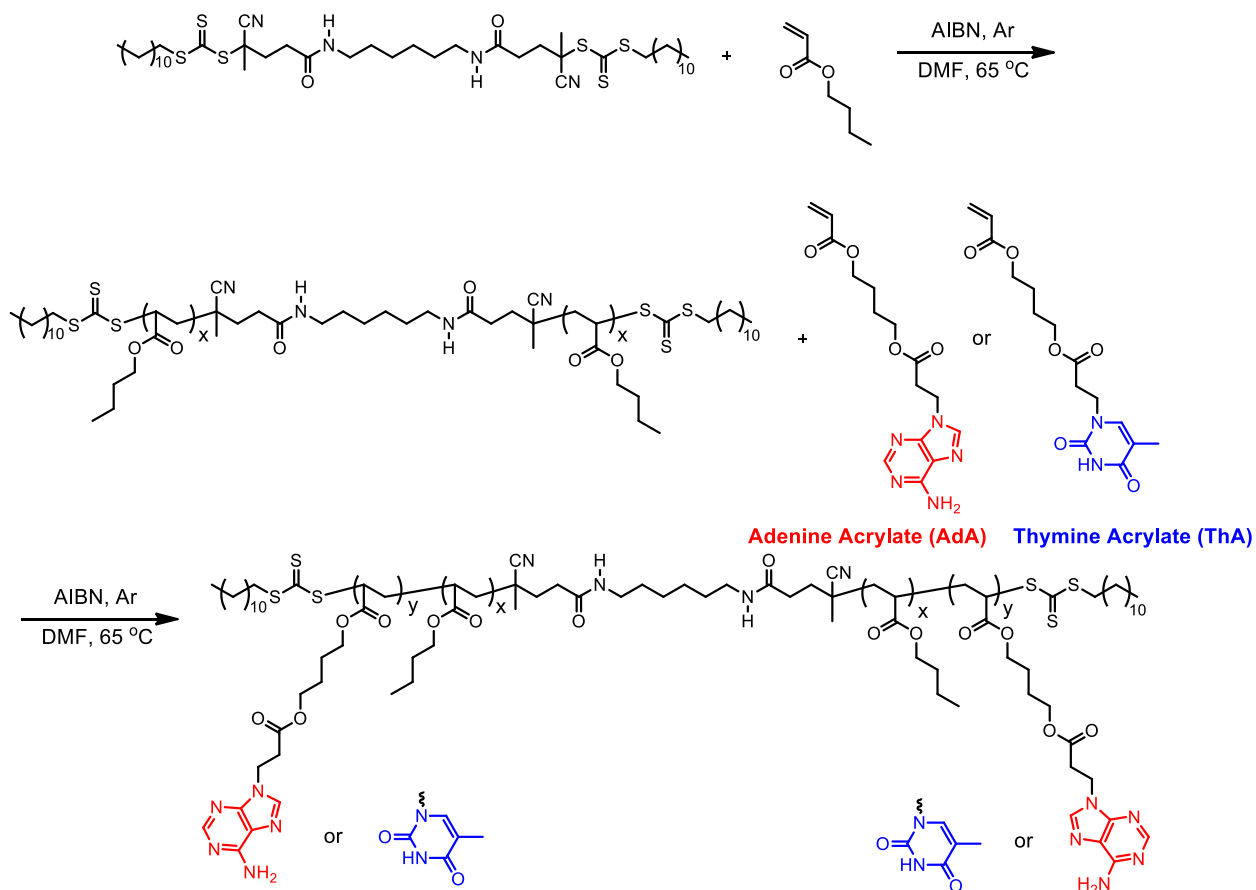
**Synthesis of acrylic ABA triblock copolymers with nucleobase-functionalized external blocks.** Controlled radical polymerization allowed the synthesis of nucleobase-functionalized ABA triblock copolymers with an acrylic backbone. Michael addition of a butanediol diacrylate with adenine or thymine afforded a convenient synthesis of the acrylic nucleobase monomers.<sup>4</sup> The acrylic backbone and flexible spacer linking the backbone to pendent nucleobases facilitated noncovalent interactions and tuned the  $T_g$ 's of the external blocks (Scheme 3.1). The butanediol spacer also promoted the solubility of nucleobase monomers in organic solvents, which allowed homogeneous copolymerization in DMF at typical concentrations.

Reversible addition-fragmentation chain transfer (RAFT) polymerization is an efficient route for synthesizing block copolymers of various compositions due to excellent functional group tolerance.<sup>53</sup> Despite the many advantages of RAFT polymerization, only a few previous reports used RAFT to synthesize nucleobase-functionalized polymers.<sup>13,14,30,54</sup> Long *et al.* previously designed and synthesized two difunctional chain transfer agents (CTA) for RAFT polymerization of ABA diblock copolymers through

divergent chain growth.<sup>52</sup> A diamide-linked difunctional CTA was used to polymerize acrylic nucleobase monomers. The difunctional CTA afforded a divergent polymerization of ABA triblock in two steps (Scheme 3.1). In the first step, dCDP-NH<sub>2</sub> controlled the polymerization of *n*BA and yielded *Pn*BA macro-initiator with absolute *M<sub>n</sub>* of 44.8 kDa and PDI of 1.13 according to SEC (Figure S3.1). Chain transfer to polymer for acrylics was suppressed due to preference for chain transfer to the CTA. Several parameters proved necessary for obtaining good control of RAFT polymerization of acrylates, including strict freeze-pump-thaw cycles, proper CTA-to-initiator ratio (10:1 for dCDP-NH<sub>2</sub>), low monomer conversion (<70%), and constant polymerization temperature. A practical threshold molecular weight for trithiocarbonate was observed near 80~100 kDa in the polymerization of acrylic monomers, where controlled polymerization diminished.

In the second step, *Pn*BA macro-initiator enabled the polymerization of nucleobase-functionalized external blocks in a divergent fashion. This divergent chain growth method eliminates possible diblock formation if cleavage of the trithiocarbonate occurs.<sup>52</sup> The diamide linker also contributed to thermal and hydrolytic stability. <sup>1</sup>H NMR spectroscopy was the primary tool for collecting structural and molecular weight information due to limited solubility of the triblock copolymers for molecular weight determination using SEC. <sup>1</sup>H NMR spectroscopic analysis of the reaction mixture immediately after polymerization provided number-average molecular weights of the nucleobase block through a comparison of monomer conversion and macroCTA molecular weight. For example, the ratio of integration of acrylic peaks (3H) at 5.8-6.4 ppm to the methylene peak (2H) adjacent to adenine at 4.2-4.4 ppm yielded a 56% conversion of the polymerization (Figure S3.2). <sup>1</sup>H NMR spectroscopic analysis of the purified copolymers determined number-average

molecular weights for the nucleobase blocks through the ratio of nucleobase to *PnBA* (Figure S3.4, S3.5). The molecular weight results of purified block copolymer products (DP<sub>2</sub> in Table S3.1) agreed with results from experimental predictions (DP<sub>1</sub> in Table S3.1). Number-average molecular weights of poly(AdA-*b-nBA-b*-AdA) and poly(ThA-*b-nBA-b*-ThA) were 27.6-44.8-27.6 kDa and 30.1-44.8-30.1 kDa, respectively. The degree of polymerization (DP) of the nucleobase-functionalized external block was calculated from the average of two calculation methods. DP of AdA external block for poly(AdA-*b-nBA-b*-AdA) was 83; DP of ThA external block for poly(ThA-*b-nBA-b*-ThA) was 93. Total number-average molecular weights of poly(AdA-*b-nBA-b*-AdA) and poly(ThA-*b-nBA-b*-ThA) were 72.4 kDa and 74.9 kDa, respectively. Similarity of the acrylic nucleobase monomers to *nBA* also eliminated possible crossover problems associated with reactivity ratio difference of monomers in controlled radical polymerization.<sup>4</sup>



**Scheme 3.1.** Synthesis of adenine- and thymine-functionalized acrylic ABA triblock copolymers using RAFT polymerization. \* For visual guidance, all adenine copolymers are labeled red; thymine copolymers are labeled blue.

**Hydrogen bonding between monomers using NMR titration.** NMR titration is a common tool to monitor reversibility of hydrogen bonding and supramolecular assembly.<sup>1,55-58</sup> NMR titration experiments at 22 °C for the AdA and ThA monomers quantified the association constant for their complementary hydrogen bonding. The concentration of ThA monomer (guest) in CDCl<sub>3</sub> remained constant while the concentration of AdA monomer (host) varied. Actual AdA concentration was calculated from the ratio of AdA to ThA in CDCl<sub>3</sub>. The hydrogen bonded proton resonance for ThA shifted from high field to low field with increasing AdA concentration (Figure S3.6). The

Connors' method provided a more accurate calculation using a non-linear fitting compared to the commonly used Benesi-Hildebrand model.<sup>58,59</sup> Figure 3.1 depicts a plot of the concentration of AdA versus the chemical shift changes ( $\delta_i$ ) of ThA hydrogen bonded proton, and non-linear fitting determined the binding constant ( $K$ ) to be  $128 \text{ M}^{-1}$  using equation (1).  $[H]_0$  and  $[G]_0$  represent the concentration of AdA (host) and ThA (guest), respectively.  $\delta_i$  is the difference between the chemical shift of observed ThA and the free ThA;  $\delta_c$  is the difference between the chemical shift of completely bonded ThA and free ThA. The binding constant of AdA and ThA agreed well with literature values.<sup>56,60</sup> The acrylic substitution on the nucleobase did not interfere with complementary hydrogen bonding between the AdA and ThA monomers.

$$[H]_0 = \frac{\frac{1}{K} - [G]_0 \left( \frac{\delta_i - 1}{\delta_c} \right)}{\frac{\delta_c}{\delta_i} - 1} \quad (1)$$

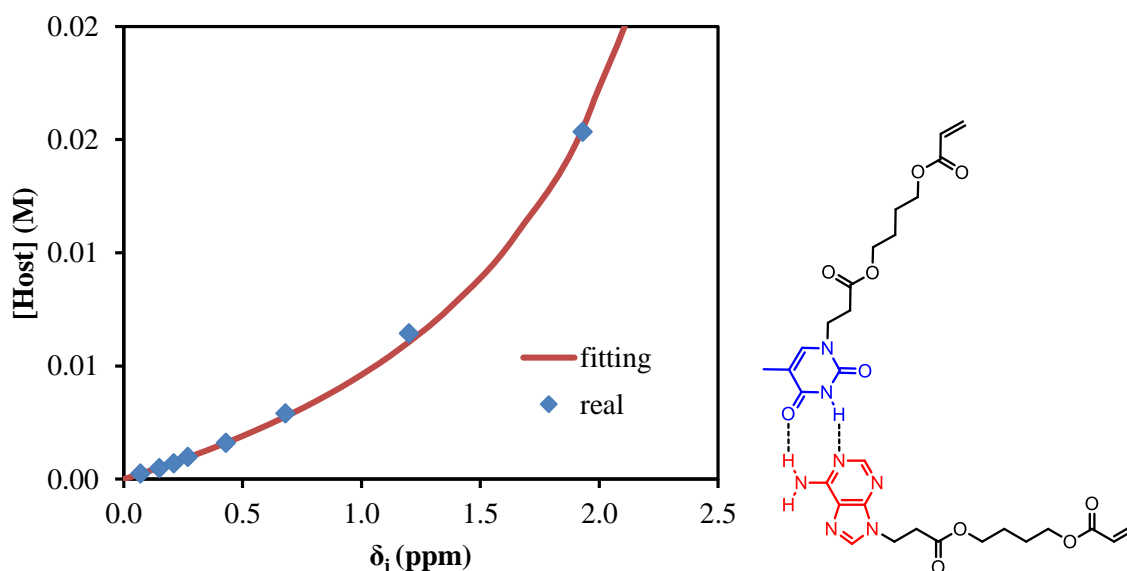


**Figure 3.1.** Non-linear fitting of NMR titration results to determine the binding constant of AdA and ThA in  $\text{CDCl}_3$  at  $22^\circ\text{C}$ .

**Thermal Transitions.** In the design of amorphous TPEs, the hard-soft-hard triblock copolymer structure is essential for mechanical integrity and elasticity. The application temperature window for TPEs lies between the  $T_g$  of the hard external blocks, which afford mechanical integrity, and the soft central block, which provides flexibility.<sup>20</sup> The nucleobase-functionalized ABA triblock copolymers contained acrylic adenine or thymine external blocks designed as the hard blocks and *PnBA* central block for the soft block. DSC determined  $T_g$ 's of poly(ThA-*b-nBA-b*-ThA) to be -40 °C and 52 °C, and  $T_g$ 's of poly(AdA-*b-nBA-b*-AdA) to be -39 °C and 76 °C (Figure S3.7). The presence of two  $T_g$ 's confirmed a block structure of the nucleobase-functionalized copolymers. The similar lower  $T_g$ 's for both ABA triblock copolymers corresponded to *PnBA* block, while the higher  $T_g$ 's correlated well with the previously reported homopolymers  $T_g$ 's.<sup>4</sup> The soft blocks  $T_g$ 's were slightly higher than poly*nBA* homopolymer  $T_g$  (-47 °C) due to phase mixing of the soft and hard phases, which was confirmed in mechanical analysis. The hard blocks  $T_g$ 's were slightly higher than the reported homopolymers  $T_g$ 's, which was presumably attributed to molecular weight differences of the nucleobase blocks from previously reported homopolymers.<sup>4</sup> The  $T_g$  difference between adenine and thymine blocks resulted from the bulkier pyrimidine structure and additional pi-pi stacking of adenine. Self-association of adenine is stronger than thymine despite their similar self-hydrogen bonding constants.<sup>60</sup> This structural difference also affected self-assembly and morphology, which is discussed below. TGA showed 5 wt% loss temperatures of poly(AdA-*b-nBA-b*-AdA) and poly(ThA-*b-nBA-b*-ThA) to be 282 °C and 285 °C, respectively, which demonstrated their thermal stability for high temperature applications such as hot melt adhesives and injection molding (Figure S3.8). To the best of our

knowledge, the acrylic nucleobase block copolymers showed the lowest  $T_g$ 's among all previously reported nucleobase-functionalized polymers.

**Thermomechanical analysis.** All triblock copolymer films showed superior mechanical integrity compared to diblock copolymers with similar nucleobase content and molecular weight. Poly(*n*BA-*b*-AdA) and poly(*n*BA-*b*-ThA) synthesized using a monofunctional CTA did not form free-standing films. As expected, the hard-soft-hard block copolymer structure proved crucial for TPE behavior. Higher  $T_g$  external blocks anchored both ends of the polymer chain, while the soft central block provided flexibility. Two different processing methods prepared block copolymer films with an identical annealing procedure. Both melt-pressed and solution-cast copolymer films exhibited microphase-separation in their thermomechanical analysis and surface morphology (Figures 3.2, 3.3a-d). In Figure 3.2, the first transition in the storage modulus-temperature curve and the first tan delta peak from the lowest temperature corresponded to the glass transition of the soft phase, followed by a plateau region where modulus remained constant with temperature. The bright and dark regions related to hard and soft phases, respectively, in AFM phase images (Figure 3.3). Both processing conditions resulted in self-assembled, microphase-separated ABA triblock copolymer films. However, DMA and AFM revealed significant morphological and mechanical differences, presumably resulting from differing processing conditions. In Figure 3.2, the solution-cast films showed higher plateau moduli on storage modulus curves compared to the melt-pressed analogs for both copolymers. The tan delta curves and AFM images (Figures 3.3a-d) also indicated more defined microphase-separation with slow evaporating solvent. Soft phase  $T_g$  (tan delta peak) of melt-pressed poly(ThA-*b*-*n*BA-*b*-ThA) and poly(AdA-*b*-*n*BA-*b*-AdA) films were -19 °C and -17 °C,



which were higher than solution-cast samples. Restricted mobility and shorter self-assembly time in the melt impeded phase separation compared to solution. A mixed soft phase that contained both nucleobase and PnBA blocks resulted in a higher soft block  $T_g$  and a lower plateau modulus, forming a kinetically trapped morphology. Further annealing at 120 °C for 5 d did not have a significant impact on the partially mixed phase separation for the melt-pressed samples. Chain mobility and time are keys to the self-assembly kinetics of block copolymers in the presence of physical crosslinks. Intermolecular hydrogen bonding also presumably further restricted chain mobility even at the annealing temperature. As a polar solvent and a hydrogen bonding acceptor, DMSO dilutes hydrogen bonding groups and screens intermolecular hydrogen bonding. Proper solvent was necessary to disrupt physical crosslinking and facilitate self-assembly. The self-assembled morphology significantly affected mechanical properties as temperature increased.

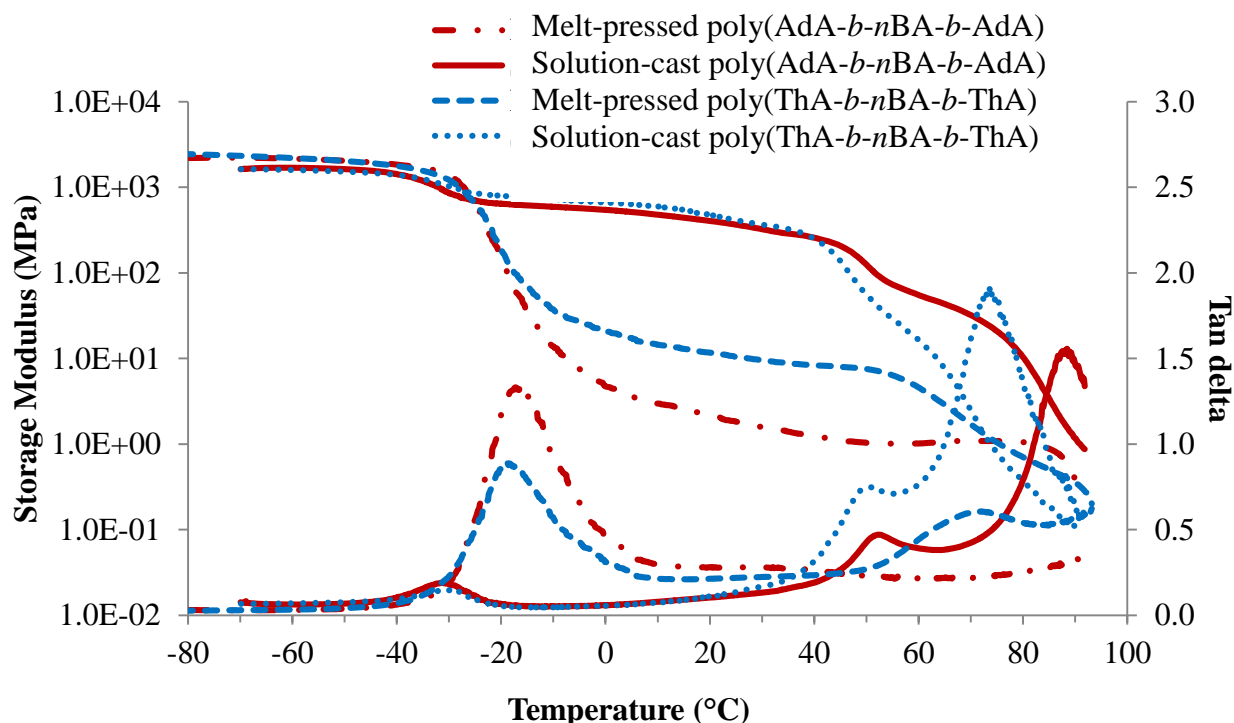


**Figure 3.2.** Effect of processing conditions on the thermomechanical properties of nucleobase-functionalized triblock copolymers.

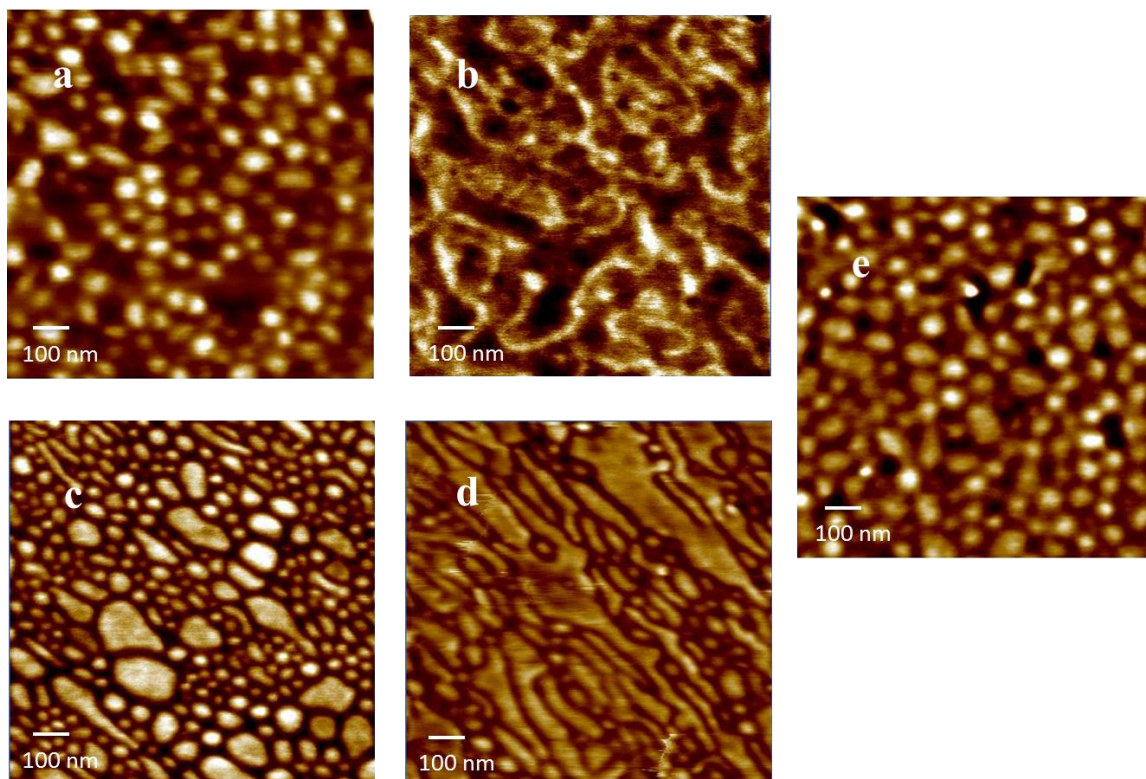


**Figure 3.3.** Tapping mode AFM phase image of (a) solution-cast poly(AdA-*b*-nBA-*b*-AdA), (b) solution-cast poly(ThA-*b*-nBA-*b*-ThA), (c) melt-pressed poly(AdA-*b*-nBA-*b*-AdA), (d) melt-pressed poly(ThA-*b*-nBA-*b*-ThA), and (e) solution-cast supramolecular blend.

Plateau moduli of melt-pressed ABA triblock copolymers were in the range of typical TPEs, while plateau moduli of solution-cast copolymers were too high for elastomers.<sup>21</sup> 38 wt% of adenine-functionalized blocks and 40 wt% of thymine-functionalized blocks self-assembled into hard phases, which restricted the flexibility of copolymers in the plateau temperature range. Decreasing the nucleobase content and block length will potentially afford nucleobase-functionalized triblock copolymer TPEs with improved elasticity.

DMA also elucidated the effect of noncovalent interactions on block copolymer thermomechanical properties. Above the  $T_g$  of the soft phase, the second drop of modulus and intermediate tan delta peak related to the  $T_g$  of the hard block for both solution-cast samples. A small second plateau followed the hard block  $T_g$  before the terminal flow. These secondary plateaus were attributed to self-association of the adenine-adenine and thymine-thymine hydrogen bonding and pi-pi stacking. Variable temperature FTIR of poly(ThA-*b*-*n*BA-*b*-ThA) and poly(AdA-*b*-*n*BA-*b*-AdA) verified the presence of weak self-hydrogen bonding (Figure S3.9, S3.10). Poly(AdA-*b*-*n*BA-*b*-AdA) showed a higher modulus above the second  $T_g$  compared to the poly(ThA-*b*-*n*BA-*b*-ThA), which correlated to stronger pi-pi stacking of the purine rings.<sup>4</sup> The noncovalent-interaction dominated region was not obvious for melt-pressed poly(ThA-*b*-*n*BA-*b*-ThA) and absent for melt-pressed poly(AdA-*b*-*n*BA-*b*-AdA) due to the poor assembly of the hard phase in the melt. The lower plateau modulus for the melt-pressed poly(AdA-*b*-*n*BA-*b*-AdA) resulted from a slower self-assembly compared to poly(ThA-*b*-*n*BA-*b*-ThA). The additional pi-pi stacking and bulkier pendant group further inhibited chain mobility of the adenine block. Melt-pressed poly(AdA-*b*-*n*BA-*b*-AdA) exhibited more phase mixing than melt-pressed poly(ThA-*b*-*n*BA-*b*-ThA) under the same annealing time. Certain features of block copolymers were necessary to reveal the noncovalent interaction-dominated plateau region. In particular, the  $T_g$  of the physically crosslinked block needs to be lower than the dissociation temperature of physical crosslinks. In addition, sufficient physical crosslinking strength is also needed. Strong crosslinks will restrict segmental motion and potentially lead to an order-disorder transition temperature above the hard block  $T_g$  as shown for supramolecular blend in Figure

3.4. Sufficient degrees of polymerization for the nucleobase blocks also ensured sufficient noncovalent interactions to influence the mechanical properties.

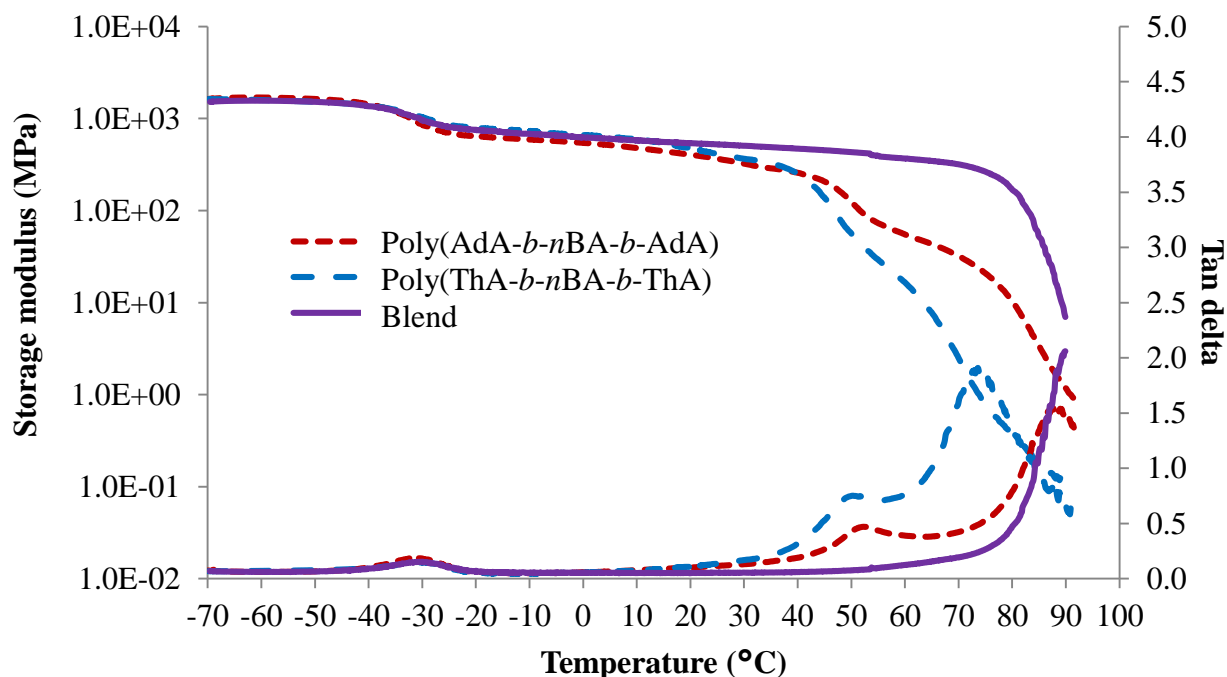


**Figure 3.4.** Thermomechanical properties of solution-cast nucleobase-functionalized triblock copolymers and their blend.

**Supramolecular blend.** Solution blend of poly(AdA-*b*-*n*BA-*b*-AdA) and poly(ThA-*b*-*n*BA-*b*-ThA) were prepared to examine the influence of complementary hydrogen bonding of A-T on mechanical performance. The supramolecular blend of poly(AdA-*b*-*n*BA-*b*-AdA) and poly(ThA-*b*-*n*BA-*b*-ThA) at 1:1 adenine:thymine molar ratio showed microphase-separation rather than macrophase-separation due to collectively strong intermolecular interactions.<sup>61</sup> AFM and DMA revealed a well-organized microphase-separated morphology for the supramolecular blend (Figures 3.3e, 3.4). Complementary hydrogen bonding between adenine and thymine is approximately 50× stronger than A-A/T-T self-association.<sup>4,60</sup> The physically crosslinked thymine and adenine-functionalized

hard blocks self-assembled into a single high  $T_g$  phase, while the soft PnBA block formed a soft phase. The plateau region of the supramolecular blend in Figure 3.4 extended beyond the  $T_g$ 's of either hard blocks. Table 3.1 summarizes observed  $T_g$ 's from DSC and DMA and the major plateau range of solution-cast poly(AdA-*b*-nBA-*b*-AdA), poly(ThA-*b*-nBA-*b*-ThA), and their blend. The blend did not exhibit an external block  $T_g$ , and an approximately 40 °C wider plateau window was observed compared to the individual components. The molecular recognition between adenine and thymine restricted the mobility of the hard blocks above  $T_g$ 's of either hard blocks. In addition, the blend showed an onset of terminal flow at a similar temperature as poly(AdA-*b*-nBA-*b*-AdA) and poly(ThA-*b*-nBA-*b*-ThA) near 90 °C, corresponding to the temperature where a majority of the hydrogen bonding dissociated. These results illustrated that noncovalent interactions extend the temperature independent modulus region, while maintaining melt processibility due to thermoreversibility of the physical crosslinks.

Dynamic mechanical analysis revealed potential benefits of the nucleobase-functionalized supramolecular blend for TPE applications. Inter-chain recognition contributed to well-defined microphase-separation, extended plateau range, and maintained melt processibility for the supramolecular blend. However, a higher plateau modulus, was observed compared to a typical TPE modulus range, limiting the elasticity of the solution-cast supramolecular blend. Further studies are underway to tune the triblock copolymer structure for a supramolecular blend with improved TPE performance.

**Table 3.1.**  $T_g$ 's and plateau temperature ranges of nucleobase-functionalized block copolymers.  $T_g^{A1}$ ,  $T_g^{A2}$  are from tan delta curves of DMA (solution-cast samples);  $T_g^{B1}$ ,  $T_g^{B2}$  are from the second heating ramps of DSC.

| Temperature (°C)                        | $T_g^{A1}$<br>(°C) | $T_g^{A2}$<br>(°C) | $T_g^{B2}$<br>(°C) | $T_g^{B2}$<br>(°C) | Plateau<br>(°C) |
|---|--------------------|--------------------|--------------------|--------------------|-----------------|
| Poly(AdA- <i>b-n</i> BA- <i>b</i> -AdA) | -31                | 52                 | -39                | 76                 | 76              |
| Poly(ThA- <i>b-n</i> BA- <i>b</i> -ThA) | -29                | 49                 | -40                | 52                 | 71              |
| A:T 1:1 Blend                           | -30                | NA                 | -47                | 74                 | 109             |

**SAXS and bulk morphology.** SAXS results were used to probe the bulk morphology of solution-cast poly(AdA-*b-n*BA-*b*-AdA), poly(ThA-*b-n*BA-*b*-ThA), and blends (Figure 3.5). The SAXS profile for each of the samples contains relatively broad scattering maxima with periodic intensity oscillations, indicative of a morphology with a distribution of characteristic dimensions (in agreement with the AFM data in Figures 3.3a,b,e). Poly(AdA-*b-n*BA-*b*-AdA) and the blend show periodic scattering maxima that roughly match the expected  $q$ ,  $\sqrt{3}q$ ,  $\sqrt{4}q$ ,  $\sqrt{7}q$ , and  $\sqrt{12}q$  peak positions that are characteristic of hexagonally packed cylinders, where  $q$  is the position of the first maximum. In contrast, for poly(ThA-*b-n*BA-*b*-ThA), both Figures 3.3b and 3.5 indicate a much less ordered morphology. The well-assembled cylindrical phase separation morphology of poly(AdA-*b-n*BA-*b*-AdA) and the blend was attributed to enhanced ordering originating from pi-pi stacking and complementary hydrogen bonding, respectively. Purine rings of poly(AdA-*b-n*BA-*b*-AdA) were shown to afford stronger pi-pi interaction than pyrimidine rings in poly(ThA-*b-n*BA-

*b*-ThA).<sup>4</sup> However, the WAXD profile (Figure S3.11) only shows a broad diffraction peak characteristic of inter-chain correlations (amorphous halo) of the *Pn*BA block.<sup>4</sup> The absence of a signature diffraction peak for pi-pi stacking is presumably due to the small, nanometer-scale size of the packed AdA domains, as compared to much longer range order of packed AdA units in the homopolymers.<sup>4,5</sup> The *d* spacings were 60.4 nm, 63.4 nm, and 58.7 nm for poly(AdA-*b*-*n*BA-*b*-AdA), poly(ThA-*b*-*n*BA-*b*-ThA), and the blend, respectively. These *d* spacings were attributed to the inter-particle distance between the phase separated domains, which also corresponded well with inter-particle distances observed in AFM. All average spacings were close to 60 nm due to the similar volume fractions of the external and internal blocks for all three samples. Overall, noncovalent interactions within the hard phase facilitated the self-assembly of block copolymers at the equilibrium self-assembled morphology. The bulk morphology and surface morphology agreed well, and both demonstrated the positive effect of noncovalent interactions on block copolymer self-assembly.

SAXS results also agreed with the trend in dynamic mechanical analysis of the solution-cast poly(AdA-*b*-*n*BA-*b*-AdA), poly(ThA-*b*-*n*BA-*b*-ThA), and the blend. Poly(ThA-*b*-*n*BA-*b*-ThA) exhibited the lowest order-disorder transition temperature due to the least ordered microphase-separation. Figure 3.6 depicts the self-assembled morphology of the supramolecular blend. The complementary hydrogen bonding facilitated self-assembly of supramolecular block copolymer blends and enhanced the mechanical performance as a function of temperature. The thermal dissociation of hydrogen bonding led to a disruption of the physically crosslinked network in the hard phase, which resulted in a modulus drop. Overall, a synergy between the noncovalent

interactions within the hard phase and the equilibrium, self-assembled morphology contributed to enhanced supramolecular polymer properties. Better phase separation led to more physical crosslinking within the hard phase and higher modulus when comparing solution-cast to melt-pressed samples. Stronger physical crosslinking within the hard phase facilitated self-assembly and reinforced the microphase-separated morphology when comparing solution-cast supramolecular blend with poly(AdA-*b*-nBA-*b*-AdA) and poly(ThA-*b*-nBA-*b*-ThA). However, noncovalent interactions decreased the rate of self-assembly in the melt.

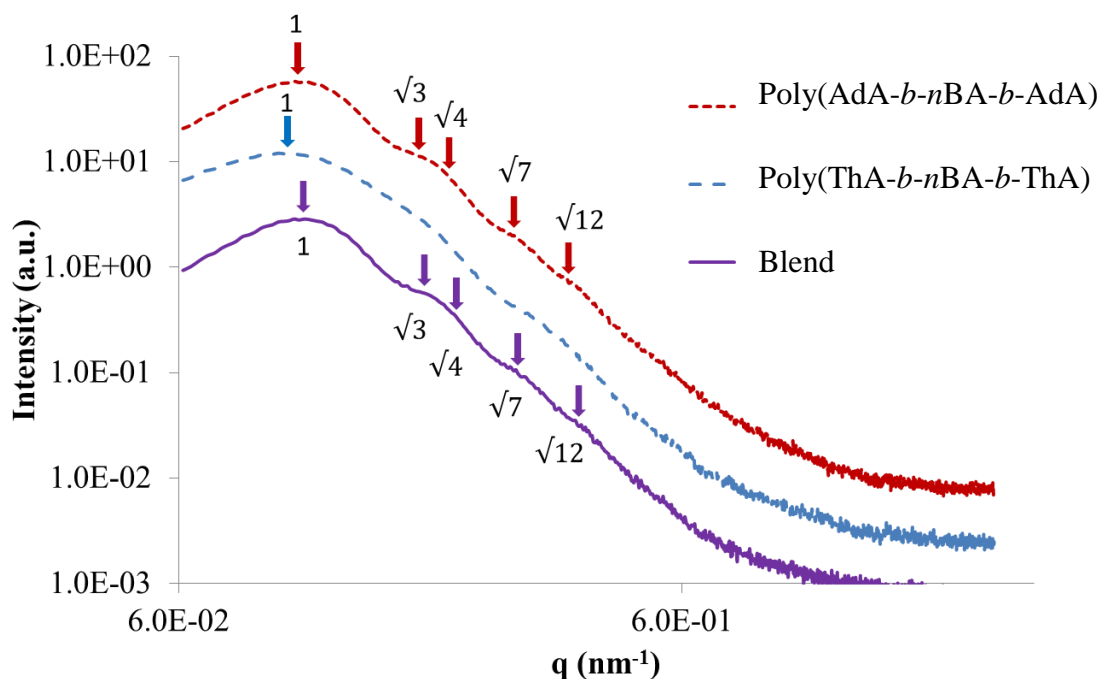


**Figure 3.5.** SAXS of solution-cast nucleobase-functionalized triblock copolymers and their blend. For clarity, data were vertically shifted by arbitrary factors.



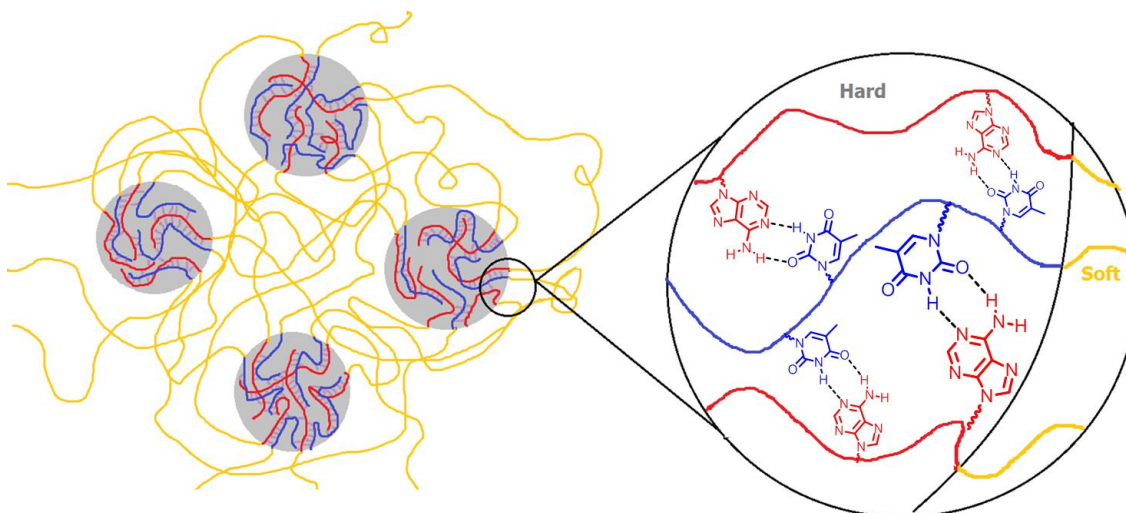


**Figure 3.6.** Pictorial representation of supramolecular blend of adenine and thymine-functionalized triblock copolymers.

**Variable temperature FTIR.** Variable temperature FTIR is suitable to monitor the thermal reversibility of hydrogen bonding in the bulk.<sup>4,55</sup> The low solubility of nucleobase-functionalized block copolymers in nonpolar solvents limited the feasibility of NMR titration despite monomer solubility. Variable temperature FTIR on poly(AdA-*b*-*n*BA-*b*-AdA), poly(ThA-*b*-*n*BA-*b*-ThA), and the blend verified the presence of hydrogen bonding and thermal reversibility. Figure 3.7 shows the scale-expanded, ATR-corrected, spectral overlay of the supramolecular blend upon a temperature ramp. Hoogsteen base pairing is shown in Figure 3.7 to label signature peaks in the spectrum. However, the association of adenine and thymine units most likely combined both Hoogsteen and Watson-Crick base pairing.<sup>22</sup> The primary absorbance at  $1730\text{ cm}^{-1}$  corresponded to C=O stretching of the carbonyl peak from the *Pn*BA block and the non-conjugated, carbonyl peak from nucleobase blocks. The broad absorbance centered at  $1670\text{ cm}^{-1}$  related to the hydrogen bonded C=O on thymine, which shifted to higher wavenumber upon heating (red arrow). Two N-H bending vibration peaks at  $1600\text{ cm}^{-1}$  and  $1645\text{ cm}^{-1}$  both shifted toward lower

wavenumbers with increasing temperature (blue arrows). Spectra collected after cooling to 30 °C shows that all hydrogen bonded absorbances shifted to their original wavenumbers. Upon cooling, hydrogen bonding formation led to a red-shift of C=O stretching vibration and a blue-shift of N-H bending vibration.<sup>4,62,63</sup> Red-shift of C=O stretching vibration was due to C=O bonding lengthening when hydrogen-bonded, where frequency decreases as force constant decreases in equation  $\bar{\nu} = \frac{1}{2\pi} \sqrt{\frac{k}{\mu}}$  (k: force constant;  $\mu$ : reduced mass).<sup>64</sup> Blue-shift of N-H bending vibration was attributed to restriction of the bending motion from hydrogen bonding. The spectral reversibility over a heat-cool cycle demonstrated the thermal reversibility of the supramolecular network. The gray peaks corresponded to free C=O and N-H that were not hydrogen bonded. The same FTIR experiment on poly(AdA-*b*-*n*BA-*b*-AdA) and poly(ThA-*b*-*n*BA-*b*-ThA) (Figures S3.9, S3.10) indicated the presence of weaker hydrogen bonding from the self-association of A-A and T-T, respectively. The FTIR results confirmed our hypothesis for the dynamic mechanical performance of the nucleobase-functionalized copolymers and the blend. The FTIR results also provided support for the morphology depicted in Figure 3.6. Thermoreversible hydrogen bonding within the hard phase contributed to a supramolecular network with a more defined, self-assembled phase-separated morphology, mechanical performance, and thermal responsiveness.

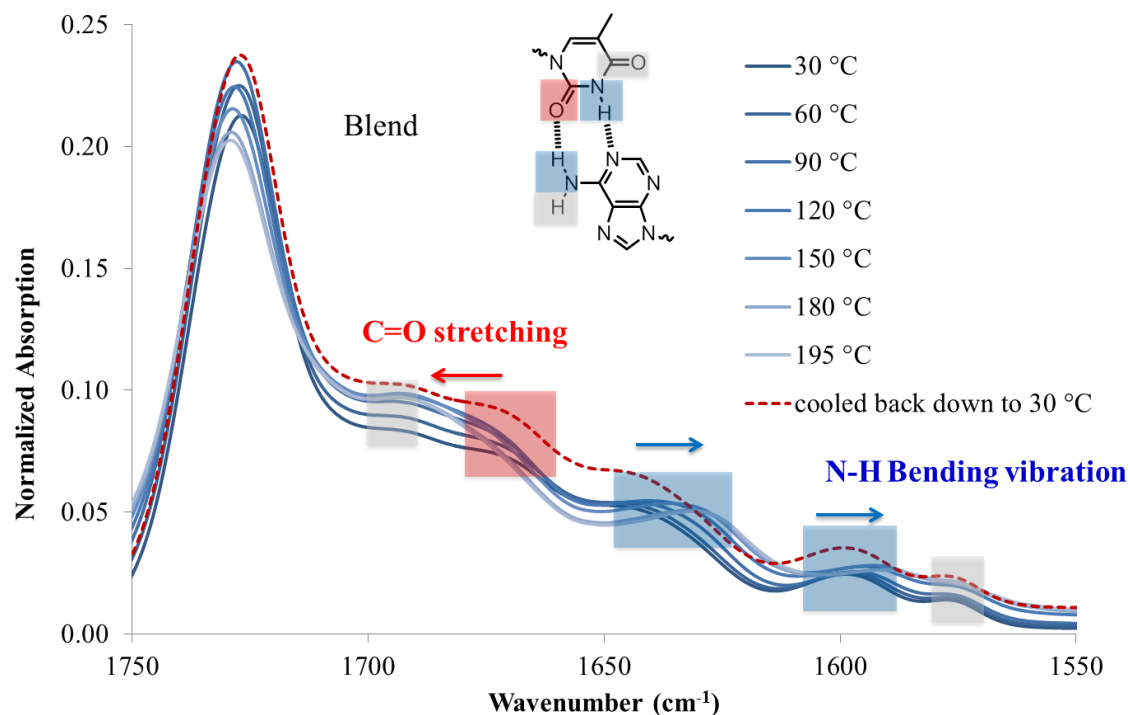


**Figure 3.7.** Variable temperature FTIR spectra in the 1500-1700  $\text{cm}^{-1}$  region for the supramolecular blend.

### 3.5 Conclusions

Divergent RAFT polymerization afforded synthesis of nucleobase-functionalized acrylic ABA triblock copolymers using a difunctional CTA. The acrylic backbone and flexible linker were crucial to lower the  $T_g$ 's for probing the effect of noncovalent interactions. Nucleobase-functionalized triblock copolymers self-assembled into microphase-separated morphologies. Hydrogen bonding and pi-stacking created physically crosslinked networks with enhanced thermomechanical properties. The performance of block copolymer films was largely dependent on their self-assembly behavior, which was affected by processing conditions. The complementary hydrogen bonding of A-T in the hard phase of the supramolecular blend contributed to an elongated plateau, while

maintaining melt processibility. We observed the synergy between physical crosslinking within the hard phase and self-assembled microphase-separation. Complementary noncovalent interactions showed potential in promoting self-assembly, enhancing mechanical strength, and introducing thermal responsiveness to improve melt processibility for block copolymers. Nucleobase-functionalized ABA copolymers offered a potential platform for future thermoplastic elastomer fabrication.

### 3.6 *Acknowledgements*

This research was supported in part by the U.S. Army Research Laboratory and the U.S. Army Research Office under Contract/Grant W911NF-07-1-0452, Ionic Liquids in Electro-Active Devices Multidisciplinary University Research Initiative (ILEAD MURI). Additionally, this work was supported in part by Henkel Corporation, and we thank Charles Paul, Cristina DeJesus, and Eric Silverberg for insightful discussions. This material is also partially based upon work supported by the National Science Foundation under Grant No. DMR-0923107. We also thank Professor Mitsuru Ueda and the Academy for Co-creative Education of Environment and Energy Science at Tokyo Institute of Technology for their support of summer research for Mr. Motohiro Aiba at Virginia Tech.

### 3.7 *References*

1. Brunsveld, L.; Folmer, B. J. B.; Meijer, E. W.; Sijbesma, R. P. *Chem. Rev.* **2001**, *101*, 4071.
2. Schalley, C.; Editor *Analytical Methods in Supramolecular Chemistry*; Wiley-VCH Verlag GmbH & Co. KGaA, **2007**.
3. Yamauchi, K.; Lizotte, J. R.; Long, T. E. *Macromolecules* **2003**, *36*, 1083.
4. Cheng, S.; Zhang, M.; Dixit, N.; Moore, R. B.; Long, T. E. *Macromolecules* **2012**, *45*, 805.
5. Sivakova, S.; Bohnsack, D. A.; Mackay, M. E.; Suwanmala, P.; Rowan, S. J. *J. Am. Chem. Soc.* **2005**, *127*, 18202.
6. Whitesides, G. M.; Grzybowski, B. *Science* **2002**, *295*, 2418.
7. Sherrington, D. C.; Taskinen, K. A. *Chem. Soc. Rev.* **2001**, *30*, 83.

8. Lehn, J. M. *Supramolecular Chemistry: Concepts and Perspectives*; VCH, **1995**.
9. Fouquey, C.; Lehn, J. M.; Levelut, A. M. *Adv. Mater.* **1990**, *2*, 254.
10. Pan, J.; Chen, M.; Warner, W.; He, M.; Dalton, L.; Hogen-Esch, T. E. *Macromolecules* **2000**, *33*, 7835.
11. Kriz, J.; Dybal, J.; Brus, J. *J. Phys. Chem. B* **2006**, *110*, 18338.
12. Mather, B. D.; Baker, M. B.; Beyer, F. L.; Berg, M. A. G.; Green, M. D.; Long, T. E. *Macromolecules* **2007**, *40*, 6834.
13. Zhang, K.; Fahs, G. B.; Aiba, M.; Moore, R. B.; Long, T. E. *Chem. Comm.* **2014**, *50*, 9145.
14. McHale, R.; Patterson, J. P.; Zetterlund, P. B.; O'Reilly, R. K. *Nat. Chem.* **2012**, *4*, 491.
15. Nowick, J. S.; Chen, J. S.; Noronha, G. *J. Am. Chem. Soc.* **1993**, *115*, 7636.
16. Spontak, R. J.; Patel, N. P. *Curr. Opin. Colloid Interface Sci.* **2000**, *5*, 334.
17. Amin, S.; Amin, M. *Rev. Adv. Mater. Sci.* **2011**, *29*, 15.
18. Antony, P.; De, S. K. *J. Macromol. Sci., Polym. Rev.* **2001**, *C41*, 41.
19. Quirk, R. P.; Kim, J. *Rubber Chem. Technol.* **1991**, *64*, 450.
20. Duchacek, V. *J. Macromol. Sci., Phys.* **1998**, *B37*, 275.
21. Drobný, J. G. *Handbook of Thermoplastic Elastomers*; William Andrew Publishing/Plastics Design Library, **2007**.
22. Sivakova, S.; Rowan, S. J. *Chem. Soc. Rev.* **2005**, *34*, 9.
23. Sijbesma, R. P.; Meijer, E. W. *Chem. Comm.* **2003**, *5*.
24. Hemp, S. T.; Long, T. E. *Macromol. Biosci.* **2012**, *12*, 29.
25. McHale, R.; O'Reilly, R. K. *Macromolecules* **2012**, *45*, 7665.
26. Yakovchuk, P.; Protozanova, E.; Frank-Kamenetskii, M. D. *Nucleic Acids Res.* **2006**, *34*, 564.
27. Kim, J. C.; Jung, J.; Rho, Y.; Kim, M.; Kwon, W.; Kim, H.; Kim, I. J.; Kim, J. R.; Ree, M. *Biomacromolecules* **2011**, *12*, 2822.
28. Egholm, M.; Buchardt, O.; Nielsen, P. E.; Berg, R. H. *J. Am. Chem. Soc.* **1992**, *114*, 1895.
29. Khan, A.; Haddleton, D. M.; Hannon, M. J.; Kukulj, D.; Marsh, A. *Macromolecules* **1999**, *32*, 6560.
30. Kang, Y.; Lu, A.; Ellington, A.; Jewett, M. C.; O'Reilly, R. K. *ACS Macro Letters* **2013**, *581*.
31. Bazzi, H. S.; Sleiman, H. F. *Macromolecules* **2002**, *35*, 9617.
32. Lo, P. K.; Sleiman, H. F. *J. Am. Chem. Soc.* **2009**, *131*, 4182.
33. Mather, B. D.; Baker, M. B.; Beyer, F. L.; Green, M. D.; Berg, M. A. G.; Long, T. E. *Macromolecules* **2007**, *40*, 4396.
34. Spijker, H. J.; Dirks, A. J.; Van, H. J. C. M. *J. Polym. Sci., Part A: Polym. Chem.* **2006**, *44*, 4242.
35. Spijker, H. J.; van, D. F. L.; van, H. J. C. M. *Macromolecules* **2007**, *40*, 12.
36. Lutz, J.-F.; Thuenemann, A. F.; Nehring, R. *J. Polym. Sci., Part A: Polym. Chem.* **2005**, *43*, 4805.
37. Lutz, J.-F.; Thuenemann, A. F.; Rurack, K. *Macromolecules* **2005**, *38*, 8124.
38. Inaki, Y.; Ebisutani, K.; Takemoto, K. *J. Polym. Sci., Part A: Polym. Chem.* **1986**, *24*, 3249.
39. Inaki, Y. *Prog. Polym. Sci.* **1992**, *17*, 515.

40. Takemoto, K.; Inaki, Y. In *Speciality Polymers*; Springer Berlin Heidelberg: 1981; Vol. 41, p 1.
41. Marsh, A.; Khan, A.; Haddleton, D. M.; Hannon, M. J. *Macromolecules* **1999**, *32*, 8725.
42. Nair, K. P.; Pollino, J. M.; Weck, M. *Macromolecules* **2006**, *39*, 931.
43. Bazzi, H. S.; Bouffard, J.; Sleiman, H. F. *Macromolecules* **2003**, *36*, 7899.
44. Lo, P. K.; Sleiman, H. F. *Macromolecules* **2008**, *41*, 5590.
45. Marsh, A.; Khan, A.; Haddleton, D. M.; Hannon, M. J. *Macromolecules* **1999**, *32*, 8725.
46. De, G. T. F. A.; Kade, M. J.; Feldman, K. E.; Kramer, E. J.; Hawker, C. J.; Meijer, E. W. *J. Polym. Sci., Part A: Polym. Chem.* **2011**, *49*, 4253.
47. Binder, W. H.; Kunz, M. J.; Kluger, C.; Hayn, G.; Saf, R. *Macromolecules* **2004**, *37*, 1749.
48. Karikari, A. S.; Edwards, W. F.; Mecham, J. B.; Long, T. E. *Biomacromolecules* **2005**, *6*, 2866.
49. Yamauchi, K.; Lizotte, J. R.; Long, T. E. *Macromolecules* **2002**, *35*, 8745.
50. *Thermal Transitions of Homopolymers* Sigma Aldrich  
[https://www.sigmaaldrich.com/content/dam/sigma-aldrich/docs/Aldrich/General\\_Information/thermal\\_transitions\\_of\\_homopolymers.pdf](https://www.sigmaaldrich.com/content/dam/sigma-aldrich/docs/Aldrich/General_Information/thermal_transitions_of_homopolymers.pdf).
51. Ahmad, N. M.; Charleux, B.; Farcet, C.; Ferguson, C. J.; Gaynor, S. G.; Hawket, B. S.; Heatley, F.; Klumperman, B.; Konkolewicz, D.; Lovell, P. A.; Matyjaszewski, K.; Venkatesh, R. *Macromol. Rapid Commun.* **2009**, *30*, 2002.
52. Allen, M. H., Jr.; Hemp, S. T.; Zhang, M.; Zhang, M.; Smith, A. E.; Moore, R. B.; Long, T. E. *Polym. Chem.* **2013**, *4*, 2333.
53. Smith, A. E.; Xu, X.; McCormick, C. L. *Prog. Polym. Sci.* **2010**, *35*, 45.
54. Tao, Y.; Satoh, K.; Kamigaito, M. *Macromol. Rapid Commun.* **2011**, *32*, 226.
55. Sijbesma, R. P.; Beijer, F. H.; Brunsveld, L.; Folmer, B. J. B.; Hirschberg, J. H. K. K.; Lange, R. F. M.; Lowe, J. K. L.; Meijer, E. W. *Science* **1997**, *278*, 1601.
56. Tamami, M.; Hemp, S. T.; Zhang, K.; Zhang, M.; Moore, R. B.; Long, T. E. *Polymer* **2013**, *54*, 1588.
57. Thordarson, P. *Chem. Soc. Rev.* **2011**, *40*, 1305.
58. Fielding, L. *Tetrahedron* **2000**, *56*, 6151.
59. Connors, K. A. *Binding constants: the measurement of molecular complex stability*; Wiley New York, **1987**.
60. Sartorius, J.; Schhneider, H.-J. *Chem. Eur. J.* **1996**, *2*, 1446.
61. Yang, Z.; Han, C. D. *Macromolecules* **2008**, *41*, 2104.
62. Tamami, M.; Zhang, K.; Dixit, N.; Moore, R. B.; Long, T. E. *Macromol. Chem. Phys.* **2014**, *215*, 2337.
63. Falk, M.; Ford, T. A. *Can. J. Chem.* **1966**, *44*, 1699.
64. Arunan, E.; Desiraju Gautam, R.; Klein Roger, A.; Sadlej, J.; Scheiner, S.; Alkorta, I.; Clary David, C.; Crabtree Robert, H.; Dannenberg Joseph, J.; Hobza, P.; Kjaergaard Henrik, G.; Legon Anthony, C.; Mennucci, B.; Nesbitt David, J. In *Pure Appl. Chem.* 2011; Vol. 83, p 1637.

### 3.8 *Supporting Information*

**Analytical Methods.** WAXD were performed using a Rigaku S-Max 3000 3 pinhole SAXS system, equipped with a rotating anode emitting X-rays with a wavelength of 0.154 nm (Cu K $\alpha$ ). Scattering from a silver behenate standard was used to calibrate the sample-to-detector distance. For WAXD, the sample-to-detector distance was 80.0 mm. WAXD two-dimensional diffraction patterns were obtained using an image plate, with an exposure time of 2 hours. All WAXD data were analyzed using the SAXSGUI software package to obtain azimuthal averaged WAXD intensity versus  $2\theta$  profiles, where  $\theta$  is one half of the scattering angle. WAXD profiles were vertically shifted to facilitate a comparison of the peak positions.

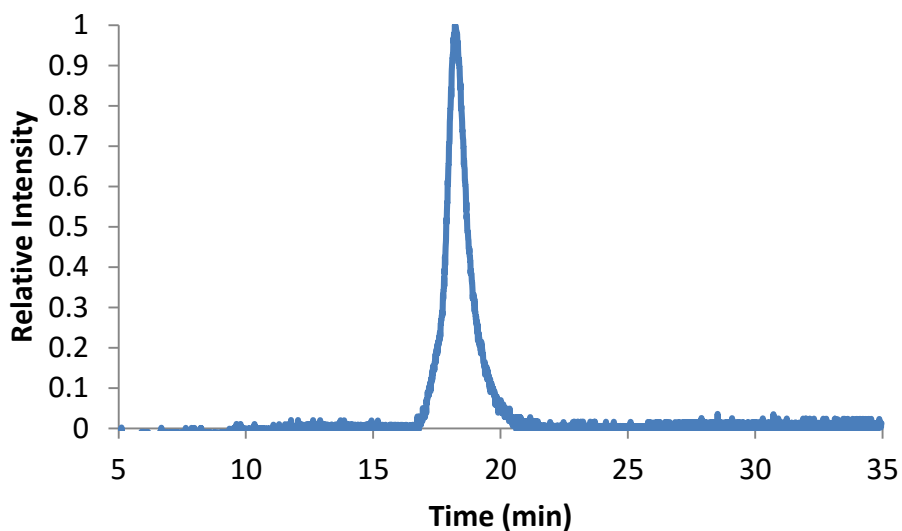


**Figure S3.1.** SEC trace of poly(*n*BA) difunctional macro-initiator.

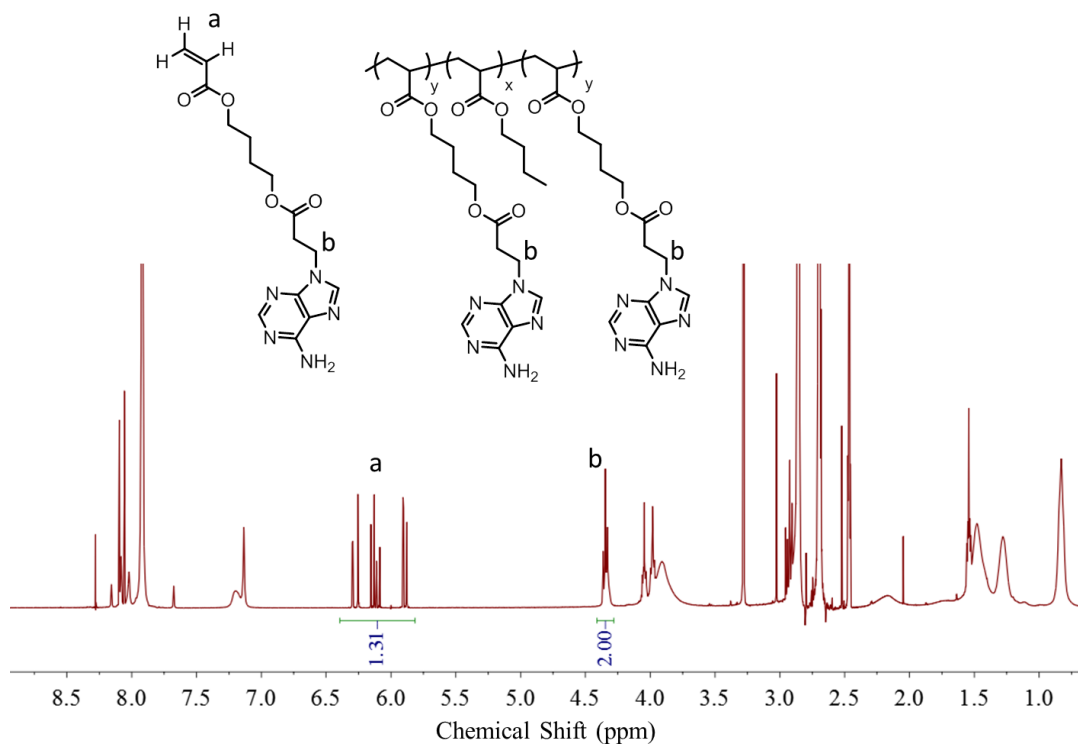


**Figure S3.2.**  $^1\text{H}$  NMR spectrum of reaction mixture after 2<sup>nd</sup> RAFT polymerization step of adenine block. The integrations of peak a and b were used to calculate conversion.

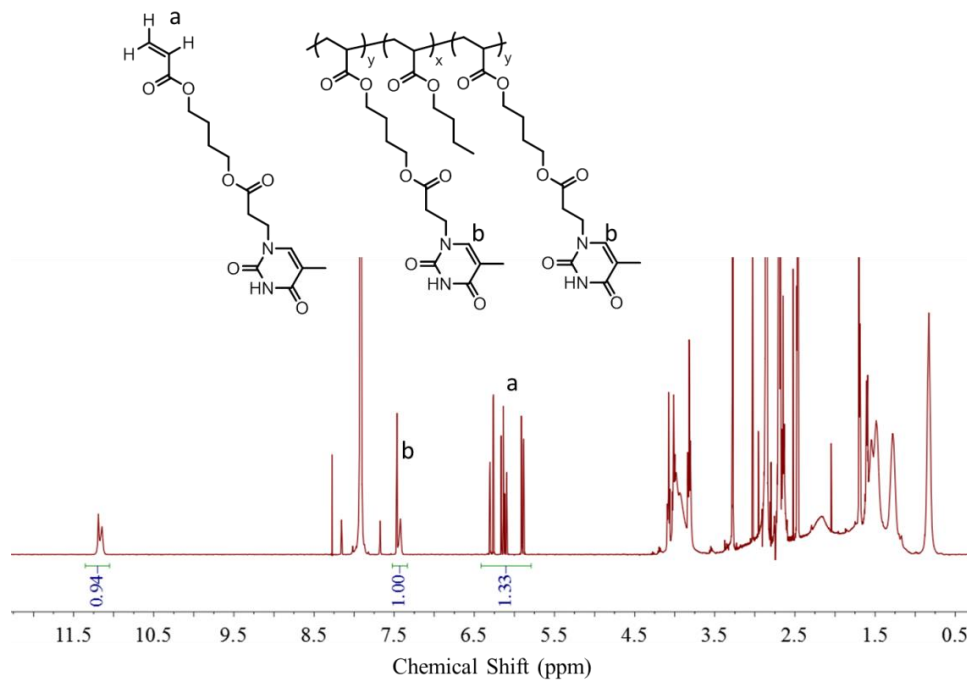




**Figure S3.3.**  $^1\text{H}$  NMR spectrum of reaction mixture after 2<sup>nd</sup> RAFT polymerization step of thymine block. The integrations of peak a and b were used to calculate conversion.

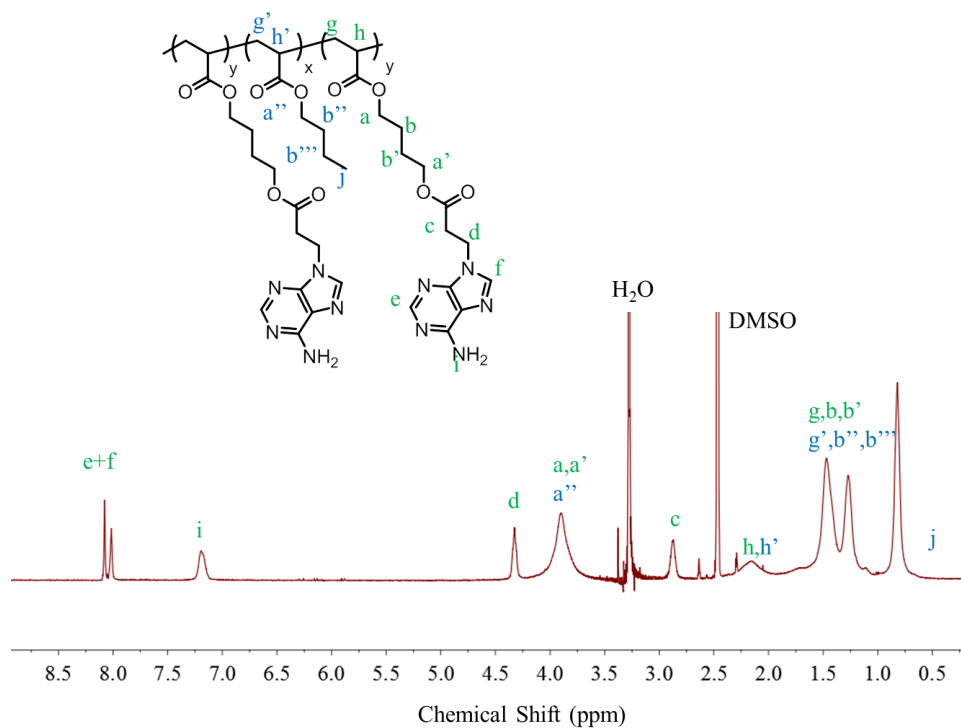


**Figure S3.4.**  $^1\text{H}$  NMR spectrum of poly(AdA-*b*-*n*BA-*b*-AdA) with 19 mol% adenine.

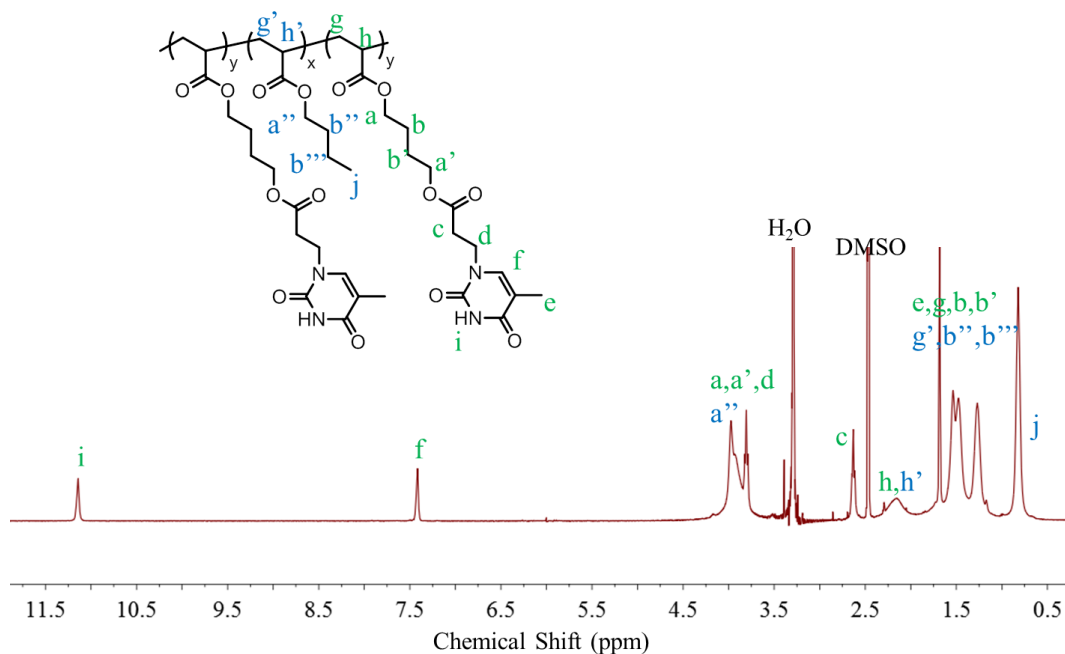


**Figure S3.5.**  $^1\text{H}$  NMR spectrum of poly(ThA-*b*-*n*BA-*b*-ThA) with 21 mol% thymine.

**Table S3.1.** DP and molecular weight from  $^1\text{H}$  NMR spectra. All data were based on the second RAFT polymerization step in Scheme 3.1, polymerization of AdA/ThA external block with PnBA macro-CTA. Conversion refers to the AdA/ThA monomer conversion. DP refers to the degree of polymerization for the nucleobase-functionalized block. DP<sub>1</sub> was calculated from  $^1\text{H}$  NMR spectroscopic analysis of the reaction mixture immediately after polymerization through a comparison of monomer conversion and targeted molecular weight from feed. DP<sub>2</sub> was calculated from  $^1\text{H}$  NMR spectroscopic analysis of the purified copolymers, using the ratio of nucleobase-functionalized block to PnBA internal block.

|   | Conversion | Targeted Mn at 100% conversion | DP <sub>1</sub> | (Nucleobase:nBA) ratio of pure copolymer | DP <sub>2</sub> | Average DP | Molecular weight | Total molecular weight |
|---|------------|--------------------------------|-----------------|--|-----------------|------------|------------------|------------------------|
| poly(AdA- <i>b</i> -nBA- <i>b</i> -AdA) | 56%        | 50.1 kDa                       | 84.5            | 4.3:1                                    | 81.3            | 83         | 27.6 kDa         | 72.4 kDa               |
| poly(ThA- <i>b</i> -nBA- <i>b</i> -ThA) | 56%        | 53.0 kDa                       | 91.1            | 3.7:1                                    | 94.6            | 93         | 30.1 kDa         | 74.9 kDa               |

The peak shift of amine group in the thymine was observed. The total concentration of adenine was varied, while that of thymine was held.

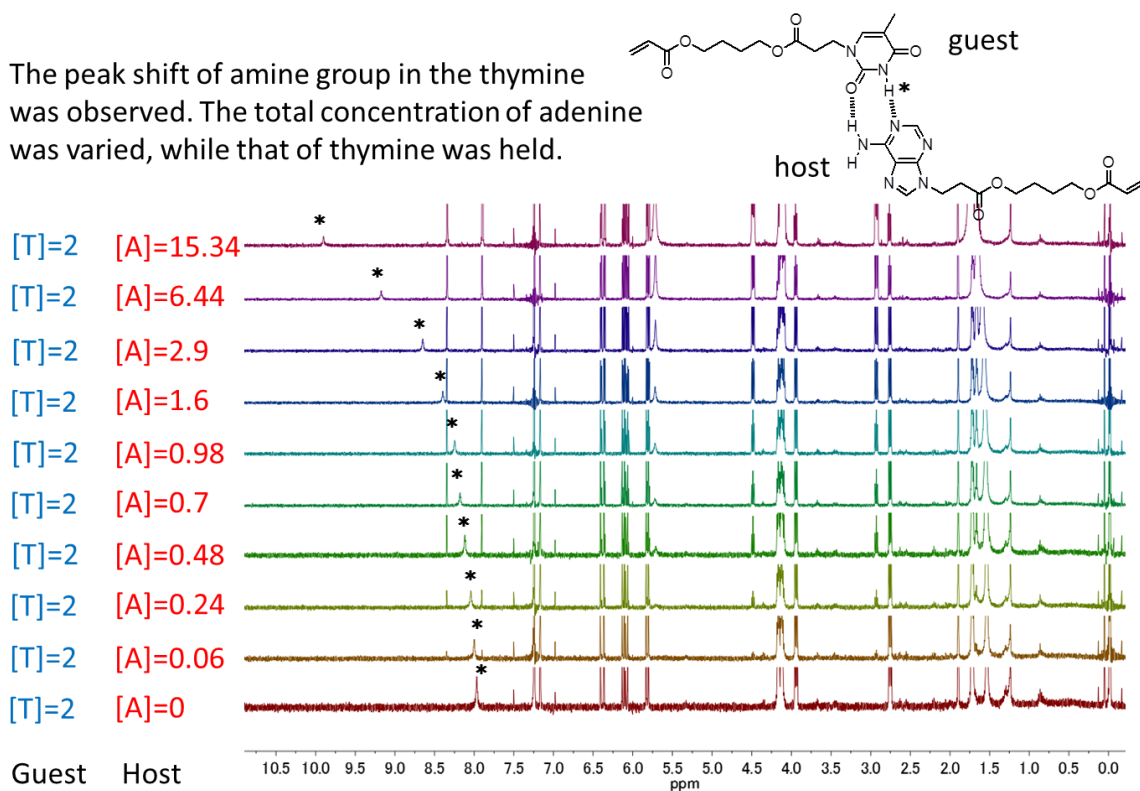


**Figure S3.6.**  $^1\text{H}$  NMR spectrum overlay of titration experiment with constant ThA concentration of 2 M and increasing AdA concentration from 0 M to 15.34 M.

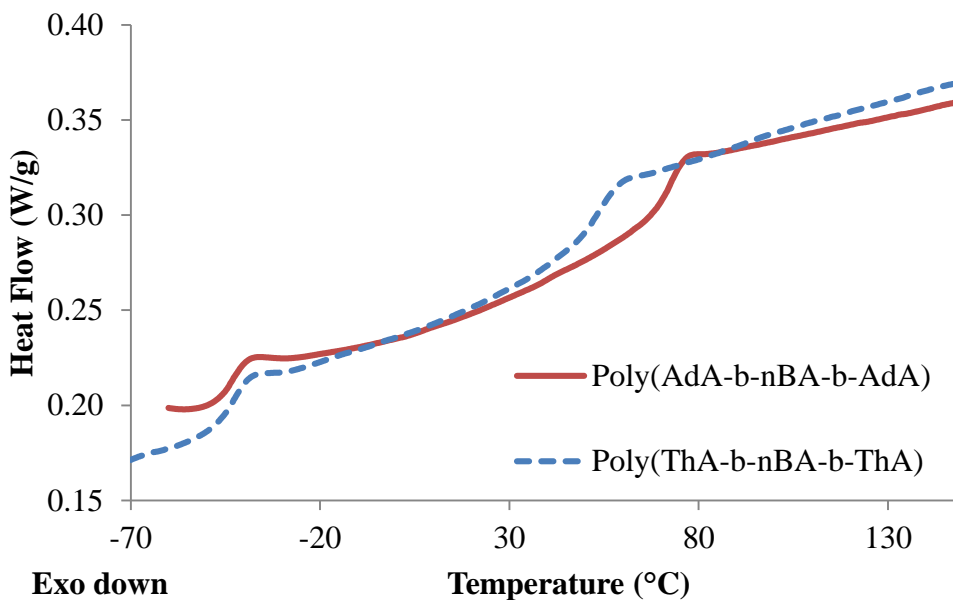


**Figure S3.7.** DSC 2<sup>nd</sup> heat of poly(ThA-*b*-*n*BA-*b*-ThA) and poly(AdA-*b*-*n*BA-*b*-AdA).

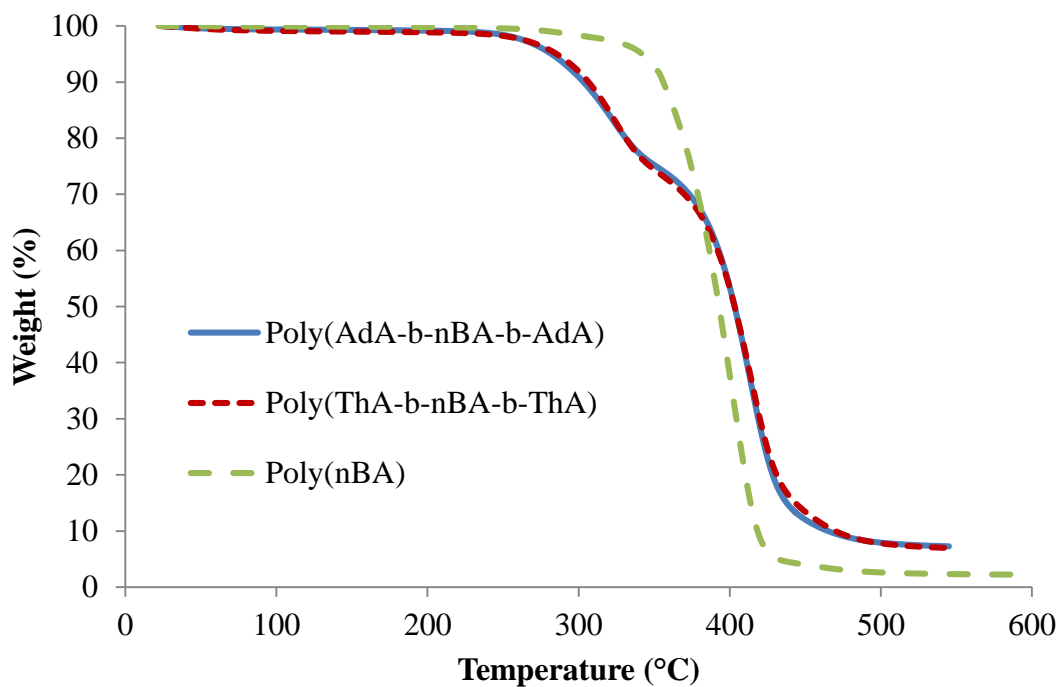


**Figure S3.8.** TGA traces of poly(ThA-*b*-*n*BA-*b*-ThA), poly(AdA-*b*-*n*BA-*b*-AdA), and poly(*n*BA).

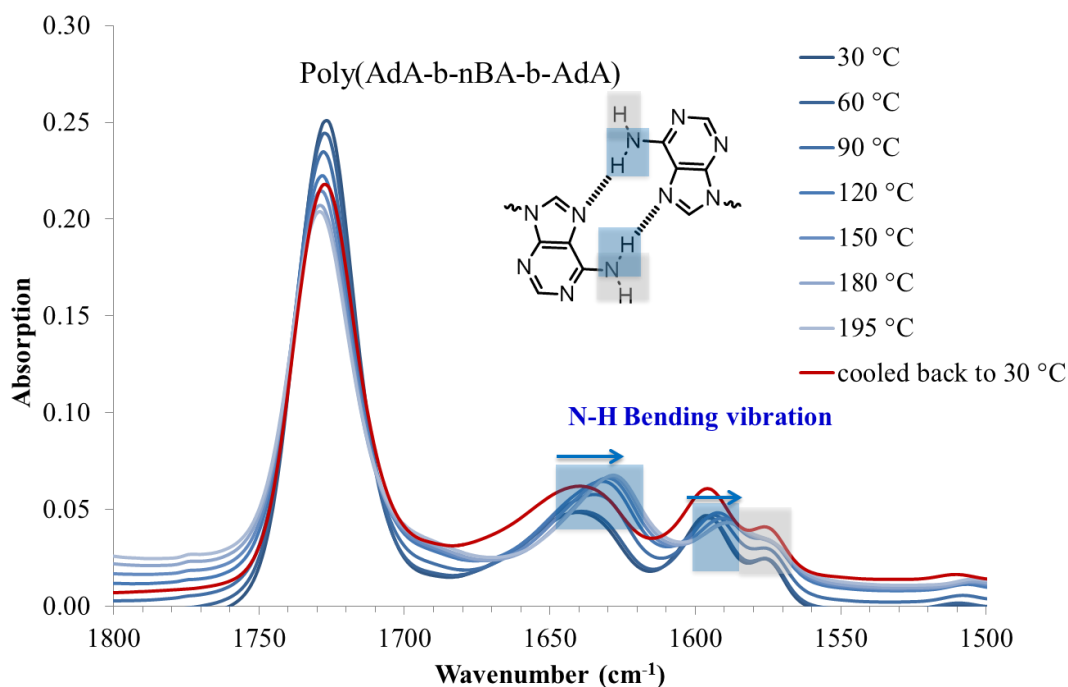


**Figure S3.9.** Variable temperature FT-IR spectra in the 1500-1800  $\text{cm}^{-1}$  region of poly(AdA-*b*-nBA-*b*-AdA).

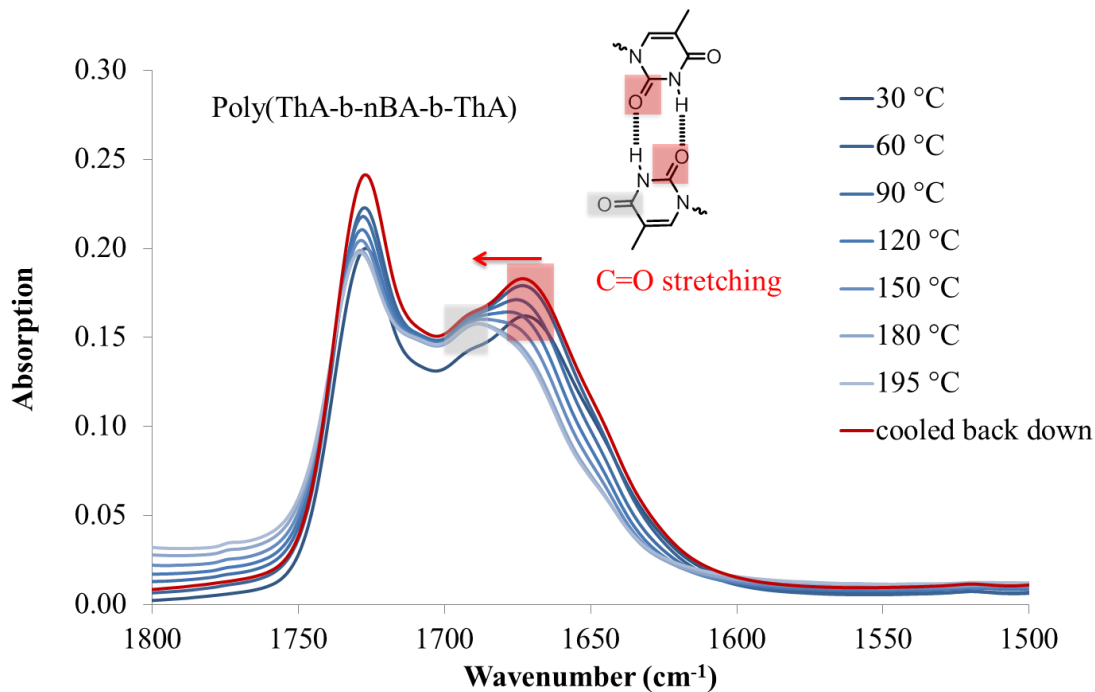


**Figure S3.10.** Variable temperature FT-IR spectra in the 1500-1800  $\text{cm}^{-1}$  region of poly(ThA-*b*-nBA-*b*-ThA).

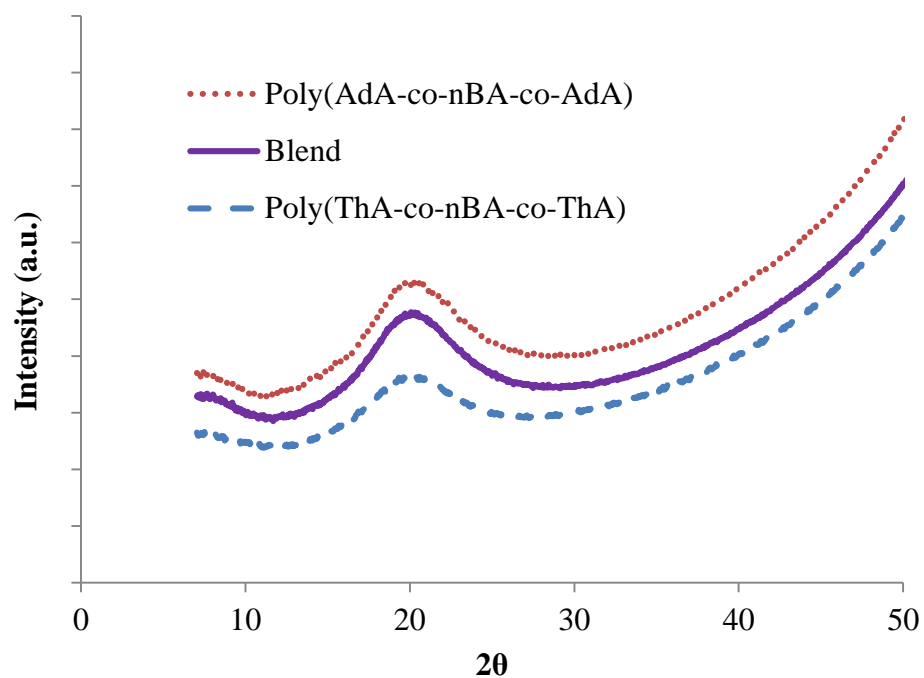


**Figure S3.11.** WAXD of solution-cast nucleobase-functionalized triblock copolymers and their blend. For clarity, data were shifted vertically by arbitrary factors.

## Chapter 4. Nucleobase-Functionalized ABC Triblock Copolymers: Self-assembly of Supramolecular Architectures

(Published in *Chemical Communication* **2014**, 50, 9145)

Keren Zhang,<sup>a</sup> Gregory B. Fahs,<sup>a</sup> Motohiro Aiba,<sup>b</sup> Robert B. Moore,<sup>a</sup> and Timothy E. Long<sup>\*a</sup>

<sup>a</sup> *Department of Chemistry, Macromolecules and Interfaces Institute  
Virginia Tech, Blacksburg, VA 24061, USA*

<sup>b</sup> *Department of Organic and Polymeric Materials, Graduate School of Science and  
Engineering, Tokyo Institute of Technology, 2-12-1, O-okayama, Meguro-ku, Tokyo 152-  
8552, Japan*

### 4.1 Abstract

RAFT polymerization afforded acrylic ABC triblock copolymers with self-complementary nucleobase-functionalized external blocks and a low- $T_g$  soft central block. ABC triblock copolymers self-assembled into well-defined lamellar microphase-separated morphologies for potential applications as thermoplastic elastomers. Complementary hydrogen bonding within the hard phase facilitated self-assembly and enhanced mechanical performance.

### 4.2 Introduction

Nature broadly employs complementary hydrogen bonding of nucleobase pairs to encode our genetic profiles. Research interest in nucleobase-containing synthetic polymers and supramolecular polymers focuses on the unique molecular recognition between the purine and pyrimidine rings: adenine-thymine (uracil) and guanine-cytosine.<sup>1-3</sup> Nucleobase incorporation significantly affects both solution and solid-state properties of polymers due to the formation of physically crosslinked networks.<sup>2,4,5</sup> Nucleobase heterocycles also restrict the segmental motion of polymer chains, leading to higher glass transition temperatures ( $T_g$ ). Most studies of nucleobase-containing polymers focus on the physical

properties and self-assembly in solution, which enable template polymerizations, biosensors, and drug therapies.<sup>2,6-9</sup> A fundamental understanding of the effect of noncovalent interactions on self-assembly in the absence of solvent is also critical to elucidate the solid-state properties of nucleobase-containing polymers. Nucleobase incorporation impacts polymer thermo-mechanical performance, solid-state self-assembly, and temperature-dependent melt viscosity.<sup>10-12</sup>

Many controlled polymerization methods provide nucleobase-containing polymers with well-defined architectures in the earlier literature. Common synthetic strategies to control the polymerization of nucleobase-functionalized monomers have included atom transfer radical polymerization (ATRP)<sup>9,13,14</sup>, nitroxide mediated polymerization (NMP)<sup>6,11,15</sup>, and ring-opening metathesis polymerization (ROMP)<sup>16-18</sup>. Reversible addition-fragmentation chain transfer (RAFT) polymerization represents a relatively new and promising method for controlling polymerization of nucleobase monomers due to superior solvent compatibility and functional group tolerance.<sup>19</sup> Advances in controlled radical polymerization methods also allow sequence and structural control for synthetic polymers that contain complementary molecular recognition sites. For example, Bazzi *et al.* observed the effect of complementary hydrogen bonding on polymer self-assembly in solution.<sup>17</sup> Tao *et al.* utilized a hydrogen-bonding mediator to control tacticity in radical polymerization.<sup>20</sup> However, the solid-state properties of polymers bearing complementary molecular recognition sites remained unexplored.

To achieve biomimetic synthetic polymers with tailored sequence and specificity, we employed RAFT polymerization for the copolymerization of acrylic adenine and thymine monomers with commercially available acrylic comonomers. Physical characterization of

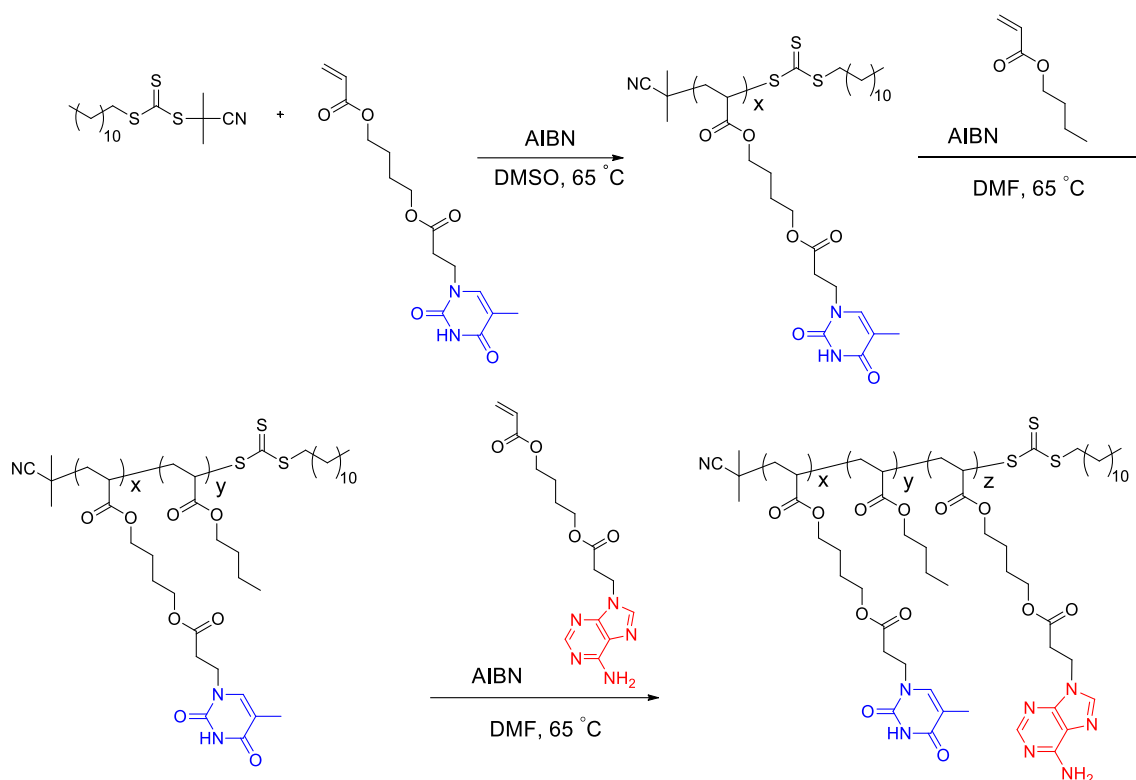


the block copolymers focused on elucidating the effect of molecular recognition and copolymer sequence on the mechanical properties and bulk self-assembly. This manuscript reports unprecedented nucleobase-functionalized ABC triblock copolymers with well-defined structures and controlled sequences.

Long *et al.* previously synthesized poly(adenine acrylate) and poly(thymine acrylate) homopolymers with glass transition temperatures of 65 °C and 43 °C, respectively, which were significantly lower than styrenic and methacrylic analogs.<sup>10,11</sup> The low  $T_g$  values aided in the elucidation of the effect of complementary hydrogen bonding on the bulk properties of nucleobase-containing copolymers. When the polymer  $T_g$  exceeds the dissociation temperature of the physical crosslinks, the polymer chains remain constrained despite disruption of the physical crosslinks. Thus, the influence of dissociation of physical crosslinks on the polymer thermo-mechanical properties is less clear. In addition, the flexible acrylic backbone and longer spacers from the backbone to the interactive nucleobase groups facilitate molecular recognition. The acrylic backbone also enables facile sequence control of nucleobase-functionalized sequences and common acrylic blocks through simply changing the order of monomer addition. More versatile monomer addition avoids common crossover inefficiencies of monomers with different propagating radical stabilities. In this study, sequential RAFT polymerization permitted the synthesis of nucleobase-functionalized ABC triblock copolymers with a fully acrylic backbone using adenine acrylate and thymine acrylate monomers (Scheme 4.1).

The poly(thymine acrylate-*b*-*n*-butyl acrylate-*b*-adenine acrylate), abbreviated as poly(ThA-*b*-*n*BA-*b*-AdA) (PTBA), represents the first example of an ABC triblock copolymer containing complementary nucleobase-functionalized external blocks. PTBA

copolymers were also solution cast into free-standing films, enabling the physical characterization of self-assembly behavior in the absence of competing solvents. The self-complementary external blocks of PTBA copolymers resulted in unique self-assembled morphologies and thermo-mechanical performance compared to poly(ThA-*b*-*n*BA-*b*-ThA) (PTBT) and poly(AdA-*b*-*n*BA-*b*-AdA) (PABA) controls. RAFT polymerization afforded novel nucleobase-containing acrylic triblock copolymers for potential thermoplastic elastomer (TPE) applications.



**Scheme 4.1.** RAFT polymerization for the preparation of poly(ThA-*b*-*n*BA-*b*-AdA) ABC triblock copolymers.

### 4.3 Results and discussion

Optimized RAFT polymerization conditions afforded ABC triblock copolymers using 2-cyano-2-propyl dodecyl trithiocarbonate as the chain transfer agent (CTA) (Scheme 4.1).

Varying monomer conversions during the two chain extension steps provided three comparative compositions of PTBA triblock copolymers with differing block lengths.  $^1\text{H}$  NMR spectroscopy was the primary tool for monitoring monomer conversions and quantifying the degree of polymerization for each block. End-group analysis determined the number-average molecular weight of poly(ThA) macro-CTA. The challenging solubility of nucleobase copolymers limited the applicability of size exclusion chromatography. The PTBA triblock copolymer series consisted of three compositions: PTBA1 9.4-19.3-6.8 kDa, PTBA2 9.4-27.2-5.3 kDa, and PTBA3 9.4-31.5-4.6 kDa. Degree of polymerizations for ThA, *n*BA, and AdA blocks (*x*, *y*, and *z* in Scheme 4.1) were: PTBA 29-151-20, PTBA2 29-213-16, and PTBA3 29-246-14. The thymine:adenine molar ratio of PTBA 1, 2, and 3 was 1.5, 1.8, and 2.1, respectively. Corresponding weight percentages of nucleobase-functionalized monomers were 46 wt%, 35 wt%, and 31 wt%.

Thermogravimetric analysis (TGA) determined 5% weight loss temperatures of PTBA copolymers near 290 °C, indicating potential tolerance for a high processing temperature. All three PTBA copolymers showed two  $T_g$ 's from differential scanning calorimetry (DSC), as summarized in Table 4.1. The lower  $T_g$  at ca. -44 °C corresponded to the central poly(*n*BA) block. The central block lengths were sufficiently high to ensure that  $T_g$  remained constant with increasing molecular weight. The  $T_g$ 's of poly(ThA) and poly(AdA) homopolymers were 43 °C and 65 °C, respectively.<sup>10</sup> However, the external blocks only showed a single  $T_g$  at ca. 70 °C, rather than two distinct  $T_g$ 's for adenine- and thymine-functionalized external blocks, presumably due to strong complementary hydrogen bonding between the adenine and thymine blocks, forming a single hard phase. The adenine block presumably restricted segmental motion of the thymine-functionalized block even

above the thymine-functionalized block's  $T_g$ , resulting in a single observable  $T_g$ . The  $T_g$  of the hard phase also increased as the adenine-functionalized block length increased.

**Table 4.1.** Transition temperatures of PTBA copolymers from DMA and DSC

| Temperature (°C)         | $T_g^1$<br>(Tan $\delta$ ) | $T_g^1$<br>(DSC) | $T_g^2$<br>(DSC) | $T_{flow}$ |
|--------------------------|----------------------------|------------------|------------------|------------|
| PTBA3 (9.4-31.5-4.6) kDa | -23                        | -44              | 66               | 80         |
| PTBA2 (9.4-27.2-5.3) kDa | -21                        | -45              | 67               | 84         |
| PTBA1 (9.4-19.3-6.8) kDa | -25                        | -44              | 72               | 85         |

Fabrication of mechanically robust block copolymer TPEs demands a specific hard-soft-hard arrangement of hard (high  $T_g$ ) and soft (low  $T_g$ ) blocks.<sup>21</sup> The triblock copolymer sequence of poly(ThA-*b*-*n*BA-*b*-AdA) was critical for preparing potential block copolymer TPEs. The nucleobase-functionalized external blocks provided mechanical reinforcement and served as physical crosslinks during the plateau window. The central poly(*n*BA) soft block provided flexibility above its  $T_g$ . The structural similarity of nucleobase-functionalized monomers and *n*BA led to similar propagating radical stability, enabling well-defined crossover at each chain extension step. The  $\chi$  parameter is also important for microphase separation of block copolymers, where enthalpic interactions between the soft and hard blocks require minimization. The relatively hydrophobic nature, thermal stability, and low  $T_g$  of poly(*n*BA) all contributed to its suitability as the soft block for designing block copolymer TPEs.

Solution-cast films of PTBA copolymers showed microphase-separated morphologies and corresponding thermo-mechanical properties. Dynamic mechanical analysis (DMA) suggested microphase separation of PTBA copolymers as depicted in Figure 4.1. The lowest thermal transitions in the storage modulus

*versus* temperature curves were assigned to the glass transitions of the PnBA soft phase. The following regions in the storage modulus analysis revealed a plateau temperature window for each sample, demonstrating feasibility for TPE applications over a wide temperature range. The service temperature window of amorphous block copolymer TPEs usually ranges from the soft phase  $T_g$  to the hard phase  $T_g$ . Among the three compositions of PTBA copolymers, the plateau modulus increased with increasing nucleobase content, which was attributed to an increased physical crosslink density. The nucleobase-functionalized copolymers displayed tunable plateau moduli with varying nucleobase block or soft block lengths. The plateau moduli of PTBA 1, 2, and 3 were higher than rubbery plateau moduli of commercial TPEs, with typical values of 2 MPa. Future work will involve synthesis of triblock copolymers with shorter nucleobase blocks and longer central blocks for TPE applications. The soft block  $T_g$ 's as determined from the tan delta curves remained constant with varying compositions, indicating that solution casting achieved microphase separation (Table 4.1). The microphase-separated morphologies and tunable plateau moduli both contribute to the potential of nucleobase-functionalized ABC triblock copolymers for TPE applications.

Complementary hydrogen bonding between the adenine-thymine nucleobase pairs enhanced the thermo-mechanical performance of PTBA copolymer films compared to ABA triblock copolymer controls. PTBT and PABA with 40 wt% and 38 wt% nucleobase were synthesized in-parallel and adopted as controls. Identical film casting procedures and thermal histories were maintained to validate the comparisons. The plateau moduli of PTBT and PABA fell between PTBA1 and

PTBA2 owing to their intermediate nucleobase contents. The plateau moduli largely depended on hard phase incorporation. The plateau region for the PTBT and PABA copolymers ended with a second glass transition belonging to the hard phase. However, PTBA did not show a second  $T_g$  in either the storage modulus or tan delta curves. This phenomenon presumably originated from the hypothesis that complementary hydrogen bonding maintained mechanical strength despite long range segmental motion of the hard blocks. The moduli of PTBA copolymer films eventually decreased upon reaching the dissociation temperature for hydrogen bonding near 80-90 °C. The complementary hydrogen bonding within the hard phase broadened the plateau window for the block copolymers and enhanced thermal response at high temperature. Thus, hydrogen bonding assisted self-assembly potentially solves the paradox of enhancing mechanical strength while improving processibility of polymeric materials.

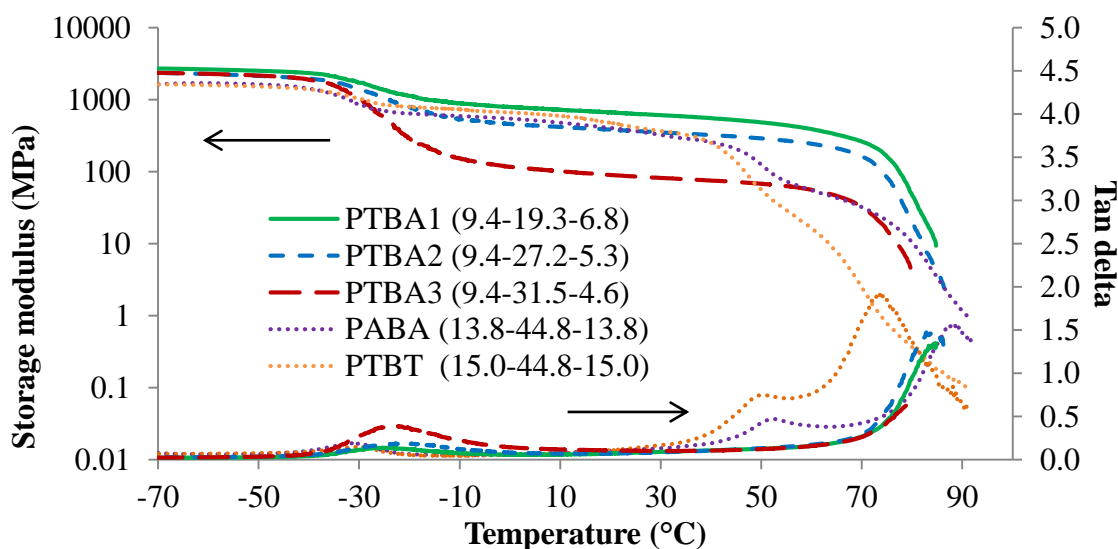


**Figure 4.1.** Dynamic mechanical temperature ramp of PTBA, copolymers with PABA and PTBT controls.

Complementary hydrogen bonding within the hard phase also contributed to a remarkably ordered microphase separated morphology of the ABC triblock copolymers. Small angle X-ray scattering (SAXS) was used to elucidate the microphase-separated bulk morphology of all three PTBA copolymers in Figure 4.2. The phase-separated morphologies of asymmetric ABC copolymers are usually more complex than symmetric ABA triblock and AB diblock copolymers.<sup>22</sup> However, all three PTBA triblock copolymers showed distinctive lamellar scattering profiles. SAXS profiles of PTBA2 and PTBA3 both exhibit primary scattering peaks and four additional secondary peaks, indicating well-organized lamellar morphologies with long-range order. The distinctive scattering peaks for ABC triblock copolymers resulted from the complementary molecular recognition, which combined two chemically different blocks into a single, precisely-ordered hard phase. Consequently, self-assembly of an ABC triblock copolymer with complementary external blocks resembled the self-assembly behavior of a symmetric ABA triblock copolymer. However, in sharp contrast, PABA with 38 wt% nucleobase content (similar to PTBA2 with 35 wt%) showed a less-ordered cylindrical microphase-separated morphology with broader SAXS scattering peaks. These analogous ABA triblock copolymers will be discussed in more detail in a forthcoming publication on nucleobase-functionalized symmetric ABA triblock copolymers. The degree of polymerization (N) difference provided one possible explanation for the morphological difference according to the phase diagram, since the morphology varies as a function of  $\chi N$ . However, the highly ordered phase

separation of PTBA copolymers was still unique for an ABC or ABA triblock copolymer, considering the presence of the complementary hydrogen bonding between two dissimilar external blocks.

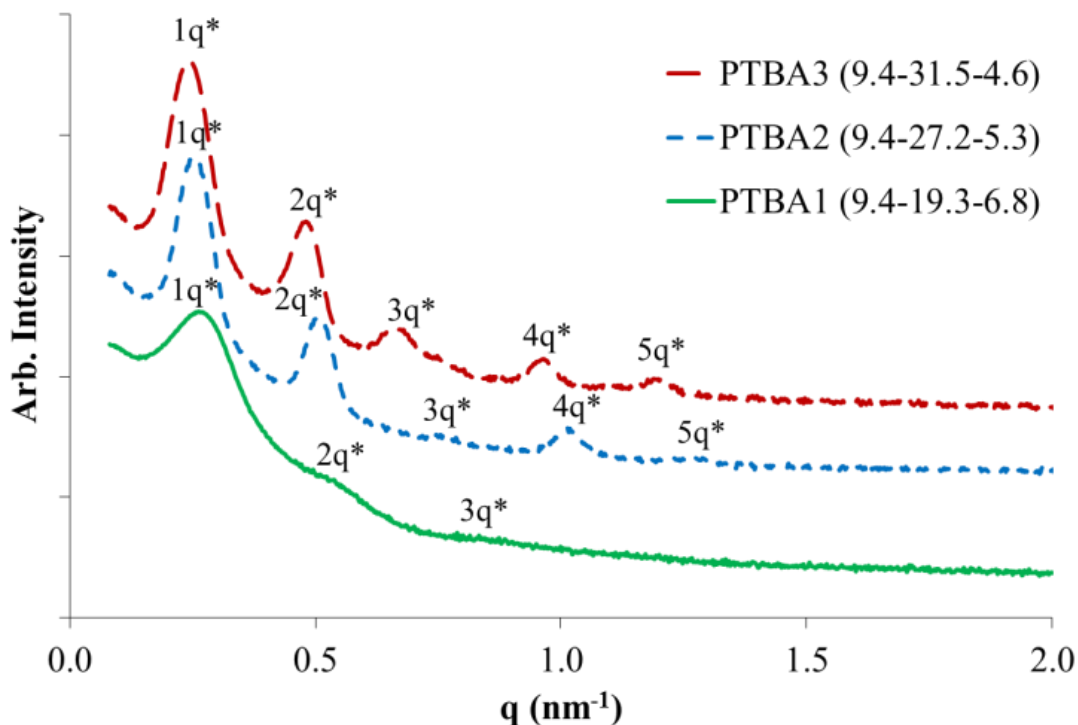


**Figure 4.2.** SAXS profiles of poly(ThA-*b*-nBA-*b*-AdA) triblock copolymers.

The domain spacing of the lamellae were 25.9 nm, 25.0 nm, and 23.4 nm for PABT3, 2, and 1, respectively. Increasing central block lengths resulted in an increased spacing between lamellae. The SAXS profile of PTBA1 showed broader scattering peaks with fewer highly ordered peaks compared to the other two compositions, suggesting a broader distribution of lamellar thicknesses and/or interlamellar dimensions, and thus less ordered domains. Two hypotheses may account for the difference in self-assembled morphologies for PTBA triblock copolymers with various compositions. The less ordered phase separation of PTBA1



was possibly a consequence of a shorter central block. The central block length was insufficient to induce well-defined microphase separation. Secondly, the highly ordered lamellar packing possibly resulted from the fact that thymine:adenine molar ratios of PTBA2 and 3 were close to 2. In the second hypothesis, each thymine-functionalized block statistically paired with two adenine blocks, facilitating the aligning of alternating soft phase and hard phase lamellae. In the latter case, the phase separated morphology would not follow the general phase diagram of ABA triblock copolymers.<sup>23</sup> Both inter-and intra-chain hydrogen bonding were presumably present according to the second hypothesis at a 2:1 thymine:adenine molar ratio. The inter-chain complexion also provided an explanation for enhanced mechanical performance compared to PABA and PTBT in Figure 4.1, resulting from increased apparent chain lengths. However, elucidation of inter-and intra-chain hydrogen bonding in the solid state is challenging due to the complexity of polymer structure compared to low molar mass molecules. Preliminary atomic force microscopic (AFM) results did not reveal a well-defined surface morphology for copolymer films, differing from the observed lamellae bulk morphology in SAXS profiles. Tuning film casting conditions and applying transmission electron microscopy (TEM) will further elucidate the morphology of nucleobase-functionalized ABC triblock copolymers. Further investigations are underway to validate two hypotheses mentioned above and understand the details of self-assembly of ABC triblock copolymers with complementary external blocks.

## 4.4 Conclusions

RAFT polymerization afforded novel self-complementary nucleobase-functionalized ABC triblock copolymers with fully acrylic backbones. Nucleobase units converted low  $T_g$  acrylics into mechanically robust polymeric films through steric restriction of segmental motion coupled with physical crosslinking. Hard-soft-hard triblock copolymers self-assembled into lamellar microphase-separated morphologies. The molecular recognition between two dissimilar hard blocks contributed to a single hard phase, and the complementary hydrogen bonding within the hard phase reinforced and facilitated the microphase-separated morphology of ABC triblock copolymers. Physical crosslinks within the hard phase broadened the plateau temperature window and improved the processibility of block copolymers for potential TPE applications.

The authors acknowledge Henkel Corporation for financial support. This material is also partially based upon work supported by the National Science Foundation under Grant No. DMR-0923107.

## 4.5 References

1. Hemp, S. T.; Long, T. E. *Macromol. Biosci.* **2012**, *12*, 29.
2. McHale, R.; O'Reilly, R. K. *Macromolecules* **2012**, *45*, 7665.
3. Sivakova, S.; Rowan, S. J. *Chem. Soc. Rev.* **2005**, *34*, 9.
4. Karikari, A. S.; Mather, B. D.; Long, T. E. *Biomacromolecules* **2006**, *8*, 302.
5. Tamami, M.; Hemp, S. T.; Zhang, K.; Zhang, M.; Moore, R. B.; Long, T. E. *Polymer* **2013**, *54*, 1588.
6. McHale, R.; Patterson, J. P.; Zetterlund, P. B.; O'Reilly, R. K. *Nat. Chem.* **2012**, *4*, 491.
7. Lutz, J.-F.; Thuenemann, A. F.; Rurack, K. *Macromolecules* **2005**, *38*, 8124.
8. Lo, P. K.; Sleiman, H. F. *Macromolecules* **2008**, *41*, 5590.
9. Spijker, H. J.; Dirks, A. J.; Van, H. J. C. M. *J. Polym. Sci., Part A: Polym. Chem.* **2006**, *44*, 4242.
10. Cheng, S.; Zhang, M.; Dixit, N.; Moore, R. B.; Long, T. E. *Macromolecules* **2012**, *45*, 805.
11. Mather, B. D.; Baker, M. B.; Beyer, F. L.; Berg, M. A. G.; Green, M. D.; Long, T. E. *Macromolecules* **2007**, *40*, 6834.
12. Yamauchi, K.; Lizotte, J. R.; Long, T. E. *Macromolecules* **2002**, *35*, 8745.

13. Spijker, H. J.; van, D. F. L.; van, H. J. C. M. *Macromolecules* **2007**, *40*, 12.
14. Lutz, J.-F.; Thuenemann, A. F.; Nehring, R. *J. Polym. Sci., Part A: Polym. Chem.* **2005**, *43*, 4805.
15. Mather, B. D.; Baker, M. B.; Beyer, F. L.; Green, M. D.; Berg, M. A. G.; Long, T. E. *Macromolecules* **2007**, *40*, 4396.
16. Bazzi, H. S.; Sleiman, H. F. *Macromolecules* **2002**, *35*, 9617.
17. Bazzi, H. S.; Bouffard, J.; Sleiman, H. F. *Macromolecules* **2003**, *36*, 7899.
18. Lo, P. K.; Sleiman, H. F. *J. Am. Chem. Soc.* **2009**, *131*, 4182.
19. Kang, Y.; Lu, A.; Ellington, A.; Jewett, M. C.; O'Reilly, R. K. *ACS Macro Letters* **2013**, 581.
20. Tao, Y.; Satoh, K.; Kamigaito, M. *Macromol. Rapid Commun.* **2011**, *32*, 226.
21. Spontak, R. J.; Patel, N. P. *Curr. Opin. Colloid Interface Sci.* **2000**, *5*, 334.
22. Stadler, R.; Auschra, C.; Beckmann, J.; Krappe, U.; Voight-Martin, I.; Leibler, L. *Macromolecules* **1995**, *28*, 3080.
23. Mayes, A. M.; Olvera de la Cruz, M. *J. Chem. Phys* **1989**, *91*, 7228.

## 4.6 Supporting Information

**Materials.** *n*-Butyl acrylate (*n*BA, 99+%) was purchased from Aldrich and passed through neutral alumina columns before use.  $\alpha,\alpha'$ -Azobis(isobutyronitrile) (AIBN, Fluka, 99%) was recrystallized from methanol. 1,4-Butanediol diacrylate (Alfa Aesar, 99%) was used without further purification. Adenine (A, 99%), thymine (T, 99%), triethylamine (TEA, 99%), potassium carbonate (99%), 2-cyano-2-propyl dodecyl trithiocarbonate (CPDT, 97%), and 2,6-di-*tert*-butyl-4-methylphenol (BHT, 99%) were purchased from Aldrich and used without further purification. Hexane (HPLC grade), chloroform (CHCl<sub>3</sub>, HPLC), tetrahydrofuran (THF, HPLC grade), *N,N*-dimethylsulfoxide (DMSO, HPLC grade) and *N,N*-dimethylformamide (DMF, HPLC grade, anhydrous) were purchased from Fisher Scientific and used as received.

**Analytical Methods.** <sup>1</sup>H NMR spectra were collected in CDCl<sub>3</sub> or DMSO-d<sub>6</sub> on a Varian INOVA spectrometer operating at 400 MHz at 23 °C. Differential scanning calorimetry (DSC) was performed under a nitrogen flush of 50 mL/min at a heating rate of 10 °C/min on a TA instruments Q1000 DSC, which was calibrated using indium (mp = 156.60 °C) and zinc (mp = 419.47 °C) standards. Glass transition temperatures were measured as the

midpoint of the transition in the second heating scan. DMA was conducted on a TA Instruments Q800 in tension mode at a frequency of 1 Hz, an oscillatory amplitude of 8  $\mu\text{m}$ , and a static force of 0.01 N. The temperature ramp was 3  $^{\circ}\text{C}/\text{min}$ . The glass transition temperature ( $T_g$ ) was determined at the peak maximum of the  $\tan \delta$  curve.

SAXS experiments were performed using a Rigaku S-Max 3000 3 pinhole SAXS system, equipped with a rotating anode emitting X-ray with a wavelength of 0.154 nm ( $\text{Cu K}\alpha$ ). The sample-to-detector distance was 1600 mm, and  $q$ -range was calibrated using a silver behenate standard. Two-dimensional SAXS patterns were obtained using a fully integrated 2D multiwire, proportional counting, gas-filled detector, with an exposure time of 2 hours. All the SAXS data were analyzed using the SAXSGUI software package to obtain radially integrated SAXS intensity versus scattering vector  $q$ , where  $q = (4\pi/\lambda)\sin(\theta)$ ,  $\theta$  is one half of the scattering angle and  $\lambda$  is the wavelength of X-ray.

**Polymerization of poly(ThA) macro-CTA.** ThA (5.0 g, 15.4 mmol), AIBN (4.1 mg, 25  $\mu\text{mol}$ ), CPDT (79.5 mg, 0.25 mmol), and DMF (29 g, 15 wt%) were charged into a single-neck Schlenk flask and subjected to four cycles of freeze-pump-thaw and subsequent refilling with argon. The flask was then sealed and thermostated at 65  $^{\circ}\text{C}$  for 3 h. The copolymer was isolated from precipitation into methanol and dried under vacuum at room temperature for 24 h. The monomer: initiator: CTA ratio was 616:1:10. End group analysis using  $^1\text{H}$  NMR revealed molecular weight  $M_n=9.4$  kDa. Conversion was 58%.

**Chain extension of poly(ThA) with  $n\text{BA}$ .** Typical synthesis of poly(ThA-*b*- $n\text{BA}$ ) was conducted as follows.  $n\text{BA}$  (1.6 mg, 12.2 mmol), AIBN (0.3 mg, 2.0  $\mu\text{mol}$ ), poly(ThA) macro-CTA (225 mg, 24.0  $\mu\text{mol}$ ), and DMF (7.1 g, 20 wt%) were charged into a single-neck Schlenk flask and subjected to four cycles of freeze-pump-thaw and subsequent

refilling with argon. The flask was then sealed and thermostated at 65 °C for 3 h. The copolymer was isolated from precipitation into methanol water mixture and dried under vacuum at room temperature for 24 h. The monomer: initiator: CTA ratio was 6100:1:10. <sup>1</sup>H NMR revealed molecular weight of poly(ThA-*b*-*n*BA)  $M_n$ = 9.4 and 19.3 kDa for each block, with a conversion of 29%.

**Chain extension of poly(ThA-*b*-*n*BA) with AdA.** Typical synthesis of poly(ThA-*b*-*n*BA-*b*-AdA) was conducted as follows. AdA (466.2 mg, 1.4 mmol), AIBN (0.4 mg, 2.3 μmol), poly(ThA-*b*-*n*BA) macro-CTA (669 mg, 23.3 μmol), and DMF (4.5 g, 20 wt%) were charged into a single-neck Schlenk flask and subjected to four cycles of freeze-pump-thaw and subsequent refilling with argon. The flask was then sealed and thermostated at 65 °C for 3 h. The copolymer was isolated from precipitation into methanol water mixture and dried under vacuum at room temperature for 24 h. The monomer: initiator: CTA ratio was 609:1:10. <sup>1</sup>H NMR revealed molecular weight of poly(ThA-*b*-*n*BA-*b*-AdA)  $M_n$ = 9.4-19.3-6.8 kDa, with a conversion of 33%.

**Solution cast copolymer films preparation.** Solution cast: PTBA copolymers were dissolved in DMSO (2 solid wt%) at 50 °C for 18 h and casted to a Teflon mold. Teflon mold was used to avoid potential deforming of the polymeric membranes during removal. The mold was placed at 80 °C for 48 h to slowly evaporate the DMSO. The dried copolymer film was then annealed in vacuum at 120 °C for 48 h.

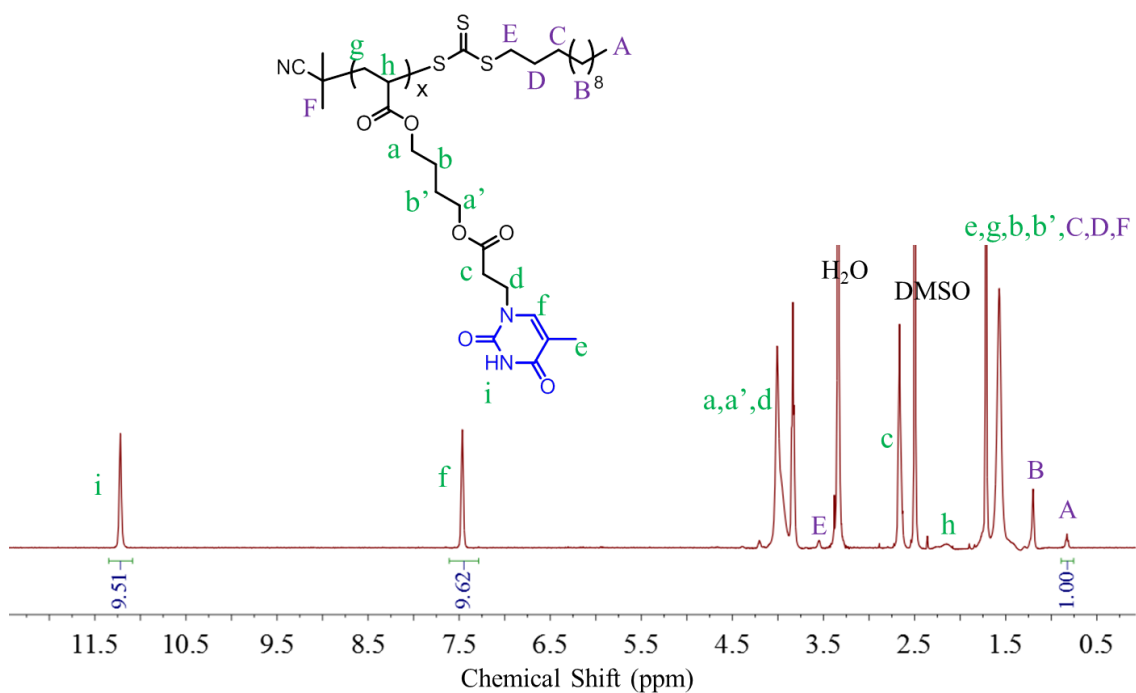


**Figure S4.1.**  $^1\text{H}$  NMR spectrum of poly(ThA) macro-CTA and end group analysis for determining molecular weight.

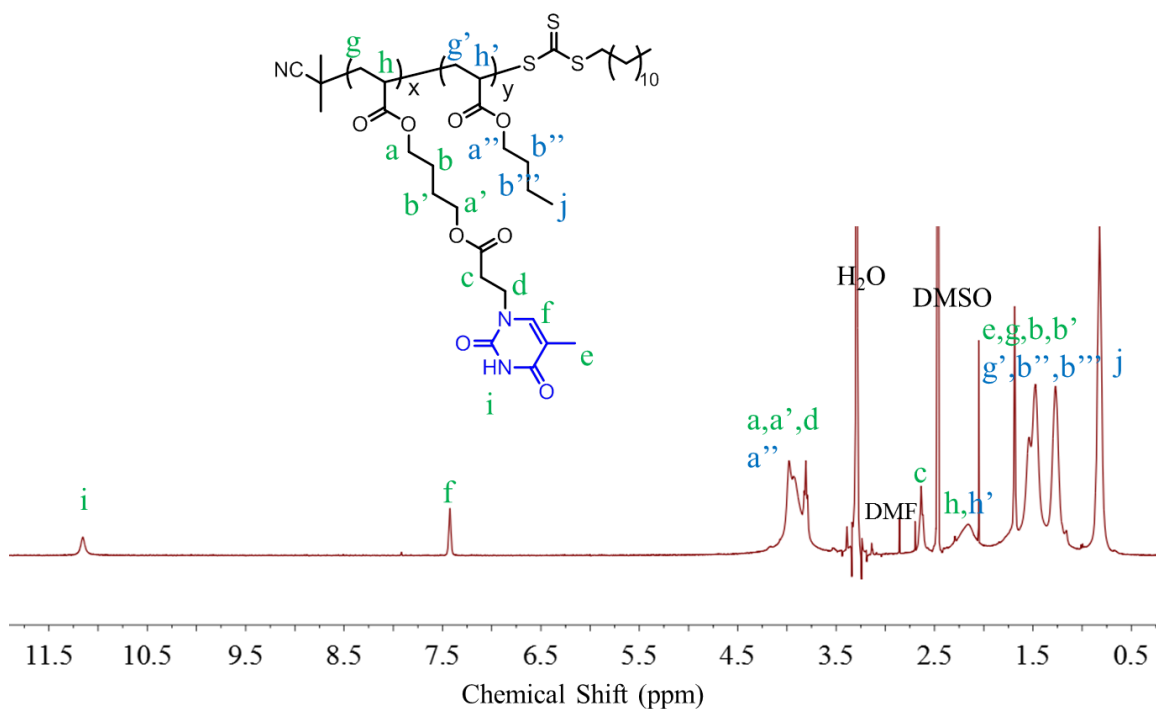


**Figure S4.2.**  $^1\text{H}$  NMR spectrum of poly(ThA-*b*-nBA) diblock copolymer macro-CTA.

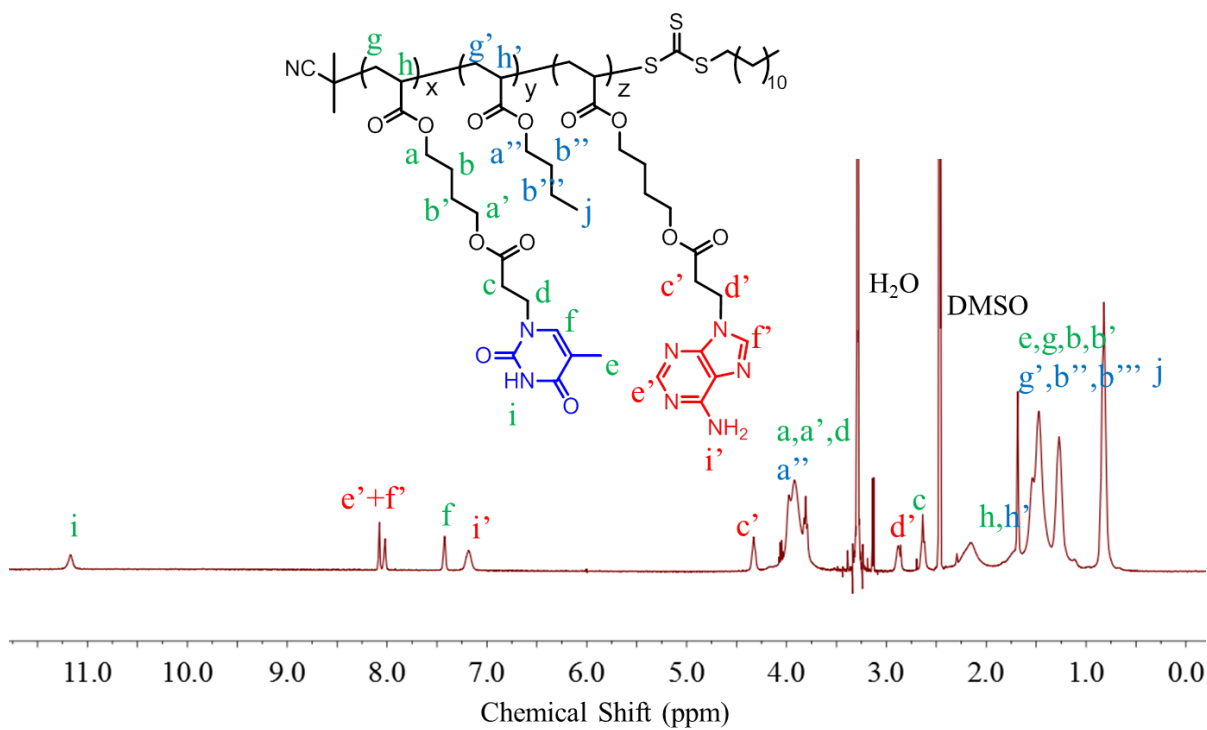


**Figure S4.3.**  $^1\text{H}$  NMR spectrum of poly(ThA-*b*-nBA-*b*-AdA) triblock copolymer.

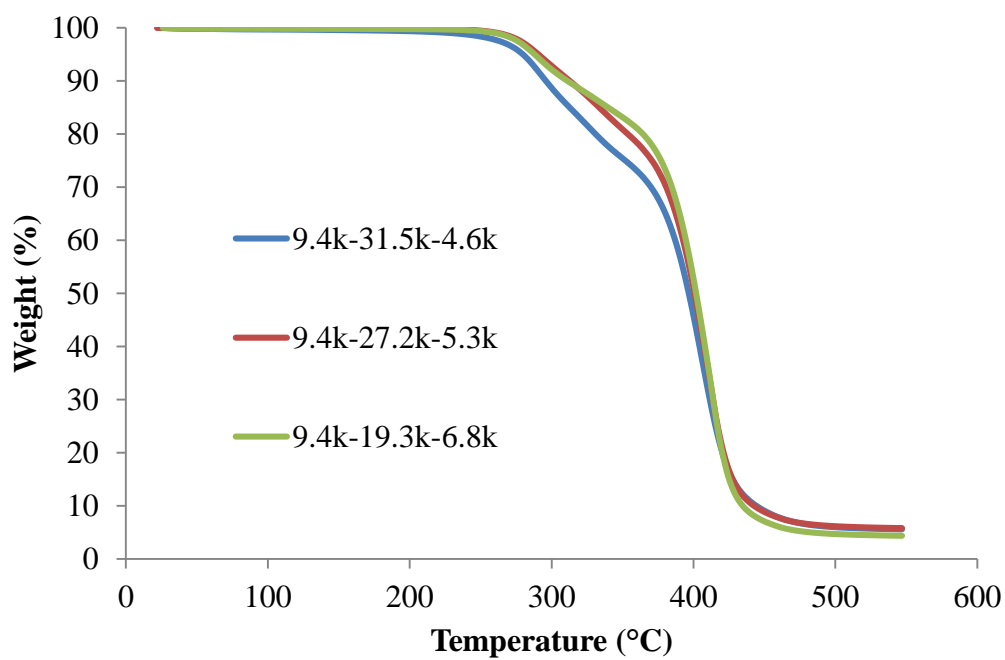


**Figure S4.4.** TGA profiles of poly(ThA-*b*-nBA-*b*-AdA) triblock copolymers.

## Chapter 5. Influence of Adenine and Thymine Binding Ratio on ABC Block Copolymer Self-Assembly

(In preparation for publishing in *Chemical Communication*)

Keren Zhang,<sup>a</sup> Samantha J. Talley<sup>a</sup>, Ya Peng Yu,<sup>b</sup> Robert B. Moore,<sup>a</sup> Mitsu Murayama,<sup>b</sup>  
and Timothy E. Long<sup>\*a</sup>

<sup>a</sup> *Department of Chemistry, Macromolecules and Interfaces Institute  
Virginia Tech, Blacksburg, VA 24061, USA*

<sup>b</sup> *Materials Science and Engineering, Virginia Tech, Blacksburg, VA 24061, USA*

Keywords: nucleobase, ABC triblock copolymer, thymine, adenine, self-assembly, block copolymer morphology

### 5.1 **Abstract**

ABC triblock copolymers bearing adenine- and thymine-functionalized external blocks self-assembled into long-range ordered lamellar microphase-separated morphology on non-patterned substrate. Intermolecular hydrogen bonding formed thymine-adenine triplets and promoted self-assembly into well-defined lamellae consisting of poly(*n*-butyl acrylate) soft domains and nucleobase hard domains, while thymine-adenine duplets contributed to superior mechanical property.

### 5.2 **Introduction**

Immiscibility of chemically different segments of block copolymers drives their self-assembly behavior, which generates various microphase-separated morphologies with periodic arrays of domains ranging from 10-100 nm in size.<sup>1-3</sup> Directed self-assembly of block copolymer thin films on patterned substrates forms well-defined periodic arrays of nano-size features with designed shapes, and the subsequent selective removal of one block enables fabrication of templates and scaffolds used in the microelectronics industry.<sup>2,4-5</sup>



Advances in polymer synthesis widened the applications of functional block copolymers to drug delivery, material templates, nanoporous membranes, photonic materials, composite materials, solar cells, adhesives, and elastomers.<sup>6-14</sup>

Nature broadly employs noncovalent interactions, such as hydrogen bonding,  $\pi$ - $\pi$  stacking, and ionic interaction, to construct well-defined supramolecular structures such as DNA and protein. Weaker than covalent bonds, noncovalent interactions provide intermediate bonding strength and directional bonding, which drive or facilitate self-assembly of natural biomacromolecules and synthetic polymers.<sup>15-18</sup> Combining noncovalent interactions with microphase-separation of block copolymers potentially provides a synergistic effect on the self-assembly behavior and enables designs of precise nano-features with additional functionality. For example, Bazzi *et al.* synthesized the first self-complementary ABC triblock copolymers and observed sequence-dependent self-assembly behavior in solution.<sup>19</sup> Xiong *et al.* demonstrated the formation of long worm-like aggregates in solution from two diblock copolymers bearing hydrogen bonding donors and acceptors, respectively.<sup>20</sup>

In the solid state, binary blends of two hydrogen-bonded diblock copolymers self-assembled into highly asymmetric lamellar morphology.<sup>21</sup> Another study showed that blends of two diblock copolymers with short associating blocks self-assembled into various hierarchical nanophase-separated morphologies with varying blending ratios and film-casting conditions.<sup>22</sup> Hybrid materials consisting of synthetic polymer blocks with biomacromolecule sequences emerged as a novel route to generate precise three-dimensional structures. For example, Sleiman *et al.* used short DNA strands to construct a block copolymer, which self-assembled into long nano-fibers through formation of three-

helix bundles.<sup>23</sup> Last but not least, hydrogen bonding proves essential in the self-assembled morphology of segmented polyurethanes and polyamides.<sup>24-28</sup>

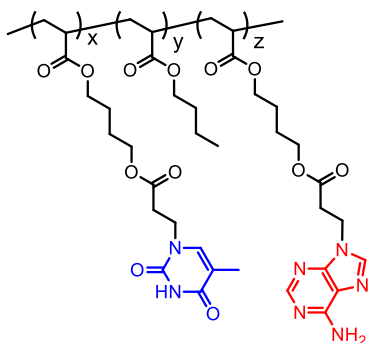
Recent advances in controlled polymerization techniques enable the synthesis of structurally diverse block copolymers. In addition to AB diblock and symmetric ABA triblock copolymers, many researchers prepared ABC triblock copolymers and investigated their self-assembled behaviors in the solid state, which generally led to rather complex morphologies with three phases.<sup>29-33</sup> Our group exploited the superior solvent and functional group tolerance of RAFT polymerization and prepared ABC triblock copolymers with two complementary, nucleobase-functionalized external blocks and a poly(*n*-butyl acrylate) (poly(*n*BA)) central block.<sup>34</sup> Preliminary SAXS results revealed highly ordered lamellae microphase-separated morphology of annealed ABC triblock copolymer films. However, the key parameters for achieving this ordered lamellar morphology remained undetermined.

Herein, this manuscript reports microphase-separated morphologies for an extended series of nucleobase-functionalized ABC triblock copolymers with varying compositions. Studying the effect of block length and thymine-adenine (T-A) binding ratio on morphology and thermomechanical properties aims to establish the structure-morphology-property relationship for ABC triblock copolymers with associating blocks. Transmission electronic microscopy (TEM) revealed a defect-free lamellar morphology with long-range order for the free-standing film of a nucleobase-functionalized ABC copolymer solution-casted onto a non-patterned PTFE surface. In addition, ABA triblock copolymers with external blocks consisting of random copolymers of adenine and thymine acrylics served as controls to determine the necessity of the asymmetric ABC architecture

in forming ordered lamellae. This study reveals synergistic effects of noncovalent interaction and phase-separation on facilitating self-assembly and enhancing thermomechanical performance of block copolymers. Using associating blocks provides a promising strategy to achieve long-range order in block copolymer microphase-separated morphology for nanolithography and patterning.

### 5.3 ***Results and Discussion***

A three-step RAFT polymerization afforded a series of ABC block copolymers with complementary nucleobase-functionalized external blocks and poly(*n*BA) central block (Scheme 5.1), following procedures from Long *et al.*<sup>34</sup> Polymerization of adenine acrylate (AdA) and thymine acrylate (ThA) monomers allowed the synthesis of adenine- and thymine-functionalized external blocks, respectively. <sup>1</sup>H NMR spectroscopy determined the number-average molecular weight ( $M_n$ ) of all poly(ThA-*b*-*n*BA-*b*-AdA) block copolymers, abbreviated as PTBA (Table S5.1). PTBA triblock copolymers were solution cast from DMSO into non-patterned PTFE molds and dried to form free-standing films ranging from 0.2 mm to 0.5 mm in thickness, in accordance with previously reported procedures.<sup>34</sup> Thermogravimetric analysis revealed  $T_{d,5wt\%}$  weight loss temperatures of PTBA copolymer ranged from 280 °C to 290 °C, and differential scanning calorimetry showed two  $T_g$ 's for each PTBA copolymer near -45 °C and 70 °C respectively (Figures S5.1, S5.2, Table S5.2). The lower  $T_g$  corresponded to the poly(*n*BA) soft phase, and the higher  $T_g$  ranged from 60 °C to 71 °C with varying adenine to thymine ratio, as poly(AdA) showed slightly higher  $T_g$  than poly(ThA).<sup>35</sup> Each PTBA copolymer exhibited only one  $T_g$  above room temperature, as the hydrogen bonding between adenine- and thymine-functionalized blocks contributed to a single hard phase, consistent with earlier work.<sup>34</sup>



**Scheme 5.1.** Chemical structure of poly(ThA-*b*-*n*BA-*b*-AdA) (PTBA) ABC triblock copolymers.

Firstly, varying poly(AdA) block length and maintaining poly(ThA) and poly(*n*BA) block length yielded a series of PTBA copolymers with different microphase-separated morphologies. The table in Figure 5.1 summarizes the compositions, thymine-adenine (T-A) ratios, and nucleobase block weight percentages (NB wt%), as well as the morphologies of solution-cast PTBA films determined using SAXS and AFM. Increasing the adenine-functionalized block length from 4.6 kDa to 10.7 kDa resulted in a decrease of thymine-adenine ratio from 2.1 to 1.1. The distinctive scattering pattern for PTBA with T-A ratio of 2.1 showed well-organized lamellar morphology, while T-A ratio of 1.5 led to a lamellar scattering profile with broader scattering peaks and only one distinguishable secondary peak at the 2 $q$  position. SAXS profile of PTBA with T-A ratio of 1.1 indicated a much less ordered morphology, and AFM showed a disordered biphasic morphology at the film surface. We previously proposed two hypotheses to account for different morphologies of PTBA copolymers with various compositions, i.e., (1) the order of microphase-separated morphology increased with increasing block length, (2) thymine-adenine ratio dominated self-assembly and affected the order of microphase-separation.<sup>34</sup> This series of copolymers in Figure 5.1 clearly determined that longer block lengths did not directly result in more

well-ordered morphology. Since copolymers in Figure 5.1 all exhibited similarly long block lengths, it was reasonable to conclude that sufficient block length alone does not necessarily lead to a well-ordered morphology. Thymine-adenine ratio played significant role in self-assembled morphology of PTBA copolymers with complementary external blocks. AFM phase images showed absence of lamellar morphology on the film surface due to different surface energy of the nucleobase domains and poly(*n*BA) domains under air. However, the TEM image of microtomed PTBA (9.4-31.5-4.6) film revealed a remarkably ordered lamellar morphology with long-range order (Figure 5.2). This long-range order likely resulted from the complementary hydrogen bonding directing the assembly of the nucleobase blocks in absence of substrate pattern.

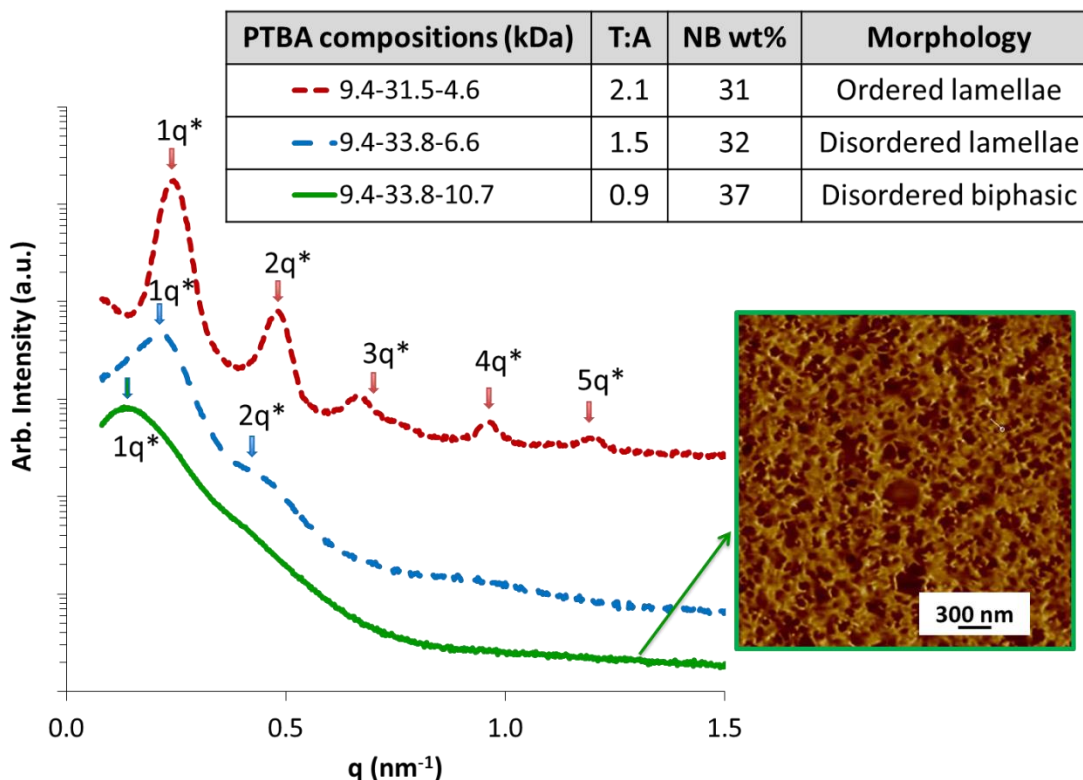


**Figure 5.1.** SAXS scattering profiles of PTBA films with varying thymine-adenine ratio; AFM phase image shows the bicontinuous surface morphology of PTBA (9.4-33.8-10.7) triblock copolymer film.

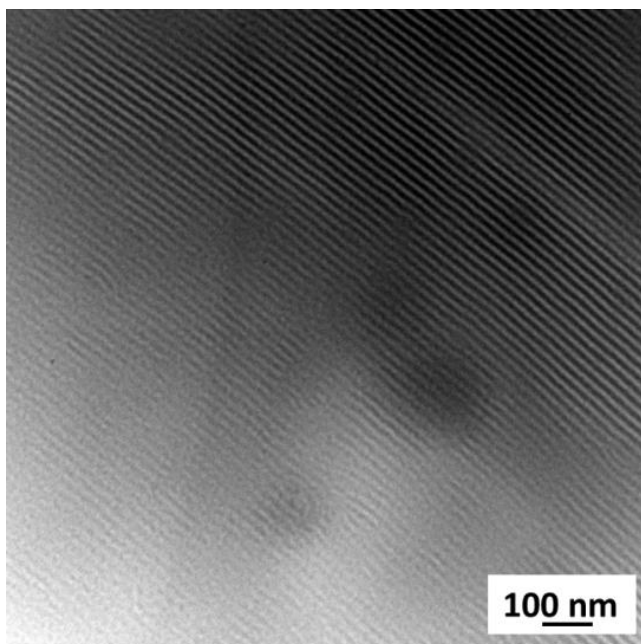


**Figure 5.2.** TEM image of PTBA (9.4-31.5-4.6) triblock copolymer film.

Dynamic mechanical analysis (DMA) compared the thermomechanical performance of three PTBA copolymers films (Figure 5.3). In contrast to the trend of morphology, the PTBA film with T-A ratio near one exhibited highest plateau modulus and widest plateau window. One to one hydrogen binding between thymine and adenine contributed to enhanced mechanical properties, and two to one binding ratio yielded the worst thermomechanical performance. Hydrogen bonding between adenine and thymine provided physical crosslinking in the hard phase, which restricted molecular mobility beyond the glass transition temperature<sup>34</sup> of the nucleobase block near 60-70 °C, observed only from DSC. The association strength of hydrogen bonding accounted for the difference in thermomechanical performance of PTBA film. One to one binding between thymine and

adenine likely formed stronger crosslinking than two to one binding. However, the increasing nucleobase weight percent from 31 wt% to 37 wt% provided another explanation for the increasing mechanical strength.

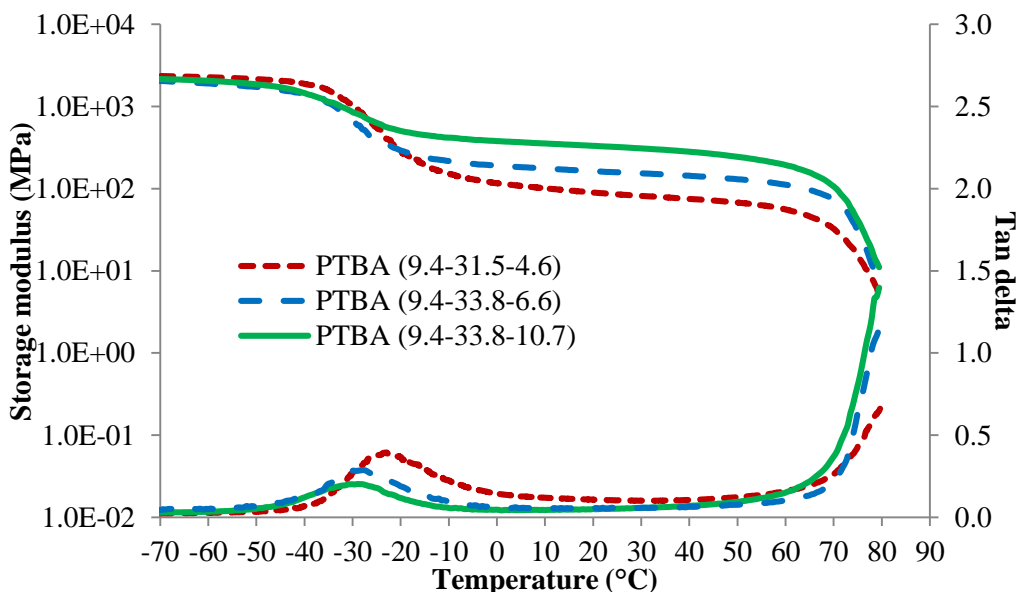


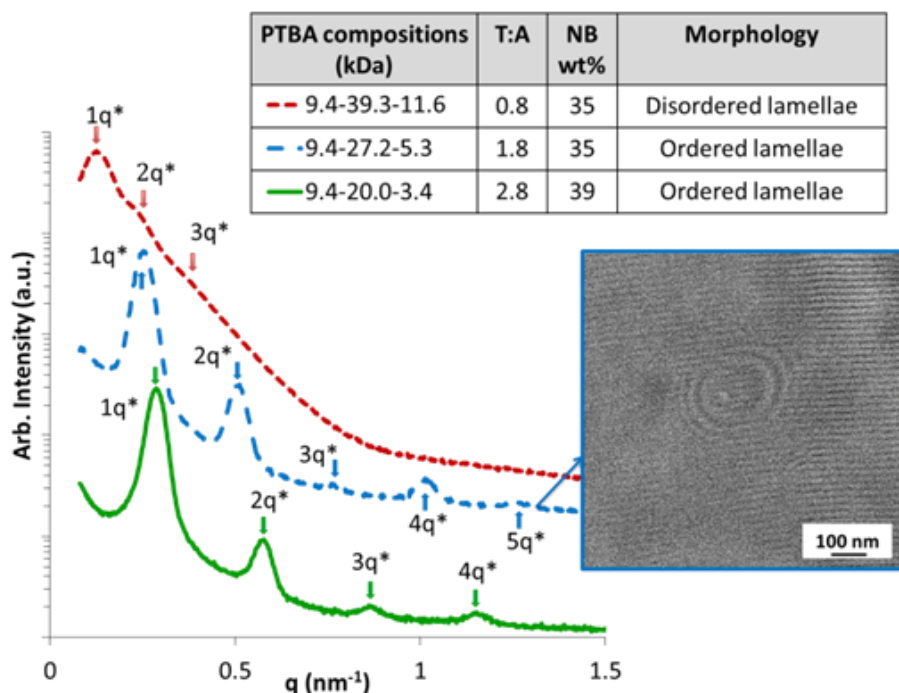
**Figure 5.3** Dynamic mechanical temperature ramps for solution-cast PTBA films with varying poly(AdA) block length.

An additional aspect of this investigation pertains to the morphological and thermomechanical differences for PTBA copolymers with similar nucleobase wt% but different T-A ratios. Fig. 5.4 depicts two PTBA copolymers with similar nucleobase weight percentages and different T-A ratios. The SAXS profile for PTBA (9.4-27.2-5.3) with a T-A molar ratio of 1.8 exhibited higher order scattering peaks up to the 5q position, indicative of an ordered lamellar morphology. On the contrary, PTBA (9.4-39.3-11.6) with T-A ratio of 0.8 displayed significantly broader scattering peaks, indicative of a disordered lamellar morphology, despite similar nucleobase wt% with PTBA (9.4-27.2-5.3). This morphological difference indicated a strong dependence of PTBA morphology on thymine-adenine binding ratio, which yielded an ordered lamellar phase when T-A molar ratio

approached 2:1. The domain spacing of lamellae in Fig. 3 significantly increased with increasing block lengths, as the primary scattering peak shifted to lower  $q$  values.

A steric effect provides a plausible explanation for the optimal T-A binding ratio in achieving ordered lamellar morphology. The conjugated purine ring of adenine occupies a larger space than the pyrimidine ring of thymine. Two thymine units bind with one adenine unit to form a base triplet (Fig. 4), previously observed in triple helix DNA molecules.<sup>37</sup> PTBA (9.4-27.2-5.3) with T-A ratio of 2.8 also self-assembled into ordered lamellae with scattering peaks up to the  $4q$  position. Additional thymine units with a higher T-A ratio than 2:1 presumably caused less disruption to the triplet formation compared to additional adenine units. As a result, PTBA with T-A of 2.8 showed more ordered lamellae compared to PTBA with T-A of 0.8. The formation of base triplets likely facilitates the development of highly ordered lamellar morphology. However, the current study only places the optimal T-A ratio near 2:1, and determining the precise optimal ratio for forming lamellae with long-range order could be achieved with complementary computational simulations and calculations. The weight percentage of overall nucleobase blocks showed an insignificant effect on self-assembled morphologies of PTBA for the entire series synthesized in this study (Table S5.1).





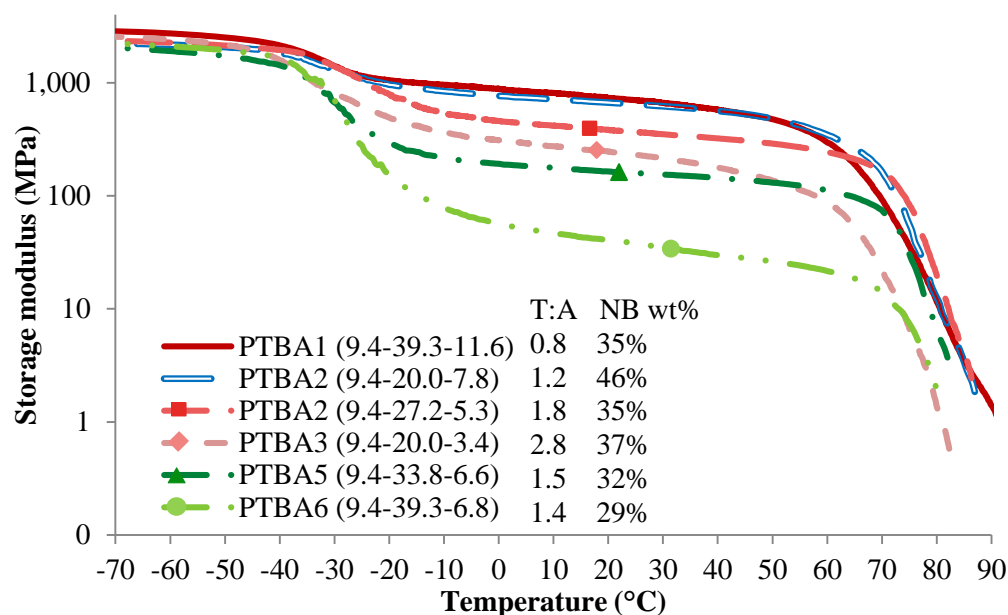
**Figure 5.4.** SAXS profiles of PTBA films with varying thymine-adenine ratio or varying nucleobase block weight percent; TEM image shows ordered lamellar morphology of a PTBA (9.4-20.0-3.4) triblock copolymer film. \*The newton’s rings are imaging artifacts due to weak phase contrast.

Figure 5.5 compares DMA modulus curves of six PTBA copolymer films with varying compositions to investigate the influence of T-A ratio and NB wt% on the thermomechanical properties. PTBA copolymer films were numbered in Figure 5.5 to ease the discussion. PTBA3 (9.4-27.2-5.3) exhibited a lower plateau modulus and a wider glass transition compared to PTBA1 (9.4-39.3-11.6), due to weaker physical crosslinking as these two copolymers shared the same NB wt%. The plateau modulus further decreased for PTBA4 (9.4-20.0-2.4) with similar NB wt% as T-A ratio increased to 2.8. This comparison confirmed the hypothesis that hydrogen bonding of thymine-adenine weakened as T-A ratio deviated from one. The viscous flow temperature also decreased

from 90 °C to 80 °C with increasing T-A ratio from 1.2 to 2.8 in presence of constant NB wt%. The similar plateau modulus of PTBA2 (9.4-20.0-7.8) compared to PTBA1 confirmed that the trend of plateau moduli of PTBA1>PTBA3>PTBA4 did not result from their molecular weight difference.

The higher NB wt% of PTBA2 did not lead to a significantly higher plateau modulus compared to PTBA1 because of their high modulus value. In the lower modulus region, the plateau modulus increased significantly with increasing NB wt% when comparing PTBA5 (9.4-33.8-6.6) and PTBA6 (9.4-39.3-6.8) with the same T-A ratio. The reinforcement of mechanical strength from physical crosslinking proved more trivial for rigid materials compared to soft materials. In summary, mechanical strength of PTBA decreased as T-A ratio deviated from one with constant NB wt%, and plateau modulus decreased as NB wt% decreased with uniform T-A ratio. The effect of NB wt% became more obvious at relatively low modulus level.

In addition, NMR titration experiment using the Job's method confirmed the one to one host-guest binding stoichiometry for the complex of thymine acrylate and adenine acrylate in CDCl<sub>3</sub> with a total concentration of 45 mM and 100 mM (Figure S5.4, S5.5).<sup>38-</sup>  
<sup>39</sup> The solubility of ThA and AdA in nonpolar solvents limited their titration at a higher concentration. One to one binding ratio between thymine and adenine was favored thermodynamically, forming stronger hydrogen bonding than the two to one base triplet.



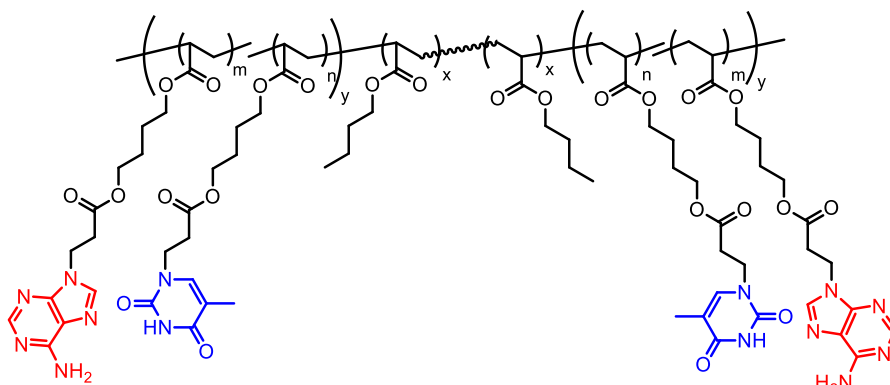
**Figure 5.5.** Dynamic mechanical temperature ramps for solution-cast PTBA films with varying poly(*n*BA) and poly(AdA) block length.

Last but not least, two symmetric ABA triblock copolymers carrying both thymine and adenine on the external blocks served as controls to investigate the necessity of asymmetric triblock structure in forming ordered lamellar morphology. A two-step RAFT polymerization with a difunctional chain transfer agent<sup>40</sup> yielded two ABA triblock copolymers poly((ThA-*co*-AdA)-*b*-*n*BA-*b*-(ThA-*co*-AdA)), abbreviated as P(TA-B-TA) using a modified procedure from Long *et al.* (Scheme 5.2, S5.1).<sup>35</sup> The external blocks were random copolymers of ThA and AdA, considering the identical structure of these two monomers near their acrylic backbones and the absence of templating effect in polar solvents.<sup>35,41</sup> The initial monomer charge ratios of 1.0 and 2.0 matched with T-A ratios of 1.0 and 1.9 in the purified block copolymers, respectively.  $M_n$  of P(TA-B-TA) with T-A 1.0 was 12.5-44.8-12.5 kDa and  $M_n$  of P(TA-B-TA) with T-A 1.9 was 9.4-44.8-9.4 kDa.

The nucleobase blocks comprised 35 wt% and 30 wt% for P(TA-B-TA) with T-A 1.0 and T-A 1.9, respectively.

The SAXS profile of P(TA-B-TA) T-A 1.0 showed broad scattering maxima with periodic intensity oscillations that roughly matched  $q$ ,  $\sqrt{3}q$ ,  $\sqrt{4}q$ ,  $\sqrt{7}q$ , and  $\sqrt{9}q$  peak positions for hexagonally packed cylindrical morphology (Figure 5.7). The AFM phase image also depicted a cylindrical surface morphology with a distribution of inter-domain spacing, agreeing with the SAXS result (Figure 5.7). On the AFM phase image, nucleobase-functionalized external blocks self-assembled into the cylindrical hard domains (light areas), distributed in the poly(*n*BA) soft matrix (dark areas), and all cylinders pointed towards the film surface. The morphology of P(TA-B-TA) T-A 1.0 matched closely with the supramolecular blend of poly(AdA-*b*-*n*BA-*b*-AdA) and poly(ThA-*b*-*n*BA-*b*-ThA) with similar block length and T-A ratio,<sup>35</sup> while the PTBA analog with T-A of 1.2 and 35 NB wt% exhibited a mixed cylindrical-lamellar morphology. SAXS and AFM results of P(TA-B-TA) T-A 1.9 showed a mixed cylindrical-lamellar morphology, distinctively different from the ordered lamellar morphology of PTBA (9.4-31.5-4.6) with similar T-A ratio and NB wt%. As a result, the presence of both thymine and adenine on a single polymer chain with optimal T-A ratio proved insufficient for ordered lamellae formation. The less ordered morphologies of symmetric ABA controls compared to PTBA likely resulted from significant amount of intramolecular hydrogen bonding. The randomly distributed thymine and adenine pendant groups predominately associated with their adjacent partners from the same block, which resulted in microphase-separated morphology of typical non-associating ABA block copolymers. The asymmetric PTBA block copolymer structure facilitated the intermolecular recognition between adenine and thymine units from different

polymer chains, which proved crucial for ordered lamellae formation. However, determining the ratio of intra- versus intermolecular hydrogen bonding of P(TA-B-TA) and PTBA remained challenging.



**Scheme 5.2.** Chemical structure of poly((ThA-co-AdA)-b-nBA-b-(ThA-co-AdA)), abbreviated as P(TA-B-TA).

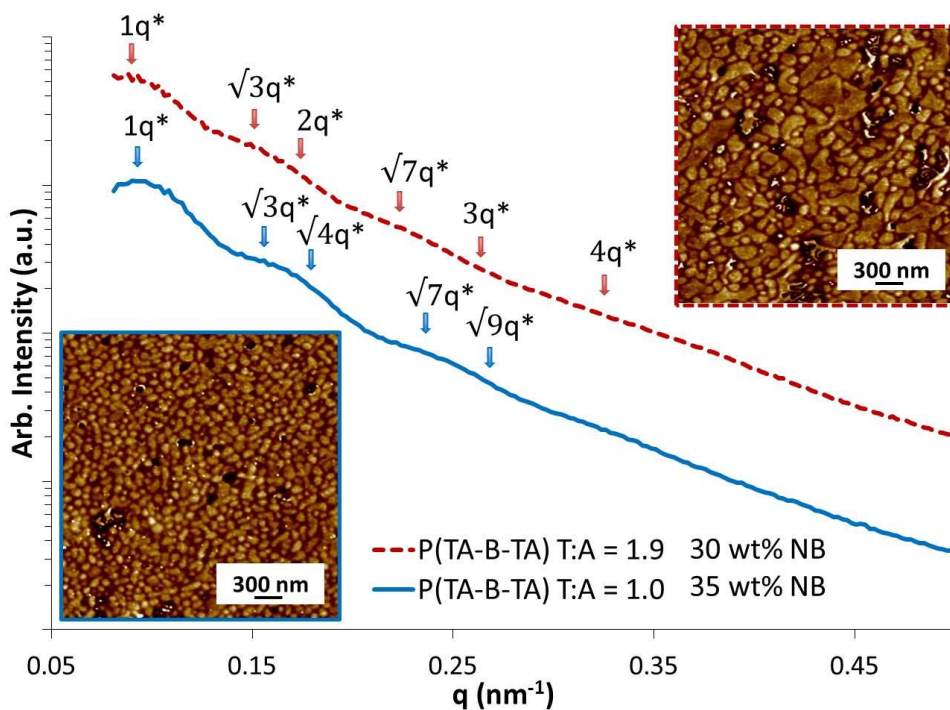


**Figure 5.6.** SAXS scattering profiles and AFM phase images of P(TA-B-TA) films with varying thymine-adenine ratio.

Figure 5.7 depicts the ordered lamellar morphology of PTBA with hydrogen bonded triplets containing two thymine units and one adenine unit. Intermolecular hydrogen bonding presumably directed the packing of alternating nucleobase blocks, which assembled into the hard domains. Well-organized lamellae with long-range order formed with optimal space matching thymine-adenine (T-A) ratio near two (Figure 5.2), while deviation of the T-A ratio resulted in curvature of the lamellae (Figure S5.6). Hydrogen bonding within the nucleobase-containing hard domains directed the morphological development of long-range ordered lamellae, and each nucleobase block preferentially bond with its complementary block rather than the poly(*n*BA) block. AFM phase images failed to show lamellar on the PBTA film surface except for PTBA (5.8-23.6-1.9) with 25 wt% NB (Figure S5.6). It is presumed that the nucleobase-containing hard domain favored the surface to air, and increasing the poly(*n*BA) content forced the soft phase to be present at the film surface.

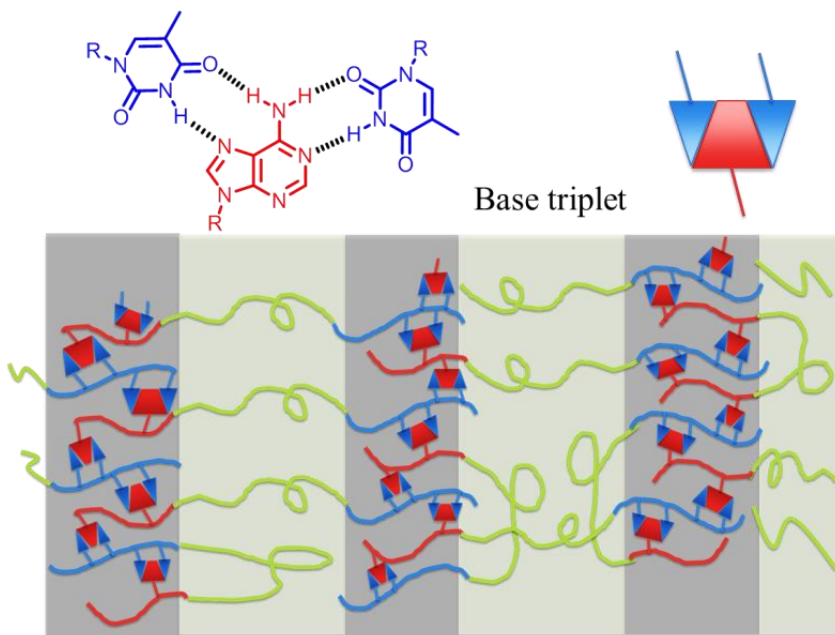


**Figure 5.7.** Proposed pictorial representation of long-range ordered lamellar morphology of PTBA triblock copolymers that contain thymine-adenine base triplets.

## 5.4 *Conclusions*

In conclusion, a series of PTBA triblock copolymers with complementary external blocks exhibited unique composition-dependent, self-assembled morphologies. This manuscript discusses in detail how thymine-adenine ratio and the nucleobase block weight percent influence bulk morphology and the thermomechanical performance of solution-cast PTBA copolymer films. An optimal thymine-adenine ratio near two promoted the formation of long-range ordered lamellar morphology without substrate patterning. However, thymine-adenine thermodynamically favored one to one binding ratio, which provided strong physical crosslinking and contributed to superior thermomechanical properties. The asymmetric structure of PTBA triblock copolymers proved crucial in forming intermolecular hydrogen bonding, which directed the block copolymer self-assembly into ordered lamellae. This study demonstrates the profound effect of noncovalent interaction on self-assembled morphology and thermomechanical performance of block copolymers. Utilizing the synergy of noncovalent interaction and block copolymer phase-separation provides a promising route for generating templates and scaffolds for nano-fabrication, and developing thermoplastics and elastomers with enhanced mechanical performance.

## 5.5 *Acknowledgements*

This work was supported in part by Henkel Corporation. We also thank insightful discussions with Dr. Charles Paul, Dr. Eric Silverberg, and Dr. Cristina DeJesus from

Henkel. This material was also partially based upon work supported by the National Science Foundation under Grant No. DMR-0923107.

## 5.6 References

1. Bates, F. S.; Fredrickson, G. H. *Annu. Rev. Phys. Chem.* **1990**, *41*, 525.
2. Bates, C. M.; Maher, M. J.; Janes, D. W.; Ellison, C. J.; Willson, C. G. *Macromolecules* **2014**, *47*, 2.
3. Koo, K.; Ahn, H.; Kim, S.-W.; Ryu, D. Y.; Russell, T. P. *Soft Matter* **2013**, *9*, 9059.
4. Kim, H.-C.; Park, S.-M.; Hinsberg, W. D. *Chem. Rev.* **2010**, *110*, 146.
5. Herr, D. J. C. *J. Mater. Res.* **2011**, *26*, 122.
6. Förster, S.; Antonietti, M. *Adv. Mater.* **1998**, *10*, 195.
7. Alexandridis, P.; Lindman, B. *Amphiphilic block copolymers: self-assembly and applications*; Elsevier, **2000**.
8. Klok, H. A.; Lecommandoux, S. *Adv. Mater.* **2001**, *13*, 1217.
9. Rösler, A.; Vandermeulen, G. W.; Klok, H.-A. *Adv. Drug Delivery Rev.* **2012**, *64*, 270.
10. Schacher, F. H.; Rupar, P. A.; Manners, I. *Angew. Chem. Int. Ed.* **2012**, *51*, 7898.
11. Peinemann, K.-V.; Abetz, V.; Simon, P. F. W. *Nat Mater* **2007**, *6*, 992.
12. Botiz, I.; Darling, S. B. *Materials Today* **2010**, *13*, 42.
13. Orilall, M. C.; Wiesner, U. *Chem. Soc. Rev.* **2011**, *40*, 520.
14. Kim, J. K.; Yang, S. Y.; Lee, Y.; Kim, Y. *Prog. Polym. Sci.* **2010**, *35*, 1325.
15. Aida, T.; Meijer, E. W.; Stupp, S. I. *Science* **2012**, *335*, 813.
16. Brunsveld, L.; Folmer, B. J. B.; Meijer, E. W.; Sijbesma, R. P. *Chem. Rev.* **2001**, *101*, 4071.
17. Yang, L.; Tan, X.; Wang, Z.; Zhang, X. *Chem. Rev.* **2015**, *115*, 7196.
18. Hemp, S. T.; Long, T. E. *Macromol. Biosci.* **2012**, *12*, 29.
19. Bazzi, H. S.; Bouffard, J.; Sleiman, H. F. *Macromolecules* **2003**, *36*, 7899.
20. Xiong, D. a.; Shi, L.; Jiang, X.; An, Y.; Chen, X.; Lü, J. *Macromol. Rapid Commun.* **2007**, *28*, 194.
21. Han, S. H.; Pryamitsyn, V.; Bae, D.; Kwak, J.; Ganesan, V.; Kim, J. K. *ACS Nano* **2012**, *6*, 7966.
22. Dobrosielska, K.; Takano, A.; Matsushita, Y. *Macromolecules (Washington, DC, U. S.)* **2010**, *43*, 1101.
23. Carneiro, K. M. M.; Aldaye, F. A.; Sleiman, H. F. *J. Am. Chem. Soc.* **2010**, *132*, 679.
24. Korley, L. T. J.; Pate, B. D.; Thomas, E. L.; Hammond, P. T. *Polymer* **2006**, *47*, 3073.
25. Gao, R.; Zhang, M.; Wang, S.-W.; Moore, R. B.; Colby, R. H.; Long, T. E. *Macromol. Chem. Phys.* **2013**, *214*, 1027.
26. Yilgor, I.; Yilgor, E.; Guclu Guler, I.; Ward, T. C.; Wilkes, G. L. *Polymer* **2006**, *47*, 4105.
27. Sheth, J. P.; Aneja, A.; Wilkes, G. L.; Yilgor, E.; Atilla, G. E.; Yilgor, I.; Beyer, F. L. *Polymer* **2004**, *45*, 6919.



28. Sami, S.; Yildirim, E.; Yurtsever, M.; Yurtsever, E.; Yilgor, E.; Yilgor, I.; Wilkes, G. L. *Polymer* **2014**, *55*, 4563.
29. Nakazawa, H.; Ohta, T. *Macromolecules* **1993**, *26*, 5503.
30. Higuchi, T.; Sugimori, H.; Jiang, X.; Hong, S.; Matsunaga, K.; Kaneko, T.; Abetz, V.; Takahara, A.; Jinnai, H. *Macromolecules* **2013**, *46*, 6991.
31. Stadler, R.; Auschra, C.; Beckmann, J.; Krappe, U.; Voight-Martin, I.; Leibler, L. *Macromolecules* **1995**, *28*, 3080.
32. Elbs, H.; Drummer, C.; Abetz, V.; Krausch, G. *Macromolecules* **2002**, *35*, 5570.
33. Mogi, Y.; Kotsuji, H.; Kaneko, Y.; Mori, K.; Matsushita, Y.; Noda, I. *Macromolecules* **1992**, *25*, 5408.
34. Zhang, K.; Fahs, G. B.; Aiba, M.; Moore, R. B.; Long, T. E. *Chem. Comm.* **2014**, *50*, 9145.
35. Zhang, K.; Aiba, M.; Fahs, G. B.; Hudson, A. G.; Chiang, W. D.; Moore, R. B.; Ueda, M.; Long, T. E. *Polym. Chem.* **2015**, *6*, 2434.
36. Kholodovych, V.; Welsh, W. J. In *Physical Properties of Polymers Handbook*; Mark, J. E., Ed.; Springer New York: New York, NY, 2007, p 611.
37. Sivakova, S.; Rowan, S. J. *Chem. Soc. Rev.* **2005**, *34*, 9.
38. Fielding, L. *Tetrahedron* **2000**, *56*, 6151.
39. Tamami, M.; Hemp, S. T.; Zhang, K.; Zhang, M.; Moore, R. B.; Long, T. E. *Polymer* **2013**, *54*, 1588.
40. Allen, M. H., Jr.; Hemp, S. T.; Zhang, M.; Zhang, M.; Smith, A. E.; Moore, R. B.; Long, T. E. *Polym. Chem.* **2013**, *4*, 2333.
41. Kang, Y.; Lu, A.; Ellington, A.; Jewett, M. C.; O'Reilly, R. K. *ACS Macro Letters* **2013**, 581.

## 5.7 Supporting Information

**Materials.** *n*-Butyl acrylate (*n*BA, 99+%) was purchased from Aldrich and passed through neutral alumina columns before use.  $\alpha,\alpha'$ -Azobis(isobutyronitrile) (AIBN, Fluka, 99%) was recrystallized from methanol. 1,4-Butanediol diacrylate (Alfa Aesar, 99%) was used without further purification. Adenine (A, 99%), thymine (T, 99%), triethylamine (TEA, 99%), potassium carbonate (99%), 2-cyano-2-propyl dodecyl trithiocarbonate (CPDT, 97%), and 2,6-di-*tert*-butyl-4-methylphenol (BHT, 99%) were purchased from Aldrich and used without further purification. Hexane (HPLC grade), chloroform (CHCl<sub>3</sub>, HPLC), tetrahydrofuran (THF, HPLC grade), dimethylsulfoxide (DMSO, HPLC grade) and *N,N*-

dimethylformamide (DMF, HPLC grade, anhydrous) were purchased from Fisher Scientific and used as received.

**Analytical Methods.**  $^1\text{H}$  NMR spectra were collected in  $\text{CDCl}_3$  or  $\text{DMSO-d}_6$  on a Varian INOVA spectrometer operating at 400 MHz at 23 °C. Differential scanning calorimetry (DSC) was performed under a nitrogen flush of 50 mL/min at a heating rate of 10 °C/min on a TA instruments Q1000 DSC, which was calibrated using indium (mp = 156.60 °C) and zinc (mp = 419.47 °C) standards. Glass transition temperatures were measured as the midpoint of the transition in the second heating scan. DMA was conducted on a TA Instruments Q800 in tension mode at a frequency of 1 Hz, an oscillatory amplitude of 8  $\mu\text{m}$ , and a static force of 0.01 N. The temperature ramp was 3 °C/min. The glass transition temperature ( $T_g$ ) was determined at the peak maximum of the  $\tan \delta$  curve.

SAXS experiments were performed using a Rigaku S-Max 3000 3 pinhole SAXS system, equipped with a rotating anode emitting X-ray with a wavelength of 0.154 nm ( $\text{Cu K}\alpha$ ). The sample-to-detector distance was 1600 mm, and q-range was calibrated using a silver behenate standard. Two-dimensional SAXS patterns were obtained using a fully integrated 2D multiwire, proportional counting, gas-filled detector, with an exposure time of 2 hours. All the SAXS data were analyzed using the SAXSGUI software package to obtain radially integrated SAXS intensity versus scattering vector  $q$ , where  $q = (4\pi/\lambda)\sin(\theta)$ ,  $\theta$  is one half of the scattering angle and  $\lambda$  is the wavelength of X-ray.

Ultrathin sections of PTBA copolymer films were prepared using a CR-X Cryosectioning System (RMC Boeckeler). Ethanol was used as a solvent for cryo-microtome with the diamond knife (Micro Star) temperature set at -85°C and cutting thickness controlled at ~100nm. Sample sections were collected on Cu TEM grids and

stained with iodine (99%) overnight. PTBA copolymer films were imaged using a transmission electron microscope (FEI Titan 300) operated at 300 kV.

ABC and ABA block copolymer synthesis, solution-cast process, and annealing conditions followed previous literature procedures.<sup>1,2</sup>

**Table S5.1.** PTBA triblock copolymer compositions, thymine-adenine (T-A) ratios, nucleobase block weight percent, and morphologies, determined using AFM and SAXS.

| Poly(ThA)<br>(kDa) | DP<br>(ThA) | Poly( <i>n</i> BA)<br>(kDa) | DP<br>( <i>n</i> BA) | Poly(AdA)<br>(kDa) | DP<br>(AdA) | T-A<br>ratio | M <sub>n</sub><br>total | NB<br>wt% | Morphology             |
|--------------------|-------------|-----------------------------|----------------------|--------------------|-------------|--------------|-------------------------|-----------|------------------------|
| 9.4                | 28.9        | 4.3                         | 333.6                | 10.1               | 30.3        | 1.0          | 23.8                    | 82        | No order               |
| 9.4                | 28.9        | 20.0                        | 156.3                | 7.8                | 23.3        | 1.2          | 37.2                    | 46        | Disordered<br>Lamellae |
| 9.4                | 28.9        | 19.3                        | 150.8                | 6.8                | 20          | 1.4          | 35.5                    | 46        | Disordered<br>Lamellae |
| 9.4                | 28.9        | 20.0                        | 156.3                | 3.4                | 10.2        | 2.8          | 32.8                    | 39        | Ordered<br>Lamellae    |
| 9.4                | 28.9        | 26.0                        | 203.1                | 10.0               | 29.9        | 1.0          | 45.4                    | 43        | Disordered<br>Lamellae |
| 9.4                | 28.9        | 27.2                        | 212.5                | 5.3                | 16          | 1.8          | 41.9                    | 35        | Ordered<br>Lamellae    |
| 9.4                | 28.9        | 33.8                        | 264.1                | 10.7               | 32.1        | 0.9          | 53.9                    | 37        | Disordered<br>biphasic |
| 9.4                | 28.9        | 33.8                        | 264.1                | 6.6                | 19.8        | 1.5          | 49.8                    | 32        | Disordered<br>Lamellae |
| 9.4                | 28.9        | 31.5                        | 246.1                | 4.6                | 14          | 2.1          | 45.5                    | 31        | Ordered<br>Lamellae    |
| 9.4                | 28.9        | 39.3                        | 307.0                | 11.6               | 34.7        | 0.8          | 60.3                    | 35        | Disordered<br>Lamellae |
| 9.4                | 28.9        | 39.3                        | 307.0                | 6.8                | 20.4        | 1.4          | 55.5                    | 29        | Disordered<br>Lamellae |
| 5.8                | 17.9        | 23.6                        | 184.4                | 1.8                | 5.55        | 3.2          | 31.2                    | 24        | Ordered<br>Lamellae    |
| 5.8                | 17.9        | 11.5                        | 89.8                 | 10.5               | 31.6        | 0.6          | 27.8                    | 59        | Cylinders              |

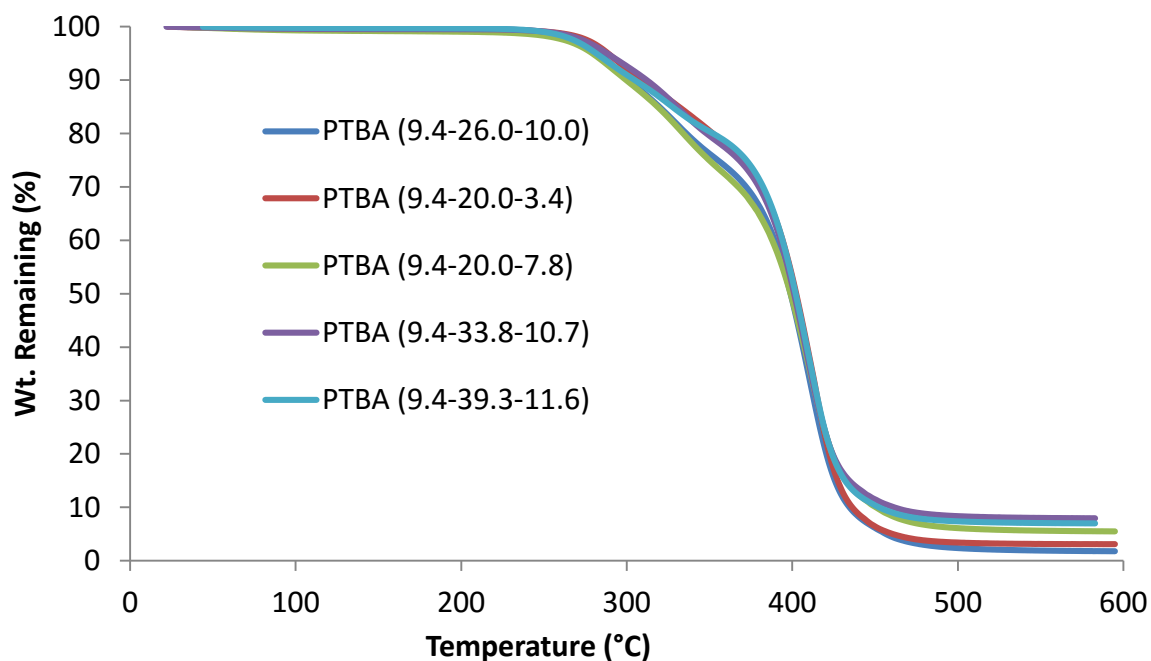


**Figure S5.1.** Representative TGA thermograms of PTBA copolymers.

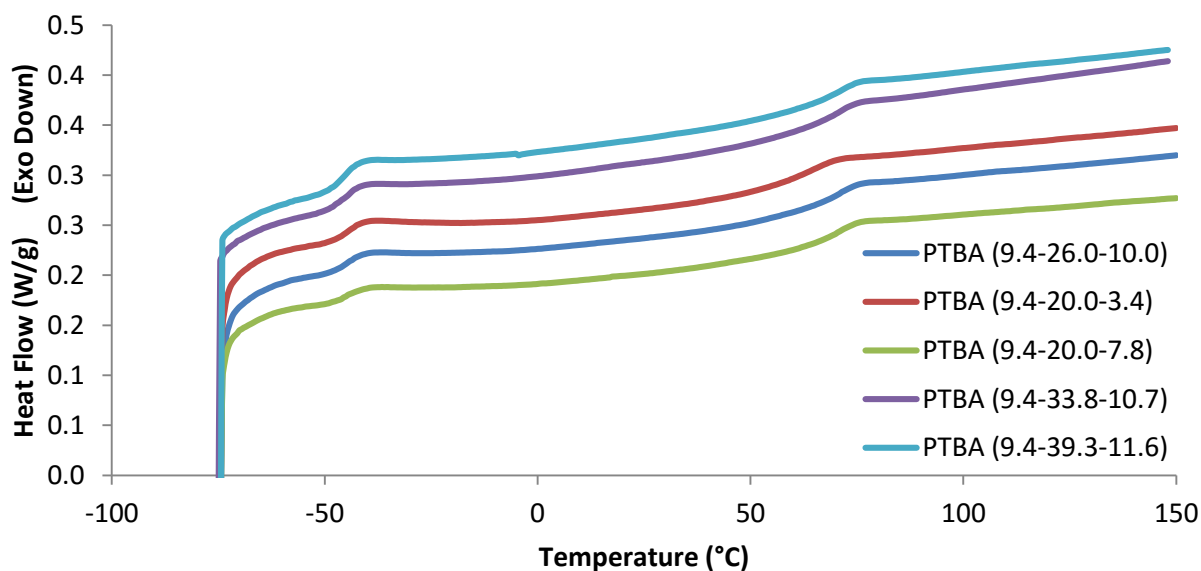
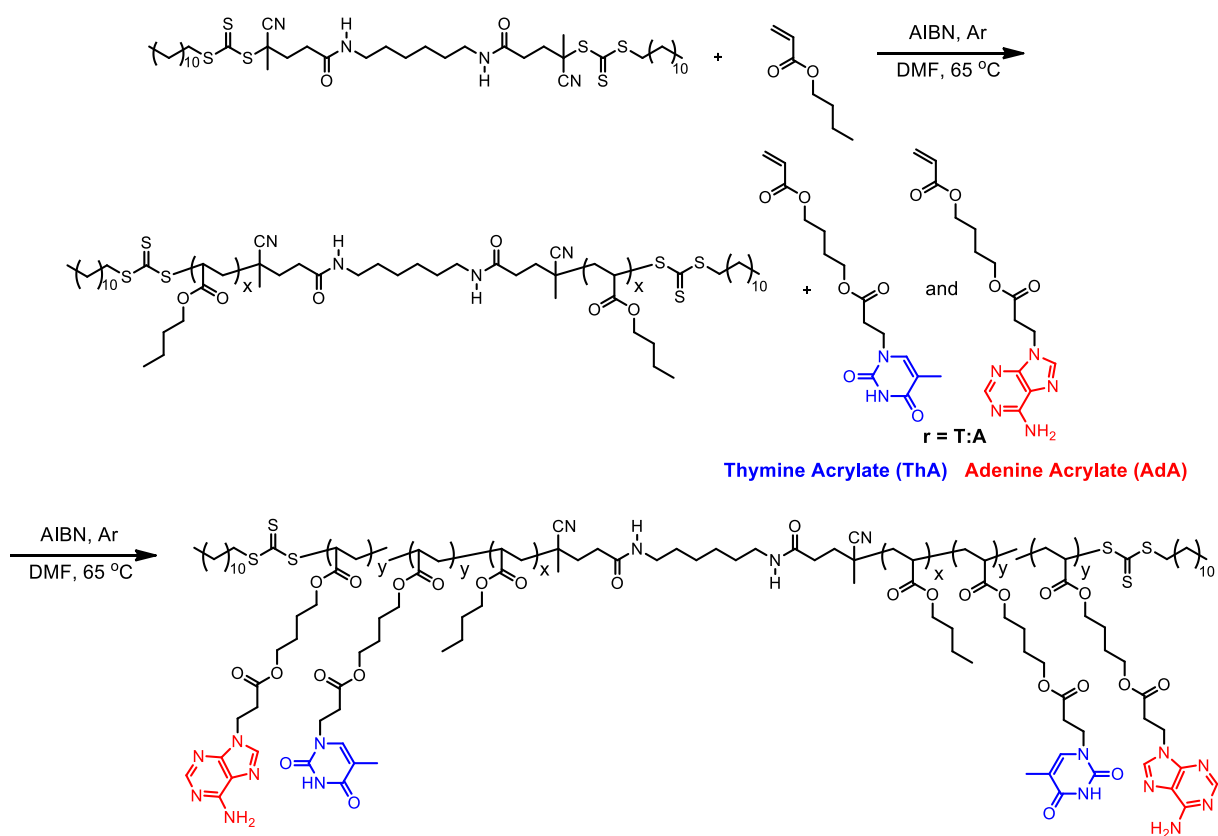


**Figure S5.2.** Representative DSC traces of PTBA copolymers.

**Table S5.2.** Compositions and thermal properties of representative PTBA copolymers.

| PTBA<br>Composition<br>(kDa) | 9.4-26.0-<br>10.0 | 9.4-20.0-<br>3.4 | 9.4-20.0-<br>7.8 | 9.4-33.8-<br>10.7 | 9.4-39.3-<br>11.6 |
|------------------------------|-------------------|------------------|------------------|-------------------|-------------------|
|------------------------------|-------------------|------------------|------------------|-------------------|-------------------|

|                           |           |           |           |           |           |
|---------------------------|-----------|-----------|-----------|-----------|-----------|
| Total (kDa)               | 45.4      | 32.8      | 37.2      | 53.9      | 60.3      |
| NB mol%                   | 23%       | 20%       | 25%       | 19%       | 17%       |
| NB wt %                   | 43%       | 39%       | 46%       | 37%       | 35%       |
| DP                        | 29-203-30 | 29-156-10 | 29-156-23 | 29-264-32 | 29-307-35 |
| T <sub>d, 5wt%</sub> (°C) | 283       | 289       | 280       | 281       | 282       |
| T <sub>g</sub> (°C)       | -45, 71   | -45, 64   | -46, 71   | -44, 71   | -45, 71   |



**Scheme S5.1.** RAFT polymerization of poly((ThA-co-AdA)-*b*-nBA-*b*-(ThA-co-AdA))

ABA triblock copolymers.

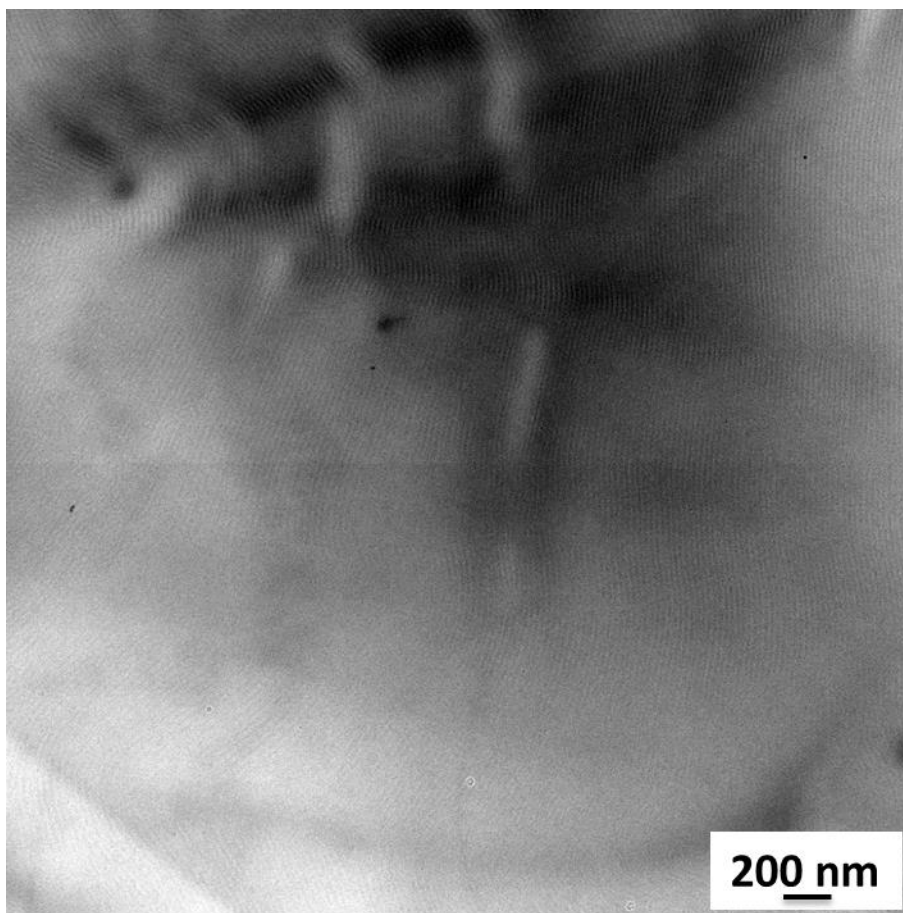


**Figure S5.3.** TEM image of PTBA (9.4-31.5-4.6) film.

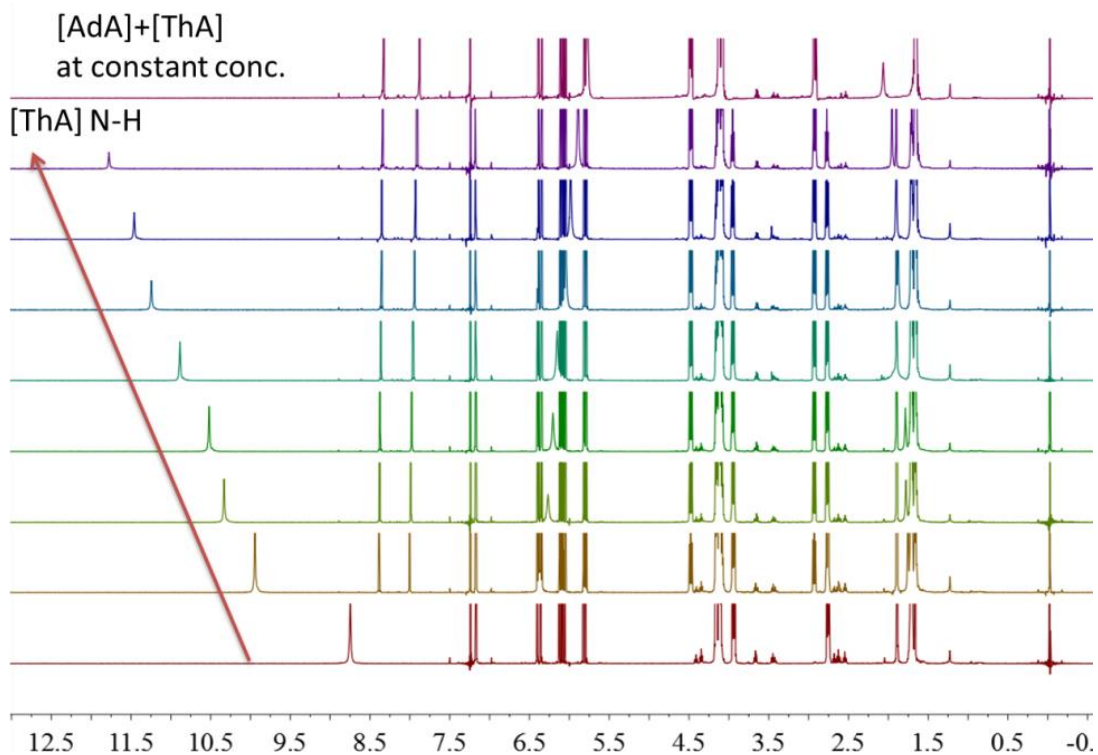


**Figure S5.4.**  $^1\text{H}$  NMR spectrum of the AdA and ThA mixture in  $\text{CDCl}_3$  with varying thymine to adenine ratio at 22  $^\circ\text{C}$ .

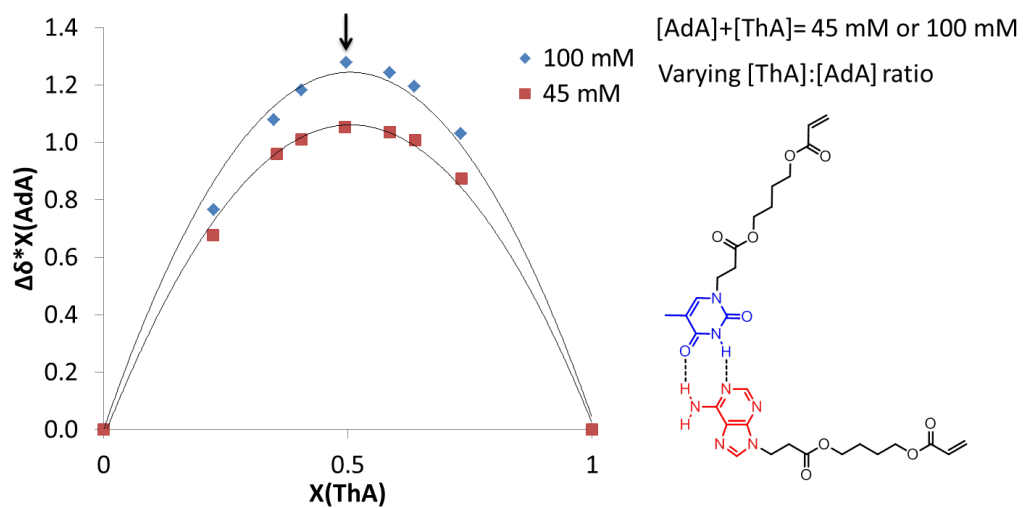


**Figure S5.5.** Job's plot of AdA and ThA in  $\text{CDCl}_3$  with overall concentration of 45 mM and 100 mM.

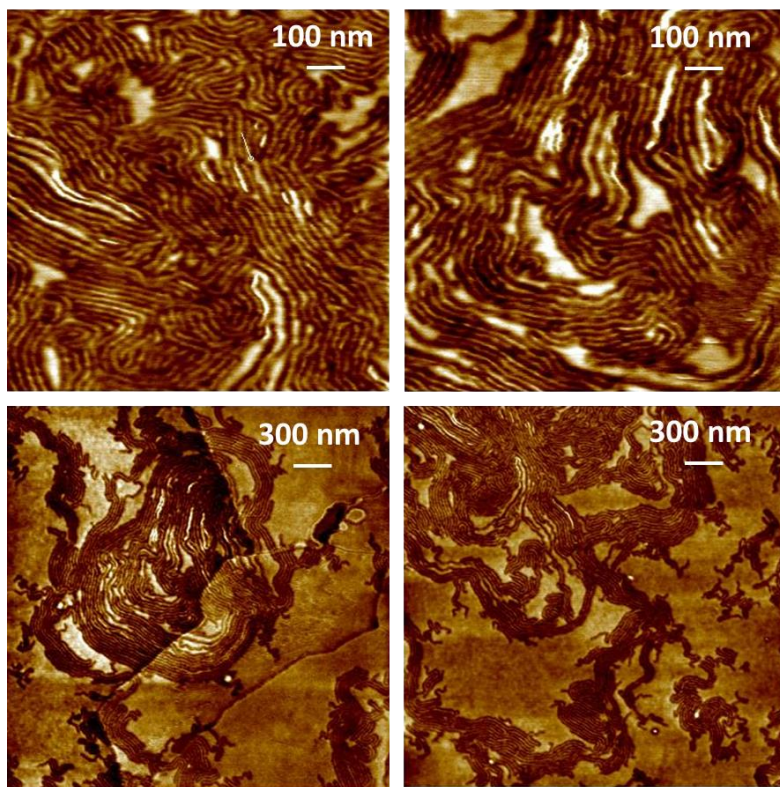


**Figure S5.6.** AFM phase images of PTBA (5.8-23.6-1.9) film surface.

#### References

1. Zhang, K.; Fahs, G. B.; Aiba, M.; Moore, R. B.; Long, T. E. *Chem. Comm.* **2014**, 50, 9145.
2. Zhang, K.; Aiba, M.; Fahs, G. B.; Hudson, A. G.; Chiang, W. D.; Moore, R. B.; Ueda, M.; Long, T. E. *Polym. Chem.* **2015**, 6, 2434.



## Chapter 6. Ureido-Cytosine and Cytosine Containing Supramolecular Polymers

*(In preparation for publishing in Polymer Chemistry)*

Keren Zhang, Mingtao Chen, Kevin J. Drummey, Samantha J. Talley, Lindsey J. Anderson, Robert B. Moore, and Timothy E. Long\*

*Department of Chemistry, Macromolecules and Interfaces Institute  
Virginia Tech, Blacksburg, VA 24061, USA*

### 6.1 **Abstract**

Regioselective Michael addition afforded *N*1-substituted cytosine acrylate monomer for the synthesis of acrylic random copolymers with cytosine pendant groups. Quantitative post-functionalization converted cytosine to ureido-cytosine (UCy) with increased self-association strength due to quadruple hydrogen bonding formation. Thermogravimetric analysis (TGA) revealed a lower onset of weight loss near 200 °C for UCy-containing copolymers, which proved more thermally stable at 130 °C and below than the cytosine-containing precursors in isothermal rheological experiments. Incorporation of UCy into random copolymers resulted in higher  $T_g$  values, enhanced mechanical performance, and better microphase-separation than the cytosine-containing precursors. Dynamic mechanical analysis and rheological analysis both revealed a rubbery plateau for each UCy-containing copolymer as well as a transition on the tan delta curve that corresponded to hydrogen bonding dissociation. On the contrary, the viscoelastic behavior of cytosine-containing random copolymers resembled entangled, non-associating polymers with increasing  $T_g$  as the cytosine content increased. A solution-cast UCy-containing copolymer film exhibited more well-defined surface morphology with nano-fibrillar hard domains compared to its cytosine control. Variable temperature FTIR verified the presence of hydrogen bonding, and thermogravimetric sorption analysis (TGASA) compared the

water uptake of UCy and cytosine-containing copolymers. UCy-containing random copolymers showed various advantages for applications in adhesives and thermoplastic elastomers compared to the cytosine copolymers, including superior cohesive strength, higher thermal stability, wider service temperature window, and lower moisture uptake.

## 6.2 *Introduction*

Supramolecular polymers serve as processable functional materials with reversibility and thermoresponsiveness for many applications including self-healing materials, adhesives, biomedical materials, controlled polymerization, and optoelectronic materials.<sup>1-12</sup> Two main types of supramolecular polymers received the most attention: ones formed through step-growth of noncovalent associating oligomers or monomers, and physically crosslinked polymers with noncovalent associating groups.<sup>1</sup> Noncovalent interactions such as hydrogen bonding, ionic interaction, and  $\pi$ - $\pi$  stacking, dominate both solution and solid-state properties of both types of supramolecular polymers. The former type gathered more scientific interest in recent years due to its unique structure and self-healing capability compared to conventional synthetic polymers. The second type of supramolecular polymer showed more potential in commercialization and industrialization of new materials due to facile formulation using traditional synthetic methods. In fact, many commercialized polymers fall into the second category of supramolecular polymer, such as Surlyn<sup>TM</sup> (poly(ethylene-*co*-methacrylate salt)), Nafion<sup>TM</sup> (sulfonated polytetrafluoroethylene), and pressure sensitive adhesives (PSA) with hydrogen bonding monomers.<sup>10,13-16</sup> The synthesis of pendant group associating supramolecular polymers generally only requires adding a functional monomer into the original formula. This produces new products without redesigning the reactors or operations, and allows

tunability in molecular weight, associating unit concentration and distribution. In addition, combination of controlled polymerization techniques with associating monomers further extends the tunability of supramolecular polymer architectures for unique self-assembly behaviors.<sup>17-21</sup>

Nature creates many biological supramolecular polymers with pendant associating groups, such as peptide and deoxyribonucleic acid (DNA). Cytosine, along with the other three nucleobases, encodes DNA using its complementary triple hydrogen bonding to guanine with a higher association constant ( $>10^4 \text{ M}^{-1}$ ) compared to its significantly weaker self-association (ca.  $40 \text{ M}^{-1}$ ).<sup>22,23</sup> However, researchers extensively investigated adenine-thymine base pair, and its effect on nucleobase-containing synthetic polymer properties due to challenging solubility and multiple nucleophilic sites of cytosine and guanine.<sup>18,24-29</sup> Hailes and coworkers recently synthesized and investigated quadruple hydrogen bonding of ureido-cytosine (UCy).<sup>23</sup> UCy contains an array of hydrogen bonding AADD (A: acceptor, D: donor) and affords quadruple self-hydrogen bonding, similar to the well-known ureido-pyrimidine (UPy) prominently researched in the Meijer group.<sup>3</sup> Ureido-cytosine self-associates into dimers through quadruple hydrogen bonding with a lower binding constant (ca.  $2.5 \times 10^5 \text{ M}^{-1}$ ) than UPy (ca.  $10^7 \text{ M}^{-1}$ ) in  $\text{CDCl}_3$ .<sup>2</sup> The relatively weak hydrogen bonding between the 5-H of cytosine and the urea carbonyl results in an equilibrium between folded and unfolded stereo-isomers, and only the unfolded configuration permits the AADD array. Hydrogen bonding at the similar position of UPy pushed the equilibrium towards the unfolded one, resulting in higher binding constant that matches theoretical prediction of quadruple binding arrays of AADD.<sup>4,23,30</sup> UPy incorporation afforded both types of supramolecular polymers through step-growth and

free radical polymerization.<sup>4,31-33</sup> Hailes *et al.* synthesized UCy-functionalized telechelic supramolecular polymers. Moreover, Cheng and coworkers prepared UCy-functionalized telechelic polypropylene glycol (PPG) oligomers, which self-assembled into semicrystalline supramolecular polymers.<sup>34,35</sup> UCy proved efficient in forming step-growth supramolecular polymers. However, functionalization of oligomers largely limits the tunability of supramolecular polymer architectures and scalability.

This manuscript details synthesis and characterization of cytosine and UCy-containing random polyacrylates with various physical properties, ranging from tacky adhesive materials to film-forming solids. Michael addition afforded a regioselective synthesis for polymerizable cytosine-functionalized acrylate monomer (CyA), which reacted with isocyanate to yield UCy-functionalized acrylate monomer (UCyA). Free radical polymerization of CyA and *n*-butyl acrylate (*n*BA) with varying feed ratios prepared a series of CyA-containing random copolymers with subsequent post-functionalization affording the corresponding UCyA-containing random copolymers. The acrylic backbone formed a low  $T_g$  soft matrix, and the flexible spacer from backbone to cytosine facilitated hydrogen bonding. Two series of copolymers provided direct comparison between weak and strong hydrogen bonding groups to investigate their effects on random copolymer properties. Systematic physical characterizations established the structure-morphology-property relationships of CyA and UCyA-containing random copolymers, including thermal, rheological, thermomechanical, and morphological analyses. This study represents the first quadruple hydrogen bonded supramolecular polymer synthesized through post-functionalization of cytosine-containing acrylics. UCyA proved more efficient in forming physical crosslinks and enhancing mechanical strength

of random copolymers compared to CyA. UCyA-containing random acrylics enable potential applications as pressure sensitive adhesives and thermoplastic elastomers.

### 6.3 *Experimental Section*

**Materials.** *n*-butyl acrylate (*n*BA, >99%) was purchased from Aldrich and passed through a neutral alumina column before use.  $\alpha,\alpha'$ -Azobis(isobutyronitrile) (AIBN, Fluka, 99%) was recrystallized twice from methanol. 1,4-butanediol diacrylate (Alfa Aesar, 99%) was used without further purification. Cytosine (C, 99%), triethylamine (TEA, 99%), 4-ethylphenyl isocyanate (98%), and 2,6-di-*tert*-butyl-4-methylphenol (BHT, 99%) were purchased from Aldrich and used without further purification. Hexane (HPLC grade), chloroform (CHCl<sub>3</sub>, HPLC), dichloromethane (DCM, ACS grade), dimethylsulfoxide (DMSO, HPLC grade), methanol (MeOH, ACS grade), and *N,N*-dimethylformamide (DMF, HPLC grade, anhydrous) were purchased from Spectrum Chemicals and used as received. Water was purified from distillation.

**Analytical Methods.** <sup>1</sup>H NMR and <sup>13</sup>C NMR spectra were collected in CDCl<sub>3</sub>, or DMSO-d<sub>6</sub>, or a mixture of CDCl<sub>3</sub> and DMSO-d<sub>6</sub> (1:1,v/v) on an Agilent U4-DD2 spectrometer operating at 400 MHz and 23 °C. High resolution TOF mass spectroscopy (HRMS) for the CyA and UCyA monomers was conducted in positive ion mode on an Agilent 6220 mass spectrometer with a TOF analyzer. Thermogravimetric analysis (TGA) of UCy and cytosine-containing copolymers was performed on a TA Instruments Q50 TGA with a heating ramp from ambient to 600 °C at a heating rate of 10 °C/min under constant nitrogen purge. Thermal degradation temperature ( $T_{d,5wt\%}$ ) corresponded to the temperature at 5% weight loss of the initial sample weight. Differential scanning calorimetry (DSC) of UCy and cytosine-containing copolymers was conducted on a TA instruments Q1000 DSC

using a heat/cool/heat procedure with heating rate of 10 °C/min and cooling rate of 10 °C/min under a nitrogen flush of 50 mL/min. The midpoint of the transition in the second heating ramp determined glass transition temperatures ( $T_g$ ).

Rheological analyses of UCy and cytosine-containing copolymers were conducted on a TA Instruments Discovery AR-G2 rheometer, using disposable aluminum parallel plates 8 mm in diameter. All measurements were strain-controlled at constant nominal strain values within the linear viscoelastic region, as determined using strain sweep experiments. Dynamic oscillatory temperature sweep experiments were performed at temperature steps from -40 °C to 130 °C with a 3 °C interval at 1 Hz. The sample was equilibrated for 1 min at each temperature. The peak of tan delta curve determined  $T_g$ . Dynamic mechanical analysis (DMA) of annealed UCy and cytosine-containing copolymer films utilized a TA Instruments Q800 dynamic mechanical analyzer in tension mode at a frequency of 1 Hz, oscillatory amplitude of 10  $\mu$ m, and a static force of 0.01 N. Rectangular film samples were cooled to -80 °C, equilibrated for 2 min, length measured, and subjected to a 3 °C/min temperature ramp.  $T_g$  values were reported as the peaks of tan delta curves. A Veeco MultiMode scanning probe microscope provided AFM phase images of UCy and cytosine-containing copolymer films using the tapping-mode. Samples were imaged with Veeco's Nanosensor silicon tips, spring constant of 42 N at approximately 0.5 set-point ratio.

Variable temperature FTIR (VT-FTIR) experiments were performed using a Varian 670-IR spectrometer (DTGS detector) with Pike Technologies variable temperature GladiATR<sup>TM</sup> attachment (diamond crystal). The spectra were collected at 4  $\text{cm}^{-1}$  resolution and as an average of 32 scans. The samples were subjected to a temperature ramp of 1 °C

/min, starting from 30 °C to 180 °C and FTIR spectra were collected every 10 °C beginning from 30 °C. A TA Instruments Q5000 thermogravimetric sorption analyzer (TGA-SA) measured the water sorption at relative humidity (RH) steps from 0 – 95% RH with a 5% increment. Each RH step continued until the sample weight equilibrated (<0.01% change over 10 min). An instrumental pre-drying method at 50 °C and 0% RH was applied to each sample until sample weight equilibrated. Water sorption was calculated based on weight gain of each pre-dried sample weight.

Small angle X-ray scattering (SAXS) experiments were performed using a Rigaku S-Max 3000 3 pinhole SAXS system, equipped with a rotating anode emitting X-ray with a wavelength of 0.154 nm (Cu K $\alpha$ ). The sample-to-detector distance was 1603 mm for SAXS, and the q-range was calibrated using a silver behenate standard. Two-dimensional SAXS patterns were obtained using a 2D multiwire, proportional counting, gas-filled detector, with an exposure time of 1 h. The SAXS data was corrected for sample thickness, and the scattering profiles were vertically shifted to facilitate a comparison of peak positions. All the scattering data was analyzed using the SAXSGUI software package to obtain radially integrated SAXS intensity versus the scattering vector q (SAXS), where  $q=(4\pi/\lambda)\sin(\theta)$ ,  $\theta$  is one half of the scattering angle and  $\lambda$  is the X-ray wavelength.

**Synthesis of 4-((3-(cytosin-1-yl)propanoyl)oxy)butyl acrylate (cytosine acrylate, CyA) monomer (Scheme 6.1).** A suspension of cytosine (5.0 g, 45.0 mmol), TEA (1.5 g, 15.0 mmol), BHT (0.3 g), and 1,4-butanediol diacrylate (13.4 g, 68.0 mol) in DMSO (100 mL) was stirred at 50 °C for 24 h. The reaction mixture was poured into water (750 mL) and washed with hexane to remove excess diacrylate. The water layer was extracted with dichloromethane (3  $\times$  100 mL). The combined extracts were dried over MgSO<sub>4</sub>, filtered,

and concentrated in a rotary evaporator to remove all the solvents. The evaporation residue was purified using flash column chromatography with  $\text{CHCl}_3$ -MeOH (10:1) on silica gel. Evaporation of the remaining eluent yielded a white solid of 5.2 g (40% yield). The structure and purity of obtained CyA monomer were confirmed using NMR spectroscopy (Figure S6.1).  $^1\text{H}$  NMR (400 MHz,  $\text{DMSO-d}_6$ ): 7.49 (d,  $J = 7.2$  Hz, 1H,  $\text{H}_a$ ), 6.99 (s, 1H,  $\text{H}_b$ ), 6.91 (s, 1H,  $\text{H}_b'$ ), 6.28 (m, 1H,  $\text{H}_c$ ), 6.13 (m, 1H,  $\text{H}_d$ ), 5.94 (m, 1H,  $\text{H}_e$ ), 5.60 (d,  $J = 7.2$  Hz, 1H,  $\text{H}_f$ ), 4.07 (m, 4H,  $\text{H}_g$ ), 3.82 (t,  $J = 6.7$  Hz, 2H,  $\text{H}_h$ ), 2.67 (t,  $J = 6.7$  Hz, 2H,  $\text{H}_i$ ), 1.63 (m, 4H,  $\text{H}_j$ ).  $^{13}\text{C}$  NMR (100 MHz,  $\text{DMSO-d}_6$ ): 171.08, 166.07, 165.50, 155.62, 146.45, 131.50, 128.34, 93.06, 63.68, 45.34, 32.84, 24.74. HRMS (ES<sup>+</sup>):  $m/z$  calculated for  $[\text{M}+\text{H}]^+$  310.1403 g/mol; found 310.1389 g/mol.

**Synthesis of 4-((3-(4-(3-(4-ethylphenyl)ureido)-cytosin-1-yl)propanoyl)oxy)butyl acrylate (ureido-cytosine acrylate, UCyA) monomer (Scheme 6.1).** Cytosine acrylate (66.4 mg, 0.2 mmol), 4-ethylphenyl isocyanate (31.6 mg, 0.2 mmol), and  $\text{CHCl}_3$  (2 mL) were added to a 25 mL, round-bottomed flask equipped with a magnetic stir bar. The reaction mixture was stirred at 0 °C for 2 h, 25 °C for 12 h, and precipitated into hexane. The resulting suspension was filtered and dried under reduced pressure (20 mmHg) at room temperature to give a white solid of 78.9 mg (81% yield). The structure and purity of obtained UCyA monomer were confirmed using NMR spectroscopy (Figure S6.2).  $^1\text{H}$  NMR (400 MHz,  $\text{DMSO-d}_6$ ): 11.24 (s, 1H,  $\text{H}_a$ ), 10.06 (s, 1H,  $\text{H}_b$ ), 7.96 (d,  $J = 7.1$  Hz, 1H,  $\text{H}_c$ ), 7.36 (d,  $J = 8.2$  Hz, 2H,  $\text{H}_d$ ), 7.15 (d,  $J = 8.2$  Hz, 2H,  $\text{H}_e$ ), 6.37-5.88 (m, 4H,  $\text{H}_{f+m}$ ), 4.25 – 3.68 (m, 6H,  $\text{H}_{g+h}$ ), 2.75 (t,  $J = 6.7$  Hz, 2H,  $\text{H}_i$ ), 2.48 (m, 2H,  $\text{H}_l$ ), 1.61 (m, 4H,  $\text{H}_j$ ), 1.14 (t,  $J = 7.6$  Hz, 3H,  $\text{H}_k$ ).  $^{13}\text{C}$  NMR (100 MHz,  $\text{DMSO-d}_6$ ): 171.28, 165.90, 162.91, 154.28, 151.62, 150.19, 139.24, 136.15, 131.85, 128.73, 128.65, 119.79, 94.63, 64.23,

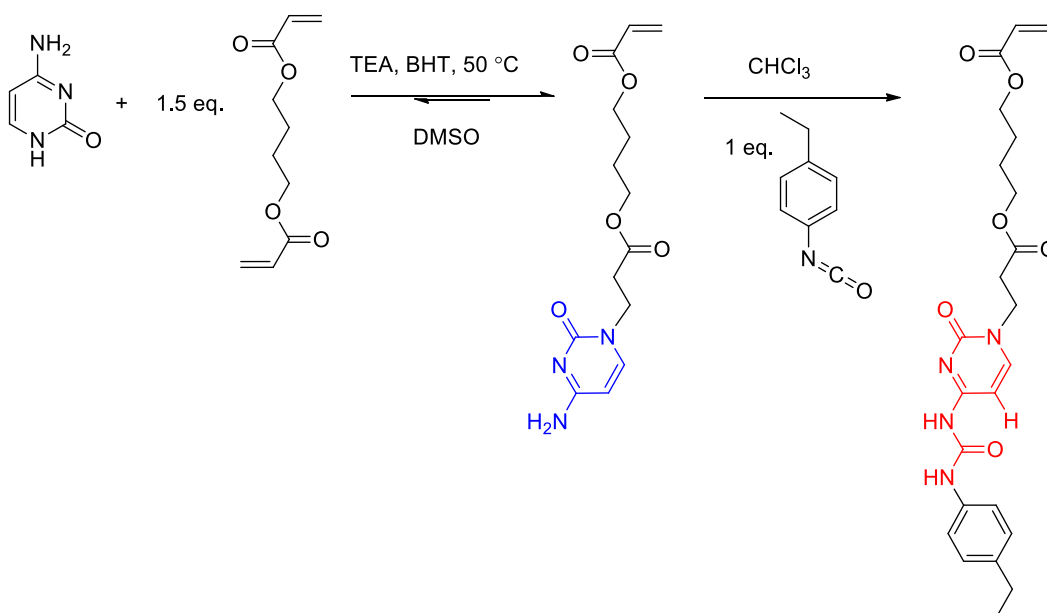


64.09, 46.54, 32.70, 27.99, 25.16, 16.12. HRMS (ES<sup>+</sup>): *m/z* calculated for [M+H]<sup>+</sup> 457.2082 g/mol; found 457.2077 g/mol.

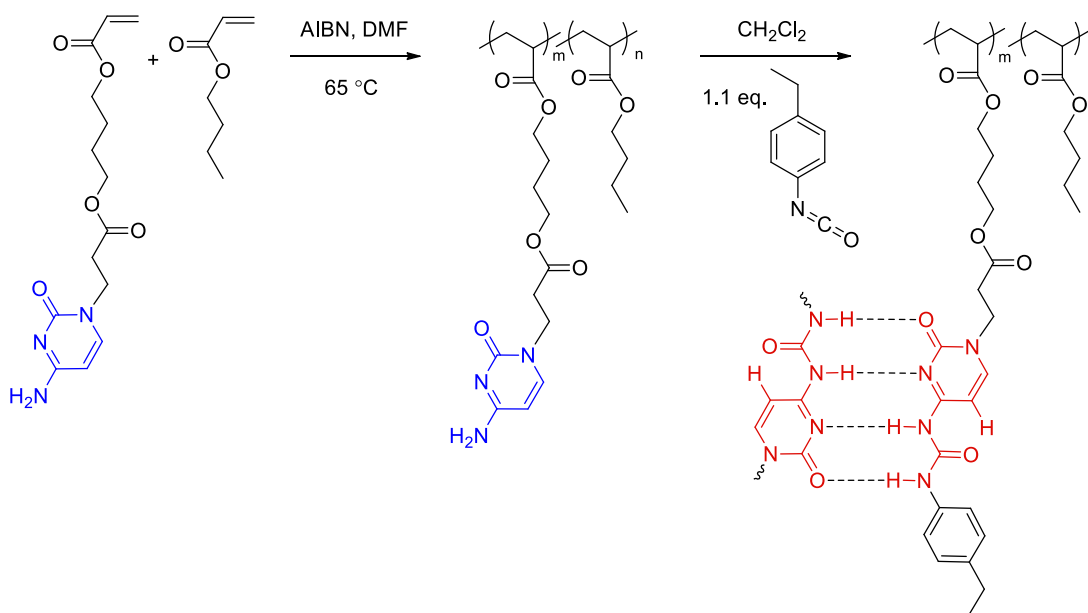
**Synthesis of poly(CyA-*co*-*n*BA) copolymers (Scheme 6.2).** Poly(CyA-*co*-*n*BA) was prepared using free radical copolymerization in DMF with AIBN as the initiator. A representative example of the polymerization was conducted as follows. A round-bottomed flask was charged with CyA (0.4 g, 1.2 mmol), *n*BA (3.0 g, 23.4 mmol), AIBN (4.0 mg, 24.0 μmol), and DMF (10 mL, 25 wt%) and sparged with N<sub>2</sub> for 20 min. The reaction mixture was stirred at 65 °C for 24 h. The resulting solution was precipitated into MeOH-water (5:1, v/v). The final products were collected and dried under reduced pressure (20 mmHg) for 24 h. The product contained 4.5 mol% CyA and 95.5 mol % *n*BA, with a yield of 80%. The structure and purity of obtained cytosine-containing copolymers were confirmed using NMR spectroscopy (Figure S6.3A).

**Synthesis of poly(UCyA-*co*-*n*BA) copolymers (Scheme 6.2).** Poly(UCyA-*co*-*n*BA) was prepared using post-functionalization of poly(CyA-*co*-*n*BA). Poly(CyA-*co*-*n*BA) (0.45 g) with 4.5 mol% CyA (47.2 mg, 0.15 mmol) and DCM (12 mL) were charged to a 50 mL, round-bottomed flask and stirred until polymer dissolved. A solution of 4-ethylphenyl isocyanate (24.7 mg, 0.17 mmol) in DCM (1 mL) was added into the flask dropwise. The reaction mixture was stirred overnight, concentrated, and precipitated into MeOH-water (6:1, v/v). The final products were collected and dried under reduced pressure (20 mmHg) for 24 h. The product contained 4.5 mol% uCyA and 95.5 mol% *n*BA, with a yield of 87%. The structure and purity of obtained UCy-containing copolymers were confirmed using NMR spectroscopy (Figure S6.3B).

**Processing and annealing conditions.** Poly(CyA-*co*-*n*BA) and poly(UCyA-*co*-*n*BA) copolymers with relatively high cytosine and UCy contents were dissolved in CHCl<sub>3</sub>-MeOH (2:1, v/v) and cast into PTFE molds. The molds were covered with glass Petri dishes and maintained at room temperature for 12 h to allow slow evaporation of the solvents. The dried samples were maintained at 50 °C for 12 h, placed under reduced pressure (20 mmHg) for 24 h at room temperature, and finally at 120 °C for 12 h. The resulting films were cooled using a step-wise procedure wherein the oven temperature was reduced 30 °C and allowed to equilibrate for 3 hours, with the process repeated until room temperature was reached. All samples were stored in a desiccator prior to any experiment.



**Scheme 6.1.** Synthesis of cytosine acrylate (CyA) and ureido-cytosine acrylate (UCyA) monomers.



**Scheme 6.2.** Synthesis of poly(CyA-*co*-*n*BA) and poly(UCyA-*co*-*n*BA) copolymers, and complementary hydrogen bonding of the ureido-cytosine. \*Poly(UCyA-*co*-*n*BA) and poly(CyA-*co*-*n*BA) samples were labeled red and blue, respectively throughout this manuscript for visual guidance.

## 6.4 Results and Discussion

**Synthesis of cytosine acrylate (CyA) and ureido-cytosine acrylate (UCyA) monomers and corresponding copolymers.** This manuscript reports a facile synthetic route for two acrylic monomers (Scheme 6.1) and corresponding copolymers that contain cytosine and UCy (Scheme 6.2), respectively. Base-catalyzed Michael addition of a diacrylate with unprotected cytosine yielded *N*1-substituted cytosine as the main product due to higher reactivity of the secondary amine compared to the primary amine.<sup>36</sup> This reaction appeared heterogeneous initially due to the challenging solubility of cytosine, and the suspension gradually dissolved as cytosine acrylate formed. Michael addition reached equilibrium when the solution turned completely clear, which served as an indication for

reaction completion. Column purification removed the *N*4-substituted isomer and the difunctionalized byproducts. Derivatization of cytosine and guanine proves challenging compared to adenine and thymine due to limiting solubility and multiple nucleophilic sites which all participate in substitution.<sup>37</sup> Michael additions of adenine and thymine with acrylates provide a viable route for synthesizing polymerizable nucleobase with regioselectivity.<sup>38</sup> Herein, the reported *N*1-substituted cytosine synthesis extended the capability of regioselective Michael addition with nucleobases using optimized catalyst, solvent, and reaction temperature. However, Michael addition of guanine with diacrylate failed in all tested solvents due to the low solubility of guanine. A reaction of purified cytosine acrylate and 4-ethylphenyl isocyanate converted the primary amine of cytosine to a urea quantitatively. UCyA with 4-ethylphenyl end proved more hydrophobic with a *R*<sub>f</sub> value of 0.72 compared to CyA with a *R*<sub>f</sub> value of 0.19 in CHCl<sub>3</sub>-MeOH 10:1 (v/v).

Free radical copolymerization of CyA and *n*BA proceeded homogeneously and afforded a series of random acrylic copolymers with varied cytosine content, controlled through changing the feed ratio of two comonomers. The feed ratios matched polymer compositions as *n*BA and CyA shared identical chemical structure near their acrylic backbones. NMR spectroscopy assisted in calculation of cytosine contents in resulting copolymers using integrations of resonances at 7.4-7.6 ppm and 0.7-1.1 ppm (Figure S6.3A), which corresponded to the chemical shifts of aromatic -CH- (*H*<sub>a</sub>) on cytosine and -CH<sub>3</sub> (*H*<sub>d</sub>) on *n*BA, respectively. Direct derivatization of cytosine units in poly(CyA-*co-n*BA) copolymers with isocyanate afforded ureido-cytosine functionalized copolymers with full conversion. This post-functionalization reaction proceeded homogeneously in DCM for poly(CyA-*co-n*BA) copolymers with less than 12 mol% CyA. The solution

viscosity of the reaction mixture for poly(CyA-*co*-*n*BA) with 9 mol% CyA increased significantly from 1.3 mPa·s to 1.3 Pa·s in approximately 70 min after the isocyanate addition (Figure S6.4), which was attributed to strong self-association of UCy compared to cytosine. The reaction of isocyanate and poly(CyA-*co*-*n*BA) copolymer with 21 mol% cytosine turned heterogeneous due to precipitation of the product in DCM. The resulting poly(UCyA-*co*-*n*BA) with 21 mol% UCyA proved insoluble in common organic solvents due to strong physical crosslinking, although UCyA proved less polar than CyA from thin layer chromatography.

Post-functionalization of cytosine copolymers proved more efficient than direct copolymerization of UCyA and *n*BA, which led to lower yield in monomer derivatization and heterogeneous polymerization. Integrations of resonances at 7.3-7.4 ppm and 0.7-1.1 ppm (Figure S6.3B) revealed the UCy contents in copolymers, as these resonances represented aromatic -CH- ( $H_i$ ) on UCy and -CH<sub>3</sub> ( $H_d$ ) on *n*BA. The compositions of poly(UCyA-*co*-*n*BA) and poly(CyA-*co*-*n*BA) matched within experimental errors, according to calculations based on <sup>1</sup>H NMR spectroscopy results before and after the post-functionalization. Table 6.1 summarizes the CyA and UCyA contents for poly(CyA-*co*-*n*BA) and poly(UCyA-*co*-*n*BA), and weight fraction of CyA or UCyA comonomer in each copolymer. All polymerization conditions and purification procedures remained identical for all acrylic copolymers to target comparable molecular weights, which included reaction temperature, time, initiator/monomer concentration, and precipitation method. However, size exclusion chromatography (SEC) results of CyA/UCyA-containing copolymers proved unreliable due to aggregation and column interactions in all available SEC mobile phases.

**Table 6.1.** Compositions and thermal properties of poly(CyA-*co*-*n*BA) and poly(UCyA-*co*-*n*BA) copolymers with varying mol% of CyA and UCyA, respectively. <sup>1</sup>reference 39.

<sup>2</sup>Fox equation  $\frac{1}{T_g} = \frac{F_1}{T_{g1}} + \frac{F_2}{T_{g2}}$  was used to calculate the predicted  $T_g$ , where  $F_1$  and  $F_2$

represent weight fraction of CyA and *n*BA respectively,  $T_{g1}$  and  $T_{g2}$  represent  $T_g$  (Kelvin) of poly(CyA) and poly(*n*BA).

|                                 | CyA/UCyA<br>in polymer<br>(mol%) | CyA/UCyA<br>in polymer<br>(wt%) | $T_{d,5wt\%}$<br>(°C) | $T_g$ (°C) | $T_g$ (°C)<br>predicted <sup>2</sup> | Calculated<br>first step<br>weight loss<br>(%) | Measured<br>first step<br>weight loss<br>(%) |
|---------------------------------|----------------------------------|---------------------------------|-----------------------|------------|--------------------------------------|--|--|
| Poly( <i>n</i> BA) <sup>1</sup> | 0.0                              | 0.0                             | 343                   | -47        |                                      | 0  | 0  |
| CyA                             | 3.0                              | 6.7                             | 331                   | -42        | -41                                  | 3  | 4  |
| uCyA                            |                                  | 9.9                             | 315                   | -38        |                                      | 6  | 6  |
| CyA                             | 4.5                              | 10.2                            | 317                   | -38        | -38                                  | 4  | 5  |
| uCyA                            |                                  | 14.4                            | 261                   | -36        |                                      | 9  | 10   |
| CyA                             | 8.8                              | 19.3                            | 295                   | -26        | -29                                  | 8  | 8  |
| uCyA                            |                                  | 25.6                            | 244                   | -18        |                                      | 17   | 16   |
| CyA                             | 10.5                             | 22.5                            | 291                   | -28        | -26                                  | 9  | 10   |
| uCyA                            |                                  | 29.0                            | 243                   | -16        |                                      | 19   | 18   |
| CyA                             | 21.4                             | 40.2                            | 283                   | 14         | -7                                   | 17   | 17   |
| uCyA                            |                                  | 48.8                            | 210                   | 28         |                                      | 35   | 29   |

**Thermal analysis.** Figure 6.1 displays representative TGA weight loss profiles of poly(CyA-*co*-*n*BA) copolymers, along with poly(UCyA-*co*-*n*BA) copolymers with similar cytosine content. All copolymers followed a two-step degradation, the first step of which corresponded to degradation of the CyA/UCyA pendant groups, leaving the acrylic backbone and cytosine solid with a melting point over 300 °C. The measured weight loss

in the first step agreed with the theoretical calculation of the linker between cytosine and the polymer backbone (Table 6.1). The second degradation step mainly involved degradation of the polymer backbone, which was consistent with previous TGA results of UPy-containing polyacrylates.<sup>33</sup> UCyA-containing copolymers exhibited lower  $T_{d,5wt\%}$  values than their CyA-containing precursors due to the incorporation of the urea bond, which started to degrade right below 200 °C.<sup>40,41</sup> Weight loss of cytosine-containing copolymers started at approximately 240 °C, while chemical crosslinking of the primary amines attacking the ester bonds occurred at much lower temperature. Isothermal rheology experiments verified the enhanced thermal stability of UCyA-containing copolymers compared to their cytosine precursors at 130 °C and below (Figures S5,S6). The complex viscosity of poly(CyA-*co*-*n*BA) increased significantly at 130 °C, while that of poly(UCyA-*co*-*n*BA) remained relatively constant.

DSC revealed thermal transitions of poly(CyA-*co*-*n*BA) and poly(UCyA-*co*-*n*BA) copolymers with varied cytosine and UCy contents, respectively (Figures 6.2,S6.7,S6.8). Copolymers in each series proved amorphous with a single  $T_g$  that increased as CyA or UCyA mol% increased. Poly(CyA) exhibited a single  $T_g$  at 90 °C, approximately 140 °C higher than  $T_g$  of poly(*n*BA) with an identical chemical structure near the backbone (Figure S6.7). Both steric hindrance and hydrogen bonding of the pyrimidine ring affected the long range segmental motion of the acrylic backbone and resulted in a higher  $T_g$  for poly(CyA).<sup>42</sup> The increasing  $T_g$  of poly(CyA-*co*-*n*BA) copolymers with increasing CyA mol% confirmed the random distribution of two comonomers, which nevertheless deviated from the Fox equation prediction, especially with relatively high CyA mol% (Figure 6.3).<sup>43</sup> This phenomenon revealed the presence of interaction between CyA and *n*BA, which

became more predominant with higher CyA incorporation.<sup>24,44</sup> Poly(UCyA-*co*-*n*BA) showed higher  $T_g$  values compared to the cytosine precursors with similar polar monomer incorporations (Figures 6.2, 6.3), resulting from bulkier UCy pendant groups and stronger hydrogen bonding (Scheme 6.2). This  $T_g$  difference between CyA and UCyA-containing copolymers appeared to increase with increasing polar monomer contents. Poly(UCyA-*co*-*n*BA) with 21 mol% UCyA exhibited a  $T_g$  of 28 °C and a second exothermic transition near 150 °C, possibly due to crystalline domain melting or hydrogen bonding dissociation.<sup>35</sup>

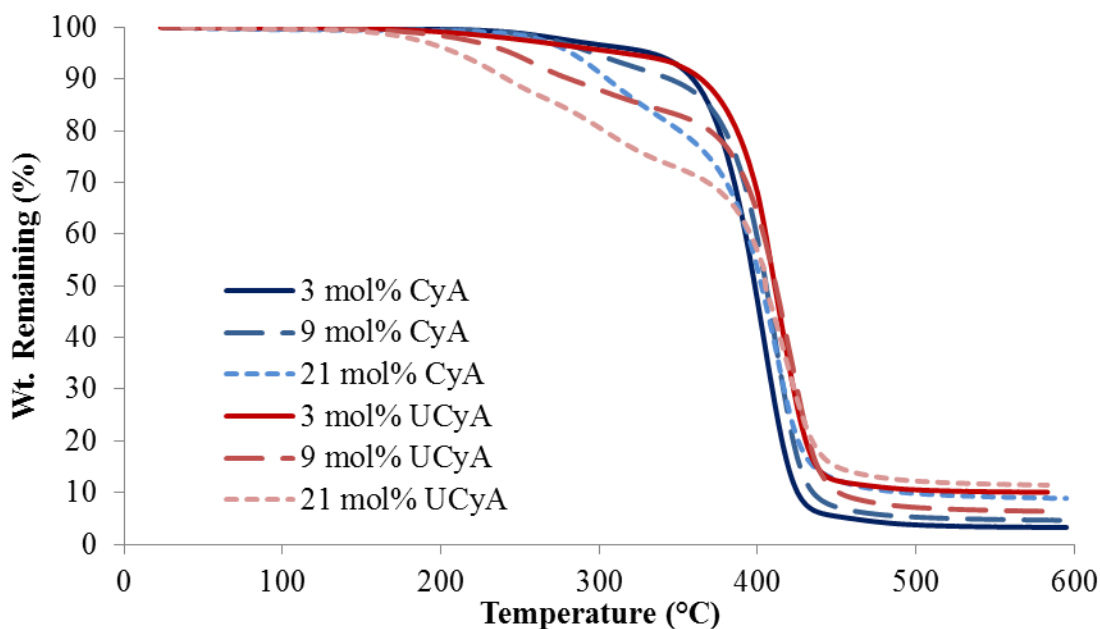


**Figure 6.1.** Representative TGA thermograms of poly(CyA-*co*-*n*BA) and poly(UCyA-*co*-*n*BA) copolymers with varied amounts of CyA and UCyA, respectively.



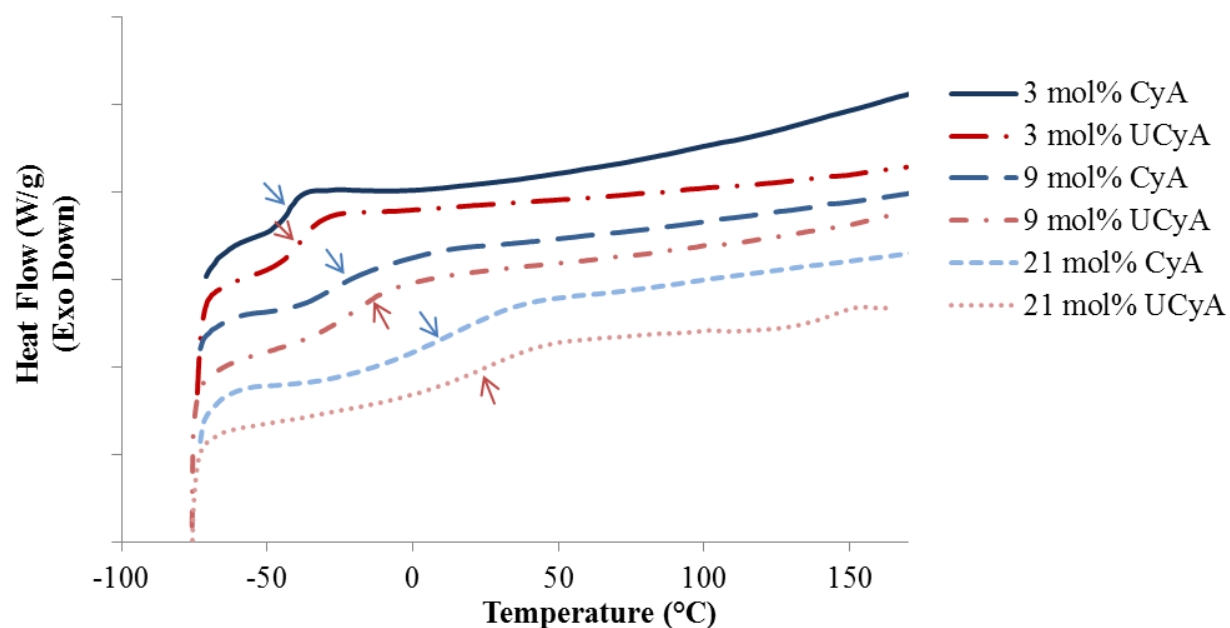


**Figure 6.2.** Representative DSC thermograms of poly(CyA-*co*-*n*BA) and poly(UCyA-*co*-*n*BA) copolymers with varied amounts of CyA and UCyA, respectively.

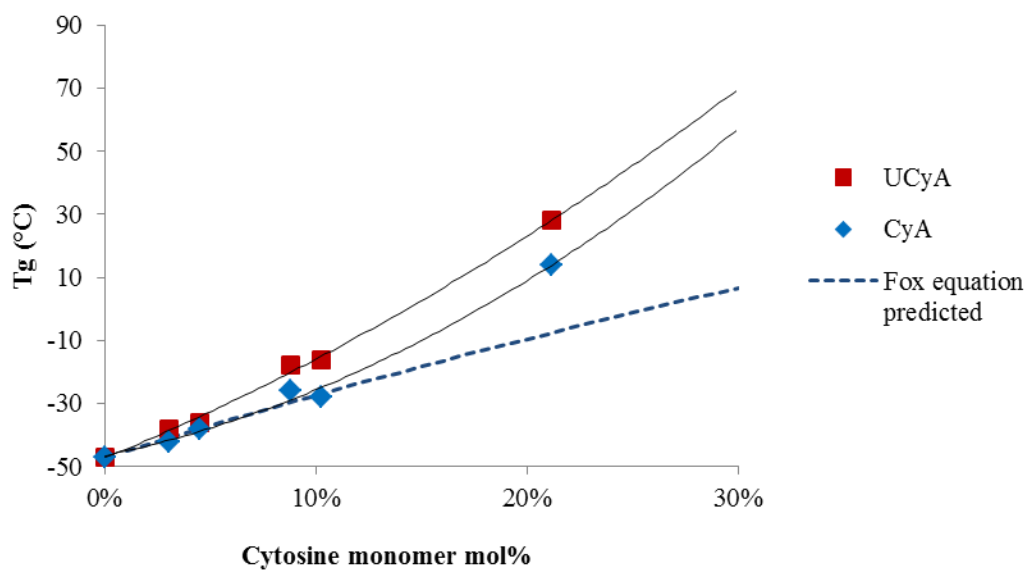


**Figure 6.3.** Relationship between CyA/UCyA mol% of poly(CyA-*co*-*n*BA) or poly(UCyA-*co*-*n*BA) and  $T_g$  values.

**Thermomechanical properties.** A rheology temperature sweep experiment investigated the viscoelastic properties of poly(UCyA-*co-n*BA) and poly(CyA-*co-n*BA) copolymers in relationship to temperature. Figure 6.4 compares storage and loss moduli ( $G'$  and  $G''$ ) of copolymers with 5 mol% of CyA and UCyA. Both samples exhibited similar moduli values before and during their glass transitions from -40 °C to -10 °C, while their viscoelastic behaviors differed significantly above -10 °C. A wide plateau of poly(UCyA-*co-n*BA) started and extended to approximately 40 °C, during which its storage modulus exceeded loss modulus. This plateau regime and the following terminal flow regime indicated the formation of a transient network of physical crosslinks from self-complementary quadruple hydrogen bonding of the ureido-cytosine units. On the contrary, the moduli of poly(CyA-*co-n*BA) continued to decrease after its glass transition and reduced to nearly 20 times lower than that of poly(UCyA-*co-n*BA) at 40 °C.

The plateau modulus of poly(UCyA-*co-n*BA) with 3 mol% UCyA approached the Dahlquist criterion, which described an empirical threshold of  $3 \times 10^5$  Pa at 25 °C and 1 Hz for the storage modulus of pressure sensitive adhesives (PSA).<sup>45</sup> Figure 6.5B shows the decreasing modulus of poly(UCyA-*co-n*BA) with lower UCyA mol%. As a result, poly(UCyA-*co-n*BA) copolymers with lower than 3 mol% UCyA serve as potential candidates for PSA with superior cohesive strength than the CyA copolymers. The plateau demonstrated superior thermal resistance of resulting adhesives with constant cohesive strength up to 45 °C. Poly(CyA-*co-n*BA) with 3 mol% CyA demonstrated sufficient tack, however weaker cohesive strength and significantly worse high temperature performance due to insufficient physical crosslinking.<sup>45</sup> The reptation onset of the UCy-containing sample occurred at 59 °C, 32 °C higher than the cytosine precursor. The viscous property

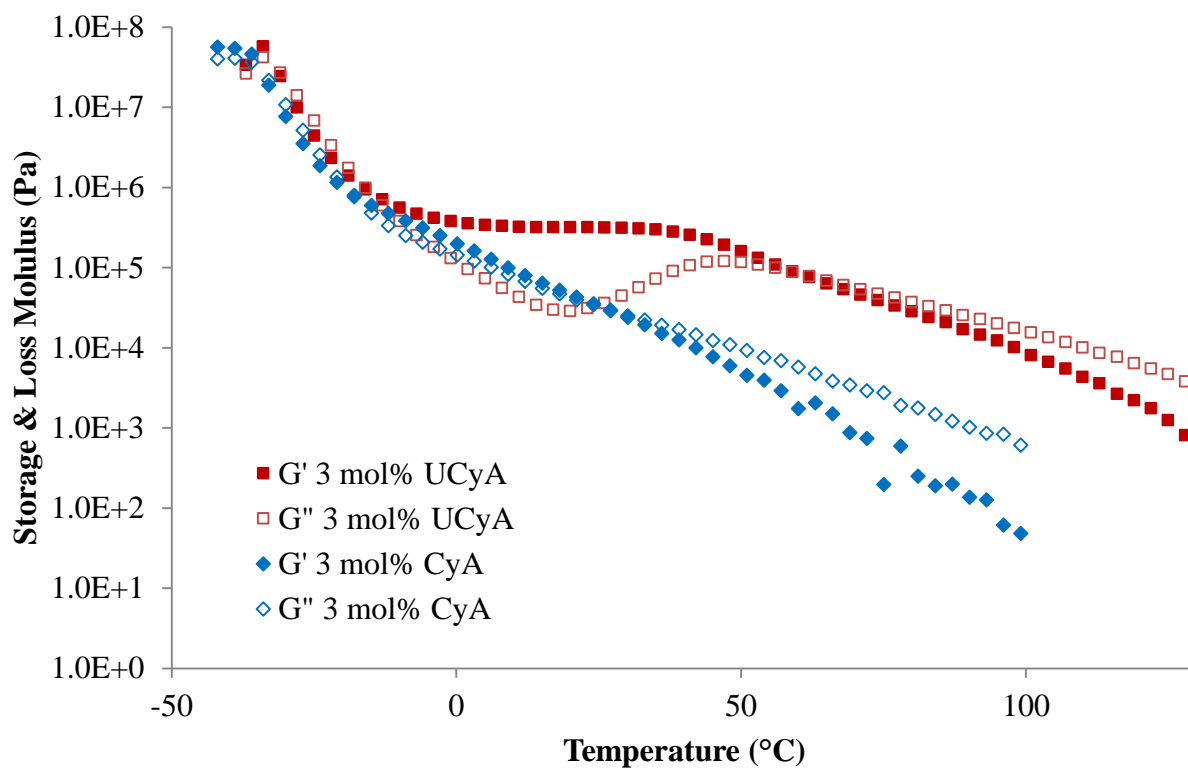
dominated after this onset, entering the terminal flow regime, where  $G''$  exceeded  $G'$ . The slopes of poly(UCyA-*co*-*n*BA) moduli curves in the terminal flow region matched closely with its CyA-containing precursor, representing an entangled polymer melt behavior.<sup>32</sup> The moduli difference between the UCy sample and the cytosine precursor remained up to 100 °C, suggesting that not all of the strong hydrogen bonding dissociated at 100 °C. Modulus measurements below 100 Pa exceeded the accuracy limits for available instrument and geometry.

Figure 6.5AB displays both  $G'$  and tan delta curves of annealed poly(CyA-*co*-*n*BA) and poly(UCyA-*co*-*n*BA) copolymer films. The sample with higher CyA mol% exhibited higher  $T_g$  and higher modulus in the tested temperature range (Figure 6.5A), due to denser physical crosslinks. The  $T_g$  increase became more significant at higher CyA mol%, which agreed with the thermal analysis results (Figure 6.3). Figure 6.5B similarly exhibited that both  $T_g$  and modulus increased with increasing UCyA content, attributed to additional hydrogen bonding. However, the tan delta curves of poly(UCyA-*co*-*n*BA) copolymer each contained an obvious transition with a peak value near 60-70 °C, which was not shown for poly(CyA-*co*-*n*BA). The DMA results of poly(UCyA-*co*-*n*BA) films with higher UCyA contents also revealed a second transition near 70 °C (Figure 6.6C). Long *et al.* previously observed similar transitions for block copolymers with functionalized blocks that formed weak noncovalent interactions.<sup>39</sup> These transitions likely reflected the majority of hydrogen bonding dissociation, which led to free volume increase with weakened physical crosslinks. The tan delta curves of poly(CyA-*co*-*n*BA) films with relatively high CyA contents also showed a secondary transition near 20-30 °C (Figure 6.6C), which presumably reflected weaker hydrogen bonding dissociation at lower temperature than

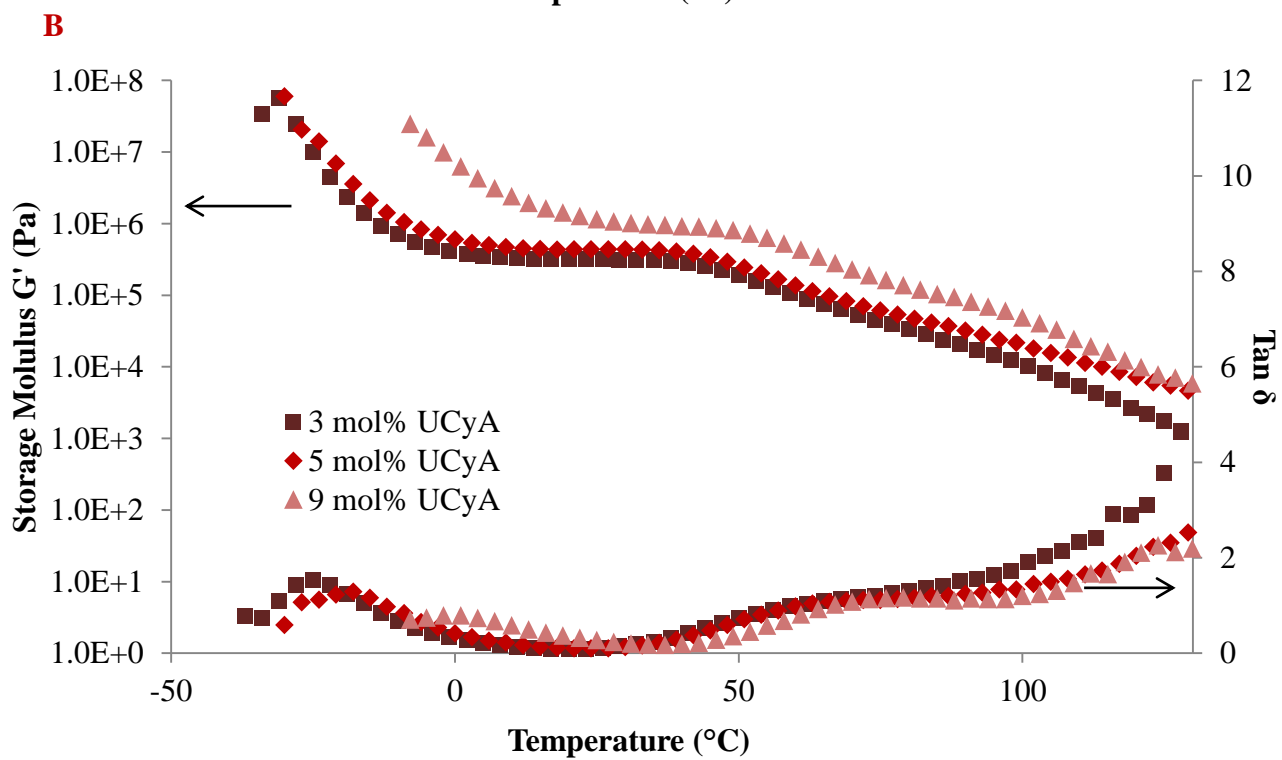
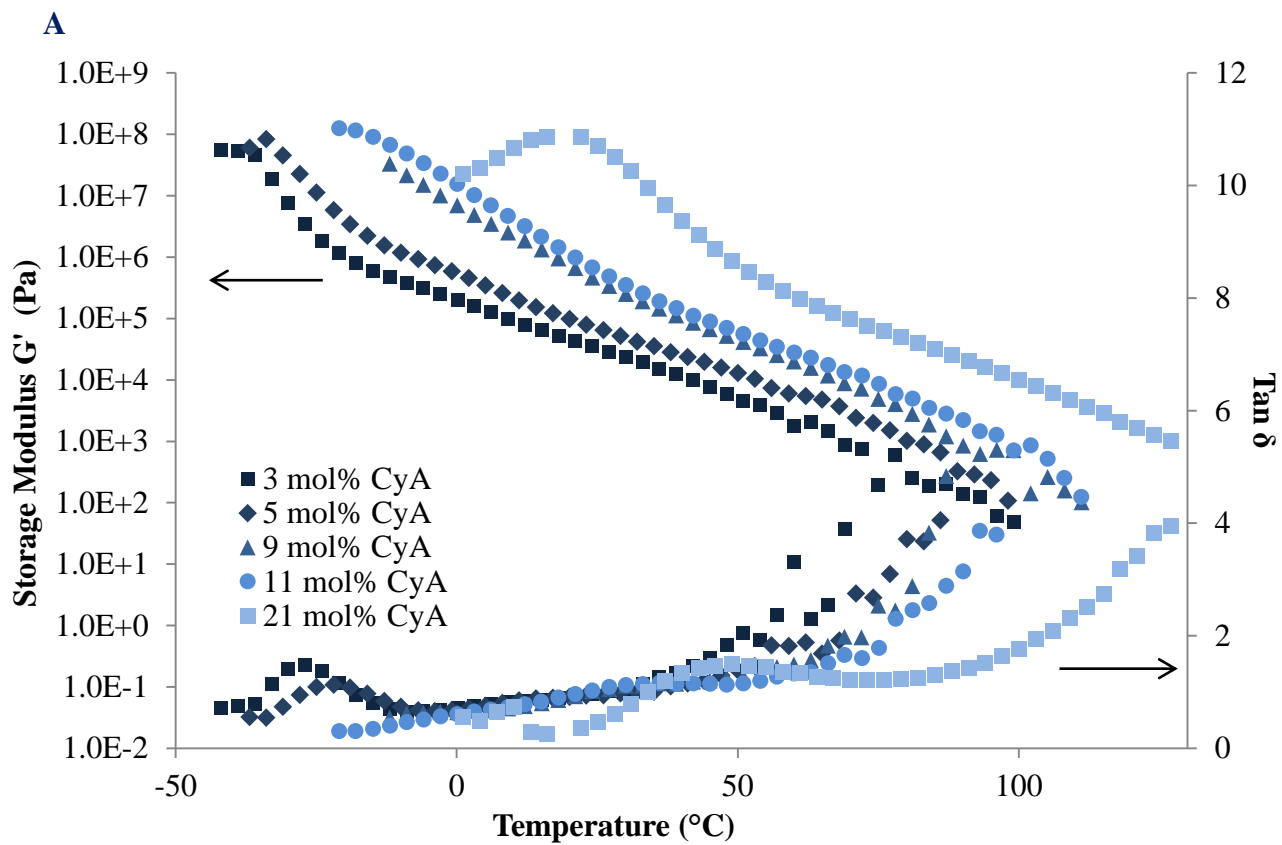
UCyA samples. Thermomechanical analyses proved capable of detecting a transition related to the dissociation of noncovalent interactions, which thermal analysis failed to reveal.

Furthermore, DMA closely compared the thermomechanical properties of solution-cast poly(UCyA-*co*-*n*BA) copolymer films with their cytosine precursors with uniaxial deformation in the oscillatory mode. The acrylic copolymer with 5 mol% UCyA formed a soft film that showed one-phase thermomechanical behavior with a single modulus drop, while its CyA precursor lacked mechanical integrity for film casting (Figure 6.6A). The other samples with higher mol% of CyA and UCyA shared similar thermodynamic behavior in the glassy regime and during glass transition (Figure 6.6B). The influence of hydrogen bonding dominated the plateau and terminal flow regimes, agreeing with rheological analysis for copolymers with lower CyA or UCyA contents. Hydrogen bonding of UCyA contributed to a well-defined plateau, the modulus of which increased with increasing UCyA concentration in the random copolymers. The flow temperature also increased with increasing UCyA content, indicating enhanced heat resistance of the copolymer mechanical strength. The plateau moduli of UCyA films fell into the rubbery range, demonstrating their potential as thermoplastic elastomers. CyA copolymer films lacked a plateau window due to insufficient physical crosslinking from the weaker self-hydrogen bonding of CyA compared to UCyA. Thermomechanical performance of poly(UCyA-*co*-*n*BA) films suggested their microphase-separated morphologies. The tan delta peak of the UCyA copolymer films beginning near 50 °C resulted from the dissociation of phase-separation enhanced hydrogen bonding of UCy units. The

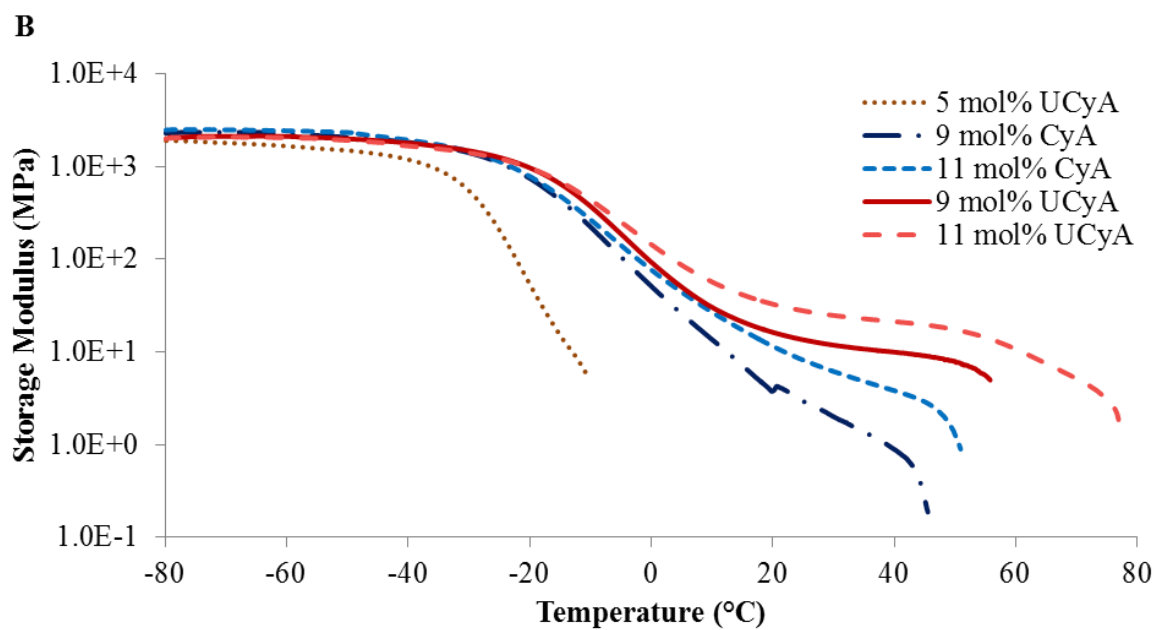
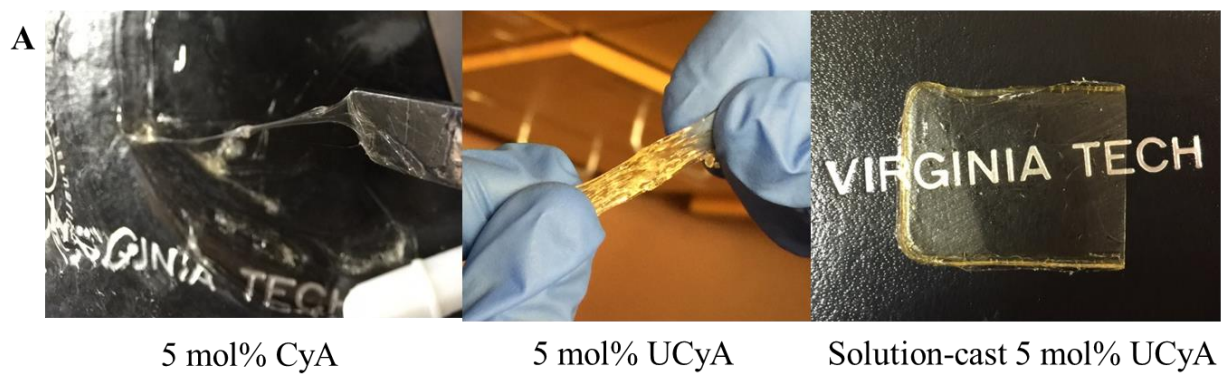
dissociation of noncovalent interactions became visible as a distinguishable transition in thermomechanical analysis because of the reinforcement from phase-separation.<sup>1,46</sup>



**Figure 6.4.** Rheological temperature sweep of poly(CyA-*co*-*n*BA) and poly(UCyA-*co*-*n*BA) with 3 mol% CyA and UCyA, respectively.



**Figure 6.5.** Rheological temperature sweep of (A) poly(CyA-*co*-nBA) and (B) poly(UCyA-*co*-nBA) with varied amounts of CyA and UCyA, respectively.



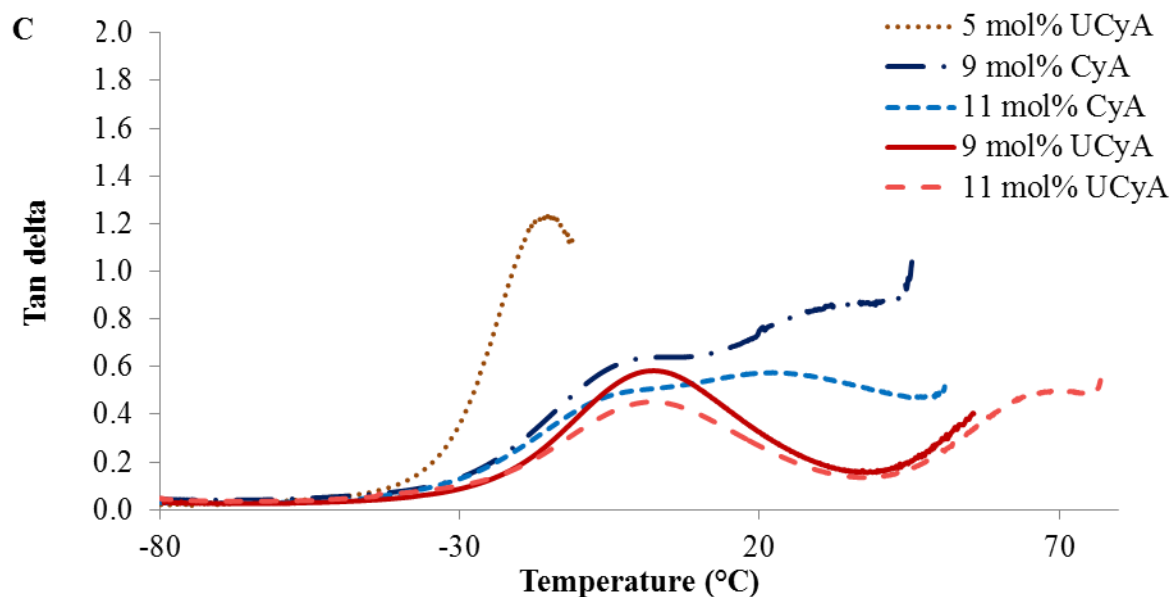


**Figure 6.6.** (A) From left to right, pictures of poly(CyA-*co*-nBA) and poly(UCyA-*co*-nBA) with 5 mol% cytosine contents, and solution-cast film of the latter. (B) Storage modulus curves and (C) tan delta curves during dynamic mechanical temperature ramps for solution-cast poly(CyA-*co*-nBA) and poly(UCyA-*co*-nBA) films with varied mol% of CyA and UCyA, respectively.

**Morphology characterization.** Small angle X-ray scattering (SAXS) elucidated the bulk morphology of annealed poly(CyA-*co*-nBA) and poly(UCyA-*co*-nBA) films (Figure 6.7). Samples were annealed at 120 °C, above the  $T_g$  of all copolymers, and step-wise cooling facilitated formation of noncovalent interactions and phase-separation. SAXS profiles of all films with > 5 mol% cytosine content exhibited relatively broad scattering maxima, suggesting a microphase-separated morphology, which resulted from immiscibility between hydrogen bonded cytosine/UCy and the acrylic polymer backbone.<sup>47</sup> The scattering peak positions remained constant with varying cytosine/UCy content for the series of poly(CyA-*co*-nBA) and poly(UCyA-*co*-nBA), indicating a relatively constant domain spacing. This phenomenon was commonly observed and well-



studied for random ionomers that contain ionic bonded aggregates. The increase in scattering peak intensity related to an overall increase in the mol% of hydrogen bonded groups, which self-assembled into the hard phase. The absence of scattering maxima for the film with 5 mol% UCyA revealed its phase-mixed morphology due to insufficient physical crosslinking, which explained the film yielding point below room temperature in DMA (Figure 6.6). Converting cytosine to UCy shifted the scattering peak from  $1.4 \text{ nm}^{-1}$  to  $0.6 \text{ nm}^{-1}$ , corresponding to a shift in the long period (spacing between hydrogen bonded hard domains) from 4.5 nm to 10 nm, respectively.

AFM images confirmed the microphase-separated surface morphology of annealed poly(CyA-*co*-*n*BA) and poly(UCyA-*co*-*n*BA) films (Figure 6.8). The dark and light areas represented the soft *n*BA phase and the hydrogen bonded hard phase, respectively. Poly(CyA-*co*-*n*BA) film contained smaller domains with irregular shapes, while poly(UCyA-*co*-*n*BA) film displayed nano-fibrillar hard domains, similar to telechelic urea-UPy supramolecular polymers.<sup>48</sup> The  $\pi$ - $\pi$  stacking of cytosines and phenyl rings presumably assisted the lateral stacking of hydrogen bonded UCyA units, which enabled the formation of nano-fibrillar hard domains. The shape and dimension differences in cytosine and UCy-containing copolymer films explained their different scattering peak positions and thermomechanical properties. Weaker hydrogen bonding of cytosine resulted in smaller hard domains with irregular shapes, resulting in shorter periodic spacing and weaker reinforcement of the mechanical strength compared to UCy. The fibrillar hard domains acted like fillers that reinforced the modulus of the soft matrix, contributing to a rubbery plateau with retained mechanical integrity over a wider temperature range.

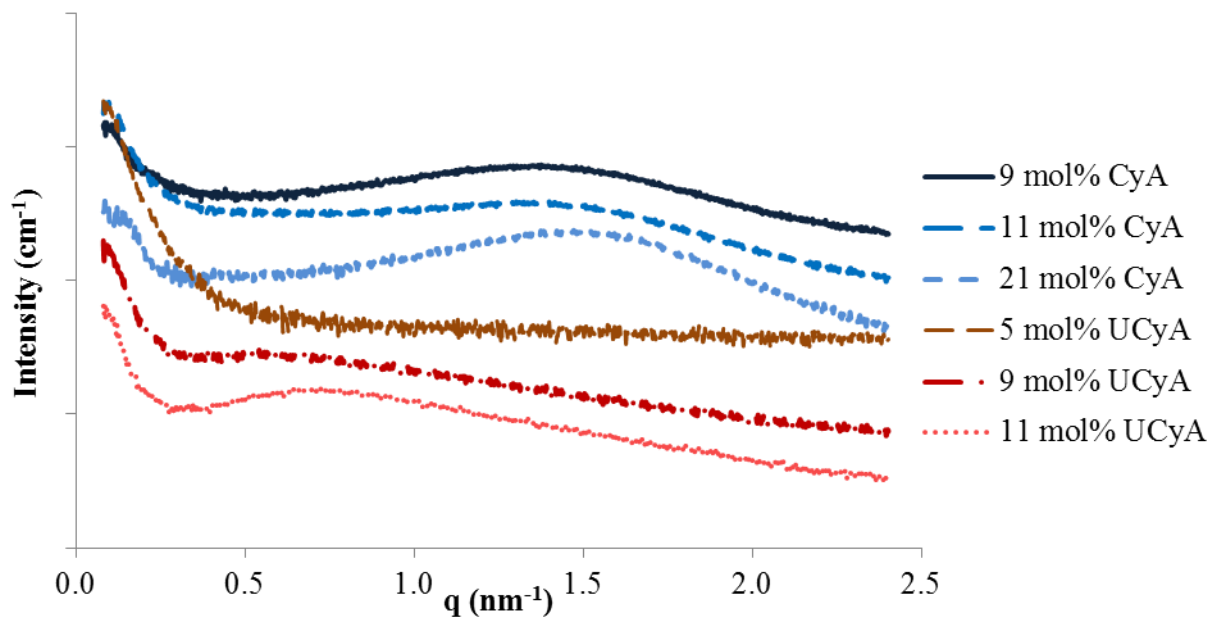


**Figure 6.7.** SAXS for solution-cast poly(CyA-*co*-nBA) and poly(UCyA-*co*-nBA) films with varied amounts of CyA and UCyA, respectively.

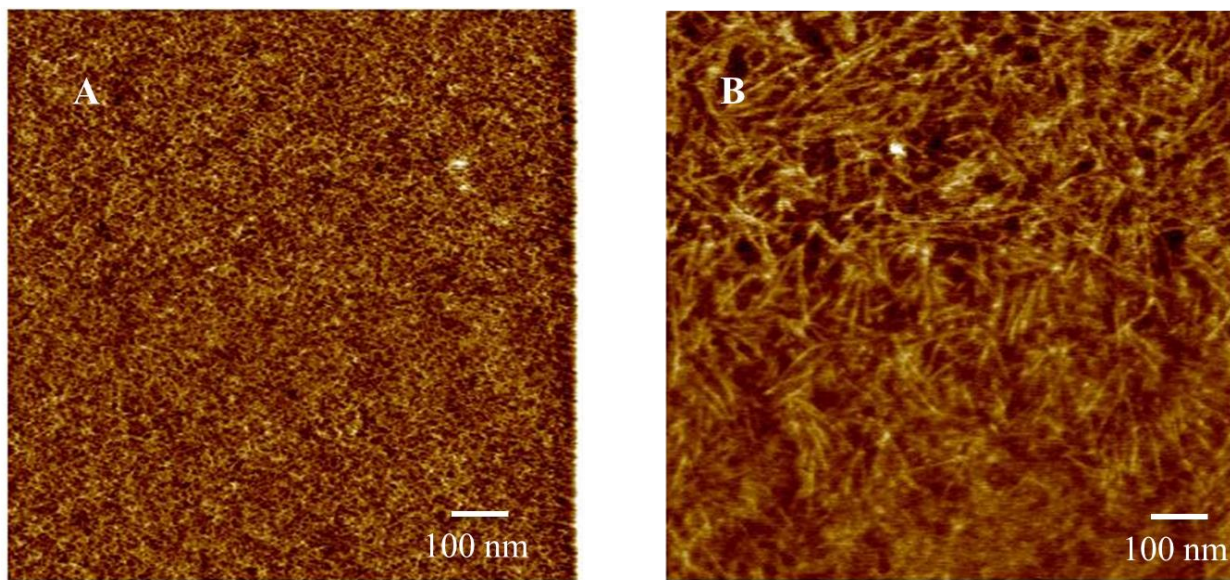
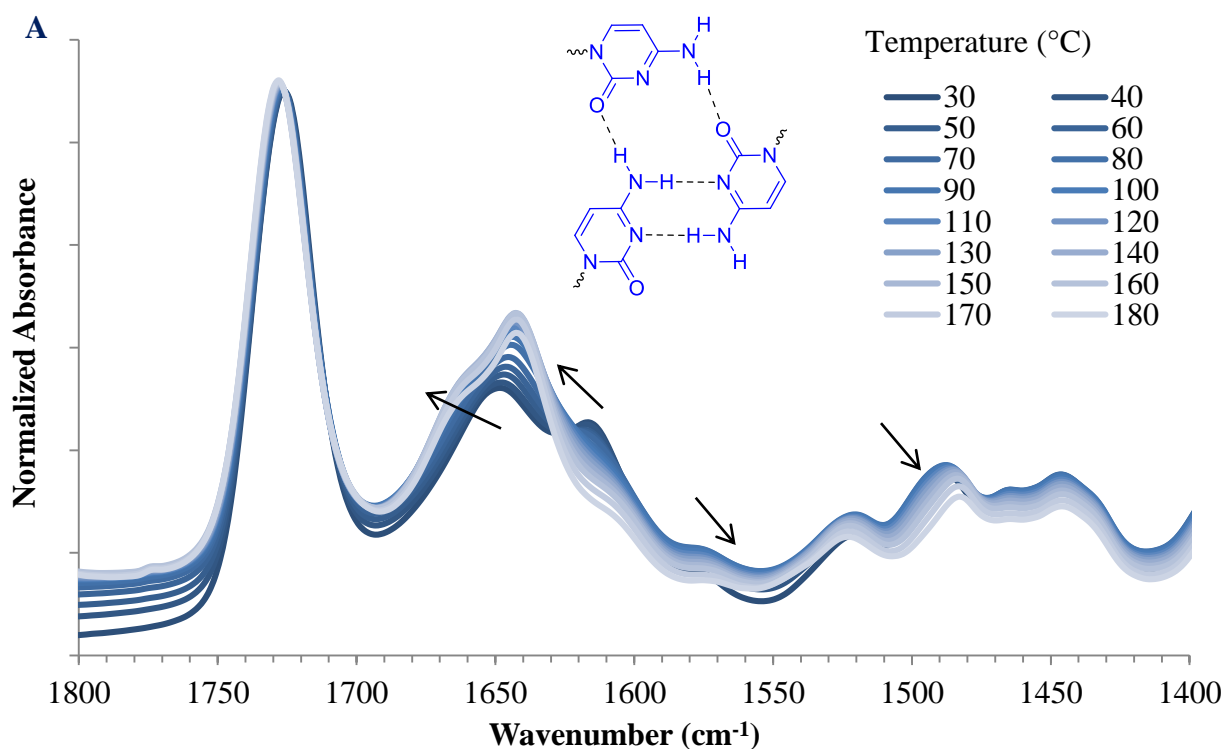


**Figure 6.8.** AFM phase images for solution-cast (A) poly(CyA-*co*-nBA) and (B) poly(UCyA-*co*-nBA) films with 11 mol% of UCyA and CyA, respectively.

**Variable temperature FTIR spectroscopy (VT-FTIR).** VT-FTIR commonly serves as a versatile tool to investigate hydrogen bonding or debonding in response to

cooling or heating.<sup>4,24,46</sup> Figure 6.9 displays FTIR absorbance spectra in the carbonyl stretching region of copolymers containing CyA or UCyA at varying temperature, demonstrating hydrogen bonding dissociation with heat. Copolymers with higher cytosine and UCy content displayed absorbance bands with higher intensity for hydrogen bonded C=O and N-H units in reference to the non-hydrogen bonded carbonyls at  $1726\text{ cm}^{-1}$  (Figure S6.9). The wavenumber of this reference band remained constant with varying temperature, which indicated that most of the carbonyls on the acrylate backbone were free from hydrogen bonding. In Figure 6.9A, the absorption band near  $1645\text{ cm}^{-1}$  and  $1622\text{ cm}^{-1}$  at  $30\text{ }^{\circ}\text{C}$  both blue-shifted to higher wavenumbers with increasing temperature, representing the stretching vibration of C=O on the cytosine units. These blue-shifts resulted from increased frequency of the C=O stretching vibration when hydrogen bond weakened and C=O bond strengthened.<sup>49,50</sup> The red-shifts of absorption bands at  $1573\text{ cm}^{-1}$  and  $1487\text{ cm}^{-1}$  from  $30\text{ }^{\circ}\text{C}$  to elevated temperatures demonstrated that the frequency of N-H bond bending vibration decreased with increasing temperature due to elimination of the anchoring restriction from hydrogen bonding.<sup>39</sup> The absorption bands near  $1521\text{ cm}^{-1}$  and  $1446\text{ cm}^{-1}$  corresponded to free N-H bending, which indicated that not all N-H formed hydrogen bonding at room temperature, agreeing with the relatively weak and non-ordered self-association of cytosine. Figure 6.9B reveals similar absorption band shifts from C=O stretching and N-H bending for poly(UCyA-*co*-nBA). The absorption band of C=O stretching near  $1710\text{ cm}^{-1}$  shifted to lower wavenumber, as the shoulder peak merged with the free C=O peak with increasing temperature. The intensity of another absorption band near  $1645\text{ cm}^{-1}$  decreased due to the blue-shift to  $1678\text{ cm}^{-1}$ , where a new peak appeared at elevated temperatures. The N-H bending absorption bands for the UCy units near  $1550\text{ cm}^{-1}$

<sup>1</sup> and 1500 cm<sup>-1</sup> clearly red-shifted to lower wavenumbers as temperature increased. The most significant shift occurred at approximately 60 °C to 90 °C for poly(CyA-*co*-*n*BA) and 100 °C to 130 °C for poly(UCyA-*co*-*n*BA), agreeing with previous DMA result that the majority of hydrogen bonding from UCyA dissociated at higher temperature than CyA. However, the heating rate and sample deformation differences of VT-FTIR and DMA led to incomparable temperature values for hydrogen bonding dissociation. Hydrogen bonding dynamically associates and dissociates within a temperature window wider than common melting point range for crystallites.



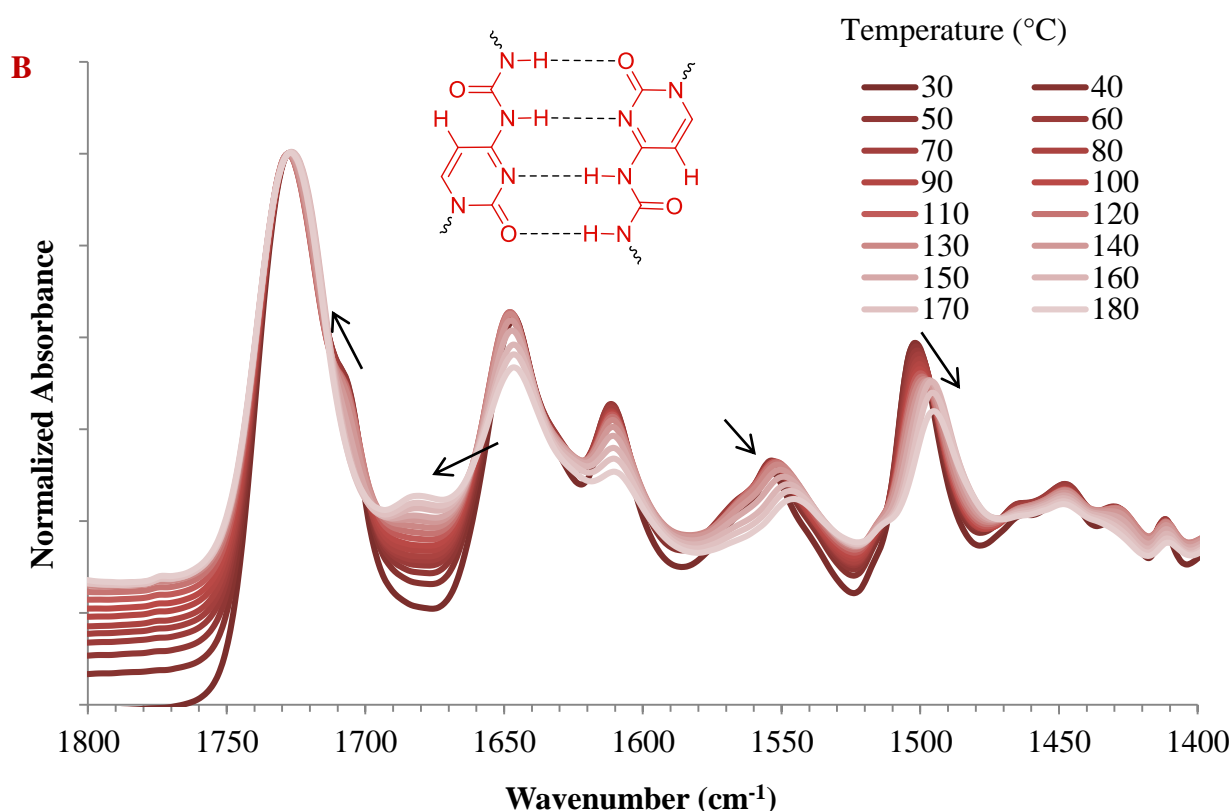


**Figure 6.9.** Variable temperature FT-IR spectra of (A) poly(UCyA-co-nBA) and (B) poly(CyA-co-nBA) with 21 mol% of UCyA and CyA, respectively, in the 1500-1700 cm<sup>-1</sup> region.

**Water sorption.** Figure 6.10 demonstrates significantly lower water uptake of poly(UCyA-co-nBA) copolymers than their CyA copolymer precursors. Poly(UCyA-co-nBA) copolymer only exhibited 0.3 wt% moisture uptake at 95% relative humidity with the highest UCyA incorporation, while the corresponding cytosine control gained up to 4.6% weight under 95% relative humidity. Water uptake of poly(CyA-co-nBA) increased with increasing mol% of CyA. Weight changes of poly(UCyA-co-nBA) from water uptake reached closely to the instrument lower limit. The increased hydrophobicity of UCy relative to cytosine contributed to lower water uptake for poly(UCyA-co-nBA). Additionally, phase-separation further repelled moisture through packing hydrogen bonding groups into the hard phase and isolating them within the nonpolar soft phase. The

low water uptake of poly(UCyA-*co*-*n*BA) largely benefits its application in adhesives as moisture generally weakens adhesion and causes degradation during melt processing.

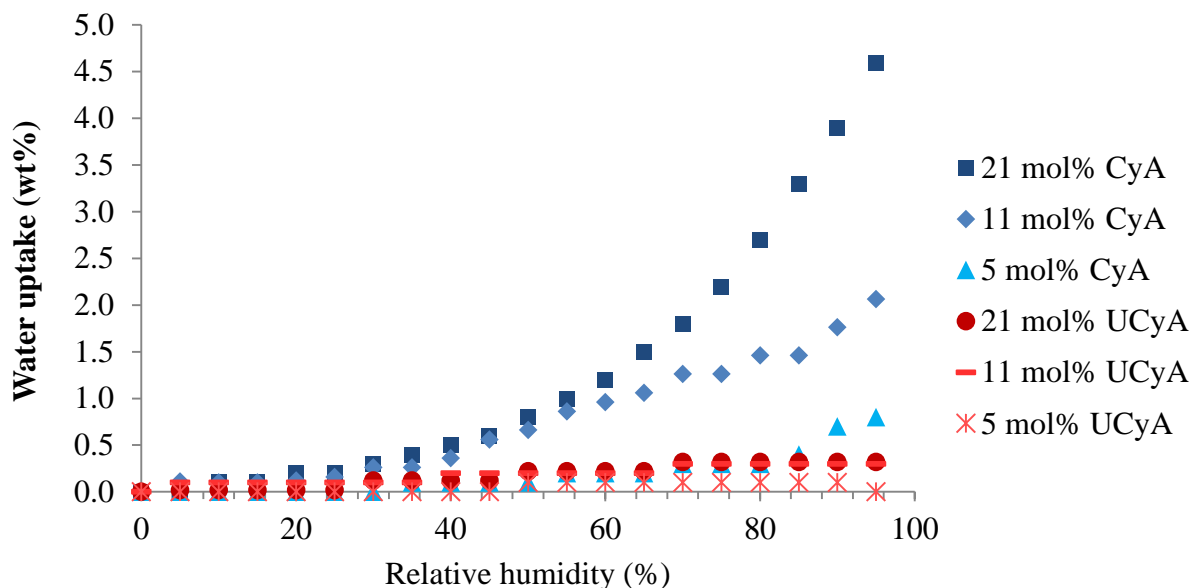


**Figure 6.10.** Equilibrium water sorption of poly(UCyA-*co*-*n*BA) and poly(UCyA-*co*-*n*BA) copolymers with varied amounts of UCyA and CyA in stepwise relative ramp from 0% to 95%.

## 6.5 Conclusions

This manuscript reports an unprecedented facile synthetic route for monomer and random copolymers that contain *N*1-substituted cytosine using Michael addition reaction of cytosine with diacrylate and free radical polymerization, respectively. Post-functionalization easily converted cytosine pendant groups to ureido-cytosines, which self-associated into quadruply hydrogen-bonded dimers. Physically crosslinked acrylic copolymers formed tacky solids with <5 mol% cytosine contents, while copolymers with  $\geq 9$  mol% associating monomers solution-casted into free-standing films. Physical

characterizations of UCy and cytosine-containing copolymers provided direct comparison of weak and strong hydrogen-bonded acrylic copolymer networks. Poly(UCyA-*co-n*BA) copolymers started to lose weight at lower temperatures in TGA heating ramps due to degradation of the urea bonds near 200 °C, while poly(CyA-*co-n*BA) thermally crosslinked into permanent gel above 130 °C. Increasing the concentrations of randomly distributed CyA or UCyA in soft acrylic matrixes contributed to viscoelastic solids with increased  $T_g$  values and higher moduli due to steric restriction and transient network formation. However, 3 mol% CyA incorporation provided sufficient physical crosslinking to afford a 50 °C wide plateau window during a rheological temperature sweep, while the cytosine control with the same mol% CyA behaved like non-associating entangled polymer melt. A copolymer with 5 mol% UCyA formed a free-standing film that allowed DMA measurement in contrast to its CyA precursor which exhibited no mechanical integrity. DMA results of UCyA copolymer films displayed superior mechanical performance relative to CyA copolymer controls, and the additional transitions on their tan delta curves corresponded to hydrogen bonding dissociation. Hydrogen bonding of cytosine and UCy drove the microphase-separation of their acrylic copolymer films, verified using SAXS, AFM, and VT-FTIR. Hydrogen bonded UCyA units stacked into nano-fibrillar hard domains, while the cytosine units lacked long-range ordering, forming less ordered domains with irregular shapes. Poly(UCyA-*co-n*BA) copolymers showed significantly lower water uptake than poly(CyA-*co-n*BA) precursors due to lower polarity and more well-defined phase-separation. Overall, quadruply hydrogen-bonded UCy units contributed to enhanced thermal stability, higher glass transitions temperature, better thermomechanical performance, wider rubbery plateau window, more well-defined

morphology, and lower water uptake for a random copolymer compared to its cytosine control. UCyA random copolymers enable potential applications as supramolecular adhesives with  $\leq 3$  mol% UCyA and thermoplastic elastomers with 9-11 mol% UCyA. The advantages of using UCyA-containing copolymers over CyA controls for adhesive applications included better melt stability during processing, enhanced cohesive strength, wider functional temperature range, and superior moisture resistance.

## 6.6 Acknowledgements

This research was partially supported by Henkel Corporation. This material is also partially based upon work supported by the National Science Foundation under Grant No. DMR-0923107.

## 6.7 References

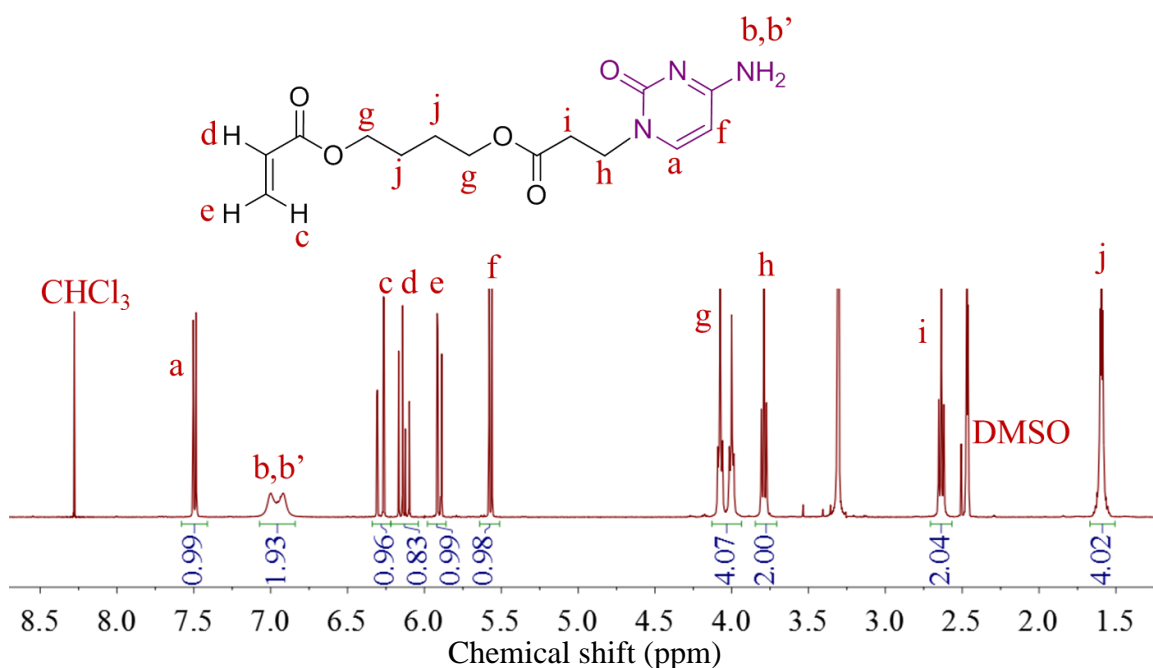
1. Seiffert, S.; Sprakel, J. *Chem. Soc. Rev.* **2012**, *41*, 909.
2. Schalley, C.; Editor *Analytical Methods in Supramolecular Chemistry*; Wiley-VCH Verlag GmbH & Co. KGaA, **2007**.
3. Sijbesma, R. P.; Beijer, F. H.; Brunsveld, L.; Folmer, B. J. B.; Hirschberg, J. H. K. K.; Lange, R. F. M.; Lowe, J. K. L.; Meijer, E. W. *Science* **1997**, *278*, 1601.
4. Brunsveld, L.; Folmer, B. J. B.; Meijer, E. W.; Sijbesma, R. P. *Chem. Rev.* **2001**, *101*, 4071.
5. Yang, L.; Tan, X.; Wang, Z.; Zhang, X. *Chem. Rev.* **2015**, *115*, 7196.
6. Khutoryanskiy, V. V. *Nat Mater* **2015**, *14*, 963.
7. Deng, R.; Liu, X. *Nat Chem* **2015**, *7*, 472.
8. Aida, T.; Meijer, E. W.; Stupp, S. I. *Science* **2012**, *335*, 813.
9. Hutin, M.; Burakowska-Meise, E.; Appel, W. P. J.; Dankers, P. Y. W.; Meijer, E. W. *Macromolecules (Washington, DC, U. S.)* **2013**, *46*, 8528.
10. Zhang, K.; Long, T. E.; Paul, C. 2015.
11. Creton, C.; Papon, E. *MRS Bull.* **2003**, *28*, 419.
12. Courtois, J.; Baroudi, I.; Nouvel, N.; Degrandi, E.; Pensec, S.; Ducouret, G.; Chaneac, C.; Bouteiller, L.; Creton, C. *Adv. Funct. Mater.* **2010**, *20*, 1803.
13. Lundberg, R. D. In *Structure and Properties of Ionomers*; Pineri, M., Eisenberg, A., Eds.; Springer Netherlands: 1987; Vol. 198, p 429.
14. Brooks, H. D.; Kelly, J. Y.; Madison, P. H.; Thatcher, C. D.; Long, T. E. *Proc. Annu. Meet. Adhes. Soc.* **2001**, *24th*, 150.
15. Griehl, W.; Ruestem, D. *Industrial & Engineering Chemistry* **1970**, *62*, 16.
16. Benedek, I. *Pressure-sensitive adhesives and applications*; CRC Press, **2004**.

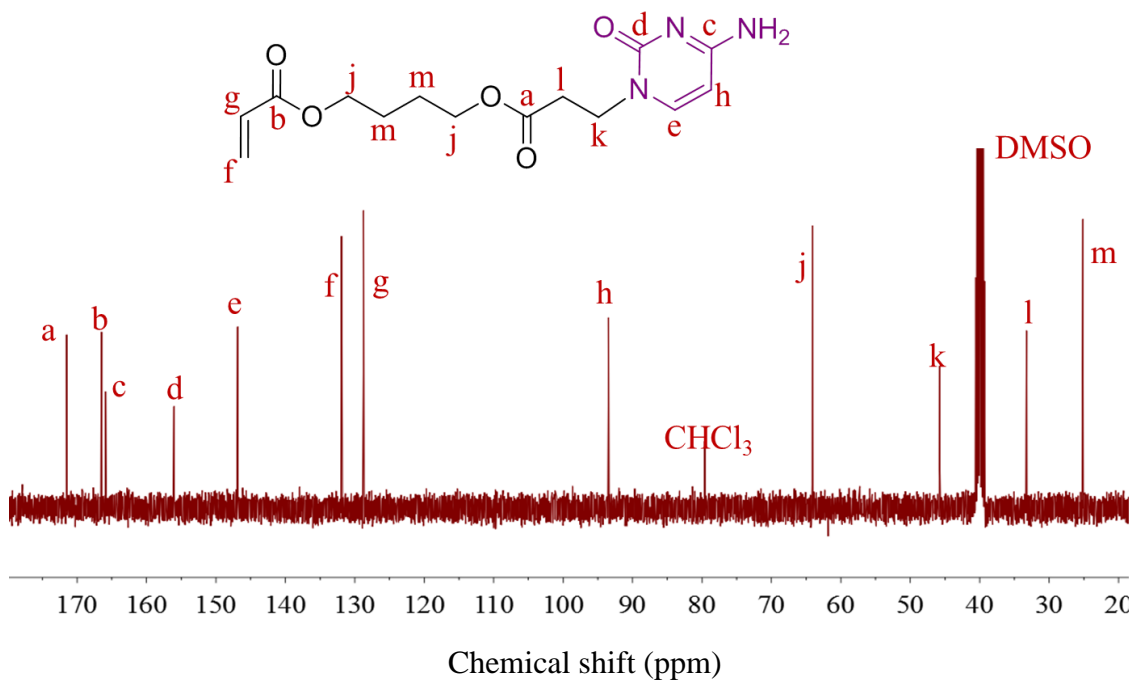


17. Han, S. H.; Pryamitsyn, V.; Bae, D.; Kwak, J.; Ganesan, V.; Kim, J. K. *ACS Nano* **2012**, *6*, 7966.
18. Zhang, K.; Fahs, G. B.; Aiba, M.; Moore, R. B.; Long, T. E. *Chem. Comm.* **2014**, *50*, 9145.
19. Bazzi, H. S.; Bouffard, J.; Sleiman, H. F. *Macromolecules* **2003**, *36*, 7899.
20. Spijker, H. J.; Dirks, A. J.; Van, H. J. C. M. *J. Polym. Sci., Part A: Polym. Chem.* **2006**, *44*, 4242.
21. Hosono, N.; Gillissen, M. A. J.; Li, Y.; Sheiko, S. S.; Palmans, A. R. A.; Meijer, E. W. *J. Am. Chem. Soc.* **2013**, *135*, 501.
22. Sartorius, J.; Schhneider, H.-J. *Chem. Eur. J.* **1996**, *2*, 1446.
23. Greco, E.; Aliev, A. E.; Lafitte, V. G. H.; Bala, K.; Duncan, D.; Pilon, L.; Golding, P.; Hailes, H. C. *New J. Chem.* **2010**, *34*, 2634.
24. Tamami, M.; Zhang, K.; Dixit, N.; Moore, R. B.; Long, T. E. *Macromol. Chem. Phys.* **2014**, *215*, 2337.
25. McHale, R.; Patterson, J. P.; Zetterlund, P. B.; O'Reilly, R. K. *Nat. Chem.* **2012**, *4*, 491.
26. McHale, R.; O'Reilly, R. K. *Macromolecules* **2012**, *45*, 7665.
27. Lo, P. K.; Sleiman, H. F. *J. Am. Chem. Soc.* **2009**, *131*, 4182.
28. Lutz, J.-F.; Thuenemann, A. F.; Rurack, K. *Macromolecules* **2005**, *38*, 8124.
29. Kim, J. C.; Jung, J.; Rho, Y.; Kim, M.; Kwon, W.; Kim, H.; Kim, I. J.; Kim, J. R.; Ree, M. *Biomacromolecules* **2011**, *12*, 2822.
30. Sijbesma, R. P.; Meijer, E. W. *Chem. Comm.* **2003**, *5*.
31. de, G. T. F. A.; Ligthart, G. B. W. L.; Lutz, M.; Spek, A. L.; Meijer, E. W.; Sijbesma, R. P. *J. Am. Chem. Soc.* **2008**, *130*, 5479.
32. Feldman, K. E.; Kade, M. J.; Meijer, E. W.; Hawker, C. J.; Kramer, E. J. *Macromolecules (Washington, DC, U. S.)* **2009**, *42*, 9072.
33. Yamauchi, K.; Lizotte, J. R.; Long, T. E. *Macromolecules* **2003**, *36*, 1083.
34. Lafitte, V. G. H.; Aliev, A. E.; Greco, E.; Bala, K.; Golding, P.; Hailes, H. C. *New J. Chem.* **2011**, *35*, 1522.
35. Cheng, C.-C.; Chang, F.-C.; Wang, J.-H.; Chu, Y.-L.; Wang, Y.-S.; Lee, D.-J.; Chuang, W.-T.; Xin, Z. *RSC Advances* **2015**, *5*, 76451.
36. Mather, B. D.; Viswanathan, K.; Miller, K. M.; Long, T. E. *Prog. Polym. Sci.* **2006**, *31*, 487.
37. Sivakova, S.; Rowan, S. J. *Chem. Soc. Rev.* **2005**, *34*, 9.
38. Cheng, S.; Zhang, M.; Dixit, N.; Moore, R. B.; Long, T. E. *Macromolecules* **2012**, *45*, 805.
39. Zhang, K.; Aiba, M.; Fahs, G. B.; Hudson, A. G.; Chiang, W. D.; Moore, R. B.; Ueda, M.; Long, T. E. *Polym. Chem.* **2015**, *6*, 2434.
40. Armstrong, G.; Buggy, M. *Materials Science and Engineering: C* **2001**, *18*, 45.
41. Ravey, M.; Pearce, E. M. *J. Appl. Polym. Sci.* **1997**, *63*, 47.
42. Odian, G. G. *Principles of polymerization*; Wiley-Interscience Hoboken, N.J, **2004**; Vol. 4th.
43. Hiemenz, P. C.; Lodge, T. P. *Polymer Chemistry, Second Edition*; Taylor & Francis, **2007**.
44. Tamami, M.; Hemp, S. T.; Zhang, K.; Zhang, M.; Moore, R. B.; Long, T. E. *Polymer* **2013**, *54*, 1588.

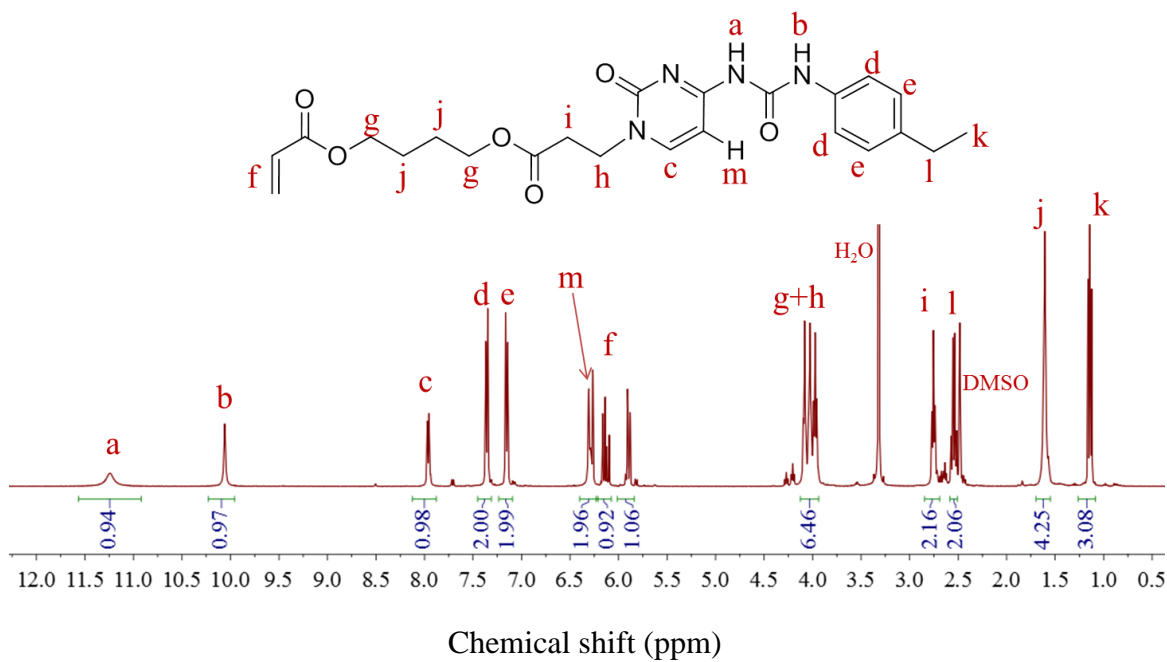
45. Chang, E. P. *J. Adhes.* **1991**, *34*, 189.
46. Sivakova, S.; Bohnsack, D. A.; Mackay, M. E.; Suwanmala, P.; Rowan, S. J. *J. Am. Chem. Soc.* **2005**, *127*, 18202.
47. Feula, A.; Pethybridge, A.; Giannakopoulos, I.; Tang, X.; Chippindale, A.; Siviour, C. R.; Buckley, C. P.; Hamley, I. W.; Hayes, W. *Macromolecules* **2015**, *48*, 6132.
48. Appel, W. P. J.; Portale, G.; Wisse, E.; Dankers, P. Y. W.; Meijer, E. W. *Macromolecules* **2011**, *44*, 6776.
49. Arunan, E.; Desiraju Gautam, R.; Klein Roger, A.; Sadlej, J.; Scheiner, S.; Alkorta, I.; Clary David, C.; Crabtree Robert, H.; Dannenberg Joseph, J.; Hobza, P.; Kjaergaard Henrik, G.; Legon Anthony, C.; Mennucci, B.; Nesbitt David, J. In *Pure Appl. Chem.* 2011; Vol. 83, p 1637.
50. Coleman, M. M.; Lee, K. H.; Skrovanek, D. J.; Painter, P. C. *Macromolecules* **1986**, *19*, 2149.

## 6.8 Supporting Information





**Figure S6.1.**  $^1\text{H}$  NMR and  $^{13}\text{C}$  NMR spectra of cytosine acrylate.



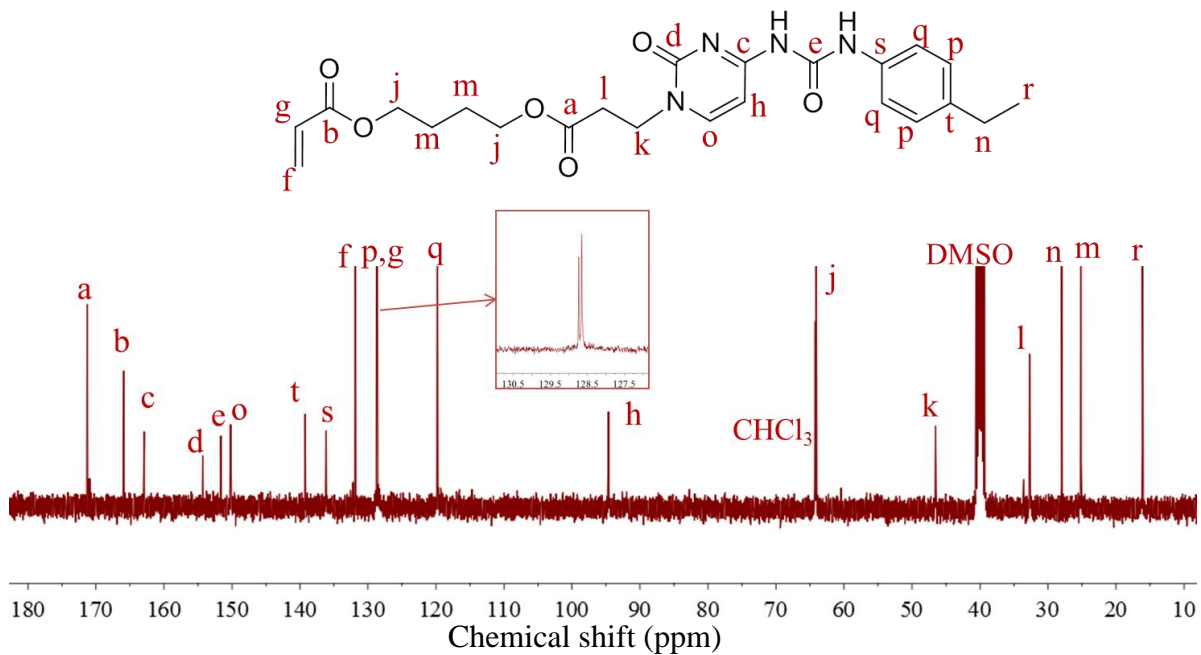


**Figure S6.2.**  $^1\text{H}$  NMR and  $^{13}\text{C}$  NMR spectra of ureido cytosine acrylate.

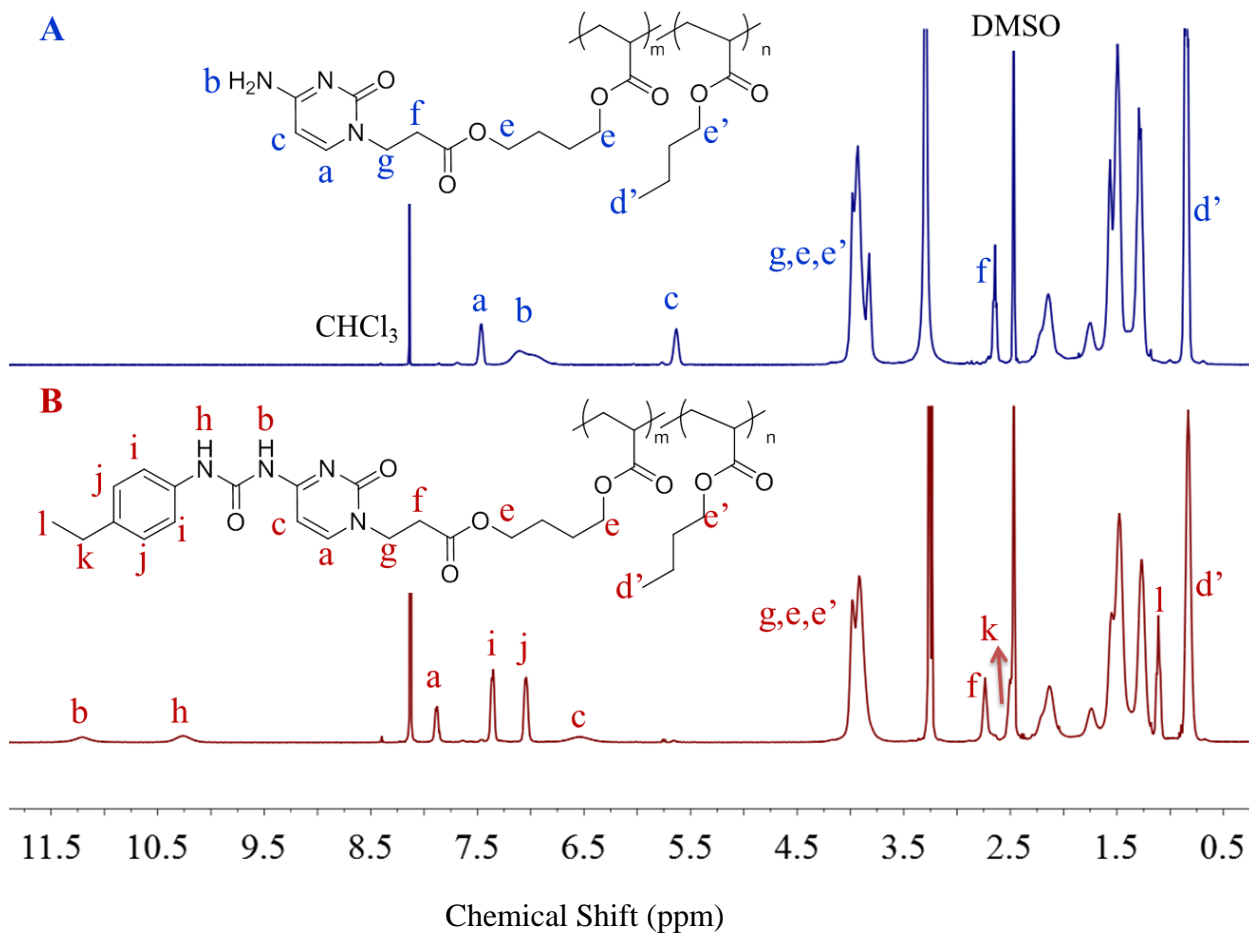


**Figure S6.3.**  $^1\text{H}$  NMR spectrum of (A) poly(CyA-*co*-nBA) and (B) poly(UCyA-*co*-nBA) copolymers in a mixture of  $\text{CDCl}_3$  and  $\text{DMSO-d}_6$ .

Specific viscosity of the reaction mixture during post-functionalization was measured on TA instrument Discovery AR-G2 rheometer, using a concentric cylinder geometry with a required liquid volume of 8 mL. The cup and spindle were enclosed with a metal cover to minimize solvent evaporation. Cytosine copolymer solution was mixed with diluted isocyanate and added to the cup, which was maintained at 25 °C. The solution was subjected to a steady shear at 10 Hz over 5 h.

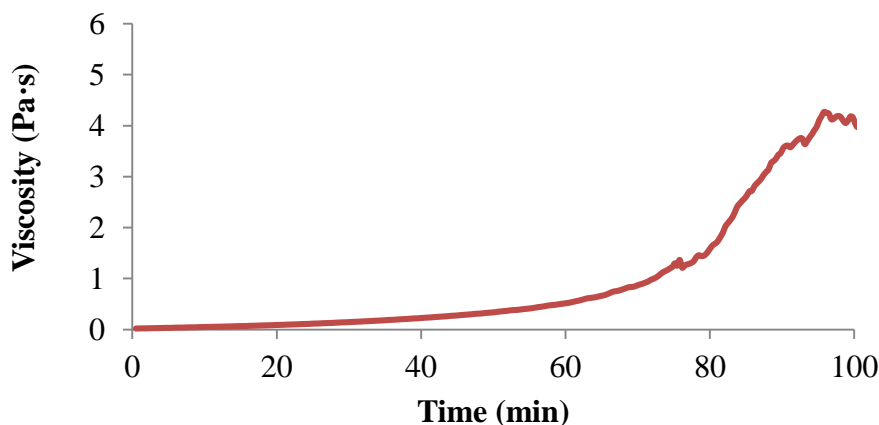


**Figure S6.4.** *In situ* specific viscosity measurement of post-functionalization reaction for and 3 wt% solution of poly(CyA-*co*-nBA) in DCM with isocyanates.

Isothermal rheological analyses of cytosine copolymers were conducted on TA Instruments Discovery AR-G2 rheometer, using disposable aluminum parallel plates of 25 mm in diameter. All measurements were strain-controlled at constant nominal strain values within the linear viscoelastic region, as determined using strain sweep experiments. Dynamic oscillatory temperature sweep experiments were performed at temperature steps

from -40 °C to 150 °C with a 3 °C interval at 1 Hz. Sample was equilibrated for 1 min at each temperature.

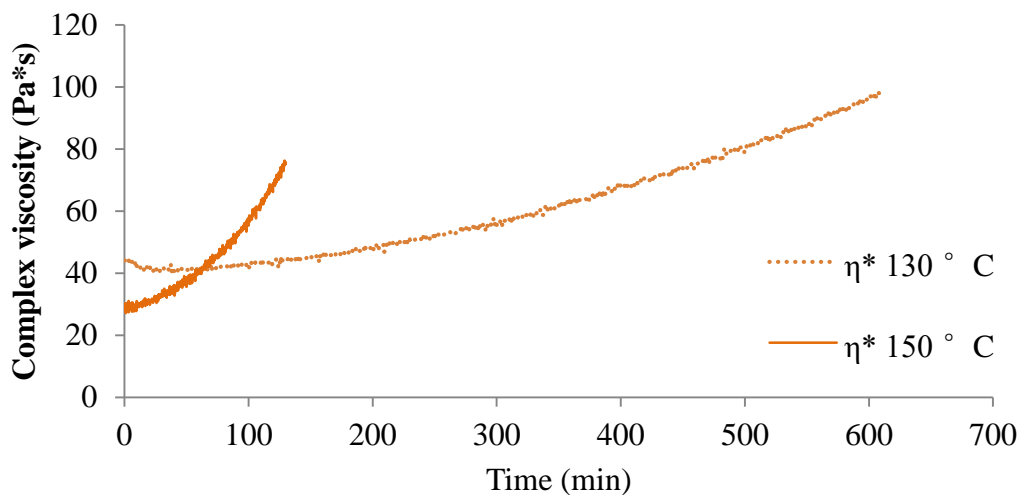


**Figure S6.5.** Isothermal rheological time sweep of poly(CyA-*co*-nBA) with 5 mol% CyA at 130 and 150 °C in air.

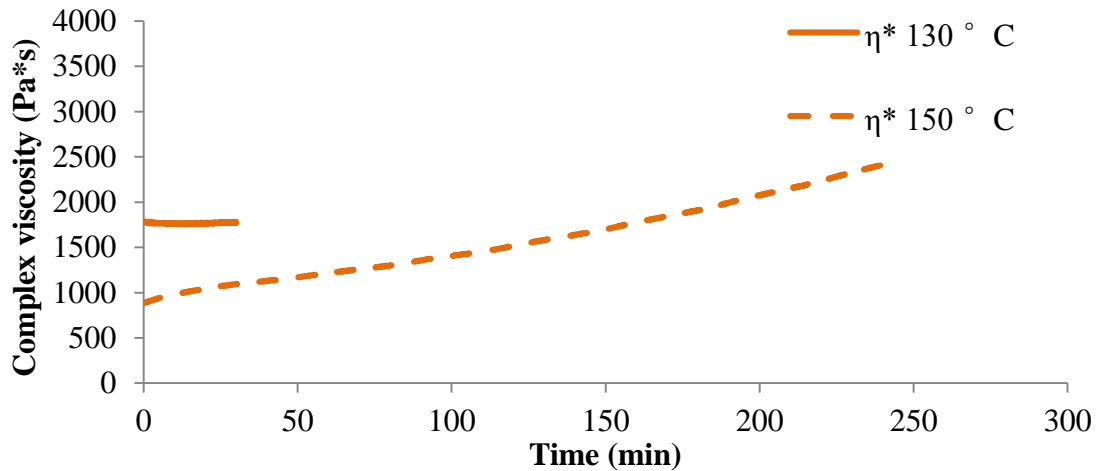


**Figure S6.6.** Isothermal rheological time sweep of poly(UCyA-*co*-nBA) with 9 mol% UCyA at 130 and 150 °C in air.

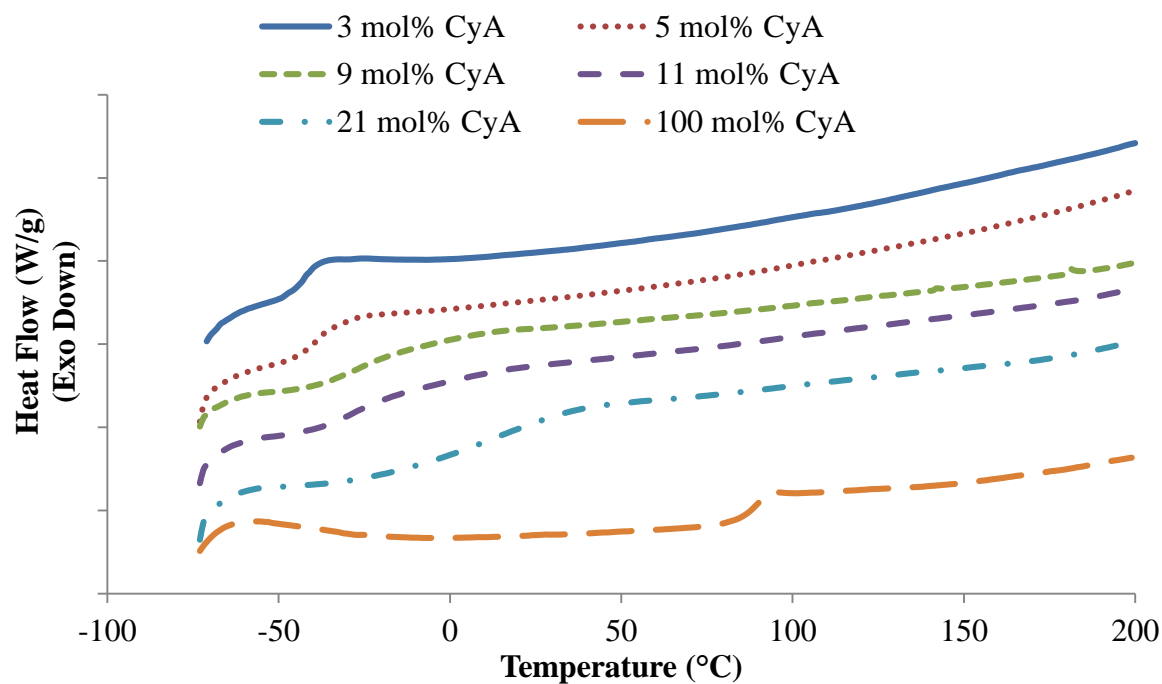


Figure S6.7. DSC thermograms of poly(CyA-co-nBA)s and poly(CyA).

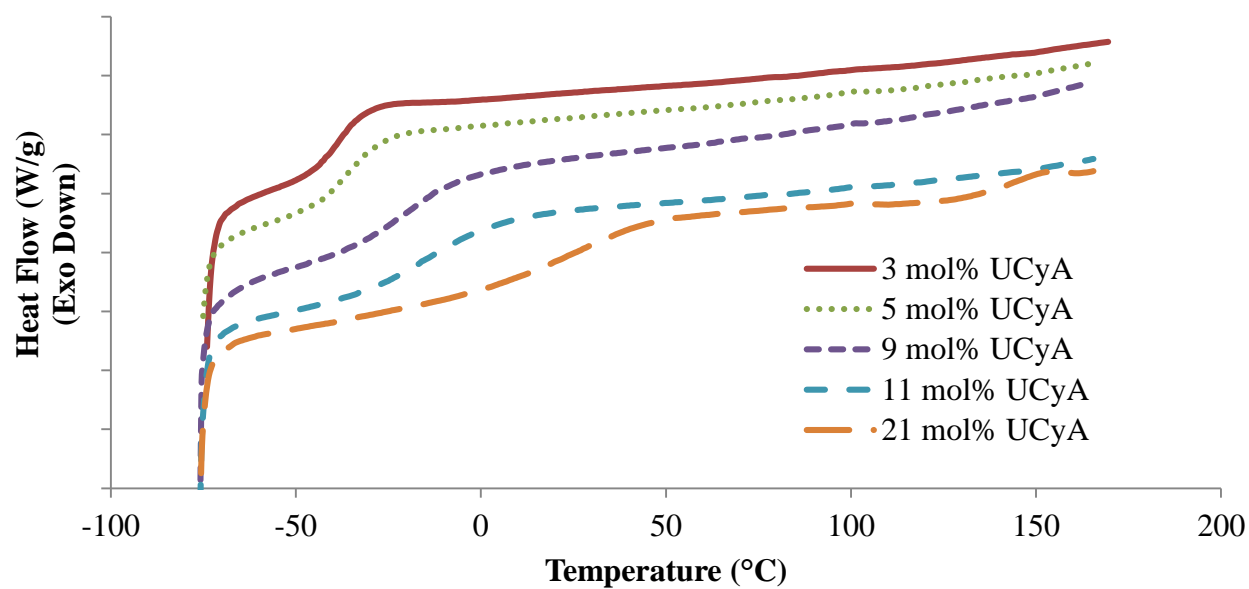
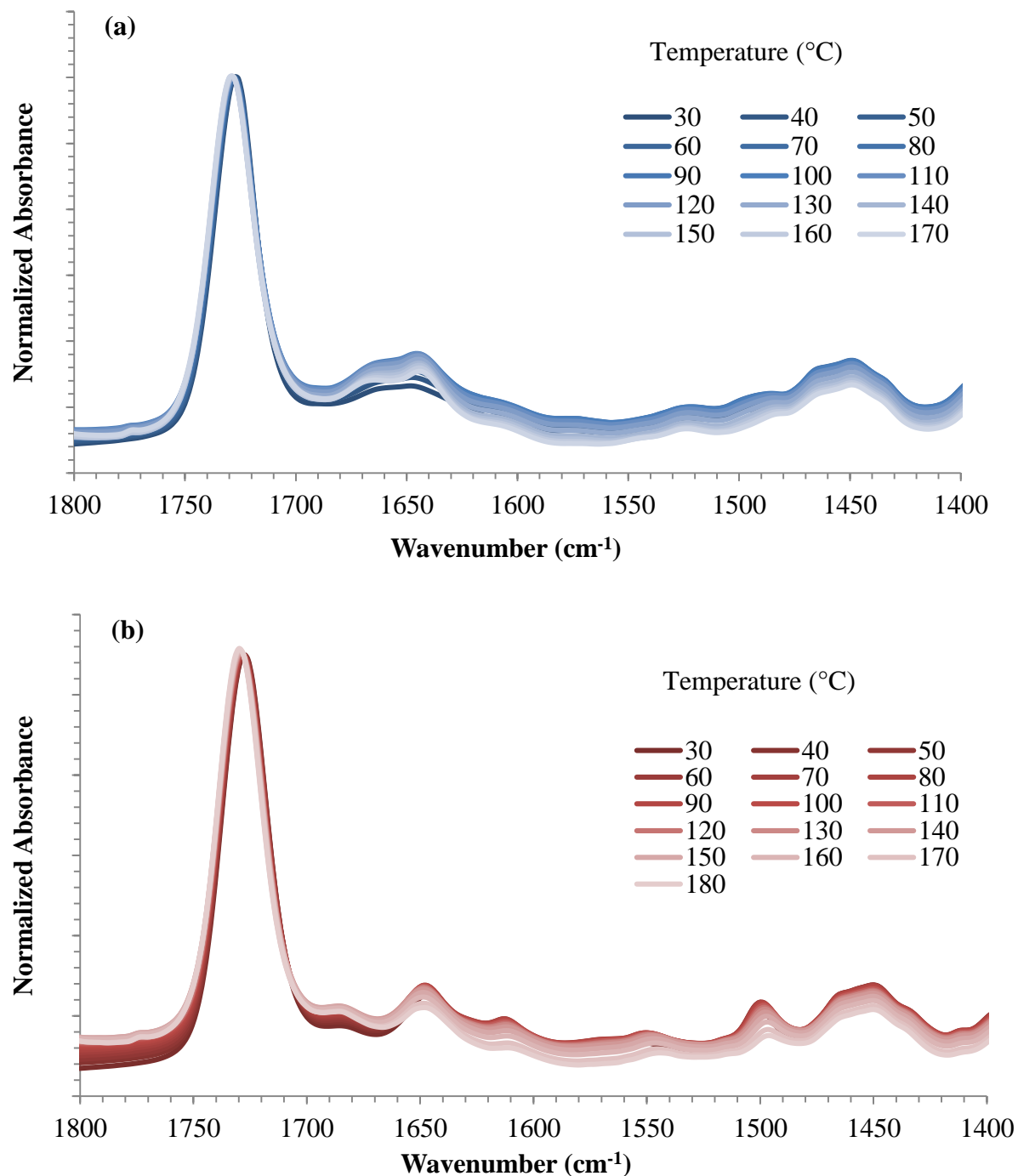


Figure S6.8. DSC thermograms of poly(UCyA-co-nBA)s.



**Figure S6.9.** Variable temperature FT-IR spectra of (a) poly(CyA-co-nBA) and (b) poly(UCyA-co-nBA) with 5 mol% CyA and UCyA in the 1800-1400  $\text{cm}^{-1}$  region at varying temperatures.



## Chapter 7. Acetyl-Protected Cytosine- and Guanine-Containing Acrylics for Supramolecular Adhesives

(In preparation for publishing in *Polymer*)

Keren Zhang, Gregory B. Fahs, Amanda G. Hudson, Robert B. Moore, and Timothy E. Long\*

*Department of Chemistry, Macromolecules and Interfaces Institute  
Virginia Tech, Blacksburg, VA 24061, USA*

**Keywords:** cytosine, guanine, pressure sensitive adhesive, hydrogen bonding

### 7.1 *Abstract*

Hydrogen bonding of nucleobase serves as an efficient noncovalent interaction for designing supramolecular polymers with desired properties for pressure sensitive adhesives. Michael additions yielded acetyl-protected cytosine and guanine-containing acrylic monomers with flexible spacers between the hydrogen bonding units to the acrylic backbone. Free radical polymerization of nucleobase-containing monomers afforded guanine and cytosine homopolymers and a series of random copolymers with *n*-butyl acrylate. Nucleobase incorporations significantly affected the physical properties of polyacrylates, including thermal, thermomechanical, rheological, morphological properties, and adhesive performance. Guanine- and cytosine-containing copolymers each exhibited a single  $T_g$  that increased with increasing nucleobase content. Self-association of acetyl cytosine and acetyl guanine units converted low  $T_g$  polyacrylate to a physically crosslinked network with mechanical integrity. Acetyl guanine-containing copolymers with 8 mol% or more guanine content solution cast into free-standing films with microphase-separation. Acetyl cytosine-containing copolymers with 15 mol% or more cytosine formed free-standing film with phase-mixed properties. NMR titration experiment established the one-to-one stoichiometry for acetyl cytosine and acetyl guanine monomers.

However, the acetyl protection group prevented the formation of triple hydrogen bonding, and yielded double hydrogen bonding between acetyl cytosine and acetyl guanine with an intermediate binding strength compared to their self-associations. Acetyl guanine-containing copolymer with 3 mol% guanine exhibited highest peel strength on stainless steel with no adhesive residue and extended service frequency range compared to the cytosine-containing copolymer and various pressure sensitive adhesive controls.

## 7.2 *Introduction*

Supramolecular polymers describe polymers that contain noncovalent interactions such as hydrogen bonding,  $\pi$ - $\pi$  stacking, and electrostatics interaction.<sup>1-3</sup> These noncovalent interactions with intermediate bond strength, lower than chemical bond and higher than van der Waals interaction, enable the formation of backbone or physical crosslinking for supramolecular polymers. Synthetic supramolecular polymers are emerging as versatile materials with superior processability due to the reversible nature of these noncovalent interactions. For example, hydrogen bonding increases apparent molecular weight and drives self-assembly of supramolecular polymers, which leads to enhanced mechanical properties,<sup>4-6</sup> ordered morphologies,<sup>7-12</sup> and stimuli-responsiveness to external triggers<sup>13,14</sup>. These unique properties of supramolecular polymers contribute to their potential application in a wide variety of forefront technologies as self-healing and mendable materials,<sup>15-17</sup> polymerization templates,<sup>18,19</sup> and nano-materials<sup>8,9,20,21</sup>. In addition, the major industrialized applications of supramolecular polymers involve a large group of traditional materials, such as adhesives, elastomers, additives, coatings, surfactants, and adsorbents, which mainly contain physically crosslinking polymers with tunable physical properties.<sup>1,22-28</sup>

Supramolecular adhesives utilize physically crosslinking mechanism instead of chemical crosslinking to obtain sufficient cohesive strength with tunable tack and adhesive strength. The reversibility of these noncovalent interactions to external triggers such as heat and solvent preserves the processability and recyclability of these transient supramolecular polymer networks. The intermediate bond strength of noncovalent interactions limits the usefulness of supramolecular polymers as structural adhesives for rigid joints, however, afford sufficient physically crosslinking for soft adhesives and reversible adhesives. Long *et al.* demonstrated the efficiency of incorporating noncovalent interactions as reversible crosslinking mechanism for acrylic adhesives using 2-ureido-4[1H]-pyrimidinone (UPy) quadruple unit, urethane, and adenine-thymine nucleobase pair.<sup>7,29,30</sup> provided noncovalent interactions. Incorporating of hydrogen bonding units onto the pendant groups within a low  $T_g$  acrylic matrix resulted in enhanced adhesive performance due to the formation of a crosslinked network and increased apparent molecular weight. The Creton group prepared bis-urea functionalized supramolecular polymers and characterized their viscoelastic and adhesive properties as soft adhesives.<sup>22,31</sup>

Adenine, thymine, cytosine, and guanine comprise the primary nucleobases in deoxyribonucleic acid (DNA). The molecular recognition of base pairing between purines and pyrimidines stabilizes the double helix structure of DNA and encodes genetic information for living organisms. These complementary hydrogen bonding associations between nucleobase pairs inspired many polymer chemists to investigate and design nucleobase-containing supramolecular polymers, in order to achieve desirable self-assembled morphologies or physical properties.<sup>8,19,32-40</sup> Among the four primary nucleobases in DNA, literature focuses on adenine and thymine derivatives due to their

relatively straight-forward synthesis.<sup>41</sup> Long *et al.* previously designed novel adenine and thymine-containing acrylic copolymers as supramolecular adhesives.<sup>7</sup> In contrast, research on cytosine and guanine-containing polymers remains relatively unexplored because of their challenging synthesis and solubility. However, the guanine-cytosine nucleobase pair affords a much stronger interaction with association constant of  $\sim 10^4 \text{ M}^{-1}$  in  $\text{CDCl}_3$  compared to adenine-thymine ( $10^2 \text{ M}^{-1}$ ) because of the triple CMHB.<sup>42</sup>

This manuscript describes the synthesis and characterization of acetyl-protected cytosine and guanine-containing acrylics, as well as their supramolecular blends. Michael addition afforded the synthesis of acetyl-protected cytosine and guanine acrylate monomers, which enabled free radical copolymerization of cytosine and guanine-containing homopolymers and copolymers with *n*-butyl acrylate (*n*BA). The identical chemical structure of cytosine and guanine acrylate monomers compared to *n*BA allowed facile control of the copolymer compositions and ensured random distribution of nucleobase on the polymer chain. Flexible spacers between the acrylic backbone and nucleobase units minimized the steric effect, providing mobility for the nucleobase and facilitated the formation of hydrogen bonding. Incorporation of acetyl cytosine and acetyl guanine units into a low  $T_g$  poly(*n*BA) matrix significantly affected the physical properties of resulting nucleobase-containing acrylics. The steric effect and hydrogen bonding of the guanine and cytosine pendant groups restricted the mobility of polymer chains, which resulted in formation of a transient physically crosslinked network. Varying the nucleobase content on the acrylic backbone contributed to a series of supramolecular polymers with different thermal and mechanical properties, ranging from tacky solid to free-standing film

to brittle solid dust. Guanine- and cytosine-containing acrylics exhibited promising viscoelastic properties and peeling strength for pressure sensitive adhesive applications.

### 7.3 *Experimental Section*

**Materials.** 1,4-Butanediol diacrylate (Alfa Aesar, 99%), and *N*4-acetylcytosine (Alfa Aesar, 99%) were used without further purification. *n*-Butyl acrylate (*n*BA, 99+%) was purchased from Sigma Aldrich and passed through neutral alumina columns before use.  $\alpha,\alpha'$ -Azobis-(isobutyronitrile) (AIBN, Fluka, 99%) was recrystallized twice from methanol. Guanine (99%), acetic anhydride (98%), lithium bromide (LiBr, 99+%), triethylamine (TEA, 99%), and 2,6-di-*tert*butyl-4-methylphenol (BHT, 99%) were purchased from Aldrich and used without further purification. All solvents were obtained from Spectrum and used as received.

**Analytical Methods.**  $^1\text{H}$  NMR and  $^{13}\text{C}$  NMR spectroscopy confirmed monomer and polymer structures using a Varian Unity 400 or an Agilent U4-DD2 spectrometer at 400 MHz in DMSO- $\text{d}_6$  or a mixture of  $\text{CDCl}_3$  and DMSO- $\text{d}_6$  (1:1, v/v) at 23 °C. Size exclusion chromatography (SEC) determined the molecular weight of polymers using a Waters size exclusion chromatograph, equipped with an auto sampler, three 5  $\mu\text{m}$  PLgel Mixed-C columns, a Waters 2410 refractive index (RI) detector operating at 880 nm, a Wyatt Technologies miniDAWN multi-angle laser light scattering (MALLS) detector operating at 690 nm, and a Viscotek 270 viscosity detector. The mobile phase contained DMF and 0.05 M LiBr with a flow rate of 1 mL/min at 50 °C. Reported molecular weights are relative to polystyrene standard. Dynamic light scattering (DLS) of polymers solution in the SEC mobile phase with 1 mg/mL concentration confirmed the absence of aggregation prior to the SEC experiment using a Malvern Zetasizer NanoZS DLS. Thermogravimetric analysis

(TGA) measured the thermal degradation temperatures ( $T_{d,5wt\%}$ ) of nucleobase-containing copolymers using a TA Instruments Q50 TGA with a heating ramp from ambient to 600 °C at a heating rate of 10 °C/min under nitrogen. Differential scanning calorimetry (DSC) measured glass transition temperatures as the midpoint of the transition in the second heating ramp with a heating rate of 10 °C/min using a TA instruments Q1000 DSC.

Nucleobase-containing copolymers with mechanical integrity were dissolved in a mixture of  $\text{CHCl}_3$ -MeOH (3:1, v/v) and cast into a PTFE Petri dish. Slow evaporation of the solvent, drying under reduced pressure (20 mmHg) at room temperature, and subsequent annealing at 50 °C for 12 h yielded free-standing films. Dynamic mechanical analysis (DMA) of free-standing copolymer films utilized a TA Instruments Q800 Dynamic Mechanical Analyzer in tension mode at a frequency of 1 Hz, an oscillatory amplitude of 15  $\mu\text{m}$ , a static force of 0.01 N, and a temperature ramp rate of 3 °C/min. Rheological experiments were performed on a TA Instruments Discovery AR-G2 rheometer in the oscillatory mode, using disposable 25 mm diameter aluminum parallel plates. Multiple temperature/frequency sweep measurements generated master curves using time-temperature superposition (TTS) principle at 20 °C according to the  $G'$  curves. All rheological measurements were strain-controlled at a constant nominal strain value within the linear viscoelastic range, determined using strain sweep experiment. Variable temperature Fourier transform infrared (VT-FTIR) experiments were performed using a Varian 670-IR spectrometer (DTGS detector) with Pike Technologies variable temperature GladiATR<sup>TM</sup> attachment (diamond crystal). Spectra were collected at 4  $\text{cm}^{-1}$  resolution and as an average of 32 scans. Samples were subjected to a temperature ramp of 1 °C /min, starting from 30 °C to 190 °C and FTIR spectra were collected every 10 °C beginning from

30 °C. Peeling strength measured the peel force per unit width on a stainless steel substrate using a Cheminstruments AR-1000 adhesion tester. Each data point represented the average of five measurements with a 180° peeling angle at a cross-head speed of 12 inch/min. The lamination and drying process of nucleobase-containing copolymers and the adhesive controls onto a 2 mil PET backing followed procedures in Long *et al.*<sup>7</sup>

Small angle X-ray scattering (SAXS) experiments were performed using a Rigaku S-Max 3000 3 pinhole SAXS system, equipped with a rotating anode emitting X-ray with a wavelength of 0.154 nm (Cu K<sub>α</sub>). The sample-to-detector distance was 1603 mm for SAXS, and the q-range was calibrated using a silver behenate standard. Two-dimensional SAXS patterns were obtained using a 2D multiwire, proportional counting, gas-filled detector, with an exposure time of 1 h. The SAXS data was corrected for sample thickness, and the scattering profiles were vertically shifted to facilitate a comparison of peak positions. All the scattering data was analyzed using the SAXSGUI software package to obtain radially integrated SAXS intensity versus the scattering vector q (SAXS), where  $q=(4\pi/\lambda)\sin(\theta)$ ,  $\theta$  is one half of the scattering angle and  $\lambda$  is the X-ray wavelength.

**Synthesis of 4-((3-(N4-Acetylcytosin-1-yl)propanoyl)oxy)butyl Acrylate (ACyA) Monomer (Scheme 7.1).** A suspension of N4-acetylcytosine (5.0 g, 30.0 mol), TEA (1.5 mL, 10.0 mol), BHT (0.6 g), and 1,4-butanediol diacrylate (12.0 mL, 60.0 mol) in dimethylsulfoxide (DMSO, 100 mL) was stirred at room temperature for 24 h. The reaction mixture was poured into a 1 L beaker containing 500 mL of water under constant stirring. The resulting solution was washed with hexane (100 mL) three times using a separation-funnel to remove excess 1,4-butanediol diacrylate. The aqueous layer was extracted with 100 mL dichloromethane four times. The combined extracts were dried over MgSO<sub>4</sub>,

filtered, and concentrated in a vacuum evaporator to remove solvents. The evaporation residue was purified using chromatography with  $\text{CHCl}_3$ –MeOH (20:1) on silica gel, yielding a white solid with 53% yield, melting at 69.9–72.3 °C. The purified ACyA monomer was stored in  $\text{CHCl}_3$  to prevent autopolymerization.  $^1\text{H}$  NMR (Figure S7.1) (400 MHz,  $\text{DMSO}-d_6$ )  $\delta$  10.76 (s, 1H,  $\text{H}_a$ ), 8.01 (d,  $J = 7.3$  Hz, 1H,  $\text{H}_b$ ), 7.08 (d,  $J = 7.2$  Hz, 1H,  $\text{H}_c$ ), 6.49 – 5.55 (m, 3H,  $\text{H}_d$ ), 4.25 – 3.78 (m, 6H,  $\text{H}_e$ ), 2.73 (t,  $J = 6.7$  Hz, 2H,  $\text{H}_f$ ), 2.04 (s, 3H,  $\text{H}_g$ ), 1.58 (m, 4H,  $\text{H}_h$ ).  $^{13}\text{C}$  NMR (101 MHz,  $\text{DMSO}-d_6$ )  $\delta$  171.29, 171.22, 165.89, 162.89, 155.48, 151.21, 131.87, 128.74, 95.25, 64.19, 64.07, 46.59, 32.63, 25.13, 24.72. HRMS (ES<sup>+</sup>):  $m/z$  calculated for  $[\text{M}+\text{H}]^+$  351.1509 g/mol; found 352.1477 g/mol.

**Synthesis of 4-((3-(*N*2-Acetylguanin-9-yl)propanoyl)oxy)butyl Acrylate (AGuA) Monomer (Scheme 7.1).** A suspension of guanine (20 g) and excess acetic anhydride (40 mL) in *N,N*-dimethylacetamide (DMAc, 200 mL) was refluxed at 130–150 °C until the solution turned clear. The reaction mixture was filtered hot, and the filtrate was cooled to room temperature. White precipitate was filtered and washed with ethanol. Drying under reduced pressure (20 mmHg) yielded a white solid of *N*2-acetylguanine with 90% yield. The ACyA synthesis procedure was followed to prepare crude AGuA that contained two isomers, 7-AGuA and 9-AGuA, with a 50:50 ratio and an overall yield of 71%.  $^1\text{H}$  NMR for the isomer mix (Figure S7.2) (400 MHz,  $\text{DMSO}-d_6$ )  $\delta$  12.01 (s, 2H,  $\text{H}_a$ ), 11.59 (s, 2H,  $\text{H}_a'$ ), 8.12 (s, 1H,  $\text{H}_{7-b}$ ), 7.95 (s, 1H,  $\text{H}_{9-b}$ ), 6.48 – 5.70 (m, 6H,  $\text{H}_c$ ), 4.48 (t,  $J = 6.7$  Hz, 2H,  $\text{H}_{7-d}$ ), 4.29 (t,  $J = 6.9$  Hz, 2H,  $\text{H}_{9-d}$ ), 4.15 – 3.95 (m, 8H,  $\text{H}_e$ ), 2.96 (m, 4H,  $\text{H}_f$ ), 2.26 – 2.07 (m, 6H,  $\text{H}_g$ ), 1.58 (m, 8H,  $\text{H}_h$ ).  $^{13}\text{C}$  NMR (101 MHz, dmso)  $\delta$  173.89, 173.76, 170.86, 165.88, 157.80, 155.27, 152.99, 149.01, 148.10, 147.36, 145.03, 140.18, 131.84, 131.81,



128.73, 120.46, 111.63, 64.33, 64.20, 64.12, 64.05, 42.73, 40.88, 39.61, 35.20, 34.04, 30.85, 25.23, 25.13, 25.10, 24.18, 24.13.

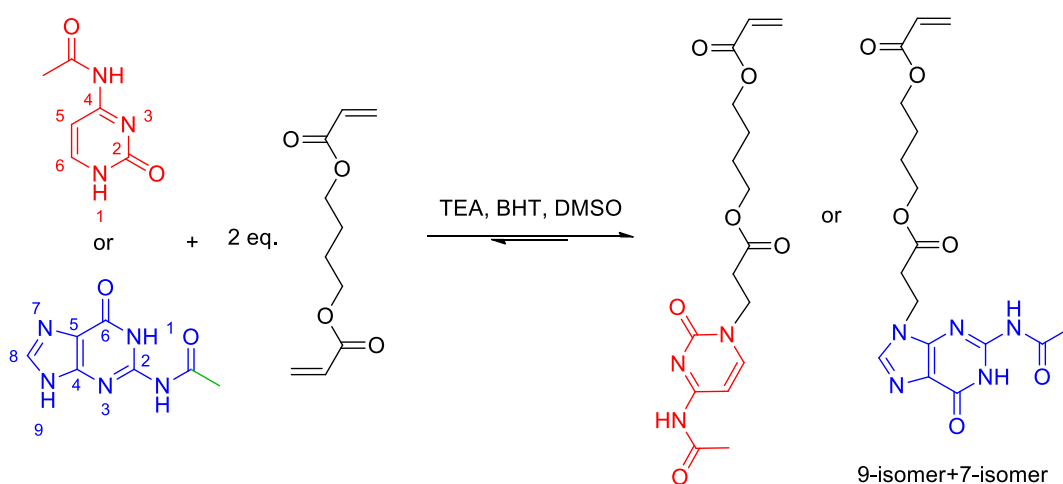
Column chromatography of crude AGuA using a mobile phase of 15:1 CH<sub>3</sub>Cl:MeOH separated 9- and 7-isomers with R<sub>f</sub> value of 0.126 and 0.259, respectively. Evaporation of eluent yielded two white solids. The 9-isomer was used throughout the polymer synthesis with a melting point of 145.7-149.9 °C. <sup>1</sup>H NMR (Figure S7.3) (400 MHz, DMSO-*d*<sub>6</sub>) δ 11.91 (s, 1H, H<sub>a</sub>), 7.95 (s, 1H, H<sub>b</sub>), 6.46 – 5.79 (m, 3H, H<sub>c</sub>), 4.29 (t, *J* = 6.9 Hz, 2H, H<sub>d</sub>), 4.16 – 3.90 (m, 4H, H<sub>e</sub>), 2.94 (t, *J* = 6.8 Hz, 2H, H<sub>f</sub>), 2.17 (s, 3H, H<sub>g</sub>), 1.58 (m, 4H, H<sub>h</sub>). <sup>13</sup>C NMR (101 MHz, DMSO-*d*<sub>6</sub>) δ 173.91, 170.85, 165.89, 155.28, 149.02, 148.13, 140.17, 131.86, 131.82, 128.72, 120.44, 64.32, 64.04, 39.60, 34.02, 25.11, 25.08, 24.19. HRMS (ES<sup>+</sup>): *m/z* calculated for [M+H]<sup>+</sup> 391.1570 g/mol; found 392.1589 g/mol.

#### **Synthesis of Nucleobase-Containing Homopolymers and Copolymers (Scheme 7.2).**

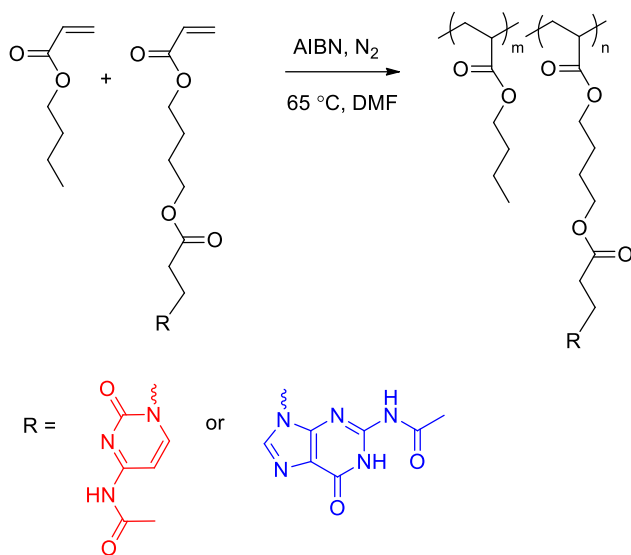
Poly(AGuA), poly(ACyA), poly(AGuA-*co-n*BA), and poly(ACyA-*co-n*BA) were prepared using solution free radical copolymerization in *N,N*-dimethylformamide (DMF) or DMSO with AIBN as initiator. A typical homopolymer synthesis was conducted as follows. A round-bottomed flask containing ACyA (216.0 mg, 0.6 mmol), AIBN (0.5 mg, 3.0 μmol), and DMSO (1.5 mL) was sparged with nitrogen for 20 min. The reaction flask was placed into an oil bath at 65 °C for 24 h with constant stirring. The resulting solution was concentrated through distillation of DMSO under reduced pressure and precipitated into CHCl<sub>3</sub>. The precipitates were collected, washed with diethyl ether, and dried under reduced pressure (22 mmHg) for 24 h, leaving 215.0 mg of brittle solid (70 % yield). <sup>1</sup>H

NMR spectroscopy confirmed the structure of Poly(AGuA) and poly(ACyA) (Figure S7.4, S7.5).

A typical copolymer synthesis was conducted as follows. A round-bottomed flask was charged with ACyA(0.75 g, 2.1 mmol), *n*BA (2.0 g, 15.6 mmol), AIBN (2.9 mg, 17.7  $\mu$ mol), and DMF (11.0 g, 20 wt%) and sparged with nitrogen for 20 min. The reaction mixture was maintained at 65 °C for 24 h with constant stirring. The resulting solution was precipitated into a MeOH-water mixture. The precipitates were collected and dried under reduce pressure (22 mmHg) for 24 h, leaving 3.0 g of solid (81% yield) that contained 10.3 mol% of poly(ACyA) and 89.7 mol% of poly(*n*BA).  $^1\text{H}$  NMR spectroscopy confirmed the structure and purity of all cytosine/guanine-containing copolymers (Figure S7.6, S7.7).



**Scheme 7.1.** Michael addition of 1,4-butanediol diacrylate with acetyl-protected guanine and cytosine.



**Scheme 7.2.** Conventional free radical copolymerization of guanine/cytosine acrylate monomer with *n*-butyl acrylate (*n*BA).

## 7.4 Results and Discussion

Michael addition reaction serves as a versatile synthetic method in polymer chemistry for monomer synthesis, post-functionalization of polymers, or chemical crosslinking.<sup>43</sup> Michael addition of thymine and adenine with a diacrylate afforded region-selective synthesis of adenine/thymine acrylate monomers.<sup>7</sup> However, Michael addition of unprotected cytosine and guanine with diacrylate proved unsuccessful due to challenging solubility of cytosine and guanine in common solvents. Acetyl protection groups on the primary amines of cytosine and guanine increased their solubility, and subsequent Michael addition of acetyl-protected cytosine and guanine with excess diacrylate yielded *N*4-acetylcytosine acrylate (ACyA) and *N*2-acetylguanine acrylate (AGuA) (Scheme 7.1), respectively. In both Michael addition reactions, the nucleobase suspension in DMSO turned clear as the Michael addition reached equilibrium with the majority of nucleobase converted to their acrylic monomers with enhanced solubility in most organic solvents. The

bis-nucleobase byproduct was removed during column chromatography. Protected guanine reacted with diacrylate on both 7- and 9- position due to tautomerization. The 9-AGuA isomer proves more polar than 7-AGuA, due to less steric effect of the acrylate group on the hydrogen bonding sites, and naturally produced DNA only contains 9-substituted guanine.

Homopolymerization of ACyA, AGuA, and *n*BA yielded poly(ACyA), poly(AGuA), and poly(*n*BA), respectively (Table 7.1). Free radical polymerization of ACyA and AGuA with *n*BA afforded a series of random copolymers with varying nucleobase contents (Scheme 7.2, Table 7.1). <sup>1</sup>H NMR spectroscopy revealed the nucleobase contents in poly(ACyA-*co-n*BA) and poly(AGuA-*co-n*BA) copolymers (Figure S7.6,S7.7), which matched closely with the feed ratios of comonomers (Table 7.1), indicating similar reactivity ratio of ACyA/AGA with *n*BA. SEC measured the molecular weights (relative to polystyrene standard) of nucleobase-containing copolymers with lower than 11 mol% ACyA and 3 mol% AGuA (Figure S7.8). These nucleobase-containing polyacrylates as well as poly(*n*BA) showed broader PDI than 2, which was attributed to chain transfer to the  $\alpha$ -proton on the acrylic backbone.<sup>44</sup> DLS proved SEC results of copolymers with higher nucleobase content unreliable due to polymer aggregation. However, the polymerization conditions for listed copolymers in Table 7.1 remained identical, including initiator concentration, monomer concentration, reaction time, and temperature.

**Table 7.1.** Relative molecular weight to polystyrene standard of nucleobase-containing acrylics and poly*n*BA. \*NA: not soluble in DMF 0.05 M LiBr. -: Polymer formed aggregates.

|               | Target<br>nucleobase<br>mol% | ACyA or<br>AGuA<br>mol% | ACyA or<br>AGuA<br>wt% | $\overline{M}_n^{a,b}$ | $\overline{M}_w^{a,b}$ | $\overline{M}_w/\overline{M}_n^{a,b}$ | T <sub>g</sub><br>(°C) |
|---------------|------------------------------|-------------------------|------------------------|------------------------|------------------------|---------------------------------------|------------------------|
| ACyA          | 3                            | 2.9                     | 7.3                    | 41k                    | 110k                   | 2.68                                  | -39                    |
|               | 5                            | 4.7                     | 11.9                   | 37k                    | 115k                   | 3.10                                  | -34                    |
|               | 12                           | 10.3                    | 24.0                   | 62k                    | 142k                   | 2.29                                  | -18                    |
|               | 15                           | 14.0                    | 30.8                   | -                      | -                      | -                                     | -11                    |
|               | 17                           | 15.3                    | 33.2                   | -                      | -                      | -                                     | -10                    |
|               | 30                           | 29.0                    | 53.1                   | -                      | -                      | -                                     | 10<br>broad            |
|               | 100.0                        | 100.0                   | 100.0                  | NA                     | NA                     | NA                                    | 67                     |
|               | 3.2                          | 2.8                     | 7.3%                   | 41k                    | 130k                   | 3.21                                  | -39<br>broad           |
| AGuA          | 8.9                          | 7.8                     | 20.5%                  | -                      | -                      | -                                     | -22<br>broad           |
|               | 12.0                         | 11.0                    | 27.4                   | -                      | -                      | -                                     | broad                  |
|               | 100.0                        | 100.0                   | 100.0                  | NA                     | NA                     | NA                                    | 118                    |
|               |                              |                         |                        |                        |                        |                                       |                        |
| poly<br>(nBA) | 0                            | 0                       | 0                      | 39k                    | 102k                   | 2.66                                  | -47                    |

Thermal weight loss profiles of guanine and cytosine-containing copolymers showed a two-step degradation process (Figure S7.9), in which the nucleobase-containing pendant groups degraded before the polymer backbone degradation, agreeing with the adenine and thymine analogs.<sup>7</sup> T<sub>d</sub> at 5% weight loss ranged from 280 °C to 320 °C with decreasing nucleobase content, and guanine-containing copolymers showed higher T<sub>d</sub> than cytosine ones. DSC revealed a single thermal transition for each nucleobase-containing homopolymers and copolymers, which corresponded to their glass transition (T<sub>g</sub>). T<sub>g</sub>'s of Poly(ACyA) and poly(AGuA) were 67 °C and 118 °C, respectively, higher than the thymine and adenine homopolymer T<sub>g</sub>'s (43 °C and 67 °C).<sup>7</sup> This presumably resulted from the stronger self-association of cytosine-cytosine and guanine-guanine, and the bulkier pendant groups than adenine and thymine. The presence of a single T<sub>g</sub> for each copolymers proved the random distribution of nucleobase-containing monomers along the acrylic backbone. The copolymer T<sub>g</sub> increased with increasing nucleobase content, though

deviated from the Fox equation<sup>11</sup> prediction to higher temperature (Figure 7.1), consistent with previous report that intermolecular interactions affected  $T_g$  of random copolymers.<sup>7,35</sup>

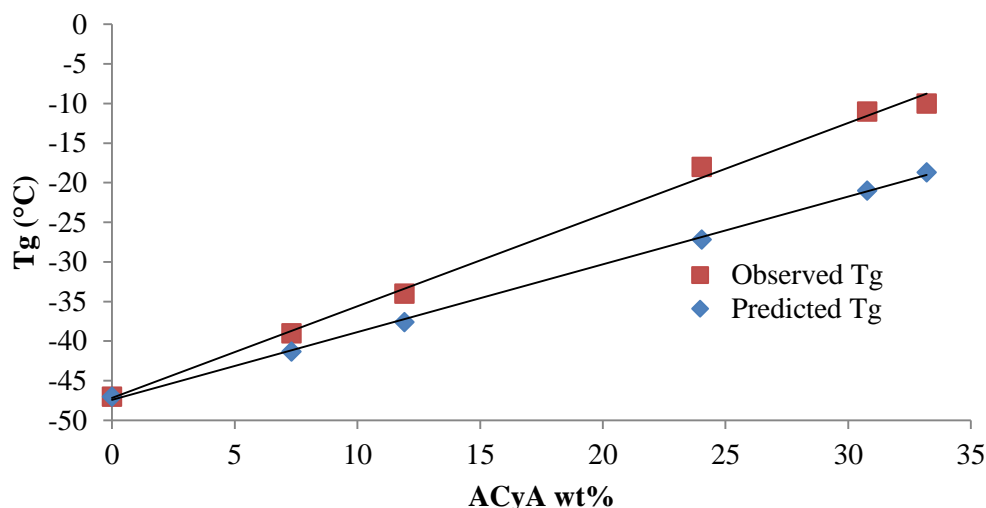


**Figure 7.1.** Relationship between observed  $T_g$  values and predicted ones based on the Fox equation for poly(ACyA-*co*-nBA) with varying ACyA mol%. Fox equation  $\frac{1}{T_g} = \frac{F_1}{T_{g1}} + \frac{F_2}{T_{g2}}$  was used to calculate the predicted  $T_g$ ,<sup>45</sup> where  $F_1$  and  $F_2$  represent weight fraction of ACyA and nBA respectively,  $T_{g1}$  and  $T_{g2}$  represent  $T_g$  (Kelvin) of poly(ACyA) and poly(nBA).

Physical properties of guanine- and cytosine-containing copolymers varied significantly with varying nucleobase content. Figure 7.2 displays pictures of poly(ACyA-*co*-nBA) and poly(AGuA-*co*-nBA) copolymers ranging from tacky solids to free standing films, and to brittle solids with increasing ACyA and AGuA mol%. The hydrogen bonding contributed to physical crosslinking, which dominated the material properties when  $T_g$  remained below room temperature. Though copolymers in Figure 7.2b and 7.2e showed

$T_g$ 's well below room temperature, the guanine and cytosine groups formed sufficient physical crosslinking to maintain the mechanical integrity of these free-standing films. Poly(AGuA-*co*-nBA) with 8 mol% AGuA formed a free-standing film, while poly(ACyA-*co*-nBA) with 10 mol% ACyA remained a tacky solid, indicating that acetyl guanine formed stronger physical crosslinking than acetyl cytosine.

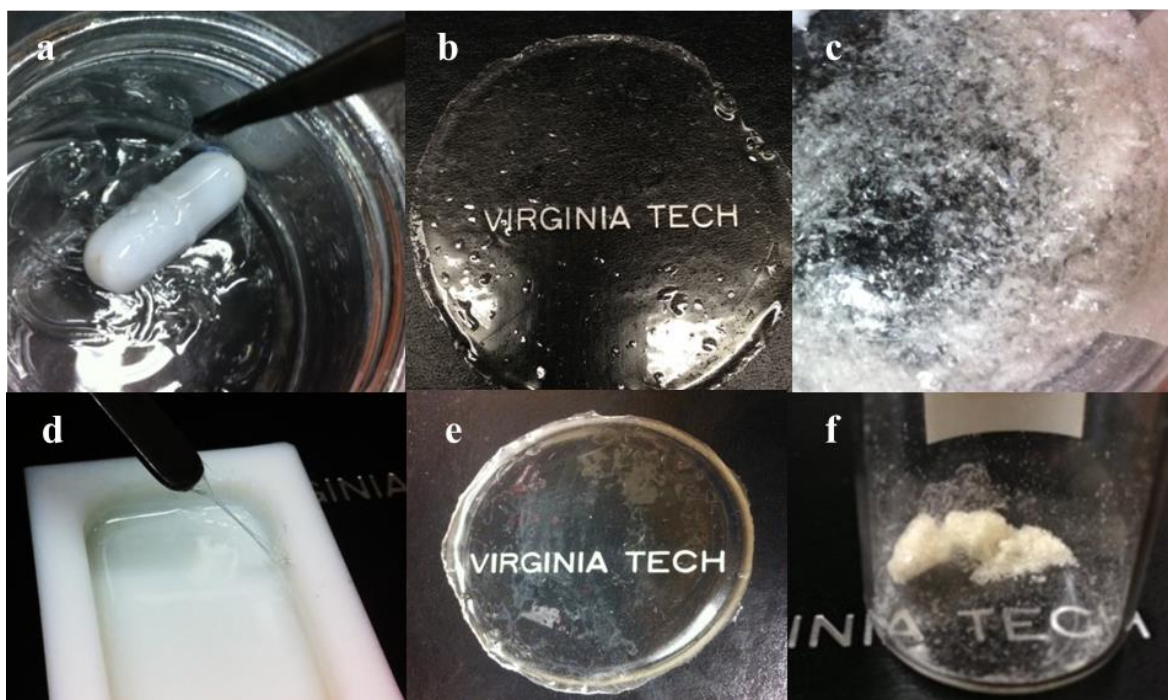


**Figure 7.2.** Pictures of poly(ACyA-*co*-nBA) with a) 4 mol%, b) 15 mol%, and c) 100 mol% ACyA. Pictures of poly(AGuA-*co*-nBA) with d) 2 mol%, b) 8 mol%, and e) 100% mol% AGuA.

Dynamic mechanical analysis (DMA) probed the thermomechanical properties of guanine- and cytosine-containing copolymer films in Figure 7.3. The storage modulus curves of copolymer films each exhibited a single gradual decrease as the glass transition

started until the viscous flow temperature near 50 °C-60 °C. The lack of well-defined plateau window suggested insufficient physical crosslinking and absence of a continuous hard phase. However, tan delta curves for poly(AGuA-*co-n*BA) continued above the broad glass transition peak from -20 °C to 10 °C, and a secondary peak near 40 °C appeared, indicative of hydrogen bonding dissociation. The hydrogen bonding of acetyl guanine provided physical crosslinking above  $T_g$ , which supported the mechanical integrity of the films until the viscous flow near 60 °C. Increasing AGuA mol% resulted in a higher modulus with no obvious  $T_g$  shift to higher temperature, suggesting microphase-separation. On the contrary, poly(ACyA-*co-n*BA) films each exhibited a broad glass transition, which increased with increasing ACyA mol%. The modulus drop of copolymer film with 15 mol% ACyA started 30 °C higher than one with 11 mol% AGuA, and ended at similar viscous flow temperature near 50 °C, which likely resulted from significant phase-mixing of the ACyA-containing copolymers. Overall, lower AGuA content in acrylic copolymers contributed to enhanced thermomechanical properties compared to ACyA analogs, indicating that acetyl guanine formed stronger physical crosslinking than acetyl cytosine.



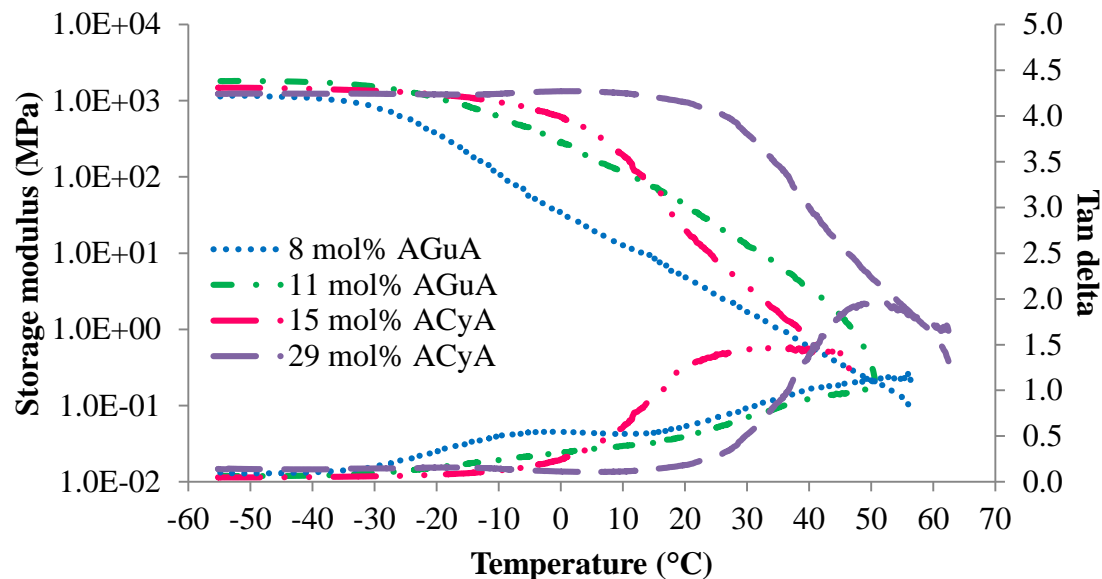


**Figure 7.3.** DMA temperature ramps of poly(ACyA-*co*-*n*BA) and poly(AGuA-*co*-*n*BA) with varied ACyA and AGuA contents, respectively.

The next step pertains to the investigation of hydrogen bonding between ACyA and AGuA, as cytosine and guanine forms complementary nucleobase pair with stronger hydrogen bonding than their self-association. Copolymers with 8 mol% AGuA and 10 mol% ACyA with a 1:1 guanine-cytosine ratio were dissolved in a solvent mixture of CHCl<sub>3</sub>-MeOH 3:1 and stirred for 24 h. Subsequent drying yielded a copolymer blend. Figure 7.4 displayed the master curves of storage modulus  $G'$  and loss modulus  $G''$  over a frequency range of eight decades generated using time-temperature superposition principle, showing partial rubbery regime and viscous flow regime. Nucleobase-containing copolymers and the blend all exhibited higher moduli compared to poly(*n*BA) control over the whole frequency range, resulting from physically crosslinked networks formation. A unique regime in a frequency range of three decades existed near the reptation onset, during which  $G'$  equaled  $G''$ .<sup>46</sup> The  $G''$  remained close to  $G'$  as the frequency decreased past the reptation

onset for nucleobase-containing copolymers, while  $G''$  promptly dominated when the non-associating poly(*n*BA) entered the flow regime. This unique regime suggested that the dynamics of hydrogen bonding among nucleobase units matched closely with the dynamics of polymer chain entanglement. In essence, hydrogen bonding among acetyl guanine and acetyl cytosine units predominately influenced the frequency range near onset of viscous flow, which also provided an explanation for the lack of plateau regime in DMA.

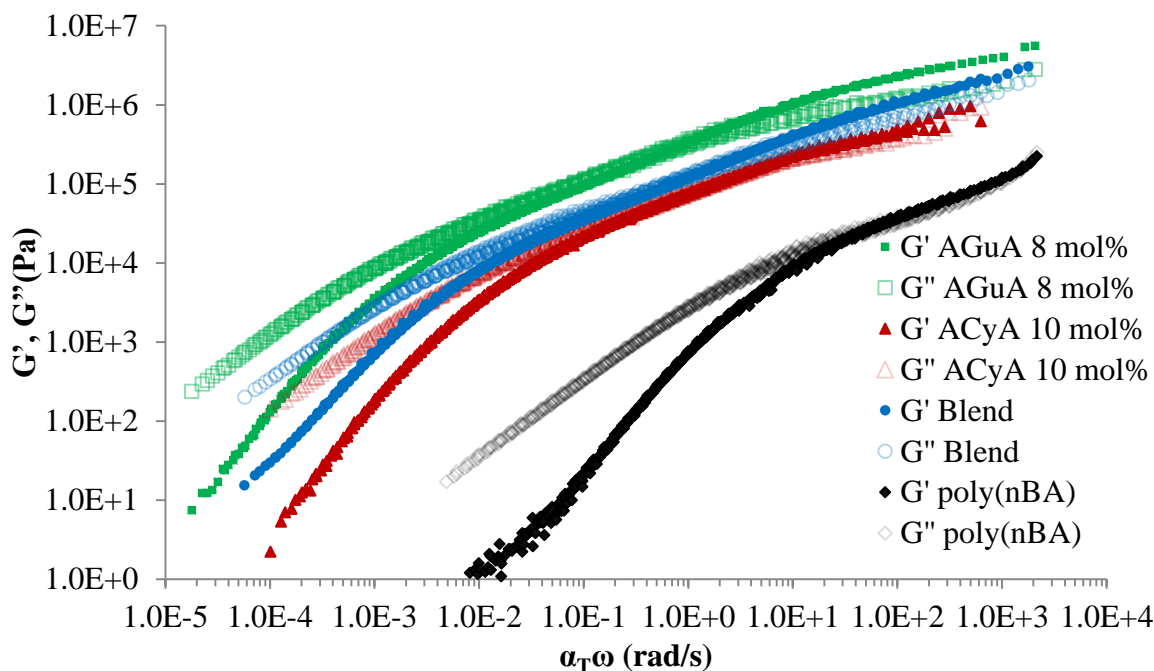


**Figure 7.4.** Rheological master curves of storage and loss moduli of poly(ACyA-*co*-*n*BA), poly(AGuA-*co*-*n*BA), and the blend, along with poly(*n*BA) control.

The copolymer with 8 mol% AGuA showed higher modulus compared to one with 10 mol% ACyA, indicative of the stronger hydrogen bonding of acetyl guanine compared to acetyl cytosine. The intermediate modulus of the blend corresponded to intermediate hydrogen bonding strength between acetyl guanine and acetyl cytosine compared to their self-association. AGuA and ACyA did not form triple complementary hydrogen bonding similar to the guanine-cytosine nucleobase pair with higher binding constant than their self-

association. The acetyl protection group likely interfered with the triple hydrogen bonding, and therefore resulted in lower binding constant compared to the guanine-cytosine association.

SAXS profile of copolymer with 8 mol% AGuA and the blend exhibited broad scattering maxima near  $1.3 \text{ nm}^{-1}$  (Figure 7.5), indicative of a microphase-separated morphology. The broadness of these scattering peaks corresponded to a distribution of inter-domain spacing, averaged at 4.8 nm. The phase contrast originated from hard domains containing hydrogen bonded nucleobase units and soft domains comprising flexible acrylic backbones. The scattering peak of copolymer with 10 mol% ACyA showed lower intensity compared to the other two sample, indicative of a weak microphase-separated morphology with significant extent of phase-mixing, consistent with the DMA result. The scattering peak intensity decreased from AGuA copolymer to the blend to ACyA copolymer, possibly due to their different extent of microphase-separation. Henceforth, AGuA afforded stronger physical crosslinking compared to ACyA, and AGuA-ACyA association provided comparable binding strength to AGuA self-association.

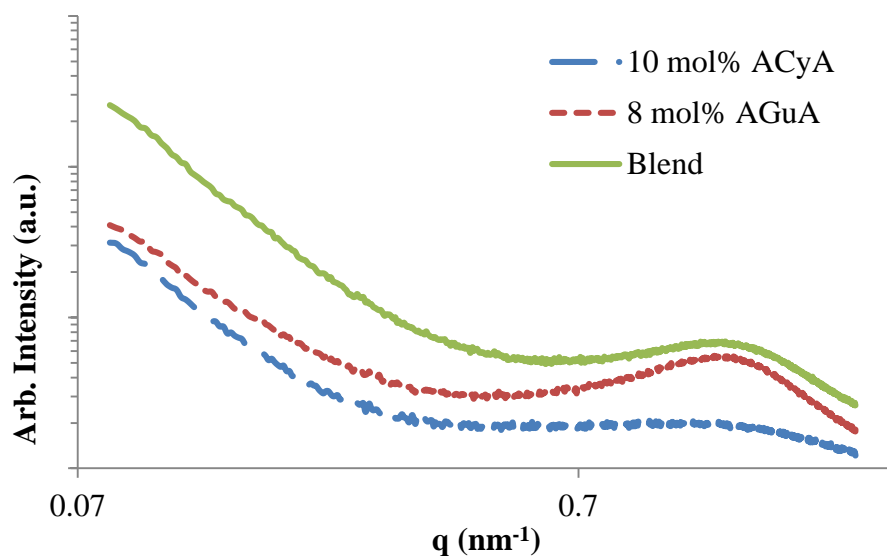


**Figure 7.5.** SAXS of poly(CyA-*co-n*BA) and poly(UCyA-*co-n*BA), as well as their blend.

$^1\text{H}$  NMR titration experiments commonly serve as quantitative measurements for the hydrogen bonding constant between nucleobase and many functional groups.<sup>4,47,48</sup> Firstly, the Job's method revealed a 1:1 binding stoichiometry between AGuA and ACyA (Figure 7.6a), in which the overall concentration remained constant while the mole ratio of AGuA varied.<sup>49</sup> Secondly, a non-linear fitting using Connor's Method<sup>50</sup> determined the binding constant ( $K$ ) to be  $265\text{ M}^{-1}$  and  $252\text{ M}^{-1}$  between AGuA and ACyA in  $\text{CDCl}_3$  (Figure 7.6b, S7.10), according to the chemical shifts of two amide protons on acetyl guanine. The similar binding constant indicated that both protons associated with ACyA in the hydrogen bonded complex. The binding constant agreed well with literature values for a double hydrogen bonding, comparable with the self-association strength for guanine-guanine and cytosine-cytosine. The titration results also explained the intermediate modulus of the blend in comparison to the AGuA and ACyA copolymers. Overall, the acetyl groups interfered with the triple hydrogen bonding between guanine and cytosine and resulted in weaker hydrogen bonding with comparable binding constant to guanine-guanine self-association.

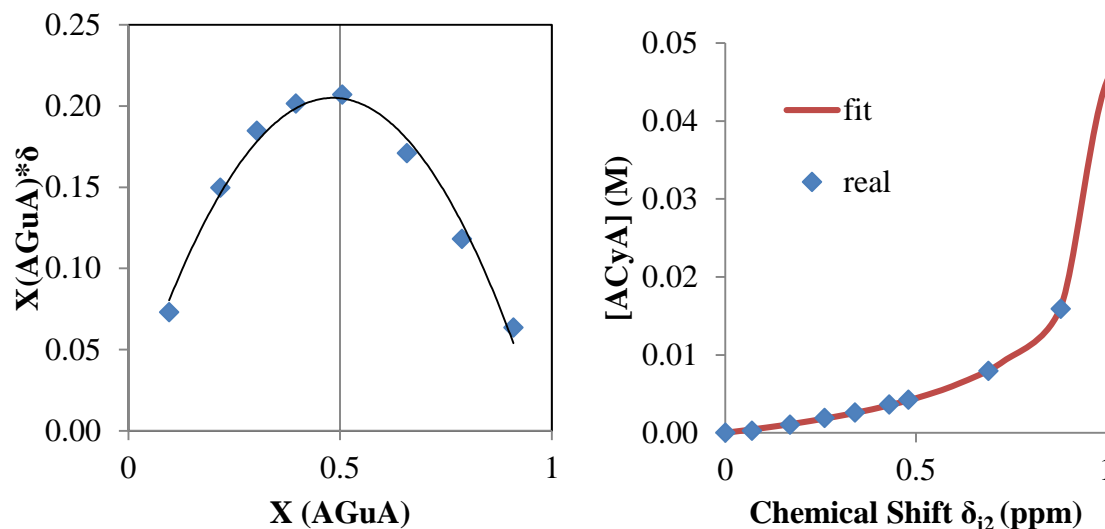
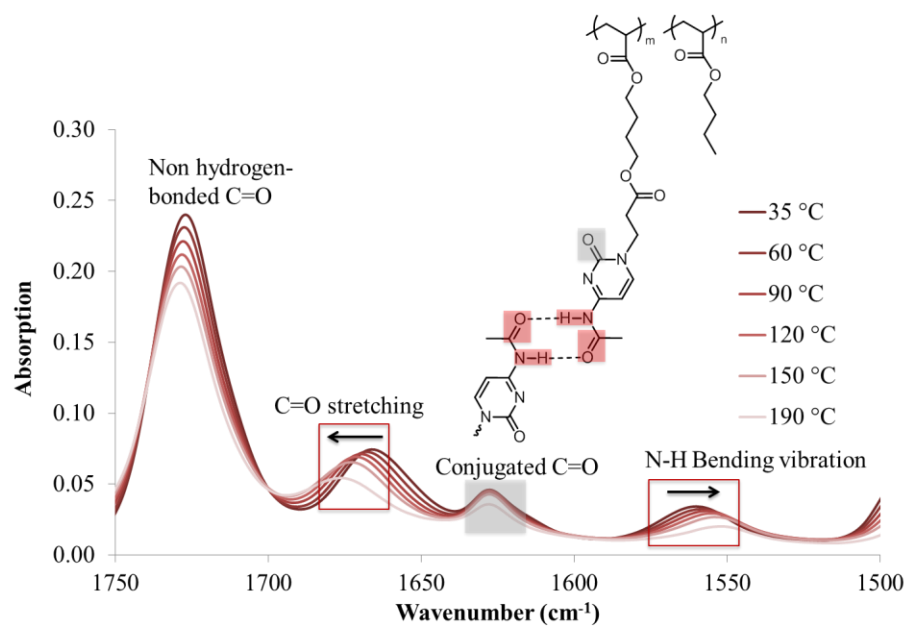


**Figure 7.6.** (a) The Job's plot for determination of binding stoichiometry of AGuA and ACyA, (b) Non-linear fitting of NMR titration results for calculation of the binding constant for ACyA and AGuA in  $\text{CDCl}_3$  at 22 °C.

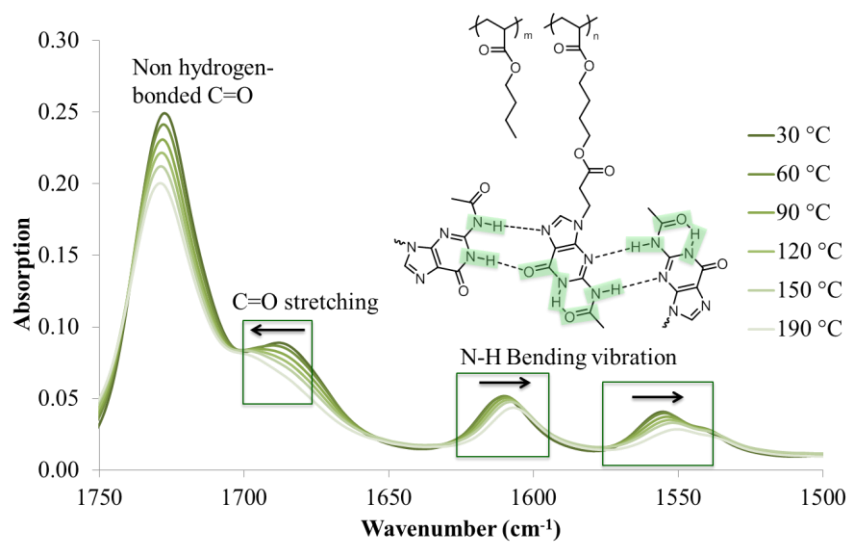
Variable temperature FTIR (VT-FTIR) spectroscopy facilely confirms the formation and dissociation of hydrogen bonding in polymer with varying temperature, as the absorption band from C=O stretching vibration blue shifts when C=O bond lengthens during hydrogen bonding dissociation and *vice versa*. Figure 7.7a,b,c showed FTIR spectra at different temperature for poly(ACyA-*co*-nBA), poly(AGuA-*co*-nBA), and the blend, respectively. The strongest absorption band near 1730  $\text{cm}^{-1}$  remained unchanged, which corresponded to the non-hydrogen-bonded acrylate carbonyls and ester carbonyls on the pendent groups. The absorption band near 1665  $\text{cm}^{-1}$  blue-shifted to 1675  $\text{cm}^{-1}$  with increasing temperature, reflecting the strengthening C=O bond from the acetyl protection group, and the C=O bond strengthened was due to hydrogen bonding dissociation with heat. However, the wavenumber of cytosine C=O absorption band remained near 1630  $\text{cm}^{-1}$  during the temperature ramp, indicating that the cytosine C=O did not form hydrogen

bonding, possibly due to steric effect of the 1-substitution group adjacent to C=O. The absorption band near  $1560\text{ cm}^{-1}$  pertained to the N-H bending vibration, and its red-shift to  $1550\text{ cm}^{-1}$  at elevated temperature confirmed that the hydrogen bonding of N-H dissociated with increasing temperature. VT FTIR results suggested that self-association of acetyl cytosine units mostly involved double hydrogen bonding of the amide groups (Figure 7.7a). VT FTIR spectra of poly(AGuA-*co-n*BA) (Figure 7.7b) showed only one broad C=O stretching absorption band, that blue-shifted from  $1690\text{ cm}^{-1}$  to  $1700\text{ cm}^{-1}$ . This band corresponded to both carbonyls on the acetyl protection group and guanine, respectively, and both carbonyls formed hydrogen bonding. Two absorption bands near  $1610\text{ cm}^{-1}$  and  $1550\text{ cm}^{-1}$  red-shifted with increasing temperature, indicating that both N-H on acetyl guanine formed hydrogen bonding. The acetyl guanine pendent group likely formed more than one hydrogen bonding per unit, illustrated in Figure 7.7b.<sup>51,52</sup> VT FTIR spectra of poly(AGuA-*co-n*BA) (Figure 7.7c) also proved the presence of hydrogen bonding through the blue-shift of C=O stretching absorption band and the red-shift of N-H bending absorption bands. The cytosine carbonyl absorption band remained unchanged, indicating that this carbonyl did not form hydrogen bonding. Therefore, one acetyl cytosine unit only formed one doubly hydrogen bonding, while each acetyl guanine formed two. This suggested that the trend of hydrogen bonding strength followed AGuA-AGuA>AGuA-ACyA>ACyA-ACyA, consistent with the rheology results.

(a)



(b)



(c)

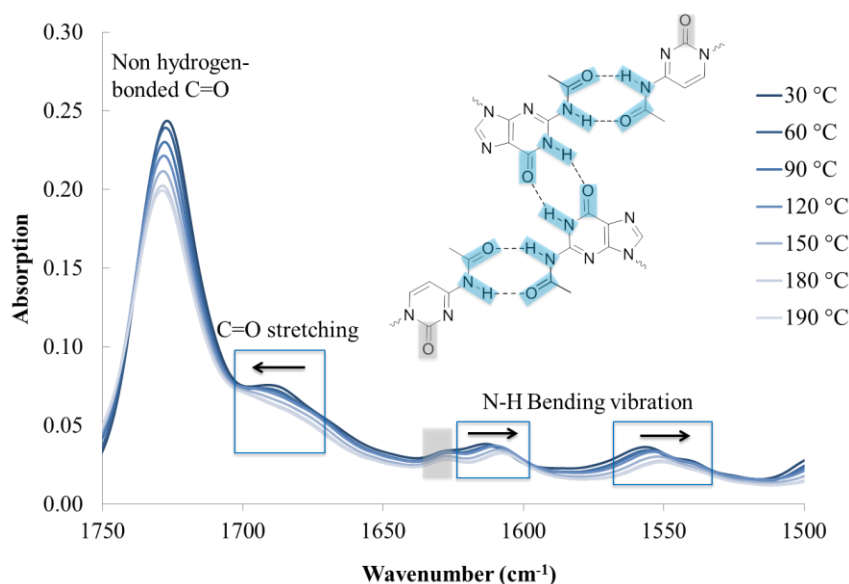


**Figure 7.7.** Variable temperature FT-IR spectra of (a) poly(ACyA-*co*-*n*BA) with 10 mol% ACyA and (b) poly(AGuA-*co*-*n*BA) with 8 mol% AGuA (c) the blend of poly(ACyA-*co*-*n*BA) and poly(AGuA-*co*-*n*BA) in the 1750-1500  $\text{cm}^{-1}$  region at varying temperatures.

Physically crosslinking acrylics serve as potential candidates for pressure sensitive adhesives (PSAs), as the low  $T_g$  acrylic matrix provides tack, and noncovalent interactions enhance cohesive strength. The Dahlquist criterion describes the upper limit for storage modulus of an adhesive to be  $3 \times 10^5$  Pa at 1Hz, room temperature for sufficient surface wetting.<sup>53,54</sup> Polyacrylates containing 3 mol% AGuA and 5 mol% ACyA, respectively, showed optimal adhesive performance within the Dahlquist criterion. Figure 7.8 lists the 180° peel strength on stainless steel for AGuA and ACyA-containing copolymers and their blend, in comparison to acrylic acid (AA)-containing copolymer and poly(*n*BA) controls. The nucleobase-containing copolymer followed a similar trend of AGuA > blend > ACyA, agreeing with the rheology and VT FTIR results. A Scotch™ tape sample served as a commercialized PSA control. All three nucleobase-containing copolymers exhibited



significantly higher peeling strength and identical adhesive failure mechanism compared to the Scotch<sup>TM</sup> tape control, leaving no adhesive residue on the substrate. The copolymer with 3 mol% AA and poly(*n*BA) homopolymer both failed cohesively, due to weak or none physically crosslinking. Henceforth, guanine and cytosine-containing acrylics enable potential applications as pressure sensitive adhesives with enhanced peel strength, and poly(AGuA-*co*-*n*BA) represented the most promising composition with lowest polar monomer content and highest peel strength.

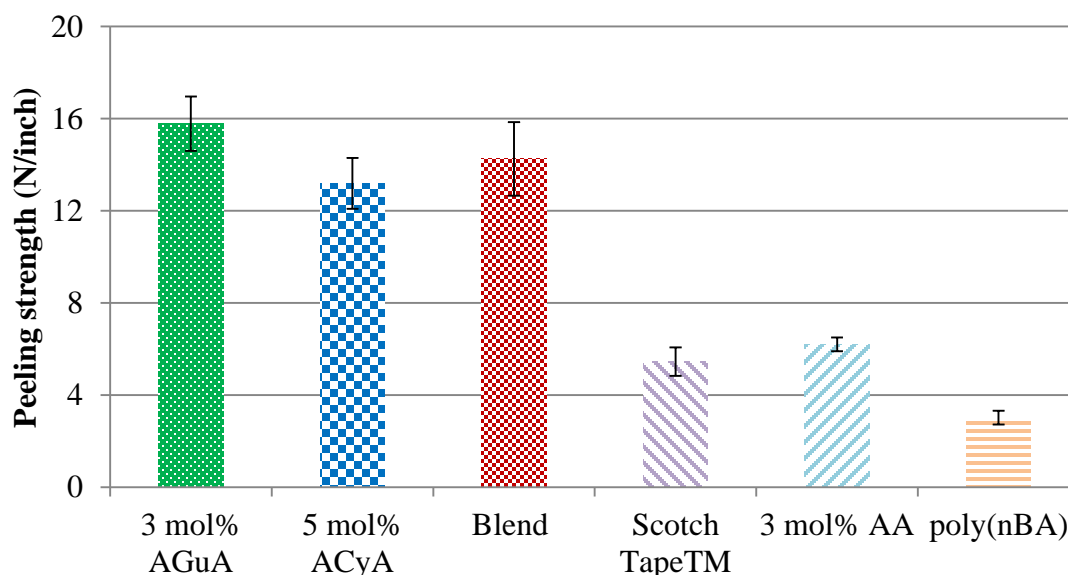


**Figure 7.8.** Peel strength of poly(ACyA-*co*-*n*BA), poly(AGuA-*co*-*n*BA), and the blend in comparison to poly(acrylic acid-*co*-*n*BA), Scotch tape<sup>TM</sup>, and poly(*n*BA) controls.

In addition, Figure 7.9 compares the storage modulus of poly(AGuA-*co*-*n*BA) with 3 mol% AGuA with several other controls to further probe the advantages of using AGuA-containing copolymers as adhesives. Poly(*t*-butyl methacrylate, *t*-BMA) exhibits  $T_g$  of 118 °C, similar to poly(AGuA) homopolymer  $T_g$ .<sup>55</sup> However, poly(*t*-BMA-*co*-*n*BA) with 3 mol% *t*-BMA showed significantly lower storage modulus and narrower plateau

frequency range compared to poly(AGuA-*co*-nBA) with similar high  $T_g$  comonomer content. Their different viscoelastic performance revealed that hydrogen bonding enhanced mechanical strength and extended the frequency range of the rubbery plateau window. More specifically, hydrogen bonding of acetyl guanine units contributed to higher cohesive strength and extended window of service time. Poly(AGuA-*co*-nBA) with 3 mol% AGuA also exhibited enhanced performance in the rubbery plateau regime and viscous flow regime compared to poly(AA-*co*-nBA) with 10 mol% AA and a bench-mark solution PSA control. Furthermore, isothermal rheological experiments at 130 °C confirmed the melt stability of AGuA containing acrylics as well as ACyA copolymers, which enabled potential applications as hot melt adhesives (Figure S7.12).

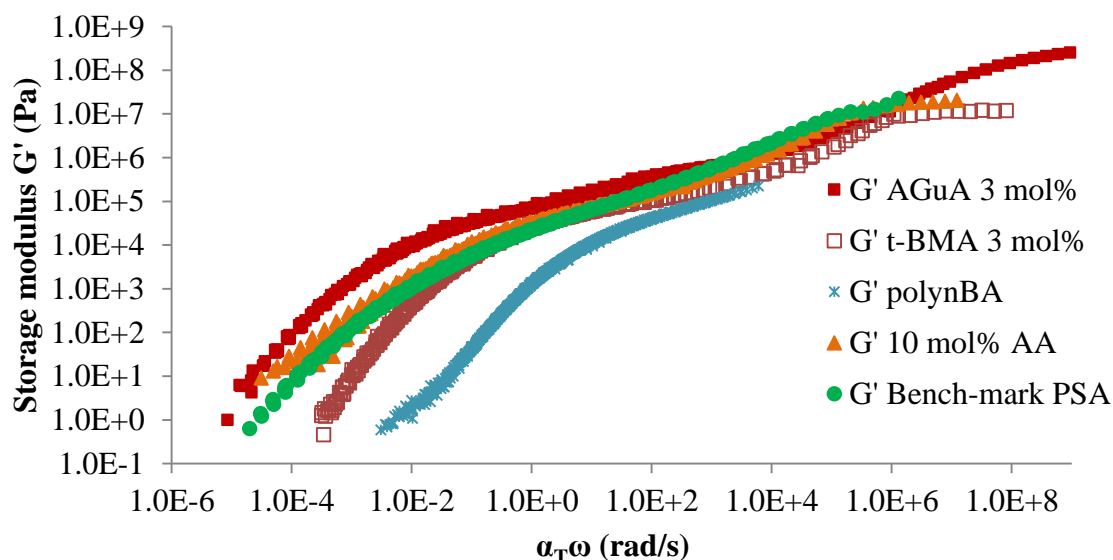


**Figure 7.9.** Storage modulus master curves of poly(AGuA-*co*-nBA) with 3 mol% AGuA in comparison to poly(t-butyl methacrylate-*co*-nBA), poly(nBA), poly(acrylic acid-*co*-nBA), and a bench-mark solution PSA control.

## 7.5 Conclusion

This manuscript reports facile synthesis of acetyl-protected cytosine and guanine-containing monomers using Michael addition reaction, and two monomers were abbreviated as AGuA and ACyA, respectively. Free radical polymerization of AGuA and ACyA afforded amorphous homopolymers with  $T_g$  of 67 °C and 118 °C, respectively. Changing the feed ratios of AGuA/ACyA with *n*-butyl acrylate (*n*BA) during copolymerization yielded a series of random copolymers with varying nucleobase contents. Acetyl cytosine and Acetyl guanine both formed self-association through doubly hydrogen bonding, which contributed to transient physically crosslinked networks and profoundly influenced the physical properties of low  $T_g$  polyacrylates. The copolymers each exhibited a single  $T_g$  that increased with increasing nucleobase content due to physical crosslinking formation and steric effect of the nucleobase-containing pendant groups. Copolymers with 8 mol% of AGuA, or 15 mol% of ACyA, or higher nucleobase contents solution-casted into free-standing films. ACyA-containing copolymers exhibited phase-mixed properties, while AGuA-containing copolymer film showed a SAXS profile of phase-separated morphology. Acetyl guanine afforded stronger self-association compared to acetyl cytosine as more hydrogen bonding donors and acceptors on acetyl guanine formed two doubly hydrogen bonding, while acetyl cytosine only afforded one doubly hydrogen bonding. AGuA and ACyA did not form triple hydrogen bonding similar to guanine-cytosine nucleobase pair due to the presence of acetyl protection group. The intermediate hydrogen bonding strength between AGuA and ACyA contributed to a blend with intermediate modulus and peel strength lower than the AGuA copolymer and higher than the ACyA copolymer. Hydrogen bonding of acetyl guanine and acetyl cytosine provided physical

crosslinking and enhanced the mechanical strength of a soft poly(*n*BA) matrix. AGuA and ACyA-containing copolymers with relatively low polar monomer incorporation served as promising candidates for pressure sensitive adhesives.

## 7.6 Acknowledgements

This research was partially supported by Henkel Corporation. This material is also partially based upon work supported by the National Science Foundation under Grant No. DMR-0923107.

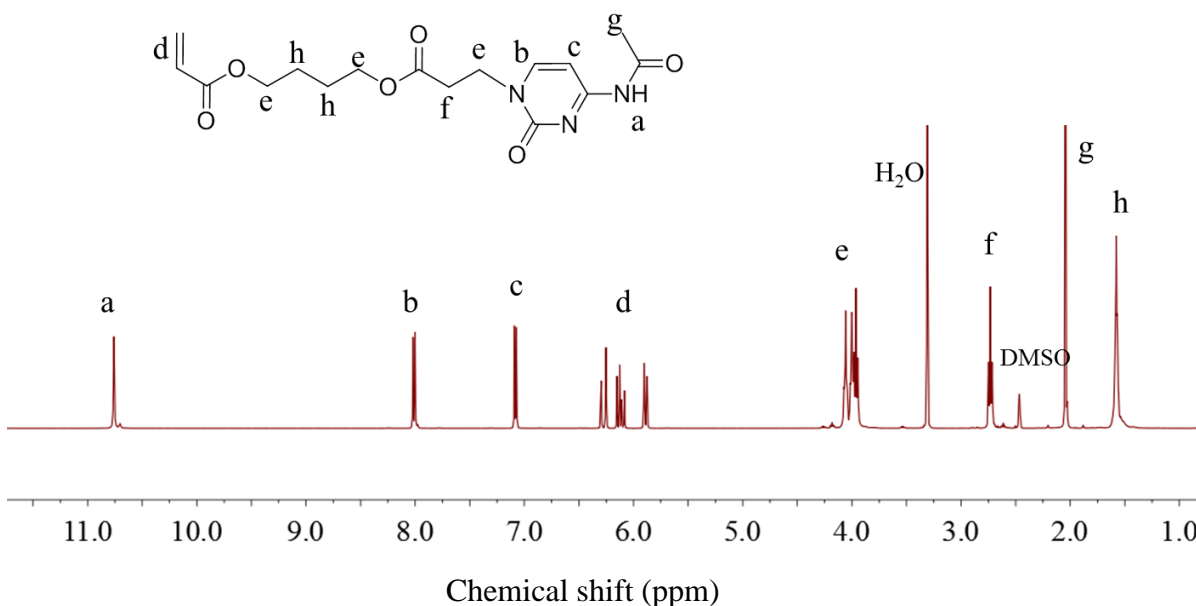
## 7.7 References

1. Brunsveld, L.; Folmer, B. J. B.; Meijer, E. W.; Sijbesma, R. P. *Chem. Rev.* **2001**, *101*, 4071.
2. Seiffert, S.; Sprakel, J. *Chem. Soc. Rev.* **2012**, *41*, 909.
3. Aida, T.; Meijer, E. W.; Stupp, S. I. *Science* **2012**, *335*, 813.
4. Zhang, K.; Aiba, M.; Fahs, G. B.; Hudson, A. G.; Chiang, W. D.; Moore, R. B.; Ueda, M.; Long, T. E. *Polym. Chem.* **2015**, *6*, 2434.
5. Karikari, A. S.; Edwards, W. F.; Mecham, J. B.; Long, T. E. *Biomacromolecules* **2005**, *6*, 2866.
6. Kautz, H.; van, B. D. J. M.; Sijbesma, R. P.; Meijer, E. W. *Macromolecules* **2006**, *39*, 4265.
7. Cheng, S.; Zhang, M.; Dixit, N.; Moore, R. B.; Long, T. E. *Macromolecules* **2012**, *45*, 805.
8. Zhang, K.; Fahs, G. B.; Aiba, M.; Moore, R. B.; Long, T. E. *Chem. Comm.* **2014**, *50*, 9145.
9. Han, S. H.; Pryamitsyn, V.; Bae, D.; Kwak, J.; Ganesan, V.; Kim, J. K. *ACS Nano* **2012**, *6*, 7966.
10. Shimizu, T.; Iwaura, R.; Masuda, M.; Hanada, T.; Yase, K. *J. Am. Chem. Soc.* **2001**, *123*, 5947.
11. Park, T.; Zimmerman, S. C. *J. Am. Chem. Soc.* **2006**, *128*, 14236.
12. Cheng, C.-C.; Chang, F.-C.; Wang, J.-H.; Chu, Y.-L.; Wang, Y.-S.; Lee, D.-J.; Chuang, W.-T.; Xin, Z. *RSC Advances* **2015**, *5*, 76451.
13. Stals, P. J. M.; Li, Y.; Burdyńska, J.; Nicolaÿ, R.; Nese, A.; Palmans, A. R. A.; Meijer, E. W.; Matyjaszewski, K.; Sheiko, S. S. *J. Am. Chem. Soc.* **2013**.
14. Stuart, M. A. C.; Huck, W. T. S.; Genzer, J.; Muller, M.; Ober, C.; Stamm, M.; Sukhorukov, G. B.; Szleifer, I.; Tsukruk, V. V.; Urban, M.; Winnik, F.; Zauscher, S.; Luzinov, I.; Minko, S. *Nat Mater* **2010**, *9*, 101.
15. Bergman, S. D.; Wudl, F. *J. Mater. Chem.* **2008**, *18*, 41.

16. Burattini, S.; Colquhoun, H. M.; Greenland, B. W.; Hayes, W.; John Wiley & Sons Ltd.: 2012; Vol. 7, p 3221.
17. Herbst, F.; Döhler, D.; Michael, P.; Binder, W. H. *Macromol. Rapid Commun.* **2013**, *34*, 203.
18. Kang, Y.; Lu, A.; Ellington, A.; Jewett, M. C.; O'Reilly, R. K. *ACS Macro Letters* **2013**, 581.
19. Lo, P. K.; Sleiman, H. F. *J. Am. Chem. Soc.* **2009**, *131*, 4182.
20. Soininen, A. J.; Rahikkala, A.; Korhonen, J. T.; Kauppinen, E. I.; Mezzenga, R.; Raula, J.; Ruokolainen, J. *Macromolecules* **2012**, *45*, 8743.
21. Dobrosielska, K.; Takano, A.; Matsushita, Y. *Macromolecules (Washington, DC, U. S.)* **2010**, *43*, 1101.
22. Courtois, J.; Baroudi, I.; Nouvel, N.; Degrandi, E.; Pensec, S.; Ducouret, G.; Chaneac, C.; Bouteiller, L.; Creton, C. *Adv. Funct. Mater.* **2010**, *20*, 1803.
23. Müller, M.; Dardin, A.; Seidel, U.; Balsamo, V.; Iván, B.; Spiess, H. W.; Stadler, R. *Macromolecules* **1996**, *29*, 2577.
24. Hilger, C.; Stadler, R. *Polymer* **1991**, *32*, 3244.
25. De Lucca Freitas, L. L.; Stadler, R. *Macromolecules* **1987**, *20*, 2478.
26. Stadler, R.; de Lucca Freitas, L. *Colloid Polym. Sci.* **1986**, *264*, 773.
27. Tant, M. R.; Mauritz, K. A.; Wilkes, G. L. *Ionomers: synthesis, structure, properties and applications*; Springer Science & Business Media, **2012**.
28. Vendamme, R.; Schüwer, N.; Eevers, W. *J. Appl. Polym. Sci.* **2014**, *131*, n/a.
29. Yamauchi, K.; Lizotte, J. R.; Long, T. E. *Macromolecules* **2003**, *36*, 1083.
30. Cashion, M. P.; Park, T.; Long, T. E. *J. Adhes.* **2009**, *85*, 1.
31. Callies, X.; Fonteneau, C.; Véchambre, C.; Pensec, S.; Chenal, J. M.; Chazeau, L.; Bouteiller, L.; Ducouret, G.; Creton, C. *Polymer* **2015**, *69*, 233.
32. McHale, R.; O'Reilly, R. K. *Macromolecules* **2012**, *45*, 7665.
33. Hemp, S. T.; Long, T. E. *Macromol. Biosci.* **2012**, *12*, 29.
34. Bazzi, H. S.; Sleiman, H. F. *Macromolecules* **2002**, *35*, 9617.
35. Tamami, M.; Zhang, K.; Dixit, N.; Moore, R. B.; Long, T. E. *Macromol. Chem. Phys.* **2014**, *215*, 2337.
36. Karikari, A. S.; Mather, B. D.; Long, T. E. *Biomacromolecules* **2007**, *8*, 302.
37. McHale, R.; Patterson, J. P.; Zetterlund, P. B.; O'Reilly, R. K. *Nat. Chem.* **2012**, *4*, 491.
38. Lutz, J.-F.; Thuenemann, A. F.; Rurack, K. *Macromolecules* **2005**, *38*, 8124.
39. Spijker, H. J.; Dirks, A. J.; Van, H. J. C. M. *J. Polym. Sci., Part A: Polym. Chem.* **2006**, *44*, 4242.
40. Kim, J. C.; Jung, J.; Rho, Y.; Kim, M.; Kwon, W.; Kim, H.; Kim, I. J.; Kim, J. R.; Ree, M. *Biomacromolecules* **2011**, *12*, 2822.
41. Sivakova, S.; Rowan, S. J. *Chem. Soc. Rev.* **2005**, *34*, 9.
42. Sartorius, J.; Schhneider, H.-J. *Chem. Eur. J.* **1996**, *2*, 1446.
43. Mather, B. D.; Viswanathan, K.; Miller, K. M.; Long, T. E. *Prog. Polym. Sci.* **2006**, *31*, 487.
44. Ahmad, N. M.; Charleux, B.; Farcet, C.; Ferguson, C. J.; Gaynor, S. G.; Hawket, B. S.; Heatley, F.; Klumperman, B.; Konkolewicz, D.; Lovell, P. A.; Matyjaszewski, K.; Venkatesh, R. *Macromol. Rapid Commun.* **2009**, *30*, 2002.

45. Odian, G. G. *Principles of polymerization*; Wiley-Interscience Hoboken, N.J, **2004**; Vol. 4th.
46. de Gennes, P. G. *J. Chem. Phys.* **1971**, 55, 572.
47. Khemtong, C.; Banerjee, D.; Liu, Y.; El, K. J. M.; Rinaldi, P. L.; Hu, J. *Supramol. Chem.* **2005**, 17, 335.
48. Thordarson, P. *Chem. Soc. Rev.* **2011**, 40, 1305.
49. Fielding, L. *Tetrahedron* **2000**, 56, 6151.
50. Connors, K. A. *Binding constants: the measurement of molecular complex stability*; Wiley New York, **1987**.
51. Giorgi, T.; Grepioni, F.; Manet, I.; Mariani, P.; Masiero, S.; Mezzina, E.; Pieraccini, S.; Saturni, L.; Spada, G. P.; Gottarelli, G. *Chemistry – A European Journal* **2002**, 8, 2143.
52. Forman, S. L.; Fetting, J. C.; Pieraccini, S.; Gottarelli, G.; Davis, J. T. *J. Am. Chem. Soc.* **2000**, 122, 4060.
53. Kraus, G.; Rollmann, K. W.; Gray, R. A. *J. Adhes.* **1979**, 10, 221.
54. Gent, A. N.; Schultz, J. *J. Adhes.* **1972**, 3, 281.
55. *Thermal Transitions of Homopolymers* Sigma Aldrich  
[https://www.sigmaaldrich.com/content/dam/sigma-aldrich/docs/Aldrich/General\\_Information/thermal\\_transitions\\_of\\_homopolymers.pdf](https://www.sigmaaldrich.com/content/dam/sigma-aldrich/docs/Aldrich/General_Information/thermal_transitions_of_homopolymers.pdf).

## 7.8 Supporting Information



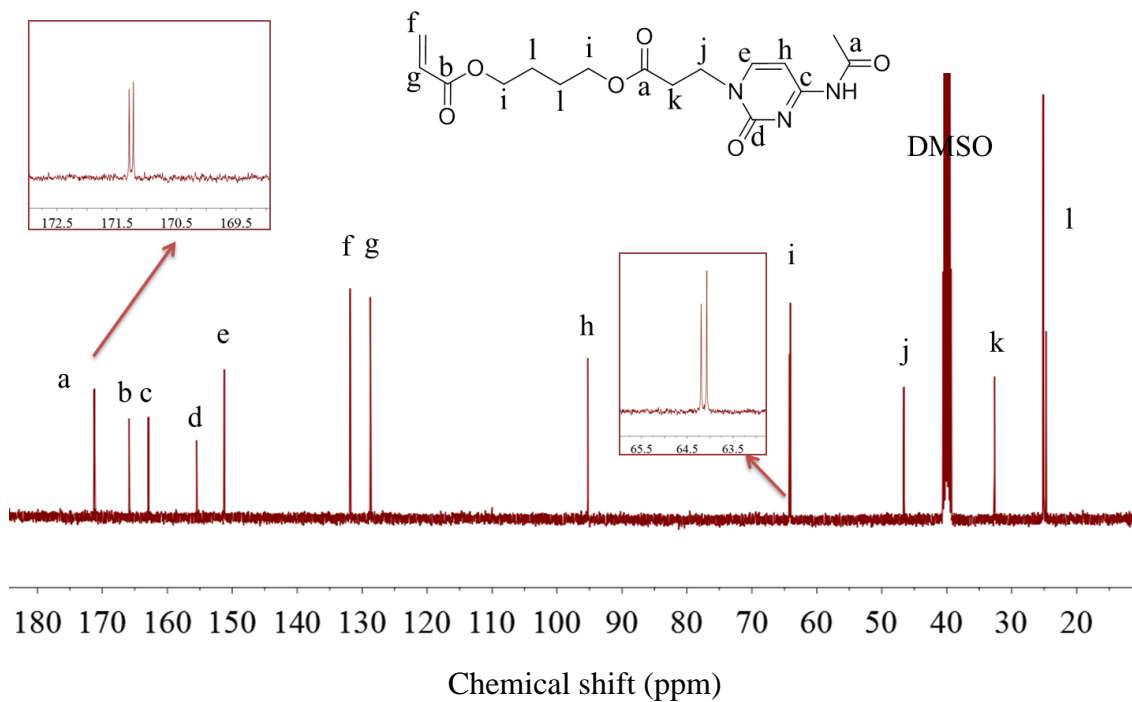


**Figure S7.1.**  $^{13}\text{C}$  NMR spectra of *N*2-acetylcytosine acrylate (ACyA).

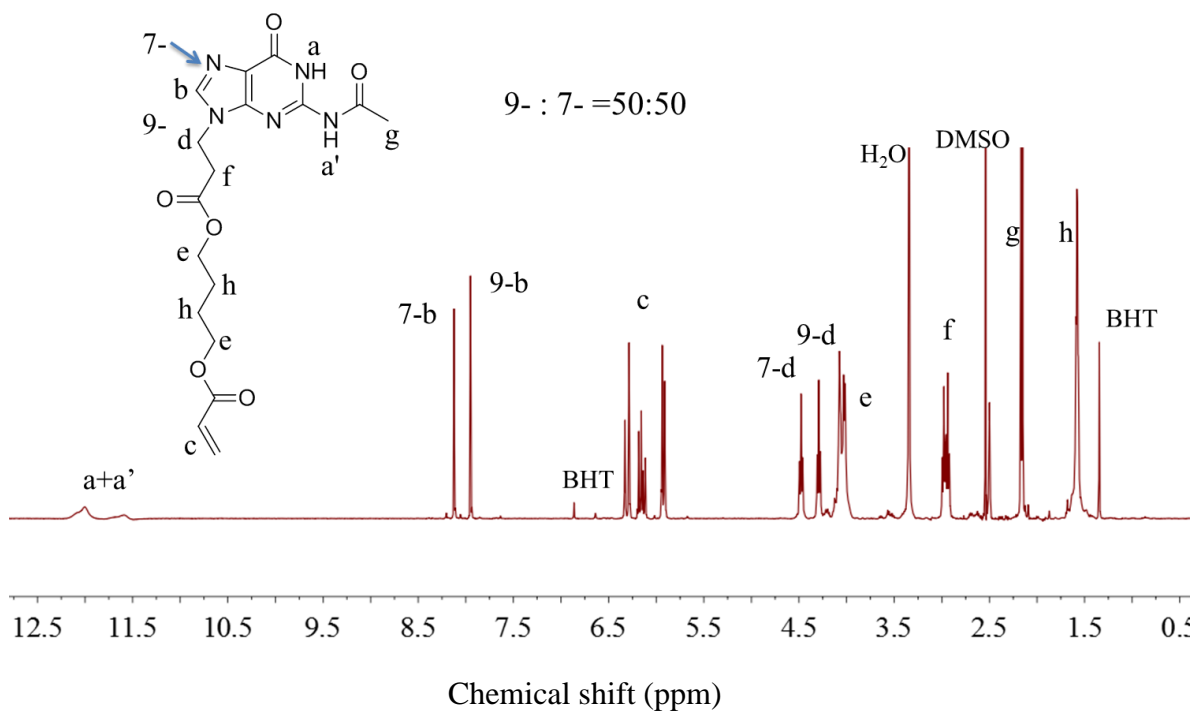


**Figure S7.2.**  $^1\text{H}$  NMR spectrum of the 9- and 7-isomer mixture of *N*4-acetylguanine acrylate (AGuA).

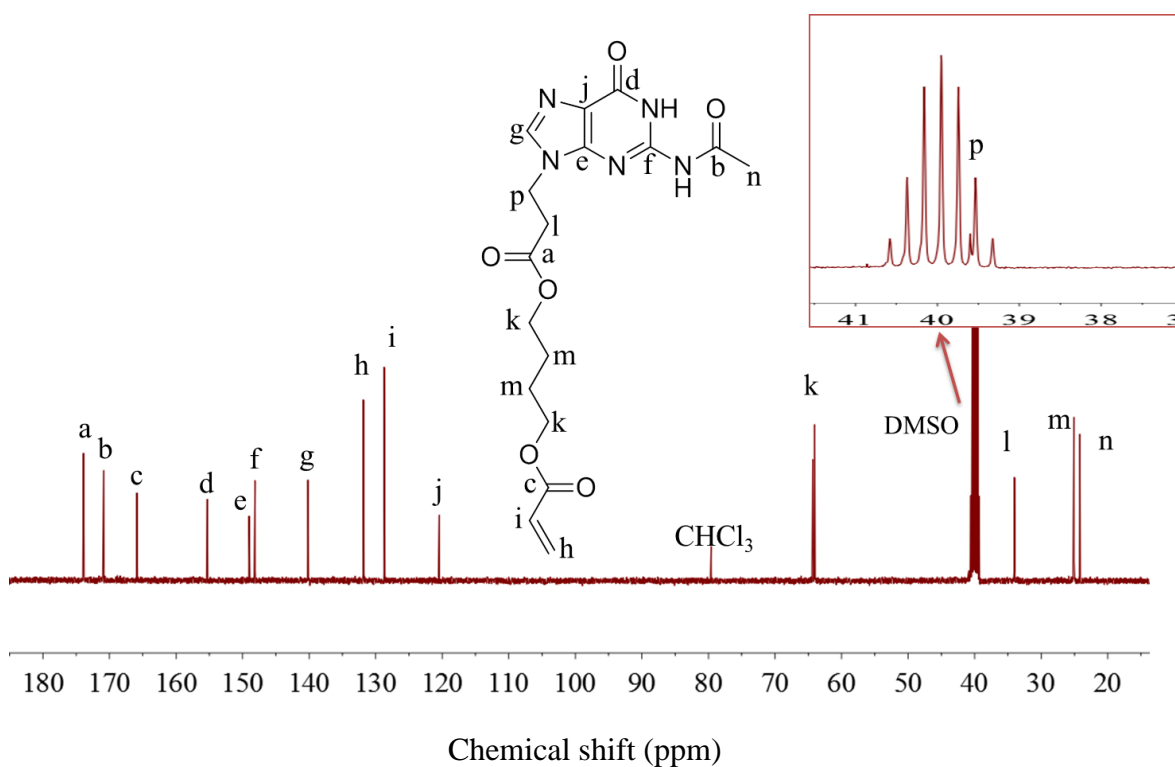
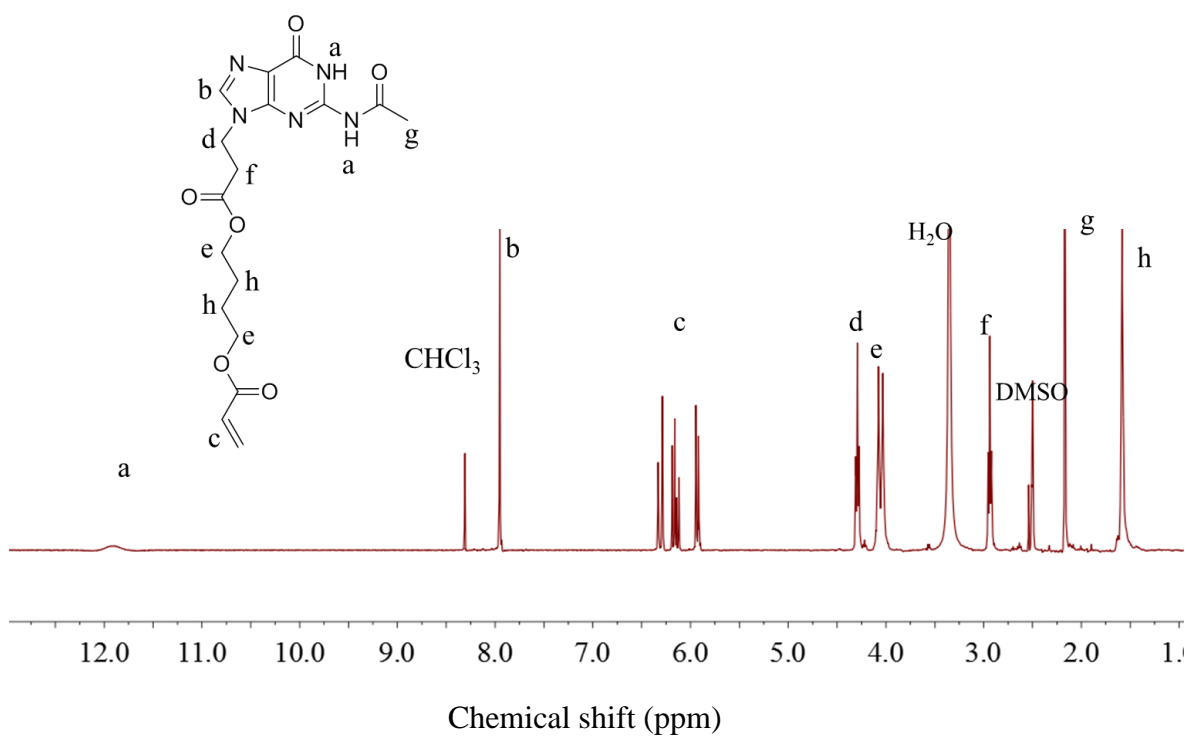


**Figure S7.3.** <sup>1</sup>H NMR and <sup>13</sup>C NMR spectra of 9-isomer of *N*4-acetylguanine acrylate (AGuA).



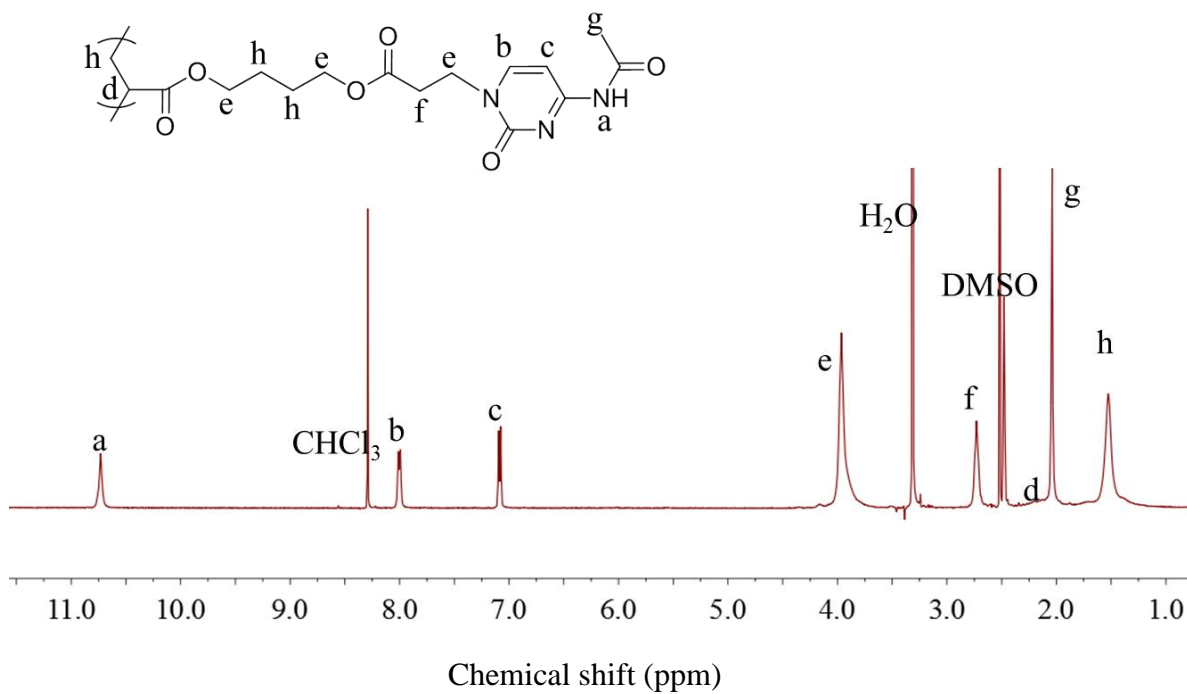


**Figure S7.4.**  $^1\text{H}$  NMR spectrum of poly (ACyA).

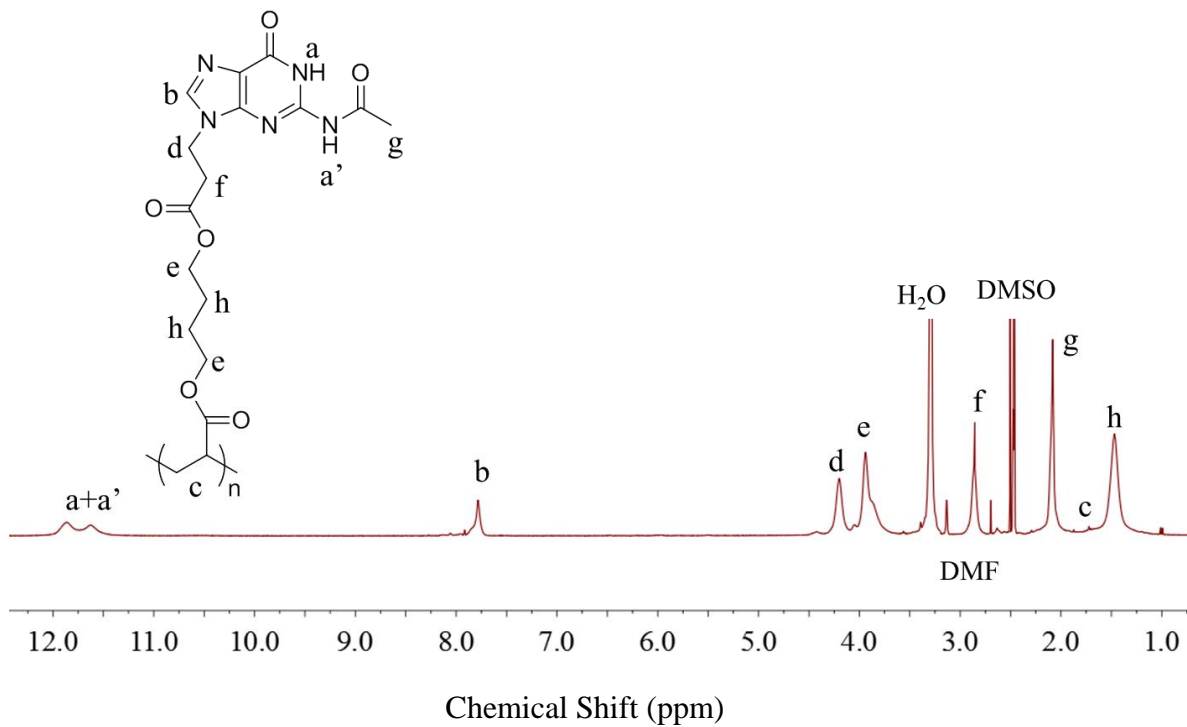


**Figure S7.5.**  $^1\text{H}$  NMR spectrum of poly (AGuA).

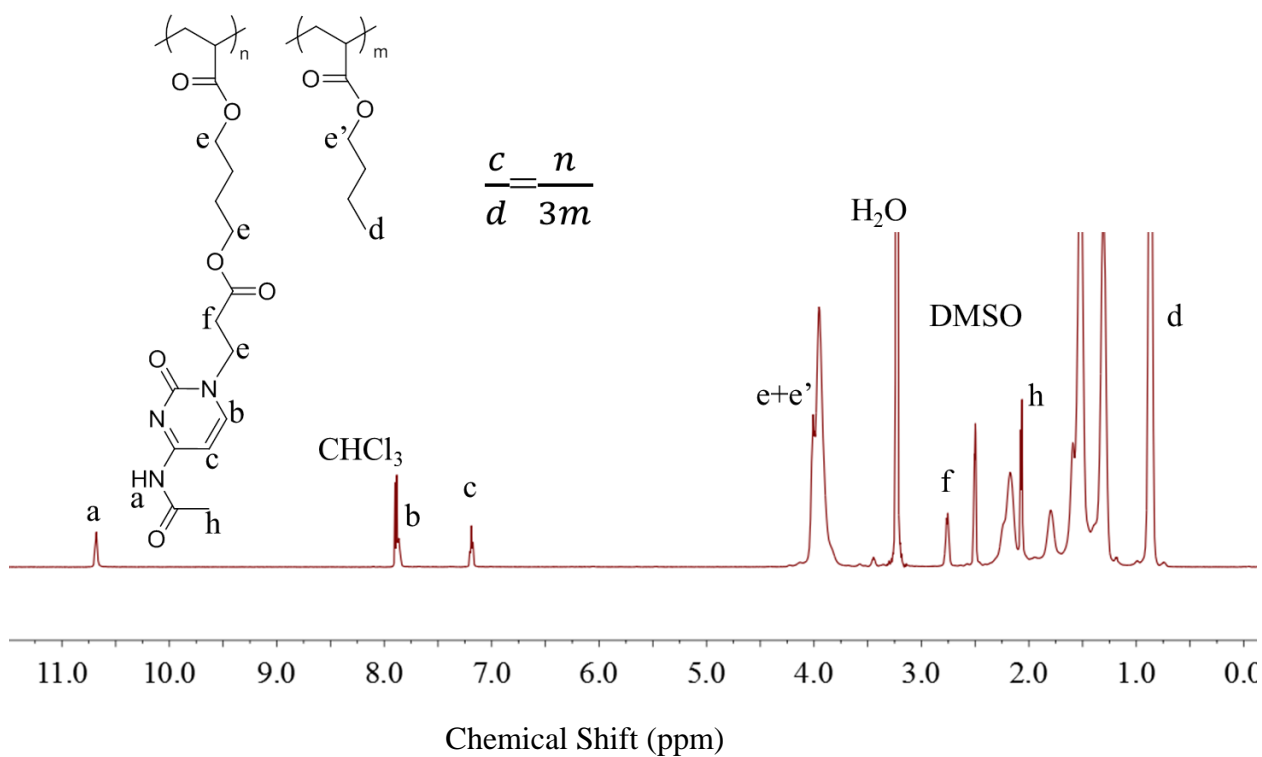
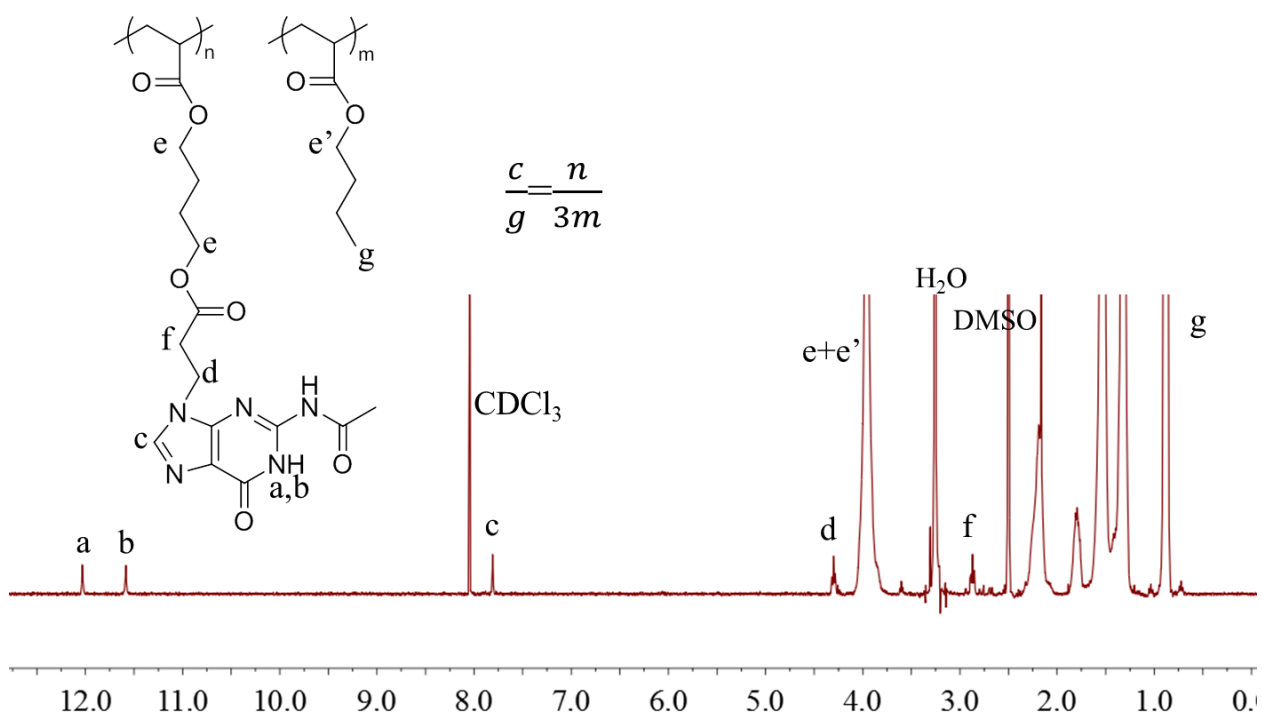


**Figure S7.6.**  $^1\text{H}$  NMR spectrum of poly(ACyA-co-nBA) in a mixture of  $\text{CDCl}_3$  and  $\text{DMSO-d}_6$ .



Chemical Shift (ppm)

**Figure S7.7.**  $^1\text{H}$  NMR spectrum of poly(AGuA-*co*-*n*BA) in a mixture of  $\text{CDCl}_3$  and  $\text{DMSO-d}_6$ .

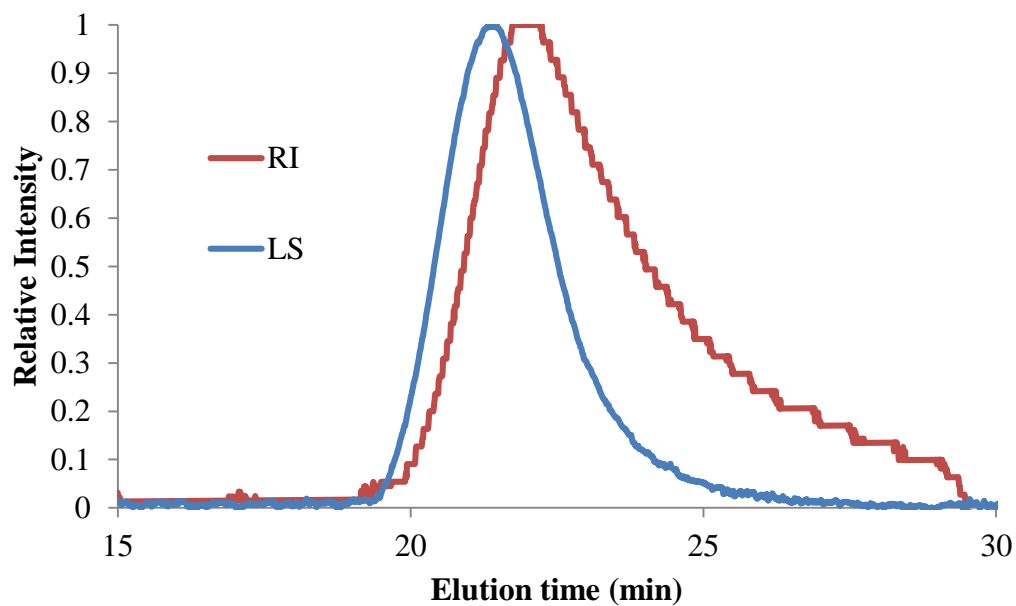
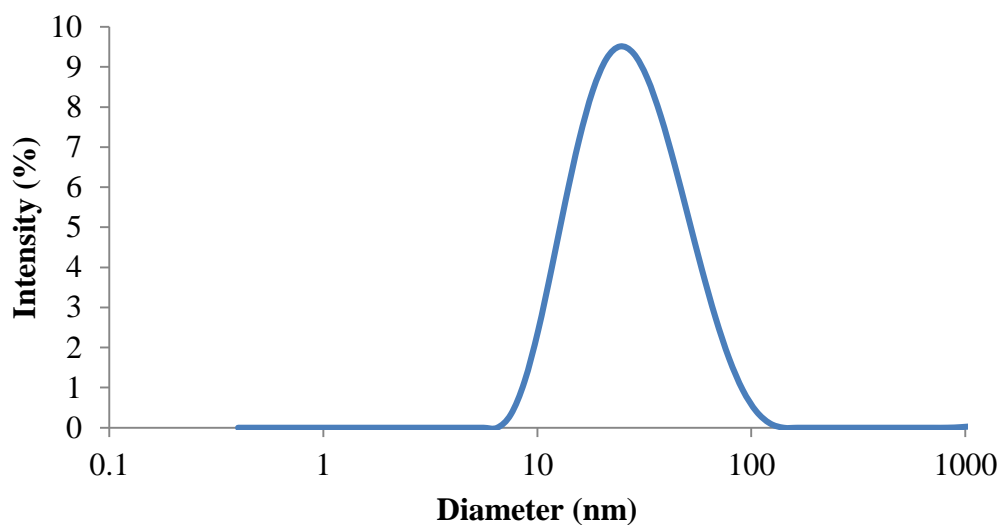


**Figure S7.8.** Representative DLS and SEC traces of poly(ACyA-*co*-*n*BA) in DMF 0.05 M LiBr at 50 °C.

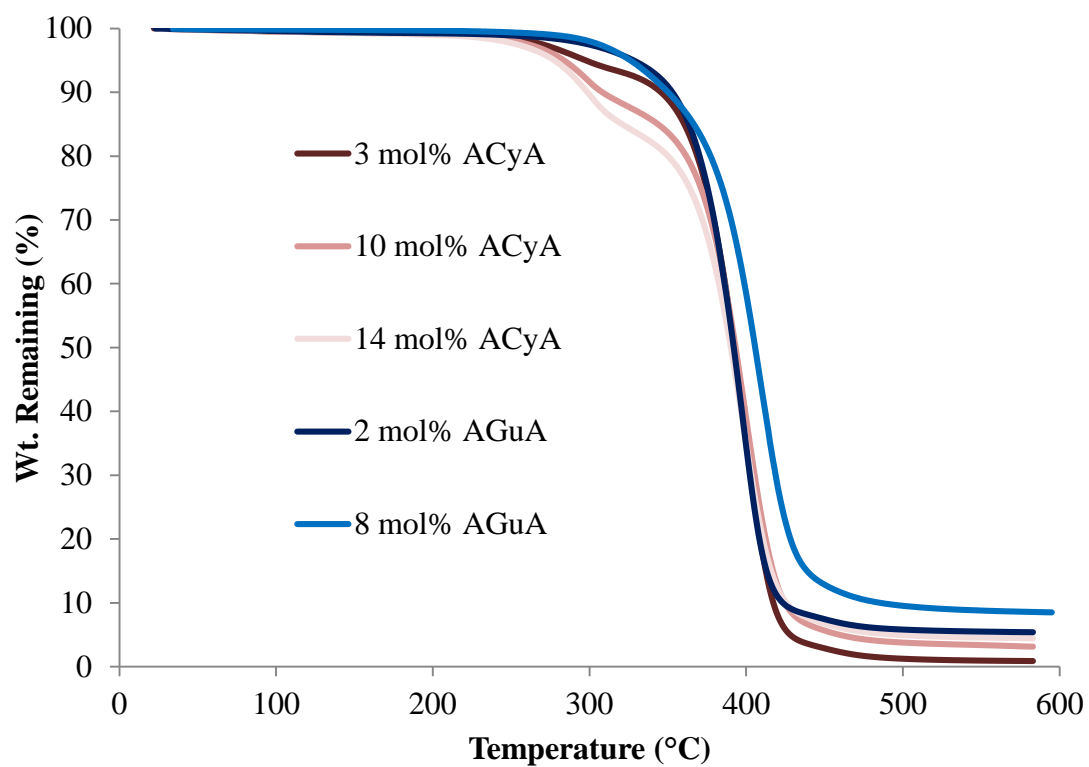


**Figure S7.9.** Representative TGA thermograms of poly(ACyA-*co*-*n*BA) and poly(AGuA-*co*-*n*BA) under nitrogen purge.

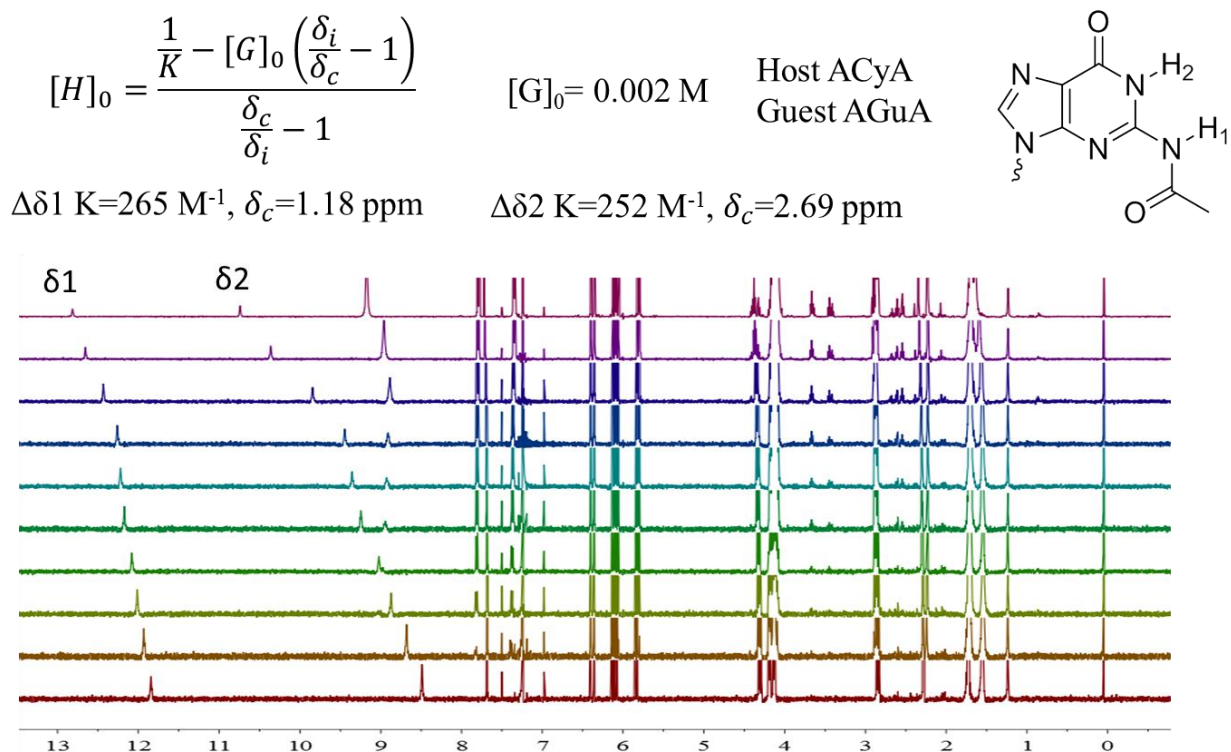


**Figure S7.10.**  $^1\text{H}$  NMR spectra of the ACyA and AGuA mixture with varying ratios in  $\text{CDCl}_3$  for the titration experiment.

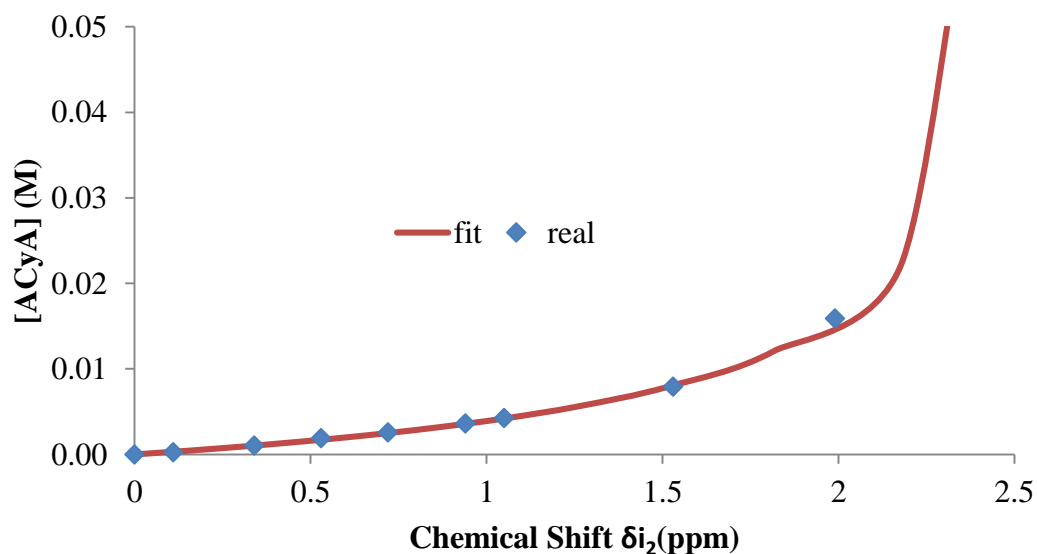


**Figure S7.11.** Non-linear fitting of NMR titration results for number two proton on AGuA to determine the binding constant of ACyA and AGuA in  $\text{CDCl}_3$  at  $22^\circ\text{C}$ .

In equation S1,  $[H]_0$  and  $[G]_0$  represent the concentration of ACyA (host) and AGuA (guest), respectively.  $\delta_c$  defines the proton chemical shift difference between completely bonded AGuA and free AGuA, and  $\delta_i$  defines the proton chemical shift difference between observed AGuA and the free AGuA. The titration experiment included a sequence of solution in  $CDCl_3$  with constant AGuA concentration and varying ACyA concentration. The chemical shift of hydrogen bonded proton on AGuA shifted from high field to low field with increasing ACyA concentration.

$$[H]_0 = \frac{\frac{1}{K} - [G]_0 (\frac{\delta_i}{\delta_c} - 1)}{\frac{\delta_c}{\delta_i} - 1} \quad (S1)$$

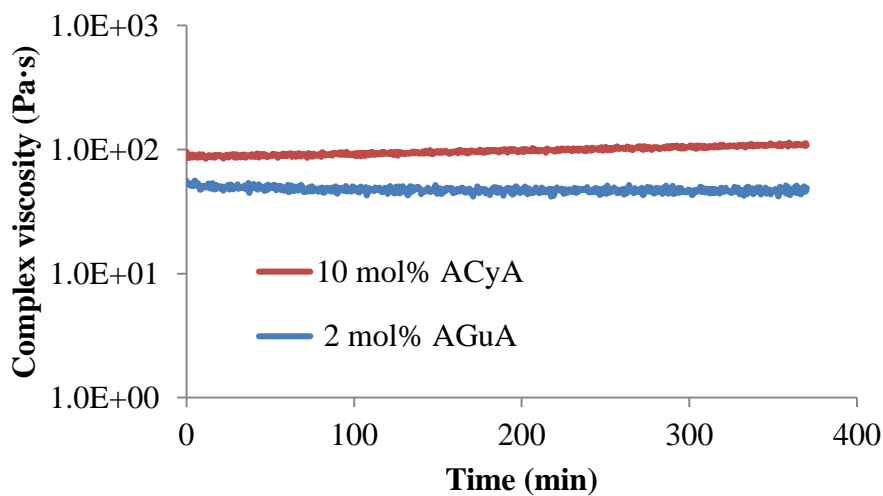


**Figure S7.12.** Isothermal time sweep of nucleobase-containing acrylics at 130 °C for 6 h.

## Chapter 8. Styrenic DABCO Salt-Containing Monomers for the Synthesis of Novel Charged Polymers

(Accepted by Polymer Chemistry)

Keren Zhang, Kevin J. Drummey, Nicholas G. Moon, William D. Chiang and Timothy E. Long \*

*Department of Chemistry, Macromolecules and Interfaces Institute  
Virginia Tech, Blacksburg, VA 24061, USA*

### 8.1 **Abstract**

A facile, two-step synthesis afforded styrenic DABCO salt monomers bearing two cyclic quaternary ammonium cations. Free radical polymerization of the DABCO salt monomers yielded homopolymers and copolymers with *n*-butyl acrylate. DABCO salt-containing random ionomers exhibited superior thermomechanical properties with extended plateau regimes compared to random ionomers bearing singly-charged pendant groups.

### 8.2 **Introduction**

Ion-containing polymers represent one of the largest families of functional polymers, and this field continues to expand due to critical commercial technologies, including water treatment, fuel cell membranes, filtration membranes, adhesives, biosensors, gene delivery, antimicrobial materials, and biomedical materials.<sup>1-7</sup> The synthesis of ion-containing polymers generally utilizes either polymerization of ionic monomers or post-functionalization of neutral polymers. Direct polymerization of charged monomers generally provides better tunability regarding ion type, concentration, and distribution within the main chain. For example, polymerizable ionic liquids, a family of charged monomers with melting points

lower than 100 °C, have received significant attention over the past decade.<sup>8</sup> Common ionic groups include, but are not limited to: ammoniums, phosphoniums, imidazoliums, sulfonates, carboxylates, and phosphates. Most polymerizable ionic monomers carry a single cation/anion with an electrostatically bonded counterion, and the effect of singly-charged monomer incorporation on polymer properties is well described.<sup>9-11</sup>

Monomers carrying multiple charges recently emerged as interesting candidates for the design of ion-containing polymers.<sup>12,13</sup> For example, a zwitterionic monomer generally contains a single covalently linked ion pair, and affords stronger association compared to singly-charged analogues, inducing more well-defined microphase-separation and superior mechanical properties.<sup>14</sup> However, only a few reports describe ionic monomers that contain two chemically bound cations or anions. Li *et al.* synthesized a polyelectrolyte with bis(trialkyl ammonium) acrylate, which displayed a lower critical aggregation value and larger aggregate sizes than the singly-charged analogues at similar charge concentrations. Quaternization of a cyclic diamine, 1,4-diazabicyclo[2.2.2]octane (DABCO), yields a doubly charged group. Salamone and Snider first synthesized DABCO based ionones using polyaddition of DABCO and dibromoalkane.<sup>15</sup> Others reported DABCO double ammonium salt (abbreviated as DABCO salt)-containing monomers for free radical polymerization. Dizman *et al.* demonstrated the antimicrobial properties of DABCO salt-containing polyelectrolytes.<sup>16</sup> Kopchinski also synthesized DABCO salt-containing polyelectrolytes for removal of phosphates from waste water.<sup>17</sup> Previous reports of these doubly-charged monomers involved



complex synthetic routes, and earlier examples of the corresponding polymers mainly focused on polyelectrolytes from charged homopolymers. This manuscript introduces a facile synthetic route to access a library of DABCO salt-containing monomers, and corresponding homopolymers and copolymers. Characterization of doubly-charged copolymers focuses on random ionomers with relatively low ionic content. Styrenic triethylammonium monomers served as singly-charged controls. Thermal characterization suggested similar thermal stability and thermal transitions of DABCO salt-containing copolymers compared to the singly-charged analogues. However, dynamic mechanical analysis (DMA) revealed distinctively different thermomechanical performance for DABCO salt-containing copolymer films compared to singly-charged analogues.

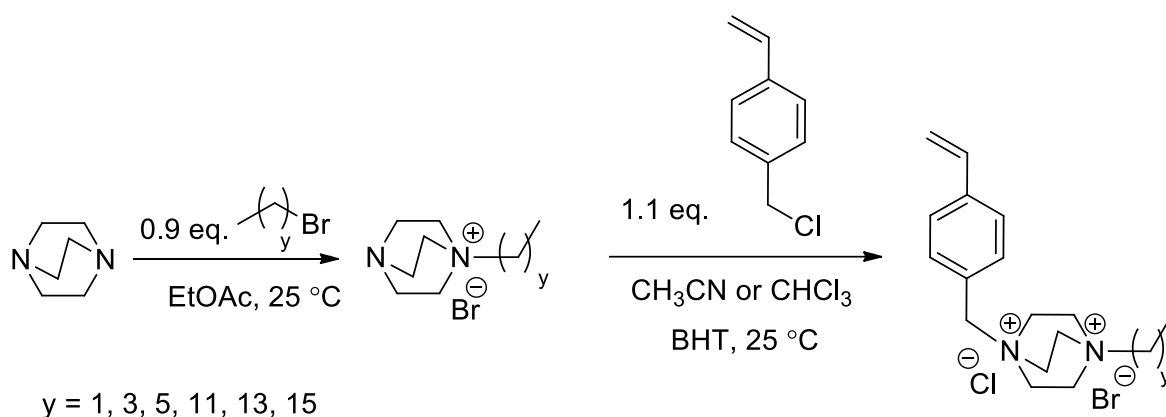
### 8.3 *Results and Discussion*

Herein, we describe an efficient synthetic strategy to access a library of *N*-4-vinylbenzyl-*N'*-alkyl DABCO BrCl (VBDC<sub>x</sub>BrCl) monomers. Two sequential nucleophilic substitutions yielded a series of VBDC<sub>x</sub>BrCl monomers with varying alkyl substituents (Scheme 8.1). In the first step, DABCO reacted with a 1-bromoalkane to form a mono-alkylated intermediate in the absence of the di-alkylated impurity. Careful solvent selection enabled precipitation of this intermediate, and the remaining tertiary amine proved less reactive than the amines before alkylation due to the nearby electron-withdrawing ammonium, which prevented the second alkylation from occurring. The subsequent reaction between the intermediate and 4-vinylbenzyl chloride (4VBCl) yielded VBDC<sub>x</sub>BrCl monomers. The reaction solvent again dissolved the starting materials and allowed

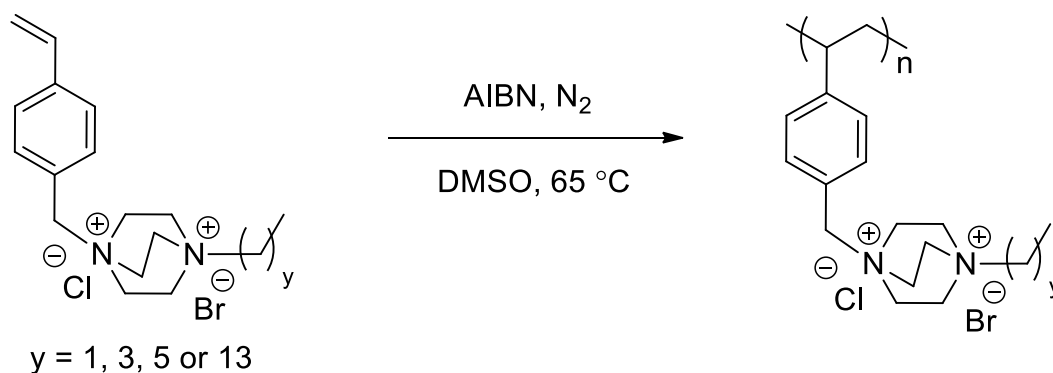
the product to precipitate, which eased purification. Monomer synthesis proved facile, high-yielding, and suitable for scale-up, with only filtration and washing required for purification. NMR spectroscopy and mass spectroscopy confirmed the chemical structure and purity of all VBDC<sub>x</sub>BrCl monomers in Scheme 8.1 (Table S8.1, Fig. S8.1,S8.2). Successful homopolymerization of four representative DABCO salt monomers demonstrated their suitability for free radical polymerization (Scheme 8.2, Figure S8.3). Triethyl-(4-vinylbenzyl)ammonium chloride (VBTEACl) was synthesized according to Long *et al.* and used as a singly-charged control.<sup>18</sup>

Among the DABCO salt-containing monomers, VBDC<sub>6</sub>BrCl and VBDC<sub>14</sub>BrCl with hexyl and tetradecyl substituents, respectively, were initially selected for copolymerization. Free radical copolymerization of *n*BA and VBDC<sub>6</sub>BrCl/VBDC<sub>14</sub>BrCl yielded random copolymers with varying ionic content (Scheme 8.3, Table 8.1). A mixture of DMSO and DMF was suitable for polymerization, and efficiently removed through precipitation and drying. It was presumed that ion-containing styrenic and acrylic monomers randomly copolymerized in a manner similar to styrenics and acrylics.<sup>19-21</sup> Random copolymers of VBTEACl and *n*BA with comparable ionic content served as controls for the comparison of doubly-charged ionic groups to their singly-charged analogues (Scheme S8.2, Table S8.2). All polymerization conditions remained identical for both DABCO salt-containing copolymers and singly-charged copolymers, including initiator and monomer concentrations, temperature, and reaction time. <sup>1</sup>H NMR spectroscopic analysis of the purified copolymers revealed their ionic contents (Fig.

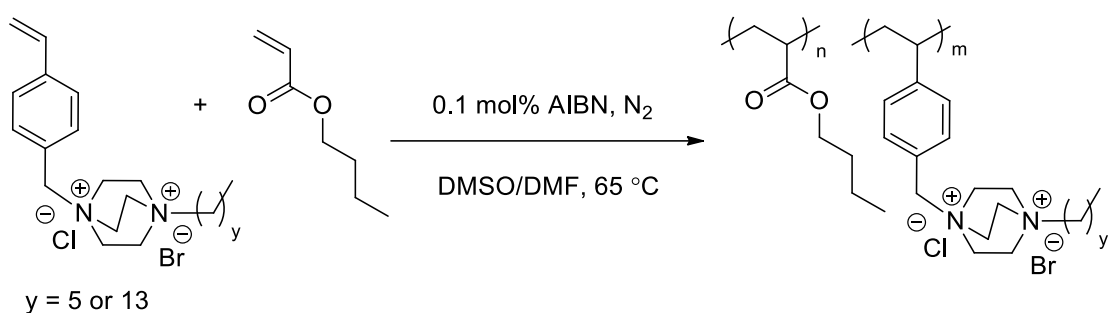
S8.4,S8.5). The copolymer compositions generally matched the feed ratios at relatively low ionic monomer incorporation. Styrenic content was higher than the feed ratio at relatively high VBDC<sub>x</sub>BrCl incorporation, consistent with previous studies reporting the preferential incorporation of styrenics over acrylics at high styrenic/acrylics feed ratios.<sup>19</sup> Although schemes depict DABCO salt units with chloride adjacent to the benzyl ammonium and bromide adjacent to the alkyl ammonium, anion exchange may occur in solution.



**Scheme 8.1.** Synthesis of *N*-4-vinylbenzyl-*N'*-alkyl DABCO-BrCl (VBDC<sub>x</sub>BrCl) monomer library, ( $x = y+1$ ).



**Scheme 8.2.** Synthesis of poly(VBDC<sub>x</sub>BrCl) homopolymers, ( $x = y+1$ ).



**Scheme 8.3.** Synthesis of poly(VBDC<sub>6</sub>BrCl-*co*-*n*BA) and poly(VBDC<sub>14</sub>BrCl-*co*-*n*BA) copolymers.

**Table 8.1.** Feed ratios of the ionic monomers and monomer incorporation in polymers for poly(VBDC<sub>6</sub>BrCl-*co*-*n*BA)s and poly(VBDC<sub>14</sub>BrCl-*co*-*n*BA)s.

| Ionic monomer<br>content | Poly(VBDC <sub>6</sub> BrCl- <i>co</i> - <i>n</i> BA) |                               | Poly(VBDC <sub>14</sub> BrCl- <i>co</i> - <i>n</i> BA) |              |
|--------------------------|---|-------------------------------|--|--------------|
|                          | Feed mol%   | Observed mol%<br>Observed wt% | Observed mol%<br>Observed wt%                          | Observed wt% |
|                          | 3   | 1<br>5                        | 2<br>7   |              |
|                          | 9   | 12<br>31                      | 8<br>28  |              |
|                          | 17  | 20<br>45                      | 20<br>51   |              |
|                          | 33  | 42<br>70                      | 38<br>72   |              |

Thermogravimetric analysis (TGA) under nitrogen revealed the thermal properties of DABCO salt-containing copolymers. Poly(VBDC<sub>14</sub>BrCl-*co*-*n*BA), poly(VBDC<sub>6</sub>BrCl-*co*-*n*BA), and poly(VBTEACl-*co*-*n*BA) displayed two-step weight-loss profiles in TGA temperature ramps (Figure 8.1,S8.6,S8.7). Thermal degradation of ammonium-containing polymers generally occurs from dequaternization of the ammonium.<sup>22</sup> Long *et al.* utilized the first-step weight-loss of trialkylammonium polyelectrolytes to determine that their dequaternization

followed a nucleophilic degradation pathway.<sup>18</sup> TGA profiles of poly(VBTEACl-*co-nBA*)s (Fig. S8.7, Table S8.4) suggested a similar degradation mechanism. However, thermal degradation of DABCO salt-containing copolymers proved more complex as the DABCO salt contained both benzylic and aliphatic ammoniums. Dequaternization of both ammonium cations occurred together in the first weight-loss step.

The dequaternization mechanism of the alkyl-substituted ammonium remained unclear without further analysis as both nucleophilic substitution and Hofmann elimination pathways would result in the same weight-loss (Scheme 8.4). Dequaternization of the ammonium adjacent to the benzyl group predominantly followed a reverse nucleophilic substitution mechanism (Scheme 8.5a), as evidenced from the weight-loss of the first step.<sup>20-21</sup> Table 8.2 summarizes theoretical weight-loss of poly(VBDC<sub>6</sub>BrCl-*co-nBA*), calculated from both Hofmann elimination and nucleophilic substitution pathways for the benzyl ammonium. Weight-loss of the first degradation step compared closely with calculations for the nucleophilic pathway of the benzyl ammonium degradation. The discrepancy between the weight-loss prediction and experimental result did not support the Hofmann elimination mechanism for the benzyl ammonium degradation (Scheme 8.5b). The second weight-loss step corresponded to the polymer backbone degradation. The char residue generally increased with increasing styrenic contents in the copolymers. TGA profiles of poly(VBDC<sub>14</sub>BrCl-*co-nBA*)s showed a similar result (Fig. S8.6, Scheme S8.3, Table S8.3). The 5 wt% loss temperature values ( $T_d$ ) of DABCO salt-containing copolymers ranged from 190 °C to 290 °C, similar to  $T_d$

values of poly(VBTEACl-*co-n*BA)s (Table 8.2,S8.3,S8.4).  $T_d$  values in each series decreased with increasing ionic content due to a decrease of the more thermally stable acrylic content.

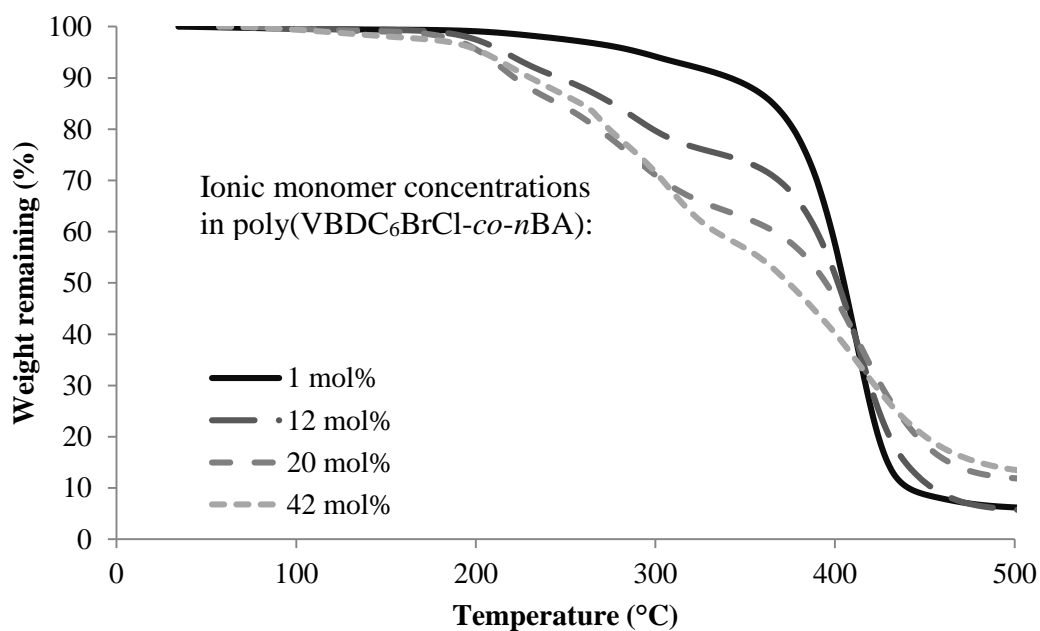
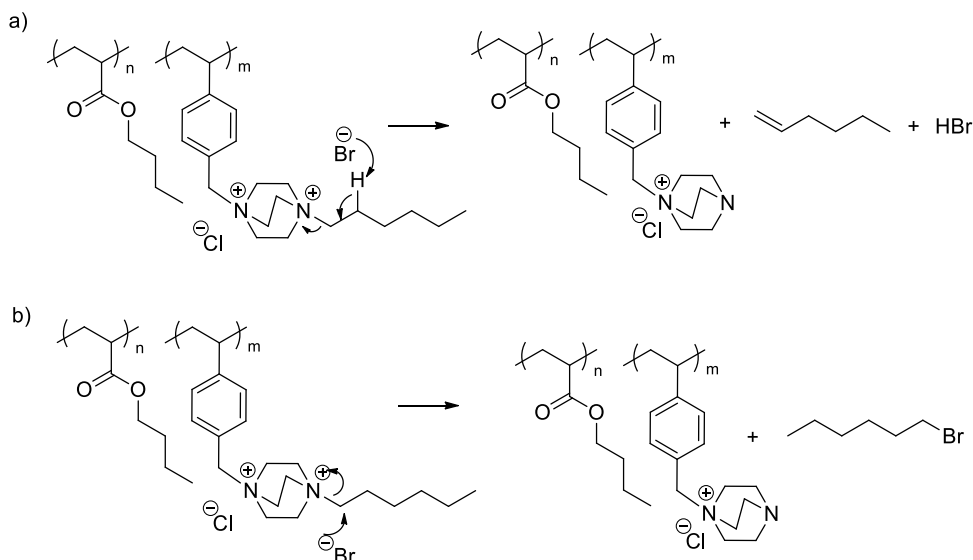
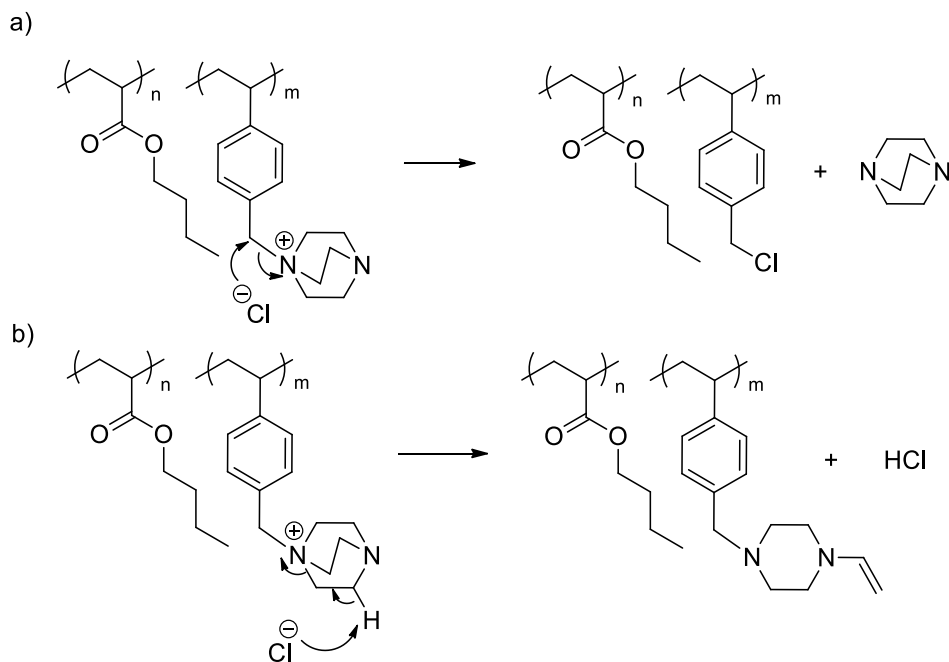


**Figure 8.1.** TGA traces of poly(VBDC<sub>6</sub>BrCl-*co-n*BA)s with varying ionic monomer concentrations.



**Scheme 8.4.** Dequaternization of the alkyl-substituted ammonium through a) nucleophilic substitution and b) Hofmann elimination.



**Scheme 8.5.** Dequaternization of the benzyl-substituted ammonium through a) nucleophilic substitution and b) Hofmann elimination.

**Table 8.2.** Temperatures at 5 % weight-loss and correlation of initial thermal weight-loss of poly(VBDC<sub>6</sub>BrCl-*co*-*n*BA)s to a nucleophilic substitution or Hofmann elimination degradation pathway.

| VBDC <sub>6</sub><br>BrCl<br>mol% | VBDC <sub>6</sub><br>BrCl<br>wt% | T <sub>d, 5wt%</sub><br>(°C) | Observed<br>weight-loss<br>1 <sup>st</sup> step (%) | Theoretical<br>weight-loss<br>1 <sup>st</sup> step Nu<br>(%) | Theoretical<br>weight-loss<br>1 <sup>st</sup> step<br>Hofmann<br>(%) |
|-----------------------------------|----------------------------------|------------------------------|---|--|--|
| 1                                 | 5                                | 291                          | 4   | 3  | 2  |
| 12                                | 31                               | 215                          | 22  | 20   | 13   |
| 20                                | 45                               | 203                          | 35  | 29   | 19   |
| 42                                | 70                               | 204                          | 42  | 45   | 28   |

Differential scanning calorimetry (DSC) revealed similar thermal transitions when comparing DABCO salt-containing polymers to their singly-charged analogues (Figure S8.8-8.10, Table S8.5). All ion-containing homopolymers and copolymers were amorphous. For homopolymers of poly(VBDC<sub>14</sub>BrCl), poly(VBDC<sub>6</sub>BrCl), and poly(VBTEACl), DSC failed to detect any glass transition temperature ( $T_g$ ) below their thermal degradation temperatures. Copolymers with lower than 25 mol% ionic monomer each exhibited a single  $T_g$  in the range from -45 °C to -36 °C, attributed to long range segmental motion of the poly(*n*BA) soft phase (homopolymer  $T_g$  -47 °C). The mild  $T_g$  increase (<10 °C) with increasing ionic content resulted from the ionic association of DABCO salt restricting adjacent chain mobility.

Poly(VBDC<sub>*x*</sub>BrCl-*co-n*BA) and poly(VBTEACl-*co-n*BA) with 3 mol% or less ionic monomer were tacky solids. Copolymers with 8 mol% or more ionic monomer were solution cast into free-standing films. Charged styrenic monomers contributed both a high  $T_g$  component and ionic associations that largely enhanced the mechanical properties of the poly(*n*BA) matrix. DMA revealed biphasic thermomechanical behavior of DABCO salt-containing copolymers with relatively low ionic contents ( $\leq 15$  mol%), consistent with typical ionomers (Figure 8.2).<sup>9,23</sup> However, the unprecedented wide and well-defined plateau window of DABCO salt-containing films indicated superior microphase-separation and stronger ionic interactions of the DABCO salt units compared to other ionomers with zwitterions or singly-charged ions.<sup>14,24-26</sup> Figure 8.2 compares storage moduli and tan delta of two ionomers films with similar incorporations of VBDC<sub>6</sub>BrCl and VBTEACl. The



poly(VBTEACl-*co-n*BA) film showed a broad glass transition, where modulus gradually decreased with increasing temperature until sample yielded. Absence of a plateau window indicated significant phase-mixing in the VBTEACl-containing copolymer film. The significant flow region difference suggested that the singly-charged control afforded weaker ionic interactions compared to the DABCO salt-containing copolymer at similar ionic content.

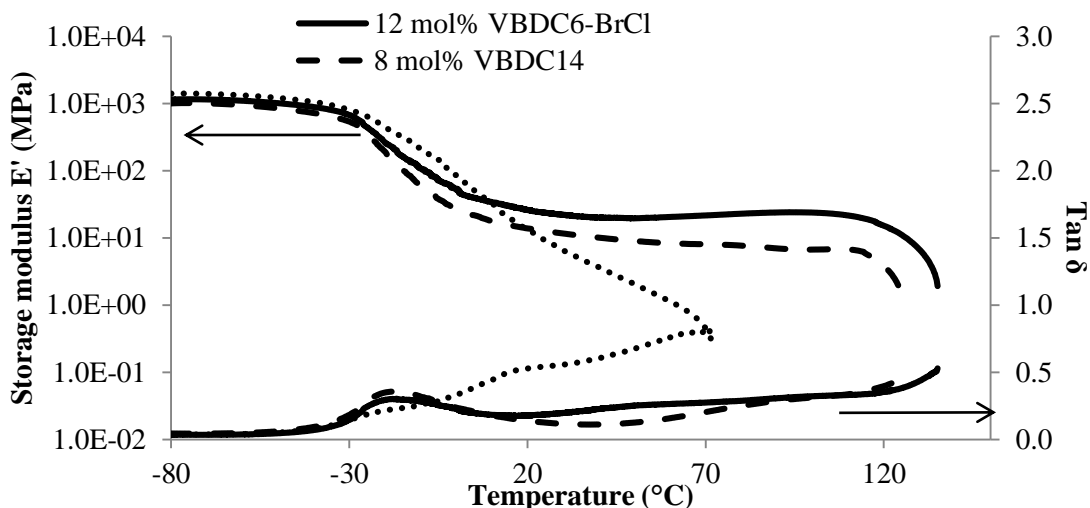
The first storage modulus drop of poly(VBDC<sub>6</sub>BrCl-*co-n*BA) and poly(VBDC<sub>14</sub>BrCl-*co-n*BA) corresponded to the glass transition of the soft phase, composed mainly of poly*n*BA. A well-defined plateau followed the soft phase T<sub>g</sub> for each DABCO salt-containing films, during which the storage modulus remained constant with increasing temperature. DABCO salt units associated with each other and formed ionic aggregates, which provided multifunctional physical crosslinking.<sup>23,27</sup> These physical crosslinks provided mechanical strength for ionomer films during the plateau window. The second modulus drop above 120 °C was attributed to motion within the ionic aggregates and dissociation of the ionic interactions according to Weiss *et al.*<sup>23</sup> Two distinct transitions before and after the plateau region originated from relaxation of polymer chains in the neutral, low T<sub>g</sub> phase and the ionic interactions in the ion-rich phase, respectively. The DMA profiles of poly(VBDC<sub>6</sub>BrCl-*co-n*BA) and poly(VBDC<sub>14</sub>BrCl-*co-n*BA) ionomer films suggested a well-defined phase-separation with strong ionic interaction.<sup>9,19</sup> Thermomechanical analysis revealed that DABCO salt units were more efficient than singly-charged analogues in forming physical crosslinks and enhancing mechanical performance of an ion-containing copolymer. A forthcoming

publication will discuss in greater detail the differences in mechanical, morphological, and rheological properties of DABCO salt-containing copolymers *vs* singly-charged controls, as well as the influence of alkyl substituent length and counterion selection.

**Figure 8.2.** Dynamic mechanical temperature analysis of poly(VBDC<sub>6</sub>BrCl-*co*-*n*BA) with 12 mol% of VBDC<sub>6</sub>BrCl, poly(VBDC<sub>14</sub>BrCl-*co*-*n*BA) with 8 mol% of VBDC<sub>14</sub>BrCl, and poly(VBTEACl-*co*-*n*BA) with 11 mol% of VBTEACl.

#### 8.4 Conclusions

We report a facile, two-step synthesis for a library of polymerizable, styrenic DABCO salt monomers. Free radical polymerization afforded DABCO salt-containing homopolymers. Two DABCO salt-containing monomers with hexyl and



tetradecyl substituents each yielded a series of random copolymers with *n*-butyl acrylate using varying feed ratios of ionic and neutral monomers. DABCO salt-containing copolymers exhibited similar thermal stability and degradation pathway compared to the triethylammonium controls. DABCO salt incorporation into a low

T<sub>g</sub> acrylic matrix resulted in a physically crosslinked network with ionic interactions. DABCO salt-containing ionomers formed free-standing films and exhibited biphasic thermomechanical properties with unprecedented well-defined plateau windows. Superior thermomechanical performance of DABCO salt-containing copolymers suggested that DABCO salt units afforded significantly stronger ionic interactions and better microphase-separation comparing to the singly-charged analogues. The library of DABCO salt monomers with tunable solubility allows facile synthesis of various ion-containing polymers. DABCO salt-containing random ionomers enable applications as elastomers and thermoplastics with superior thermal resistance and processability.

## 8.5 *Acknowledgements*

The authors acknowledge Henkel Corporation for financial support and insightful discussions with Dr. Charles Paul, Dr. Eric Silverberg, and Dr. Cristina DeJesus. We also thank Dr. Motohiro Aiba from Tokyo Institute of Technology for his assistance with polymer synthesis.

## 8.6 *References*

1. Bolto, B.; Gregory, J. *Water Res.* **2007**, *41*, 2301.
2. Hickner, M. A. *Mater. Today* **2010**, *13*, 34.
3. Couture, G.; Alaaeddine, A.; Boschet, F.; Ameduri, B. *Prog. Polym. Sci.* **2011**, *36*, 1521.
4. Merle, G.; Wessling, M.; Nijmeijer, K. *J. Membr. Sci.* **2011**, *377*, 1.
5. Williams, S. R.; Long, T. E. *Prog. Polym. Sci.* **2009**, *34*, 762.
6. Zhang, K.; Long, T. E.; VIRGINIA TECH INTELLECTUAL PROPERTIES, INC. : 2015.
7. Zhang, M.; Gao, R.; June, S. M.; Cheng, S.; Long, T. E. *Proc. Annu. Meet. Adhes. Soc.* **2011**, *34th*, zhang2/1.
8. Mecerreyes, D. *Prog. Polym. Sci.* **2011**, *36*, 1629.

9. Tant, M. R.; Mauritz, K. A.; Wilkes, G. L. *Ionomers: synthesis, structure, properties, and applications*; Blackie Academic & Professional New York; London, **1997**.
10. Pineri, M.; Eisenberg, A. *Structure and properties of ionomers*; Springer Science & Business Media, **2012**; Vol. 198.
11. Eisenberg, A.; King, M. *Ion-containing polymers: physical properties and structure*; Academic Press New York, **1977**; Vol. 2; 2.
12. Laschewsky, A. *Polymers* **2014**, 6, 1544.
13. Xuan, F.; Liu, J. *Polym. Int.* **2009**, 58, 1350.
14. Wu, T.; Beyer, F. L.; Brown, R. H.; Moore, R. B.; Long, T. E. *Macromolecules* **2011**, 44, 8056.
15. Salamone, J. C.; Snider, B. *J. Polym. Sci., Part A: Polym. Chem.* **1970**, 8, 3495.
16. Dizman, B.; Elasri, M. O.; Mathias, L. J. *J. Appl. Polym. Sci.* **2004**, 94, 635.
17. Kopchinski, A. F., Kansas State University, 1994.
18. Hemp, S. T.; Zhang, M. Q.; Allen, M. H.; Cheng, S. J.; Moore, R. B.; Long, T. E. *Macromol. Chem. Phys.* **2013**, 214, 2099.
19. Cheng, S.; Zhang, M.; Wu, T.; Hemp, S. T.; Mather, B. D.; Moore, R. B.; Long, T. E. *J. Polym. Sci., Part A: Polym. Chem.* **2012**, 50, 166.
20. Ziaee, F.; Nekoomanesh, M. *Polymer* **1998**, 39, 203.
21. Hawker, C. J.; Elce, E.; Dao, J.; Volksen, W.; Russell, T. P.; Barclay, G. G. *Macromolecules* **1996**, 29, 2686.
22. Williams, S. R.; Borgerding, E. M.; Layman, J. M.; Wang, W.; Winey, K. I.; Long, T. E. *Macromolecules* **2008**, 41, 5216.
23. Weiss, R. A.; Fitzgerald, J. J.; Kim, D. *Macromolecules* **1991**, 24, 1071.
24. Gauthier, M.; Carrozzella, T.; Snell, G. *J. Polym. Sci., Part B: Polym. Phys.* **2002**, 40, 2303.
25. Ehrmann, M.; Muller, R.; Galin, J. C.; Bazuin, C. G. *Macromolecules* **1993**, 26, 4910.
26. Bazuin, C. G.; Eisenberg, A. *J. Chem. Educ.* **1981**, 58, 938.
27. Eisenberg, A.; Hird, B.; Moore, R. B. *Macromolecules* **1990**, 23, 4098.

## 8.7 Supporting Information

**Materials.** *n*-Butyl acrylate (*n*BA, 99+%) was purchased from Aldrich and passed through neutral alumina columns before use.  $\alpha,\alpha'$ -Azobis-(isobutyronitrile) (AIBN, Fluka, 99%) was recrystallized from methanol twice. 1-bromoethane (98+%), 1-bromobutane (98+%), 1-bromohexane (98+%), 1-bromododecane (98+%), and 1-bromohexadecane (98+%) were purchased from Alfa Aesar and used without further purification. DABCO (99+%), 4-vinyl benzyl chloride (4VBCl, 99%), 2,6-di-*tert*-butyl-4-methylphenol (BHT, 99%),

triethylamine (TEA, 99+), sodium tetrafluoroborate (NaBF<sub>4</sub>, 98%), and bis(trifluoromethane)sulfonimide lithium (Li-Tf<sub>2</sub>N) were purchased from Aldrich and used without further purification. Ethyl acetate (EtOAc, HPLC grade), chloroform (CHCl<sub>3</sub>, HPLC grade), acetone (HPLC grade), methanol (MeOH, HPLC grade), *N,N*-dimethylsulfoxide (DMSO, HPLC grade) and *N,N*-dimethylformamide (DMF, HPLC grade) were obtained from Spectrum and used as received.

**Analytical Methods.** <sup>1</sup>H NMR and <sup>13</sup>C NMR spectroscopy was conducted on a Varian Unity 400 at 400 MHz in deuterated DMSO, deuterated MeOD, or CDCl<sub>3</sub>. Thermogravimetric analysis (TGA) was performed on a TA Instruments Q500 TGA with heating ramps from ambient to 600 °C at 10 °C/min. Thermal degradation temperatures (T<sub>d</sub>) corresponded to 5% weight-loss. Differential scanning calorimetry (DSC) provided heat/cool/heat cycles with a heating rate of 10 °C/min and cooling rate of 10 °C/min on a TA instruments Q1000 DSC. DSC experiments used a nitrogen flush of 50 mL/min. DSC calibration utilized indium (mp = 156.60 °C) and zinc (mp = 419.47 °C) standards. The midpoint of the transition in the second heating ramp determined glass transition temperatures (T<sub>g</sub>). Dynamic mechanical analysis (DMA) utilized a TA Instruments Q800 Dynamic Mechanical Analyzer in tension mode at a frequency of 1 Hz, oscillatory amplitude of 15 μm, and a static force of 0.01 N. The temperature ramp was 3 °C/min. The peak maxima of tan delta curves determined T<sub>g</sub> values.

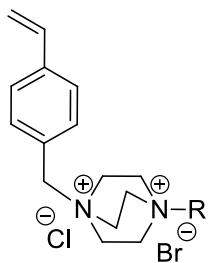
**Synthesis of *N*-4VinylBenzyl-*N'*-alkyl DABCO BrCl (VBDC<sub>x</sub>BrCl) monomers.** In a representative DABCO salt-containing monomer synthesis (Scheme 8.1), DABCO (5.6 g, 50.0 mmol) and 1-bromohexane (6.3 mL, 45.0 mmol) were dissolved in 100 mL of ethyl acetate and stirred overnight. White suspension was filtered, washed with ethyl acetate,

and dried *in vacuo* at room temperature. The mono-alkylated DABCO intermediate was used without further purification. Alkylated DABCO (12.2 g, 44.1 mmol) and 4VBCl (7.4 g, 48.5 mmol) were dissolved in 100 mL acetonitrile and stirred overnight. The white suspension was filtered, washed with acetonitrile, and dried *in vacuo* at room temperature to give a white solid (13.9 g, 72% yield).  $^1\text{H}$  NMR (400 MHz,  $d_6$ -DMSO, Figure S8.1): 7.65-7.57 (m, 4H,  $\text{H}_{\text{a+b}}$ ), 6.81 (dd, 1H,  $J_1 = 10.9$  Hz,  $J_2 = 17.6$  Hz,  $\text{H}_{\text{c}}$ ), 5.98 (d, 1H,  $J = 17.6$  Hz,  $\text{H}_{\text{d}}$ ), 5.39 (d, 1H,  $J = 10.9$  Hz,  $\text{H}_{\text{e}}$ ), 4.96 (s, 2H,  $\text{H}_{\text{f}}$ ), 3.94 (s, 12H,  $\text{H}_{\text{g}}$ ), 3.52 (m, 2H,  $\text{H}_{\text{h}}$ ), 1.65 (m, 2H,  $\text{H}_{\text{i}}$ ), 1.27 (s, 6H,  $\text{H}_{\text{j}}$ ), 0.86 (s, 3H,  $\text{H}_{\text{m}}$ ).  $^{13}\text{C}$  NMR (100 MHz,  $d_6$ -DMSO): 139.76, 136.18, 133.83, 127.17, 126.40, 116.95, 66.09, 63.76, 50.74, 50.49, 31.00, 25.62, 22.23, 21.67, 14.24. HRMS (ESI+):  $m/z$  calculated for  $[\text{VBDC}_x\text{Br}^+]$  393.1900 g/mol; found 393.1897 g/mol.

**Synthesis of DABCO Salt-Containing Homopolymers and Copolymers.** A typical homopolymerization was conducted as follows (Scheme 8.2, 8.3). VBDC<sub>6</sub>BrCl (2.0 g, 5.0 mmol), AIBN (8.2 mg, 0.05 mmol), DMSO (4.0 mL), and MeOH (2.0 mL) were added to a 100 mL, round-bottomed flask equipped with magnetic stirrer. The solution was purged with nitrogen for 20 min and stirred at 65 °C for 24 h. The resulting solution was dialyzed against MeOH and dried *in vacuo* to obtain a brittle clear solid of (2.4 g, 87% yield).  $^1\text{H}$  NMR spectroscopy confirmed the structure of poly(VBDC<sub>6</sub>BrCl) (Figure S8.3). A typical copolymerization was conducted as follows: *n*BA (2.0 g, 15.6 mmol), AIBN (2.8 mg, 0.017 mmol), VBDC<sub>6</sub>BrCl (0.669 g, 1.6 mmol) and DMSO-DMF mixture (10.7 g) were added to a round-bottomed flask equipped with magnetic stirrer. The solution was purged with argon for 20 min and stirred at 65 °C for 24 h. The resulting solution was precipitated into a MeOH-H<sub>2</sub>O mixture. The precipitate was collected and dried *in vacuo* to obtain an solid

of (2.4 g, 90% yield). Calculation based on the  $^1\text{H}$  NMR spectrum of poly(VBDC<sub>6</sub>BrCl-*co-n*BA) showed 11.5 mol% incorporation of VBDC<sub>6</sub>BrCl (Figure S8.4).

SEC analysis was unable to produce reliable molecular weight information of ion-containing copolymers. Dynamic light scattering showed aggregate formations for all poly(VBDC<sub>x</sub>BrCl)s, poly(VBDC<sub>x</sub>BrCl-*co-n*BA)s, and poly(VBTEACl-*co-n*BA)s in various SEC solvents. However, all polymerizations were conducted with 0.1 mol% AIBN in DMF-DMSO mixture with 20 wt% solids, and stirred at 65 °C for 24 h. Polymerization conditions generally dominate the molecular weight in conventional free radical polymerizations, even with ionic monomer presence.<sup>1-4</sup>



**Scheme S8.1.** N-4-Vinylbenzyl-N'-alkyl DABCO-BrCl (VBDC<sub>x</sub>BrCl) monomer library.

**Table S8.1.** Mass spectroscopy, NMR, yield, yellowing temperature, and solubility in water of VBDC<sub>x</sub>BrCl monomer library.

| R   | Step1<br>NMR | Step2<br>NMR | m/z*<br>Observed<br>(g/mol) | m/z*<br>Predicted<br>(g/mol) | Yield<br>(%) | Transition*<br>(°C) | Solubility<br>in H <sub>2</sub> O |
|-----|--------------|--------------|-----------------------------|------------------------------|--------------|---------------------|-----------------------------------|
| C2  | √            | √            | 337.1274                    | 337.1274                     | 97           | 223.4               | Y                                 |
| C4  | √            | √            | 365.1592                    | 365.1587                     | 92           | 216.2               | Y                                 |
| C6  | √            | √            | 393.1897                    | 393.1900                     | 72           | 203.9               | Y                                 |
| C12 | √            | √            | 477.2848                    | 477.2839                     | 50           | 189                 | N                                 |

|     |   |   |          |          |    |     |   |
|-----|---|---|----------|----------|----|-----|---|
| C14 | √ | √ | 505.3152 | 505.3152 | 82 | 191 | N |
| C16 | √ | √ | 533.3444 | 533.3465 | 63 | 189 | N |

\* HRMS ESI+ m/z calculated for [VBDC<sub>x</sub>Br<sup>+</sup>]

\*Transition: Yellowing of solid powder. No melting.

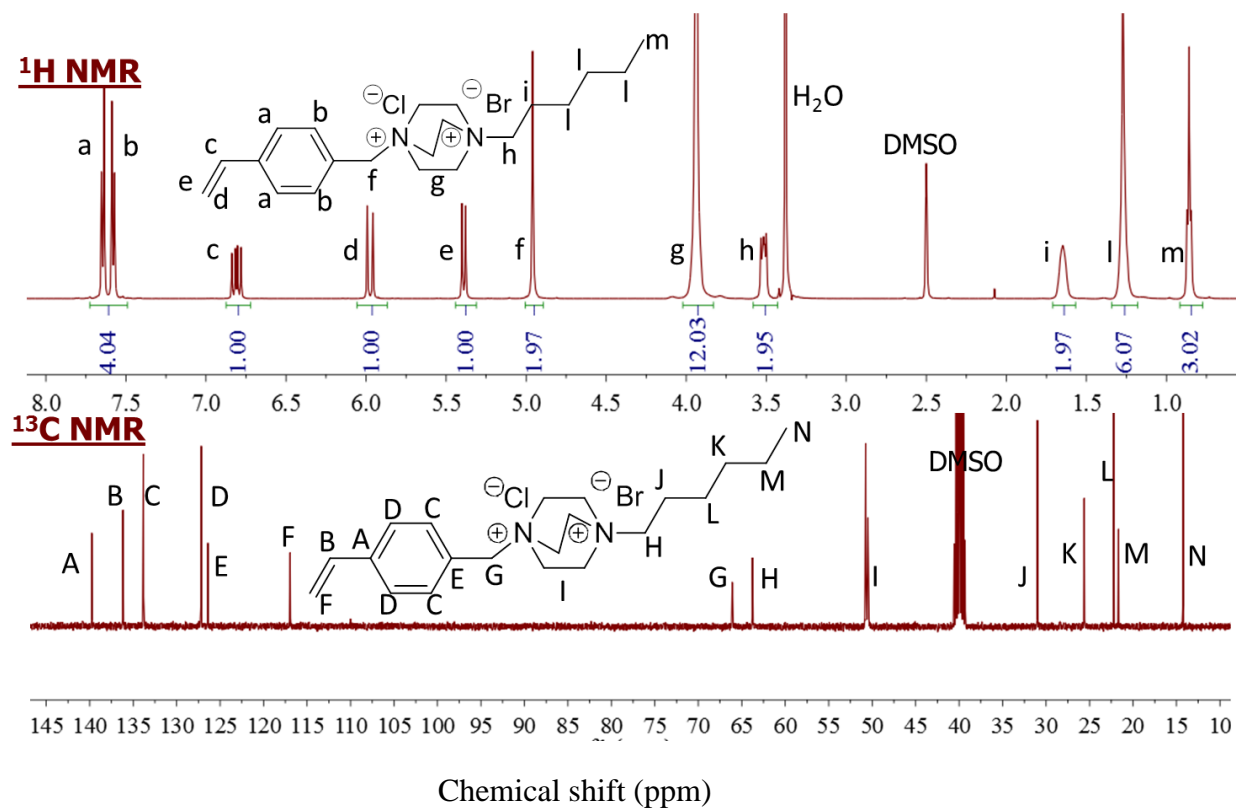


**Figure S8.1.** <sup>1</sup>H NMR and <sup>13</sup>C NMR spectra of VBDC<sub>6</sub>BrCl.



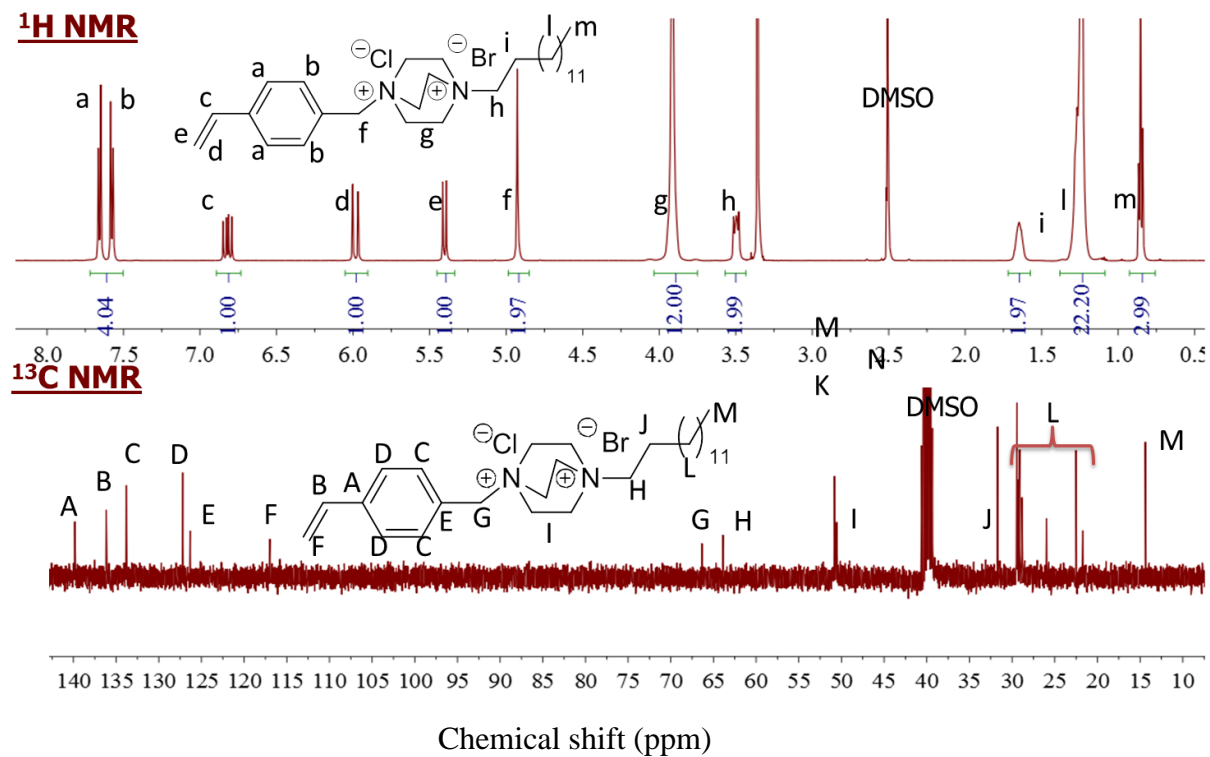


**Figure S8.2.** <sup>1</sup>H NMR and <sup>13</sup>C NMR spectra of VBDC<sub>14</sub>BrCl.

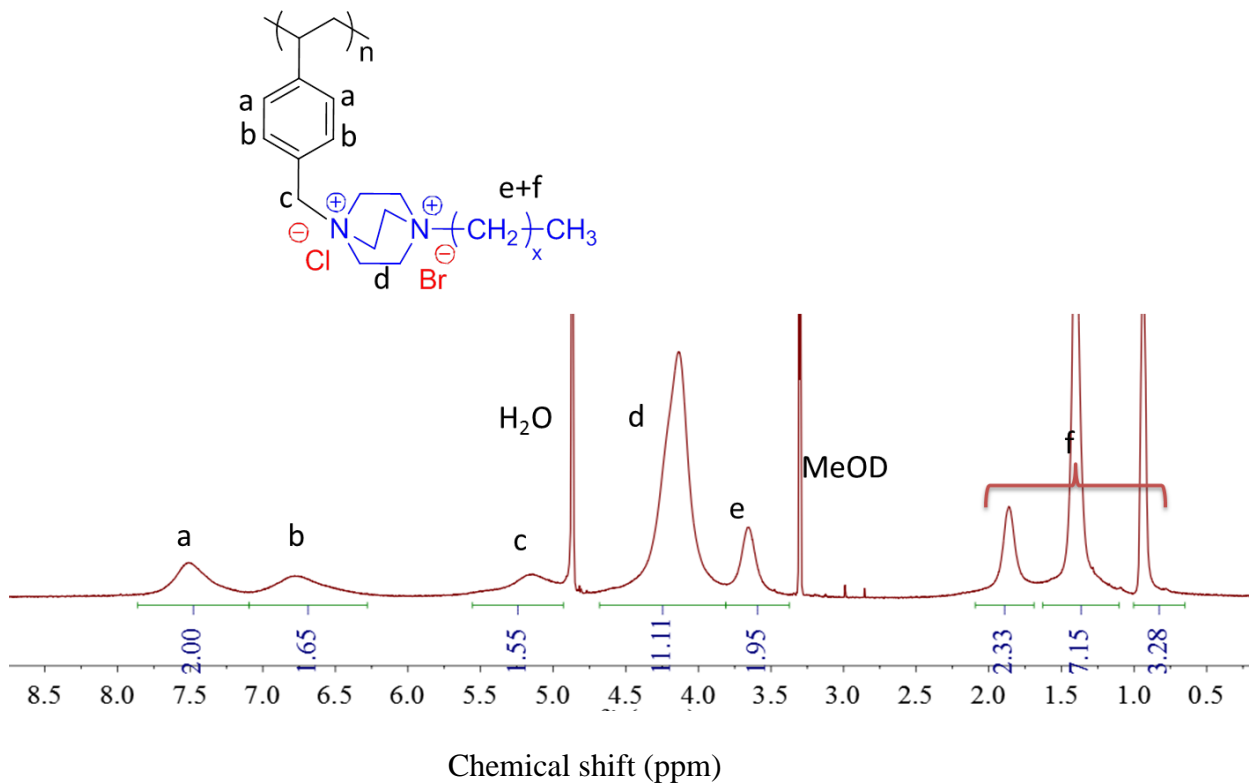


**Figure S8.3.** <sup>1</sup>H NMR spectrum of poly(VBDC<sub>6</sub>BrCl).

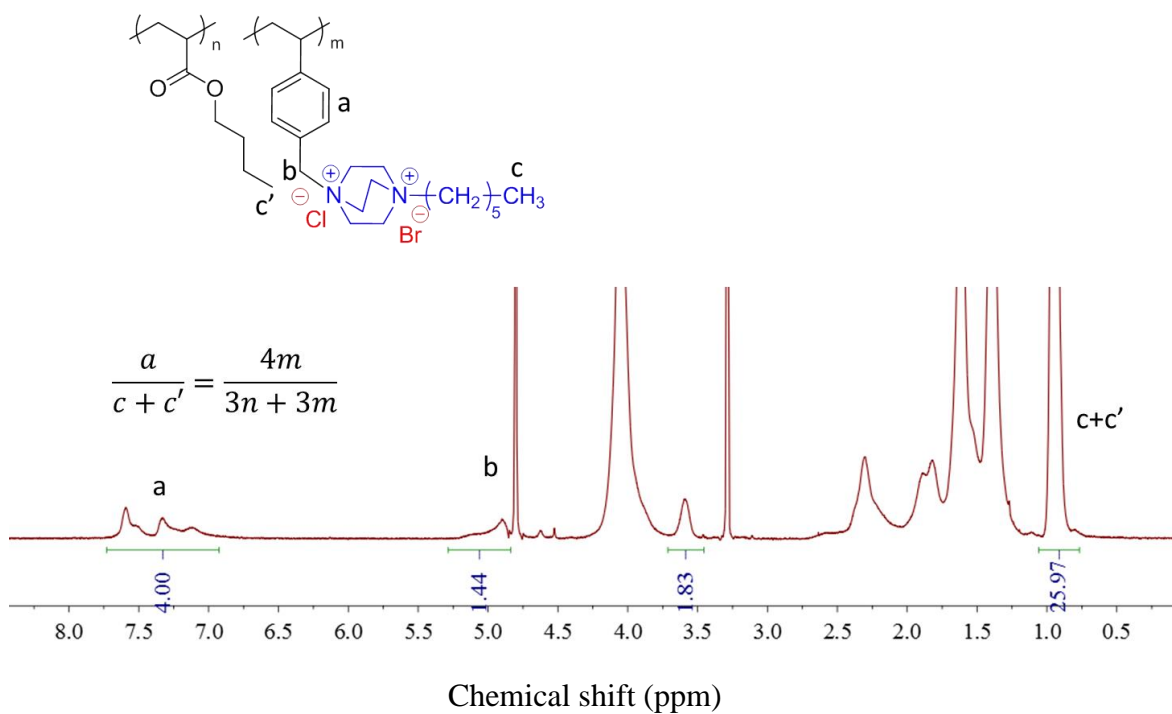
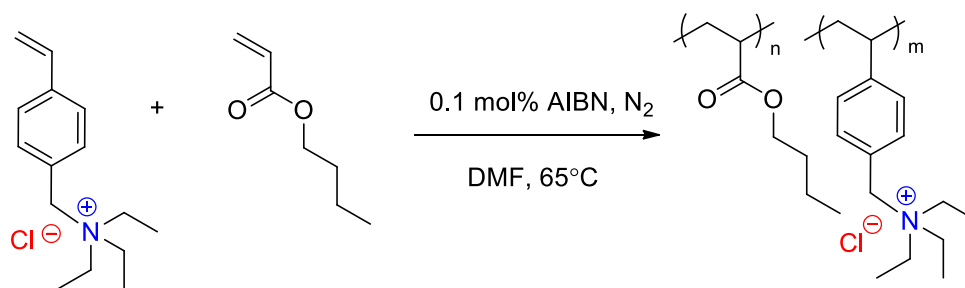


**Figure S8.4.**  $^1\text{H}$  NMR spectrum of poly(VBDC<sub>6</sub>BrCl-*co*-*n*BA) with 12 mol% VBDC<sub>6</sub>BrCl.



**Scheme S8.2.** Synthesis of poly(VBTEACl-*co*-*n*BA). Triethyl-(4-vinylbenzyl) ammonium chloride (VBTEACl)

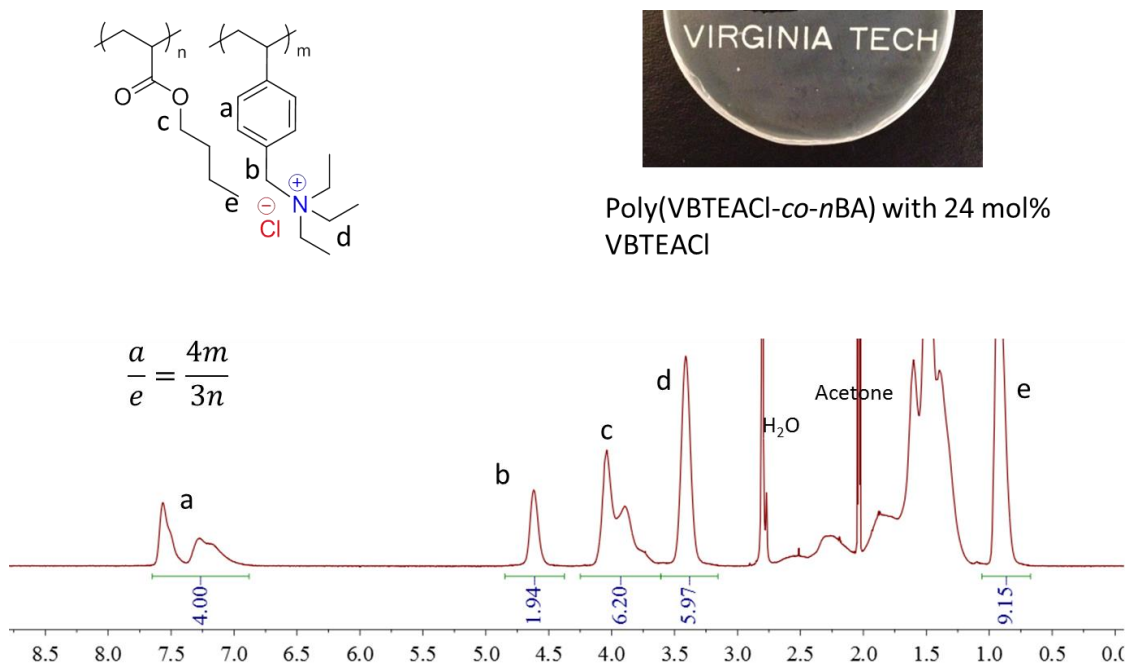


**Figure S8.5.**  $^1\text{H}$  NMR spectrum and the solution-cast film of poly(VBTEACl-*co*-*n*BA) with 24 mol% VBTEACl.

**Table S8.2.** Ionic monomer in feed and in polymer for poly(VBTEACl-*co*-*n*BA)s.

| Poly(VBTEACl- <i>co</i> - <i>n</i> BA) |               |              |
|--|---------------|--------------|
| Feed mol%                              | Observed mol% | Observed wt% |
| 3                                      | 3             | 6            |
| 9                                      | 11            | 19           |
| 17                                     | 24            | 39           |
| 33                                     | 48            | 64           |

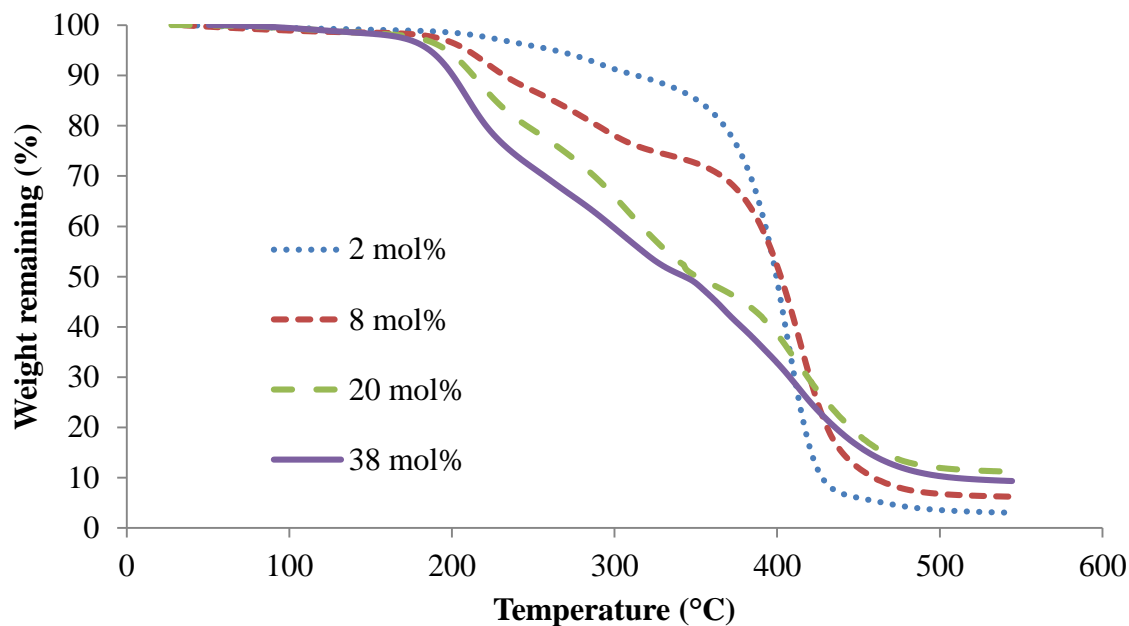
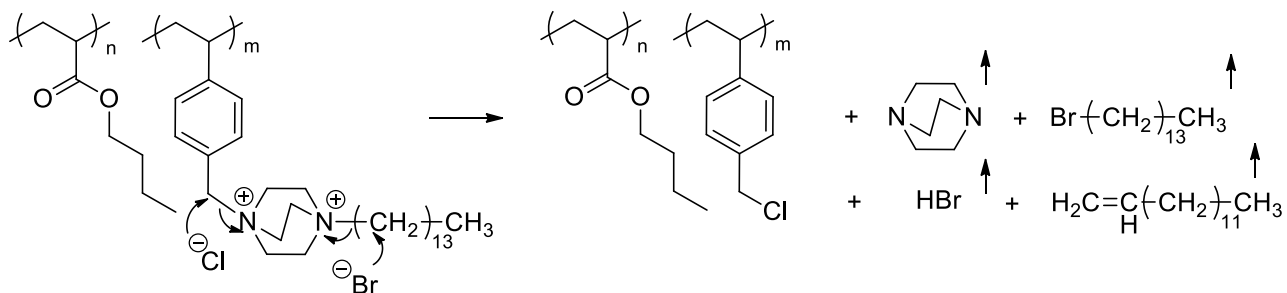


**Figure S8.6.** TGA traces of poly(VBDC<sub>14</sub>BrCl-*co-n*BA)s with varying ionic monomer concentrations.



**Scheme S8.3.** Thermal degradation of poly(VBDC<sub>14</sub>BrCl-*co-n*BA)s through a nucleophilic substitution mechanism.

**Table S8.3.** 5 wt% loss temperatures and correlation of first weight-loss step of poly(VBDC<sub>14</sub>BrCl-*co-n*BA)s to a nucleophilic substitution degradation pathway.

| VBDC <sub>14</sub> BrCl<br>mol% | T <sub>d</sub><br>(°C)<br>5 wt% | Observed weight-<br>loss 1 <sup>st</sup> step (%) | Theoretical<br>weight-loss 1 <sup>st</sup><br>step Nu(%) | Theoretical<br>weight-loss 1 <sup>st</sup><br>step Hoffman<br>(%) |
|---------------------------------|---------------------------------|---|--|---|
|---------------------------------|---------------------------------|---|--|---|

|    |     |    |    |    |
|----|-----|----|----|----|
| 2  | 262 | 8  | 6  | 4  |
| 8  | 209 | 24 | 21 | 16 |
| 20 | 197 | 43 | 40 | 30 |
| 38 | 186 | 60 | 56 | 41 |

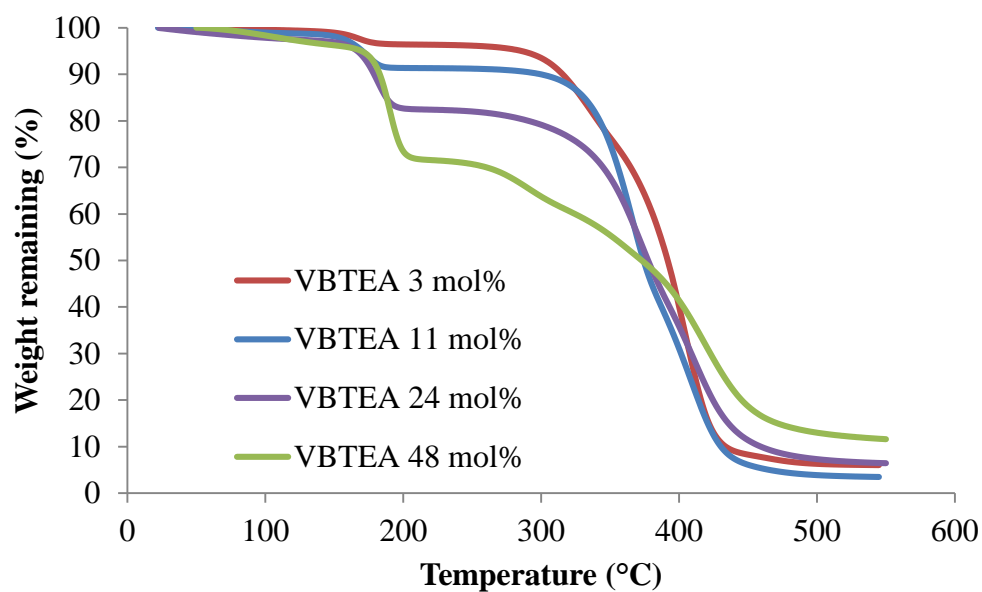
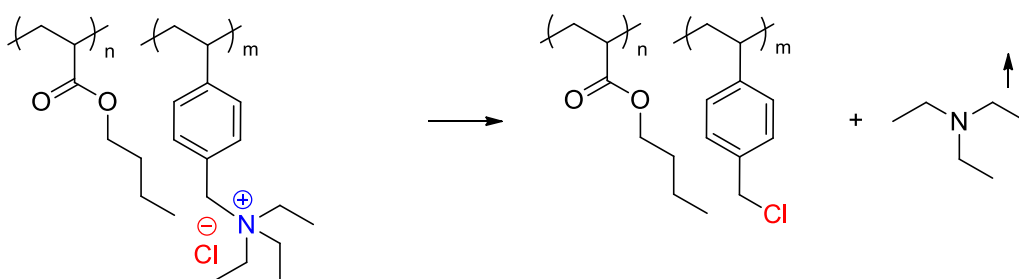


**Figure S8.7.** TGA traces of poly(VBTEACl-*co*-*n*BA)s with varying ionic monomer concentrations.



**Scheme S8.4.** Thermal degradation of poly(VBTEACl-*co*-*n*BA) through a nucleophilic substitution mechanism.

**Table S8.4.** 5 wt% loss temperatures and correlation of first weight-loss step of poly(VBTEACl-*co*-*n*BA)s to a nucleophilic substitution degradation pathway.

| VBTEACl mol%     | T <sub>d</sub> (°C)<br>5 wt% | Observed<br>weight-loss 1 <sup>st</sup><br>step (%) | Theoretical<br>weight-loss 1 <sup>st</sup> step |
|------------------|------------------------------|---|---|
| 3                | 286                          | 3   | 2   |
| 11               | 170                          | 8   | 8   |
| 24               | 167                          | 14  | 14  |
| 48               | 170                          | 25  | 26  |
| 100 <sup>5</sup> | 200                          | 41  | 40  |

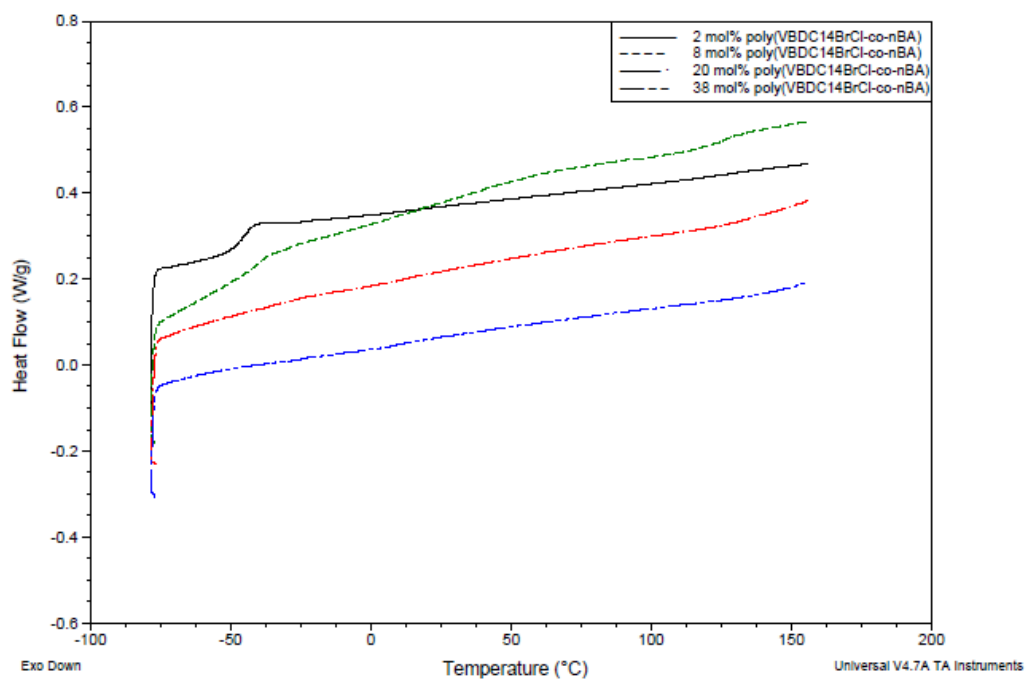


**Figure S8.8.** DSC second heating ramps of poly(VBDC<sub>14</sub>BrCl-*co*-*n*BA)s with varying ionic monomer concentrations.

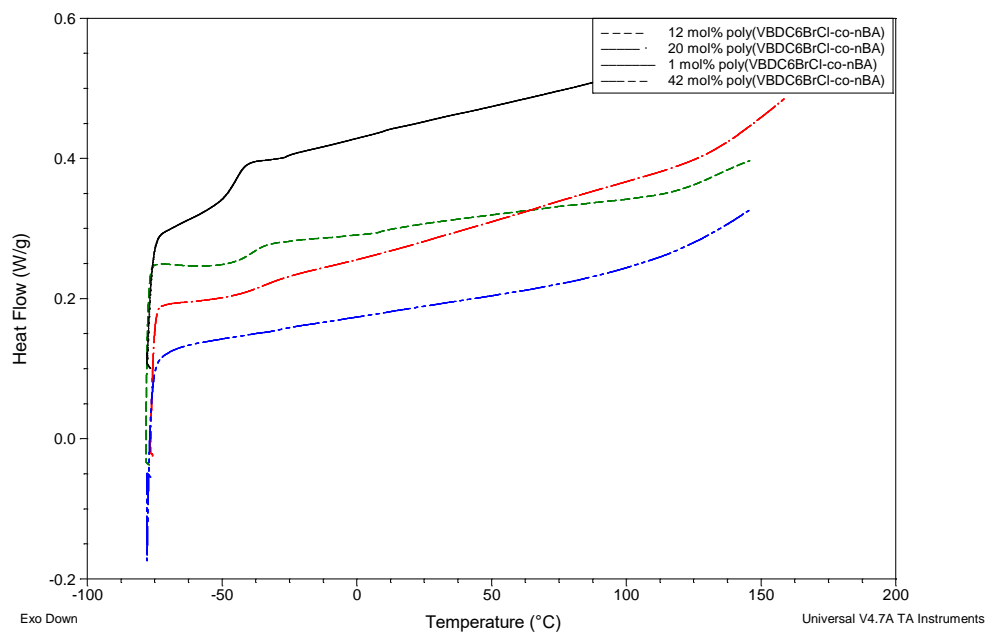


**Figure S8.9.** DSC second heating ramps of poly(VBDC<sub>6</sub>BrCl-*co*-nBA)s with varying ionic monomer concentrations.

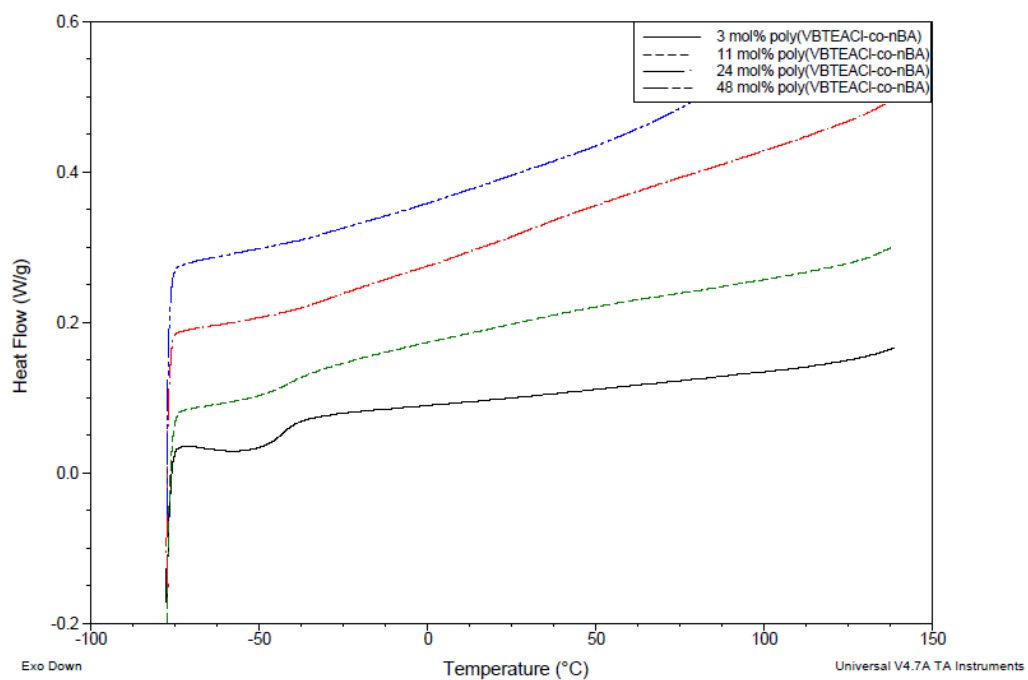


**Figure S8.10.** DSC second heating ramps of poly(VBTEACl-*co*-nBA)s with varying ionic monomer concentrations.

**Table S8.5.** T<sub>g</sub> values of poly(VBDC<sub>14</sub>BrCl-*co*-*n*BA)s, poly(VBDC<sub>6</sub>BrCl-*co*-*n*BA)s, poly(VBTEACl-*co*-*n*BA)s with varying ionic monomer concentrations. ND: not observed.

| Poly(VBDC <sub>6</sub> BrCl- <i>co</i> - <i>n</i> BA) |                     | Poly(VBDC <sub>14</sub> BrCl- <i>co</i> - <i>n</i> BA) |                     | Poly(VBTEACl- <i>co</i> - <i>n</i> BA) |                     |
|---|---------------------|--|---------------------|--|---------------------|
| Ionic monomer mol%                                    | T <sub>g</sub> (°C) | Ionic monomer mol%                                     | T <sub>g</sub> (°C) | Ionic monomer mol%                     | T <sub>g</sub> (°C) |
| 1   | -45                 | 2  | -45                 | 3                                      | -44                 |
| 12  | -39                 | 8  | -40                 | 11                                     | -42                 |
| 20  | -35                 | 20   | ND                  | 24                                     | -36                 |
| 42  | ND                  | 38   | ND                  | 48                                     | ND                  |

## References

1. Cheng, S.; Zhang, M.; Dixit, N.; Moore, R. B.; Long, T. E. *Macromolecules* **2012**, *45*, 805.
2. Cheng, S.; Zhang, M.; Wu, T.; Hemp, S. T.; Mather, B. D.; Moore, R. B.; Long, T. E. *J. Polym. Sci., Part A: Polym. Chem.* **2012**, *50*, 166.
3. Pojman, J. A.; Willis, J.; Fortenberry, D.; Ilyashenko, V.; Khan, A. M. *J. Polym. Sci., Part A: Polym. Chem.* **1995**, *33*, 643.
4. Gauthier, M.; Carrozzella, T.; Snell, G. *J. Polym. Sci., Part B: Polym. Phys.* **2002**, *40*, 2303.
5. Hemp, S. T.; Zhang, M. Q.; Allen, M. H.; Cheng, S. J.; Moore, R. B.; Long, T. E. *Macromol. Chem. Phys.* **2013**, *214*, 2099.



## Chapter 9. Doubly-Charged Random Ionomers with Enhanced Microphase-Separation

*(Submitted to Macromolecules)*

Keren Zhang, Gregory B. Fahs, Kevin J. Drummey, Robert B. Moore, and Timothy E. Long\*

*Department of Chemistry, Macromolecules and Interfaces Institute  
Virginia Tech, Blacksburg, VA 24061, USA*

**Keywords:** DABCO salt, trialkyl ammonium, random ionomers, microphase-separation, ionic interaction, ionic aggregate.

### 9.1 *Abstract*

Two styrenic DABCO salt monomers allowed the synthesis of DABCO salt-containing random copolymers with two quaternized nitrogen cations on each ionic pendant group. Triethyl-(4-vinylbenzyl)ammonium chloride (VBTEACl)-containing random copolymers served as singly-charged controls. DABCO salt-containing copolymers with 20 mol% or lower ionic contents exhibited microphase-separated morphologies, consistent with typical random ionomer morphology. Thermomechanical, morphological, and rheological analyses revealed that doubly-charged DABCO salts promoted more well-defined microphase-separation than singly-charged analogs. Stronger ionic association of DABCO salts compared to trialkyl ammoniums resulted in superior thermomechanical and tensile properties of DABCO salt-containing ionomers. The doubly-charged copolymers exhibited less water uptake per charge than the singly-charged analogs. Anion exchange of the halides to more hydrophobic anions led to enhanced thermal stability, increased phase-mixing, and reduced water uptake for DABCO salt-containing copolymers and their singly-charged controls. Alkyl substituent lengths on the

DABCO salts affected water uptake of DABCO salt-containing copolymers. However, thermomechanical properties and thermal stability did not differ significantly between copolymers with hexyl and tetradecyl substituents.

## 9.2 *Introduction*

Industrial interests in ionomers surged from the 1950s with the commercialization of Dupont's Hypalon<sup>TM</sup> (chlorosulfonated polyethylene) and Surllyn<sup>TM</sup> (poly(ethylene-*co*-methacrylate salt)).<sup>1</sup> Today, ionomers dominate a large market share of elastomers, membranes, resins, coatings, adhesives, and biomedical materials.<sup>2,3</sup> Ionic interactions prove essential for the viscoelastic and mechanical performance of ionomers. Ionic interactions between multiple ion pairs induce the formation of ionic aggregates, which was also known as mutiplets.<sup>4</sup> A region that contains high density of multiplets and ions form an ionic domain with significant ionic association and restricted polymer chain mobility. Dispersing ionic domains into a low  $T_g$  (lower than the application temperature) soft matrix affords flexibility and elastomeric properties for random ionomers. In addition, ionomers with limited or no flexible component serve as thermoplastics. Ionomers typically offer superior processability compared to covalently crosslinked polymers due to reversible ionic interactions. Other physical crosslinking mechanisms such as hydrogen bonding and chain entanglement also contribute to thermo-reversibility, and often serve as a supplementary means for improving mechanical strength due to their weaker association strength than ionic interactions.<sup>2,5,6</sup>

Combining ionic interactions with segmented or block copolymer architectures affords a higher order of microphase-separation and superior physical properties for ionomers, such as ion-containing polyurethanes.<sup>7,8</sup> However, the preparation of segmented

and block copolymers generally requires complex synthetic routes. Thus, random ionomers represent preferential materials for processable thermoplastics and elastomers if the ionic groups induce phase-separation and retain a physically crosslinked network with desirable mechanical performance.<sup>1,2</sup> Furthermore, water uptake and ion transport properties of ionomers enable a wide variety of membrane applications.<sup>9,10</sup> Mechanical integrity and ion/water transport properties of ionomers such as Nafion™ proves essential for their applications as proton exchange membrane (PEM) in fuel cells.<sup>11</sup> Establishing structure-property relationships for novel random ionomers will assist the property optimization of these polymers and determine their potential commercial impacts for various applications.

Recently, an emerging design feature for novel ion-containing polymers involves monomers carrying more than one ionic site.<sup>12-17</sup> These multiply-charged monomers led to superior properties than their singly-charged controls. Li *et al.* synthesized a polyelectrolyte with bis(trialkyl ammonium) acrylate, displaying a lower critical aggregation value and larger aggregate sizes than its singly-charged analog at similar charge concentration.<sup>16</sup> Laschewsky and others reviewed various zwitterion-containing polymers with unique properties.<sup>12,18-20</sup> Many other researchers explored the potential of multiply-charged polyelectrolytes for water treatment, gene delivery, and antimicrobial material.<sup>14,21-24</sup> However, earlier studies focused on multiply-charged polyelectrolytes and their solution properties while multiply-charged ionomers and their solid-state properties remained relatively unexplored. Moreover, the difference between multiply-charged and singly-charged ionic groups demands more comprehensive investigations. Long *et al.* recently reported the synthesis of styrenic monomers that contained quaternized 1,4-diazabicyclo[2.2.2]octane (DABCO) groups (Chapter 8). Copolymerization of *n*-butyl

acrylate (*n*BA) and styrenic DABCO salt monomers afforded random copolymers with a pair of ammonium cations on each ionic pendant group, the properties of which were compared to singly-charged trialkylammonium-containing random copolymer controls. Previous results demonstrated similar thermal stability and thermal transitions of the DABCO salt-containing copolymer as their singly-charged analogs while thermomechanical properties differed greatly (Chapter 8).

This manuscript provides an anion exchange strategy to enhance the thermal stability of DABCO salt-containing copolymers, and detailed investigations to examine their physical properties. Varying ionic contents, counterion types, and alkyl substituent lengths of DABCO salt-containing copolymers afforded mechanically robust ionomers with tunable properties and morphologies. A series of characterizations established structure-morphology-property relationships of DABCO salt-containing copolymers and their singly-charged analogs, which included thermomechanical, rheological, morphological, moisture sorption, and tensile analyses. This study reports unprecedented well-defined microphase-separation of random ionomers that contain doubly-charged cationic pendant groups. Furthermore, systematic investigations compared, for the first time, the effects of doubly-charged and singly-charged monomer incorporations on the solid-state properties of random ionomers.

### 9.3 *Experimental Section*

**Materials.** Sodium tetrafluoroborate (NaBF<sub>4</sub>, 98%), bis(trifluoromethane)sulfonimide lithium (Li-Tf<sub>2</sub>N), and silver nitrate were purchased from Aldrich and used without further purification. Ethyl acetate (EtOAc, HPLC grade), chloroform (CHCl<sub>3</sub>, HPLC grade),

acetone (HPLC grade), methanol (MeOH, HPLC grade) were obtained from Spectrum and used as received.

**Analytical Methods.** Polymers were dissolved in methanol or acetone and casted into PTFE Petri dishes. The solutions were maintained at room temperature for 24 h to allow solvent evaporation, placed in *vacuo* for 24 h at room temperature, and finally at 40 °C in *vacuo* for 24 h. All film samples remained in a desiccator prior to any experiment. Dynamic mechanical analysis (DMA) utilized a TA Instruments Q800 Dynamic Mechanical Analyzer in tension mode at a frequency of 1 Hz, oscillatory amplitude of 15  $\mu$ m, and a static force of 0.01 N. The temperature ramp was 3 °C/min. The peak maxima of tan delta curves determined  $T_g$  values. A Veeco MultiMode scanning probe microscope provided atomic force microscopy (AFM) images using the tapping-mode. Samples were imaged with Veeco's Nanosensor silicon tips, spring constant of 42 N. The set-point ratio was approximately 0.7.

A TA Instruments Q5000 thermogravimetric sorption analyzer (TGA-SA) probed the water sorption behavior of ammonium-containing copolymer samples using a relative humidity (RH) sweep procedure from 0 – 95% RH with 5% increase in each step. Each RH step proceeded until the sample weight equilibrated (<0.01% change over 10 min). An instrumental pre-drying method at 50 °C and 0% RH was applied to each sample until the sample weight equilibrated before the experiment. Water uptake per charge ( $\lambda$ ) was calculated based on the weight gain of each sample as a function of initial weight and charge density. An Instron 5500R universal testing instrument characterized tensile properties of the solution-cast DABCO-containing copolymer films at a crosshead speed

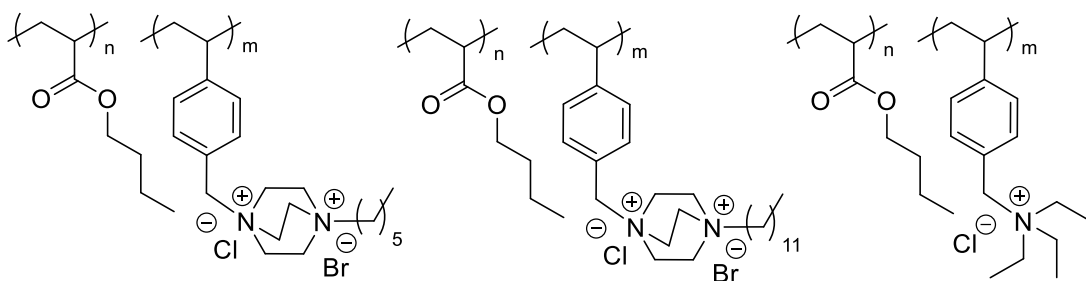
of 50 mm/min. Tensile analysis results represented an average of five specimens with calculated standard deviations.

A TA Instruments Discovery AR-G2 rheometer provided rheological analysis for ammonium-containing copolymers with relatively low ionic contents using disposable aluminum parallel plates of 8 mm in diameter. All measurements were strain-controlled at constant nominal strain values within the linear viscoelastic region, as determined using strain sweep experiments. Dynamic oscillatory frequency sweep experiments were performed at temperature steps from -40 °C to 150 °C with a 10 °C interval. The storage modulus ( $G'$ ) and loss modulus ( $G''$ ) as a function of frequency curves for different temperatures were shifted to partially overlap. Horizontal shifts with shifting factors generated pseudo-master curves from the temperature/frequency sweep measurements using time-temperature superposition (TTS).  $G'$  and  $G''$  curves were both fitted in the range of -40 to 100 °C to generate the shift factors ( $a_T$ ).  $G''$  was used as the reference for the fitting above 100 °C. Shift factors near polymer  $T_g$  (-40 to 50 °C) were fitted to the Williams-Landel-Ferry equation. Shift factors above 100 °C were fitted to the Arrhenius equation.

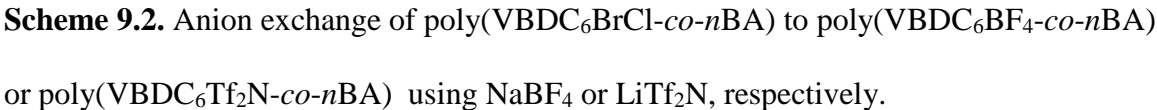
SAXS experiments were performed using a Rigaku S-Max 3000 3 pinhole SAXS system, equipped with a rotating anode emitting X-ray with a wavelength of 0.154 nm (Cu  $K\alpha$ ). The sample-to-detector distance was 1603 mm, and the  $q$ -range was calibrated using a silver behenate standard. Two-dimensional SAXS patterns were obtained using a fully integrated 2D multiwire, proportional counting, gas-filled detector with an exposure time of 2 h. All SAXS data were analyzed using the SAXSGUI software package to obtain

radially integrated SAXS intensity *versus* scattering vector  $q$ , where  $q = (4\pi/\lambda)\sin(\theta)$ ,  $\theta$  is one half of the scattering angle and  $\lambda$  is the wavelength of X-ray.

**Anion Exchange of DABCO Salt-Containing Copolymers.** *N*-4VinylBenzyl-*N'*-alkyl DABCO BrCl (VBDC<sub>*x*</sub>BrCl) monomers and copolymers were synthesized as reported in Chapter 8. Triethyl-(4-vinylbenzyl)ammonium chloride (VBTEACl) and the copolymers was prepared according to Long *et al.*<sup>25</sup> A typical anion exchange experiment was conducted as follows (Scheme 9.2): 0.5 g copolymer (0.45 mmol of DABCO salt) was dissolved in 5 mL methanol and added dropwise to a solution of NaBF<sub>4</sub> (0.49 g, 4.5 mmol) in 50 mL MeOH. A white precipitate formed, and the heterogeneous solution was stirred overnight. The precipitate was filtered from the solvent, washed thoroughly with deionized water, and dried in *vacuo*. Silver nitrate solution (1 M) was used to confirm absence of halide counterions. <sup>1</sup>H NMR spectroscopy confirmed the compositions of DABCO salt-containing copolymers after anion exchange experiments.



**Scheme 9.1.** Chemical structures of poly(VBDC<sub>6</sub>BrCl-*co*-*n*BA), poly(VBDC<sub>14</sub>BrCl-*co*-*n*BA), and poly(VBTEACl-*co*-*n*BA) random copolymers.



**Thermal properties.** Previous thermal analysis revealed that thermal degradation of DABCO salt-containing copolymers initiated from dequaternization of the ammonium cations near 180 °C. Anion exchange of the halides to more hydrophobic anions such as  $\text{Tf}_2\text{N}^-$  and  $\text{BF}_4^-$  contributed to higher degradation onsets for DABCO salt-containing copolymers at approximately 270 °C (Figures S9.1,S9.2). Literature widely acknowledges the effect of counterions on thermal stability of ammonium-containing polymers.<sup>26-28</sup> Bulkier anions such as  $\text{Tf}_2\text{N}^-$  and  $\text{BF}_4^-$  are less nucleophilic than halides due to the delocalization of the negative charges and steric effect, which inhibits dequaternization through nucleophilic substitution or Hofmann elimination. Anion-exchanged DABCO salt-containing copolymers with  $\text{Tf}_2\text{N}^-$  and  $\text{BF}_4^-$  showed higher  $T_{d,5 \text{ wt}\%}$  values compared to their precursors with halides (Tables S9.1,S9.2). TGA experiments of singly-charged controls also exhibited enhanced thermal stability after anion exchange to  $\text{Tf}_2\text{N}^-$  and  $\text{BF}_4^-$  (Figure S9.3, Table S9.1). DSC thermograms of DABCO salt-containing copolymers agreed well with the thermal properties of typical microphase-separated ionomers. DSC detected a single  $T_g$  ranging from -45 °C to -36 °C for each DABCO salt-containing copolymer with



less than 21 mol% ionic content, which corresponded to glass transition of the neutral soft phase. Lack of detectable glass transition for the anion-exchanged DABCO salt-containing copolymers indicated more phase-mixing. The singly-charged controls exhibited similar thermal transitions.

**Thermomechanical properties.** Figure 9.1 depicts uniaxial storage modulus and tan delta curves over a temperature ramp for poly(VBDC<sub>6</sub>BrCl-*co-n*BA) with 12 or 20 mol% of VBDC<sub>6</sub>BrCl and poly(VBTEACl-*co-n*BA) with 11 or 24 mol% of VBTEACl. DMA modulus curves of poly(VBDC<sub>6</sub>BrCl-*co-n*BA) each contained a well-defined plateau between the glass transition of the soft phase and the terminal flow region, which suggested significant phase-separation of the ionic domains and the soft domains.<sup>2,29</sup> The temperature windows of these plateaus proved longer than 100 °C and more well-defined than other random ionomers previously reported in literature.<sup>20,29,30</sup> The plateau moduli increased from 20 MPa to 140 MPa, and the flow temperature increased from 135 °C to 157 °C with increasing DABCO salt content. Ionic interactions of the DABCO salts provided multifunctional, electrostatic crosslinking and affected the moduli of the plateau region and the flow temperatures.<sup>29</sup> Tan delta curves of poly(VBDC<sub>6</sub>BrCl-*co-n*BA) with 12 and 20 mol% of VBDC<sub>6</sub>BrCl reached maxima at -17 °C and -7 °C (Table 9.1), respectively. This relatively small T<sub>g</sub> increase originated from partial phase-mixing between the polynBA phase and the ionic phase, which agreed with the T<sub>g</sub> measurements from DSC. This mild T<sub>g</sub> increment (ca. 0.8 °C/mol%) was similar to reported zwitterion-containing random ionomers and smaller than singly-charged ionomers, which suggested higher degree of phase-separation of DABCO salt-containing ionomers than the singly-charged ones.<sup>31-33</sup>

The intensity of tan delta peaks also decreased with increasing ionic content due to decreasing volume percentage of the soft phase.<sup>33</sup>

Narrower or no plateau window on the modulus curves of poly(VBTEACl-*co-n*BA) indicated more phase-mixing compared to the DABCO salt films. The modulus of poly(VBTEACl-*co-n*BA) with 11 mol% VBTEA gradually decreased in a single step, and the one with 24 mol% VBTEA contained a plateau approximately 60 °C narrower than poly(VBDC<sub>6</sub>BrCl-*co-n*BA) with similar extent of ionic monomer incorporation. The flow temperatures of the singly-charged controls also proved significantly lower than DABCO salt copolymers with similar ionic content. The temperature range of a plateau window from DMA directly relates to the available service temperature range of a thermoplastic material.<sup>5,34</sup> Higher flow temperatures offer better heat resistance before losing mechanical integrity. DABCO salt monomers proved more efficient than singly-charged monomers in enhancing the thermomechanical properties of an ion-containing random ionomer. More importantly, copolymers containing DABCO salt exhibited better phase-separation than singly-charged analogs with the same charge density. Because each DABCO salt monomer incorporates two ammonium cations, poly(VBDC<sub>6</sub>BrCl-*co-n*BA) with 12 mol% VBDC<sub>6</sub>BrCl and poly(VBTEACl-*co-n*BA) with 24 mol% VBTEA contained the same charge density along their neutral polymer chains. In Figure 9.1, the wider plateau temperature window, higher flow temperature, and lower plateau modulus of poly(VBDC<sub>6</sub>BrCl-*co-n*BA) demonstrated the presence of more well-defined phase-separation compared to poly(VBTEACl-*co-n*BA) with the same charge density. This comparison revealed that each DABCO salt unit afforded a stronger ionic interaction than did two triethylammonium groups, which presumably resulted from the unique structure

of DABCO salt. On a DABCO salt unit, the spatial restraint arising from the bridged structure of three ethylene substituents likely minimized the screening effects of the alkyl chains on the charged center.

Similar thermomechanical properties of DABCO salt-containing ionomer films with tetradecyl and hexyl substituents demonstrated that alkyl chain length did not significantly affect the ionic interactions (Figure S9.4). Long *et al.* previously observed a different phenomenon where trioctyl phosphonium exhibited significantly weaker ionic association than tributyl phosphonium from DMA results for random copolymers.<sup>35</sup> This different effect of alkyl chain length on DABCO salts and trialkyl phosphoniums possibly resulted from the different extents of screening effect from the alkyl substituents.

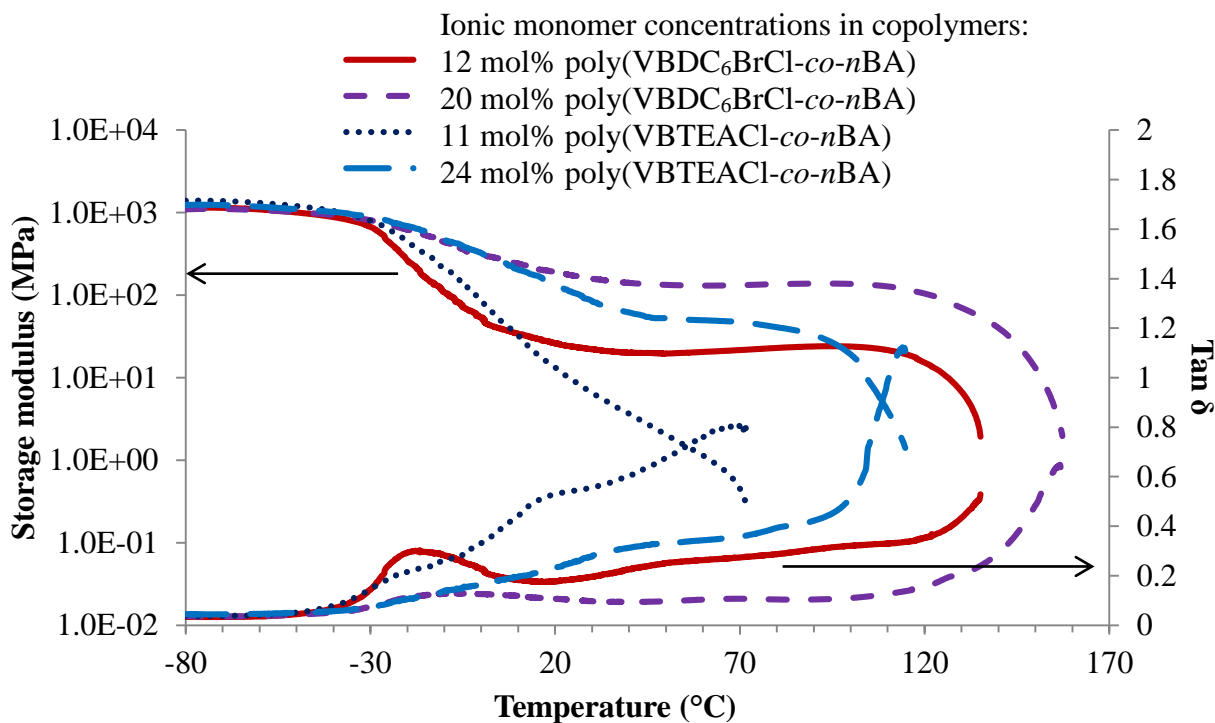


**Figure 9.1.** Dynamic mechanical temperature analysis of poly(VBDC<sub>6</sub>BrCl-*co*-*n*BA) with varied amounts of VBDC<sub>6</sub>BrCl and poly(VBTEACl-*co*-*n*BA) with similar amounts of VBTEACl.

**Table 9.1.**  $T_g$  values and plateau temperature ranges of poly(VBDC<sub>6</sub>BrCl-*co-n*BA) and poly(VBTEACl-*co-n*BA).  $T_g^1$  values are from maxima of peaks on tan delta curves of DMA;  $T_g^2$  values are from the second heating scans of DSC. NO: no observable transition.

| Ionic monomer concentrations in copolymers           | $T_g^1$ (°C) | $T_g^2$ (°C) | $T_{flow}$ (°C) | Plateau (°C) |
|--|--------------|--------------|-----------------|--------------|
| 12 mol% poly(VBDC <sub>6</sub> BrCl- <i>co-n</i> BA) | -17          | -39          | 135             | 110          |
| 20 mol% poly(VBDC <sub>6</sub> BrCl- <i>co-n</i> BA) | -7           | -35          | 157             | 120          |
| 11 mol% poly(VBTEACl- <i>co-n</i> BA)                | -20          | -42          | 72              | NA           |
| 24 mol% poly(VBTEACl- <i>co-n</i> BA)                | NO           | NO           | 115             | 70           |

DMA also investigated the effect of counterions on the thermomechanical properties of DABCO salt-containing copolymers (Figure 9.2). Poly(VBDC<sub>6</sub>BF<sub>4</sub>-*co-n*BA) exhibited more phase-mixing after anion exchange with a broader glass transition and a less well-defined plateau. Poly(VBDC<sub>6</sub>TF<sub>2</sub>N-*co-n*BA) were mainly phase-mixed with a 10 °C wide plateau from the modulus curve and no detectable  $T_g$  from the tan delta curve. Poly(VBDC<sub>14</sub>BF<sub>4</sub>-*co-n*BA) and poly(VBDC<sub>14</sub>TF<sub>2</sub>N-*co-n*BA) displayed similar properties to their counterparts with hexyl substituents (Figure S9.5). The extent of phase-mixing increased with weakening ionic associations, which agreed with the trend of counterion size and charge delocalization: Cl<sup>-</sup>, Br<sup>-</sup> < BF<sub>4</sub><sup>-</sup> < TF<sub>2</sub>N<sup>-</sup>. However, the ionic interactions of DABCO salts with BF<sub>4</sub><sup>-</sup> and TF<sub>2</sub>N<sup>-</sup> proved sufficient to yield plateau windows on their DMA modulus curves, while the singly-charged ammoniums with BF<sub>4</sub><sup>-</sup> and TF<sub>2</sub>N<sup>-</sup> yielded completely phase-mixed copolymers without any plateau window (Figure S9.6). This confirmed stronger ionic associations of DABCO salts relative to the single ammonium controls regardless of counterion types.

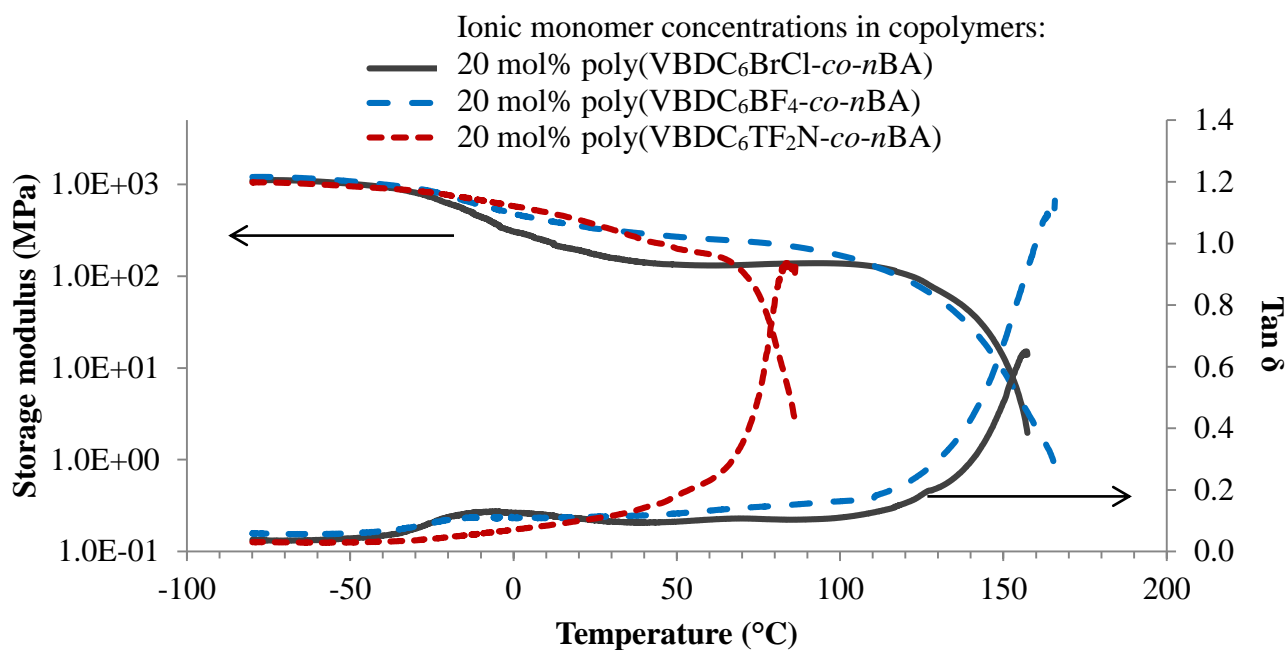


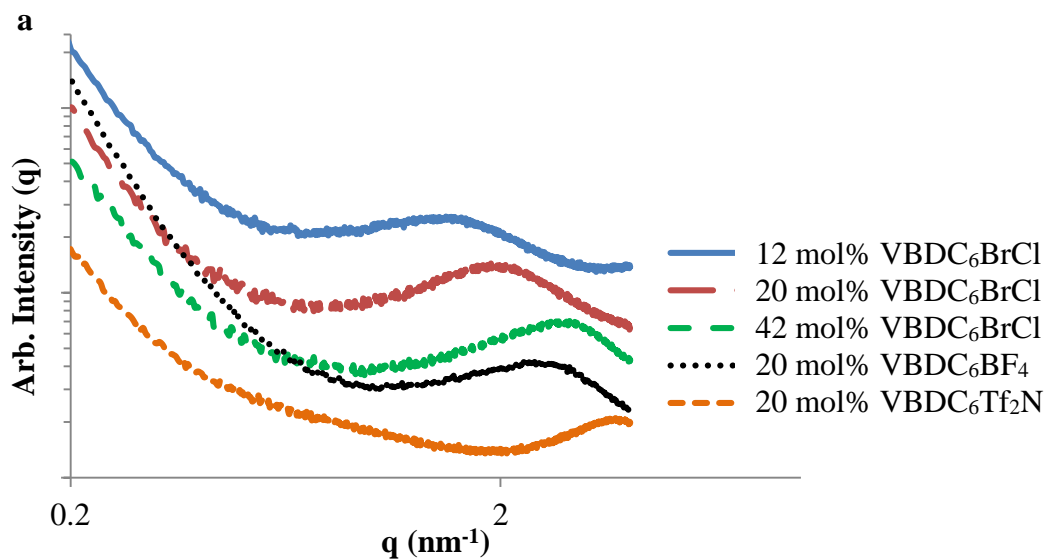
**Figure 9.2.** Dynamic mechanical analysis for poly(VBDC<sub>6</sub>BrCl-*co-n*BA), poly(VBDC<sub>6</sub>BF<sub>4</sub>-*co-n*BA), and poly(VBDC<sub>6</sub>Tf<sub>2</sub>N-*co-n*BA) containing 20 mol% ionic monomers.

**Morphological analysis.** Small angle X-ray scattering (SAXS) elucidated the bulk morphology of DABCO salt-containing copolymers in Figure 9.3ab in comparison to the VBTEA analogs (Figure S9.7). SAXS profiles of DABCO salt-containing copolymers exhibited a relatively broad scattering maxima, indicative of a microphase-separated morphology with a distribution of characteristic dimensions, correlated to the inter-aggregate distances.<sup>4</sup> To further elucidate the morphological features of the ionic domains, the SAXS curves were fit using a liquid-like hard sphere model according to Kinning and Thomas (Table 9.2),<sup>36</sup> following a formulation for the SAXS modeling interference terms (structure factors) defined by Winey *et al.*<sup>37</sup> These fits provided quantitative insight concerning the center-to-center distance between ionic domains and the size of aggregates. The liquid-like hard sphere model describes collections of aggregates with respect to three

principle spatial parameters: the radius of the spherical aggregate ( $R_1$ ), the radius of closest approach ( $R_{ca}$ ), and the average center-to-center aggregate separation ( $2R_{is}$ ). The fitting data in Table 9.2 provided reasonable explanations for the observable trends in Figure 9.3ab. In Figure 9.3a, the  $q$ -value of the scattering maximum for VBD<sub>6</sub>BrCl-containing copolymers increases as the ionic content increases from 12 mol% to 42 mol%. The fitting data for VBD<sub>6</sub>BrCl-containing copolymers suggested that both aggregate size  $R_1$  and average interparticle separation  $R_{is}$  decreased with increasing ion content, consistent with the observed scattering peak shift to higher  $q$ -value. Overall, poly(VBDC<sub>6</sub>BrCl-*co-n*BA) copolymers tended to form a larger number of smaller aggregates that were closer together with higher ion content.

Poly(VBDC<sub>14</sub>BrCl-*co-n*BA) exhibited a different trend with increasing ion content. In Figure 9.3b, the  $q$ -value of the scattering maximum for VBD<sub>14</sub>BrCl-containing polymers remains near  $1.9 \text{ nm}^{-1}$ , independent of varying DABCO salt concentrations from 8 mol% to 38 mol%, more commonly observed for random ionomers with relative high ionic contents.<sup>38,39</sup> The constant  $q$ -value pertained to a nearly constant inter-aggregate dimension with varying ion content. However, the size of the aggregates  $R_1$  significantly increased, accommodating the increased ion content. SAXS profiles of VBDC<sub>14</sub> salt-containing copolymers exhibited sharper scattering peaks compared to VBDC<sub>6</sub> salt-containing copolymers, reflecting the effect of alkyl chain length on the formation of ionic aggregates. Longer alkyl chains likely enhanced mobility of ions and facilitated the formation of aggregates, leading to a narrower distribution of inter-aggregate spacing for poly(VBDC<sub>14</sub>BrCl-*co-n*BA) compared to poly(VBDC<sub>6</sub>BrCl-*co-n*BA).<sup>40,41</sup>

The  $q$ -value at the scattering maximum for copolymer with 20 mol% DABCO salt increased with varying anions from  $\text{Cl}^-$ ,  $\text{Br}^-$  to  $\text{BF}_4^-$  to  $\text{TF}_2\text{N}^-$  in both Figure 9.3a and 9.3b. This was due to size increase and charge density decrease of these associated counterions. Table 9.2 indicated that VBDC<sub>6</sub>-containing copolymer with halide counterions contained smaller aggregates with shorter inter-aggregate distance compared to the copolymer with  $\text{BF}_4^-$ , consistent with the  $q$ -value change. A similar change existed for VBDC<sub>14</sub>-containing copolymer, where the bulkier anion contributed to smaller aggregates with less spacing in between. This phenomenon likely resulted from the dipole-dipole interaction diminishing with bulkier anions, which led to the formation of smaller aggregates.<sup>42</sup> The fitting for samples with  $\text{TF}_2\text{N}^-$  proved inaccurate due to poor agreement between the Kinning and Thomas model and the data.



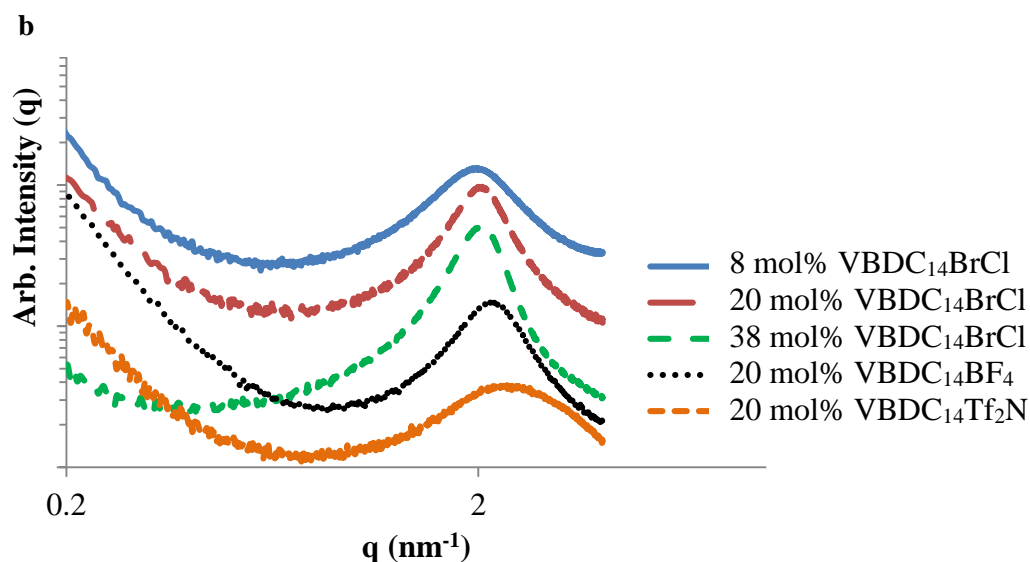


**Figure 9.3.** (a) SAXS of solution-cast poly(VBDC<sub>6</sub>BrCl-*co*-*n*BA), poly(VBDC<sub>6</sub>BF<sub>4</sub>-*co*-*n*BA), and poly(VBDC<sub>6</sub>Tf<sub>2</sub>N-*co*-*n*BA); (b) SAXS of solution-cast poly(VBDC<sub>14</sub>BrCl-*co*-*n*BA), poly(VBDC<sub>14</sub>BF<sub>4</sub>-*co*-*n*BA), and poly(VBDC<sub>14</sub>Tf<sub>2</sub>N-*co*-*n*BA). For clarity, data were shifted by arbitrary factors vertically.

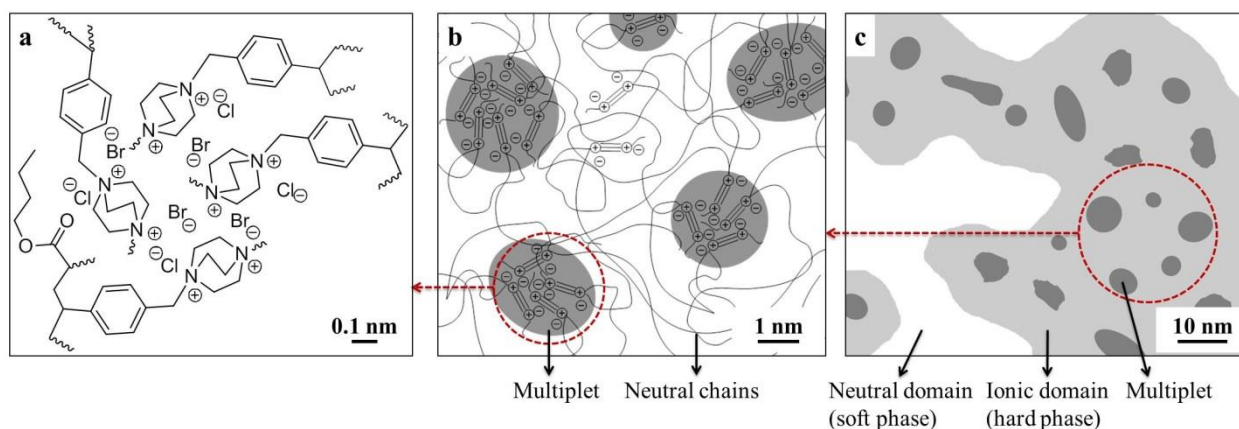
**Table 9.2.** Fitting parameters from the Kinning and Thomas model for SAXS curves of DABCO salt-containing copolymers with various counterions.  $R_1$  represents the radius of the spherical aggregate,  $R_{ca}$  represents the radius of closest approach, and  $2R_{is}$  pertains to the average center-to-center aggregate separation. NA: not accurate.

| Ionic monomer mol%  | $R_1$ (nm)      | $R_{ca}$ (nm)   | $R_{is}$ (nm)  |
|---|-----------------|-----------------|----------------|
| 12 mol% poly(VBDC <sub>6</sub> BrCl- <i>co</i> - <i>n</i> BA)             | $1.11 \pm 0.01$ | $1.76 \pm 0.01$ | $3.76 \pm .05$ |
| 20 mol% poly(VBDC <sub>6</sub> BrCl- <i>co</i> - <i>n</i> BA)             | $0.87 \pm 0.04$ | $1.41 \pm 0.01$ | $2.45 \pm .03$ |
| 42 mol% poly(VBDC <sub>6</sub> BrCl- <i>co</i> - <i>n</i> BA)             | $0.61 \pm 0.04$ | $0.74 \pm 0.07$ | $1.72 \pm .17$ |
| 20 mol% poly(VBDC <sub>6</sub> BF <sub>4</sub> - <i>co</i> - <i>n</i> BA) | $0.56 \pm 0.03$ | $0.98 \pm 0.02$ | $2.14 \pm .05$ |



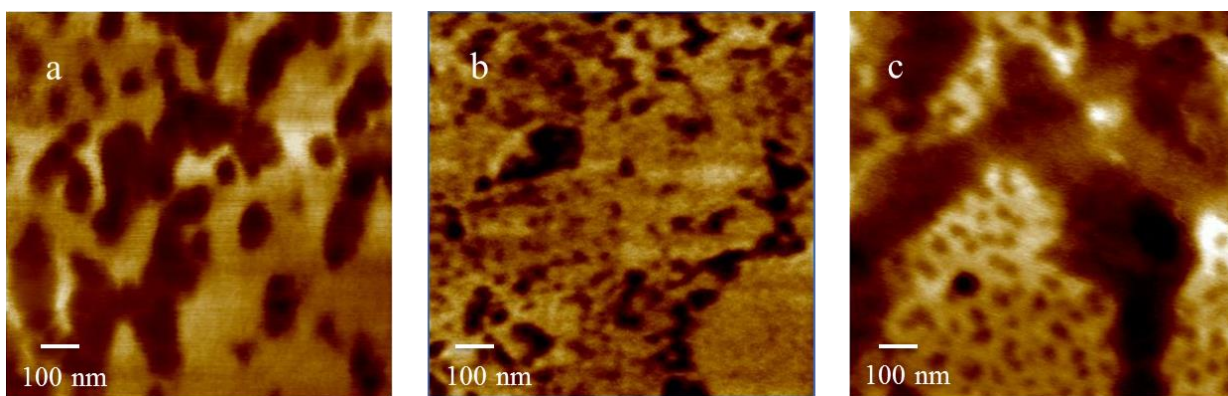
|   |             |             |            |
|---|-------------|-------------|------------|
| 8 mol% poly(VBDC <sub>14</sub> BrCl- <i>co-n</i> BA)              | 0.71 ± 0.01 | 1.53 ± 0.01 | 2.35 ± .01 |
| 20 mol% poly(VBDC <sub>14</sub> BrCl- <i>co-n</i> BA)             | 0.92 ± 0.01 | 1.58 ± 0.01 | 2.19 ± .01 |
| 38 mol% poly(VBDC <sub>14</sub> BrCl- <i>co-n</i> BA)             | 1.00 ± 0.01 | 1.60 ± 0.01 | 2.20 ± .01 |
| 20 mol% poly(VBDC <sub>14</sub> BF <sub>4</sub> - <i>co-n</i> BA) | 0.79 ± 0.01 | 1.44 ± 0.01 | 2.10 ± .01 |

Figure 9.4 depicts the spatial arrangement of DABCO salt units in random copolymers over a range of length scales, agreeing with typical ionomer behavior.<sup>4</sup> Figure 9.4 describes (a) aggregation of ions driven by dipole-dipole (columbic) interactions, (b) spatial arrangement of multiplets, note some ion pairs not able to associate with a specific multiplet, (c) spatial heterogeneity of ionic domains (hard phase) containing a high density of ions and multiplets, dispersed with neutral domains (soft phase).<sup>40</sup> Within a typical aggregate, the number of DABCO salt units ranges from 10 to 60, calculated based on space filling of DABCO salt unit (assuming a volume per unit of  $6.23 \times 10^{-3} \text{ nm}^3$ ) into an aggregate volume of  $V = \frac{4}{3}\pi(R_1)^3$ . The DABCO salt unit was approximated as a sphere with diameter of 0.559 nm, determined using the distance between two carbons adjacent to the two quaternary ammonium cations of the DABCO salt unit in the crystallography data of a di-alkylated DABCO salt.<sup>43</sup>



**Figure 9.4.** Pictorial representation for the intersection of a DABCO salt aggregates, multiplets, and ionic domains of poly(VBDC<sub>x</sub>BrCl-*co*-*n*BA) with halide counterions.

Tapping-mode AFM revealed the surface morphologies of poly(VBDC<sub>6</sub>BrCl-*co*-*n*BA), poly(VBDC<sub>14</sub>BrCl-*co*-*n*BA), and poly(VBTEACl-*co*-*n*BA) with comparable ionic content. Representative AFM phase images in Figure 9.5 showed microphase-separated surface morphology, consistent with the schematic representation of ionic domains (Figure 9.4c) based on the scattering results. The dark areas correspond to the neutral soft phase, and light areas represent the ionic hard phase. The absence of well-ordered domain shape proved the random distribution of ionic pendant groups along polymer chains. The wide distributions of domain size and shape on the surface explained the broad scattering peaks in Figure 9.3. The hard phases of DABCO salt copolymers in Figure 9.5a,b appeared more continuous than that of the singly-charged analog in Figure 9.5c. DABCO salt-containing copolymers exhibited larger area of the hard phase on the surface than their singly-charged analogs with similar ionic contents. This confirmed the previous conclusion that DABCO salts afforded stronger ionic associations than trialkyl ammoniums.



**Figure 9.5.** Tapping mode AFM phase images of (a) poly(VBDC<sub>6</sub>BrCl-*co*-*n*BA) with 20 mol% VBDC<sub>6</sub>BrCl, (b) poly(VBDC<sub>14</sub>BrCl-*co*-*n*BA) with 20 mol% VBDC<sub>14</sub>BrCl, and (c) poly(VBTEACl-*co*-*n*BA) with 24 mol% VBTEACl.

**Rheological analysis.** Time-temperature superposition (TTS) examined the viscoelastic properties of DABCO salt-containing ionomers and their singly-charged analogs with relatively low ionic contents ( $\leq 11$  mol%) over a frequency range of approximately 15 decades (Figure 9.6, S9.8). Frequency sweeps from 0.1-100 rad/s at temperatures ranging from -40 to 150 °C with a 10 °C interval were shifted to generate the pseudo-master curves at 20 °C. All three DABCO salt-containing samples clearly failed time-temperature superposition in the intermediate frequency range from 0.01 to 10 rad/sec. The higher and lower frequency regions, separated by this rheologically complex region, described relaxation of the soft phase and the ionic phase, respectively. The failures of TTS resulted from two different relaxation mechanisms functioning in the same intermediate frequency range. On the contrary, the master curve of singly-charged copolymers with 3 mol% VBTEACl followed TTS principle without obvious deviation (Figure S9.8). Though ionomers generally exhibit rheological complexity, ionomers with relatively low ionic contents and weak ionic interactions do not noticeably deviate from TTS principle if the restricted domains surrounding multiplets are relatively small and isolated. TTS starts to break down significantly at the onset of clustering, when ionic domains become continuous (Figure 9.5).<sup>2,44</sup> Increasing ionic contents and incorporating stronger ionic interactions will both induce clustering due to increasing the number and area of ionic domains, respectively.<sup>44,45</sup> Poly(VBTEACl-*co*-*n*BA) with 11 mol% VBTEACl failed TTS due to increased ionic content. DABCO salt-containing copolymers with less than 3 mol% ionic monomer failed TTS as DABCO salts induced clustering and afforded stronger ionic association than singly-charged ammoniums. Pseudo-master curve of poly(VBTEACl-*co*-

*n*BA) with 11 mol% VBTEACl displayed TTS discrepancy in the low frequency region ( $10^{-5}$ ~ $10^{-2}$  rad/sec), suggesting the co-occurrence of glass transition and ionic interactions in this region. The broad glass transition over a frequency range of nine decades indicated significant phase-mixing, which agreed with the DMA results (Figure 9.1). The different frequency ranges of TTS failures for DABCO salt and VBTEA containing copolymers again proved the higher efficiency of DABCO salts for inducing microphase-separation. DABCO salt-containing ionomers with  $\leq 2$  mol% DABCO salt monomers obeyed the Dahlquist criterion, which ensured tack for pressure sensitive adhesive (PSA) applications. DABCO salt-containing ionomers serve as potential candidates for ionic PSAs, as ionic interactions reinforce the cohesive strength and the low  $T_g$  acrylic matrix provides tack.<sup>46</sup>

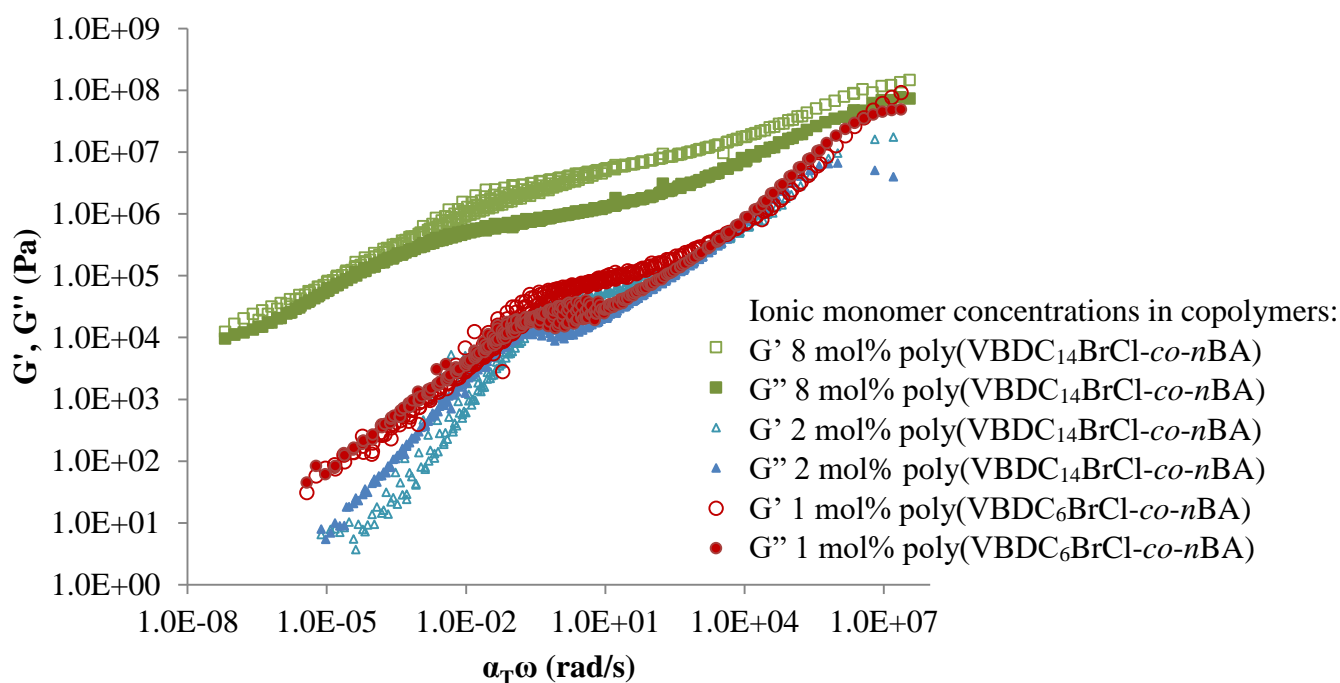


**Figure 9.6.** Rheological pseudo master curves of storage and loss modulus for poly(VBDC<sub>14</sub>BrCl-*co-n*BA) and poly(VBDC<sub>6</sub>BrCl-*co-n*BA) with varied amounts of DABCO salt incorporations.

The pseudo-master curves of DABCO salt-containing copolymers clearly revealed two frequency regions with different relaxation mechanisms. Diffusion dominated the high frequency region near glass transition where TTS shift factors ( $a_T$ ) obeyed the free volume theory. Thus,  $a_T$  values in the temperature range near  $T_g$  followed the WLF equations (1).<sup>47</sup>

$$\log(a_T) = \frac{-C_1(T - T_r)}{C_2 + (T - T_r)} \quad (1)$$

Fittings to equation 1 generated  $C_1$  and  $C_2$  based on the reference temperature  $T_r$ , which was 20 °C (Figure S9).  $C_1$  and  $C_2$  were normalized against  $T_g$  values for each sample using equation (2) and (3), yielding constants  $C_1^g$  and  $C_2^g$  for direct comparisons to literature values.  $C_1^g$  is inversely proportional to polymer fractional free volume at  $T_g$  ( $f_g$ ) in equation (4). The thermal expansion coefficient ( $\alpha_f$ ) relates to  $C_1^g$  and  $C_2^g$  through equation (5). Doolittle and other researchers typically assume  $B=1$ .<sup>48,49</sup> Ionic interaction dominated the low frequency range (high temperature), where shift factors followed the Arrhenius equation (6) to calculate the flow activation energies ( $E_a$ ) (Figure S9.10). Table 9.3 summarizes the WLF constants,  $T_g$  values, and flow activation energies for DABCO salt-containing ionomers and their singly-charged analogs. Rheological complexity prevented WLF and Arrhenius equations from generating proper fit for shift factors in the region where TTS failed. Ferry listed  $C_1^g$  and  $C_2^g$  for many neutral and non-associating polymers, which were regressed to be  $16.79 \pm 5.43$  and  $51.6 \pm 28.1$  K, respectively.<sup>47</sup> These constants prove specific for different polymer types without general correlation across the entire collection.<sup>27,49</sup> Most  $C_1^g$  and  $C_2^g$  values in Table 9.3 occurred within error of neutral polymer constants, as they both characterized the neutral phase of listed ionomers. However, significant phase-mixing of poly(VBTEACl-*co-n*BA) with 11 mol% VBTEA led to deviations of its WLF constants from neutral polymers, as these constants described

a mixed phase with both neutral chains and ionic units. Table 9.3 also revealed a decrease of fractional free volume ( $f_g$ ) and an increase of flow activation energy with increasing ionic content for poly(VBDC<sub>14</sub>BrCl-*co-n*BA) and poly(VBTEACl-*co-n*BA) series. These trends agreed with previous observations from Weiss *et al.* and Eisenberg *et al.*<sup>29,44</sup> The free volume decreased as the residual ionic units in the soft phase densified the matrix. Ionic interactions in the hard phase hindered the flow of polymer chains, resulting in higher flow activation energy for the sample with higher ionic content. DABCO salt-containing ionomers with lower ionic contents exhibited higher flow activation energy compared to their singly-charged analogs, which verified stronger ionic interaction of DABCO salts compared to trialkyl ammoniums.

$$C_1^g = \frac{C_1 C_2}{C_2 + (T_g - T_r)} \quad (2)$$

$$C_2^g = C_2 + (T_g - T_r) \quad (3)$$

$$f_g = \frac{B}{2.303 C_1^g} \quad (4)$$

$$\alpha_f = \frac{B}{2.303 C_1^g C_2^g} \quad (5)$$

$$\log \alpha_f = -\frac{E_a}{RT} \quad (6)$$

**Table 9.3.** WLF constants,  $T_g$  values, and activation energy of flow for DABCO salt-containing copolymers and their single ammonium analogs.

|                           | $C_1$ | $C_2$<br>(K) | $C_1^g$ | $C_2^g$<br>(K) | $T_g$<br>(°C)* | $f_g$ | $\alpha_f (10^{-4} K^{-1})$ | $E_a$<br>(kJ/mol) |
|---------------------------|-------|--------------|---------|----------------|----------------|-------|-----------------------------|-------------------|
| 1 mol% VBDC <sub>6</sub>  | 3.5   | 99.3         | 10.3    | 34.3           | -45            | 0.042 | 12.4                        | 171               |
| 2 mol% VBDC <sub>14</sub> | 3.8   | 101.5        | 10.5    | 36.5           | -45            | 0.041 | 11.3                        | 155               |

|                           |     |       |      |      |     |       |     |     |
|---------------------------|-----|-------|------|------|-----|-------|-----|-----|
| 8 mol% VBDC <sub>14</sub> | 5.3 | 107.5 | 12.0 | 47.5 | -40 | 0.036 | 7.6 | 221 |
| 3 mol% VBTEA              | 7.0 | 141.8 | 12.7 | 77.8 | -44 | 0.034 | 4.4 | 65  |
| 11 mol% VBTEA             | 7.4 | 74.5  | 43.8 | 12.5 | -42 | 0.010 | 7.9 | 103 |

**Tensile properties.** Figure 9.7a,b depicts representative engineering stress-strain curves of DABCO salt-containing copolymers and their singly-charged analogs. Table 9.4 summarizes averaged tensile properties with standard deviations for each sample. Most ionomer films exhibited typical tensile properties for thermoplastics with yield points, except for poly(VBTEACl-*co*-*n*BA) with 11 mol% VBTEACl. Within each ionomer series, Young's modulus increased, stress at break increased, and strain at break decreased as the ionic content increased. Higher ionic content contributed to denser physically crosslinked networks, which resulted in lower extensions and higher moduli. However, similar incorporations of DABCO salts and single ammoniums resulted in drastically different tensile properties. Both Figure 9.7a and 9.7b revealed higher Young's moduli and stresses at break of DABCO salt ionomers compared to their singly-charged analogs with the same mol% of ionic monomers. Ionomer films with 24 mol% VBTEACl and 12 mol% VBDC<sub>6</sub>BrCl exhibited different tensile strengths despite of their similar charge densities. DABCO salt-containing samples exhibited higher moduli and toughness than the single ammonium analogs, which was attributed to stronger ionic interactions of DABCO salts. Tensile results elucidated that DABCO salts provided better mechanical performance for random ionomers than singly-charged analogs with the same charge density, and verified the conclusion that DABCO salts associated stronger than the trialkyl ammoniums. Stress-

strain profiles of DABCO salt-containing copolymers also revealed their potential as thermoplastics with tunable mechanical properties.<sup>2,3</sup>

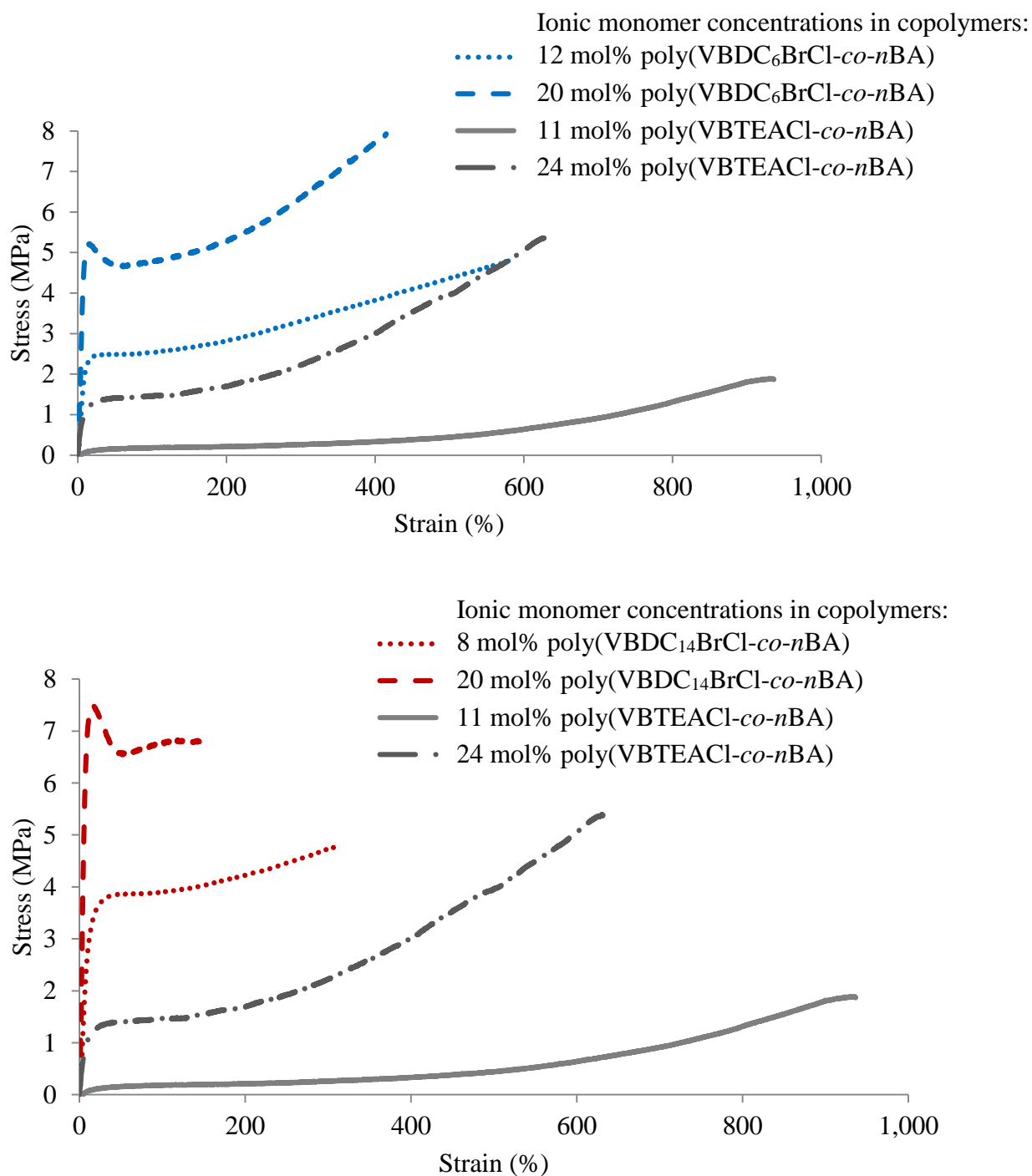


**Figure 9.7.** (a) Stress-strain curves of poly(VBDC<sub>6</sub>BrCl-*co*-*n*BA) and poly(VBTEACl-*co*-*n*BA) with varying ionic monomer concentrations. (b) Stress-strain curves of



poly(VBDC<sub>14</sub>BrCl-*co-n*BA) and poly(VBTEACl-*co-n*BA) with varying ionic monomer concentrations.

**Table 9.4.** Tensile testing results of poly(VBDC<sub>6</sub>BrCl-*co-n*BA), poly(VBDC<sub>14</sub>BrCl-*co-n*BA), and poly(VBTEACl-*co-n*BA) with varying ionic monomer concentrations.

\*Toughness: integrations of the areas under stress-strain curves.

| Ionic monomer concentrations       | Young's modulus (MPa) | Yield stress (MPa)<br>Yield strain (%) | Stress at break (MPa) | Strain at break (%) | Toughness (MPa) |
|------------------------------------|-----------------------|--|-----------------------|---------------------|-----------------|
| 8 mol%<br>VBDC <sub>14</sub> BrCl  | 40 ± 4                | 4 ± 0, 25 ± 5                          | 5 ± 0                 | 284 ± 25            | 12 ± 1          |
| 20 mol%<br>VBDC <sub>14</sub> BrCl | 120 ± 10              | 8 ± 1, 16 ± 3                          | 7 ± 1                 | 122 ± 29            | 9 ± 1           |
|                                    |                       |  |                       |                     |                 |
| 12 mol%<br>VBDC <sub>6</sub> BrCl  | 29 ± 6                | 2 ± 0, 12 ± 1                          | 4 ± 1                 | 610 ± 39            | 20 ± 1          |
| 20 mol%<br>VBDC <sub>6</sub> BrCl  | 78 ± 17               | 5 ± 1, 9 ± 1                           | 7 ± 1                 | 368 ± 42            | 21 ± 3          |
|                                    |                       |  |                       |                     |                 |
| 11 mol%<br>VBTEACl                 | 0.5 ± 0.1             | NA                                     | 2 ± 0                 | 1026 ± 78           | 6 ± 0           |
| 24 mol%<br>VBTEACl                 | 13 ± 3                | 1.4 ± 0.2, 0.4 ± 0.1                   | 5 ± 1                 | 561 ± 79            | 14 ± 3          |

**Water sorption.** Moisture generally proves detrimental to the mechanical performance of ionomers, as it screens ionic interactions and swells ionic aggregates.<sup>50</sup> Water also serves as a solvent or an additive for ion-containing polymers to enhance conductivity.<sup>51,52</sup> Thermogravimetric sorption analysis (TGASA) probed the water uptake of both DABCO salt-containing copolymers and their singly-charged analogs at 25 °C. Figure 9.8 compares the equilibrium water uptake per charge ( $\lambda$ ) at each relative humidity (RH) in the range of 0 % to 95 %. Each data point of the weight gain was normalized against the concentration of ammonium cations (one for VBTEA, two for DABCO salt) in

the copolymers to calculate the  $\lambda$  values.  $\lambda$  values proved constant for each series of ammonium-containing copolymers and homopolymers, independent of ionic monomer concentration (Figure S9.11-S9.13). The curves of  $\lambda$  in relation to RH exhibited sigmoidal shapes similar to results from Kutsumizu *et al.*<sup>9</sup> Slow increase of  $\lambda$  at low relative humidity (RH<70%) indicated a Langmuir-type sorption profile, where water was absorbed onto ionic groups in the amorphous region and at the ionic cluster surfaces.<sup>9</sup> The slope started to increase above 70% RH, suggesting water absorption into the ionic clusters. DABCO salt-containing copolymers exhibited much lower water uptakes per charge compared to their single ammonium analogs (Table 9.5), likely due to better phase-separation and higher physical crosslinking density.<sup>50</sup> DABCO salt-containing copolymers with tetradecyl substituents absorbed slightly less water than the ones with hexyl substituents, due to the hydrophobicity increase with increasing alkyl length. Water uptake per charge decreased significantly after anion exchanging halides to  $\text{Tf}_2\text{N}^-$  due to increased hydrophobicity.

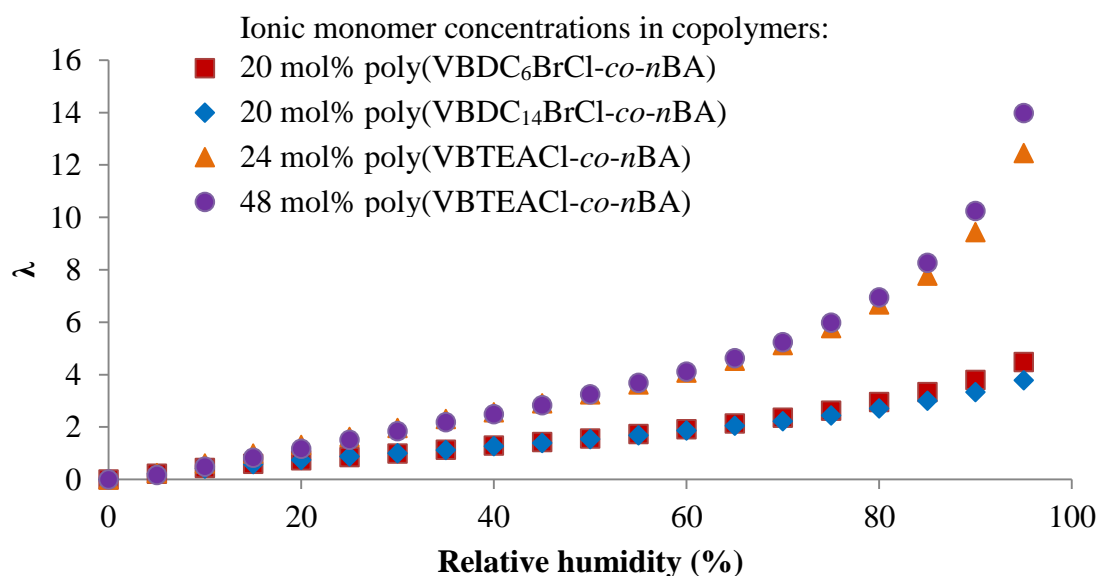


**Figure 9.8.** Water uptake per charge of poly(VBDC<sub>6</sub>BrCl-*co-n*BA), poly(VBDC<sub>14</sub>BrCl-*co-n*BA), and poly(VBTEACl-*co-n*BA) at a range of relative humidity.

**Table 9.5.** Water uptake per charge of poly(VBDC<sub>6</sub>-*co*-*n*BA), poly(VBDC<sub>14</sub>-*co*-*n*BA), and poly(VBTEA-*co*-*n*BA) at 95% relative humidity.

| $\lambda$ (H <sub>2</sub> O uptake per charge) | VBTEA | VBDC <sub>6</sub> | VBDC <sub>14</sub> |
|--|-------|-------------------|--------------------|
| Halide   | 14.0  | 4.5               | 3.8                |
| Tf <sub>2</sub> N                              | 1.2   | 1.8               | 0.9                |

## 9.5 *Conclusions*

Facile monomer synthesis and free radical polymerization yielded two series of DABCO salt-containing random ionomers with hexyl and tetradecyl substituents. Trialkyl ammonium-containing random ionomers with similar mol% ionic monomer and similar charge density served as controls to elucidate different effects from DABCO salts and single ammoniums on ionomers. Thermal analysis demonstrated similar thermal properties of DABCO salt-containing copolymers and their singly-charged analogs, agreeing with common ammonium-containing polymers. Anion exchange of halides to more hydrophobic anions enhanced thermal stability of both DABCO salt-containing copolymers and the controls. Solution-cast DABCO salt ionomers formed free-standing films with microphase-separated morphologies. Thermomechanical, morphological, rheological, and tensile analyses revealed stronger ionic interaction of DABCO salts than trialkyl ammoniums in forming random ionomers. Incorporating DABCO salts into random ionomers proved more efficient in creating physical crosslinking and inducing microphase-separation than using single ammonium salts with the same charge density. In addition, DABCO salt-containing copolymers exhibited much lower water uptake per charge than singly-charged analogs. Hydrophobic anions such as BF<sub>4</sub><sup>-</sup> and Tf<sub>2</sub>N<sup>-</sup> weakened

ionic interactions compared to halides, resulting in more phase-mixing and less water uptake. Comparisons of DABCO salt-containing ionomers with hexyl and tetradecyl substituents illustrated that alkyl substituent lengths did not significantly affect the ionic interaction, opposed to the behavior seen in trialkyl ammonium/phosphonium salts. However, the alkyl substituents influenced the solubility and water uptake of DABCO salt-containing monomers and polymers.

## 9.6 *Acknowledgements*

This research was supported in part by the U.S. Army Research Laboratory and the U.S. Army Research Office under Contract/Grant W911NF-07-1-0452, Ionic Liquids in Electro-Active Devices Multidisciplinary University Research Initiative (ILEAD MURI). Additionally, this work was supported in part by Henkel Corporation. We also thank insightful discussions with Dr. Charles Paul, Dr. Eric Silverberg, and Dr. Christina DeJesus from Henkel. This material is also partially based upon work supported by the National Science Foundation under Grant No. DMR-0923107.

## 9.7 *References*

1. Lundberg, R. D. In *Structure and Properties of Ionomers*; Pineri, M., Eisenberg, A., Eds.; Springer Netherlands: 1987; Vol. 198, p 429.
2. Tant, M. R.; Mauritz, K. A.; Wilkes, G. L. *Ionomers: synthesis, structure, properties, and applications*; Blackie Academic & Professional: New York; London, 1997.
3. Bagrodia, S.; Mohajer, Y.; Wilkes, G.; Storey, R.; Kennedy, J. *Polym. Bull.* **1983**, 9, 174.
4. Eisenberg, A.; Hird, B.; Moore, R. B. *Macromolecules* **1990**, 23, 4098.
5. Zhang, K.; Aiba, M.; Fahs, G. B.; Hudson, A. G.; Chiang, W. D.; Moore, R. B.; Ueda, M.; Long, T. E. *Polym. Chem.* **2015**, 6, 2434.
6. Schalley, C.; Editor *Analytical Methods in Supramolecular Chemistry*; Wiley-VCH Verlag GmbH & Co. KGaA, 2007.
7. Nelson, A. M.; Long, T. E. *Macromol. Chem. Phys.* **2014**, 215, 2161.
8. Gao, R.; Zhang, M.; Wang, S.-W.; Moore, R. B.; Colby, R. H.; Long, T. E. *Macromol. Chem. Phys.* **2013**, 214, 1027.

9. Kutsumizu, S.; Nagao, N.; Tadano, K.; Tachino, H.; Hirasawa, E.; Yano, S. *Macromolecules* **1992**, *25*, 6829.
10. Bazuin, C. G.; Eisenberg, A. *J. Chem. Educ.* **1981**, *58*, 938.
11. Hickner, M. A.; Ghassemi, H.; Kim, Y. S.; Einsla, B. R.; McGrath, J. E. *Chem. Rev.* **2004**, *104*, 4587.
12. Laschewsky, A. *Polymers* **2014**, *6*, 1544.
13. Xuan, F.; Liu, J. *Polym. Int.* **2009**, *58*, 1350.
14. Dizman, B.; Elasri, M. O.; Mathias, L. J. *J. Appl. Polym. Sci.* **2004**, *94*, 635.
15. Losada, R.; Wandrey, C. *Macromolecules* **2009**, *42*, 3285.
16. Li, R.; Wei, L.; Hu, C.; Xu, C.; Wang, J. *The Journal of Physical Chemistry B* **2010**, *114*, 12448.
17. Lall, S.; Behaj, V.; Mancheno, D.; Casiano, R.; Thomas, M.; Rikin, A.; Gaillard, J.; Raju, R.; Scumpia, A.; Castro, S.; Engel, R.; Cohen, J. L. I. *Synthesis* **2002**, 1530.
18. Mi, L.; Jiang, S. *Angew. Chem. Int. Ed.* **2014**, *53*, 1746.
19. Lowe, A. B.; McCormick, C. L. *Chem. Rev.* **2002**, *102*, 4177.
20. Wu, T.; Beyer, F. L.; Brown, R. H.; Moore, R. B.; Long, T. E. *Macromolecules* **2011**, *44*, 8056.
21. Kopchinski, A. F., Kansas State University, 1994.
22. Xue, Y.; Xiao, H.; Zhang, Y. *Int. J. Mol. Sci.* **2015**, *16*, 3626.
23. Tamami, M.; Hemp, S. T.; Zhang, K.; Zhang, M.; Moore, R. B.; Long, T. E. *Polymer* **2013**, *54*, 1588.
24. Tamami, M.; Zhang, K.; Dixit, N.; Moore, R. B.; Long, T. E. *Macromol. Chem. Phys.* **2014**, *215*, 2337.
25. Hemp, S. T.; Zhang, M. Q.; Allen, M. H.; Cheng, S. J.; Moore, R. B.; Long, T. E. *Macromol. Chem. Phys.* **2013**, *214*, 2099.
26. Mecerreyes, D. *Prog. Polym. Sci.* **2011**, *36*, 1629.
27. Ye, Y.; Elabd, Y. A. *Polymer* **2011**, *52*, 1309.
28. Green, M. D.; Salas-de la Cruz, D.; Ye, Y.; Layman, J. M.; Elabd, Y. A.; Winey, K. I.; Long, T. E. *Macromol. Chem. Phys.* **2011**, *212*, 2522.
29. Weiss, R. A.; Fitzgerald, J. J.; Kim, D. *Macromolecules* **1991**, *24*, 1071.
30. Gauthier, M.; Carrozzella, T.; Snell, G. *J. Polym. Sci., Part B: Polym. Phys.* **2002**, *40*, 2303.
31. Eisenberg, A.; King, M. *Ion-containing polymers: physical properties and structure*; Academic Press: New York, 1977; Vol. 2; 2.
32. Gauthier, M.; Eisenberg, A. *Macromolecules* **1990**, *23*, 2066.
33. Ehrmann, M.; Muller, R.; Galin, J. C.; Bazuin, C. G. *Macromolecules* **1993**, *26*, 4910.
34. Zhang, K.; Fahs, G. B.; Aiba, M.; Moore, R. B.; Long, T. E. *Chem. Comm.* **2014**, *50*, 9145.
35. Cheng, S.; Zhang, M.; Wu, T.; Hemp, S. T.; Mather, B. D.; Moore, R. B.; Long, T. E. *J. Polym. Sci., Part A: Polym. Chem.* **2012**, *50*, 166.
36. Kinning, D. J.; Thomas, E. L. *Macromolecules* **1984**, *17*, 1712.
37. Zhou, N. C.; Chan, C. D.; Winey, K. I. *Macromolecules* **2008**, *41*, 6134.
38. Kim, J.-S.; Jackman, R. J.; Eisenberg, A. *Macromolecules* **1994**, *27*, 2789.
39. Jiang, M.; Gronowski, A. A.; Yeager, H. L.; Wu, G.; Kim, J. S.; Eisenberg, A. *Macromolecules* **1994**, *27*, 6541.

40. Moore, R. B.; Gauthier, M.; Williams, C. E.; Eisenberg, A. *Macromolecules* **1992**, 25, 5769.
41. Moore, R. B.; Bittencourt, D.; Gauthier, M.; Williams, C. E.; Eisenberg, A. *Macromolecules* **1991**, 24, 1376.
42. Orler, E. B.; Calhoun, B. H.; Moore, R. B. *Macromolecules* **1996**, 29, 5965.
43. Ishioka, T.; Matsuda, N.; Kitagawa, Y.; Nakamura, K. T. *Bull. Chem. Soc. Jpn.* **2000**, 73, 2725.
44. Eisenberg, A.; Navratil, M. *J. Polym. Sci. [B]* **1972**, 10, 537.
45. Eisenberg, A.; Navratil, M. *Macromolecules* **1974**, 7, 90.
46. Zhang, K.; Long, T. E. US2014/061229 **2015**.
47. Ferry, J. *Viscoelastic properties of polymers*; Wiley: New York, 1980.
48. Doolittle, A. K. *J. Appl. Phys.* **1951**, 22, 1471.
49. Hemp, S. T.; Zhang, M. S.; Tamami, M.; Long, T. E. *Polym. Chem.* **2013**, 4, 3582.
50. Pineri, M.; Eisenberg, A. *Structure and properties of ionomers*; Springer Science & Business Media, 2012; Vol. 198.
51. Siu, A.; Schmeisser, J.; Holdcroft, S. *J. Phys. Chem. B* **2006**, 110, 6072.
52. Khoroushi, M.; Keshani, F. *Dent. Res. J.* **2013**, 10, 411.

## 9.8 Supporting Information

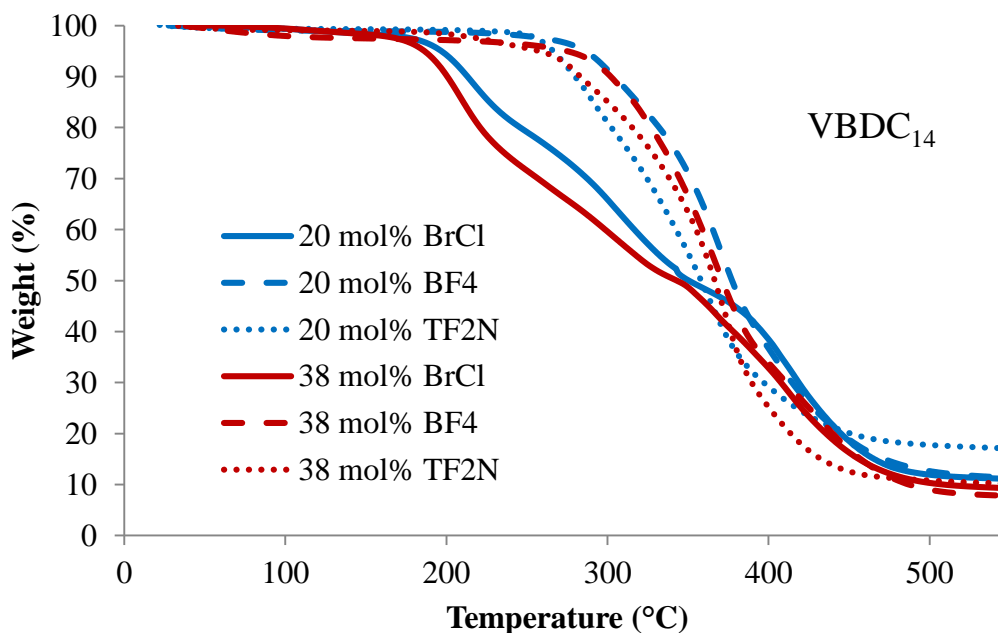


**Figure S9.1.** TGA traces of poly(VBDC<sub>14</sub>BrCl-*co-n*BA)s, poly(VBDC<sub>14</sub>BF<sub>4</sub>-*co-n*BA)s, and poly(VBDC<sub>14</sub>Tf<sub>2</sub>N-*co-n*BA)s with varying ionic monomer concentrations.

**Table S9.1.** 5 wt% loss temperatures of poly(VBDC<sub>14</sub>BrCl-*co-n*BA)s, poly(VBDC<sub>14</sub>BF<sub>4</sub>-*co-n*BA)s, and poly(VBDC<sub>14</sub>Tf<sub>2</sub>N-*co-n*BA)s.

| T <sub>d</sub> (°C) C <sub>14</sub> | BrCl | BF <sub>4</sub> | TF <sub>2</sub> N |
|-------------------------------------|------|-----------------|-------------------|
| 20 mol%                             | 197  | 286             | 266               |
| 38 mol%                             | 186  | 274             | 257               |

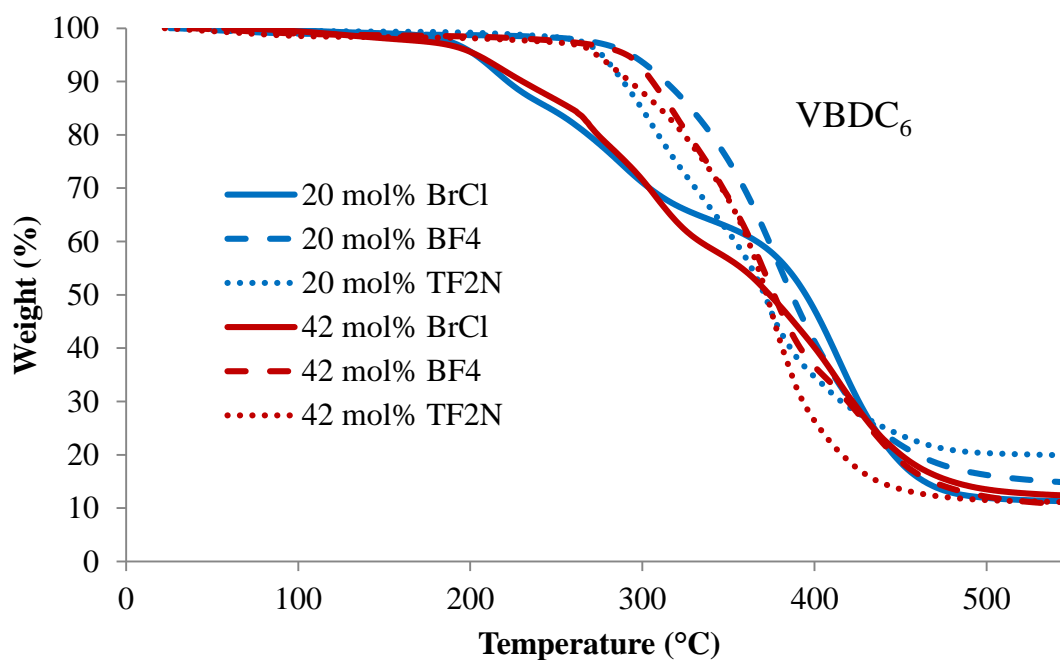


**Figure S9.2.** TGA traces of poly(VBDC<sub>6</sub>BrCl-*co-n*BA), poly(VBDC<sub>6</sub>BF<sub>4</sub>-*co-n*BA), and poly(VBDC<sub>6</sub>Tf<sub>2</sub>N-*co-n*BA) with varying ionic monomer concentrations.

**Table S9.2.** 5 wt% loss temperatures of poly(VBDC<sub>6</sub>BrCl-*co-n*BA)s, poly(VBDC<sub>6</sub>BF<sub>4</sub>-*co-n*BA)s, and poly(VBDC<sub>6</sub>Tf<sub>2</sub>N-*co-n*BA)s.

| T <sub>d</sub> (°C) C <sub>6</sub> | BrCl | BF <sub>4</sub> | TF <sub>2</sub> N |
|------------------------------------|------|-----------------|-------------------|
| 20 mol%                            | 203  | 293             | 276               |
| 42 mol%                            | 204  | 291             | 273               |

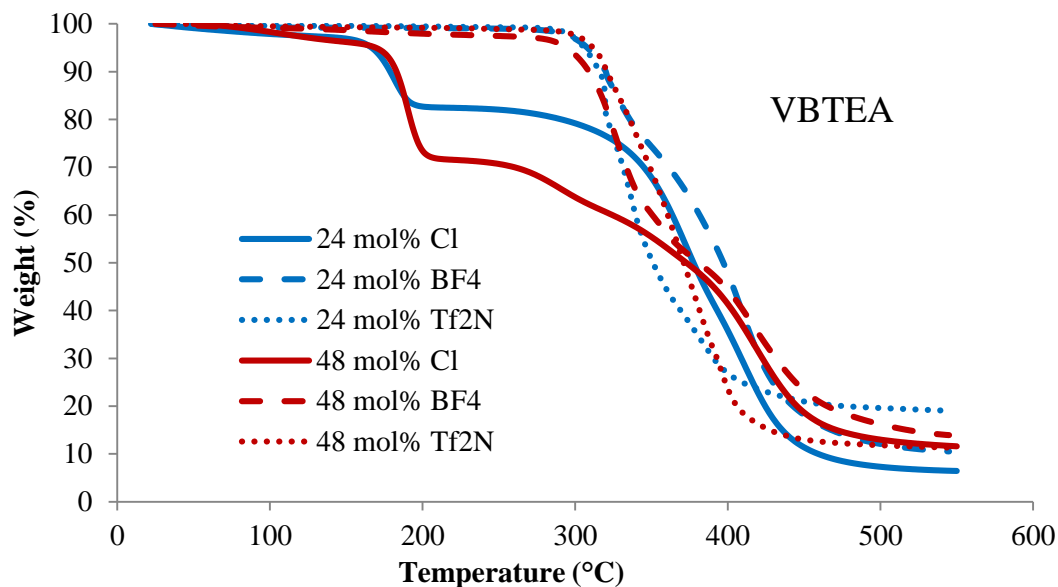


**Figure S9.3.** TGA traces of poly(VBTEACl-*co-nBA*)s, poly(VBTEABF<sub>4</sub>-*co-nBA*)s, and poly(VBTEATf<sub>2</sub>N-*co-nBA*)s with varying ionic monomer concentrations.

**Table S9.3.** 5 wt% loss temperatures of poly(VBTEACl-*co-nBA*)s, poly(VBTEABF<sub>4</sub>-*co-nBA*)s, and poly(VBTEATf<sub>2</sub>N-*co-nBA*)s.

| T <sub>d</sub> (°C) VBTEA | Cl  | BF <sub>4</sub> | Tf <sub>2</sub> N |
|---------------------------|-----|-----------------|-------------------|
| 20 mol%                   | 167 | 308             | 306               |
| 38 mol%                   | 180 | 294             | 312               |



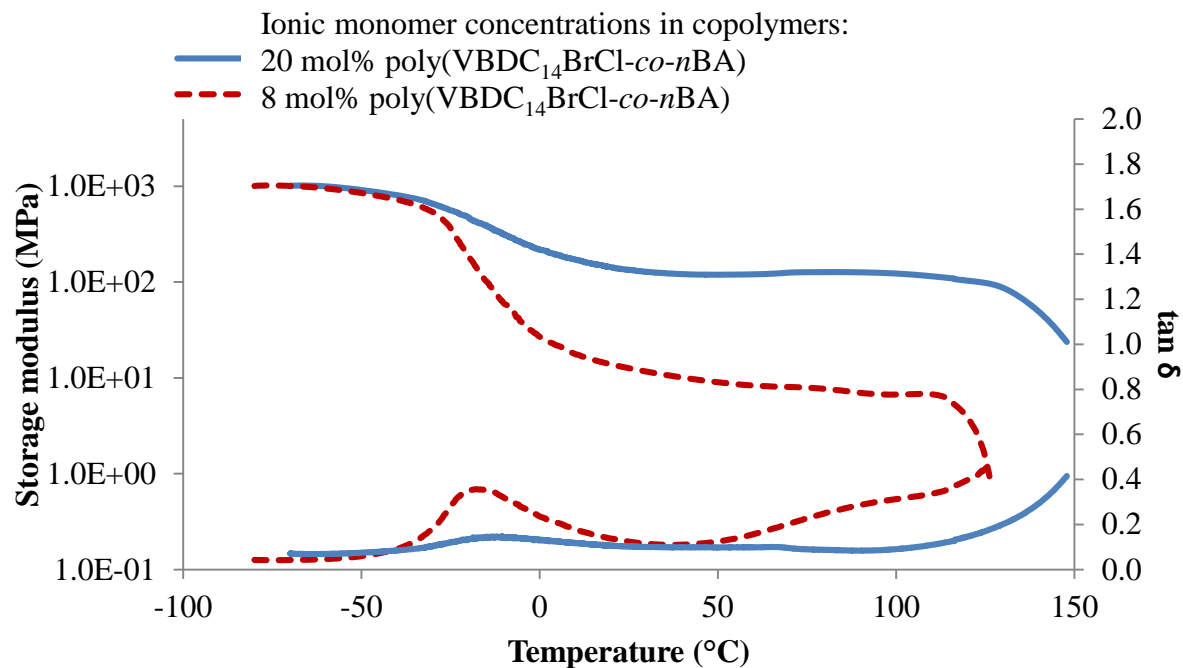


**Figure S9.4.** Dynamic mechanical temperature analysis of poly(VBDC<sub>14</sub>BrCl-*co*-*n*BA) with 8, 20 mol% of VBDC<sub>14</sub>BrCl.

**Table S9.4.**  $T_g$ 's and plateau temperature ranges of poly(VBDC<sub>14</sub>BrCl-*co*-*n*BA)s.  $T_g^1$  values are from maxima of peaks on tan delta curves of DMA;  $T_g^2$  values are from the second heating scans of DSC.

| Ionic monomer concentration        | $T_g^1$<br>(tan $\delta$ ) | $T_g^2$<br>(2 <sup>nd</sup> heat) | $T_{flow}$ | Plateau window |
|------------------------------------|----------------------------|-----------------------------------|------------|----------------|
| 8 mol%<br>VBDC <sub>14</sub> BrCl  | -18 °C                     | -40 °C                            | 127 °C     | 110 °C         |
| 20 mol%<br>VBDC <sub>14</sub> BrCl | -11 °C                     | NA                                | 148 °C     | 125 °C         |

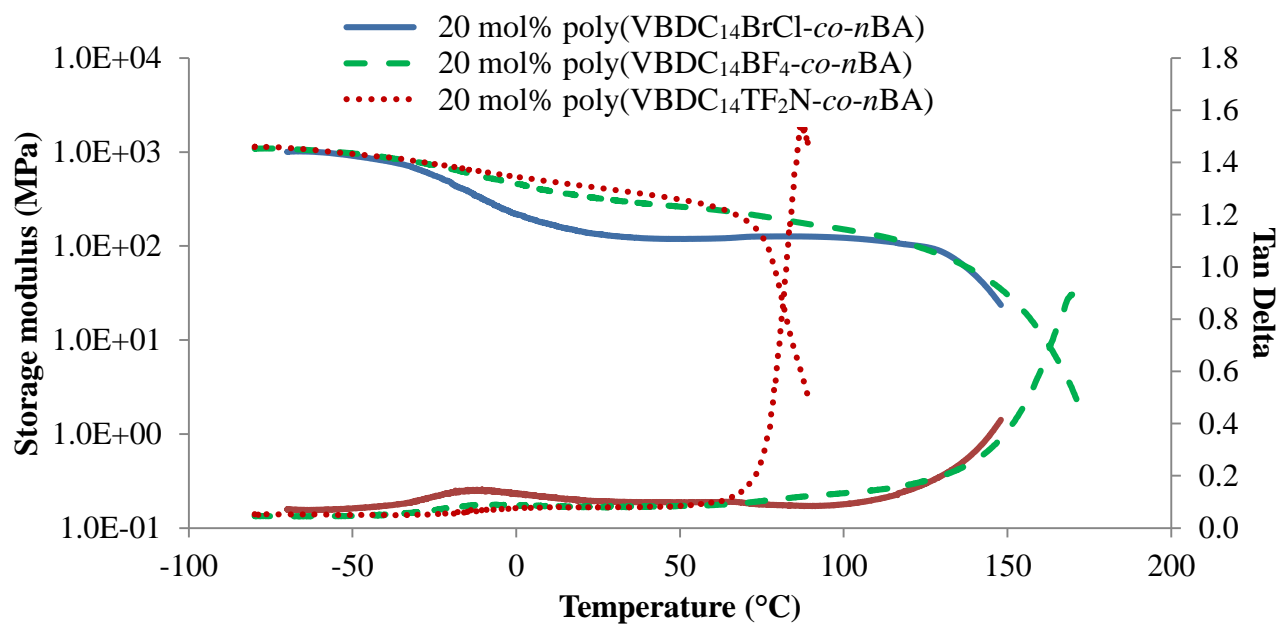


**Figure S9.5.** Dynamic mechanical analysis for poly(VBDC<sub>14</sub>BrCl-*co*-nBA), poly(VBDC<sub>14</sub>BF<sub>4</sub>-*co*-nBA), and poly(VBDC<sub>14</sub>TF<sub>2</sub>N-*co*-nBA) containing 20 mol% ionic monomers.

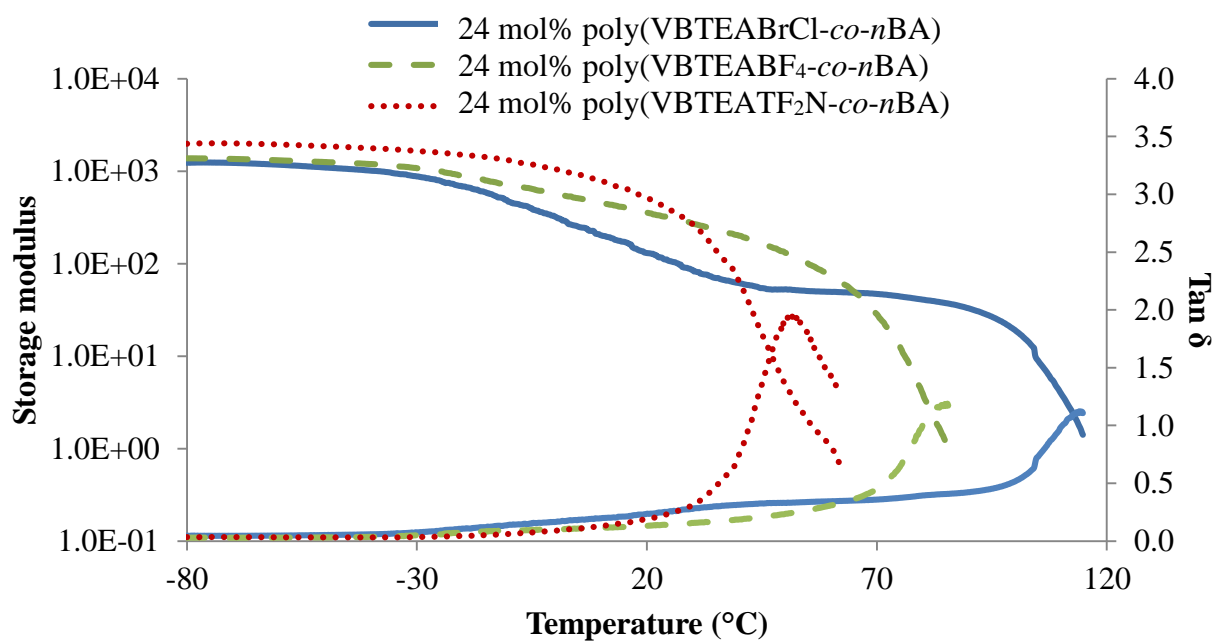


**Figure S9.6.** Dynamic mechanical analysis for poly(VBTEABrCl-*co-n*BA), poly(VBTEABF<sub>4</sub>-*co-n*BA), and poly(VBTEATf<sub>2</sub>N-*co-n*BA) containing 24 mol% ionic monomers.

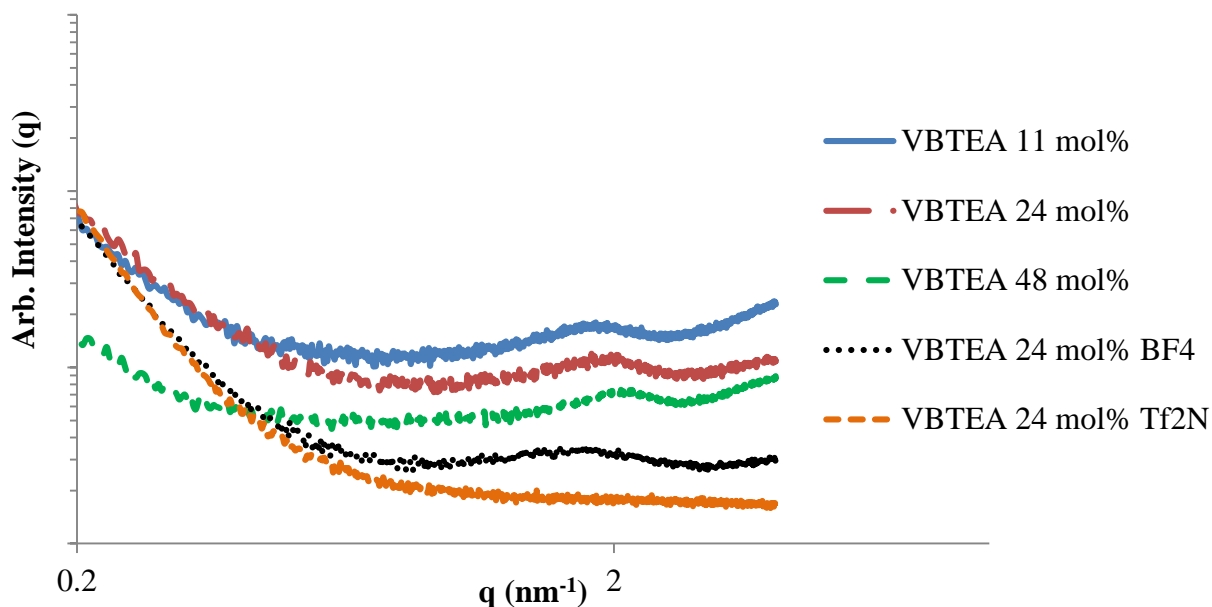


**Figure S9.7.** SAXS of solution-cast poly(VBTEACl-*co-n*BA)s, poly(VBTEABF<sub>4</sub>-*co-n*BA), and poly(VBTEATf<sub>2</sub>N-*co-n*BA).

**Table S9.5.** Fitting parameters for the Kinning and Thomas model for poly(VBTEA R-*co-n*BA)

|  | $R_1$ (nm)      | $R_{ca}$ (nm)   | $V_p$ (nm <sup>3</sup> ) |
|--|-----------------|-----------------|--------------------------|
| 11 mol% poly(VBTEA Cl- <i>co-n</i> BA)               | $0.73 \pm 0.04$ | $1.66 \pm 0.01$ | $2.69 \pm .02$           |
| 24 mol% poly(VBTEA Cl- <i>co-n</i> BA)               | $0.72 \pm 0.05$ | $1.60 \pm 0.01$ | $2.48 \pm .02$           |
| 48 mol% poly(VBTEA Cl- <i>co-n</i> BA)               | $0.81 \pm 0.08$ | $1.43 \pm 0.01$ | $2.40 \pm .05$           |
| 24 mol% poly(VBTEA BF <sub>4</sub> - <i>co-n</i> BA) | $0.74 \pm 0.15$ | $1.52 \pm 0.02$ | $3.16 \pm .20$           |

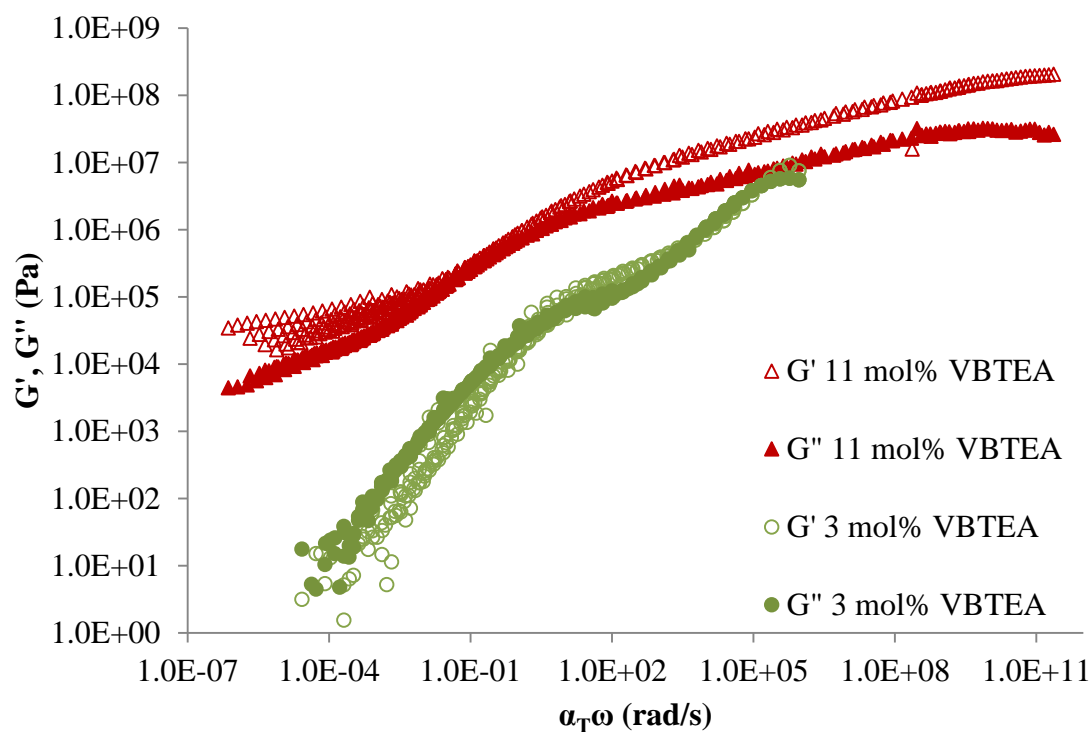


**Figure S9.8.** Rheological TTS master curves poly(VBTEACl-*co*-*n*BA) with 3 mol% and 11 mol% ionic monomer.

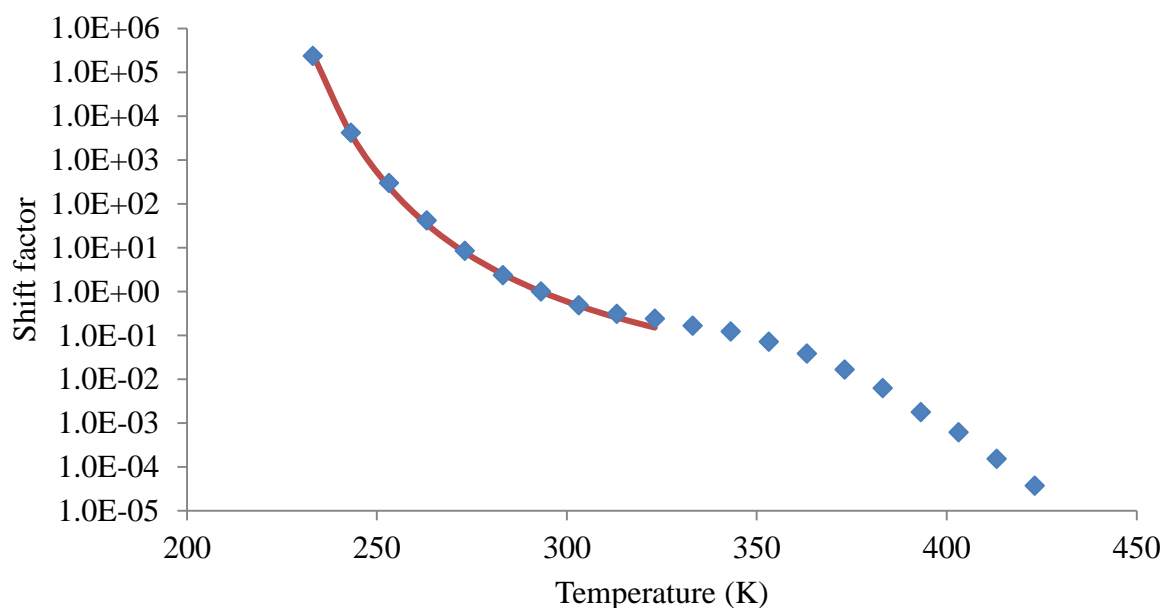


**Figure S9.9.** Shifting factor fitting to WLF equation for poly(VBDC<sub>6</sub>BrCl-*co*-*n*BA) with 1 mol% VBDC<sub>6</sub>BrCl.

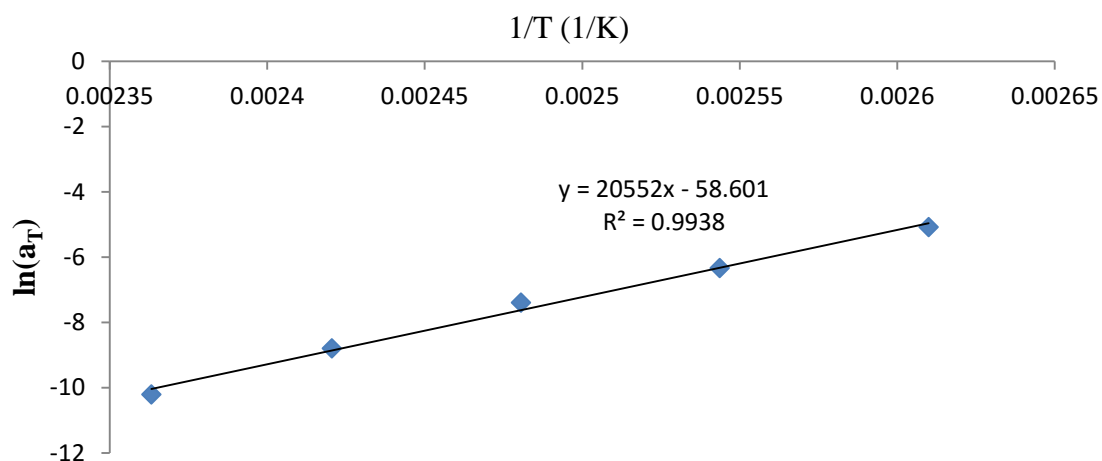


**Figure S9.10.** Shifting factor fitting to Arrhenius equation for poly(VBDC<sub>6</sub>BrCl-*co*-nBA) with 1 mol% VBDC<sub>6</sub>BrCl.

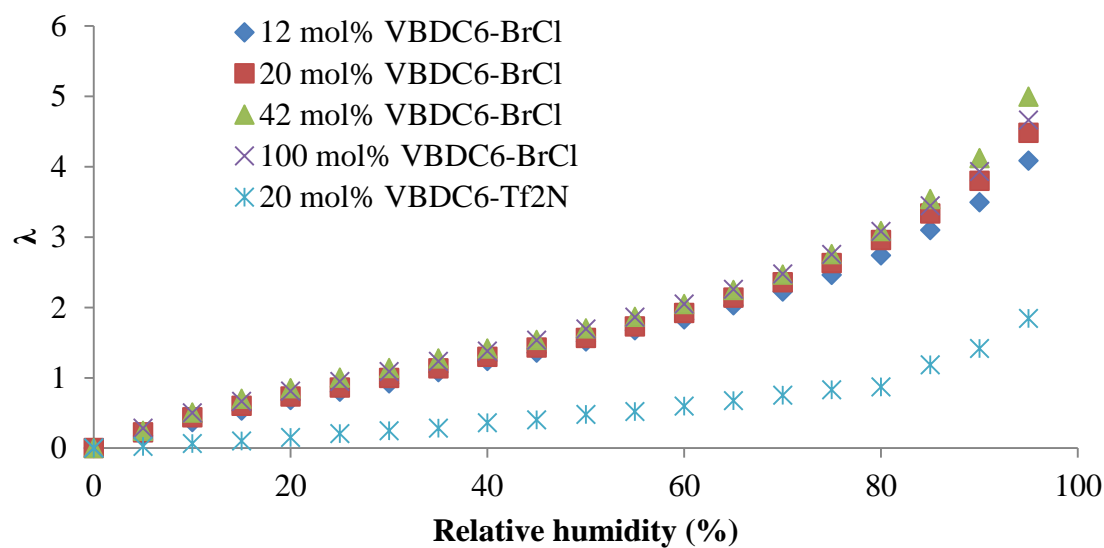


**Figure S9.11.** Water uptake per charge of poly(VBDC<sub>6</sub>BrCl), poly(VBDC<sub>6</sub>Tf<sub>2</sub>N-*co*-nBA) and poly(VBDC<sub>6</sub>BrCl-*co*-nBA) with various ionic concentration at a range of relative humidity.

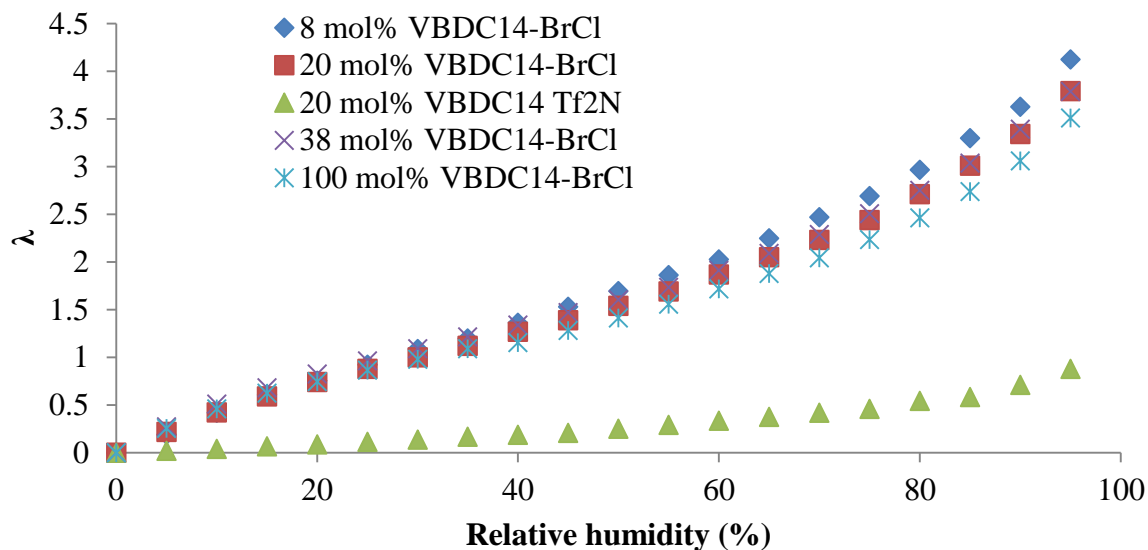


**Figure S9.12.** Water uptake per charge of poly(VBDC<sub>14</sub>BrCl), poly(VBDC<sub>14</sub>Tf<sub>2</sub>N-*co*-*n*BA) and poly(VBDC<sub>14</sub>BrCl-*co*-*n*BA) with various ionic concentration at a range of relative humidity.

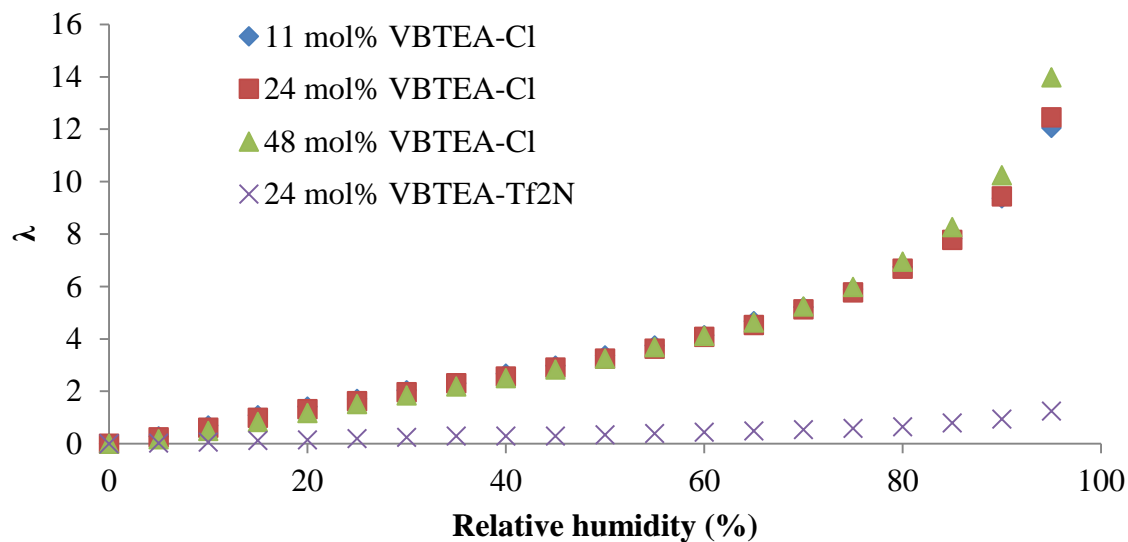


**Figure S9.13.** Water uptake per charge of poly(VBTEACl-*co*-*n*BA) and poly(VBTEATf<sub>2</sub>N-*co*-*n*BA) with various ionic concentration at a range of relative humidity.

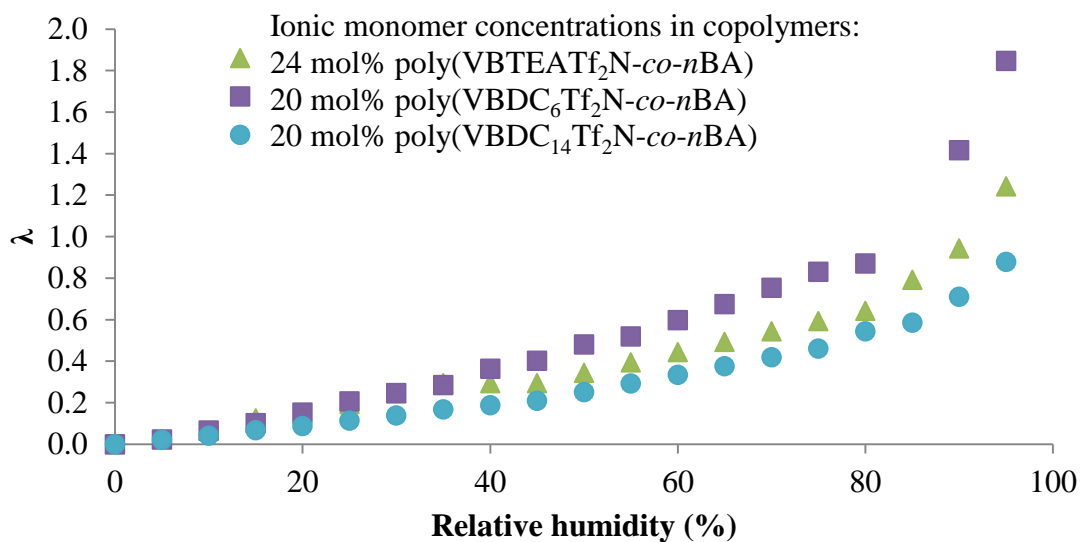


**Figure S9.14.** Water uptake per charge of poly(VBDC<sub>6</sub>Tf<sub>2</sub>N-*co-n*BA), poly(VBDC<sub>14</sub>Tf<sub>2</sub>N-*co-n*BA), and poly(VBTEATf<sub>2</sub>N-*co-n*BA) at a range of relative humidity.

#### References

1. Hemp, S. T.; Zhang, M. Q.; Allen, M. H.; Cheng, S. J.; Moore, R. B.; Long, T. E. *Macromol. Chem. Phys.* **2013**, 214, 2099.

## Chapter 10. Non-Isocyanate Poly(amide-hydroxyurethane)s from Sustainable Resources

*(Submitted to Green Chemistry)*

*Keren Zhang, Samantha J. Talley, Mingtao Chen, Amanda G. Hudson, Evan Margaretta, Ashley*

*M. Nelson, Robert B. Moore, and Timothy E. Long\**

*Department of Chemistry, Macromolecules and Interfaces Institute*

*Virginia Tech, Blacksburg, VA 24061, USA*

**Keywords:** Non-isocyanate polyurethane, cyclic carbonate, amidation, poly(amide-hydroxyurethane), sustainable resources, structure-morphology-property relationship

### 10.1 *Abstract*

A two-step facile synthesis afforded a hetero-functional AB monomer with cyclic carbonate and methyl ester (CC-ME) on each end using plant oil-based methyl 9-decenoate and CO<sub>2</sub>. A unprecedented one-pot synthetic platform of CC-ME with 1,12-diaminododecane and poly(tetramethylene oxide) (PTMO)-based polyether diamine allowed synthesis of both nonsegmented poly(amide-hydroxyurethane) (PA<sub>12</sub>HU) and segmented PA<sub>12</sub>HU-PTMOs with varying polyether contents. <sup>1</sup>H NMR spectroscopy confirmed complete conversions of cyclic carbonates and methylesters to hydroxyurethanes and amides, respectively. Thermal analysis revealed distinctive thermal properties of PA<sub>12</sub>HU and PA<sub>12</sub>HU-PTMOs compared to their starting materials and model compound oligomers. PA<sub>12</sub>HU and PA<sub>12</sub>HU-PTMOs were melt compression molded into semicrystalline, free-standing films, except for PA<sub>12</sub>HU-PTMO100 with 100% polyether diamine. PA<sub>12</sub>HU-PTMO100 was a viscous liquid with a glass transition temperature (T<sub>g</sub>)



of -64 °C and zero-shear viscosity of 449 Pa·s. PA<sub>12</sub>HU formed a semicrystalline, rigid film with T<sub>g</sub> of 11 °C. Polyether incorporations afforded creasable PA<sub>12</sub>HU-PTMO films with broad glass transitions near -50 °C. Thermal and thermomechanical analysis revealed phase-mixing properties of the annealed PA<sub>12</sub>HU-PTMO films. Polyether soft segments intermixed with the amorphous hard segments, forming a soft phase; crystallizable hard segments with ordered hydrogen bonding formed a hard phase. Surface morphology analysis of each PA<sub>12</sub>HU-PTMO film displayed ribbon-like, hard domains with composition-dependent aspect ratios. PA<sub>12</sub>HU-PTMOs exhibited higher moisture uptake than traditional thermoplastic polyurethane (TPU) due to additional hydroxyls. Variable temperature FTIR spectroscopy demonstrated that ordered hydrogen bonding in the crystalline domains was disrupted or dissociated as the crystallites melted. Though tensile properties of segmented PA<sub>12</sub>HU-PTMOs were weaker than traditional polyurethanes due to phase-mixing, these are the first examples of film-forming, linear isocyanate-free polyurethanes with mechanical integrity and processability.

## 10.2 *Introduction*

Sustainable and environmentally friendly materials attract attention due to decreasing petroleum storage and arising environmental concerns. Polyurethanes provide thermoplastics and thermosets for many applications such as adhesives, sealants, coatings, commodities, automotive, packaging, and insulations materials. However, isocyanates, key starting materials for polyurethane synthesis, exhibit high reactivity and toxicity. Side reactions of isocyanates with moisture affect cost and demand many safety precautions during storage, transportation, and production of polyurethanes. Furthermore, isocyanate production commonly utilizes phosgene, a more reactive and toxic gas that causes acute

safety and environmental hazards. Therefore, developing a more environmentally benign synthetic strategy for polyurethanes to avoid isocyanate usage remains a priority for many researchers. Literature from the past two decades highlights three main phosgene-free synthetic routes for preparing non-isocyanate polyurethanes (NIPUs): polyaddition reactions between five-membered cyclic carbonates and amines;<sup>1,2</sup> polycondensation of carbonates with amines;<sup>3,4</sup> polycondensation of AB type monomer containing acyl-azides with hydroxyls.<sup>5</sup> Endo *et al.* proved quantitative reaction of a cyclic carbonate with a primary amine after 24 h at room temperature, yielding an isomer mixture of hydroxyurethanes with primary and secondary hydroxyls.<sup>6</sup> This ring opening reaction has become the most promising method to substitute the urethane-forming reaction of isocyanate and alcohol. Cyclic carbonates led to a synthetic route for creating polymer backbones or chemical crosslinks, allowing the synthesis of linear or crosslinked NIPUs for thermoplastics and thermosets, respectively. Webster first reviewed the progress of cyclic carbonate-functionalized monomers and NIPU synthesis, and others comprehensively summarized the most recent efforts in developing NIPUs.<sup>7-11</sup> The earliest studies synthesized cyclic carbonate-containing acrylic, methacrylic, and vinyl monomers that allowed post-functionalization of free radically polymerized polymers, mostly used for thermoset materials.<sup>12-14</sup> Several studies utilized sustainable resources to produce bio-based NIPUs, the synthesis of which generally involves three steps: epoxidation of the carbon-carbon double bonds on an unsaturated fatty acid produces multi-oxiranes; carbon dioxide insertion converts oxiranes to cyclic carbonates; reaction of cyclic carbonates with amines affords crosslinked polyhydroxyurethane network. Wilkes *et al.* synthesized a crosslinked NIPU with cyclic carbonate-functionalized soybean oil and amines, and

measured their thermomechanical and tensile properties.<sup>2,15</sup> Javni *et al.* also prepared soybean oil-derived, crosslinked NIPU thermosets with the highest stress at break near 6-7 MPa.<sup>16,17</sup> Hybrid systems such as carbonated soybean oil-containing epoxy resins have shown comparable toughness with unmodified resins when cured with amines.<sup>18</sup> Though requiring further optimizations, crosslinked NIPUs have demonstrated potential in matching the mechanical performance of conventional polyurethane thermosets.

However, the progress lags on developing linear or branched NIPUs to compete with conventional thermoplastic polyurethanes (TPUs). Endo and many others utilized polyaddition of bis(cyclic carbonate)s and diamine to synthesize linear NIPU.<sup>1,19-23</sup> Cramail *et al.* recently reported the synthesis of aliphatic bis(6-membered cyclic carbonate)s using castor oil-based methyl undecenoate. Polymerization of the cyclic carbonates and diamine produced NIPUs with relative  $M_n$  as high as 23 kDa.<sup>22</sup> Another study from the same group also used methyl undecenoate to synthesize amide-containing bis(cyclic carbonate), the melt polymerization of which yielded amide-containing NIPUs. However, the products were blends due to heterogeneous mixtures of amines and cyclic carbonates. Despite many efforts devoted to developing linear NIPUs for thermoplastics, most studies were limited to the synthesis, spectroscopic validations, and thermal properties. Only Nanclares *et al.* very recently reported stress-strain profiles of segmented bisphenol A-based NIPUs with elastomeric properties.<sup>24</sup> To our knowledge, no report exists of bio-based NIPU thermoplastics with mechanical integrity or detailed morphology analysis.

This manuscript details the synthesis and characterization of a series of nonsegmented and segmented NIPUs with various physical properties, ranging from film-

forming solids to viscous liquid. A commercialized biochemical refinery produced methyl 9-decenoate using metathesis reactions of unsaturated fatty acids. Sequential epoxidation and carbonation yielded a cyclic carbonate-methyl ester (CC-ME) monomer, a stable solid at room temperature. An one-pot synthetic platform afforded a series of novel bio-based poly(amide hydroxyurethane)s (PAHUs) using CC-ME, an aliphatic diamine, and a polyether diamine. Polymerization proceeded through ring opening of five-membered cyclic carbonates and amidation of the methyl esters, forming both hydroxyurethanes and amides on the polymer backbone. The reported PAHU series spans both nonsegmented and segmented polyurethanes with tunable thermal, thermomechanical properties, and crystallinity. The segmented PAHUs with aliphatic diamine incorporation were homogeneous melts during polymerization and compression molded into free-standing films. In addition, atomic force microscopy (AFM) and X-ray scattering experiments elucidated the influence of hard segment percentage on the morphology of annealed PAHU films. The PAHU with the highest soft segment percentage was a clear, viscous liquid that displayed shear thinning during rheological shear-sweep experiment. This manuscript represents the first report of bio-based, semicrystalline NIPUs with mechanical integrity, microphase-separated morphology, and processability. Various physical characterization techniques assisted in establishing the structure-morphology-property relationship of synthesized PAHUs. This versatile synthetic platform also opens a window for preparing a wide variety of NIPUs with tunable properties using many other diamines and cyclic carbonate-ester monomers.

### 10.3 *Experimental Section*

**Materials.** Methyl 9-decenoate (9-DAME) was provided from Elevance Renewable Sciences, Inc. and used as received. *meta*-Chloroperoxybenzoic acid (m-CPBA,  $\leq 77\%$ ), 1,12-diaminododecane (98%), lithium bromide (LiBr,  $\geq 99\%$ ), 1,5,7-triazabicyclo[4.4.0]dec-5-ene (TBD, 98%), sodium hydroxide solution (NaOH, 1.0 M in water), magnesium sulfate (MgSO<sub>4</sub>, 99%) sodium sulfite (NaSO<sub>3</sub>,  $\geq 98\%$ ), sodium bicarbonate (NaHCO<sub>3</sub>,  $\geq 99\%$ ), N-methyl-2-pyrrolidone (NMP, ACS grade), and sodium chloride (NaCl,  $\geq 99\%$ ) were obtained from Sigma-Aldrich and used as received. Jeffamine® THF-100 was poly(tetramethylene oxide)/poly(propylene glycol) copolymer based diamine with 1 kDa molecular weight, obtained from Huntsman Corporation sample department and used as received. Bone-dry CO<sub>2</sub> was obtained from Airgas and used as received. Ethyl acetate (EtOAc, ACS grade) and dichloromethane (DCM, ACS grade) were purchased from Spectrum Chemicals and used as received. Water was purified from distillation.

**Analytical Methods.** <sup>1</sup>H NMR and <sup>13</sup>C NMR spectra were collected in CDCl<sub>3</sub>, deuterated trifluoroacetic acid (TFA), or deuterated hexafluoroisopropanol (HFIP) on an Agilent U4-DD2 spectrometer operating at 400 MHz, 23 °C. High resolution TOF mass spectroscopy (HRMS) was conducted on an Agilent 6220 mass spectrometer with a TOF analyzer in positive ion mode. Melting point was measured on an Electrothermal IA9000 melting point apparatus with heating rate of 10 °C/min. TA Instruments Q50 provided thermogravimetric analysis (TGA) results using a heating ramp with 10 °C/min heating rate from ambient to 600 °C under nitrogen purge. Thermal degradation temperatures (T<sub>d,5wt%</sub>) corresponded to the temperature at 5% weight loss. Differential scanning calorimetry (DSC) experiments

of all PAHU samples were conducted on a TA instruments Q1000 DSC utilizing a heat/cool/heat procedure under nitrogen flush of 50 mL/min. Both heating and cooling rates were 10 °C/min. Cryo-DSC was utilized to characterize thermal transitions below 80 °C on TA instruments Q100 using liquid nitrogen. Cryo-DSC used a heat/cool/heat procedure with heating rate of 10 °C/min and cooling rate of 100 °C/min. The midpoint of the transition in the second heating ramp determined glass transition temperatures ( $T_g$ ).

Dynamic mechanical analysis (DMA) utilized a TA Instruments Q800 dynamic mechanical analyzer in tension mode at an oscillatory amplitude of 10  $\mu$ m, a frequency of 1 Hz, and a static force of 0.01 N. Rectangular film samples were cooled to -100 °C, equilibrated for 2 min, length measured, and ramped up temperature at a rate of 3 °C/min. The peaks of tan delta curves determined  $T_g$  values. A Veeco MultiMode scanning probe microscope provided AFM phase and height images using the tapping mode. Samples were imaged with Veeco's Nanosensor silicon tips, spring constant of 10-100 N at approximately 0.7 set-point ratio. A TA Instruments Q5000 thermogravimetric sorption analyzer (TGA-SA) measured the water sorption of compression molded PAHU samples at 25 °C with relative humidity (RH) steps from 0 – 95% RH, 5% increment after each step. Each RH step proceeded until the sample weight equilibrated with less than 0.01% weight change in 10 min. An instrumental pre-drying method at 25 °C and 0% RH was applied to each sample until sample weight equilibrated. Water sorption was calculated based on weight gain of each pre-dried sample weight. An Instron 5500R universal testing instrument measured tensile properties of several segmented PA<sub>12</sub>HU-PTMO film samples at a crosshead speed of 10 mm/min. Tensile analysis data represented an average of five specimens with calculated standard deviations.

Small angle X-ray scattering (SAXS) and wide-angle X-ray diffraction (WAXD) experiments were performed using a Rigaku S-Max 3000 3 pinhole SAXS system, equipped with a rotating anode emitting X-ray with a wavelength of 0.154 nm (Cu K $\alpha$ ). The sample-to-detector distance was 1603 mm for SAXS and 109 mm for WAXD, and the q-range was calibrated using a silver behenate standard. Two-dimensional SAXS patterns were obtained using a 2D multiwire, proportional counting, gas-filled detector, with an exposure time of 1 h. Two-dimensional WAXD diffraction patterns were obtained using an image plate with an exposure time of 1 h. The SAXS data were corrected for sample thickness, and the SAXS/WAXD profiles were vertically shifted to facilitate a comparison of peak positions. All the SAXS and WAXD data were analyzed using the SAXSGUI software package to obtain radially integrated SAXS and WAXD intensity versus the scattering vector q (SAXS) or 2 $\theta$  (WAXD) respectively, where  $q=(4\pi/\lambda)\sin(\theta)$ ,  $\theta$  is one half of the scattering angle and  $\lambda$  is the X-ray wavelength.

Variable temperature FTIR (VT-FTIR) experiments were performed using a Varian 670-IR spectrometer (DTGS detector) with Pike Technologies variable temperature GladiATR<sup>TM</sup> attachment (diamond crystal). The spectra were collected at 4 cm<sup>-1</sup> resolution and as an average of 32 scans. The samples were subjected to a temperature ramp of 1 °C /min, starting from 30 °C to 180 °C and FTIR spectra were collected every 10 °C beginning from 30 °C. Rheology experiments were conducted on TA instrument Discovery AR-G2 rheometer with cone and plate geometry (20 mm in diameter, 2° cone angle, truncation gap 60  $\mu$ m). The samples were subjected to a shear sweep ramping from 1 s<sup>-1</sup> to 200 s<sup>-1</sup>. All samples were kept in a desiccator prior to any experiment.

**Synthesis of 9,10-cyclic carbonate-methyl decanoate (CC-ME) monomer (Scheme 10.1).** In the first step, *m*-CPBA (33 g, 0.14 mol) and DCM (200 mL) were added to a 500 mL, round-bottomed flask equipped with a magnetic stir bar. The flask was placed into an ice bath with constant stirring until *m*-CPBA dissolved. 9-DAME (20 g, 0.11 mol) was then added into the solution and allowed to stir overnight. White precipitate was removed from the solution using vacuum filtration. DCM was then removed using a rotary evaporator. Additional white precipitate was removed again with vacuum filtration. The filtrate was washed with saturated NaSO<sub>3</sub> solution 2 times, aqueous NaOH (1.0 M) 3 times, NaHCO<sub>3</sub> 2 times, and brine 2 times. The resulting light yellow oil was placed at -20 °C overnight, filtered through a 5 µm membrane filter, and dried in *vacuo* (15 g, 69% yield). The structure and purity of obtained methyl 9,10-epoxydecanoate intermediate were confirmed using NMR spectroscopy (Figure S10.1). <sup>1</sup>H NMR (400 MHz, CDCl<sub>3</sub>): 3.64 (s, 3H, H<sub>a</sub>), 2.87 (m, 1H, H<sub>b</sub>), 2.72 (dd, 1H, *J*<sub>1</sub> = 3.9 Hz, *J*<sub>2</sub> = 5.0 Hz, H<sub>c</sub>), 2.44 (dd, 1H, *J*<sub>1</sub> = 2.8 Hz, *J*<sub>2</sub> = 5.0 Hz, H<sub>d</sub>), 2.28 (t, 2H, *J* = 7.5 Hz, H<sub>e</sub>), 1.59 (m, 2H, H<sub>f</sub>), 1.50 (m, 2H, H<sub>g</sub>), 1.46-1.19 (m, 8H, H<sub>h</sub>). <sup>13</sup>C NMR (100 MHz, CDCl<sub>3</sub>): 174.16, 52.25, 51.36, 47.01, 34.00, 32.39, 29.16, 29.08, 28.95, 25.84, 24.84. HRMS (ES<sup>+</sup>): *m/z* calculated for [M+H]<sup>+</sup> 201.1485 g/mol; found 201.1481 g/mol.

In the second step, methyl 9,10-epoxydecanoate (4.0 g, 20 mmol), NMP (10 mL), and LiBr (0.087 g, 1.0 mmol) were added into a 100 mL, round-bottomed flask equipped with a magnetic stir bar. The reaction mixture was stirred at 80 °C with constant CO<sub>2</sub> bubbling for 24 h. After cooling back to room temperature, the reaction mixture was dissolved in 100 mL EtOAc and washed with 150 mL brine. The organic phase was dried with MgSO<sub>4</sub> and rotatory evaporated to remove EtOAc. Resulted light brown oil was dried



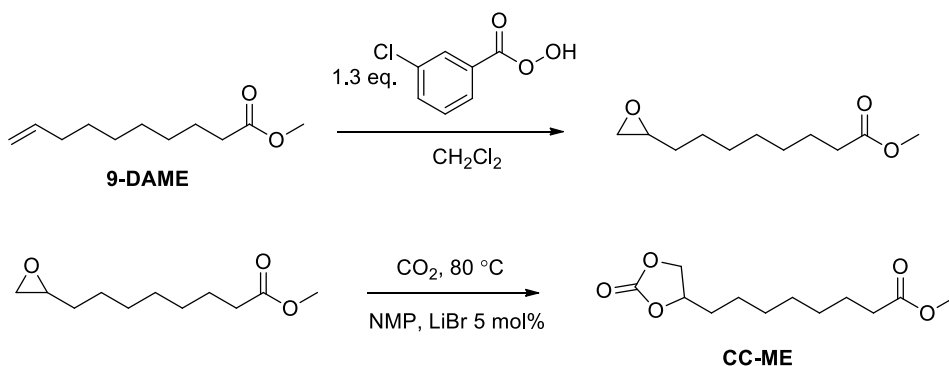
in *vacuo* at 50 °C for 24 h and cooled to room temperature to obtain a salmon color solid (4.9 g, 89% yield) (Figure S10.2). <sup>1</sup>H NMR (400 MHz, CDCl<sub>3</sub>, Figure S10.2): 4.67 (m, 1H, H<sub>a</sub>), 4.50 (dd, 1H, *J*<sub>1</sub> = 8.2 Hz, *J*<sub>2</sub> = 8.4 Hz, H<sub>b</sub>), 4.05 (dd, 1H, *J*<sub>1</sub> = 7.2 Hz, *J*<sub>2</sub> = 8.4 Hz, H<sub>c</sub>), 3.65 (s, 3H, H<sub>d</sub>), 2.29 (t, 2H, H<sub>f</sub>), 1.82-1.55 (m, 4H, H<sub>g</sub>), 1.46-1.28 (m, 8H, H<sub>h</sub>). <sup>13</sup>C NMR (100 MHz, CDCl<sub>3</sub>): 174.14, 154.98, 76.93, 69.32, 51.44, 33.95, 33.84, 28.92, 28.88, 28.85, 24.77, 24.28. HRMS (ES<sup>+</sup>): *m/z* calculated for [M+H]<sup>+</sup> 245.1384 g/mol; found 245.1384 g/mol. Melting point 36-37 °C.

**One-pot melt polymerization of nonsegmented poly(amide-hydroxyurethane) (PA<sub>12</sub>HU) (Scheme 10.2).** 9,10-cyclic carbonate-methyl decanoate (CC-ME) (2.0 g, 8.2 mmol), 1,12-diaminododecane (2.5 g, 8.9 mmol), and TBD (0.057 g, 0.41 mmol) were charged to a dry, 100 mL, round-bottomed flask. The flask was equipped with an overhead stir rod, argon inlet, and connection to vacuum through a dry ice-IPA trap. After argon purge for 30 min, the flask was heated to 70 °C to allow melting of the solids. The flask was then heated from 70 °C to 190 °C with constant stirring over 24 h, and the pressure was subsequently reduced to 0.06 mbar at 190 °C for additional 2 h. The resulting polymer was collected without further purification.

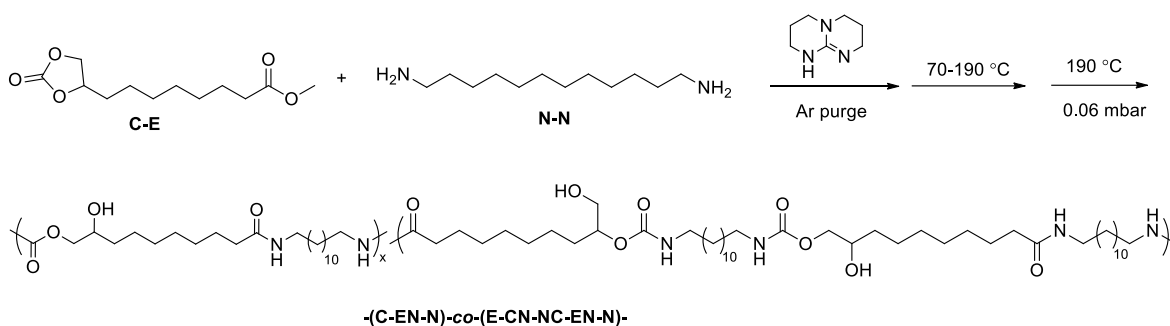
**One-pot melt polymerization of segmented poly(amide-hydroxyurethane) with PTMO soft segment (PA<sub>12</sub>HU-PTMO) (Scheme 10.3).** A typical polymerization of segmented PAHU-PTMO was conducted as following: 9,10-cyclic carbonate-methyl decanoate (CC-ME) (2.0 g, 8.2 mmol), 1,12-diaminododecane (0.84 g, 4.2 mmol), PTMO-diamine (THF-100 Jeffamine®) (4.2 g, 4.1 mmol), and TBD (0.057 g, 0.41 mmol) were charged to a dry, 100 mL, round-bottomed flask. The flask was equipped with an overhead stir rod, argon inlet, and connection to vacuum through a dry ice-IPA trap. After argon

purge for 30 min, the flask was heated to 70 °C to allow melting of the solids. The flask was then heated from 70 °C to 180 °C with constant stirring over 3 d, and the pressure was subsequently reduced to 0.06 mbar at 180 °C for additional 3 h. The resulting polymer was collected without further purification.

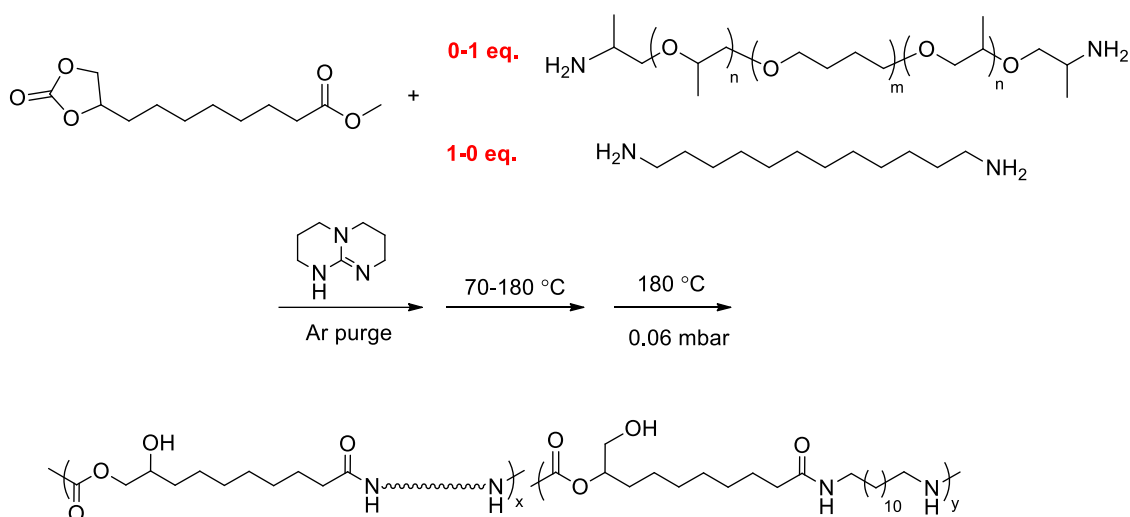
**Processing and annealing conditions.** Nonsegmented PA<sub>12</sub>HU was melt compression molded at 160 °C for 5 min under 3 ton of compression force and cooled to room temperature, sandwiched between two Kapton® sheets and two steel plates. All segmented PA<sub>12</sub>HU-PTMO, except for PAHU-PTMO100, were melt compression molded at 130 °C for 5 min under 3 ton of compression force and cooled to room temperature, sandwiched between two Kapton® sheets and two steel plates. Compression molded films were annealed in *vacuo* for 12 h at 130 °C. Films were cooled using a step-wise procedure wherein the oven temperature was reduced 30 °C and allowed to equilibrate for 3 hours, with the process repeated until room temperature was reached.



**Scheme 10.1.** Synthesis of cyclic carbonate-methyl ester (CC-ME) monomers.



**Scheme 10.2.** Synthesis of nonsegmented poly(amide-hydroxyurethane) (PA<sub>12</sub>HU) copolymers.



**Scheme 10.3.** One-pot melt polymerization of segmented poly(amide-hydroxyurethane) with PTMO-based polyether 1 kDa soft segment (PA<sub>12</sub>HU-PTMO).

## 10.4 Results and Discussion

**Synthesis of CC-ME hetero-difunctional AB monomer.** This manuscript reports a scalable synthetic route for synthesizing a difunctional AB monomer with cyclic carbonate and methyl ester from renewable resources. A proprietary olefin metathesis technology of Elevance Renewable Sciences, Inc. afforded multifunctional small molecules from plant oils. Methyl 9-decenoate (9-DAME), one of the produced difunctional small molecules, was epoxidized to methyl 9,10-epoxydecanoate (Scheme

10.1). Complete removal of the byproduct *meta*-chlorobenzoic acid was confirmed through TLC and NMR spectroscopy to prevent contamination of mono-functional small molecules. In the second step, insertion of a CO<sub>2</sub> molecule to the epoxy ring generated a five-membered cyclic carbonate (Scheme 10.2). The CO<sub>2</sub> insertion was quantitative after 24 h. Another one-pot method from Davies *et al.* was also effective in converting olefins to cyclic carbonates but less efficient.<sup>25</sup> Purified CC-ME monomer was synthesized in 20 g scale with potential scalability. Figure 10.1a summarizes the entire process from plant oil to polymerizable, multi-functional monomer. This synthetic route provided an efficient way in using greenhouse gas as a carbon source for functional monomer and polymer synthesis.

**Nonsegmented PA<sub>12</sub>HU synthesis.** High conversion is crucial for step growth polymerization.<sup>26</sup> Successful polymerization of CC-ME monomer requires quantitative reactions for both methyl ester and cyclic carbonate. Model compound reactions were described in the supplementary information, which assisted the optimization of reaction conditions for hydroxyurethane formation and amidation. Scheme 10.2 illustrates synthesis of a nonsegmented PAHU using one-pot melt polymerization of CC-ME and 1,12-diaminododecane. Starting materials and catalyst were added into the reaction all at once. The melt polymerization proceeded under an inert atmosphere in one pot. The initial temperature at 70 °C melted the starting materials and minimized sublimation. The final vacuum step aimed to completely remove the byproduct methanol and reach high conversion. 1,12-diaminododecane was chosen over 1,6-diaminohexane to reduce sublimation, which was noted as subscript 12 in the abbreviation, PA<sub>12</sub>HU. PA<sub>12</sub>HU was a hard solid that dissolved in TFA and HFIP, insoluble in common organic solvents for

conventional TPUs. Size exclusion chromatography (SEC) was unavailable to determine the molecular weight of PA<sub>12</sub>HU due to the challenging solubility in common SEC solvents. Overlaying NMR spectra of PA<sub>12</sub>HU and CC-ME in deuterated TFA verified the complete conversion of cyclic carbonates and methyl esters (Figure S10.9, S10.10). <sup>1</sup>H NMR spectrum in deuterated HFIP confirmed the structure of PA<sub>12</sub>HU using a model compound hydroxyurethane methyl ester as the reference (Figure S10.11). PA<sub>12</sub>HU contained two repeating units as shown in Scheme 10.2: (C-EN-N) and (E-CN-NC-EN-N) (C: cyclic carbonate, E: methyl ester, N: primary amine). Each repeating unit consisted of isomers with primary and secondary hydroxyls in ratio of 12:88, respectively.

**Segmented PA<sub>12</sub>HU-PTMO synthesis.** Scheme 10.3 illustrates the synthesis of segmented PA<sub>12</sub>HUs with polyether soft segments using a one-pot melt polymerization. Telechelic polyether oligomers with low glass transitions often serve as soft segments for synthesizing segmented polyurethanes, polyureas, and polyamides.<sup>27,28</sup> This study utilized commercially available Jeffamine® THF-100, a PTMO-based polyether diamine with approximately 1 kDa molecular weight. Differing the ratio of PTMO-diamine to 1,12-diaminododecane yielded a series of segmented PA<sub>12</sub>HU-PTMOs with varying extent of soft segment incorporation (Table 10.1). Stoichiometric balance for the amount of total diamines and CC-ME was kept for all PAHUs. A segmented PA<sub>12</sub>HU with x mol% of PTMO diamine in the total amines was named PA<sub>12</sub>HU-PTMO<sub>x</sub>. Synthesis of PA<sub>12</sub>HU-PTMO followed a similar procedure as nonsegmented PA<sub>12</sub>HU synthesis. Overall reaction time was longer for PA<sub>12</sub>HU-PTMO with increasing polyether diamine mol% due to decreasing concentration of reactive groups in the mixture. THF-100 Jeffamine® features primary amines bonded to secondary carbons rather than primary carbons of 1,12-

diaminododecane, which also affected reactivity. PA<sub>12</sub>HU-PTMO10 to PA<sub>12</sub>HU-PTMO67 were compression molded to homogeneous, free-standing films. PA<sub>12</sub>HU-PTMO10 film was rigid, similar to nonsegmented PA<sub>12</sub>HU, while PA<sub>12</sub>HU-PTMO25-67 films were creasable. PA<sub>12</sub>HU-PTMO100 was a transparent, viscous liquid. Figure 10.1b summarizes the physical appearance of rigid nonsegmented PA<sub>12</sub>HU film, creasable PA<sub>12</sub>HU-PTMO films, and viscous liquid PA<sub>12</sub>HU-PTMO100. Figure 10.1a summarizes the whole isocyanate-free synthetic route of linear poly(amide-urethane)s using unsaturated fatty acid and CO<sub>2</sub>, which allows many potential applications as thermoplastics.

A rheology shear-sweep experiment measured specific viscosities of PA<sub>12</sub>HU-PTMO100 and 1 kDa PTMO diamine to be 449 Pa·s and 0.2 Pa·s at 25 °C, respectively (Figure S10.16). PA<sub>12</sub>HU-PTMO100 started to shear thin near a shear rate of 25 s<sup>-1</sup>, while 1 kDa PTMO diamine remained in the linear viscoelastic region up to 200 s<sup>-1</sup>. The higher viscosity and shear thinning proved the higher molecular weight of PA<sub>12</sub>HU-PTMO100 compared to the 1 kDa precursor. Hydrogen bonding of the urethanes and amides also contributed to higher viscosity and longer relaxation time for PAHU. Direct calculation of molecular weight for PAHUs based on specific viscosity was challenging. PA<sub>12</sub>HU-PTMO solids only dissolved in HFIP and TFA, which limited the availability of molecular weight characterization through SEC. PA<sub>12</sub>HU-PTMO100 was miscible with DMF. However, column interaction prohibited the elution of PA<sub>12</sub>HU-PTMO100 from the SEC with a DMF 0.05 M LiBr mobile phase.

**Table 10.1.** Compositions and thermal properties of nonsegmented PA<sub>12</sub>HU and segmented PA<sub>12</sub>HU-PTMOs with various PTMO mol% among total amines.

|                                 | PA <sub>12</sub> HU | PA <sub>12</sub> HU-PTMO10 | PA <sub>12</sub> HU-PTMO25 | PA <sub>12</sub> HU-PTMO33 | PA <sub>12</sub> HU-PTMO50 | PA <sub>12</sub> HU-PTMO67 | PA <sub>12</sub> HU-PTMO100 | PTMO-diamine |
|---------------------------------|---------------------|----------------------------|----------------------------|----------------------------|----------------------------|----------------------------|-----------------------------|--------------|
| PTMO mol% in total amines       | 0%                  | 10%                        | 25%                        | 33%                        | 50%                        | 67%                        | 100%                        | NA           |
| Soft segment wt%                | 0%                  | 19%                        | 39%                        | 47%                        | 59%                        | 68%                        | 80%                         | NA           |
| T <sub>d</sub> (°C, 5 wt%)      | 272                 | 273                        | 302                        | 296                        | 305                        | 316                        | 319                         | 273          |
| T <sub>g</sub> (°C)             | 11                  | NA                         | -44                        | -47                        | -53                        | -59                        | -64                         | -85          |
| T <sub>m</sub> (°C)             | 113, 128, 152       | 103, 143                   | 61, 96, 127                | 54, 90, 139                | 46, 76, 103                | 39, 68, 93                 | NA                          | 9            |
| ΔH <sub>m</sub> (J/g)           | 98                  | 67                         | 52                         | 41                         | 25                         | 15                         | 0                           | 29           |
| Percent of crystallinity (WAXD) | 25                  | 19                         | 12                         | 13                         | 9                          | 9                          | 0                           | NA           |

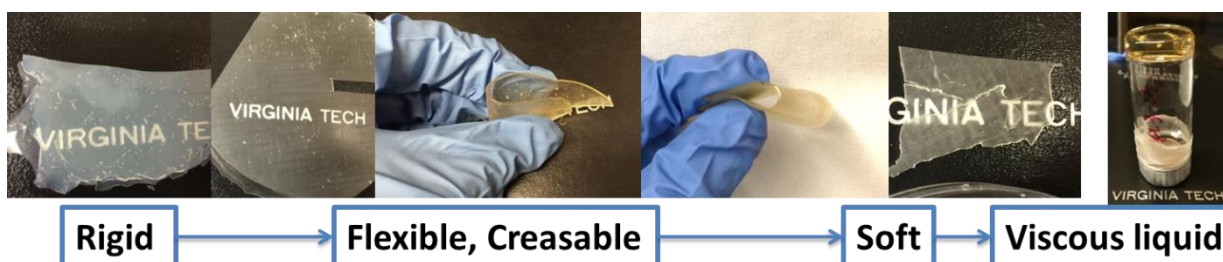
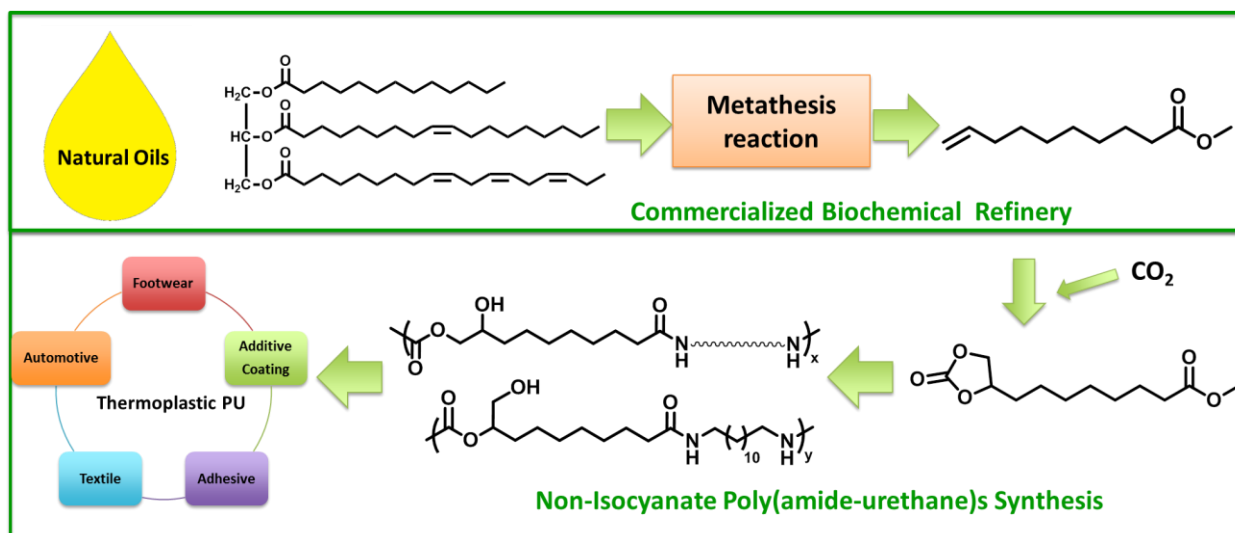


**Figure 10.1.** (a) Process of linear segmented PA<sub>12</sub>HU-PTMO synthesis from unsaturated fatty acid for thermoplastic applications. (b) Melt compression molded films of nonsegmented PA<sub>12</sub>HU and segmented PA<sub>12</sub>HU-PTMOs and a liquid of PA<sub>12</sub>HU-PTMO100, with increasing PTMO mol% from left to right. NA: not applicable.

**Thermal analysis.** Figure 10.2 shows representative TGA weight loss profiles of PA<sub>12</sub>HU and PA<sub>12</sub>HU-PTMOs, along with CC-ME monomer and PTMO-diamine controls. Both PA<sub>12</sub>HU and PA<sub>12</sub>HU-PTMO demonstrated enhanced thermal stability compared to CC-ME due to polymer formation. T<sub>d,5wt%</sub> of PA<sub>12</sub>HU matched conventional polyurethanes, with urethane bond degradation above 210 °C.<sup>29</sup> PA<sub>12</sub>HU clearly exhibited a two-step degradation profile. The second step started near 400 °C, consistent with polyamide degradation.<sup>30</sup> Weight loss of PTMO-diamine started near 300 °C and progressed in a single step. PA<sub>12</sub>HU-PTMOs displayed higher onsets of weight loss with increasing polyether incorporations compared to PA<sub>12</sub>HU, due to decreasing amount of urethane bonds. PA<sub>12</sub>HU-PTMOs each followed a single weight loss step due to polyamide content decreasing with increasing polyether incorporation. PA<sub>12</sub>HU and PA<sub>12</sub>HU-PTMOs also displayed higher thermal stability than trimers in the model compound analyses, proving polymer formation (Figure S10.13, 10.14).

DSC revealed thermal transitions of PA<sub>12</sub>HU and PA<sub>12</sub>HU-PTMOs, comparing to PTMO diamine (Figure 10.3), CC-ME monomer (Melting point 36-37 °C), and trimers (Figure S10.14). The differences between their thermal transitions again confirmed polymer formation. Table 10.1 summarizes compositions and thermal properties of PA<sub>12</sub>HU and PA<sub>12</sub>HU-PTMOs. Heat of fusion ( $\Delta H_m$ ) was normalized against weight percent of the hard segments. PA<sub>12</sub>HU was a semicrystalline polymer with a T<sub>g</sub> of 11 °C



and multiple melting exothermic peaks. The complex melting exotherms presumably resulted from different crystalline structures, possibly due to differences in packing of the dodecane units flanked by amides or hydroxyurethanes. However, other explanations such as recrystallization of imperfect crystals and re-melting lamellae with different thicknesses should not be ruled out without further investigation.<sup>31</sup> Bidentate hydrogen bonding of amide and urethane units generally assists crystallization in polyamides and polyurethanes, respectively.<sup>28</sup> The highest melting point of PA<sub>12</sub>HU was significantly lower than typical nylon melting points (180-270 °C),<sup>32</sup> due to hydroxyurethane units disrupting the long range periodical packing of polyamide segments. Shorter amide segment length generally results in thinner lamellae with lower melting points. The primary hydroxyls and secondary hydroxyls on the polymer chains also possibly interfered with chain packing, as most reported poly(hydroxyurethane)s were amorphous.<sup>10</sup>

DSC thermograms of segmented PA<sub>12</sub>HU-PTMOs contained melting exothermic peaks except for amorphous PA<sub>12</sub>HU-PTMO100 (Figure 10.3). However, the  $\Delta H_m$  values were significantly lower than the nonsegmented PA<sub>12</sub>HU (Table 10.1). Furthermore,  $\Delta H_m$  decreased with increasing soft segment content. Because crystallinities were not calculated due to unknown  $\Delta H_m$  for fully crystalline PAHU, only qualitative comparisons were discussed herein. Although DSC profile of PTMO-diamine showed an exothermic melting peak around 0 °C, PA<sub>12</sub>HU-PTMOs did not exhibit any thermal transition indicative of crystallinity of the soft segments. Polymer formation and relatively low polyether molecular weight (1 kDa) hindered the crystallization of the soft segments, as commonly seen in segmented polyurethanes and polyamides.<sup>27,33,34</sup> Higher polyether incorporations led to lower crystallinities and melting temperatures, mainly due to a dilution effect of

crystallizable hard segments.<sup>35,36</sup> Hydrogen bonding in close proximity typically proves more effective in forming ordered structure due to cooperative effect. Flexible polyether segments between the hydrogen bonding groups resulted in shorter hard segment lengths and therefore weaker neighboring cooperative effects. This interference became stronger when the hard segments phase-mixed with polyether segments.

Amorphous PA<sub>12</sub>HU-PTMO100 showed a single T<sub>g</sub> at -63 °C, nearly 20 °C higher than the PTMO diamine (T<sub>g</sub> = -85 °C), indicative of complete phase-mixing of polyether segments and urethane/amide-containing segments. Hydrogen bonding of the urethanes and amides resulted in higher T<sub>g</sub> of PA<sub>12</sub>HU-PTMO100 relative to PTMO diamine. T<sub>g</sub> values of segmented PA<sub>12</sub>HU-PTMOs increased and broadened with increasing hard segment content, indicative of phase-mixing (Figure S10.15). This phase-mixing likely resulted from relatively short polyether segment (low degree of polymerization, N), similar polarity of hard segments and polyether segments (small Flory-Huggins interaction parameter,  $\chi$ ), or both.<sup>38</sup> Yu *et al.* observed similar phase-mixing properties of segmented polyamides with 460 g/mol poly(propylene oxide) soft segment.<sup>31</sup> The aliphatic spacers in CC-ME monomer and 1,12-diaminododecane contributed to more hydrophobic hard segments of PA<sub>12</sub>HU-PTMOs than conventional segmented polyurethanes, which commonly utilize butane diol/ethylene diol for the chain extenders.

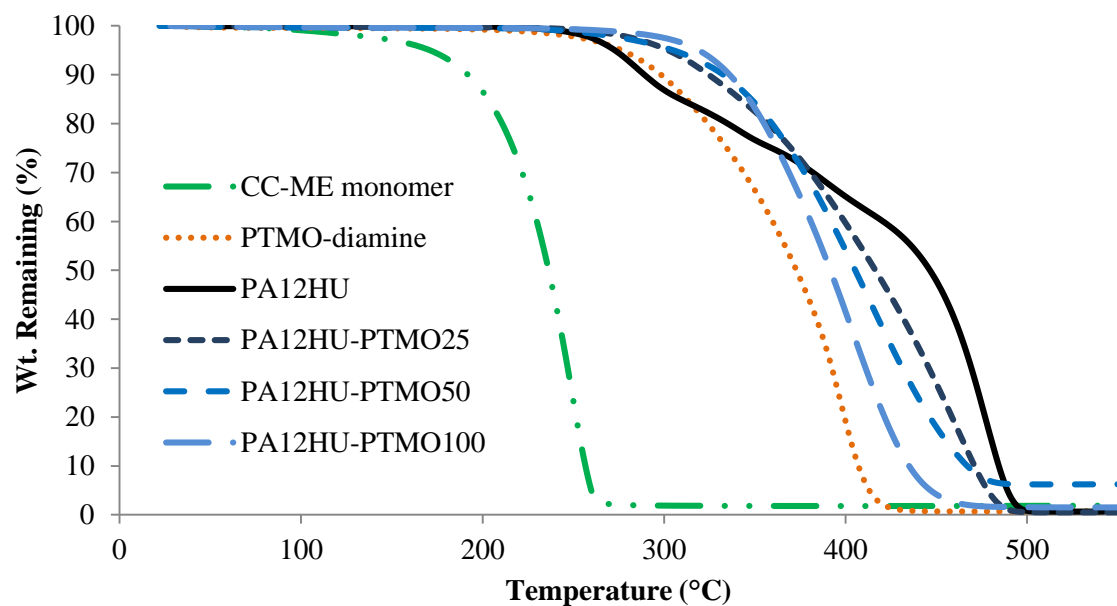


**Figure 10.2.** Representative TGA thermograms of nonsegmented PA<sub>12</sub>HU and segmented PA<sub>12</sub>HU-PTMOs, along with PTMO-diamine precursor and CC-ME monomer under nitrogen purge.

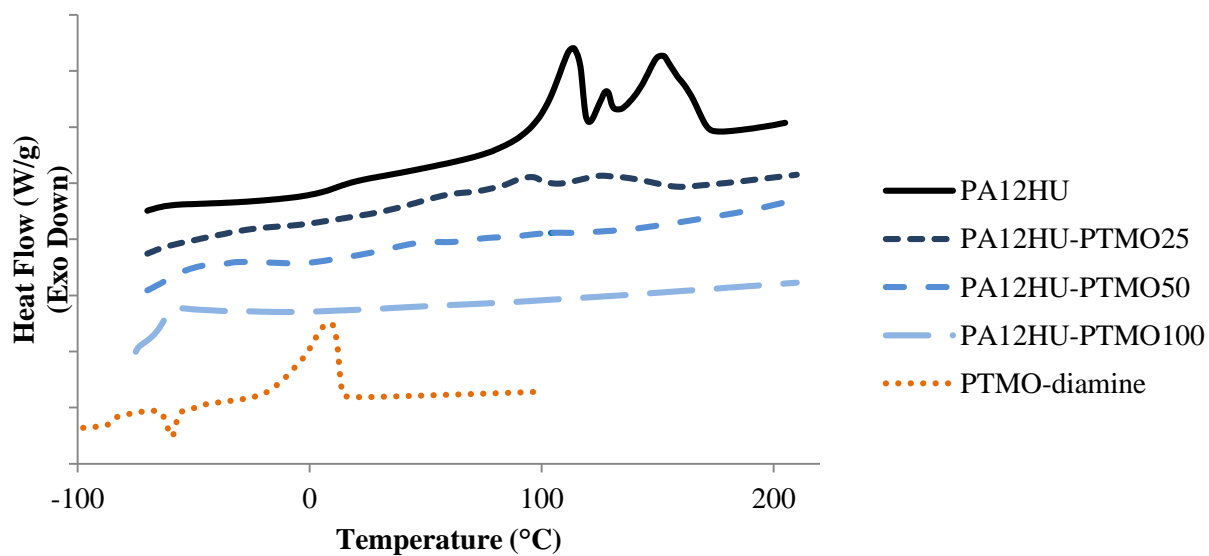


**Figure 10.3.** Representative DSC thermograms of nonsegmented PA<sub>12</sub>HU and segmented PA<sub>12</sub>HU-PTMOs, compared with PTMO-diamine 1 kDa.

DMA investigated the thermomechanical properties of segmented PA<sub>12</sub>HU-PTMOs from -100 °C to 100 °C (Figure 10.4). All compression molded films showed similar moduli in the glassy region below -70 °C. Modulus curves started to drop near -60 °C, representing onset of the glass transition. The following gradual decreases of moduli and broad tan delta peaks indicated significant phase-mixing of the soft segments and the amorphous hard segments, which agreed with the DSC results. Tan delta peaks shifted to lower temperature with increasing polyether contents, which was attributed to increasing low T<sub>g</sub> component of the amorphous phase. The crystalline phase maintained the mechanical integrity for PA<sub>12</sub>HU-PTMO films, affording small plateau windows from 0 °C to 40 °C, more distinguishable with higher polyether contents. Crystalline domains of segmented PA<sub>12</sub>HU-PTMO films served as reinforcing fillers to preserve the modulus level with increasing temperature until the onset of melting. The final drop in moduli corresponded to crystallites melting, and the observed temperature agreed well with melting temperatures from DSC.

Comparing the series of PA<sub>12</sub>HU-PTMOs with varying soft segment contents, samples with higher polyether mol% exhibited lower moduli and bigger tan delta peaks. The magnitude of tan delta peak generally correlates to the relative amount of the amorphous phase, which undergoes glass transition.<sup>31</sup> PA<sub>12</sub>HU-PTMOs with higher polyether contents proved less crystalline, demonstrating a similar trend to the DSC results (Table 10.1). Increasing soft segment also led to earlier onset of flow due to reduced crystallinity and less hydrogen bonding. Two broad tan delta peaks of PA<sub>12</sub>HU-PTMO10 near -70 °C and 10 °C suggested the presence of phase-separation. The tan delta peak of

PA<sub>12</sub>HU-PTMO67 also contained a shoulder around 0 °C. However, phase-mixing still dominated the thermomechanical properties of PA<sub>12</sub>HU-PTMOs. Annealing at 130 °C afforded no significant effect on the DMA results for PA<sub>12</sub>HU-PTMO films. The lack of annealing effect indicated that the phase-mixing of hard segments and polyether soft segments was not due to kinetically trapped morphology.

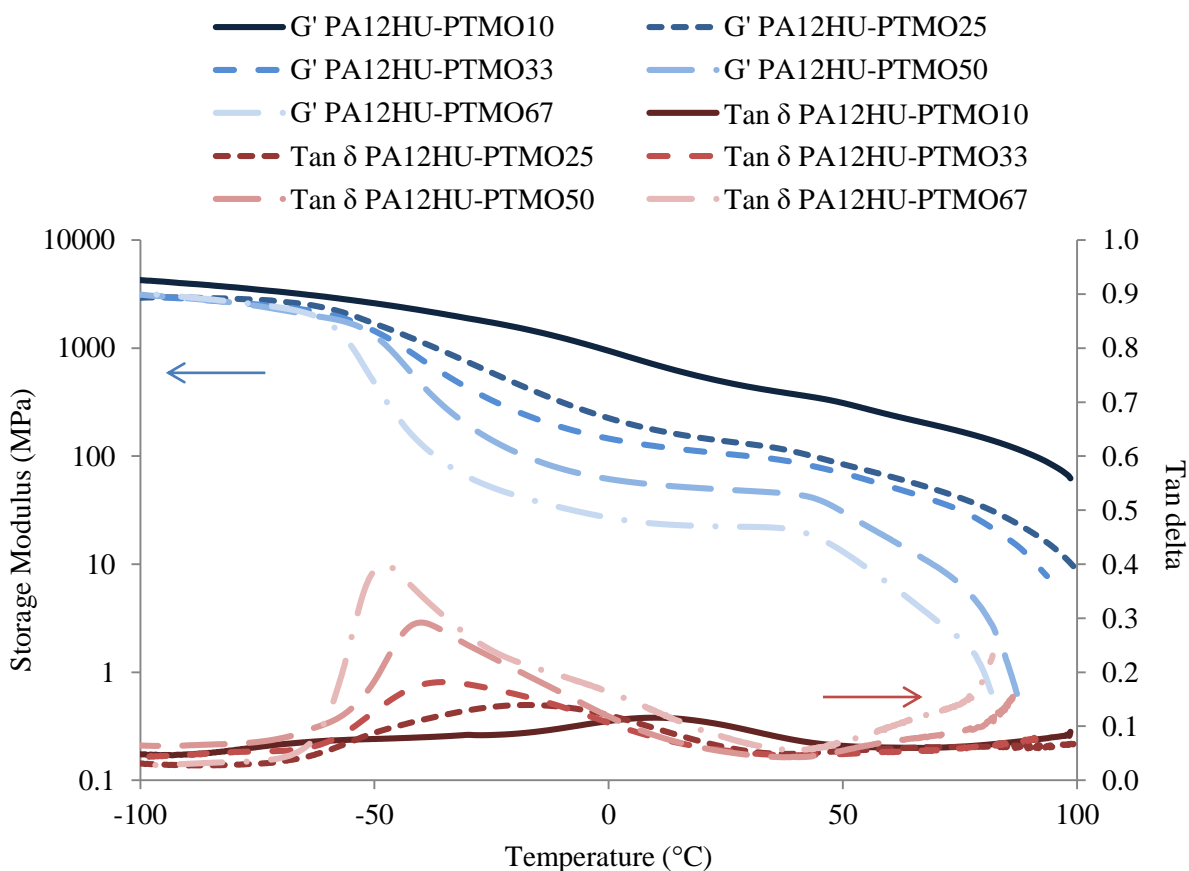


**Figure 10.4.** Dynamic mechanical temperature ramps for compression molded segmented PA<sub>12</sub>HU-PTMO films.

**Morphology characterization.** Small angle X-ray scattering (SAXS) elucidated the bulk morphology of annealed PA<sub>12</sub>HU and PA<sub>12</sub>HU-PTMO films (Figure 10.5). Samples were annealed at 130 °C, above the T<sub>g</sub> of all PA<sub>12</sub>HU-PTMOs and near the T<sub>m</sub> of

nonsegmented PA<sub>12</sub>HU. Slow, step-wise cooling facilitated crystallization of segmented PA<sub>12</sub>HU-PTMOs. Figure 10.5 reveals the microphase-separated bulk morphology of these semicrystalline PA<sub>12</sub>HU-PTMO films, which contain a crystalline phase and an amorphous phase. The amorphous phase consisted of intermixed polyether segments and non-crystallizable portion of the hard segments. SAXS profiles exhibit relatively broad scattering maxima, attributed to interlamellar scattering from PA<sub>12</sub>HU crystallites. Increasing polyether contents shifted the scattering peak from 0.6 nm<sup>-1</sup> to 0.4 nm<sup>-1</sup>, corresponding to a shift in the long period (interlamellar spacing between crystallites) from 10.5 nm to 15.7 nm, respectively. The decrease in scattering peak intensity related to an overall decrease in % crystallinity ( $X_c$ ), consistent with DSC (Figure 10.3) and WAXD (Figure 10.6, Table 10.1). Additionally, the decrease in intensity is likely attributed to a decrease in long range interlamellar ordering as the amorphous contents fill spaces between the lamella.

WAXD enabled characterization of the degree of crystallinity of annealed PA<sub>12</sub>HU and PA<sub>12</sub>HU-PTMO films (Figure 10.6). Before the analyses, the samples were annealed at 130 °C for 12 hours followed by slow step-wise cooling to promote crystallization. Prominent crystalline peaks are observed for nonsegmented PA<sub>12</sub>HU and WAXD measurements were taken at room temperature, above the  $T_m$  of pure PTMO (Table 10.1). Therefore, these peaks are attributed to the crystalline order of the poly(amide-hydroxyurethane) segment in PA<sub>12</sub>HU-PTMO films. As shown in Figure 10.6, these crystalline reflections appear at 6.5°, 20.0°, and 23.0°. The degree of crystallinity,  $X_c$ , summarized in Table 10.1 was calculated for each copolymer using the WAXD data. Crystalline peaks were deconvoluted by a fit of Gaussian and Lorentzian functions with

minimized residuals (Figure S10.18). Degree of crystallinity was calculated as the ratio of the combined area under the three crystalline peaks to the total area. As expected, the degree of crystallinity in the segmented block copolymer decreases with increasing polyether contents (i.e. a decrease in the amount of the crystallizable hard segment).

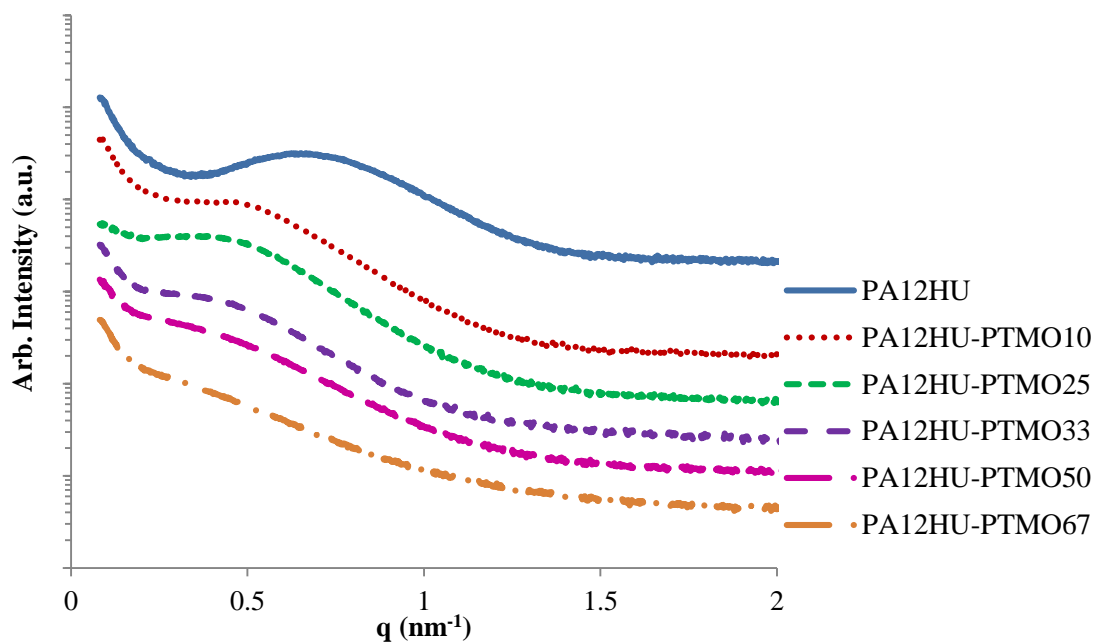


**Figure 10.5.** SAXS for compression molded films of nonsegmented PA<sub>12</sub>HU and segmented PA<sub>12</sub>HU-PTMOs after annealing at 130 °C for 12 h.

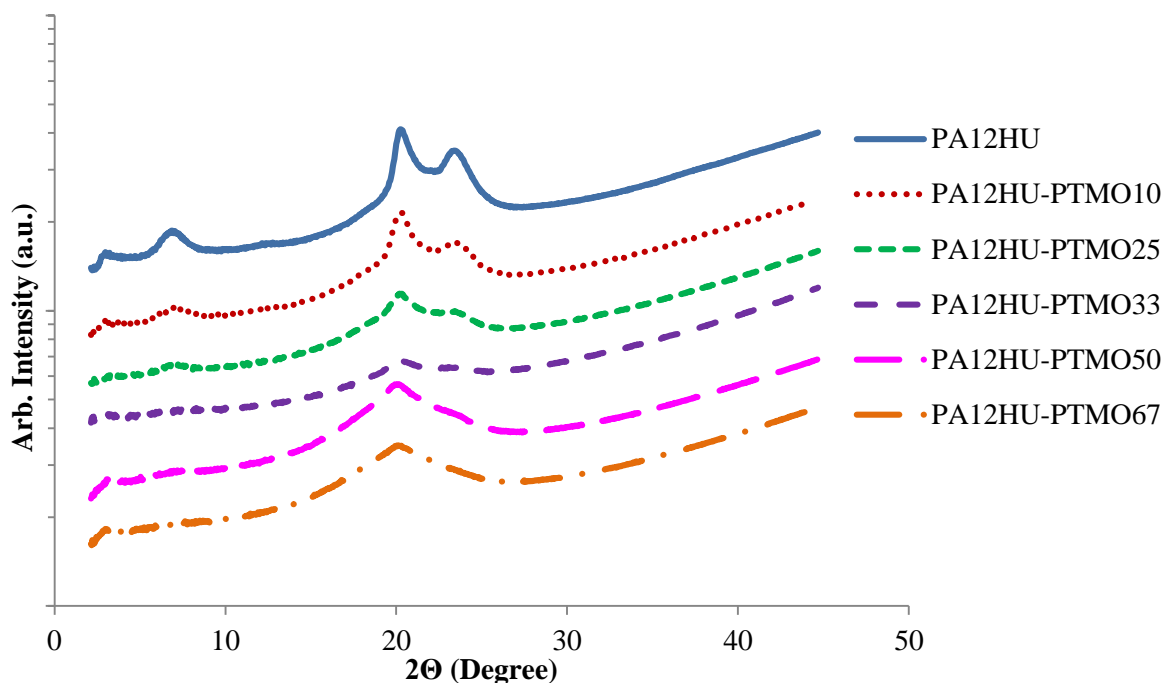


**Figure 10.6.** WAXD for compression molded films of nonsegmented PA<sub>12</sub>HU and segmented PA<sub>12</sub>HU-PTMOs after annealing at 130 °C for 12 h. Curves were shifted vertically for visual clarity.

Atomic force microscopy (AFM) commonly applies to surface morphological characterization of segmented polyurethanes and polyamides.<sup>39</sup> Figure 10.7 reveals the microphase-separated surface morphologies of annealed PA<sub>12</sub>HU-PTMO films. The light areas represent the hard, crystalline domains, and the dark areas represent the amorphous, soft domains, which contained intermixed polyether segments and non-crystallized hard segments. All PA<sub>12</sub>HU-PTMO samples displayed ribbon-like crystalline domains on the surface. AFM image of nonsegmented PA<sub>12</sub>HU showed a continuous crystalline matrix with isolated amorphous domains (Figure S10.17), which explained its rigidity. The incorporation of polyether segments contributed to densely packed ribbons for PA<sub>12</sub>HU-



PTMO25 and PA<sub>12</sub>HU-PTMO33. With increasing soft segment content, the crystalline phase formed more loosely packed ribbons randomly dispersed in the amorphous matrix for PA<sub>12</sub>HU-PTMO50 and PA<sub>12</sub>HU-PTMO67. The wider-field images (upper row) more clearly depict the general trend of light, crystalline phase shrinking with increasing polyether incorporation, agreeing with both DSC and WAXD results. The width of these ribbons appeared rather constant with changing hard segment contents, likely due to the chain-folding mechanism.<sup>40</sup> However, the lengths of crystalline ribbons appeared to increase with decreasing hard segment content from PA<sub>12</sub>HU-PTMO10 to 50. Increasing the content of polyether incorporation in the mixed amorphous phase led to lower T<sub>g</sub> and higher chain mobility, which facilitated long-range packing of the crystallizable hard segments. The increasing lengths of the crystalline domains compensated for their loosening distribution as polyether content increases, which explained the relatively constant interlamellar spacing from the SAXS profiles of PA<sub>12</sub>HU-PTMOs. When polyether content increased beyond 50 mol%, the hard segment content was insufficient to form one-micron size ribbons, accounting for the shorter crystalline domains in PA<sub>12</sub>HU-PTMO67. The crystalline domains of PA<sub>12</sub>HU-PTMO67 displayed more curvature, which explained the disappearance of scattering peak in Figure 5 for the SAXS profile of PA<sub>12</sub>HU-PTMO67.

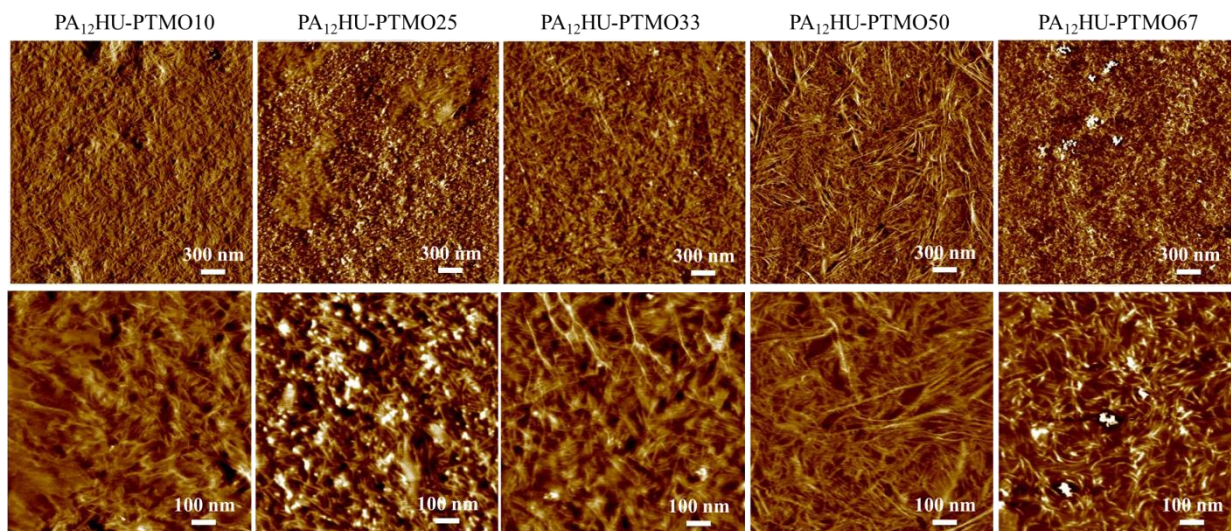
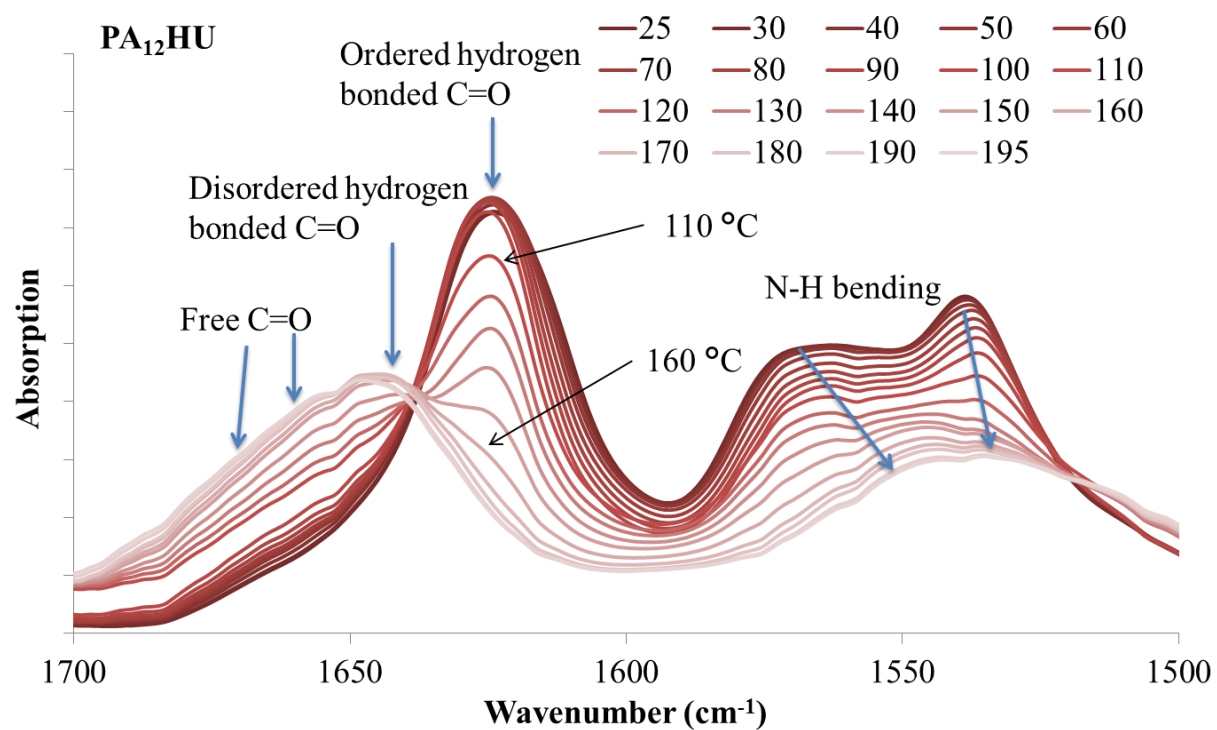


**Figure 10.7.** AFM phase images of compression molded segmented PA<sub>12</sub>HU-PTMOs after annealing at 130 °C for 12 h.

**Variable temperature FTIR spectroscopy (VT-FTIR).** Hydrogen bonding plays significant role in the crystallization and morphology of polyamides and polyurethanes. When C=O and N-H units of amides and urethanes form hydrogen bonds, their signature infrared absorption frequencies shift due to bond length changes. In poly(amide-hydroxyurethane), the hydroxyls also provide hydrogen bonding donors and acceptors. VT-FTIR is a valuable tool for monitoring hydrogen bonding association and dissociation with changing temperature.<sup>41-43</sup> Figure 10.8a demonstrates VT-FTIR spectra of nonsegmented PA<sub>12</sub>HU in the 1500-1700 cm<sup>-1</sup> region with increasing temperature from dark to light curves. This carbonyl stretching region contains three distinctive contributions: ordered hydrogen bonded, disordered hydrogen bonded, and free (non-hydrogen bonded) carbonyls near 1624 cm<sup>-1</sup>, 1645 cm<sup>-1</sup>, and 1670 cm<sup>-1</sup>, respectively. Hydrogen bonding formation results in the red shift of C=O stretching vibration band, due to bond lengthening.<sup>41</sup> Increasing temperature leads to a blue shift of the C=O stretching vibration

band to higher frequency when hydrogen bond weakens or dissociates. In Figure 10.8a, a sharp absorption band near  $1624\text{ cm}^{-1}$  decreased with increasing temperature and a broad band gradually increased at higher frequency, indicating a blue shift due to hydrogen bond weakening and dissociation. This onset occurred near  $100\text{ }^{\circ}\text{C}$ , which correlated to the melting onset of nonsegmented  $\text{PA}_{12}\text{HU}$  in Figure 10.3. Melting of  $\text{PA}_{12}\text{HU}$  finished near  $170\text{ }^{\circ}\text{C}$  in DSC, when the ordered hydrogen bonded carbonyl absorption disappeared completely. This indicated that ordered hydrogen bonded carbonyls existed mostly within the crystalline domains. Disordered hydrogen bonded and free carbonyls became predominant above  $170\text{ }^{\circ}\text{C}$  due to melting of the crystallites. N-H bending absorption red-shifted to lower frequency with decreasing intensity due to weakening hydrogen bonding as temperature increased.<sup>41,43,44</sup> Figure 10.8b illustrates that N-H and O-H stretching vibration bands shifted to higher wavenumbers with increasing temperature, which is attributed to hydrogen bond weakening. A decrease in the absorption coefficient accounted for the dramatic band intensity decrease due to hydrogen bonding weakening.<sup>43</sup> Segmented  $\text{PA}_{12}\text{HU-PTMO50}$  exhibited a similar phenomenon in Figure 10.9. The absorption band of ordered hydrogen bonded carbonyls blue-shifted with increasing temperature. This shift started above  $30\text{ }^{\circ}\text{C}$  until ordered hydrogen bonded band disappeared near  $120\text{ }^{\circ}\text{C}$ , which matched closely to the melting range of  $\text{PA}_{12}\text{HU-PTMO50}$  in Figure 10.3. VT-FTIR revealed the melting point difference between segmented  $\text{PA}_{12}\text{HU-PTMO50}$  and nonsegmented  $\text{PA}_{12}\text{HU}$ . FTIR spectrum of  $\text{PA}_{12}\text{HU-PTMO50}$  at  $30\text{ }^{\circ}\text{C}$  contained a more obvious, relatively broader shoulder from the disordered hydrogen bonded and free carbonyls, compared to nonsegmented  $\text{PA}_{12}\text{HU}$  at  $30\text{ }^{\circ}\text{C}$ . Polyether incorporation disrupted

ordered hydrogen bonding formation, and resulted in a higher percentage of disordered and free hydrogen bonding donors and acceptors for PA<sub>12</sub>HU-PTMO50.



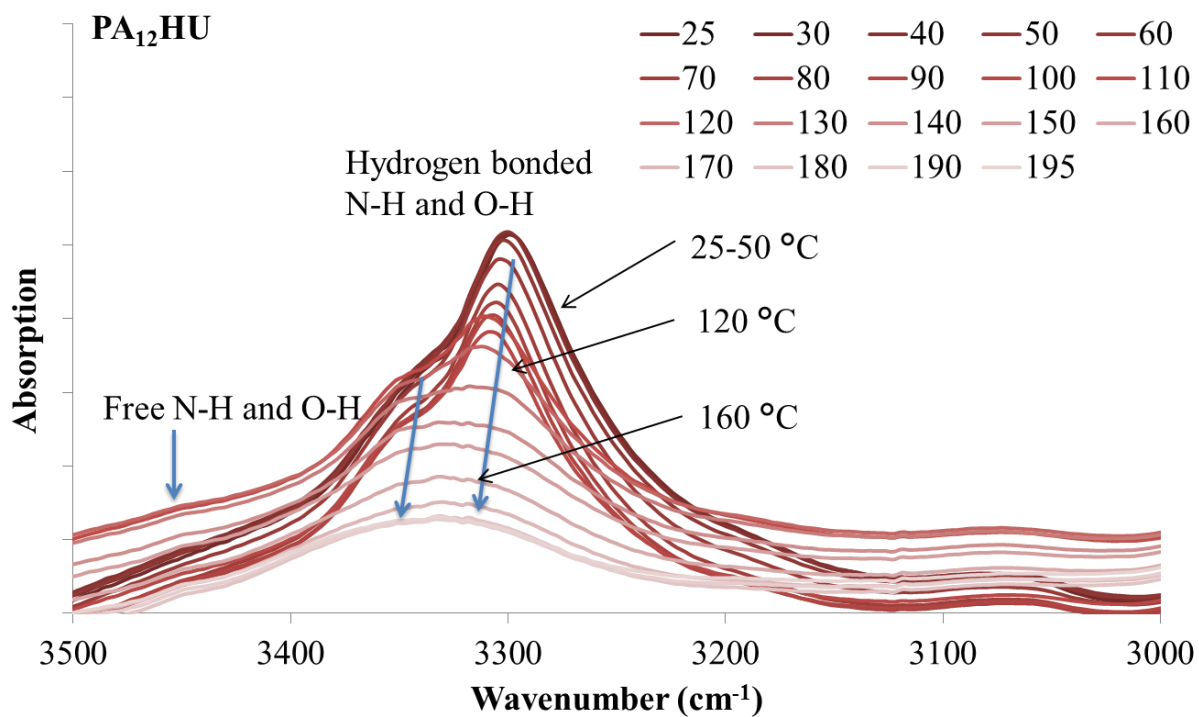


**Figure 10.8.** Variable temperature FT-IR spectra of nonsegmented PA<sub>12</sub>HU (a) in the 1500-1700 cm<sup>-1</sup> region and (b) in the 3000-3500 cm<sup>-1</sup> region.

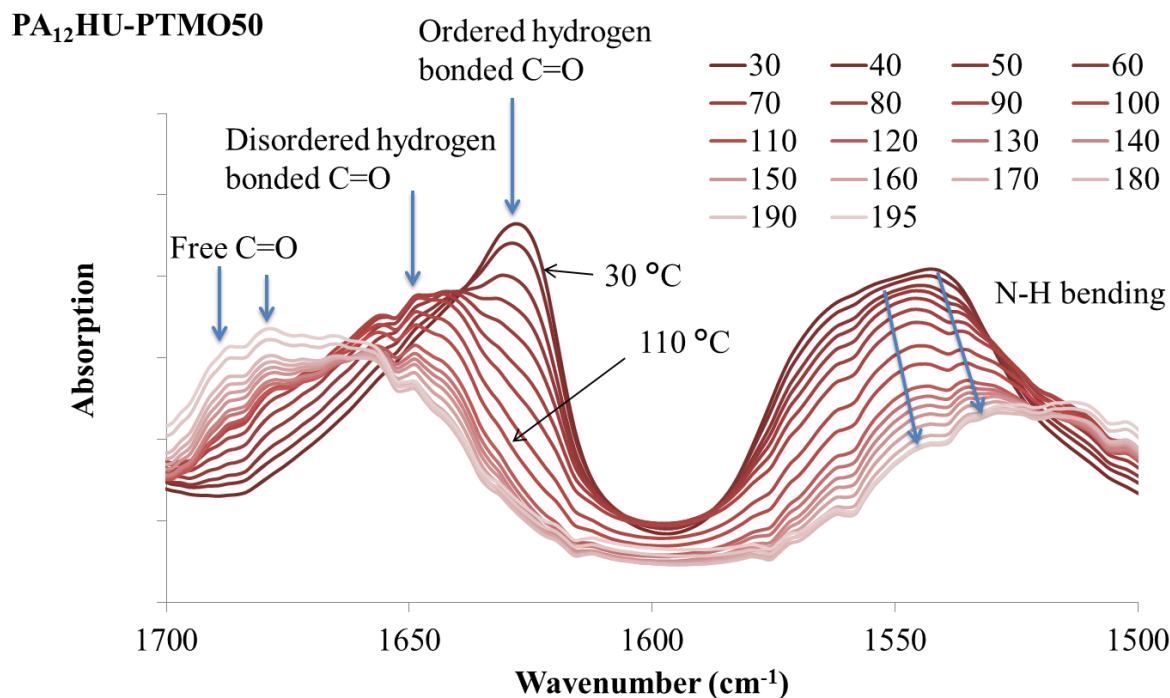


**Figure 10.9.** Variable temperature FT-IR spectra of segmented PA<sub>12</sub>HU-PTMO50 (a) in the 1500-1700 cm<sup>-1</sup> region.

**Water sorption.** Figure 10.10 depicts water uptake of nonsegmented PA<sub>12</sub>HU and segmented PA<sub>12</sub>HU-PTMOs in 0% to 95% relative humidity (RH) at 25 °C. PA<sub>12</sub>HU lacked detectable water uptake until 90% RH, due to its relatively high crystallinity and T<sub>g</sub> near room temperature (11 °C). PA<sub>12</sub>HU only showed 0.5 wt% uptake of water at 95% RH, possibly attributed to water condensed on the surface. Segmented PA<sub>12</sub>HU-PTMOs exhibited much higher water uptake compared to PA<sub>12</sub>HU due to lower crystallinity and lower T<sub>g</sub> values (Table 10.1). Water uptake of PA<sub>12</sub>HU-PTMOs increased with increasing RH, reaching approximately 3.6-4.9 wt% at 95% RH and 1.6-2.0% at 65% RH, which was slightly higher than commercial Spandex® (thermoplastic polyurethane 0.75-1.3% at 65% RH), due to the additional hydroxyls.<sup>45</sup> Water uptake of PA<sub>12</sub>HU-PTMOs proved

independent of the polyether weight content, which confirmed the similar polarity of the hard segments and the polyether segments.

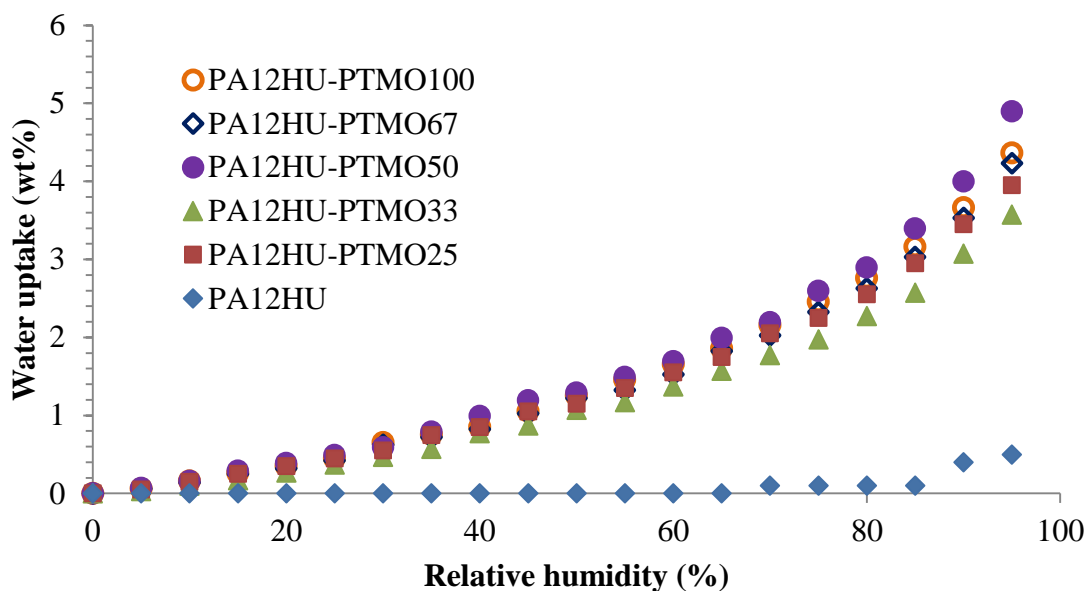


**Figure 10.10.** Equilibrium water sorption of nonsegmented PA<sub>12</sub>HU and segmented PA<sub>12</sub>HU-PTMOs in relative humidity steps from 0% to 95%.

**Tensile properties.** Figure 10.11 displays representative engineering stress-strain curves of PA<sub>12</sub>HU-PTMOs. Table 10.2 summarizes their tensile properties, including stress at break, strain at break, and Young's modulus. Compression molded films of PA<sub>12</sub>HU-PTMO25-50 exhibited enough mechanical integrity to yield statistically reliable tensile testing results. However, their tensile properties proved weaker than conventional segmented polyurethanes or segmented polyamides, likely due to the phase-mixed nature of the hard segments and polyether soft segments. Multiple thermal, dynamic mechanical, morphological analyses confirmed that the amorphous phase of each PA<sub>12</sub>HU-PTMO contained both hard and soft segments with a broad glass transition. The lack of long plateau window in DMA curves agreed with the low strain at break values of PA<sub>12</sub>HU-

PTMOs due to the broad  $T_g$ . Crystallinities of PA<sub>12</sub>HU-PTMOs also significantly limited the strains at break. The molecular weights of these PA<sub>12</sub>HU-PTMOs were adequate for compression molding into free-standing films, however, not sufficient to reach comparable tensile properties to commercial polyurethanes. Further optimization of PAHUs requires two main considerations: improving the phase-separation of hard and soft segments, and establishing SEC systems for molecular weight determination.

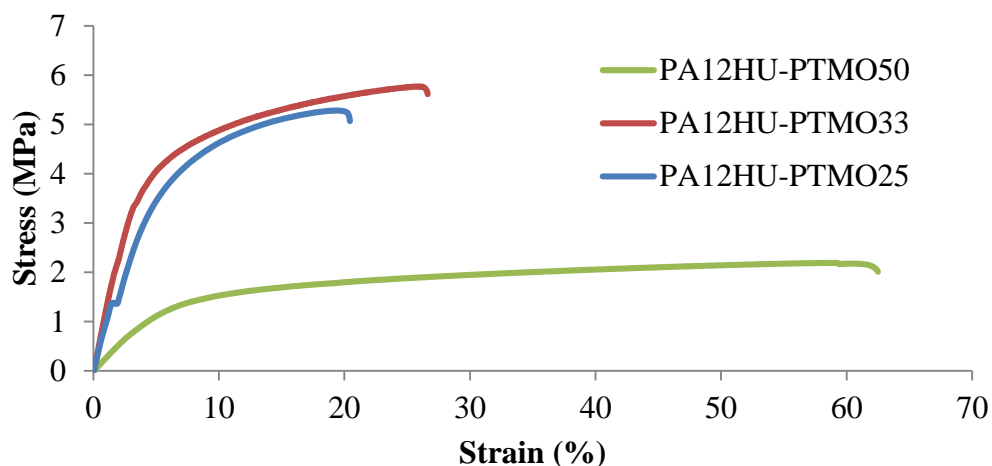


**Figure 10.11.** Stress-strain curves of compression molded segmented PA<sub>12</sub>HU-PTMOs with 25-50 mol% soft segments.

**Table 10.2.** Tensile properties of compression molded segmented PA<sub>12</sub>HU-PTMOs with 25-50 mol% soft segments.

|                            | Young's modulus (MPa) | Strain at break (%) | Stress at break (MPa) |
|----------------------------|-----------------------|---------------------|-----------------------|
| PA <sub>12</sub> HU-PTMO25 | 94.2 ± 24.5           | 25 ± 8              | 5.7 ± 0.4             |
| PA <sub>12</sub> HU-PTMO33 | 108.8 ± 8.1           | 21 ± 6              | 5.3 ± 0.5             |
| PA <sub>12</sub> HU-PTMO50 | 26.5 ± 2.3            | 51 ± 4              | 2.1 ± 0.0             |



## 10.5 *Conclusions*

This manuscript demonstrates an unprecedented, facile synthetic platform for both nonsegmented and segmented poly(amide-hydroxyurethane)s using sustainable resources. These PAHUs represent the first examples of film-forming, isocyanate-free polyurethanes with both melt and solution processability. A variety of physical characterizations established the structure-morphology-property relationship of the synthesized PAHU series with varying compositions.

A scalable, two-step synthesis converted methyl 9-decenoate from the biorefinery of unsaturated fatty acids to CC-ME monomer using CO<sub>2</sub>. A one-pot melt polymerization of CC-ME with diamines afforded synthesis of isocyanate-free PAHUs. Diaminododecane reacted with CC-ME to synthesize nonsegmented PA<sub>12</sub>HU, which was a semicrystalline copolymer with T<sub>g</sub> of 11 °C and multiple melting exotherms at 100~150 °C. Incorporation of a low T<sub>g</sub> 1 kDa polyether diamine added flexibility to segmented PA<sub>12</sub>HU-PTMOs. Segmented PA<sub>12</sub>HU-PTMOs exhibited broad glass transitions near -60~-50 °C from DSC and lower crystallinity compared to nonsegmented PA<sub>12</sub>HU. Increasing ratio of polyether diamine to dodecane diamine resulted in lower crystallinity and lower melting point of PA<sub>12</sub>HU-PTMO due to shorter and fewer hard segments. Both DSC and DMA results indicated significant phase-mixing of polyether segments and the hard segments. Crystallizable hard segments formed crystalline domains, which supported mechanical strength of segmented PA<sub>12</sub>HU-PTMOs. The ribbon-like crystalline domains of PA<sub>12</sub>HU-PTMOs exhibited constant width and varying lengths with different extent of polyether incorporation. VT-FTIR proved that most ordered hydrogen bonded carbonyls existed within the crystalline domains. The carbonyl vibration band shifts occurred in the same

temperature range as melting of the crystalline domains of PA<sub>12</sub>HU or PA<sub>12</sub>HU-PTMOs, according to the DSC results. PA<sub>12</sub>HU exhibited minimal water uptake due to relatively high crystallinity. PA<sub>12</sub>HU-PTMOs showed slightly higher water uptake than conventional segmented polyurethanes. Reported poly(amide-hydroxyurethane)s displayed similar thermal degradation temperature as conventional polyurethanes, however lacked tensile strength due to their phase-mixed morphologies and possibly low molecular weights.

## 10.6 *Acknowledgements*

This research was supported by Elevance Renewable Science, Inc. This material is also partially based upon work supported by the National Science Foundation under Grant No. DMR-0923107. We also thank Professor Garth L. Wilkes for insightful discussion and Huntsman Corporation for material support.

## 10.7 *References*

1. Ochiai, B.; Sato, S.-I.; Endo, T. *J. Polym. Sci., Part A: Polym. Chem.* **2007**, *45*, 3408.
2. Tamami, B.; Sohn, S.; Wilkes, G. L. *J. Appl. Polym. Sci.* **2004**, *92*, 883.
3. Ochiai, B.; Utsuno, T. *J. Polym. Sci., Part A: Polym. Chem.* **2013**, *51*, 525.
4. Ubaghs, L.; Fricke, N.; Keul, H.; Höcker, H. *Macromol. Rapid Commun.* **2004**, *25*, 517.
5. Palaskar, D. V.; Boyer, A.; Cloutet, E.; Alfos, C.; Cramail, H. *Biomacromolecules* **2010**, *11*, 1202.
6. Kihara, N.; Endo, T. *J. Polym. Sci., Part A: Polym. Chem.* **1993**, *31*, 2765.
7. Webster, D. C. *Prog. Org. Coat.* **2003**, *47*, 77.
8. Guan, J.; Song, Y.; Lin, Y.; Yin, X.; Zuo, M.; Zhao, Y.; Tao, X.; Zheng, Q. *Ind. Eng. Chem. Res.* **2011**, *50*, 6517.
9. Rokicki, G.; Parzuchowski, P. G.; Mazurek, M. *Polym. Adv. Technol.* **2015**, *26*, 707.
10. Blattmann, H.; Fleischer, M.; Bähr, M.; Mülhaupt, R. *Macromol. Rapid Commun.* **2014**, *35*, 1238.
11. Sardon, H.; Pascual, A.; Mecerreyes, D.; Taton, D.; Cramail, H.; Hedrick, J. L. *Macromolecules* **2015**, *48*, 3153.
12. Kihara, N.; Endo, T. *Die Makromolekulare Chemie* **1992**, *193*, 1481.
13. Couvret, D.; Brosse, J.-C.; Chevalier, S.; Senet, J.-P. *Die Makromolekulare Chemie* **1990**, *191*, 1311.

14. Webster, D. C.; Crain, A. L. *Prog. Org. Coat.* **2000**, *40*, 275.
15. Sohn, S.; Tamami, B.; Wilkes, G.; Google Patents: 2004.
16. Javni, I.; Hong, D. P.; Petrović, Z. S. *J. Appl. Polym. Sci.* **2008**, *108*, 3867.
17. Javni, I.; Hong, D. P.; Petrović, Z. S. *J. Appl. Polym. Sci.* **2013**, *128*, 566.
18. Parzuchowski, P. G.; Jurczyk-Kowalska, M.; Ryszkowska, J.; Rokicki, G. *J. Appl. Polym. Sci.* **2006**, *102*, 2904.
19. Ochiai, B.; Inoue, S.; Endo, T. *J. Polym. Sci., Part A: Polym. Chem.* **2005**, *43*, 6613.
20. Tomita, H.; Sanda, F.; Endo, T. *J. Polym. Sci., Part A: Polym. Chem.* **2001**, *39*, 851.
21. Kim, M.-R.; Kim, H.-S.; Ha, C.-S.; Park, D.-W.; Lee, J.-K. *J. Appl. Polym. Sci.* **2001**, *81*, 2735.
22. Maisonneuve, L.; More, A. S.; Foltran, S.; Alfes, C.; Robert, F.; Landais, Y.; Tassaing, T.; Grau, E.; Cramail, H. *RSC Advances* **2014**, *4*, 25795.
23. Boyer, A.; Cloutet, E.; Tassaing, T.; Gadenne, B.; Alfes, C.; Cramail, H. *Green Chemistry* **2010**, *12*, 2205.
24. Nanclares, J.; Petrović, Z. S.; Javni, I.; Ionescu, M.; Jaramillo, F. *J. Appl. Polym. Sci.* **2015**, *132*, n/a.
25. Davies, S. G.; Fletcher, A. M.; Kurosawa, W.; Lee, J. A.; Poce, G.; Roberts, P. M.; Thomson, J. E.; Williamson, D. M. *The Journal of Organic Chemistry* **2010**, *75*, 7745.
26. Odian, G. G. *Principles of polymerization*; Wiley-Interscience Hoboken, N.J, **2004**; Vol. 4th.
27. Korley, L. T. J.; Pate, B. D.; Thomas, E. L.; Hammond, P. T. *Polymer* **2006**, *47*, 3073.
28. Buckwalter, D. J.; Dennis, J. M.; Long, T. E. *Prog. Polym. Sci.*
29. Ravey, M.; Pearce, E. M. *J. Appl. Polym. Sci.* **1997**, *63*, 47.
30. Levchik, S. V.; Weil, E. D.; Lewin, M. *Polym. Int.* **1999**, *48*, 532.
31. Yu, Y. C.; Jo, W. H. *J. Appl. Polym. Sci.* **1995**, *56*, 895.
32. *Thermal Transitions of Homopolymers* Sigma Aldrich  
[https://www.sigmaaldrich.com/content/dam/sigma-aldrich/docs/Aldrich/General\\_Information/thermal\\_transitions\\_of\\_homopolymers.pdf](https://www.sigmaaldrich.com/content/dam/sigma-aldrich/docs/Aldrich/General_Information/thermal_transitions_of_homopolymers.pdf).
33. Paik Sung, C. S.; Hu, C. B.; Wu, C. S. *Macromolecules* **1980**, *13*, 111.
34. Niesten, M. C. E. J.; Feijen, J.; Gaymans, R. J. *Polymer* **2000**, *41*, 8487.
35. Van Der Schuur, M.; Gaymans, R. J. *J. Polym. Sci., Part A: Polym. Chem.* **2006**, *44*, 4769.
36. Flory, P. J. *Principles of polymer chemistry*; Conell Univerisity Press, **1953**.
37. Sperling, L. H. *Introduction to physical polymer science*; John Wiley & Sons, **2015**.
38. Robeson, L. M. *A Comprehensive Review, Leseprobe* **2007**.
39. McLean, R. S.; Sauer, B. B. *Macromolecules* **1997**, *30*, 8314.
40. Chool Yu, Y.; Jo, W. H.; Lee, M. S. *J. Appl. Polym. Sci.* **1997**, *64*, 2155.
41. Zhang, K.; Aiba, M.; Fahs, G. B.; Hudson, A. G.; Chiang, W. D.; Moore, R. B.; Ueda, M.; Long, T. E. *Polym. Chem.* **2015**, *6*, 2434.
42. Skrovanek, D. J.; Painter, P. C.; Coleman, M. M. *Macromolecules* **1986**, *19*, 699.
43. Coleman, M. M.; Lee, K. H.; Skrovanek, D. J.; Painter, P. C. *Macromolecules* **1986**, *19*, 2149.

44. Tamami, M.; Zhang, K.; Dixit, N.; Moore, R. B.; Long, T. E. *Macromol. Chem. Phys.* **2014**, *215*, 2337.
45. Cook, J. G. *Handbook of textile fibres: man-made fibres*; Elsevier, **1984**; Vol. 2.

## 10.8 *Supporting Information*

**Synthesis of hydroxyurethane methylester.** CC-ME (0.7 g, 3.0 mmol), DCM (10 mL), and 1-aminohexane (0.4 g, 4.0 mmol) were added into a 100 mL round-bottomed flask equipped with a magnetic stir bar. The reaction mixture was stirred at 40 °C for 3 h. After cooling back to room temperature, the reaction mixture was washed with 1 M HCl to remove excess amine. DCM was removed and product was washed with diethyl ether. Product was decanted off diethyl ether and dried in vacuo, yielding yellow viscous oil. HRMS (ES<sup>+</sup>): m/z calcd for [M+H]<sup>+</sup> 346.2588 g/mol; found 346.2602 g/mol.

**Synthesis of bis(hydroxyurethane) dimethylester.** CC-ME (3.0 g, 12.3 mmol) and 1,6-diaminohexane (0.7 g, 5.9 mmol) were added into a 100 mL round-bottomed flask equipped with a magnetic stir bar. The reaction mixture was stirred at 80 °C for 12 h, yielding viscous yellow oil. After cooling back to room temperature, 3 mL of DCM was added and stirred to dissolve the oil. The mixture was precipitated to a hexane-ether 2:6 mixture. The precipitant was dissolved in DCM and reprecipitated in hexane-ether 3:1 mixture. The precipitant was dried in vacuo, yielding a yellow wax-like solid-liquid mixture. Evaporation of half the decanted off solvent left white powder on the side of the beaker. The white powder was collected and dried in vacuo. The yellow wax contained both isomers; the white powder only contained the isomer with primary hydroxyl groups. Mass spectroscopy showed the same m/z for both products. HRMS (ES<sup>+</sup>): m/z calcd for [M+H]<sup>+</sup> 605.4013 g/mol; found 605.3989 g/mol.

**Synthesis of hexanediamide diene or dodecanediamide diene.** 9-DAME (25 g, 0.13 mol), 5 mol% La(OTf)<sub>3</sub> or TBD and 1,6-diaminohexane (6.3 g, 54 mmol) were added into a 250 mL round-bottomed flask equipped with a magnetic stir bar. The reaction mixture was melted at 80 °C and stirred for 5 h with slow nitrogen purge until the mixture solidified. The reaction was allowed to stir overnight. The resulted mixture was filtered and washed with MeOH. The solid was recrystallized from IPA and dried in vacuo, giving higher than 80% isolated yield. Dodecanediamide diene was synthesized using the same procedure with more than 80% isolated yield. Hexanediamide diene melting point was 128-130 °C. HRMS (ES<sup>+</sup>): m/z calcd for [M+H]<sup>+</sup> 421.3794 g/mol; found 421.3789 g/mol. Dodecanediamide diene melting point was 125-126 °C. HRMS (ES<sup>+</sup>): m/z calcd for [M+H]<sup>+</sup> 505.4733 g/mol; found 505.4719 g/mol.

**Model compound reactions for hydroxylurethane formation and amidation.** The well-known aminolysis of cyclic carbonates was verified using CC-ME monomer and 1-aminohexane (Scheme S10.1).<sup>1</sup> The reaction finished in 3 h according to NMR spectroscopy. The purified product was an isomer mixture of hydroxyurethane methylester with 70% of secondary hydroxyls and 30% of primary hydroxyls, determined through <sup>1</sup>H NMR spectroscopy (Figure S10.3). Secondary hydroxyls dominated due to the O=C-O single bond length difference on the cyclic carbonate.<sup>1</sup> The ratios reported in literature varied from 85/15 to 56/44, depending on solvents, catalysts, and amines.<sup>1-3</sup> FTIR also revealed the wavenumber shift of the signature absorption peak of carbonyls when cyclic carbonates converted to urethanes (Figure S10.5). CC-ME was also reacted with 1,6-diaminohexane to obtain bis(hydroxyurethane) dimethylester, yielding three isomers (Scheme S10.2). The isomer with only primary hydroxyls was isolated and used as

reference to correctly assign proton and carbon peaks in NMR spectroscopy (Figure S10.3,S10.4,S10.6,S10.7). Secondly, amidation of ester is generally problematic due to low reactivity of the esters.<sup>4</sup> Lanthanum triflate and TBD were proved to be effective catalyst for quantitative amidation of methyl ester with efficient byproduct removal using constant nitrogen purge (Scheme S10.3).<sup>5,6</sup> Both 1,6-diaminohexane and 1,12-diaminododecane reacted with 9-DAME quantitatively at 80 °C in bulk. Mass spectroscopy and NMR spectroscopy confirmed the structure and purity of the produced diamide diene (Figure S10.8).

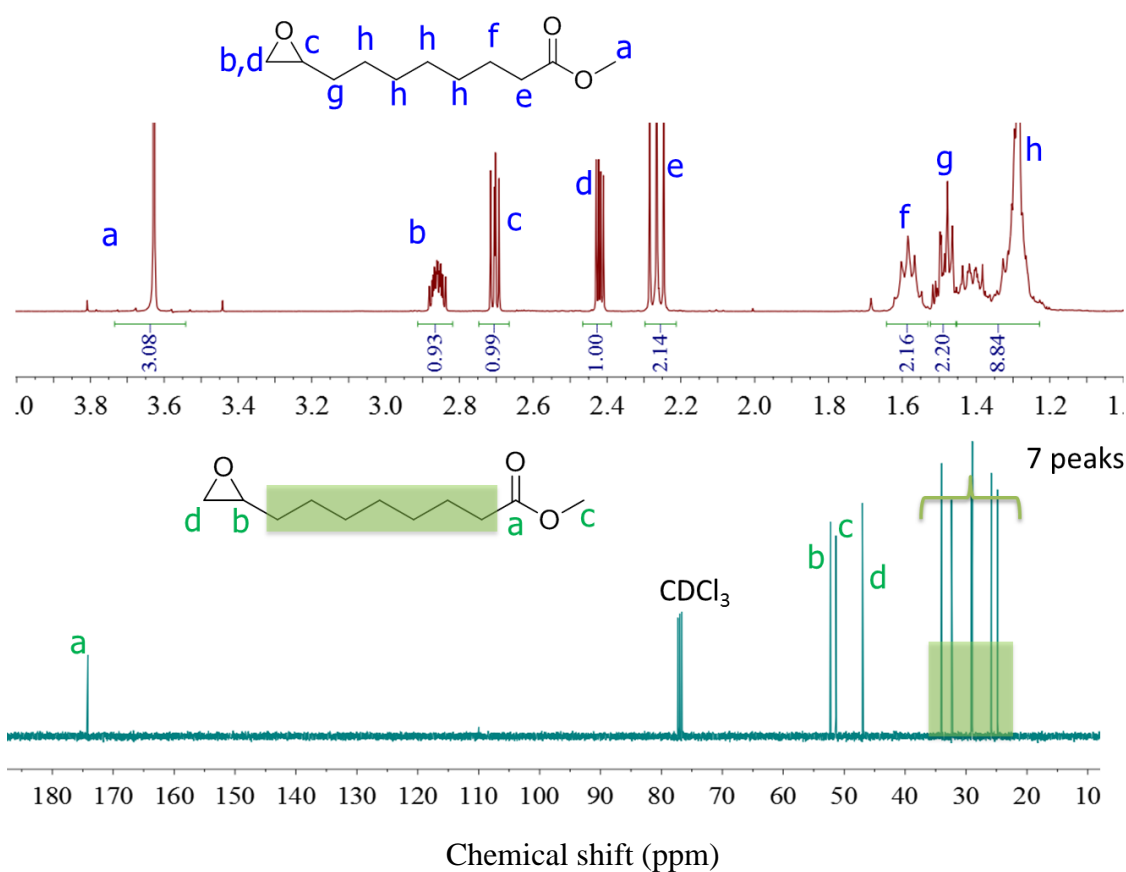


**Figure S10.1.**  $^1\text{H}$  NMR and  $^{13}\text{C}$  NMR spectra of methyl 9,10-epoxydecanoate.

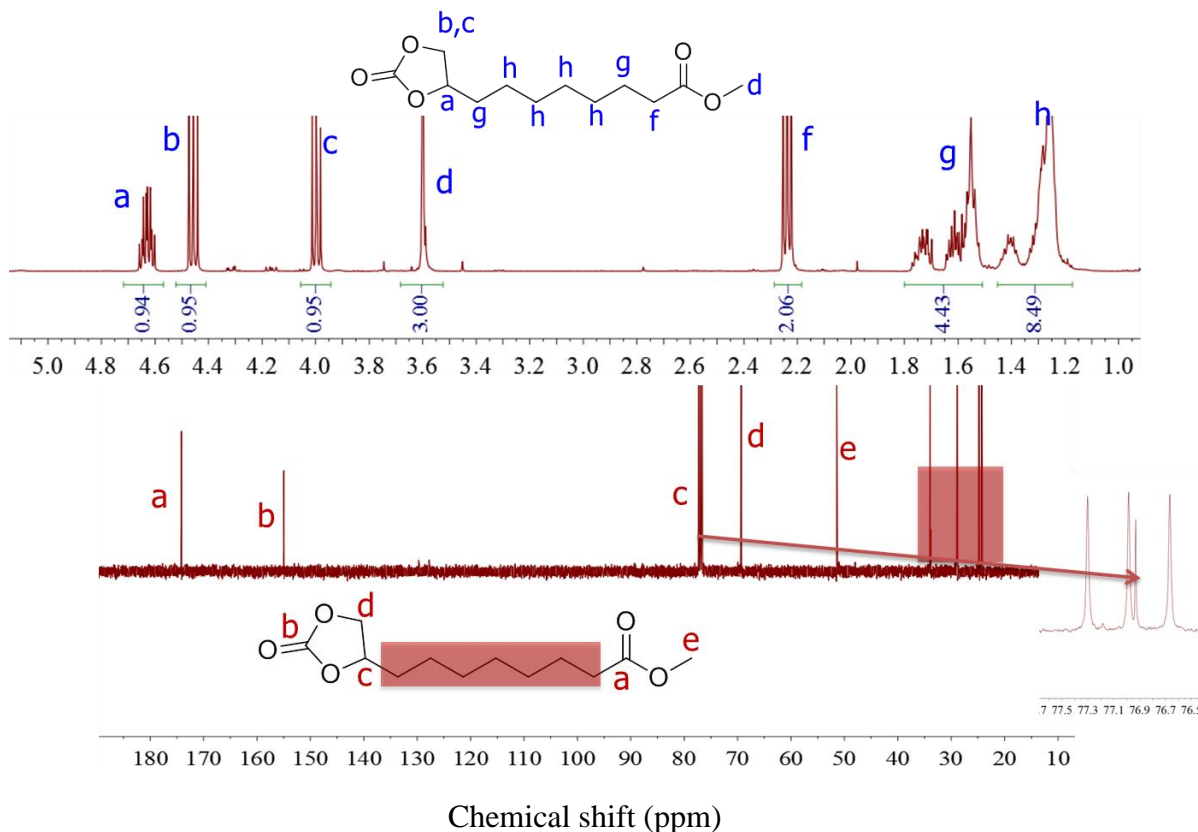
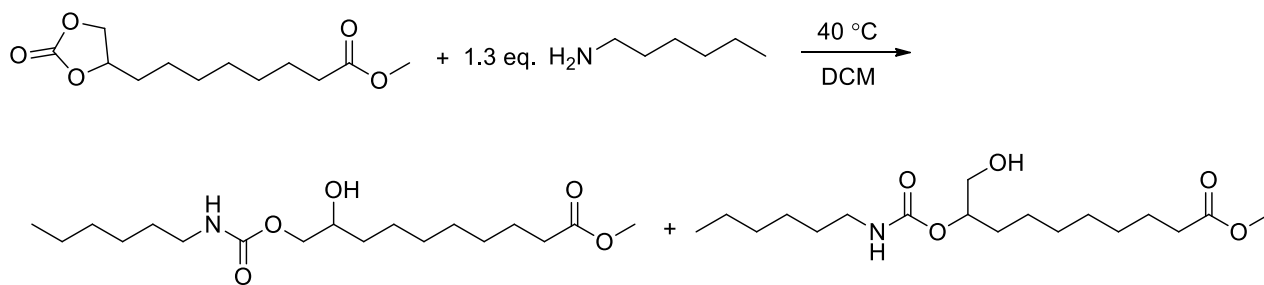


**Figure S10.2.**  $^1\text{H}$  NMR and  $^{13}\text{C}$  NMR spectra of CC-ME monomer.



**Scheme S10.1.** Model compound reaction between CC-ME with 1-aminoheptane, generating isomer mixture of hydroxyurethane methylester with primary and secondary hydroxyl groups.

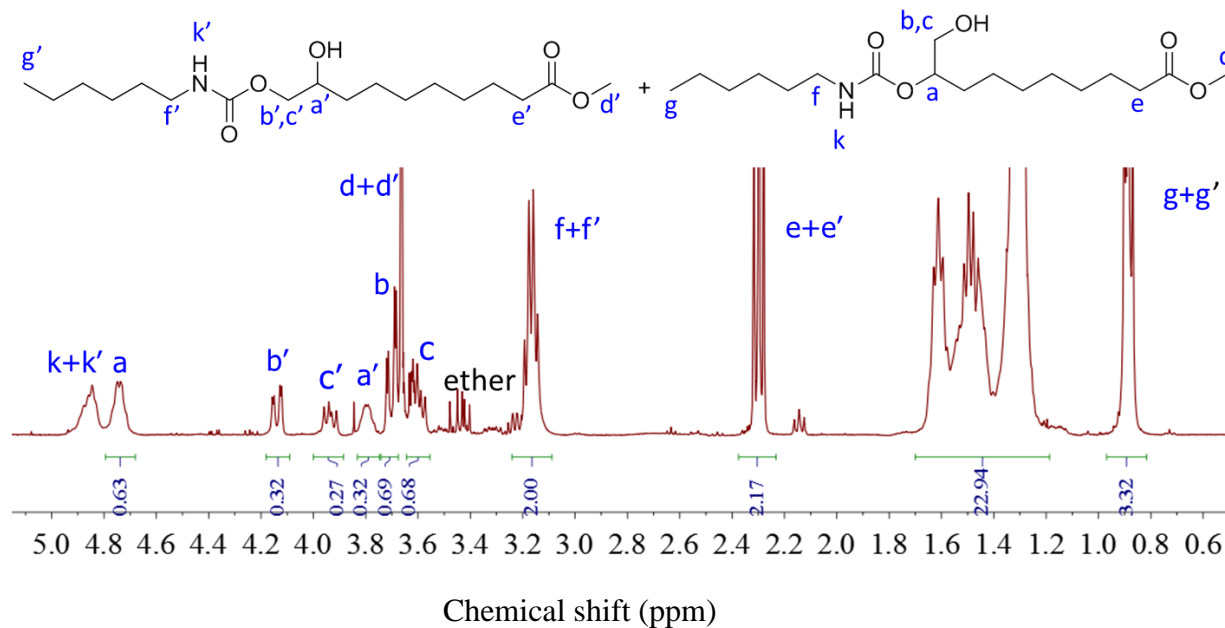


**Figure S10.3.**  $^1\text{H}$  NMR spectrum of hydroxyurethane methylester isomer mixture.

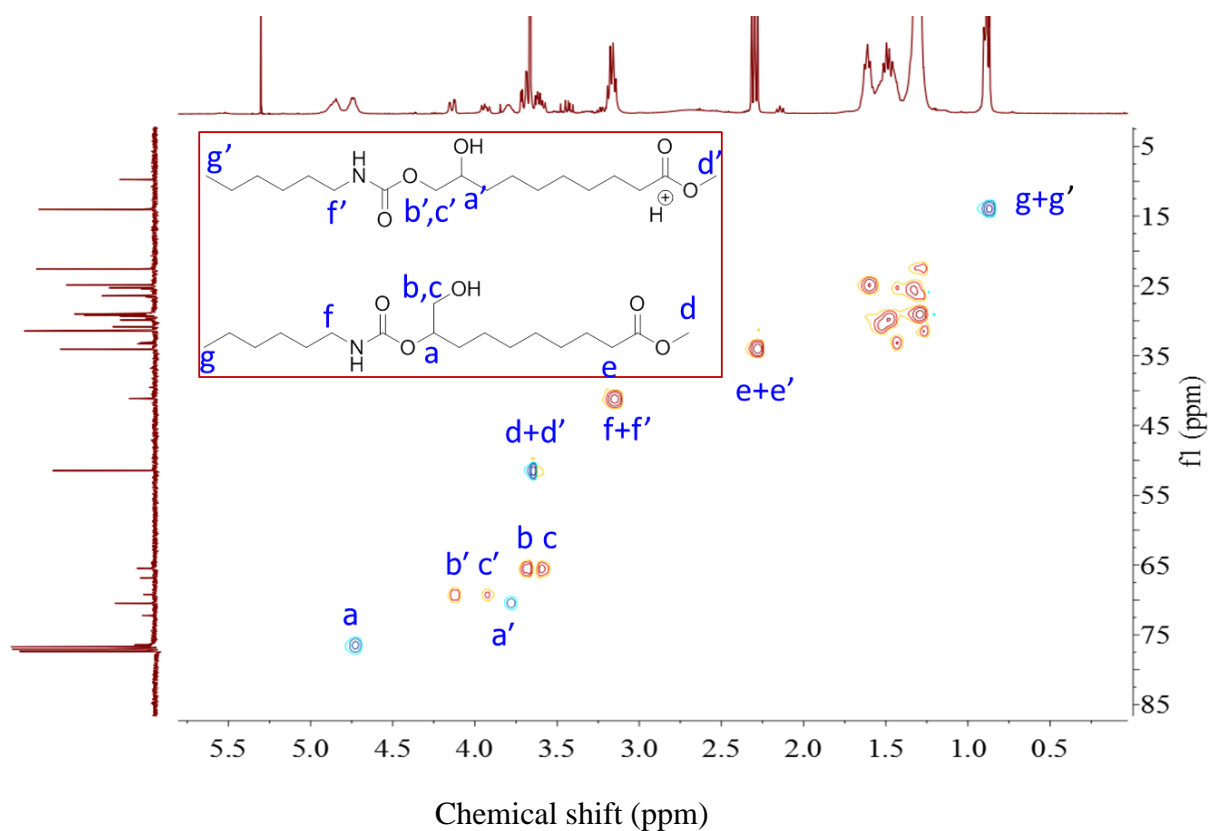


**Figure S10.4.** HSQC 2D NMR spectrum of the mixture of hydroxyurethane methylester isomers with primary and secondary hydroxyl groups.



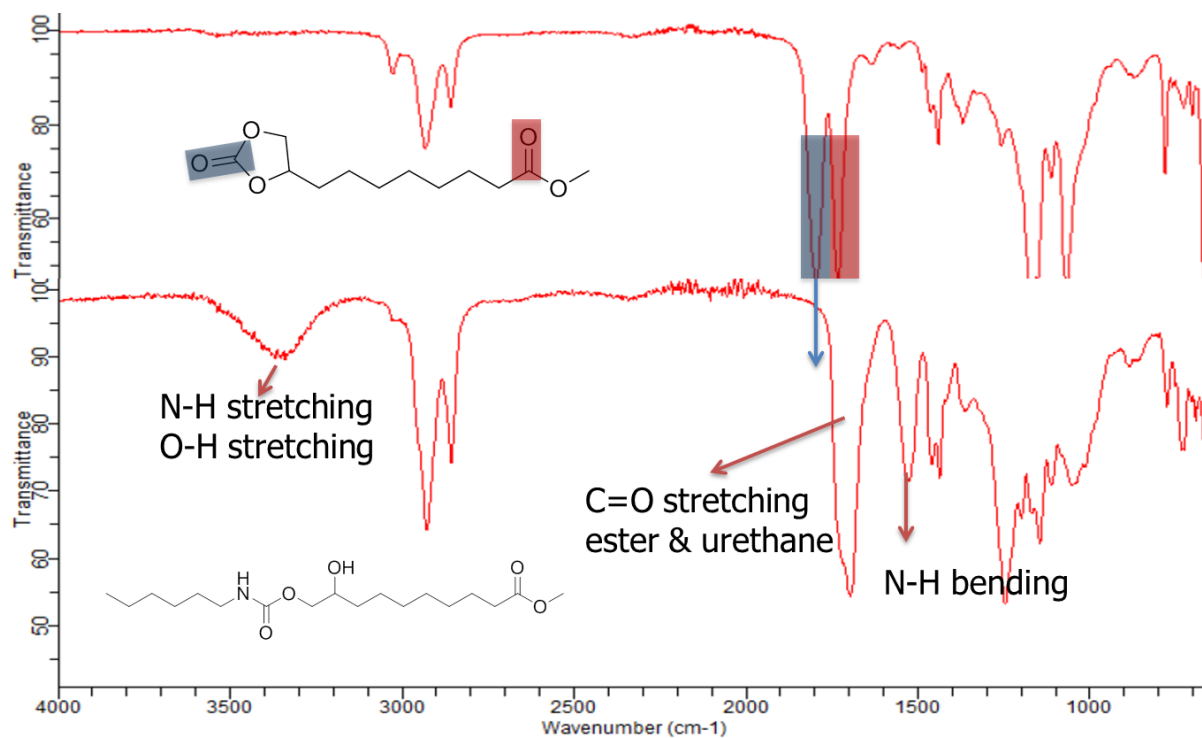
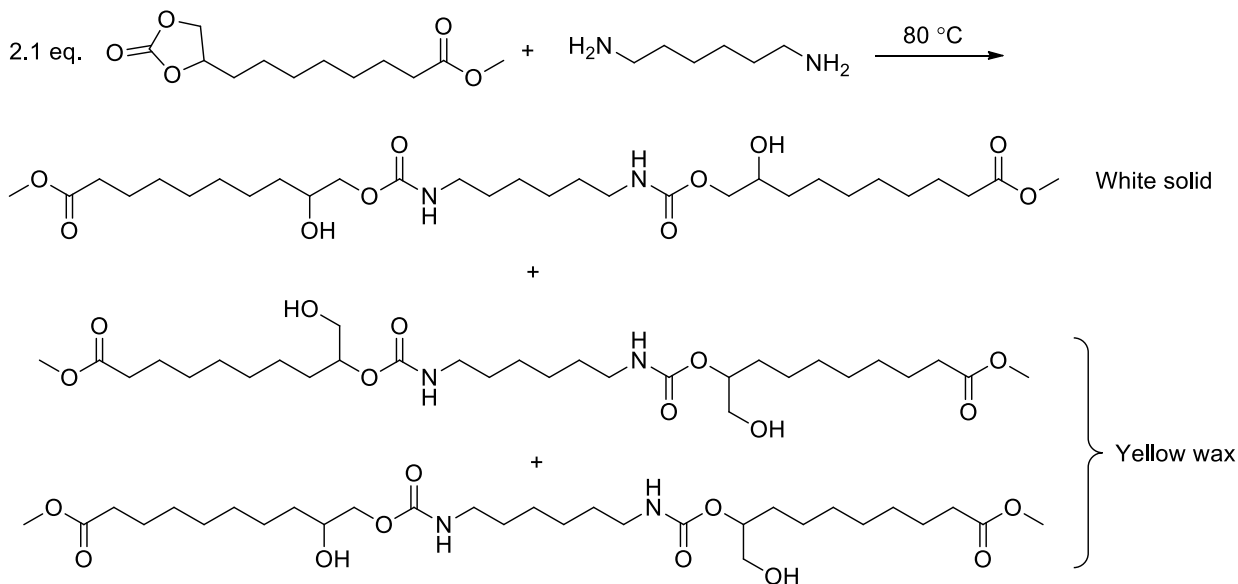


**Figure S10.5.** FTIR spectra of CC-ME and bis(hydroxyurethane) dimethylester.



**Scheme S10.2.** Model compound reaction between CC-ME with 1,6-diaminohexane, generating isomer mixture of bis(hydroxyurethane) dimethylester with primary and secondary hydroxyl groups, fractionated using precipitation.

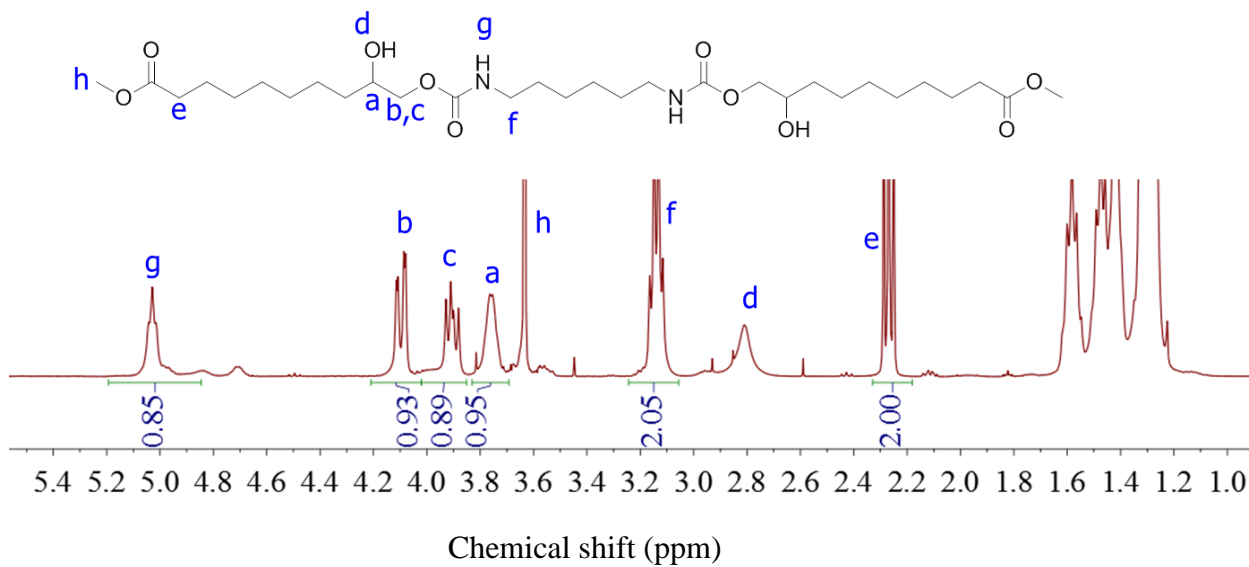


**Figure S10.6.** <sup>1</sup>H NMR spectrum of isolated bis(hydroxyurethane) dimethylester isomer with secondary hydroxyl groups.

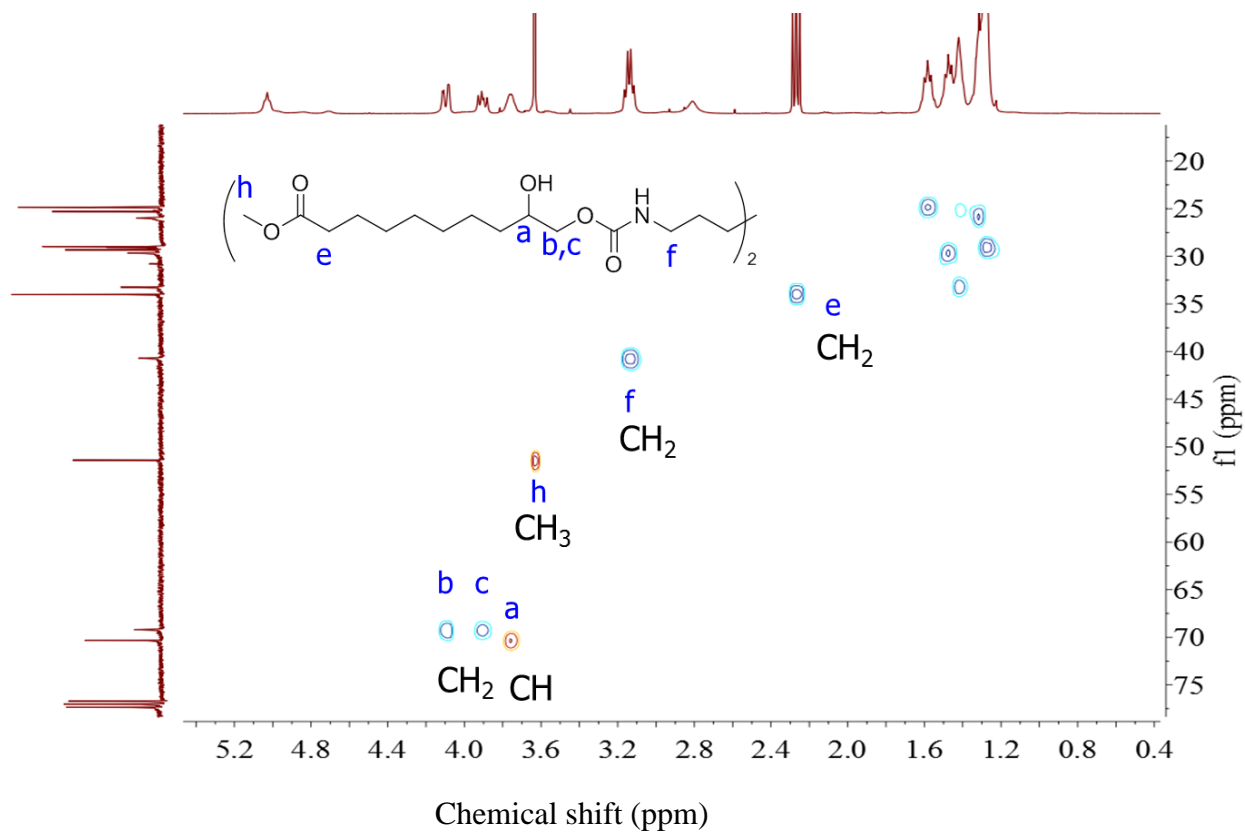
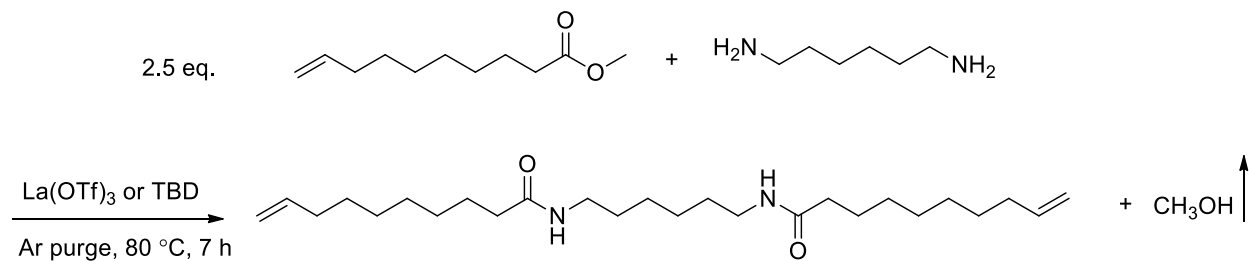


**Figure S10.7.** HSQC 2D NMR spectrum of isolated bis(hydroxyurethane) dimethylester with secondary hydroxyl groups.



**Scheme S10.3.** Model amidation reaction between 2 equivalent of 9-DAME with 1 equivalent of 1,6-diaminohexane, generating a hexanediamide diene.

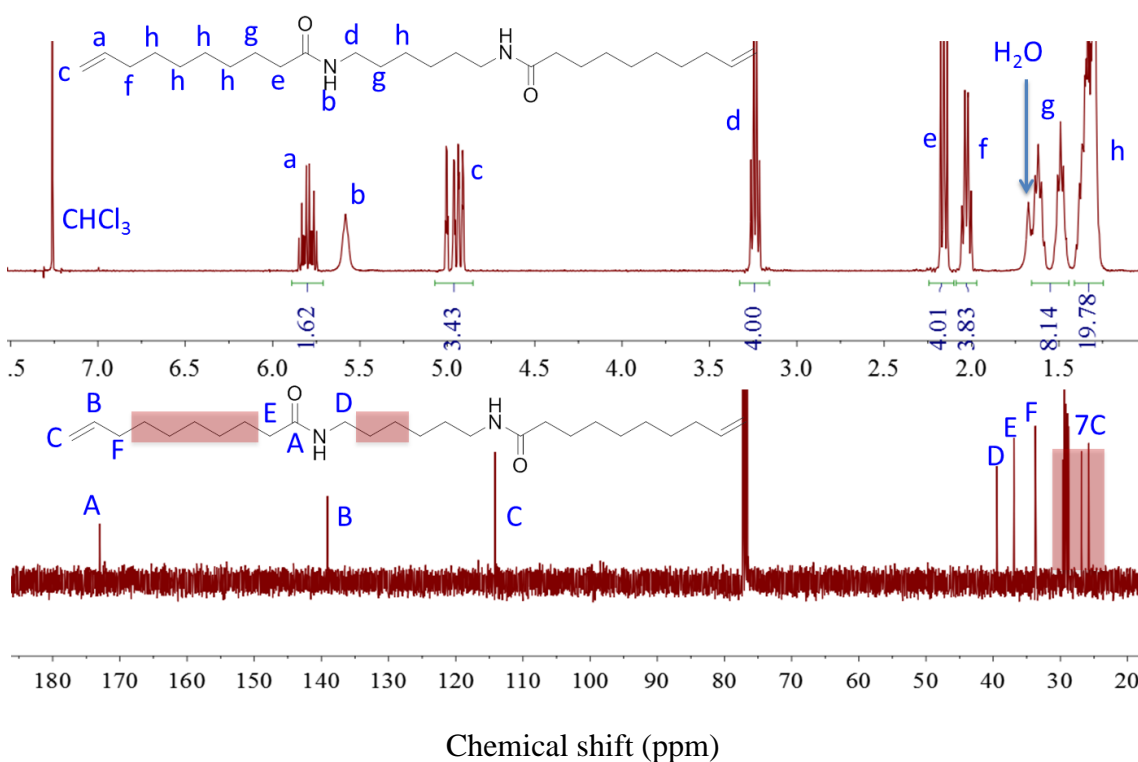


**Figure S10.8.**  $^1\text{H}$  and  $^{13}\text{C}$  NMR spectrum of hexanediamide diene.

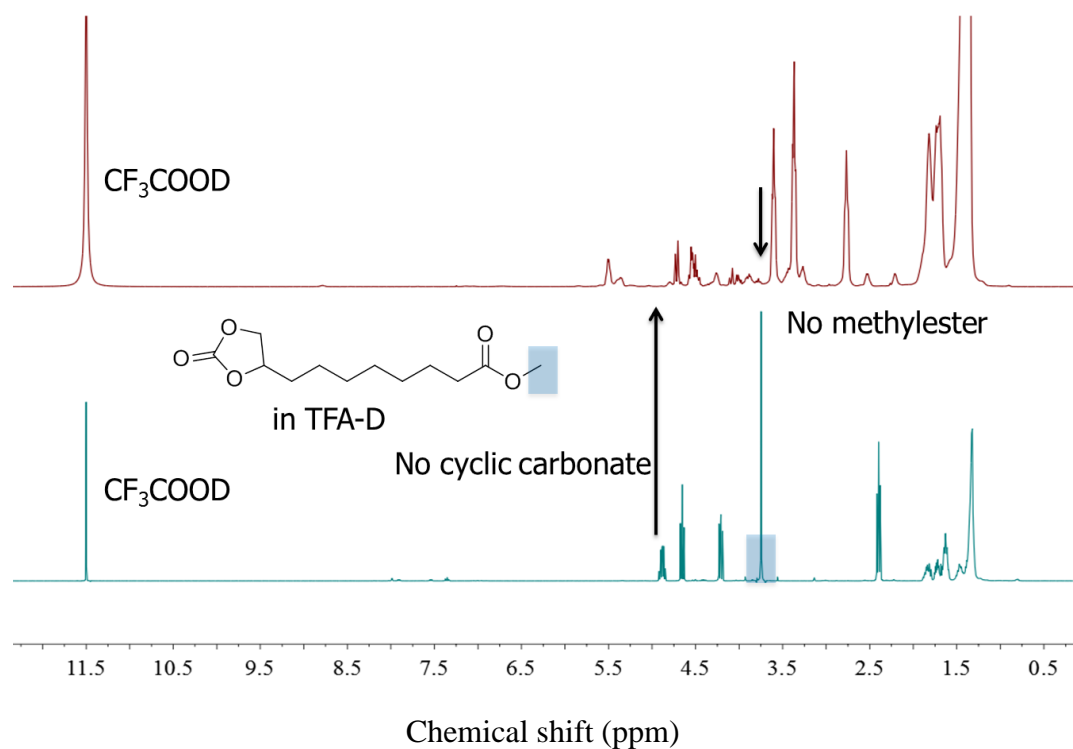


**Figure S10.9.** <sup>1</sup>H NMR spectra overlay of PA<sub>12</sub>HU and CC-ME monomer in deuterated TFA, demonstrating full conversion of cyclic carbonate and methylester groups.

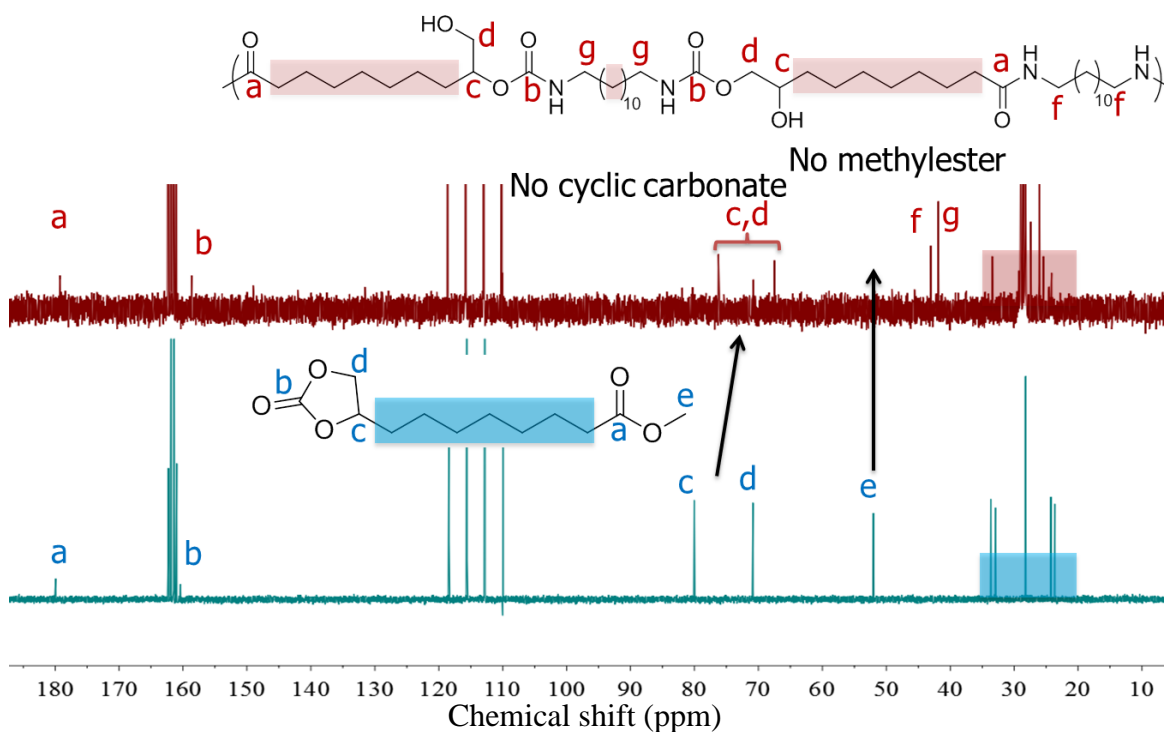


**Figure S10.10.**  $^{13}\text{C}$  NMR spectra overlay of PA<sub>12</sub>HU and CC-ME monomer in deuterated TFA, demonstrating full conversion of cyclic carbonate and methylester groups.

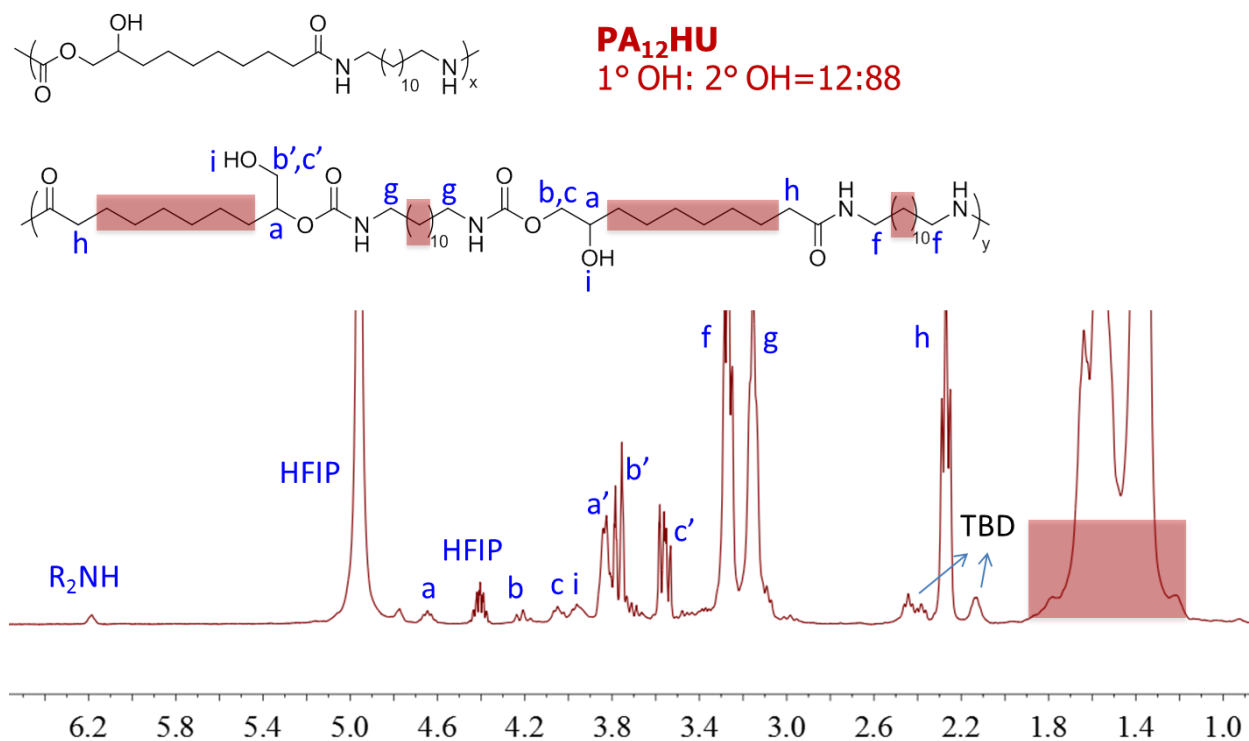


**Figure S10.11.**  $^1\text{H}$  NMR spectra of PA<sub>12</sub>HU.

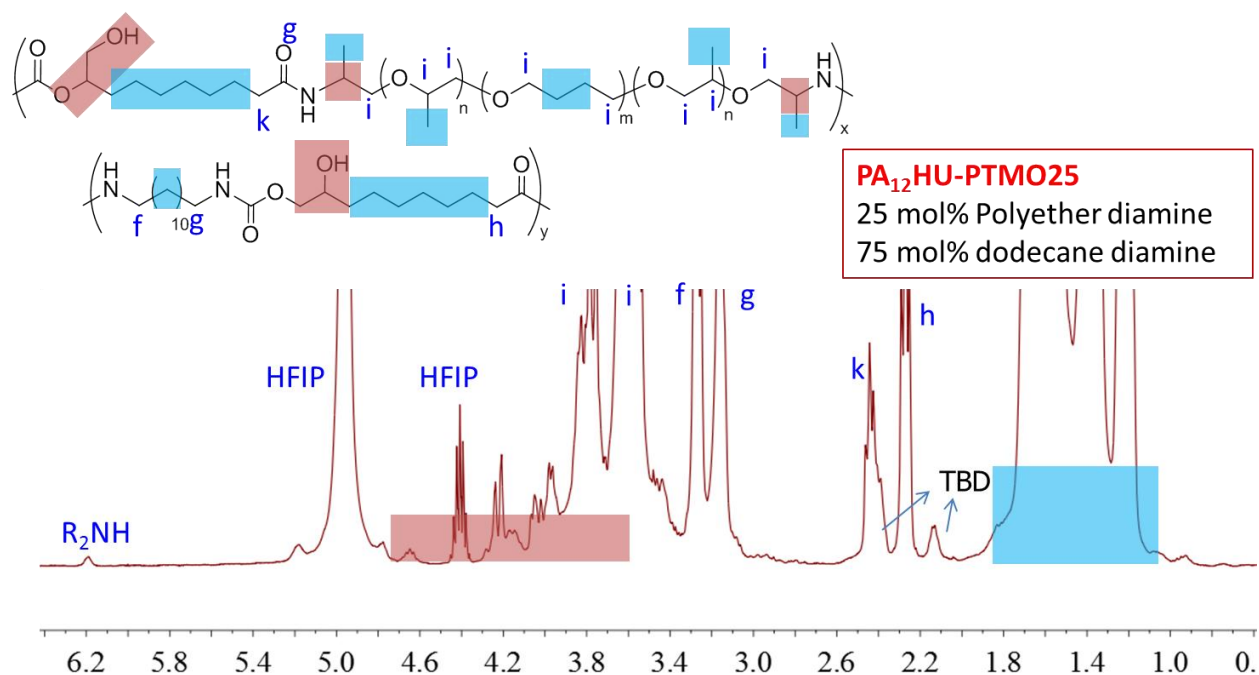
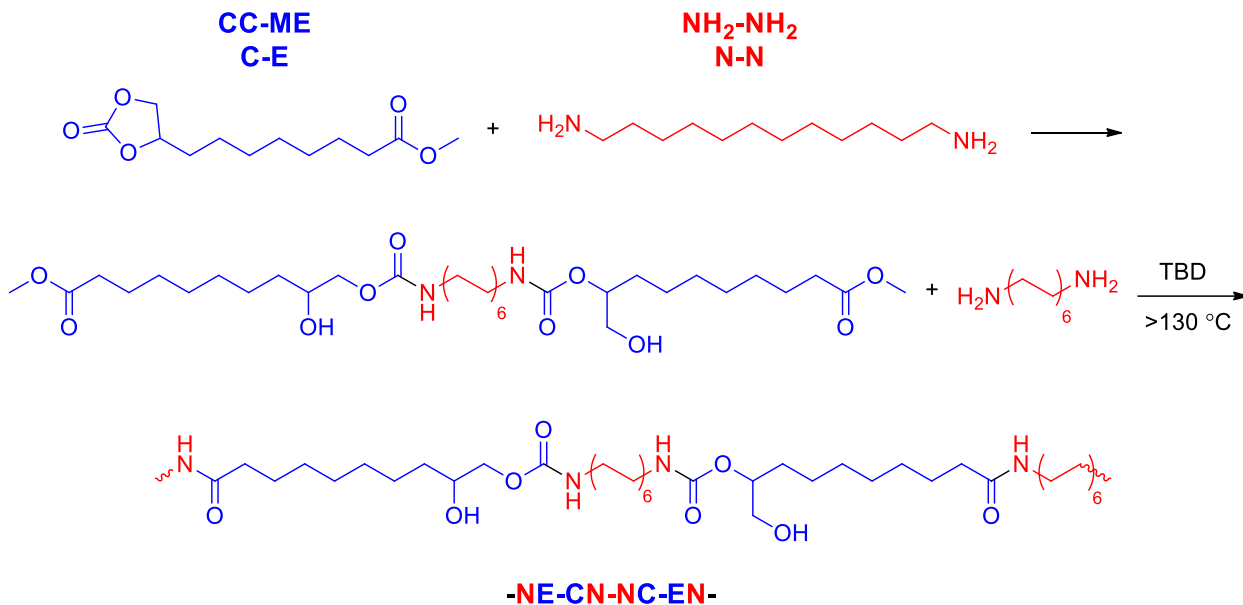


**Figure S10.12.**  $^1\text{H}$  NMR spectra of  $\text{PA}_{12}\text{HU}$ -PTMO25.



**Scheme S10.4.** Formation of the E-CN-NC-EN-N repeating unit in the structure of  $\text{PA}_{12}\text{HU}$  -(C-EN-N)- and -(E-CN-NC-EN-N)-.

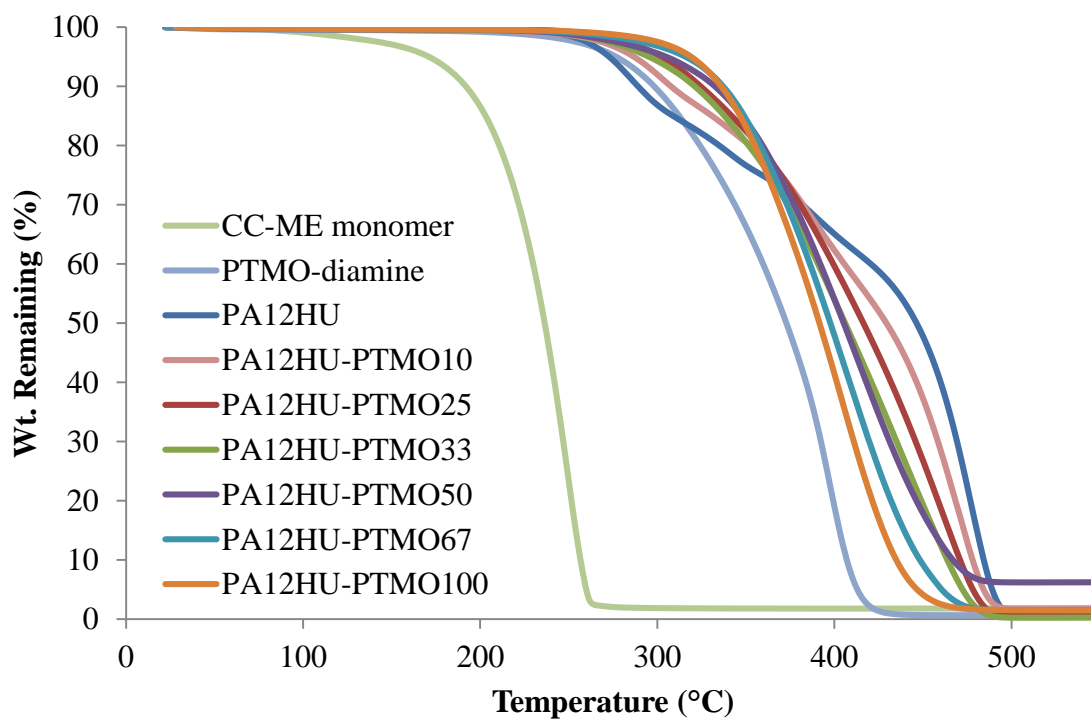


**Figure S10.13.** TGA thermograms of nonsegmented PA<sub>12</sub>HU and segmented PA<sub>12</sub>HU-PTMOs, compared with PTMO-diamine precursor and CC-ME monomer under nitrogen purge.

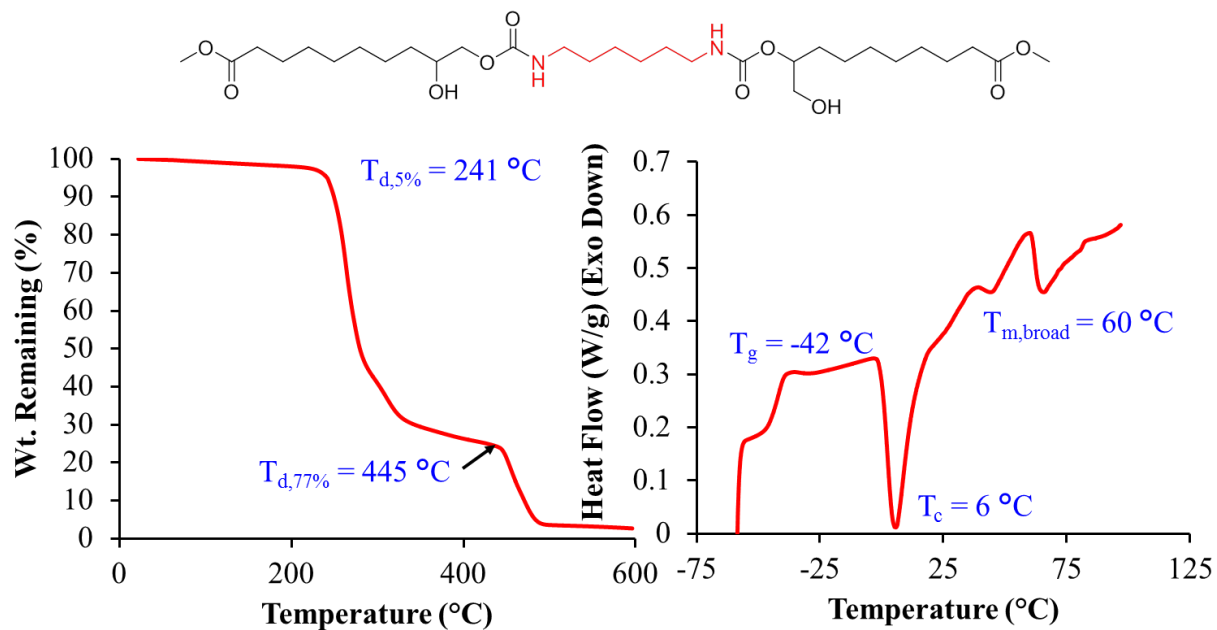


**Figure S10.14.** Thermal properties of the model compound bis(hydroxyurethane) dimethylester.

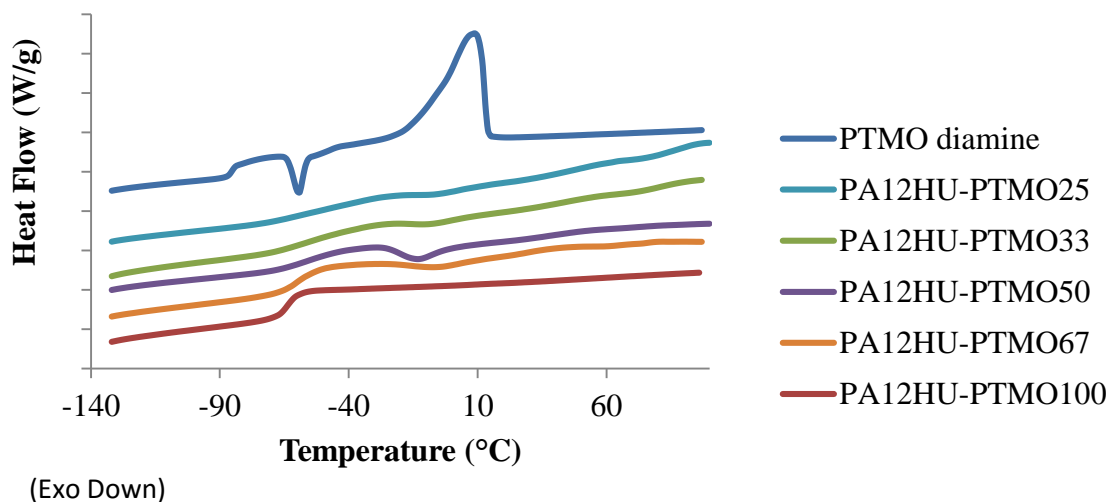


**Figure S10.15.** Cryo DSC traces of segmented PA<sub>12</sub>HU-PTMOs, compared with PTMO-diamine 1 kDa. Second heat reported with 10 °C/min heating rate after quench cooling from 100 °C.

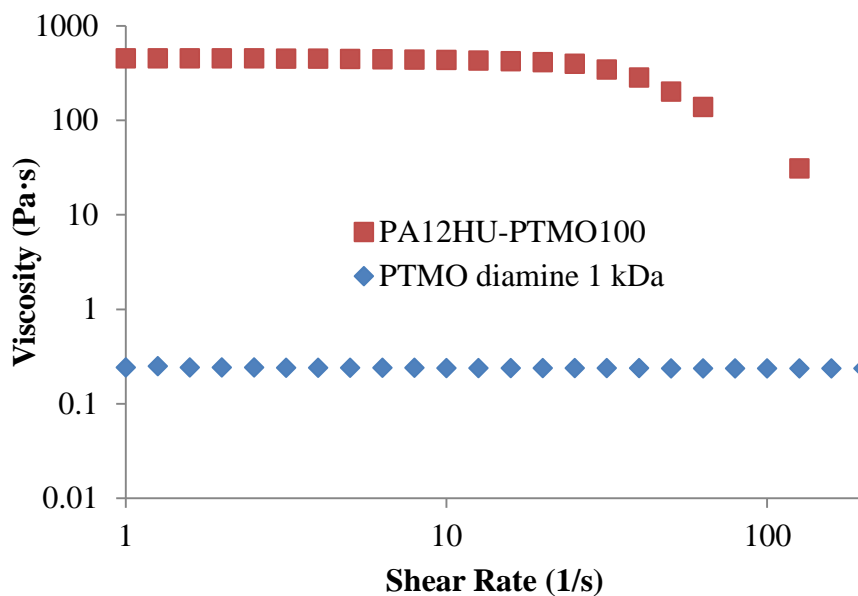


**Figure S10.16.** Shear rate sweep of PA<sub>12</sub>HU-PTMO100 and 1 kDa PTMO diamine.

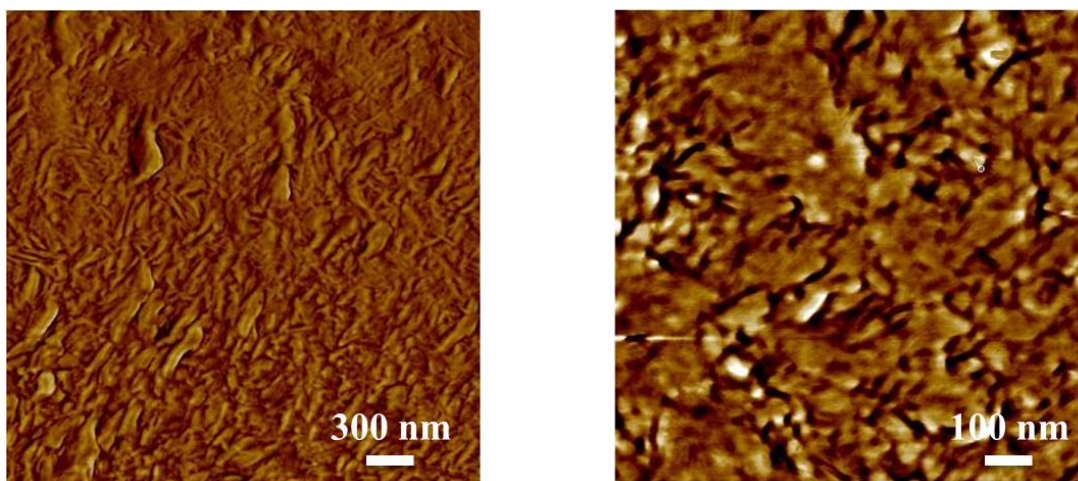


**Figure S10.17.** AFM tapping mode phase image of non-segmented PA<sub>12</sub>HU.



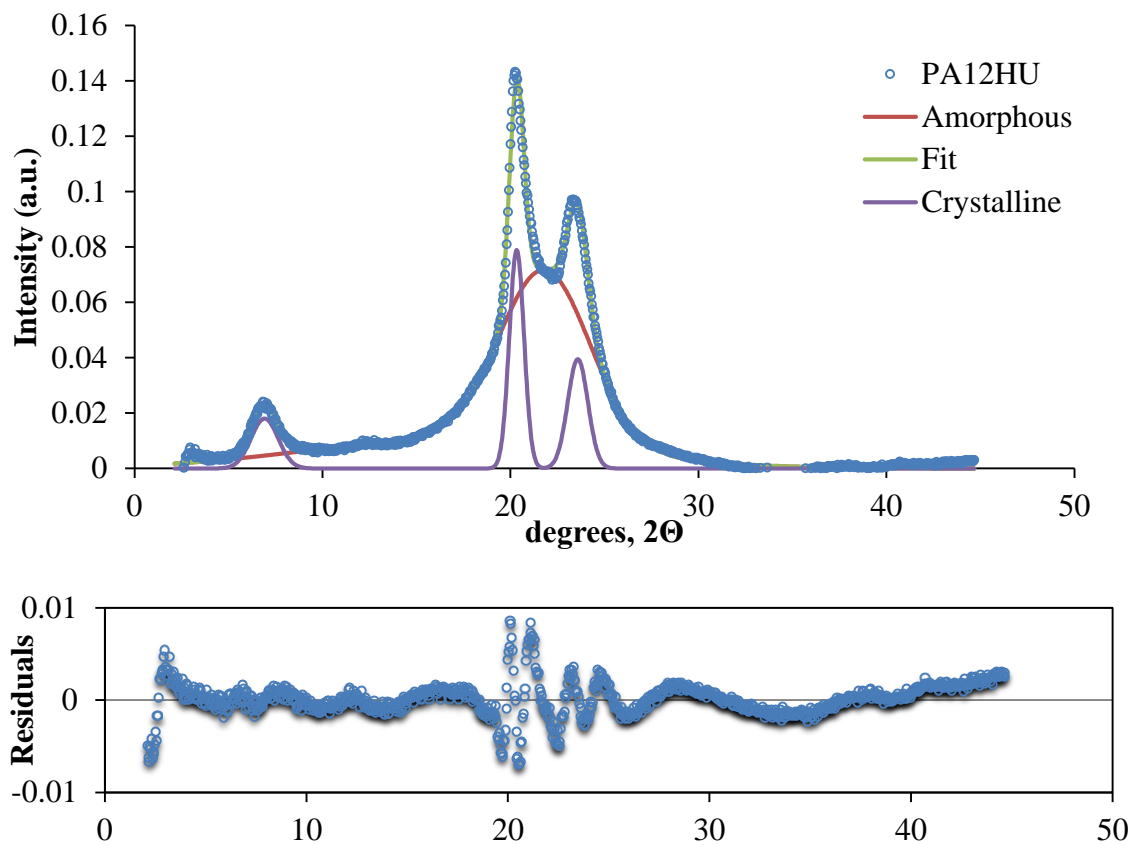


**Figure S10.18.** Peak deconvolution and residuals of the WAXD profile of non-segmented PA<sub>12</sub>HU using Gaussian and Lorentzian functions.

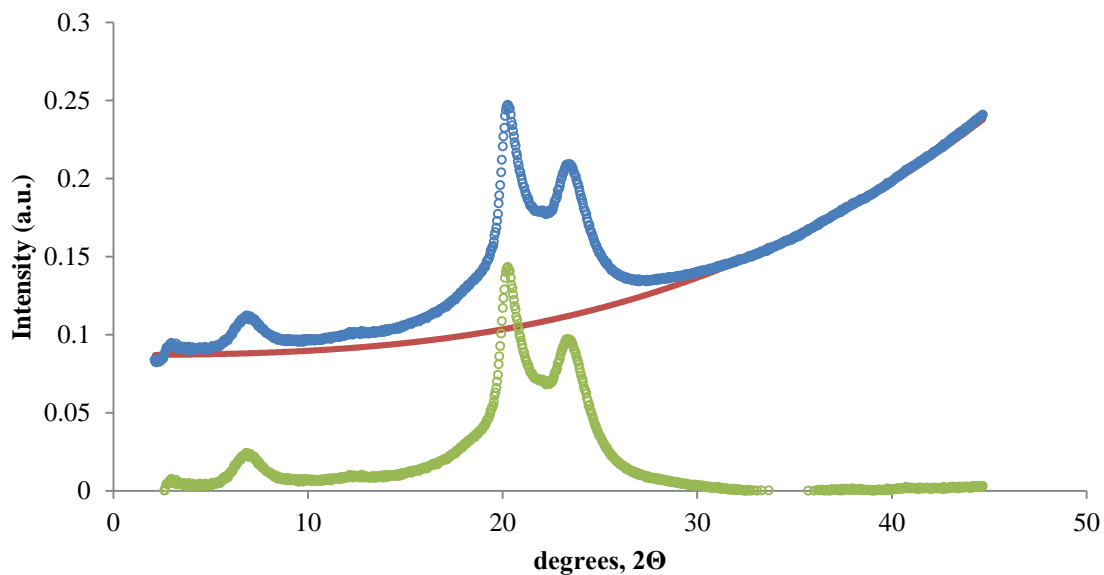


**Figure S10.19.** Baseline correction of the WAXD profile of non-segmented PA<sub>12</sub>HU.

## References

1. Tomita, H.; Sanda, F.; Endo, T. J. Polym. Sci., Part A: Polym. Chem. **2001**, 39, 851.
2. Ochiai, B.; Inoue, S.; Endo, T. J. Polym. Sci., Part A: Polym. Chem. **2005**, 43, 6613.
3. Maisonneuve, L.; More, A. S.; Foltran, S.; Alfes, C.; Robert, F.; Landais, Y.; Tassaing, T.; Grau, E.; Cramail, H. RSC Advances **2014**, 4, 25795.
4. Kim, B. R.; Lee, H.-G.; Kang, S.-B.; Sung, G. H.; Kim, J.-J.; Park, J. K.; Lee, S.-G.; Yoon, Y.-J. Synthesis **2012**, 44, 42.
5. Mutlu, H.; Meier, M. A. R. Macromol. Chem. Phys. **2009**, 210, 1019.
6. Morimoto, H.; Fujiwara, R.; Shimizu, Y.; Morisaki, K.; Ohshima, T. Organic Letters **2014**.

## Chapter 11. Electrospinning of Plant Oil-based, Non-Isocyanate Polyurethanes for Biomedical Applications

*(In preparation for publishing in ACS applied materials & interfaces)*

Donald C. Aduba, Jr.<sup>1,2\*\*</sup>, Keren Zhang<sup>2,3\*\*</sup>, Akanksha Kanitkar<sup>2,4</sup>, Justin Sirrine<sup>2,3</sup>,  
Timothy E. Long<sup>2,3</sup>

<sup>1</sup>*Department of Mechanical Engineering, Virginia Tech, Blacksburg, VA 24061.*

<sup>2</sup>*Macromolecules Innovation Institute, Virginia Tech, Blacksburg, VA 24061.*

<sup>3</sup>*Department of Chemistry, Virginia Tech, Blacksburg, VA 24061.*

<sup>4</sup>*Department of Biomedical Engineering and Mechanics, Virginia Tech, Blacksburg, VA 24061.*

### 11.1 **Abstract**

A one-pot melt polymerization of plant oil-based monomer and diamines yielded isocyanate-free, segmented poly(amide hydroxyurethane)s (PAHUs) with polyether soft segments. Successful electrospinning of segmented PAHUs afforded randomly orientated, semicrystalline fibers that formed stretchable, free-standing fiber mats. A variety of characterization experiments aimed to establish the structure-processing-property relationships of electrospun PAHU fibers. Comparing electrospun fiber mats to compression-molded films evaluated the effect of processing conditions on physical properties of segment PAHUs. A conventional segmented polyurethane with comparable soft segment content to segmented PAHU served as isocyanate-based control to relate their structural difference to thermal and mechanical properties. Morphology studies proved uniform PAHU fibers in the nanoscale, with average fiber diameters ranging from 718 to 862 nanometers. The thermal stability of PAHU remained after electrospinning, while electrospun PAHU fibers exhibited lower crystallinity than annealed compression-molded films. Dynamic mechanical analysis revealed significantly lower moduli of electrospun

fiber mats compared to bulk films, and tensile studies demonstrated suitable Young's modulus values of electrospun PAHU fiber mats near 7 MPa for tissue engineering applications. The electrospun PAHU fibers exhibited faster and higher water uptake than bulk films and isocyanate-based polyurethane, respectively. The chemical composition of the polymer was retained after electrospinning and tested for its biocompatibility using live/dead staining assays. Primary human fibroblasts were seeded and successfully adhered onto electrospun PAHU fibers with viabilities over 90% after a 3-day period. The results highlight the electrospinning of biocompatible polyurethanes using sustainable chemistries useful in biomaterials development.

## 11.2 *Introduction*

Electrospinning is a simple material processing system which has been in use since Formhals patented the technology in 1934.<sup>1</sup> This process involves the application of electrostatic charges on a syringe containing polymer solution. The charged viscoelastic solution travels as a jet across space and deposits micro to nano sized fibers onto a collector plate. These fibers form a non-woven mesh that has indicated uses in textile manufacturing<sup>2</sup>, filtration membranes<sup>3</sup>, tissue engineered scaffolds<sup>4</sup>, wound dressing materials<sup>5</sup>, medical devices<sup>6</sup>, drug delivery vehicles<sup>7,8</sup> and sensors<sup>9</sup>. Electrospinning has become popular over the last twenty years across interdisciplinary fields.<sup>10</sup> Electrospun fiber materials have advantages of having a high surface to volume ratio, high porosity, and high conformability. Also, it is ideal for materials fabrication because of its ease of use, cost-effective, and has a large library of synthetic and natural polymers from which electrospun fibers can be formed.<sup>11</sup>

Segmented polyurethanes represent an important family of industrialized synthetic polymers widely used as thermoplastics. The tunable chemical composition of TPU influences the resulting material properties such as crystallinity, thermal and mechanical properties. Traditional thermoplastic polyurethane (TPU) synthesis utilizes polyols and di-isocyanates as starting materials, and electrospinning of TPU yields nanofiber mats with elastomeric property.<sup>12,6</sup> Polyurethane can be dissolved in many organic solvents to form the electrospinning solution. Polyurethanes are relatively simple to synthesize or purchase which makes fabrication scalability possible. There are many applications of electrospun polyurethane fibers as: filtration membranes<sup>3</sup>, shape-memory materials<sup>13</sup>, wound dressings<sup>14</sup>, tissue engineering scaffolds<sup>15</sup> and support structures for carbon nanotubes<sup>16</sup>. However, isocyanate proves highly reactive and hazardous to eyes and the respiratory system.<sup>17</sup> Therefore, many researchers devote their effort in synthesizing non-isocyanate polyurethanes (NIPU), especially using sustainable starting materials such as plant oils and carbon dioxide.<sup>18–22</sup> However, most studies focus on crosslinked NIPU for thermosets, and the inadequate mechanical integrity of reported linear NIPU precludes the preparation of electrospun fibers from NIPU. Long *et al.* recently reported a novel synthesis approach to prepare linear segmented poly(amide hydroxyurethane)s (PAHUs) with mechanical integrity using isocyanate-free starting materials, namely cyclic carbonate methyl ester (CC-ME), an aliphatic diamine, and a polyether diamine. This manuscript describes, for the first time, successful electrospinning of NIPU into nanofibers, and thorough physical characterization of NIPU nanofibers in comparison to the annealed compression molded films. Using isocyanate free electrospun fibers hopes to encourage green chemistry and

fabrication of sustainable materials that possess appropriate material and biocompatibility properties for a variety of biomedical applications.

### 11.3 *Experimental Section*

**Materials.** Methyl 9-decenoate (9-DAME) was provided from Elevance Renewable Sciences, Inc. and used as received. Jeffamine® THF-100 was poly(tetramethylene oxide)/poly(propylene glycol) copolymer based diamine with 1 kDa molecular weight, obtained from Huntsman Corporation sample department and used as received. Magnesium sulfate ( $\text{MgSO}_4$ , 99%), sodium sulfite ( $\text{NaSO}_3$ ,  $\geq 98\%$ ), sodium bicarbonate ( $\text{NaHCO}_3$ ,  $\geq 99\%$ ), 1,12-diaminododecane (98%), lithium bromide ( $\text{LiBr}$ ,  $\geq 99\%$ ), 1,5,7-triazabicyclo[4.4.0]dec-5-ene (TBD, 98%), *meta*-Chloroperoxybenzoic acid (m-CPBA,  $\leq 77\%$ ), sodium hydroxide solution ( $\text{NaOH}$ , 1.0 M in water), *N*-methyl-2-pyrrolidone (NMP, ACS grade), hexafluoro-2-propanol (HFIP,  $\geq 99\%$ ), and sodium chloride ( $\text{NaCl}$ ,  $\geq 99\%$ ) were obtained from Sigma-Aldrich and used as received. Poly(tetramethylene oxide) (PTMO) ( $M_n$  2,000 g/mol) and 1,4-butanediol were purchased from Sigma Aldrich and dried under reduced pressure for 12 h at 40 °C before use. Dicyclohexylmethane-4,4'-diisocyanate (HMDI) (99.5%) was kindly provided by Bayer MaterialScience and used as received. *N,N*-dimethylformamide (DMF) (HPLC grade) was purchased from Spectrum and dried with an Innovative Technology PureSolv solvent purification system before use. Dibutyltin dilaurate (95%) (DBTDL) was purchased from Sigma Aldrich and used as a 1 wt % solution in THF. Bone-dry  $\text{CO}_2$  was obtained from Airgas and used as received. Ethyl acetate ( $\text{EtOAc}$ , ACS grade) and dichloromethane (DCM, ACS grade) were purchased from Spectrum Chemicals and used as received. Water was purified from distillation.

**Synthesis of segmented PA<sub>12</sub>HU-PTMOs and TPU control.** Segmented PA<sub>12</sub>HU-PTMOs was synthesized according to Chapter 10. (**Scheme 11.1**) Synthesis of TPU control followed a two-step, one-pot synthetic route under nitrogen. (**Scheme 11.2**) A three-necked, 250 mL round-bottomed flask was fitted with an addition funnel, nitrogen inlet, outlet bubbler, overhead mechanical stirrer, and condenser column, and subsequently flame-dried while under nitrogen purge. After cooling, all the glass joints were sealed with Teflon® tape and Parafilm®. HMDI (66.8 mmol, 17.536 g) was added dropwise to the reaction flask containing PTMO (15.0 mmol, 29.990 g) and 50 ppm DBTDL at 80 °C over 10 min, and reacted for 4 h to form the isocyanate-terminated prepolymer. Dry DMF (100 mL) was then introduced, followed with dropwise addition of 1,4-butanediol (51.8 mmol, 4.672 g) over 10 min. The addition funnel was rinsed with dry DMF, bringing the total solvent to 140 mL (40 % solids). The 1,4-butanediol was allowed to react for 24 h, and the solution remained homogeneous throughout the polymerization. The resulting reaction solution was concentrated and precipitated into diethyl ether, then re-dissolved in chloroform and re-precipitated into diethyl ether. The resulting white, elastomeric product was subsequently dried in *vacuo* at 50 °C for 12 h.

**Annealing conditions.** Synthesized non-isocyanate segmented PA<sub>12</sub>HU-PTMO<sub>25</sub> and PA<sub>12</sub>HU-PTMO<sub>33</sub> were melt compression molded at 130 °C for 5 min under 3-ton compression force sandwiched between two Kapton® sheets and two steel plates, and cooled to room temperature. Compression molded films were annealed in *vacuo* for 12 h at 130 °C. PAHU films were cooled using a step-wise procedure wherein the oven temperature was reduced 30 °C and allowed to equilibrate for 3 hours, with the process repeated until room temperature was reached. The synthesized isocyanate-based

segmented polyurethane was dissolved in  $\text{CHCl}_3$  at 40 wt % and directly cast into a polytetrafluoroethylene (PTFE) mold. Films were dried in air at 23 °C for 24 h and annealed under reduced pressure at 100 °C for an additional 24 h. Samples were stored in a desiccator at 23 °C prior to characterization.

**Electrospinning conditions.** The  $\text{PA}_{12}\text{HU-PTMO}_{25}$  and  $\text{PA}_{12}\text{HU-PTMO}_{33}$  melt pressed films were minced and 800 mg was weighed and added to 2 mL of HFIP. The same mass quantity was used to weigh TPU control films but 3 mL of HFIP was added to reduce solution viscosity for electrospinning. All solutions were placed on a shaker plate and dissolved overnight. To fabricate electrospun fibers, the  $\text{PA}_{12}\text{HU-PTMO}_{25}$  and  $\text{PA}_{12}\text{HU-PTMO}_{33}$  polyurethane solutions were drawn up through the blunted needle (18G $\times$ 1½ in) of a 3 ml syringe. The syringe was loaded into a syringe pump, propelling solution out of the needle 30 cm away from a grounded cylindrical collector at a rate of 1.5 ml/hr. TPU control solution was propelled 27 cm away from the collector at a 1.5 ml/hr flow rate. The needle was connected to a positive electrode of a high voltage power supply (Ultravolt HV-RACK-4-250-00387). A voltage of 16 and 20 kilovolts was applied to the syringe needle containing  $\text{PA}_{12}\text{HU-PTMO}$ s and TPU control polyurethanes respectively. This voltage and charge density created an electric field in the air gap between the needle and collector which allowed the polymer solution to overcome its surface tension and viscoelastic properties at the needle tip. These conditions (**Table 11.1**) generated a Taylor cone which enabled the charged polyurethane solution, in a jet like fashion to become suspended in air from the needle to the grounded collecting plate. (**Figure 11.1**) As the polyurethane solution was streamed from the needle tip, HFIP solvent evaporated, allowing the fibers to dry. Randomly aligned nanofibers were collected on a cylindrical, stainless steel collector



with 5 cm diameter and 20 cm length rotating at approximately 200 revolutions per minute.

The fibers were extracted from the collector and desiccated overnight for storage.

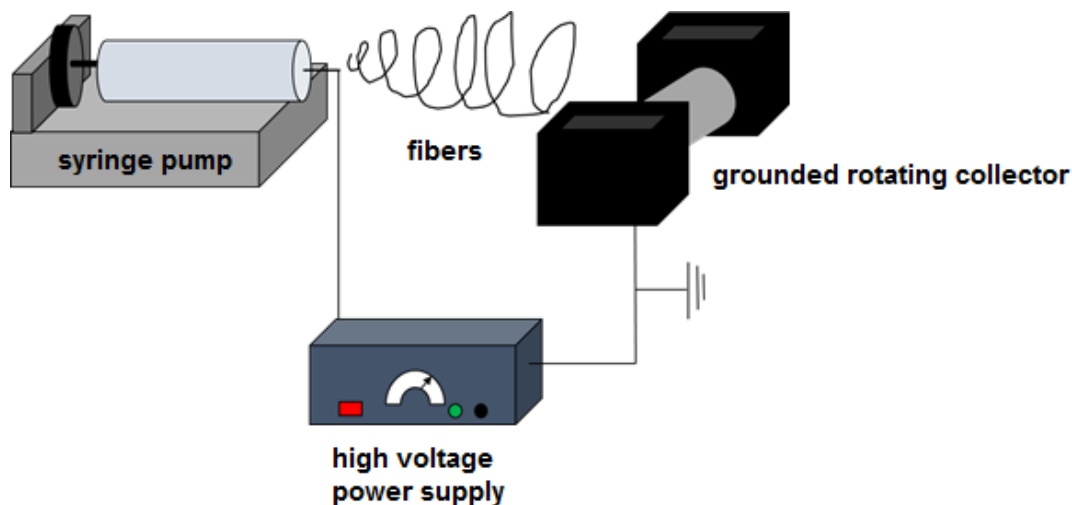


**Figure 11.1:** Electrospinning setup illustrating random deposition of fibers from polymer solution to collector driven by syringe pump and electric field.

**Table 11.1.** Summary of solution and electrospinning parameters

| Sample                        | Viscosity (cPs) | Concentration of polymer in HFIP (w/v%) | Voltage (kV) | Air-gap distance (cm) | Flow-rate (mL/h) | Average thickness (mm) |
|-------------------------------|-----------------|---|--------------|-----------------------|------------------|------------------------|
| ES PA <sub>12</sub> HU-PTMO25 | 95.0            | 40                                      | 20           | 30                    | 1.5              | 0.062 ± 0.002          |
| ES PA <sub>12</sub> HU-PTMO33 | 111             | 40                                      | 20           | 30                    | 1.5              | 0.025 ± 0.004          |
| ES TPU control                | 308             | 27                                      | 16           | 27                    | 1.5              | 0.314 ± 0.048          |

## Analytical methods

To evaluate fiber morphology post-electrospinning, the electrospun mats were placed on a 1 cm diameter stub and placed on a specimen holder for analysis using Scanning Electron Microscopy (SEM). Images were taken and analyzed under JEOL NeoScope JCM-5000 Scanning Electron Microscope. Fifty randomly chosen fibers in each SEM image were analyzed with ImageJ software for fiber diameter measurements. Viscosity of electrospun solutions was measured on Brookfield DV-E viscometer with s18 conical spindle adapter. Solutions underwent oscillatory shear between 20-100 revolutions per minute until viscosity readings in centipoise (cPs) equilibrated to a constant value.

Thermogravimetric analysis (TGA) was performed on a TA Instruments Q50 TGA with a heating ramp from ambient temperature to 600 °C at 10 °C/min under nitrogen purge. Thermal degradation temperatures ( $T_{d,5wt\%}$ ) corresponded to the temperature at 5% weight loss. Differential scanning calorimetry (DSC) was conducted on a TA instruments Q1000 DSC using a cool/heat/cool/heat procedure with heating rate of 10 °C/min and cooling rate of 10 °C/min under nitrogen flush of 50 mL/min. The samples were cut from annealed films or electrospun mats and subjected to cooling before the first heat to elucidate the effect of processing conditions on thermal properties. The midpoint of the transition in the first heating ramp determined glass transition temperatures ( $T_g$ ).

A TA Instruments Q5000 thermogravimetric sorption analyzer (TGA-SA) measured the water sorption at relative humidity (RH) steps from 0 – 95% RH at 5% increments. Each RH step continued until the sample weight equilibrated (<0.01% change over 10 min). An instrumental pre-drying method at 50 °C and 0% RH was applied to each sample until sample weight equilibrated. Water sorption was calculated based on weight gain of each pre-dried sample weight. Dynamic mechanical analysis (DMA) utilized a TA

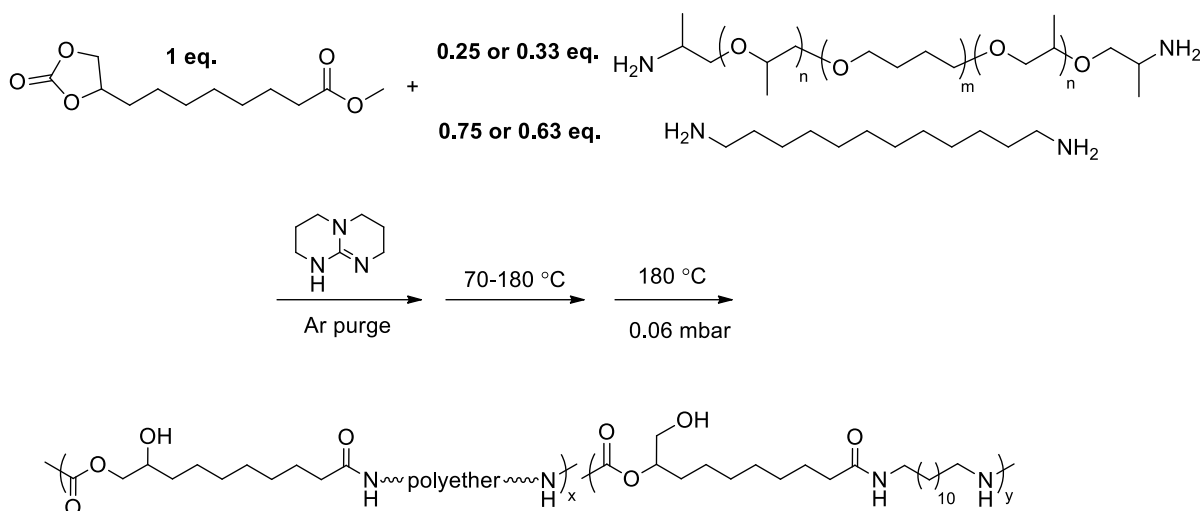
Instruments Q800 dynamic mechanical analyzer in tension mode at a frequency of 1 Hz, oscillatory amplitude of 10  $\mu\text{m}$ , and a static force of 0.01 N. Rectangular film samples were cooled to -100  $^{\circ}\text{C}$ , equilibrated for 2 min, length measured, and ramped up temperature at a rate of 3  $^{\circ}\text{C}/\text{min}$ . The peaks of tan delta curves determined  $T_g$  values. Instron 5500R universal testing instrument evaluated tensile properties of annealed film and electrospun film samples at a crosshead speed of 10 mm/min. Tensile analysis data represented an average of five specimens with calculated standard deviations.

Synthesized segmented ES PA<sub>12</sub>HU-PTMO25, ES PA<sub>12</sub>HU-PTMO33 and ES TPU control samples were sterilized by soaking in ethanol overnight and dried under air. The samples were then weighed and placed in 5 ml of RPMI media in 15 mL centrifuge tubes. These were then placed on a shaker plate for specified time (1 and 3 days). After each time period, electrospun polyurethane samples were separated from the media and its extracts were filtered using 0.22  $\mu\text{m}$  filters and refrigerated until further use. Primary human fibroblasts (passage 2) were seeded in a 96-well plate at 25,000 cells/well and incubated for 24 h. The media in each well was replaced by 100  $\mu\text{l}$  of filtered media extracts from the samples (day 1 and 3 extracts). The 96-well plate containing fibroblasts-RPMI media extract was incubated at 37 $^{\circ}\text{C}$  in 5% CO<sub>2</sub> for 24 h. Plate containing hASC-stromal media extract was incubated at 37 $^{\circ}\text{C}$  in 5% CO<sub>2</sub> for 24 h.

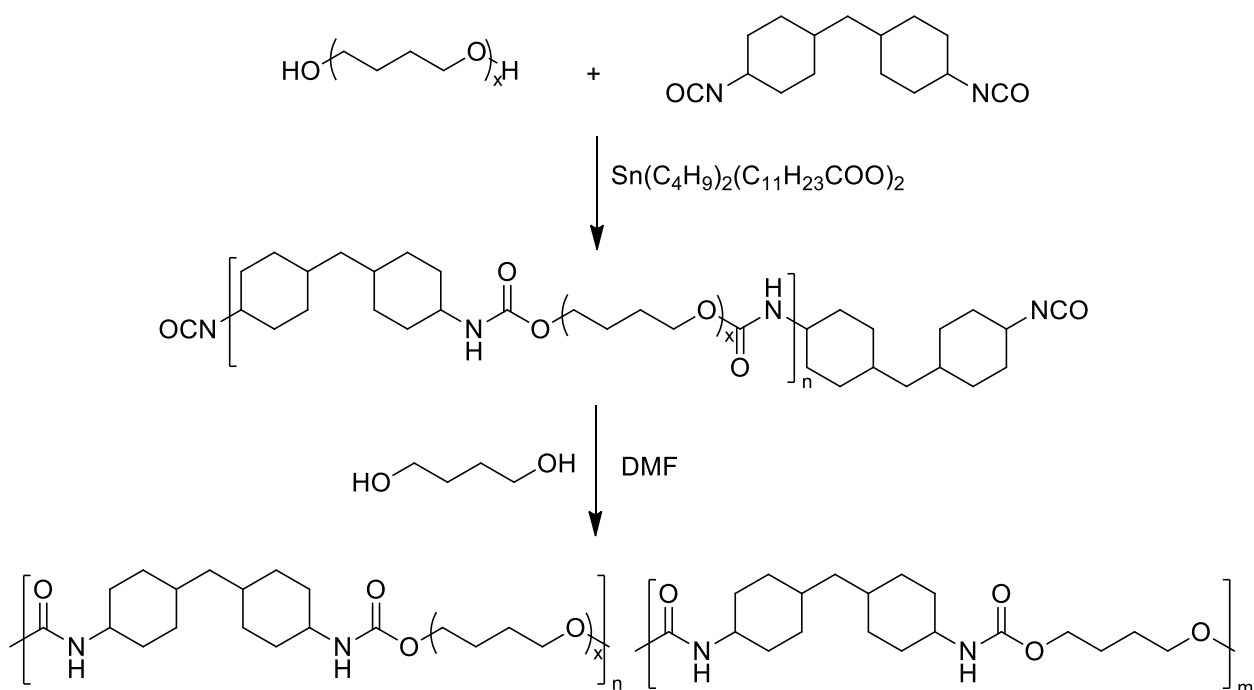
The toxicity of the media extracts towards fibroblasts was quantitatively determined using alamarBlue® assay. 10  $\mu\text{l}$  of alamarBlue® reagent (10% of the volume of stromal media in each well) was added to each well containing fibroblasts in RPMI media extracts and re-incubated at 37 $^{\circ}\text{C}$  in 5% CO<sub>2</sub> environment for 5 h. At the end of 5 h, fluorescence was measured at an excitation wavelength of 530 nm and an emission

wavelength of 595 nm using a Molecular Devices microplate reader. Fibroblasts cultured with RPMI media in tissue cultured 96-well plate served as positive control, while fibroblasts cultured in ethanol (70%) served as negative control. RPMI media extracts without cells served as blank to subtract background fluorescence.

Surface adherent biocompatibility of fibroblasts on segmented ES PA<sub>12</sub>HU-PTMO25, ES PA<sub>12</sub>HU-PTMO33 and ES TPU control samples was analyzed using Biotium Live/Dead™ stain and following the manufacturer's protocol. Prior to loading of cells, electrospun mats were cut to fit a 24 well plate then were sterilized, and soaked in RPMI media for 2 h. Later the RPMI media was removed and 50,000 cells were seeded on top of each of the samples. After 30 min of incubation, RPMI media was added to each well and electrospun mats loaded with fibroblasts were incubated at 37°C in 5% CO<sub>2</sub> environment for 1 and 3 days. At the end of each time point, working solution of 2 µM calcein AM and 4 µM EthD-III was prepared in phosphate-buffered saline. RPMI media was removed from each samples well and the live/dead dye working solution was directly added to each sample. The samples were incubated for 30-45 minutes and imaged using a Zeiss Observer Z1 microscope fluorescent microscope.



**Scheme 11.1.** One-pot synthesis of segmented PA<sub>12</sub>HU-PTMO25 and PA<sub>12</sub>HU-PTMO33 using non-isocyanate starting materials from sustainable resources and diamines.



**Scheme 11.2.** One-pot, two-step synthesis of conventional segmented polyurethane with isocyanate and diols.

## 11.4 *Results and discussion*

**Polymer synthesis.** A one-pot melt polymerization of cyclic carbonate-methyl ester (CC-ME) and 1,12-diaminododecane and Jeffamine® with 1 kDa molecular weight afforded segmented poly(amide-hydroxyurethane) with PTMO-based soft segments, abbreviated as PA<sub>12</sub>HU-PTMO (**Scheme 11.1**). The stoichiometry amount of diamines and CC-ME was charged into the reaction flask, along with 5 mol% TBD as the catalyst and 5 mol% excess of 1,12-dodecanediamine to accommodate for sublimation. Table 11.2 summarizes the molar percentage of polyether diamine within the overall amount of diamines, which is used to distinguish different compositions, ca. PA<sub>12</sub>HU-PTMO25 with 25 mol% of PTMO diamine. This melt polymerization proceeded under inert atmosphere over 2 days, followed with a final vacuum step to remove the byproduct methanol and to drive the reaction towards completion. This one-pot melt polymerization featured solvent-free and purification-free synthesis, facile process with a single charge of starting materials, and moisture tolerance. The conventional segmented polyurethane synthesis required a two-step process in a non-aprotic, high boiling point solvent, moisture-free operation, and purification procedures (**Scheme 11.2**). More importantly, CC-ME proved a stable and non-volatile solid, derived from plant oil and CO<sub>2</sub>, which enables formation of urethane bonds without using isocyanate. Isocyanate-free synthesis for processable polyurethane thermoplastics envisions many advantages over traditional isocyanate chemistry such as reduced toxic by-products. Sustainable feedstock provides starting materials for both CC-ME and 1,12-diaminododecane, further emphasizing the impact of these materials on green chemistry.

**Table 11.2.** Compositions and thermal properties of annealed films and electrospun fiber mats of segmented PA<sub>12</sub>HU-PTMOs and a TPU control.

| Sample                     |                            | Soft segment wt% | T <sub>d,5</sub> wt% (°C) | T <sub>g</sub> (°C) | T <sub>m</sub> (°C)   | ΔH <sub>m</sub> First heat (J/g) | ΔH <sub>m</sub> Second heat (J/g) |
|----------------------------|----------------------------|------------------|---------------------------|---------------------|-----------------------|----------------------------------|-----------------------------------|
| PA <sub>12</sub> HU-PTMO25 |                            | 39%              | 302                       | -56 broad           | 56, 82, 95, 105, 121  | 79                               | 53                                |
| PA <sub>12</sub> HU-PTMO33 |                            | 47%              | 296                       | -59 broad           | 57, 96, 110, 129, 151 | 72                               | 39                                |
| TPU control                |                            | 43%              | 278                       | -77                 | 65, 124               | 38                               | 0                                 |
| ES                         | PA <sub>12</sub> HU-PTMO25 | 39%              | 305                       | -56 broad           | 51, 101, 125          | 73                               | 49                                |
| ES                         | PA <sub>12</sub> HU-PTMO33 | 47%              | 297                       | -56 broad           | 49, 101, 133          | 64                               | 39                                |
| ES                         | TPU control                | 43%              | 278                       | -76                 | 75, 133               | 28                               | 0                                 |

**Morphology and solution viscosity.** Both segmented ES PA<sub>12</sub>HU-PTMO and the ES TPU control formed homogeneous solutions in HFIP, while the TPU solution appeared more viscous than PA<sub>12</sub>HU-PTMO solutions with lower concentration, suggesting a higher molecular weight. A solution of TPU with lower solid weight percent in HFIP afforded electrospun fiber mat of ES TPU compared to ES PA<sub>12</sub>HU-PTMO. Successful electrospinning under optimized conditions yielded white, free-standing fiber mats for ES PA<sub>12</sub>HU-PTMO25, ES PA<sub>12</sub>HU-PTMO33, and the ES TPU control (**Figure 11.2**). ES PA<sub>12</sub>HU-PTMO25 and ES PA<sub>12</sub>HU-PTMO33 fiber mats exhibited randomly aligned fibers with a ribbon-like morphology. Electrospun polyurethane fibers were more packed with respect to the increase in soft segment and decrease in crystallinity. The fiber diameters of ES PA<sub>12</sub>HU-PTMO25 and ES PA<sub>12</sub>HU-PTMO33 were predominantly in the nanoscale and have bi-modal and uni-modal distributions with average fiber diameters of  $862 \pm 238$  and

718  $\pm$  328 nm respectively. (**Figures 11.3, 11.4**) ES TPU control mats primarily possessed micron scaled fibers, 4.58  $\pm$  0.881  $\mu\text{m}$ , significantly higher average diameters than of ES PA<sub>12</sub>HU-PTMO mats. This phenomenon may be attributed to the high viscosity of the polymer which led to very large fibers being deposited on the collector. Overall, the morphology of the ES PA<sub>12</sub>HU-PTMOs fibers proved more in the nanoscale than ES TPU controls. This enables high surface to volume ratio needed to function as interfacing materials with flexible and elastic properties.

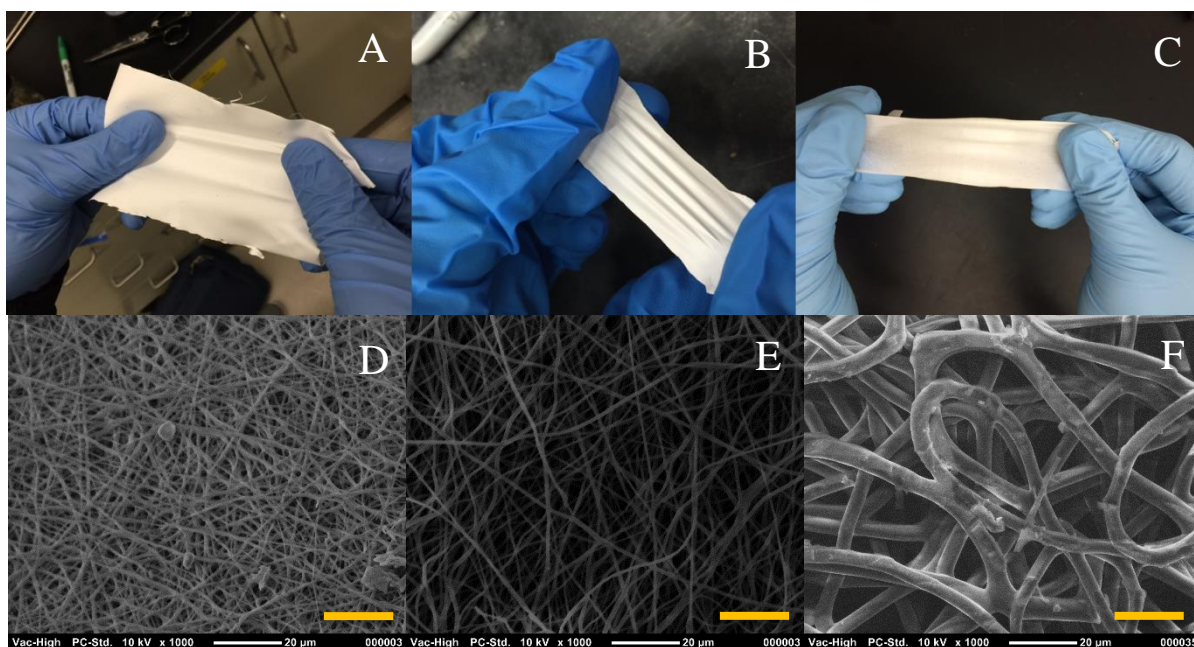


**Figure 11.2:** Pictures of fiber mats of A) ES PA<sub>12</sub>HU-PTMO25; B) ES PA<sub>12</sub>HU-PTMO33; C) ES TPU control. SEM of ES PA<sub>12</sub>HU-PTMOs fibers: D) ES PA<sub>12</sub>HU-PTMO25; E) ES PA<sub>12</sub>HU-PTMO33; F) ES TPU control. Scale bars: 20  $\mu\text{m}$ .



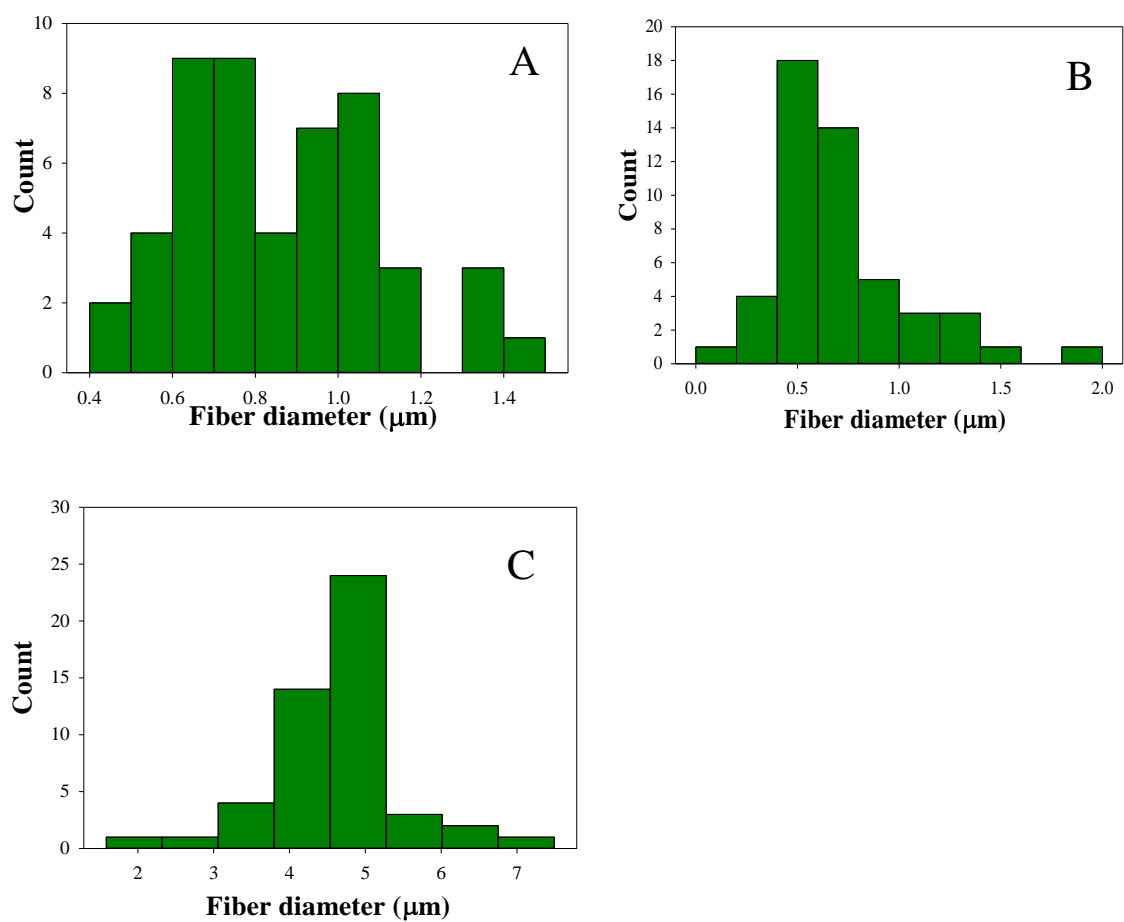


**Figure 11.3:** Fiber diameter distribution of electrospun PA<sub>12</sub>HU-PTMO fibers: **A)** ES PA<sub>12</sub>HU-PTMO25; **B)** ES PA<sub>12</sub>HU-PTMO33; **C)** ES TPU control

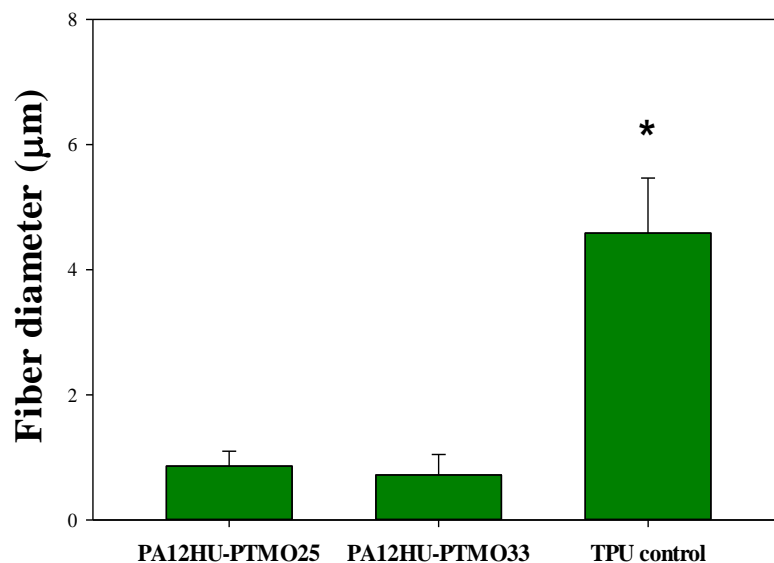


**Figure 11.4:** Average fiber diameter measurement of ES PA<sub>12</sub>HU-PTMOs and ES TPU control. (n = 50) (\*p < 0.05; significant differences between control and test groups.)

**Thermal properties.** Figure 11.5 shows TGA weight loss profiles of segmented PA<sub>12</sub>HU-PTMO and TPU control before and after electrospinning from HFIP, which matched closely within experimental error. The electrospinning process did not affect the thermal stability of PA<sub>12</sub>HU and TPU. <sup>1</sup>H NMR spectrum of PA<sub>12</sub>HU and TPU in deuterated HFIP remained unchanged, while deuterated TFA reacted with PAHU over time, which was avoided for electrospinning. Segmented PA<sub>12</sub>HU-PTMO samples exhibited higher T<sub>d, 5wt%</sub> than isocyanate-based TPU control sample likely due to additional amide bonds that proved more stable than urethane bonds (**Table 11.2**).<sup>23,24</sup> All polymer samples lack weight loss in the range of 130-230 °C where the monomer evaporated or degraded, indicating complete conversion of CC-ME monomer during polymerization.

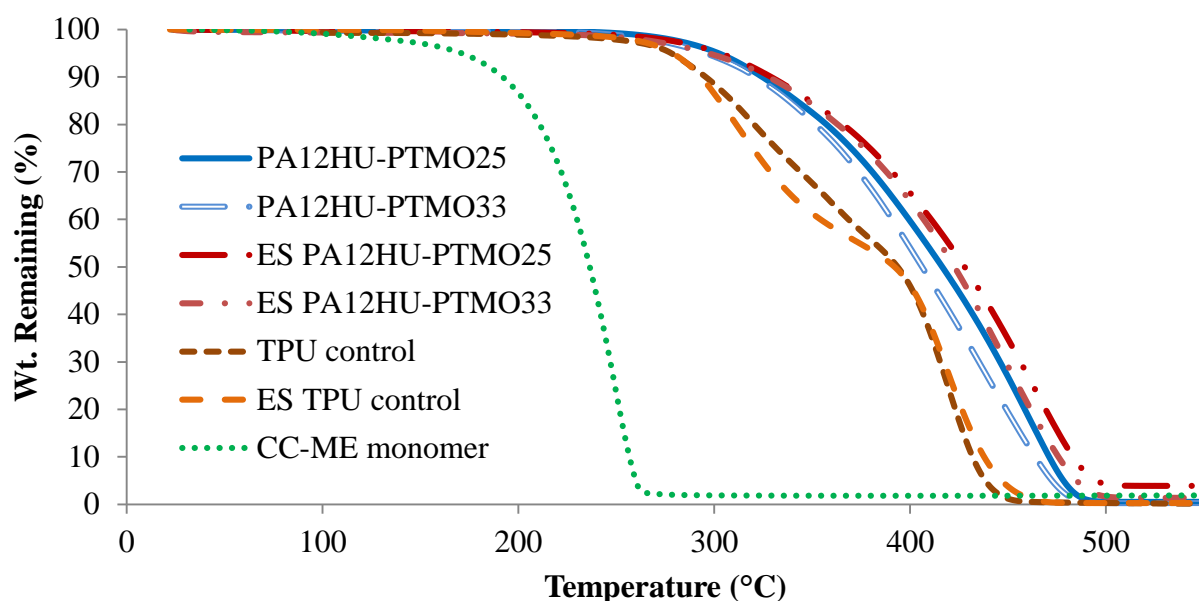


**Figure 11.5:** TGA thermograms of segmented PA<sub>12</sub>HU-PTMOs and the TPU control before and after electrospinning, along with CC-ME monomer under nitrogen purge.

The thermal history of annealed bulk films and electrospun fiber samples for both PAHUs and the TPU control was compared and shown in **Figure 11.6**. The first heating ramps of the annealed samples contained multiple isolated exothermic peaks, while electrospun samples exhibited broad overlapping exothermic peaks. The enthalpy of fusion for the first heating ramp listed in **Table 11.2** indicated that electrospinning yielded fibers with lower crystallinity than annealed bulk films. However, electrospinning resulted in significantly higher crystallinity than 10 °C/min cooling from 220 °C, comparing the enthalpy of fusion from the first and the second heating ramps. The electrospun TPU sample also exhibited exotherm peaks near 90-140 °C, attributing to the crystallization of the hard segments, while the 10 °C/min cooling process failed to induce any crystallinity. This crystallinity difference agreed with previous results that electrospinning facilitates crystallization.<sup>25</sup> However, annealing above the melting point combined with slow cooling

contributed to higher crystallinity than electrospinning.  $T_g$  values of annealed films and electrospun fibers matched closely, suggesting that annealing and electrospinning contributed to similar extent of phase-separation. However, the TPU control showed approximately 20 °C lower  $T_g$  than PA<sub>12</sub>HU-PTMO25 and PA<sub>12</sub>HU-PTMO33 with similar soft segment weight percentages, resulting from significant phase-mixing of the hard and soft segment in PA<sub>12</sub>HU-PTMOs in Chapter 10. In summary, electrospinning proved non-disruptive to the chemical compositions and phase-separation of PAHU and conventional TPU, and contributed to crystallinity lower than the annealing process and higher than 10 °C/min cooling.

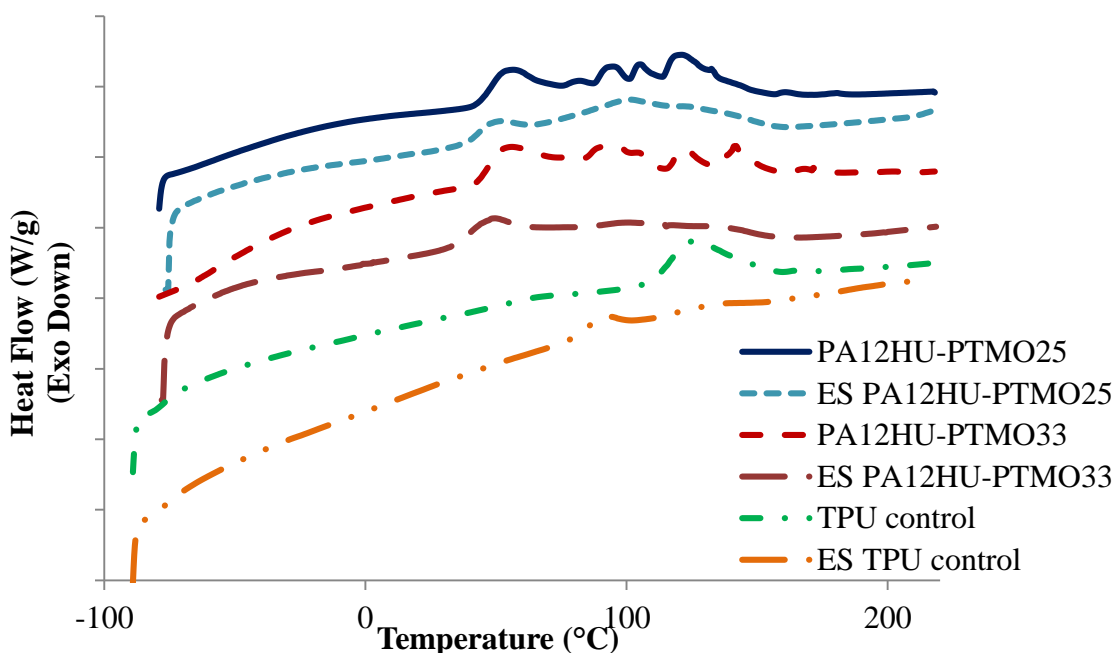


**Figure 11.6.** DSC thermograms of segmented PA<sub>12</sub>HU-PTMOs and the TPU control before and after electrospinning.

**Water sorption.** **Figure 11.7A** displays equilibrium water uptake of PA<sub>12</sub>HU-PTMO and the TPU control in 0% to 95% relative humidity (RH) at 25 °C. Comparison of annealed films and electrospun samples revealed that both processing conditions yielded similar water uptake as annealing and electrospinning maintained the chemical compositions for all polymers. The water uptake of PA<sub>12</sub>HU-PTMOs electrospun fibers and films reached approximately 4 wt% on average at 95% RH, independent of their soft segment percentage. The TPU controls exhibited water uptake near 1.2% at 95% RH, more than three times lower than PA<sub>12</sub>HU-PTMOs with comparable soft segments percentage (**Table 11.2**). The difference in water uptake of PA<sub>12</sub>HU-PTMOs and TPU likely resulted from the additional hydroxyls next to each urethane unit on the poly(amide-hydroxyurethane) backbone. Higher hydrophilicity potentially benefits the performance of PA<sub>12</sub>HU-PTMOs in biomedical application as a wound dressing material whose functions, fluid absorption and moisture exchange allow wounds to heal properly.<sup>14</sup> Also, water uptake will enable another application as a drug release scaffold.<sup>26</sup>

In addition, **Figure 11.7B** reveals that the electrospun samples require a significantly shorter time to reach equilibrium water uptake compared to the film samples, which pertained to the surface area difference from different processing methods. The time before equilibrium sorption generally increased with increasing RH for each sample, and the difference in rate of water uptake between electrospun and film samples increased with increasing RH. PA<sub>12</sub>HU-PTMO films required more than 20 h before reaching equilibrium at 95% RH, while electrospun PA<sub>12</sub>HU-PTMO fibers only need 35 minutes before equilibrium at identical RH. The TPU film sample needed shorter time to achieve equilibrium of water uptake compared to PA<sub>12</sub>HU-PTMO films, which proved nearly 100

times longer compared to the electrospun TPU sample. The faster water sorption and larger surface area of electrospun fiber mats will contribute to larger cell contact area and better permeability, which can help facilitate cell adhesion, nutrient exchange, oxygen exchange, and cell growth for tissue scaffolds. The electrospun mats enable applications as drug delivery materials, in which large surface area proves critical for burst or controlled release of potential drugs and biological mediators into physiological media.<sup>7,26</sup>

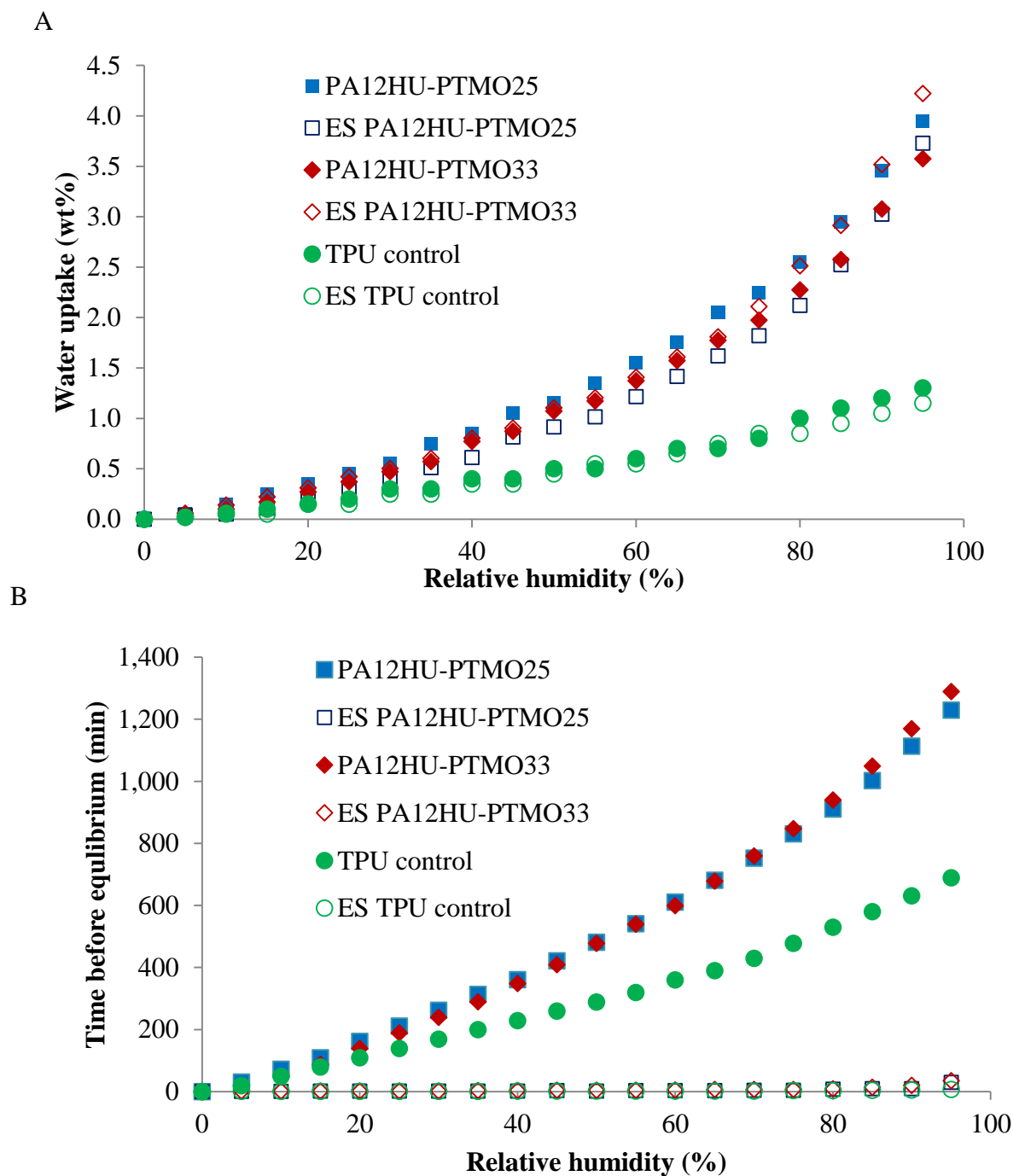


**Figure 11.7.** A) Equilibrium water sorption of compression molded and electrospun segmented PA<sub>12</sub>HU-PTMO samples in comparison to TPU controls. B) Time to reach equilibrium water sorption for compression molded and electrospun samples.

**Mechanical analysis.** DMA compared the thermomechanical properties of annealed segmented PA<sub>12</sub>HU-PTMO with TPU control from -100 °C to 130 °C. PA<sub>12</sub>HU-PTMO25 exhibited similar biphasic thermomechanical response with the TPU control (**Figure 11.8**), indicating a microphase-separated morphology. The urethane and amide-containing hard segments of PA<sub>12</sub>HU-PTMO self-assembled into a crystallizable hard domain, which served as physical crosslinking to yield a plateau region on the modulus curve, so did the TPU control. The moduli of annealed PA<sub>12</sub>HU-PTMO25 and TPU film matched closely in the glassy regime, while the TPU film exhibited lower modulus in the plateau and terminal flow regimes likely due to lower crystallinity compared to PA<sub>12</sub>HU-PTMO25. The modulus curve of TPU film started to decrease near -73 °C, approximately 10 °C earlier compared to PA<sub>12</sub>HU-PTMO25, which suggested a lower T<sub>g</sub> and agreed with the thermal analysis result from **Table 11.2**. The tan delta peak of TPU near -65 °C also revealed a lower temperature and narrower glass transition, indicating a better phase-separation for TPU compared to PA<sub>12</sub>HU-PTMO25. The phase-mixing of the soft and hard segments of PA<sub>12</sub>HU-PTMO25 resulted from the relatively short 1 kDa polyether segment, while TPU contained polyether soft segment with 2 kDa molecular weight which afforded better phase-separation. Furthermore, the composition difference between PAHU and TPU likely yielded different Flory-Huggins interaction parameters  $\chi$ , which affected the extent of phase-separation.<sup>27</sup> PA<sub>12</sub>HU-PTMO33 exhibited similar biphasic thermomechanical performance with lower modulus in the plateau and flow regimes compared to PA<sub>12</sub>HU-PTMO25 due to lower hard segment content (**Figure 11.9**). The larger tan delta peak of PA<sub>12</sub>HU-PTMO33 corresponded to a lower crystallinity compared to PA<sub>12</sub>HU-PTMO25.



DMA also investigated the thermomechanical properties of electrospun fiber mats of segmented PAHUs and the TPU control (**Figures 11.8,11.9**). The ES PA<sub>12</sub>HU-PTMO fiber mats proved thinner than ES TPU fiber mat, and not strong enough to withhold the preloaded force during the oscillatory experiment at room temperature. The ES PA<sub>12</sub>HU-PTMO samples were cooled below their glass transitions and subjected to the oscillatory experiment. The glassy moduli of electrospun fiber mats proved significantly lower than the annealed films for both PA<sub>12</sub>HU-PTMO25 and the TPU control. This phenomenon resulted from the non-continuous morphology of electrospun fiber mats with sub-micron porosity between the randomly orientated fibers.<sup>12</sup> The electrospun TPU mat showed higher glassy modulus than PA<sub>12</sub>HU-PTMO25 due to its larger overlapped area and larger fiber diameter. Thermomechanical transitions of electrospun TPU matched closely with the annealed TPU film with a glass transition starting near -70 °C. However, the modulus of electrospun TPU fiber mat decreased with a faster rate in the flow regime, and yielded at lower temperature compared to the annealed film. This difference likely resulted from the lower crystallinity of electrospun fiber mats and their porous morphologies, which enabled faster heat transfer under the same heating rate. ES PA<sub>12</sub>HU-PTMO25 fiber mat also exhibited a similar T<sub>g</sub> as the bulk film, however, it yielded at much lower temperature. ES PA<sub>12</sub>HU-PTMO25 fiber mat exhibited weaker thermomechanical properties mainly due to its lower thickness and lower molecular weight compared to ES TPU (**Table 11.1**). Comparing two samples with the same modulus, the one with lower thickness will afford weaker force that is below the accuracy of DMA force sensor. The storage modulus of ES PA<sub>12</sub>HU-PTMO25 fiber mat measured to be approximately 2 MPa, which enabled its

application as a tissue scaffold.<sup>13,15</sup> ES PA<sub>12</sub>HU-PTMO33 displayed similar thermomechanical properties to electrospun PA<sub>12</sub>HU-PTMO25.

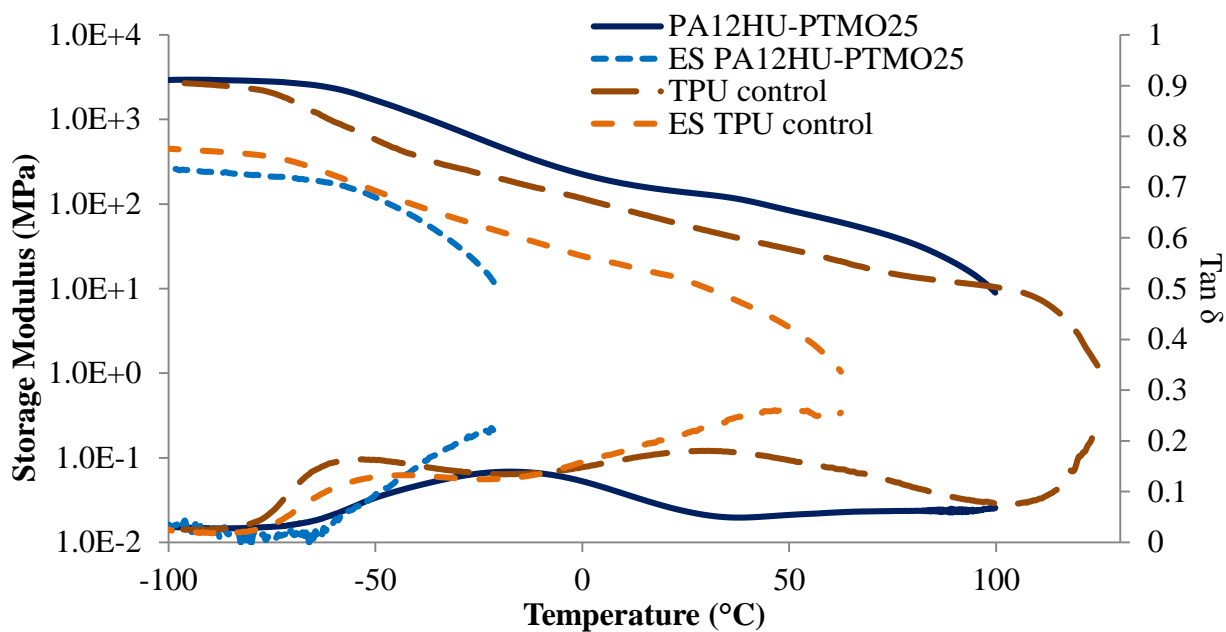


**Figure 11.8.** Dynamic mechanical temperature ramps for segmented PA<sub>12</sub>HU-PTMO25 and the TPU control before and after electrospinning.

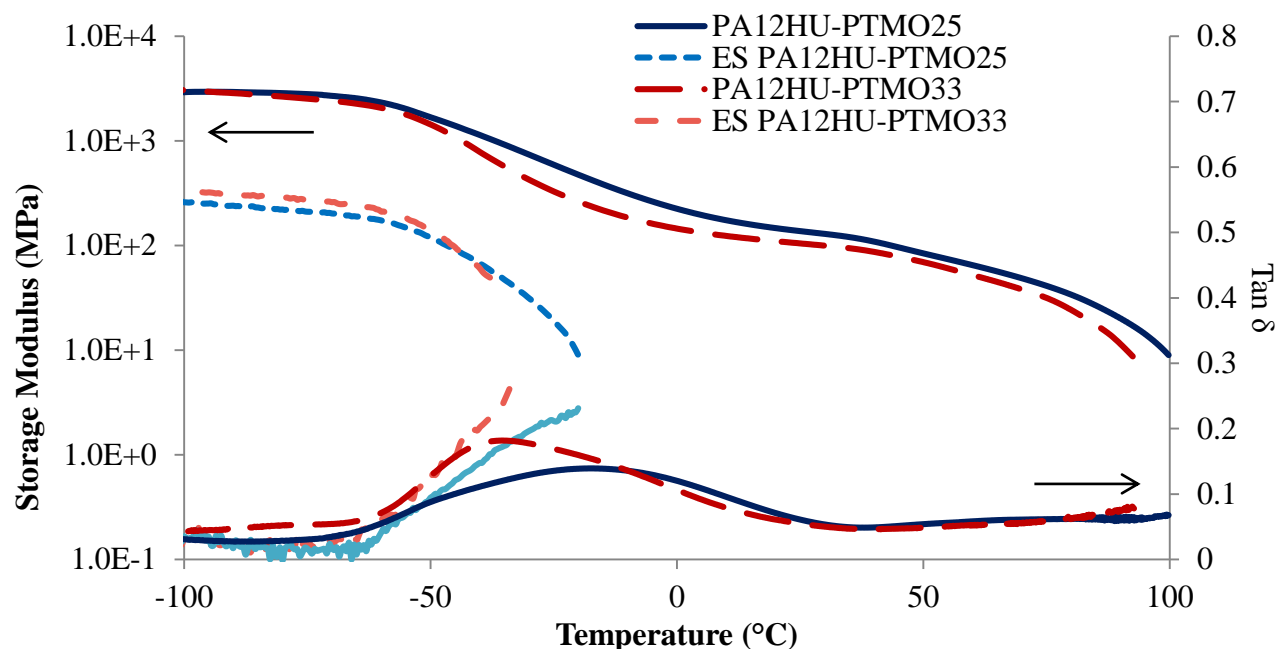


**Figure 11.9.** Dynamic mechanical temperature ramps for segmented PA<sub>12</sub>HU-PTMO25 and PA<sub>12</sub>HU-PTMO33 before and after electrospinning.

Electrospun fibers and annealed polyurethanes films were analyzed on the Instron Microtester to evaluate their tensile properties with respect to the amount of PTMO soft segment. ES PA<sub>12</sub>HU-PTMO25 and ES PA<sub>12</sub>HU-PTMO33 underwent failure at 1.56 and 1.50 MPa respectively while ES TPU controls failed at 1.59 MPa, similar to values of electrospun polyurethanes fibers in literature.<sup>26</sup> (**Table 11.3**). When looking at strain at break data, more revealing observations show TPU controls proved to be significantly more elastic than ES PA<sub>12</sub>HU-PTMO fibers, experiencing failure at 128% and 807% for electrospun fibers and films respectively. ES PA<sub>12</sub>HU-PTMO25 and ES PA<sub>12</sub>HU-PTMO33 experienced strain at break at 20.9 and 16.3 percent respectively. The differences in mechanical properties between ES PA<sub>12</sub>HU-PTMO and ES TPU control fibers may be due to the greater mat thickness and solution viscosity in the TPU materials. Overall, these electrospun fibers are soft, elastomeric mats which deform at smaller loads when compared

to their film counterparts. Increasing the mat thickness for ES PA<sub>12</sub>HU-PTMO mats would improve mechanical integrity at greater loads while maintaining its elastomeric profile.

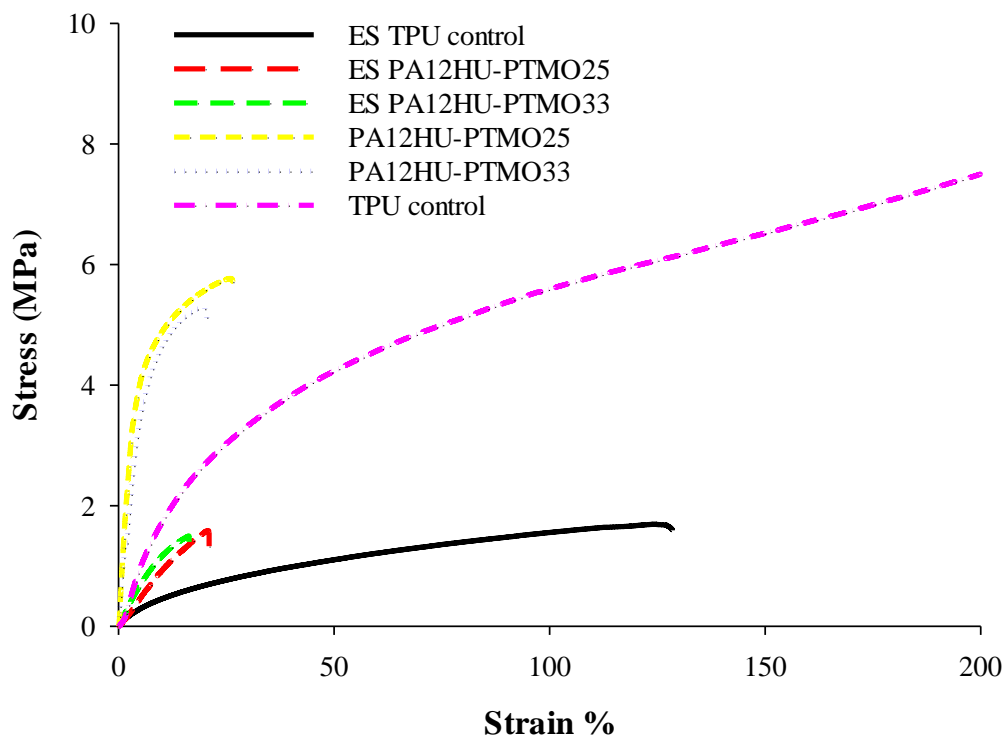


**Figure 11.10:** Stress-strain curves of PA<sub>12</sub>HU-PTMO materials up to 200% strain.

**Table 11.3.** Tensile properties of PA<sub>12</sub>HU-PTMOs with 25-50 mol% soft segments.

| Sample                        | Young's Modulus (MPa) | Strain at break (%) | Stress at break (MPa) |
|-------------------------------|-----------------------|---------------------|-----------------------|
| ES PA <sub>12</sub> HU-PTMO25 | 6.71 ± 1.09           | 20.9 ± 2.91         | 1.56 ± 0.277          |
| ES PA <sub>12</sub> HU-PTMO33 | 8.03 ± 1.04           | 16.3 ± 1.02         | 1.50 ± 0.099          |
| ES TPU control                | 0.874 ± 0.163         | 128 ± 4.99          | 1.59 ± 0.320          |
| PA <sub>12</sub> HU-PTMO25    | 94.2 ± 24.5           | 24.9 ± 8.27         | 5.71 ± 0.387          |
| PA <sub>12</sub> HU-PTMO33    | 109 ± 8.10            | 21.4 ± 5.92         | 5.30 ± 0.485          |
| TPU control                   | 20.1 ± 2.52           | 807 ± 66.9          | 22.9 ± 2.86           |

**Cell studies.** To afford the use of these materials in biological applications such as wound dressings or drug delivery vehicles, their biocompatibility with human primary fibroblasts was tested. The first step involved analyzing the effect of media extracts exposed to these mats on the viability of fibroblasts. **Figure 11.11** depicts the viability of cells exposed to RPMI media extracts from polymers after 1 and 3 days relative to positive control containing no polymer extracts as analyzed by alamar blue staining. Samples are normalized to positive control for each day. As compared to the positive control, cells exposed to all the ES PA<sub>12</sub>HU-PTMO samples were 90-97% viable at the end of 3 days. This indicates that the degradation products, if any, are non-toxic to the growth of cells and implies their potential for use in biomedical applications.

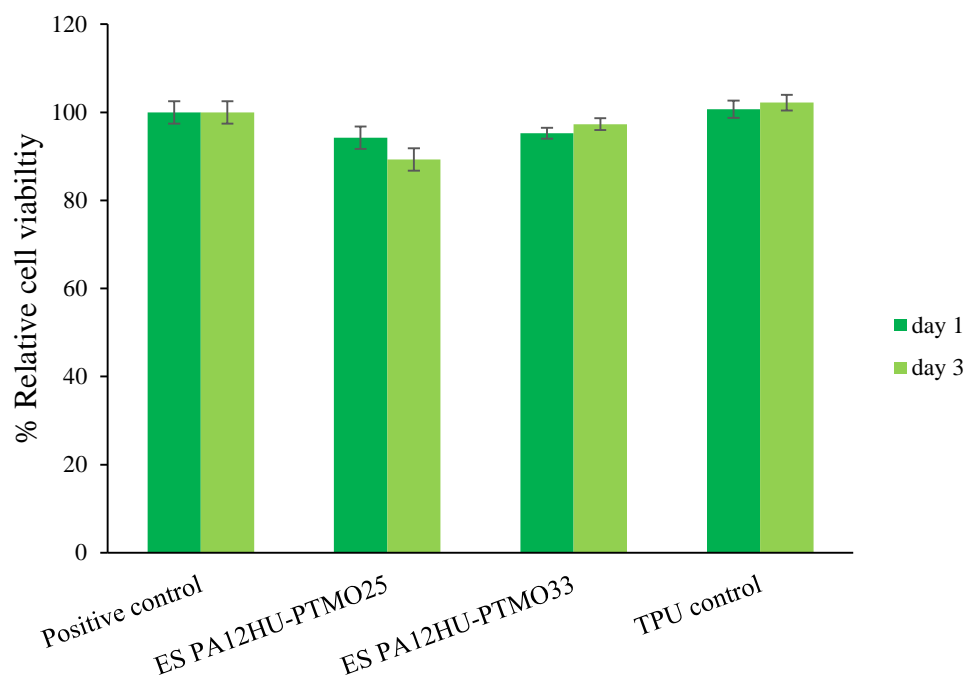


**Figure 11.11:** Cell viability study for electrospun PA<sub>12</sub>HU-PTMO samples in comparison to TPU controls.

To further confirm the attachment of fibroblasts to these mats and the effect on cell viability, fibroblasts were directly seeded on the polymers and viability was analyzed using Live/Dead™ stain. As seen in **Figure 11.12**, the top panel shows fibroblasts attaching to ES PA<sub>12</sub>HU-PTMO samples at the end of day 1. Live cells stained with Calcein AM fluoresced green while the dead cells stained with EthD III fluoresced red. These images revealed that cells attached and spread onto the electrospun PU samples while a significant majority remained viable. At the end of day 3, cells on all the samples showed regular morphology.<sup>28</sup> Cell proliferation on the electrospun PA<sub>12</sub>HU-PTMO samples was higher than the ES TPU controls as seen in **Figure 11.12** possibly due to the additional hydroxyl groups for PA<sub>12</sub>HU-PTMO and higher water uptake. The fiber morphology may be another reason as PA<sub>12</sub>HU-PTMO fiber mat contained thinner fibers with higher surface area. This data suggests the importance of low cytotoxicity of ES PA<sub>12</sub>HU-PTMO on cells over a 3-day period which underscores the ability to support growth and proliferation of cells on the material surface. These are vital properties for a viable wound dressing material.

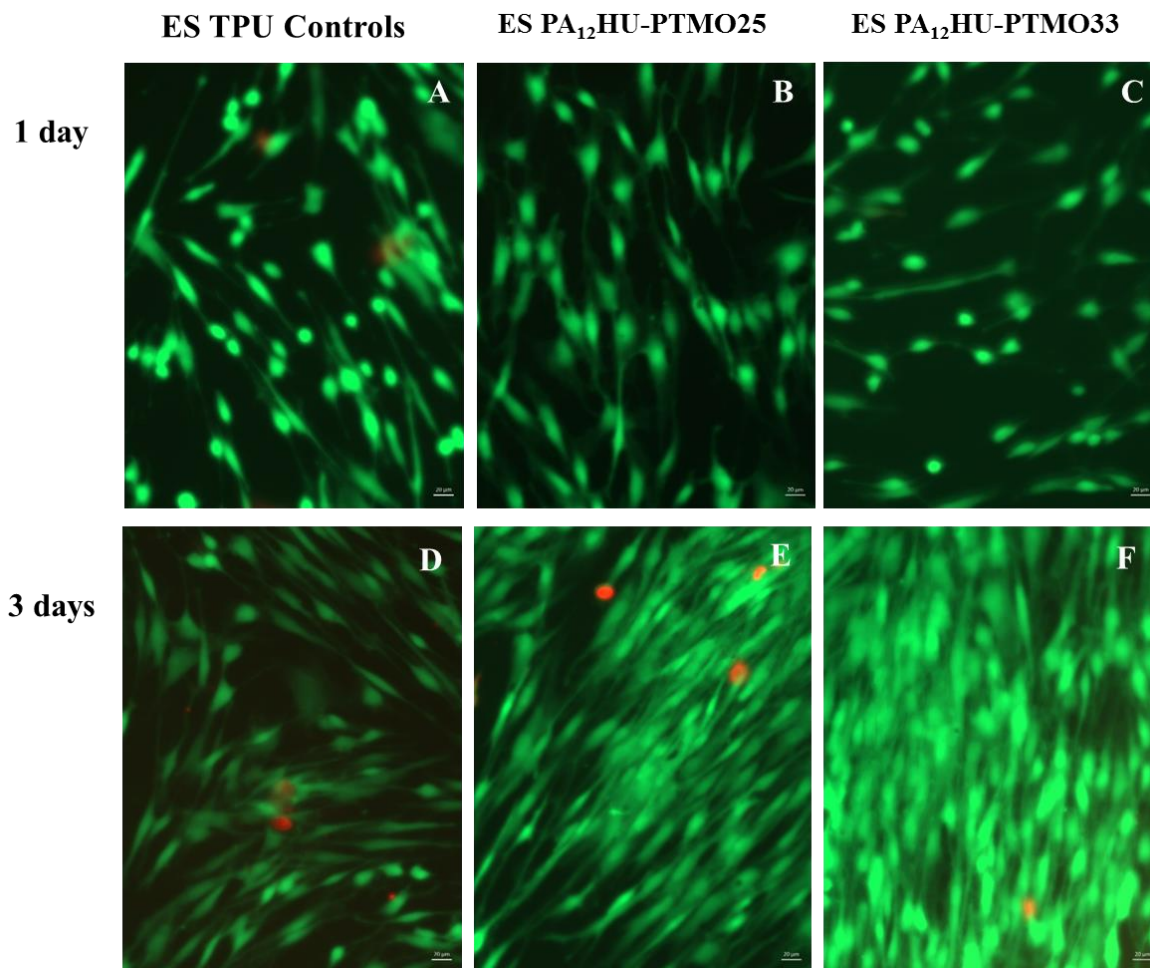


**Figure 11.12:** Fluorescent microscopy images of fibroblasts on ES PA<sub>12</sub>HU-PTMO samples in comparison to ES TPU controls. Fibroblasts were stained with Live/Dead™ stain (green: viable cells, red: non-viable cells). Upper panel (A, B, C): cells on fiber mats at day 1; Lower panel (D, E, F): cells on fiber mats at day 3.

## 11.5 Conclusions

This study reports successful electrospinning of non-isocyanate polyurethanes from sustainable resources to prepare nanofibers and evaluation of their structure-processing-property relationships. Electrospun PA<sub>12</sub>HU-PTMO fibers exhibited nanoscale fiber

morphology with uniform size distribution. Thermal analysis suggested that electrospinning did not affect the thermal stability of PA<sub>12</sub>HU-PTMO and the TPU control, while the electrospun fibers showed slightly lower crystallinity than the annealed films. The tensile and thermomechanical properties of electrospun PA<sub>12</sub>HU-PTMO fibers proved weaker than annealed films due to the porous fiber morphology and lower thickness. However, the high surface areas of electrospun fibers enabled faster fluid sorption than annealed films. The electrospun conventional TPU control showed stronger mechanical performance than PA<sub>12</sub>HU-PTMO, presumably due to higher molecular weight. However, PA<sub>12</sub>HU-PTMOs exhibited higher water uptake than TPU control, beneficial for biomedical applications.

Cell viability and attachment studies illustrated the high biocompatibility of electrospun PA<sub>12</sub>HU-PTMO fibers which enabled its use in biomedical applications, including tissue engineering, drug delivery, and wound dressing development. Polyurethanes represent a class of polymers that are ubiquitously used in society. Therefore, considerations must be taken to account for potential health hazards such as isocyanate. The work in this study successfully evaluated the properties of electrospun polyurethane fibers using sustainable materials applicable in the medical device industry. The findings in this study support the need to further explore green synthesis of polyurethanes and its conversion into functional materials.

## 11.6 *Acknowledgements*

This research was partially supported by Elevance Renewable Science, Inc. We also thank Huntsman Corporation for material support, as well as Lindsey Anderson and Jeremy Beach from Dr. Robert Moore's group for use of their electrospinning setup.



Authors thank Alexis Trent from Dr. Van Dyke's laboratory for providing primary fibroblasts used in the study, Robert Accolla for his assistance with biocompatibility studies, and Kevin Drummey for his contribution on the viscosity measurements.

## 11.7 References

- (1) Anton, F. " U.S. Patent No. 1,975,504. October 2, 1934.
- (2) Deitzel, J. .; Kleinmeyer, J.; Harris, D.; Beck Tan, N. . *Polymer (Guildf)*. **2001**, 42 (1), 261–272.
- (3) Gibson, P.; Schreuder-Gibson, H.; Rivin, D. *Colloids Surfaces A Physicochem. Eng. Asp.* **2001**, 187-188, 469–481.
- (4) Barnes, C. P.; Sell, S. A.; Boland, E. D.; Simpson, D. G.; Bowlin, G. L. *Adv. Drug Deliv. Rev.* **2007**, 59 (14), 1413–1433.
- (5) Min, B.-M.; Lee, G.; Kim, S. H.; Nam, Y. S.; Lee, T. S.; Park, W. H. *Biomaterials* **2004**, 25 (7-8), 1289–1297.
- (6) Zdrahala, R. J.; Zdrahala, I. J. *J Biomater Appl* **1999**, 14 (1), 67–90.
- (7) Aduba, D. C.; Hammer, J. a.; Yuan, Q.; Andrew Yeudall, W.; Bowlin, G. L.; Yang, H. *Acta Biomater.* **2013**, 9 (5), 6576–6584.
- (8) Aduba, D. C.; Overlin, J. W.; Frierson, C. D.; Bowlin, G. L.; Yang, H. *Mater. Sci. Eng. C* **2015**, 56, 189–194.
- (9) Wang, X.; Drew, C.; Lee, S.-H.; Senecal, K. J.; Kumar, J.; Samuelson, L. A. *Nano Lett.* **2002**, 2 (11), 1273–1275.
- (10) Adams, Jonathan, Pendlebury, D. *Global Research Report: MATERIALS SCIENCE AND TECHNOLOG*; Leeds, United Kingdom, 2011.
- (11) Trinca, R. B.; Abraham, G. A.; Felisberti, M. I. *Mater. Sci. Eng. C. Mater. Biol. Appl.* **2015**, 56, 511–517.
- (12) McKee, M. G.; Park, T.; Unal, S.; Yilgor, I.; Long, T. E. *Polymer (Guildf)*. **2005**, 46 (7), 2011–2015.
- (13) Cha, D. Il; Kim, H. Y.; Lee, K. H.; Jung, Y. C.; Cho, J. W.; Chun, B. C. *J. Appl. Polym. Sci.* **2005**, 96 (2), 460–465.
- (14) Khil, M.-S.; Cha, D.-I.; Kim, H.-Y.; Kim, I.-S.; Bhattarai, N. *J. Biomed. Mater. Res. B. Appl. Biomater.* **2003**, 67 (2), 675–679.
- (15) Chen, R.; Huang, C.; Ke, Q.; He, C.; Wang, H.; Mo, X. *Colloids Surf. B. Biointerfaces* **2010**, 79 (2), 315–325.
- (16) Sen, R.; Zhao, B.; Perea, D.; Itkis, M. E.; Hu, H.; Love, J.; Bekyarova, E.; Haddon, R. C. *Nano Lett.* **2004**, 4 (3), 459–464.
- (17) CDC - Isocyanates - NIOSH Workplace Safety and Health Topic <http://www.cdc.gov/niosh/topics/isocyanates/> (accessed Feb 2, 2016).
- (18) Webster, D. C. *Prog. Org. Coatings* **2003**, 47 (1), 77–86.
- (19) Blattmann, H.; Fleischer, M.; Bähr, M.; Mülhaupt, R. *Macromol. Rapid Commun.* **2014**, 35 (14), 1238–1254.
- (20) Rokicki, G.; Parzuchowski, P. G.; Mazurek, M. *Polym. Adv. Technol.* **2015**, 26 (7), 707–761.
- (21) Maisonneuve, L.; More, A. S.; Foltran, S.; Alfes, C.; Robert, F.; Landais, Y.;

- Tassaing, T.; Grau, E.; Cramail, H. *RSC Adv.* **2014**, 4 (49), 25795.
- (22) Guan, J.; Song, Y.; Lin, Y.; Yin, X.; Zuo, M.; Zhao, Y.; Tao, X.; Zheng, Q. *Ind. Eng. Chem. Res.* **2011**, 50 (11), 6517–6527.
- (23) Ravey, M.; Pearce, E. M. *J. Appl. Polym. Sci.* **1997**, 63 (1), 47–74.
- (24) Levchik, S. V.; Weil, E. D.; Lewin, M. *Polym. Int.* **1999**, 48 (7), 532–557.
- (25) Yanilmaz, M.; Kalaoglu, F.; Karakas, H.; Sarac, A. S. *J. Appl. Polym. Sci.* **2012**, 125 (5), 4100–4108.
- (26) Xu, C.; Huang, Y.; Wu, J.; Tang, L.; Hong, Y. *ACS Appl. Mater. Interfaces* **2015**, 7 (36), 20377–20388.
- (27) Robeson, L. M. *Leseprobe* **2007**, 10–23.
- (28) Healey, C.; Forgione, P.; Lounsbury, K. M.; Corrow, K.; Osler, T.; Ricci, M. A.; Stanley, A. *J. Vasc. Surg.* **2003**, 38 (5), 1099–1105.

## Chapter 12. Nucleobase Functionalized Polymers for Enhanced Interlayer Adhesion in 3D Printing

Keren Zhang,<sup>a</sup> Kristen S. Wek,<sup>a</sup> Ye-Won Rhee,<sup>a</sup> Andrea Sweet,<sup>a</sup> and Timothy E. Long<sup>a\*</sup>

<sup>a</sup>*Virginia Tech, Department of Chemistry, Macromolecules and Interfaces Institute (MII)  
Blacksburg, Virginia 24061*

<sup>b</sup>*Department of Macromolecular Science and Engineering  
Case Western Reserve University, Cleveland, OH, 44106*

### 12.1 **Abstract**

Additive manufacturing offers immense promise at the interface of tailored polymeric materials and lithographic manufacturing technologies. This project focus on the potential synergy of 3D printing technique and bio-based supramolecular polymers for manufacturing designed polymeric objects with smart materials. Nucleobase-containing polymers have shown their potentials as smart materials with biological activities. Michael addition of polyethylene glycol (PEG) diacrylate and adenine/thymine affords synthesis of nucleobase-functionalized monomers under mild conditions. Reaction mixture will be directly used to prepare materials for 3D printing, while eliminating purification procedures. Nucleobase-functionalized monomers will allow facile incorporation of nucleobases into photo-crosslinked networks. Varying the amount of di-acrylate *vs* mono-acrylate provides tunable crosslinking density for the final product. Our fully PEG-based crosslinked network also ensures sufficient biocompatibility for biomedical applications.

Mask projection micro-stereolithography enabled the design of micron scale objects with nanostructural control. However, absence of strong interlayer bonding generally limits mechanical performance of 3D printed objects. The complementary hydrogen bonding between a nucleobase pair serves as an additional adhesion mechanism

between the printed layers besides weak van der Waals interaction. Interlayer adhesion reinforcement from hydrogen bonding will contribute to enhanced mechanical performance for 3D printed parts. We will probe the effect of nucleobase incorporation on thermal, mechanical, rheological, and biological properties of 3D printed objects using various instrumental tools in our polymer characterization laboratory. Stimuli-responsiveness and biological activities of nucleobase also enables potential applications such as tissue scaffold, protein separation column, antibacterial coating, and stimuli-responsive gel.

## 12.2 *Introduction*

Additive manufacturing is a rapidly emerging technique for producing designed objects with precise dimensional control and compatibility for various raw materials. Interdisciplinary research opportunities arise from the interface of tailored polymeric materials and lithographic manufacturing technologies. This project focus on the potential synergy of 3D printing technique and bio-based supramolecular polymers for manufacturing designed polymeric objects with smart materials. Nucleobase-containing polymers have shown their potentials as smart materials with biological activities.<sup>1,2</sup> Kim *et. al.* demonstrated the biological activities of adenine-rich polymer surface, including selective protein absorption, suppressed bacteria adherence, and good compatibility both *in vivo* and *in vitro*.<sup>1</sup> Long *et. al.* improved the adhesive performance of acrylic polymers when nucleobase were added on the pendant groups, providing physical crosslinking.<sup>3,4</sup> Many research groups have demonstrated the potential of nucleobase-containing polymers in DNA-mimicking materials, biomedical sensors, tissue scaffolds, protein separation membranes, templating polymerizations, and stimuli-responsive materials.<sup>2,5-8</sup> Most of

these applications require a precisely controlled manufacture process that is capable to accommodate for a range of raw materials from fragile gels to tough blocks.

The emerging additive manufacturing offers great opportunities for producing biomedical products with precise shape and a wide range of toughness. Mask projection micro-stereolithography enables the design of micron scale objects with nanostructural control. However, absence of strong interlayer bonding generally limits mechanical performance of 3D printed objects. Complementary hydrogen between nucleobase pairs may serve as an additional adhesion mechanism between the printed layers, besides the weak van der Waals interaction. Interlayer adhesion reinforcement from hydrogen bonding possibly contributes to enhanced mechanical performance for 3D printed parts. Herein, we designed a nucleobase-containing crosslinked polymer platform for 3D printable smart materials. Among four primary nucleobases in deoxyribonucleic acid (DNA), we will focus on the adenine and thymine nucleobase pair due to their synthetic versatility. This PEG-based crosslinked network also ensures sufficient biocompatibility for biomedical applications.

### 12.3 *Experimental Section*

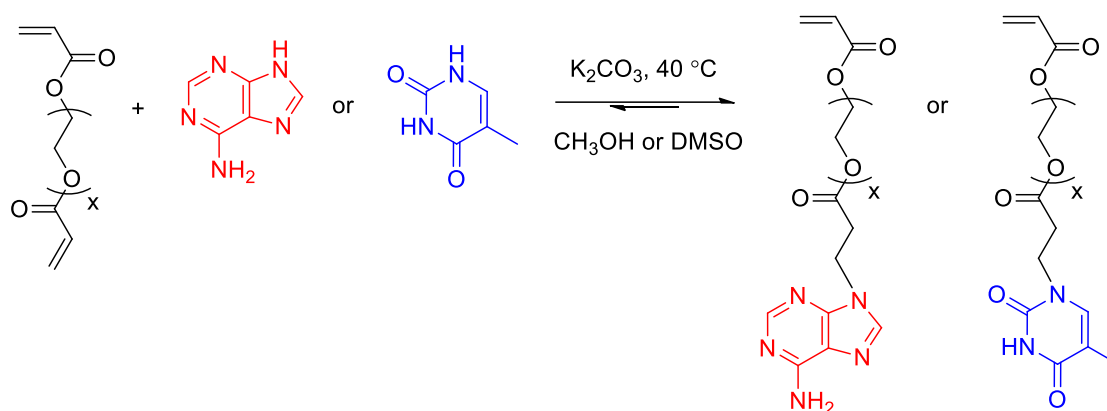
**Materials.** Adenine (A, 99%), thymine (T, 99%), potassium carbonate ( $K_2CO_3$ , 99%), 2-Hydroxy-4'-(2-hydroxyethoxy)-2-methylpropiophenone (I2959, 98%), and poly(ethylene glycol) diacrylate (PEGDA,  $M_w$  575 g/mol and 700 g/mol) were purchased from Sigma Aldrich and used without further purification. Dimethylsulfoxide (DMSO, HPLC grade), methanol (MeOH, HPLC grade), and isopropyl alcohol (IPA, HPLC grade) were purchased from Spectrum Chemicals and used as received. Water was purified from distillation.

**Analytical Methods.**  $^1\text{H}$  NMR spectroscopy confirmed the chemical structure of nucleobase-containing PEG acrylate monomers in  $\text{DMSO-d}_6$  using an Agilent U4-DD2 spectrometer operating at 400 MHz at 23 °C. *In situ* FTIR analysis utilized a Mettler Toledo ReactIR 45M attenuated total reflectance reaction apparatus equipped with a light conduit and DiComp (diamond composite) insertion probe. Thermogravimetric analysis (TGA) of nucleobase-containing PEGDA gels and control PEGDA gels was performed on a TA Instruments Q50 TGA with a heating ramp from ambient to 600 °C at a heating rate of 10 °C/min under constant nitrogen purge. Thermal degradation temperature ( $T_{\text{d},5\text{wt}\%}$ ) corresponded to the temperature at 5% weight loss of the initial sample weight. Differential scanning calorimetry (DSC) of nucleobase-containing PEGDA gels and control PEGDA gels was conducted on a TA instruments Q1000 DSC using a heat/cool/heat procedure with heating rate of 10 °C/min and cooling rate of 10 °C/min under a nitrogen flush of 50 mL/min. The midpoint of the transition in the second heating ramp determined glass transition temperatures ( $T_g$ ).

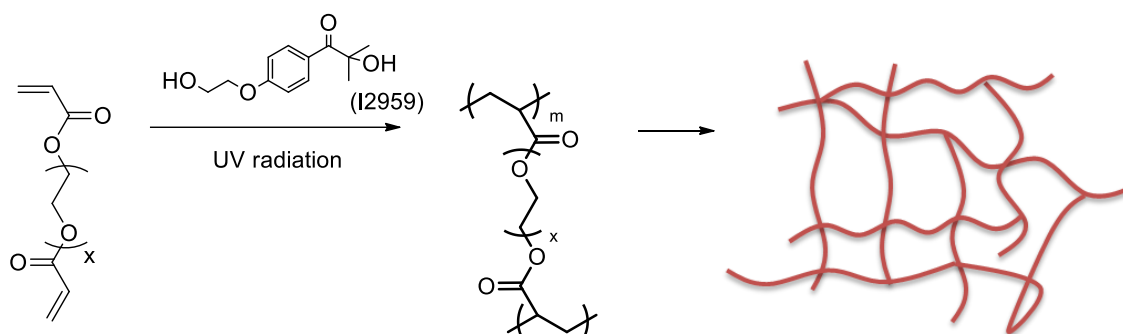
Dynamic mechanical analysis (DMA) of nucleobase-containing PEGDA gels and control PEGDA gels utilized a TA Instruments Q800 in tension mode at a frequency of 1 Hz, oscillatory amplitude of 15  $\mu\text{m}$ , and a static force of 0.01 N. Rectangular gel samples were cooled to -80 °C, equilibrated for 2 min, length measured, and subjected to a 3 °C/min temperature ramp. An Instron 5500R universal testing instrument characterized tensile properties of nucleobase-containing PEGDA gels and control PEGDA gels at a crosshead speed of 50 mm/min. Tensile analysis results represented an average of five specimens with calculated standard deviations.

**Synthesis of adenine and thymine poly(ethylene glycol) acrylates, abbreviated as APA and TPA, respectively (Scheme 12.1).** Adenine or thymine (1.0 g), one equivalent of PEGDA ( $M_w$  of 575 g/mol),  $K_2CO_3$  (60.0 mg) were charged into a round-bottomed flask with MeOH (20 mL) or DMSO (20 mL), respectively. The reaction mixture was allowed to stir at 40 °C for 3.5 h for the thymine reaction in MeOH and 50 °C for 0.5 h for the adenine reaction in DMSO. The reaction mixture in MeOH was concentrated in a rotary evaporator to remove the solvent. DMSO was distilled off under reduced pressure. Solvent removal resulted in two white solids with over 95% yield.  $^1H$  NMR confirmed the structure of both nucleobase PEG acrylates and revealed the reaction conversion near 90%. The resulting APA and TPA monomer with ca. 10% PEG diacrylate were used directly for photopolymerization without further purification step.

**Photopolymerization Process (Scheme 12.2).** Control samples were prepared using PEGDA (700  $M_w$ , 10.0 g) with I2959 (0.25 wt%, 25.0 mg) photoinitiator in water as shown in Scheme 12.2. Diluted solutions with 17, 10, and 5 wt% of PEGDA in water were prepared. Adenine and thymine-containing resins were prepared through adding APA and TPA (1.0 g) to a solution of PEGDA (3.0 g,  $M_w$  of 700 g/mol), I2959 (80 mg, 2 wt%), in 4.0 g MeOH. These solutions were poured into PTFE molds and cured using a UV Fusion under speed 6 fpm or 20 fpm. The resulting crosslinked gels were then dipped into IPA to remove any unreacted resin, and dried overnight at room temperature *in vacuo*.



**Scheme 12.1.** Synthesis of adenine PEG acrylate (APA) and thymine PEG acrylate (TPA).



**Scheme 12.2.** Photopolymerization of PEG diacrylate into chemically crosslinked gels.

## 12.4 Results and Discussion

Michael addition serves as a widely used synthetic method for preparing polymers with designed architectures and functional groups.<sup>9</sup> Our group previously used a Michael addition of 1, 4-butanediol diacrylate with adenine/thymine to synthesize organic soluble acrylic adenine/thymine monomers under mild conditions.<sup>4</sup> Under similar conditions, Michael addition of polyethylene glycol (PEG) diacrylate and adenine/thymine afforded synthesis of nucleobase-functionalized monomers with a PEG spacer between the acrylic backbone and nucleobase group (Scheme 12.1).  $^1\text{H}$  NMR spectroscopy results (Figure S12.1, S12.2) confirmed the successful synthesis of adenine/thymine PEG acrylate monomers. Low amount of  $K_2CO_3$  catalyst proved non-disruptive to the curing process and



biocompatible. Methanol mainly served the purpose of dissolving the photo-initiator and nucleobase monomers. Residue solvent was easily removed under vacuum after photocuring. Unreacted diacrylate served as crosslinkers for the curing process. Reaction mixtures from Michael addition were directly used to prepare UV resins for photocrosslinking without further purification.

*In situ* FTIR monitored the Michael reaction kinetics of thymine and PEG diacrylate. Figure 12.1 displayed the FTIR spectra changing as the Michael reaction proceeded over time. The absorption band at  $1679\text{ cm}^{-1}$  corresponded to the stretching vibration of the carbonyl adjacent to nucleobase on thymine PEG acrylate (TPA) monomer. The intensity of this absorption band correlated to the amount of TPA increase as reaction proceeded. The 2D plot of intensity over reaction time revealed the reaction kinetic in Figure 12.2. In first two hours, the reaction followed first order reaction kinetics as the thymine concentration remained saturated in MeOH. The rate of reaction was proportional to the concentration of starting material PEG diacrylate. The reaction rate constant in the first two hours was calculated to be  $0.01\text{ min}^{-1}$ . The end of this phase matched the observation of reaction turning clear, leading to the start of the second phase. The second phase followed a second order reaction kinetics as reaction rate depends on concentrations of both starting materials. Finally the reaction reached equilibrium at 3.3 hours.

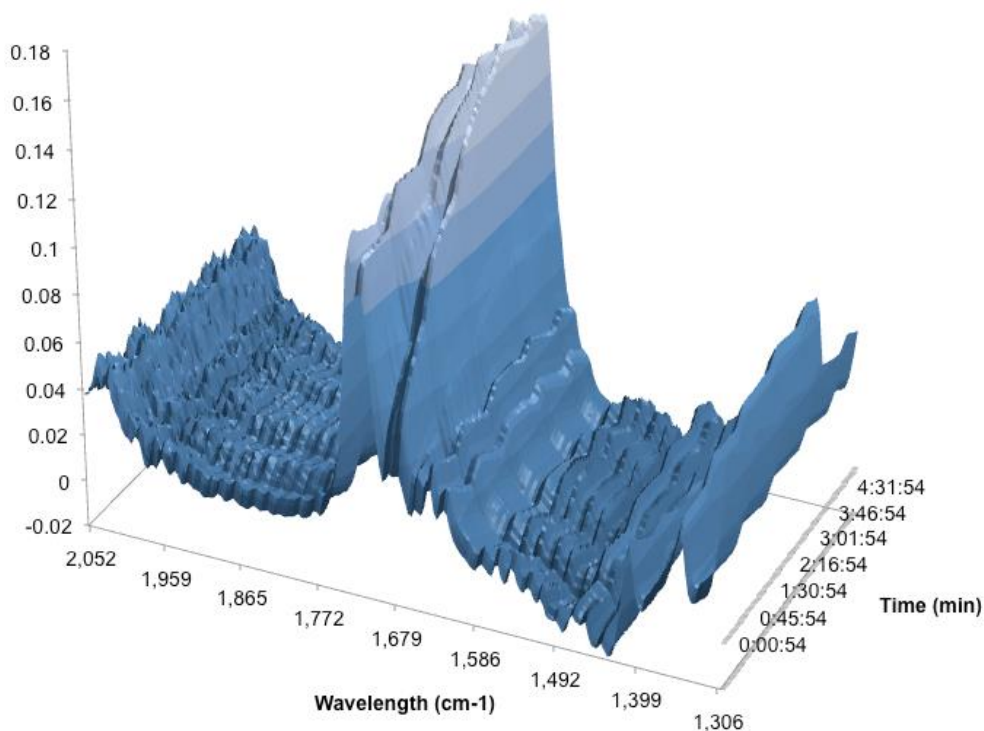


**Figure 12.1.** 3D waterfall plot of *in situ* FTIR spectra monitoring Michael reaction between thymine and PEG diacrylate.

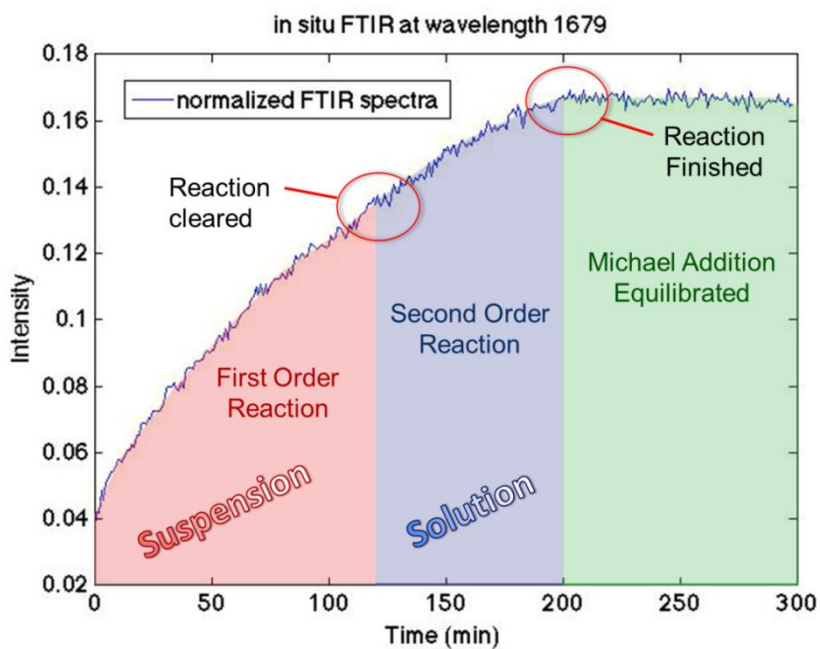


**Figure 12.2.** The intensity of absorption band at 1679 cm<sup>-1</sup> over time.

Synthesis of two nucleobase-functionalized PEG acrylate monomers, APA and TPA, allowed facile incorporation of nucleobases into photo-crosslinked acrylic networks (Figure 12.3). Direct photo-crosslinking of PEG diacrylate provided control samples to study the solvent effect on UV curing. Stock solutions of PEG diacrylate in water were prepared with varied concentration, UV cured, and dried to remove water. The resulting chemically crosslinked gels all exhibited identical thermal stability and  $T_g$  values near -41 °C. Solvent showed no significant effect on thermal stability of crosslinked gels. The PEG diacrylate with 50 solid wt% served as the control to study the nucleobase incorporation on physical properties of diacrylate gels. Crosslinked adenine and thymine-containing samples showed lower thermal stability and  $T_g$  values near -45 °C, attributing to decreased crosslinked density. DMA results in Figure 12.4 also proved the  $T_g$  decrease with nucleobase incorporation, and the plateau moduli decreased slightly due to a combined effect from crosslinked density decreasing and physical crosslinking increasing with nucleobase incorporation.

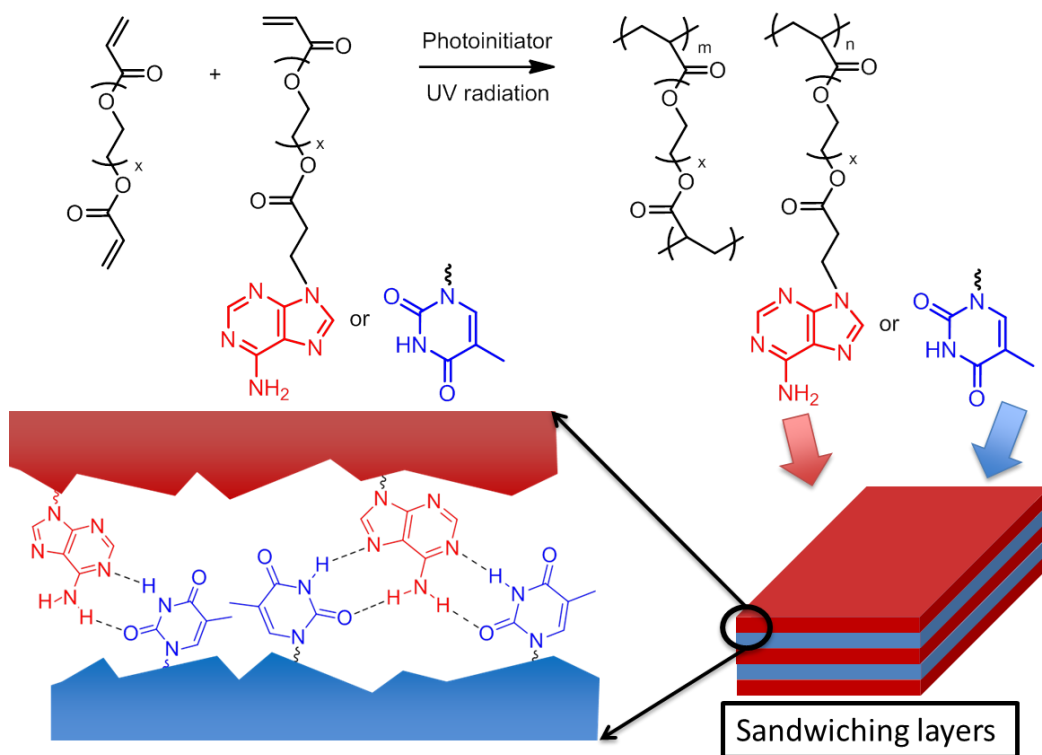


**Figure 12.3.** Photo-polymerization of nucleobase-containing resins and the proposed hydrogen bonding at the interface between layers.

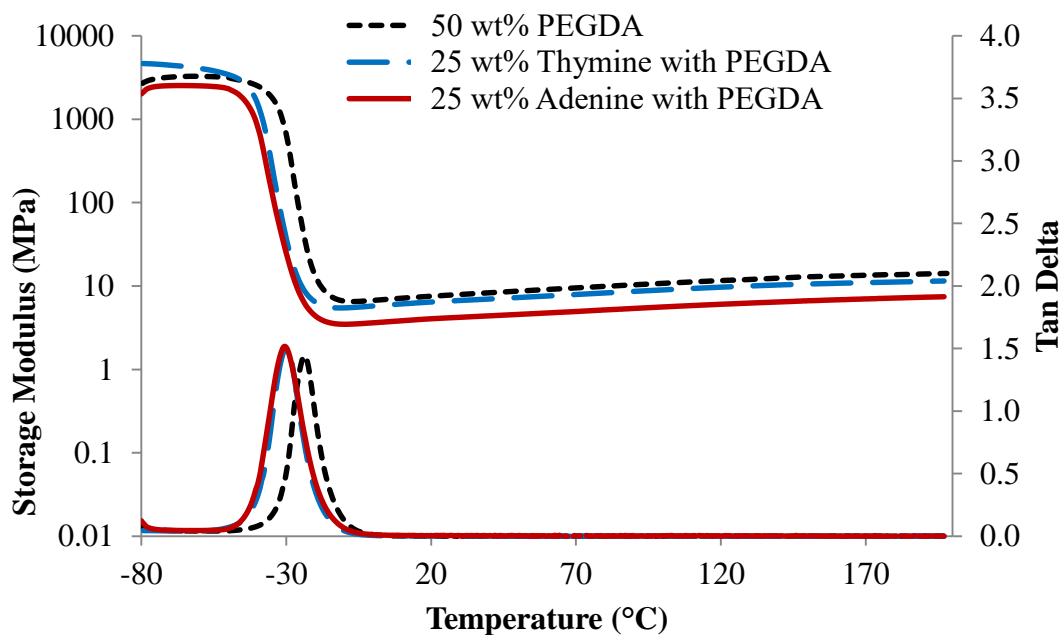


**Figure 12.4.** DMA modulus and tan delta curves of flat crosslinked thymine and adenine-containing gels in comparison to the crosslinked PEGDA control.

To simulate 3D printing process, a designed curing process was described in Figure 12.5. A layered popsicle sample and a shear sample was prepared to evaluate the adhesion strength at the interface between different UV-crosslinked layers. Tensile testing evaluated the mechanical strength of layered popsicle sample and a shear sample containing only crosslinked PEG diacrylate (Figure 12.6a). The result indicated that both sample showed significantly weaker mechanical strength compared to the control with a one-step cured flat sample. Most layered popsicle sample broke along the interface, suggesting that the poor interfacial adhesion compromised the mechanical integrity of the sample as a whole. However, some samples broke along the clamp or inside the gel due to defect and damages from clamping the sample onto the instron. Almost all shear samples broke on the interface. The one-step cured thymine and adenine-containing controls showed similar tensile strength to the PEG diacrylate control. However, the layered popsicle and shear samples with complementary nucleobase interfaces did not exhibited enhanced mechanical strength as expected. The layered popsicle sample exhibited a mixed failure mode at the interfaces and along the clamp. The shear sample mostly broke at the edge of the interface, indicative of weakly enhanced shear strength at the interface.

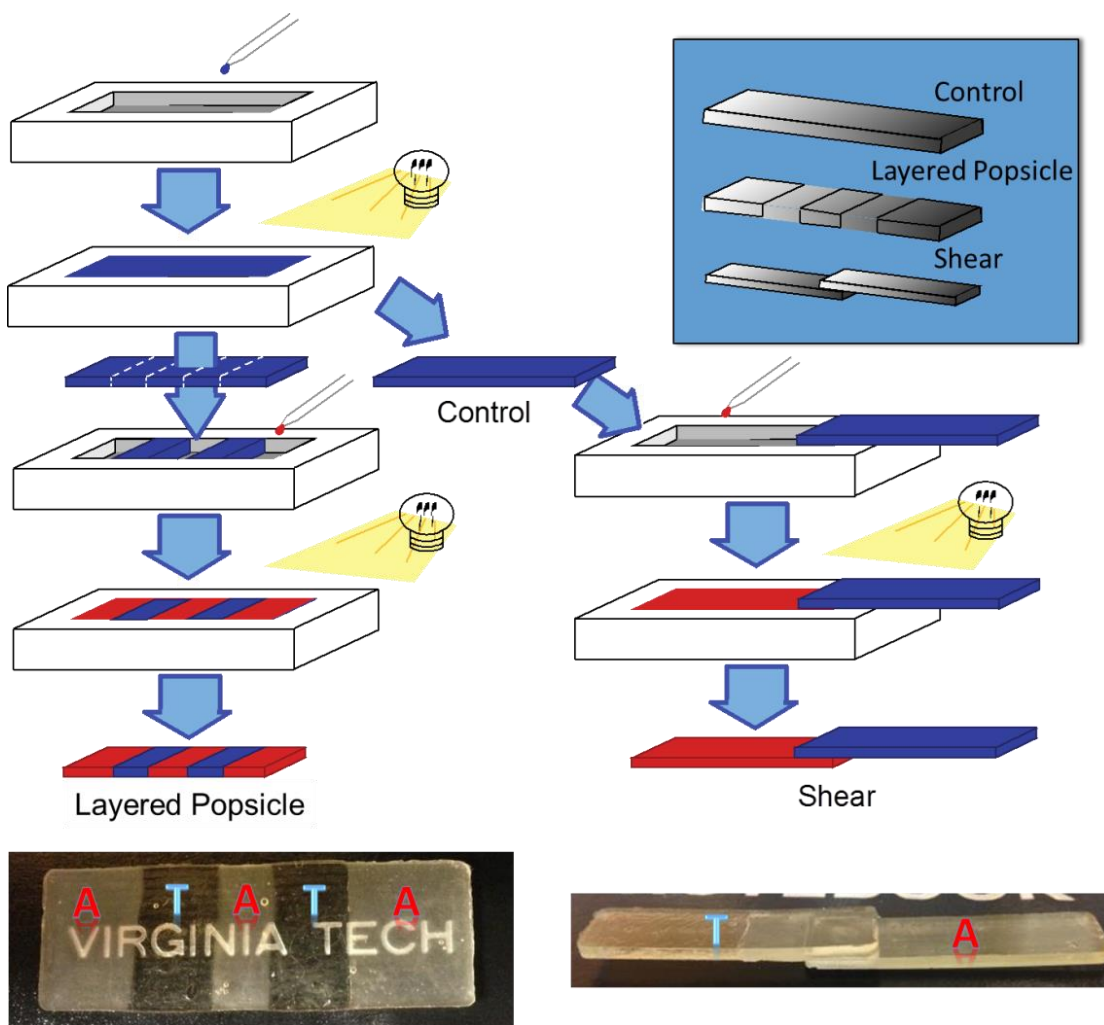


**Figure 12.5.** Fabrication of layered popsicle and shear sample geometry to test the interfacial strength of simulated 3D printed samples.

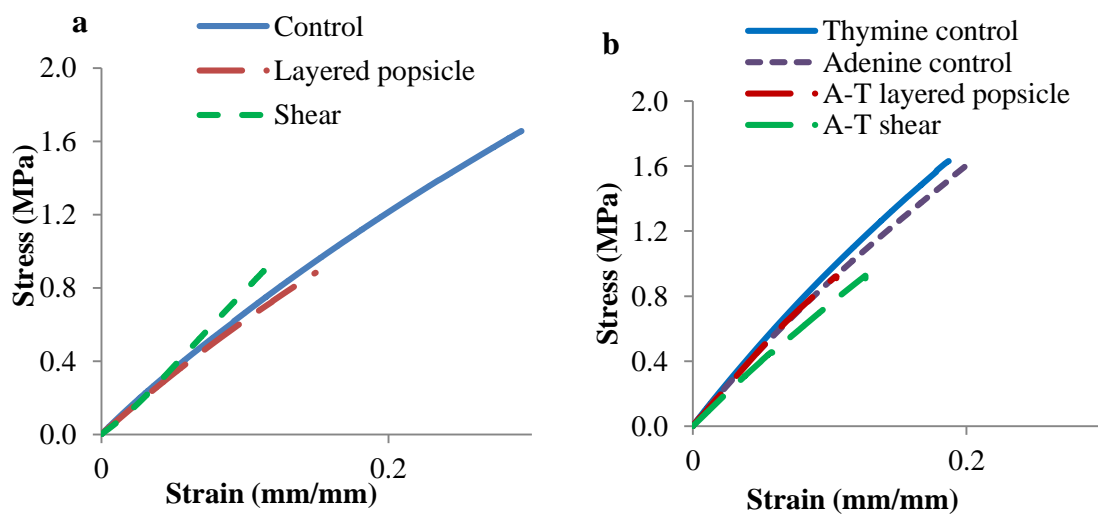


**Figure 12.6.** Stress-strain curves of (a) crosslinked PEG diacrylate samples (b) crosslinked nucleobase-containing PEG diacrylate samples with different geometries.

**Table 12.1.** Tensile analysis result for crosslinked PEG diacrylate samples and crosslinked nucleobase-containing PEG diacrylate samples with different geometries.

| Sample         | Young's Moduli (MPa) | Strain (mm/mm) | Stress (MPa) | Shear (N/cm <sup>2</sup> ) |
|----------------|----------------------|----------------|--------------|----------------------------|
| PEGDA flat     | 7.26 ± 0.84          | 0.24 ± 0.03    | 1.29 ± 0.23  | -                          |
| PEGDA popsicle | 6.69 ± 0.76          | 0.11 ± 0.03    | 0.71 ± 0.14  | -                          |
| PEGDA shear    | 4.76 ± 1.70          | 0.22 ± 0.31    | 0.42 ± 0.38  | 1.62 ± 1.0                 |
| A-control      | 9.32 ± 0.36          | 0.22 ± 0.02    | 1.63 ± 0.11  | -                          |
| T-control      | 8.89 ± 0.52          | 0.26 ± 0.10    | 1.49 ± 0.23  | -                          |
| A-T popsicle   | 9.11 ± 1.80          | 0.07 ± 0.04    | 0.44 ± 0.30  | -                          |
| A-T shear      | 8.95 ± 1.50          | 0.09 ± 0.03    | 0.67 ± 0.17  | 1.17 ± 0.3                 |

## 12.5 *Conclusions*

Novel adenine and thymine nucleobase PEG acrylates have been successfully synthesized through Michael addition reactions. Instron tests for with three sample geometries was developed and used to compare the interlayer adhesion of the adenine and thymine layered samples with PEGDA control. Preliminary studies failed to observe any enhanced interfacial adhesion due to nucleobase incorporation, presumably due to the limited hydrogen bonding strength between thymine and adenine. Hydrogen bonding with stronger association constant or ionic interaction may lead to promising result in the future.

## 12.6 References

1. Kim, J. C.; Jung, J.; Rho, Y.; Kim, M.; Kwon, W.; Kim, H.; Kim, I. J.; Kim, J. R.; Ree, M. *Biomacromolecules* **2011**, *12*, 2822.
2. Sivakova, S.; Rowan, S. J. *Chem. Soc. Rev.* **2005**, *34*, 9.
3. Yamauchi, K.; Lizotte, J. R.; Long, T. E. *Macromolecules* **2003**, *36*, 1083.
4. Cheng, S.; Zhang, M.; Dixit, N.; Moore, R. B.; Long, T. E. *Macromolecules* **2012**, *45*, 805.
5. McHale, R.; O'Reilly, R. K. *Macromolecules* **2012**, *45*, 7665.
6. McHale, R.; Patterson, J. P.; Zetterlund, P. B.; O'Reilly, R. K. *Nat. Chem.* **2012**, *4*, 491.
7. Hemp, S. T.; Long, T. E. *Macromol. Biosci.* **2012**, *12*, 29.
8. Lutz, J.-F.; Thuenemann, A. F.; Rurack, K. *Macromolecules* **2005**, *38*, 8124.
9. Mather, B. D.; Viswanathan, K.; Miller, K. M.; Long, T. E. *Prog. Polym. Sci.* **2006**, *31*, 487.

## 12.7 Supporting Information

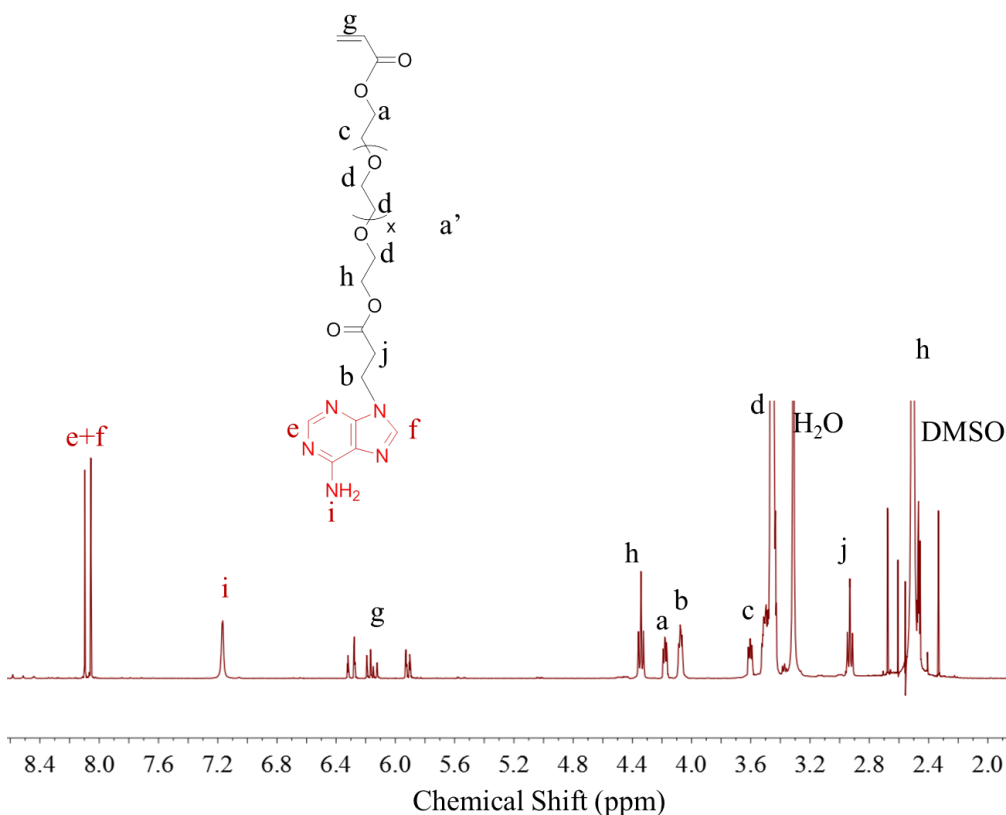


**Figure S12.1.**  $^1\text{H}$  NMR spectrum of adenine PEG acrylate monomer.



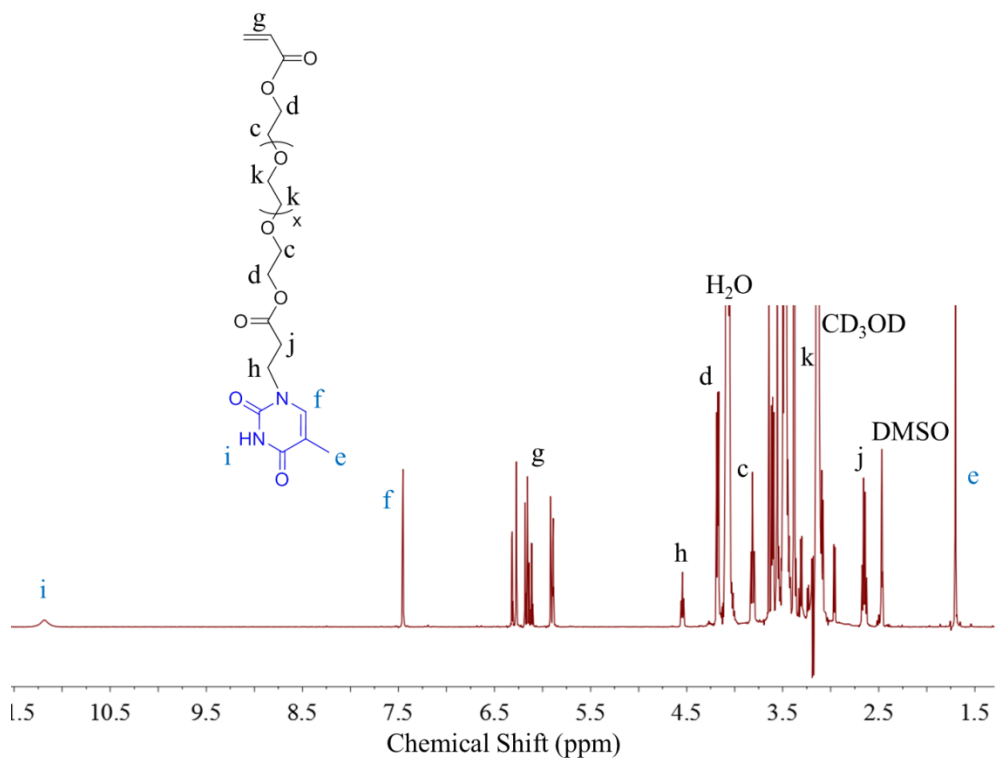


**Figure S12.2.** <sup>1</sup>H NMR spectrum of thymine PEG acrylate monomer.

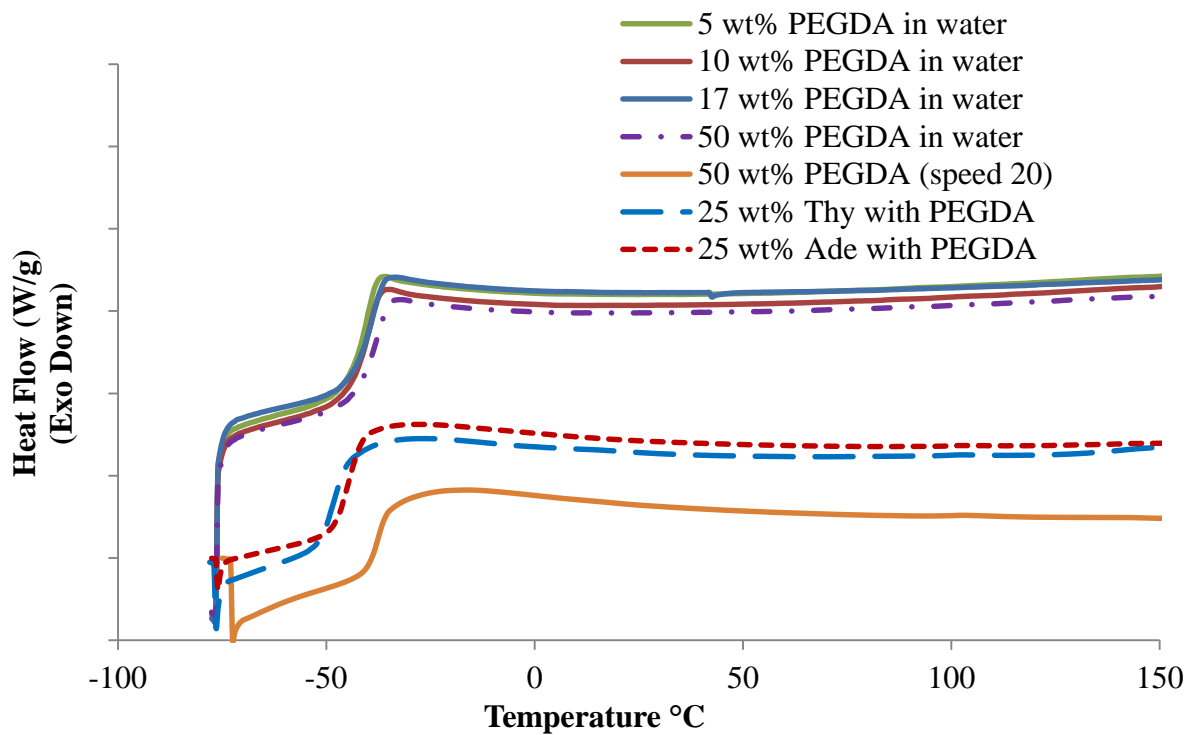


**Figure S12.3.** DSC thermograms of PEGDA crosslinked in presence of various water content and different UV radiation time, as well as thymine/adenine-containing PEGDA samples.

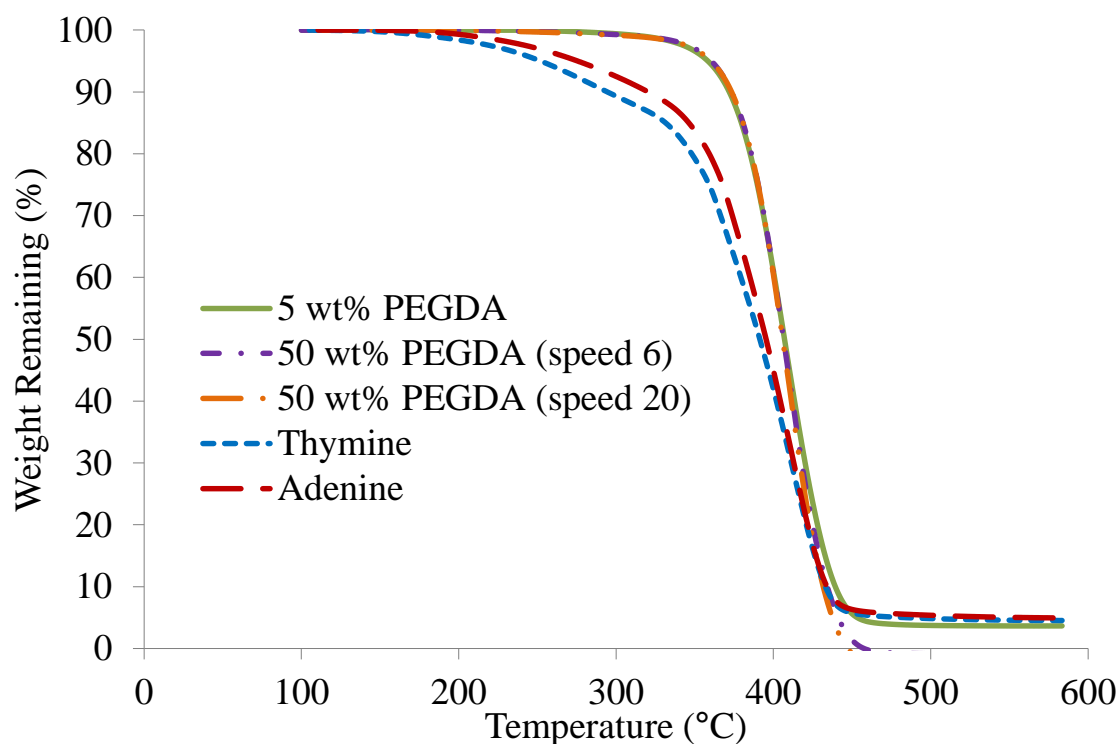


**Figure S12.4.** TGA thermograms of PEGDA crosslinked in presence of various water content and UV radiation time, as well as thymine/adenine-containing PEGDA samples.

## Chapter 13. Overall Conclusions

This dissertation introduces synthesis of unprecedented, bio-inspired supramolecular polymers with noncovalently associating functionalities that provide hydrogen bonding or ionic interaction. The incorporation of these functional groups into polymers relied on novel monomer synthesis, including nucleobase-containing acrylates, DABCO salt-containing styrenics, and cyclic carbonate-based AB monomer using scalable chemical reactions such as Michael addition and nucleophilic substitution. Free radical polymerization, controlled radical polymerization, and step-growth polymerization afforded random copolymers, block copolymers, and segmented copolymers, respectively, with well-defined polymer structures. The associating functional group resided on the pendant groups of a radically polymerized copolymer, and *n*-butyl acrylate (*n*BA) represented the low  $T_g$  comonomers that formed the soft polymer matrix. Urethane and amide groups on polymer backbone provided hydrogen bonding for poly(amide-hydroxyurethane) synthesized from step-growth polymerization. Post-functionalization reactions further derivatized unprotected cytosine to ureido-cytosine, anion exchange yielded DABCO salt-containing copolymers with fluorinated anions with delocalized charges.

Noncovalent interactions introduced physical crosslinking through inter- and intramolecular interactions, which increased the effective molecular weight of copolymers and drives microphase-separation of the associating group-containing hard phase and acrylic soft phase. Thermal analyses indicated that incorporation of functional group generally decreased thermal stability of acrylics due to relatively weak chemical bonds connecting these functional groups to polymers, such as the N-C bonds in nucleobase acrylic

monomers and DABCO salt monomers. Hydrogen bonded random copolymers each showed a single  $T_g$  that increased with increasing associating group with a positive deviation from the Fox equation prediction based on poly(*n*BA) and nucleobase-functionalized homopolymer. Ionomers displayed a single  $T_g$  that mildly increased with increasing ionic content due to strong phase separation of the ionic domains and the soft neutral domains. Hydrogen bonding also led to different thermomechanical performance for random copolymers compared to ionic interaction from dynamic mechanical and rheological analysis. Nucleobase incorporation into random copolymers contributed to slower molecular dynamics, namely, higher modulus at the same frequency compared to poly(*n*BA), and flow temperature of 40-60 °C. Ureido-cytosine, however, resulted in a 40 °C wide rubbery plateau window where modulus remained constant with increasing temperature and higher viscous flow temperature near 80 °C compared to cytosine copolymers. The morphology analysis revealed that ureido-cytosine units self-assembled into nano-fibrillar hard domains that performed as fillers that maintained mechanical strength during the plateau window. DABCO-containing ionomers showed plateau windows over 100 °C wide and flow temperatures near 130-150 °C, significantly higher than studied hydrogen bonded copolymers, and morphology analysis revealed distinctive microphase-separated scattering profiles.

The explanation for different structure-property-morphology relationships of hydrogen bonded and ionically crosslinked copolymers centralized to the noncovalent bond strength and their ability in driving microphase-separation. The electrostatic interaction of ion pairs drove ionic aggregation that restricted mobility of adjacent polymer chains and formed ionic domains. These ionic domains reinforced mechanical strength of

copolymers, and ionic bonding strength dominated the mechanical performance at the plateau regime and viscous flow regime of copolymers. Bulkier anions with delocalized charges weakened the dipole-dipole interactions among ion pairs, resulting in narrower plateau window and lower flow temperature. Ureido-cytosine formed stronger quadruple hydrogen bonding compared to self-association of underivatized nucleobase, which resulted in a well-defined plateau window. Well-aligned noncovalent interactions benefited phase-separation of the associated domains from the neutral soft domains, which also led to plateau windows. For example,  $\pi$ - $\pi$  stacking of adenine-containing random copolymers and nucleobase-functionalized block copolymers exhibited plateau window on their modulus-temperature curves.

Structure-property-morphology relationship of nucleobase-functionalized block copolymers revealed the synergistic effect of noncovalent interaction and block copolymer phase-separation on mechanical performance and self-assembly behavior of polymers. The block copolymer architecture placed nucleobase units adjacent to each other, and facilitated the formation of noncovalent interactions within the nucleobase domains. Noncovalent interactions provided physically crosslinking for the hard domains. Sufficiently strong hydrogen bonding (thymine-adenine doubly hydrogen bonding) restricted polymer chain mobility even above the  $T_g$  of nucleobase block in the ABA triblock blend and ABC triblock copolymers. Nucleobase-functionalized block copolymer exhibited more well-defined plateau regime and higher viscous flow temperature compared to the nucleobase-containing random copolymers. Furthermore, intermolecular hydrogen bonding within the nucleobase blocks directed the self-assembly of ABC triblock copolymer into remarkably well-defined lamellar morphology with long-range order. Physically crosslinking block

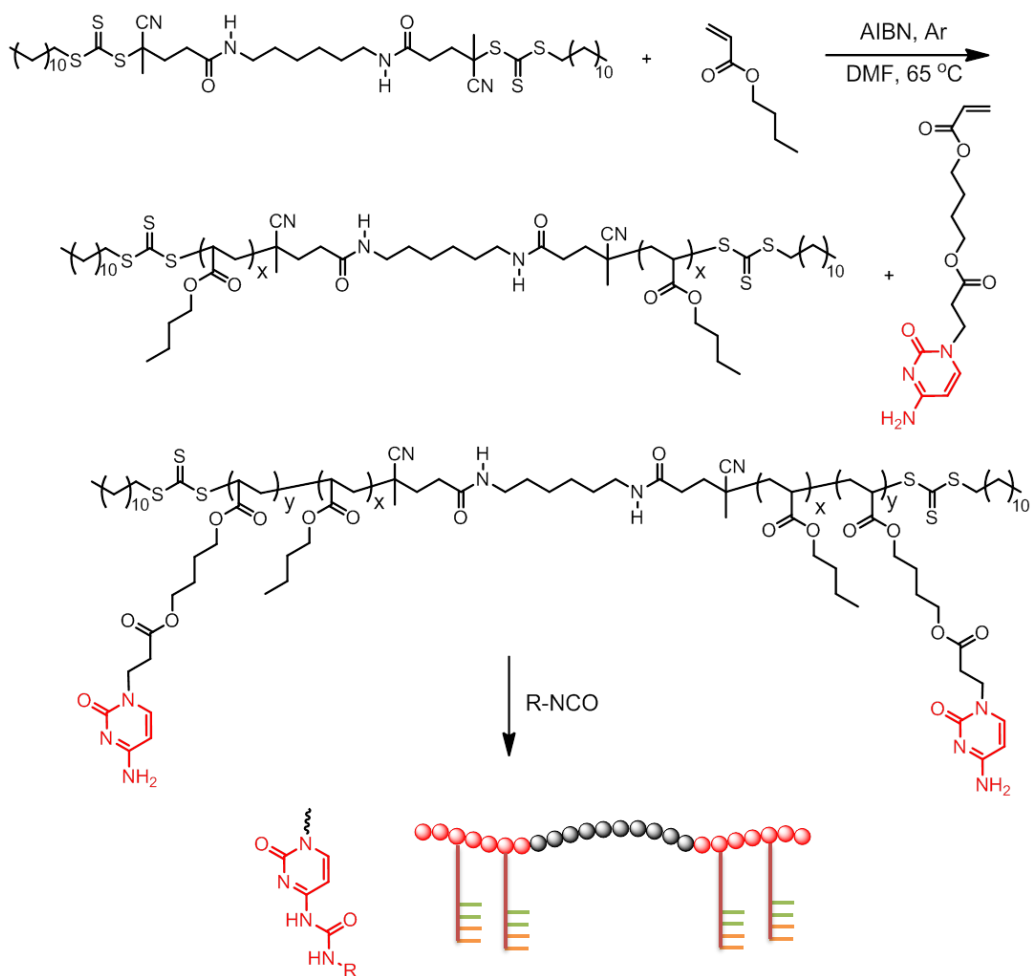
copolymers offer promises in novel thermoplastic elastomers with enhanced mechanical properties and well-defined morphologies for nano-fabrication.

Last but not least, hydrogen bonding influence mechanical properties, crystallinity, and water sorption of semicrystalline, step-growth polymers. Hydrogen bonding enabled periodic chain packing of the aliphatic amide-containing segments and assisted crystallization of poly(amide-hydroxyurethane). Ordered hydrogen-bonded carbonyls mainly existed within the crystalline domains, and these nano-fibrillar hard domains served as physical crosslinking in the amorphous matrix to reinforce the mechanical strength of segmented poly(amide-hydroxyurethane). The crystallite structure also prevented the dissociation of hydrogen bonding below melting point. The additional pendant hydroxyls near urethane bonds contributed to higher water uptake of poly(amide-hydroxyurethane) compared to conventional isocyanate-based polyurethane control.

## Chapter 14. Suggested Future Work

### 14.1 *Ureido-cytosine functionalized triblock copolymers*

Future work would focus on utilizing the synergy of complementary quadruple hydrogen bonding of ureido-cytosine and block copolymer phase-separation. The successful synthesis of unprotected cytosine acrylate monomer and its quantitative reaction with isocyanate enable One question remained from the ureido-cytosine chapter: whether the 2-ethylphenyl group on ureido-cytosine formed  $\pi$ - $\pi$  stacking and enabled the self-assembly into nano-fibrillar hard domains. Wide angle scattering studies and synthesis of ureido-cytosine copolymer with alkyl substituents would provide an answer to this question. The effect of substituent on random copolymer self-assembly would determine what isocyanate to use in Scheme 14.1 for ureido-cytosine functionalized ABA triblock copolymer synthesis. RAFT polymerization using a difunctional CTA would enable synthesis of ABA triblock copolymers with ureido-cytosine functionalized external blocks and poly(*n*BA) central block in two steps. Varying the block lengths for the low  $T_g$  central block and ureido-cytosine block would produce a series of film-forming copolymers with varying plateau modulus for thermoplastics or elastomers. The quadruple complementary hydrogen bonding would influence the self-assembly behavior of ABA triblock copolymer in bulk and in solution. In addition, incorporation of a ureido-cytosine-containing guest molecule would open other avenues for tuning block copolymer morphology and introducing a secondary functionality such as ionic group.



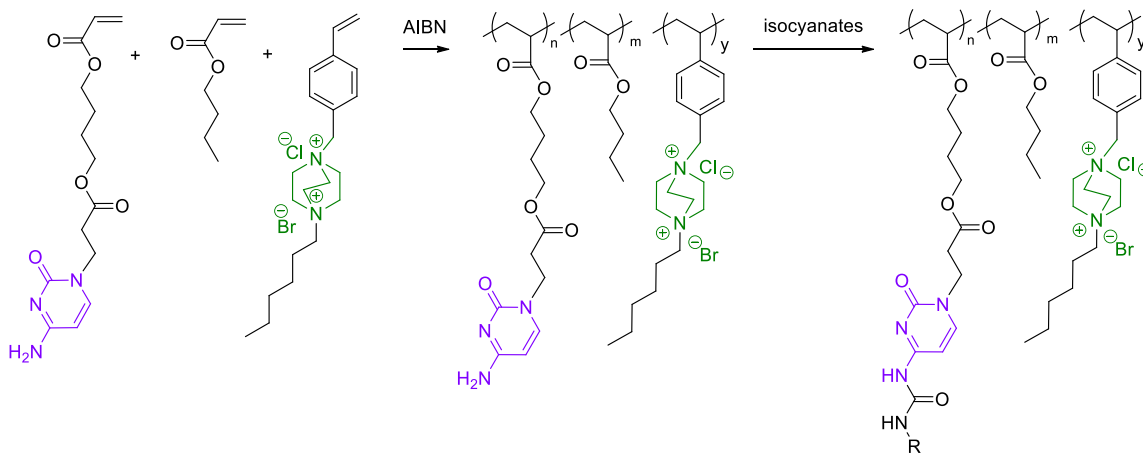
**Scheme 14.1.** RAFT polymerization to synthesize ureido-cytosine functionalized ABA triblock copolymer.

## 14.2 Synergy of hydrogen bonding and ionic interaction in random copolymers

Previous random copolymer work focused on the effect of a single noncovalent interaction on the physical properties and morphology. Many biomacromolecules with complex and hierarchical structures wouldn't exist without synergist effect of two or more noncovalent interactions. Both hydrogen bonding and electrostatic interaction proved crucial in forming and stabilizing the double helical structure of DNA molecules. However, combining hydrogen bonding with ionic interaction into a synthetic polymer may present



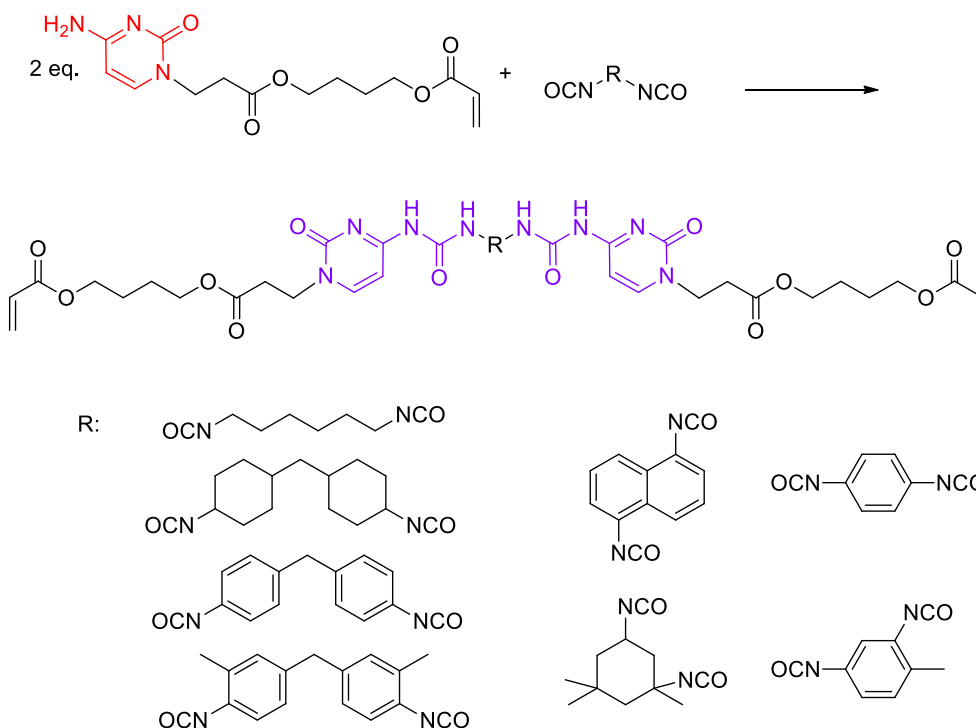
a double-edged sword. Incorporation of DABCO salt and ureido-cytosine group randomly would be a suitable starting point to probe whether hydrogen bonding and ionic interaction act synergistically in a terpolymer. As ionic interaction formed stronger association than hydrogen bonding, it may interfere with the prefer geometry for quadruple hydrogen bonding. Probing the bulk and surface morphology of this terpolymer would elucidate whether ionic aggregates and hydrogen bonded aggregates form two different hard domains or combine into one hard phase. Varying the content of one functional monomer with constant comonomers composition would provide a series of samples to compare their thermomechanical, rheological, and morphological properties. Solution properties would also be interesting to examine the terpolymer micelle properties using light scattering and transmission electron microscopy. The study of random terpolymers with hydrogen bonded and ionic groups could be a starting point for a detailed investigation on how to synthetically prepare biomimetic macromolecules with complex structures.



**Scheme 14.2.** Free radical polymerization of ureido-cytosine and DABCO salt-containing terpolymers.

### 14.3 *Bis(ureido cytosine) diacrylate crosslinkers for 3D printing*

Previous work on novel polymer resin for 3D printing failed to show enhanced interlayer adhesion mainly due to relatively weak hydrogen bonding strength between adenine and thymine. Future work would pertain to synthesis of UV crosslinkable resin containing stronger hydrogen bonding, and the quadruple self-association of ureido-cytosine would be suitable for this purpose. Herein, two equivalents of unprotected cytosine acrylate monomer reacts with one equivalent of di-isocyanate (Scheme 14.3), forming bis(ureido-cytosine) diacrylates that serve as crosslinkers for photopolymerization. Various commercial available di-isocyanates would provide tunable molecular structure for the crosslinkers to achieve optimal hydrogen bonding. Combining quadruple hydrogen bonding and additional  $\pi$ - $\pi$  stacking of the aromatic groups from the isocyanates may contributed to unique self-assembly behavior of the crosslinkers prior to UV radiation. One or multiple radically polymerizable comonomers would be added to the recipe of UV resin to tune the bulk modulus of UV-cured product. Interfacial hydrogen bonding of ureido-cytosine groups on the surfaces of adjacent UV crosslinked layers may enhance interlayer adhesion of 3D printed objects.

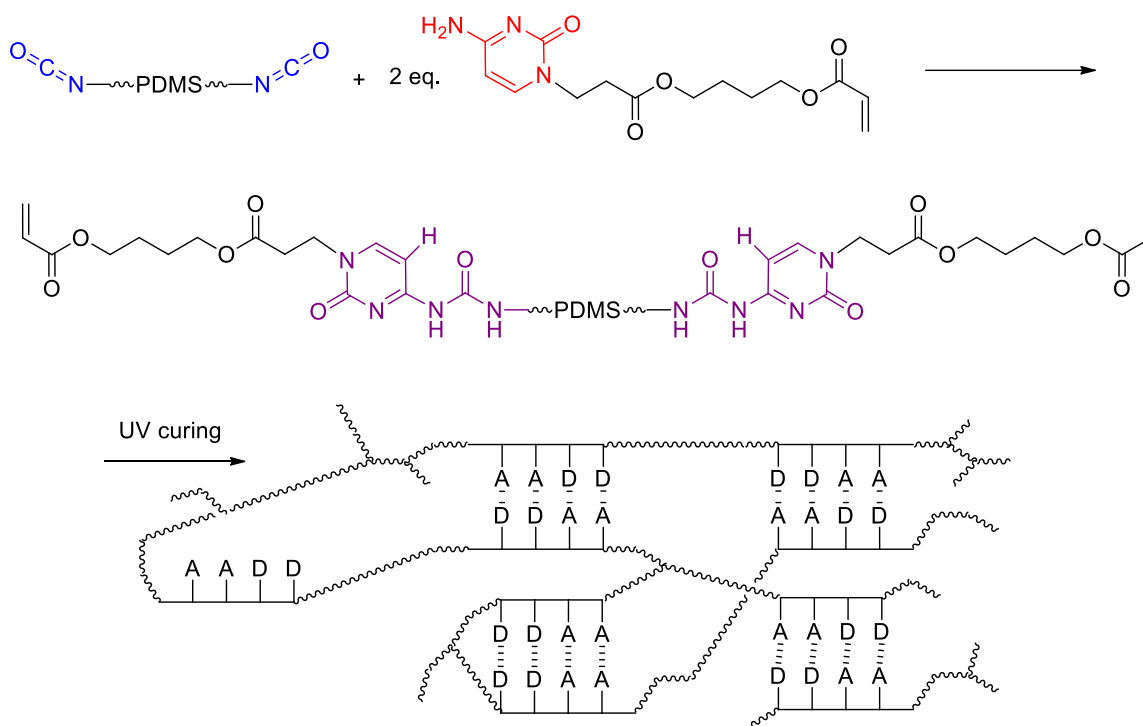


**Scheme 14.3.** Reaction of cytosine acrylate with di-isocyanate.

#### 14.4 *Ureido-cytosine containing resins for extrusion 3D printing and self-healing materials*

An extension of bis(ureido cytosine) diacrylate crosslinker synthesis involves using isocyanate end-functionalized prepolymer instead of small molecule di-isocyanates. Commercial production of segmented polyurethane generally utilizes a two-step method, which yields isocyanate end-functionalized polyester, polyether, or PDMS prepolymers in the first step.<sup>1</sup> Reaction between an isocyanate-functionalized prepolymer, PDMS di-isocyanate for example, and two equivalents of cytosine acrylate monomer would yield an ureido-cytosine flanked PDMS with acrylate end functionality (Scheme 14.4). Typically the polyurethane prepolymer product contains excess di-isocyanate, which continues to the second step reaction and forms the hard segment. Stoichiometric cytosine acrylate would be added to react with excess di-isocyanate, forming a diacrylate molecule without PDMS.

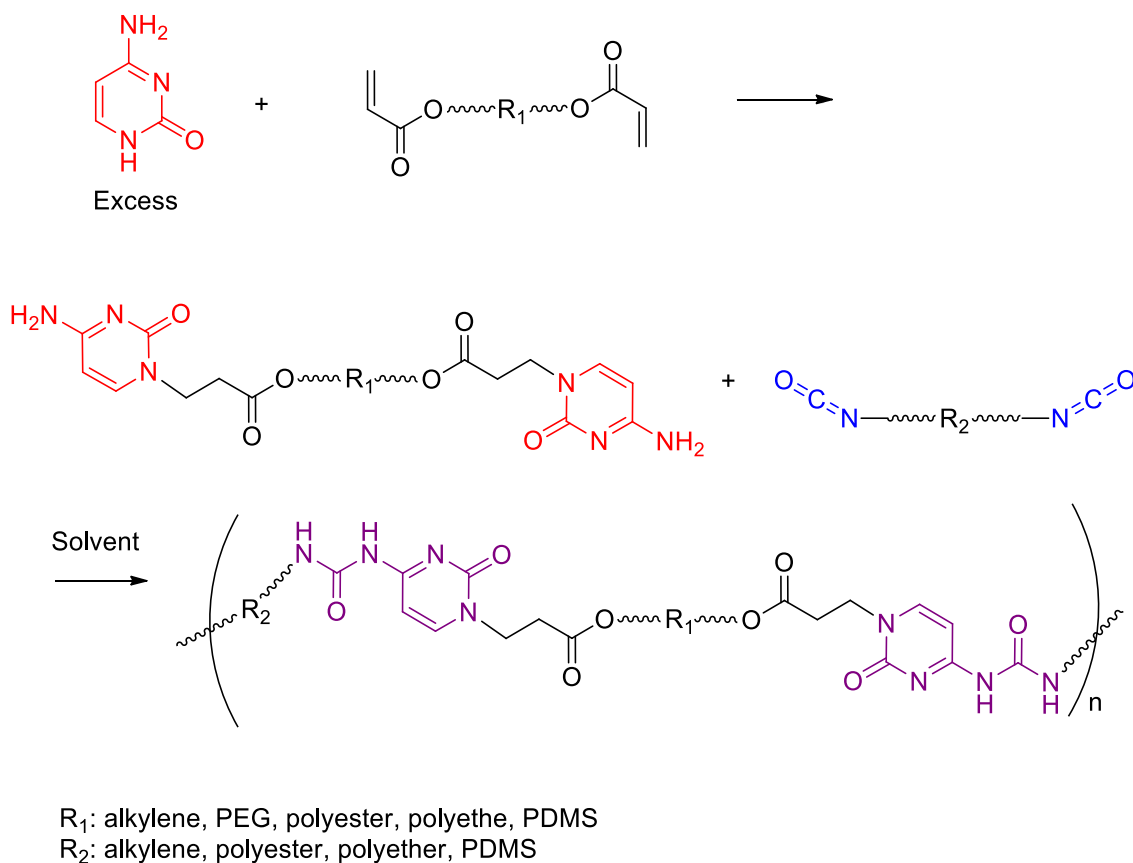
Strong quadruple hydrogen bonding of ureido-cytosine units contributes to formation of a supramolecular polymer with increased apparent molecular weight and mechanical integrity. In addition, the viscosity of this supramolecular polymer would significantly decrease above the dissociation temperature of hydrogen near 80-100 °C. This would allow extrusion of this supramolecular precursor, and cooling to room temperature would reform hydrogen bonding and retain the printed shape. Finally, UV radiation of the entire piece of printed object would induce photo-polymerization within layers and across layers, increasing the interlayer adhesion and reinforce the mechanical strength of printed part. Thermodynamic analysis before and after UV radiation would assist determination of the 3D printing parameters and provide insight of the influence from both crosslinking mechanisms on mechanical properties.



**Scheme 14.4.** Reaction of isocyanate-functionalized PDMS with cytosine acrylate, and UV-crosslinking of resulting supramolecular precursor.

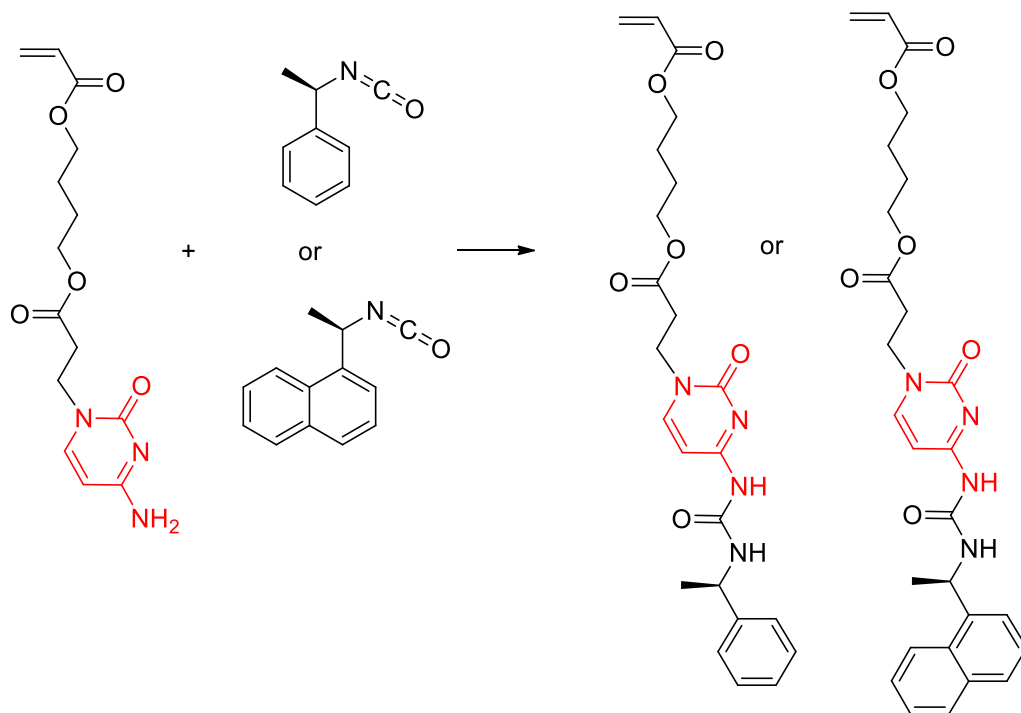
### 14.5 *Synthesis of poly(ureido-cytosine ester)*

The quantitative reaction between cytosine and isocyanate may be used as a polymerization reaction. Scheme 14.5 proposes a bis-cytosine monomer synthesis and subsequent polymerization with di-isocyanate. Optimizing polymerization conditions would afford polyester with two ureido-cytosine groups in each repeating unit. This polymer enables potential applications as self-healing materials and elastomeric materials.



**Scheme 14.5.** Synthesis and polymerization of bis-cytosine monomer with di-isocyanate, forming poly(ureido-cytosine ester).

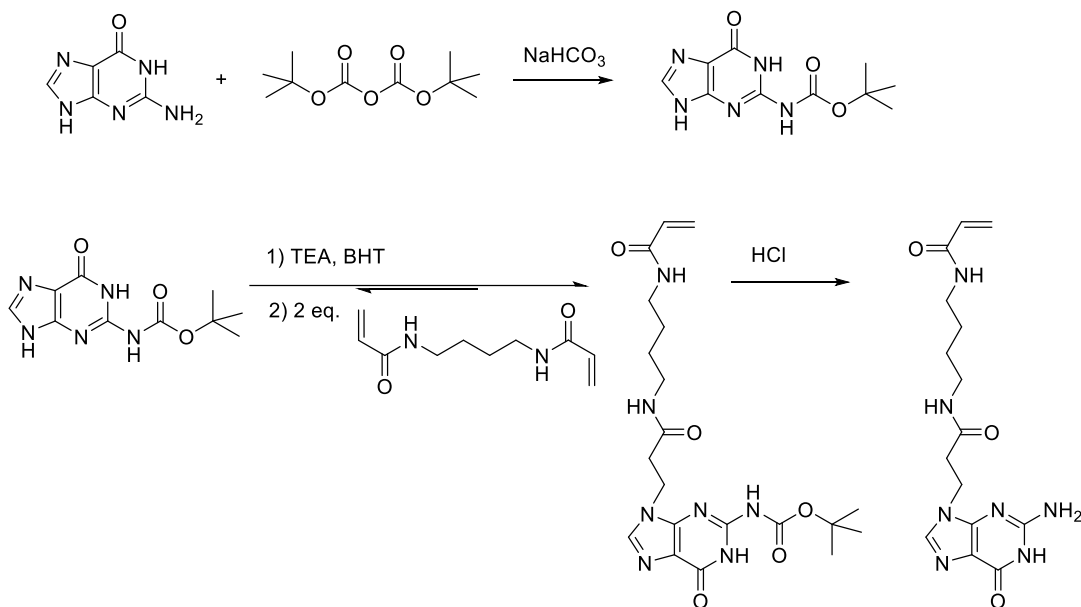
### 14.6 *Chirality, pi-pi stacking, complement hydrogen bonding in concert for supramolecular polymer self-assembly*



**Scheme 14.6.** Synthesis of acrylic ureido-cytosine monomers with aromatic substituents and chiral centers.

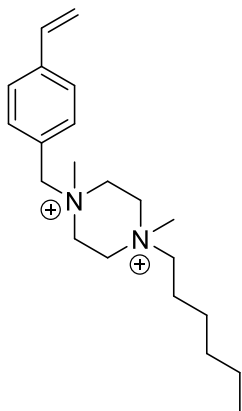
The Meijer group reported that discotic triamides with chiral alkyl chains self-assembled into helical columnar aggregates in solution.<sup>2</sup> Ureido-pyrimidinone-based supramolecular polymer with chiral centers also self-assembled into helical fibers.<sup>3</sup> Adding a chiral center near the ureido-cytosine group may also enable self-assembled helical structure. Scheme 6 lists synthesis of two ureido-cytosine acrylate monomers with chiral centers. Radical polymerization would afford copolymers with quadruple hydrogen bonding groups, aromatic rings, and chiral centers. UV-vis, circular dichroism spectroscopy, and dynamic light scattering will be primary characterization techniques to study the self-assembly behavior.

## 14.7 Synthesis of guanine-containing acrylamide monomer



**Scheme 14.7.** Potential synthetic route for guanine acrylamide monomers.

## 14.8 Doubly-charged monomers



**Scheme 14.8.** Potential interesting doubly-charged monomer.

## 14.9 References

1. He, Y.; Xie, D.; Zhang, X. *J. Mater. Sci.* **2014**, *49*, 7339.
2. Smulders, M. M. J.; Schenning, A. P. H. J.; Meijer, E. W. *J. Am. Chem. Soc.* **2008**, *130*, 606.
3. Ramaekers, M.; de Feijter, I.; Bomans, P. H. H.; Sommerdijk, N. A. J. M.; Dankers, P. Y. W.; Meijer, E. W. *Macromolecules* **2014**, *47*, 3823.